ISSN 0288-4534
CODEN: KONAE7

KONA

POWDER AND PARTICLE

No. 13(1995)

Published by Hosokawa Powder Technology Foundation

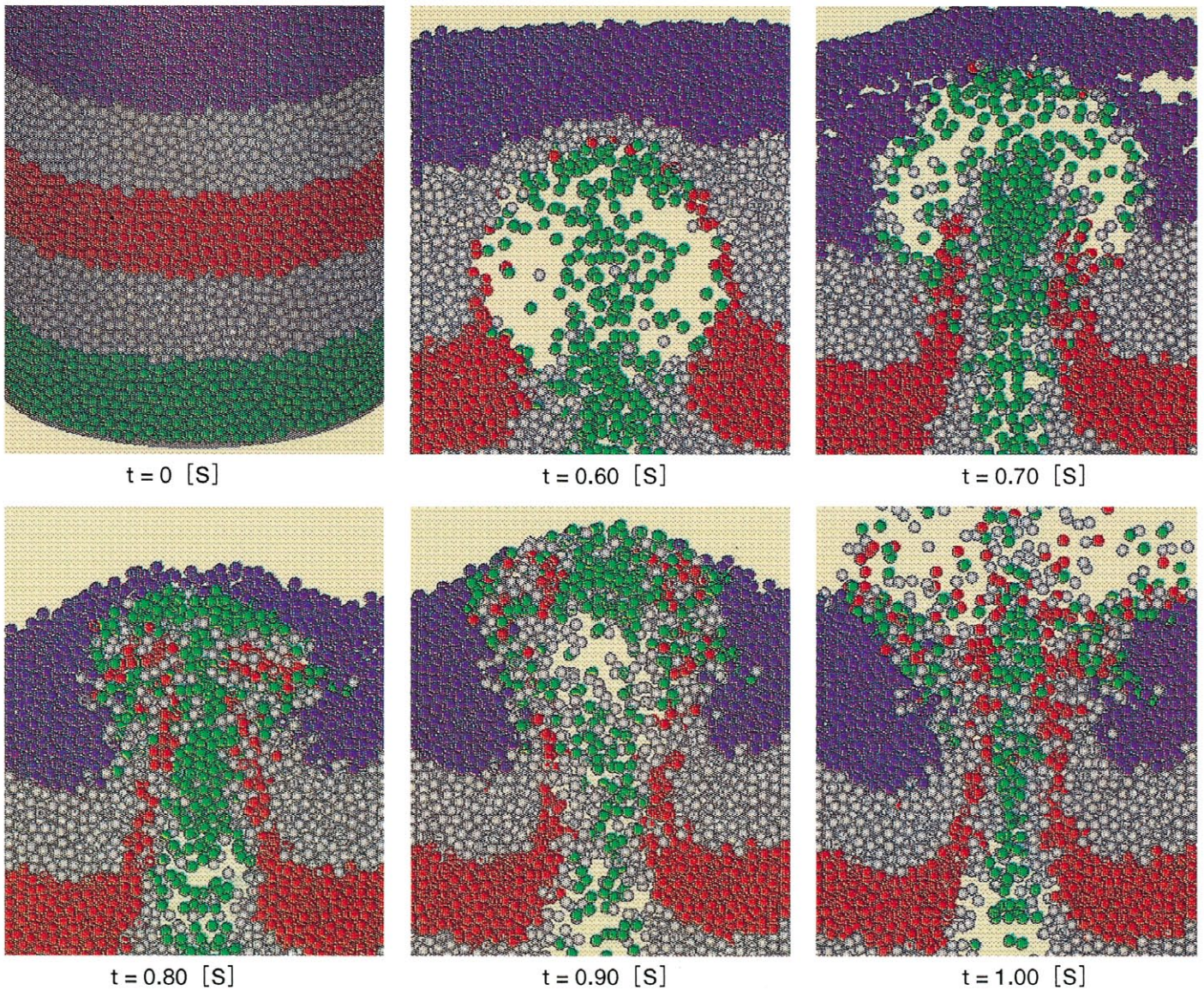

KONA

POWDER AND PARTICLE

KONA, issued annually since 1983 by Hosokawa Powder Technology Foundation, Japan, is a refereed journal publishing the articles on powder sciences and technology, and is distributed to the interested persons and institutions throughout the world.

About the Cover of Journal "KONA"

The chinese character "粉" is pronounced as "KONA" in Japanese, and means "Powder". The hand written "粉" is after the late Mr. Eiichi Hosokawa, the founder of Hosokawa Micron Corporation.

Hosokawa Micron Corporation and its R&D Center

■ Publication Office

Hosokawa Powder Technology Foundation (Japan)
in **Hosokawa Micron Corporation**
No. 9, 1-chome, Shoudai Tajika, Hirakata-shi, Osaka 573 Japan

■ Notes

○ Hosokawa Powder Technology Foundation has entrusted the editorial duty to the editorial board organized by the Council of Powder Technology, Japan.

(Complimentary Copy)

Printed in Japan

The Letter from the Editor

KONA journal had been published by the Council of Powder Technology, Japan (CPT) from No.1 to No.12 issues, under the sponsorships of Hosokawa Micron Corporation (No.1 to No.9) and Hosokawa Powder Technology Foundation (No.10 to No.12).

From this No. 13 issue and on, the Foundation has taken over the role of KONA publisher from the CPT and the Foundation has entrusted the editorial duty to the present KONA editorial board organized by the CPT without requesting any shift in our present editorial policies.

This switching of publisher is simply and only to make the aim and scope of the Foundation definite. Essentially no change shall be ovserved in continuously editing and publishing this journal except in the designation on a part of the journal cover.

Kei Miyanami,
Editor-in-Chief

KONA

GENERAL INFORMATION

HISTORY OF THE JOURNAL

The Council of Power Technology (CPT), Japan, has been established in 1969 as a non-profit organization to enhance the activities of research and development on powder science and technology in Japan under the sponsorship of Hosokawa Micron Corporation. In 1983, the CPT has decided to issue an international journal named "KONA", which publishes the excellent articles appeared in Japanese Journals concerning with powder science and technology, translated into English, throughout the world. After the seventh volume issued in 1989, the CPT has changed its policy to internationalize the "KONA" from the 8th issue (1990) on by incorporating the monographs originally written in English from the authors throughout the world.
From issue of No.13 the publisher has changed to Hosokawa Powder Technology Foundation.

AIMS AND SCOPE OF THE JOURNAL

KONA Journal is to publish the papers in a broad field of powder sciences and technology, ranging from fundamental principles to practical applications. The papers discussing technological experiences and critical reviews of existing knowledge in specialized areas will be welcome.

These papers will be published only when they are judged, by the Editor, to be suitable for the progress of powder sciences and technology, and are approved by each Block Editorial Committee. The paper submitted to the Editorial Secretariat should not have been previously published except the translated papers which would be selected by the Block Editorial Committees.

CATEGORY OF PAPERS

- Invited papers
  Original research and review papers invited by the Block KONA Editorial committees.
- Contributed papers
  Original research and review papers submitted to the Block KONA Editorial Committees, and refereed by the Editors.
- Translated papers
  Papers translated into English, previously published in other languages, selected by the Block KONA Editorial Committees with the permission of the authors and/or the copyright holder.

SUBMISSION OF PAPERS

Papers should be sent to each Block KONA Editorial Secretariat.

- Asian Block Editorial Secretariat
  F. Nakagawa
  Hosokawa Micron Corporation Micromeritics Laboratory
  1-9, Shoudai Tajika, Hirakata, 573 JAPAN
- European Block Editorial Secretariat
  Dr. W. Peukert
  Hosokawa Mikropul
  Welserstr. 9-11, 51149 Köln
  Postfach 900749, 51117 Köln
  GERMANY
- American Block Editorial Secretariat
  Hosokawa Micron International Inc.
  Dr. I. Pikus or D.A. Scott
  10 Chatham Road, Summit, NJ 07901 USA

FREQUENCY

KONA will be issued once each calendar year.

SUBSCRIPTION

KONA is distributed free of charge to senior researchers at universities and laboratories as well as to institutions and libraries in the field throughout the world. The publisher is always glad to consider the addition of names of those who wish to obtain this journal regularly to the mailing list. Distribution of KONA is made by each Block Secretariat.

INSTRUCTIONS TO AUTHORS

(1) Manuscript format

- Two copies should be submitted to the Editorial Secretariat, in double-spaces typing on pages of uniform size.
- Authorship is to give author's names, and the mailing address where the work has been carried out on the title page.
- Abstract of 100-180 words should be given at the beginning of the paper.
- Nomenclature should appear at the end of each paper. Symbols and units are listed in alphabetical order with their definitions and dimensions in SI units.
- Literature references should be numbered and listed together at the end of paper, not in footnotes. Alphabetical order is accepted. Please give information as in the following examples:
  1) Carslaw, H.C. and J.C. Jaeger: "Conduction of Heat in Solids", 2nd ed., Clarendon Press, Oxford, England (1960).
  2) Howell, P.A.: US Patent, 3,334,603 (1963).
  3) Rushton, J.H., S. Nagata and D.L. Engle: AIChE J., 10. 298 (1964).
  4) Seborg, D.E.: Ph. D. Dissertation, Princeton Univ., N.J., U.S.A (1969).
- Original figures with each single copy should be submitted, on separate sheets. Authors' names and figure numbers are marked in the corner.
- Figure numbers and captions are listed on a separate sheet.
- Place of figure insertion is to be indicated in the margin of the manuscript.
- Tables should be typed on separated sheets.
- Submit an IBM-readable floppy disk (3½) with your unformatted text file in ASCII code. If you use either WORD or WORD PERFECT – as word processing system, please add the formatted text file.

(2) Reprints

- The authors shall receive 50 free reprints. Additional reprints will be furnished when ordered with return of galley proofs.

(3) Publication policy

- All papers submitted for publication become immediately the property of the CPT and remain so unless withdrawn by the author prior to acceptance for publication or unless released by the Editor. Papers are not to be reproduced or published in any form without the written permission of the CPT.

KONA Powder and Particle No. 13 (1995)

Contents

<Review>

- Grinding Aids — *D.W. Fuerstenau* 5
- Optimum Design for Fine and Ultrafine Grinding Mechanisms Using Grinding Media — *T. Tanaka* 19
- Ultrasonic Particle Sizing — *P. Khatchikian, U. Riebel and U. Krduter* .. 31
- Nanostructures: The Next Generation of High Performance Bulk Materials and Coatings — *B.H. Kear and P.R. Strutt* 45
- Comparative Study of Particle Size Analyses Using Common Samples — *H. Yamamoto and T. Matsuyama* 57

<Original Research Paper>

- Dispersants in Stirred Ball Mill Grinding — *Y. Wang and E. Forssberg* 67
- Characterization of Nanocrystalline Oxide Powders Prepared by CO_2 Laser Evaporation — *E. Müller, Ch. Oestreich, U. Popp G. Michel, G. Staupendahl and K.-H. Henneberg* 79
- Relationships Between Surface Areas of Red Tropical Soils Measured by Different Methods — *H.C. Ferreira, T.H. Topper and G.A. Neves* 91
- Investigation of the Behaviour of Cohesive Powder in the Biaxial Tester — *H. Feise and J. Schwedes* 99
- An Experimental Study of the Wear at Hopper Walls — *G.D. Corder and R.B. Thorpe* 105
- Investigations into Fine Grinding — *J. Dodds, C. Frances, P. Guigon and A. Thomas* 113
- Air Entrainment and Dust Generation from a Falling Stream of Bulk Material — *P. Cooper and P.C. Arnold* 125
- Constitutive Model for Dry Cohesive Powders with Application to Powder Compaction — *V.M. Puri, H.A. Tripodi, H.B. Manbeck and G.L. Messing* 135
- Ball Charge Dynamics in a Planetary Mill — *B.K. Mishra* 151

<Translated Research Paper>

- Contamination and Sinterability of Planetary－milled Alumina — *O. Abe* 159
- Simultaneous process of Granulation, Grinding and Separation in a Continuous Tumbling Conical Granulator －On the Shape Evaluation of the Granules and Granulating Conditions－ — *M. Sugimoto, N. Yokota and H. Miyanaga* 167
- An XPS Study on the Interaction at the Fe_3O_4/SiO_2 Boundary on the Surface of Composite Microspheres Prepared via a Shear－Compressive Mechanical Route — *I. Saito and M. Senna* 177
- Simultaneous Measurement of Particle Size and Electrostatic Charge by Using Laser Doppler Method — *N. Kaya, H. Tsujimoto, S. Sasabe, S. Yoshikawa and M.K. Mazumder* 185
- The Effect of Humidity on the Removal of Fine Particles on a Solid Surface using High-speed Air Jet — *K. Gotoh, S. Takebe, H. Masuda and Y. Banba* 191
- Flow Mechanism of Granular Materials Discharging from Bin－Hopper System — *J. Hidaka, J. Kano and A. Shimosaka* 205

- Adhesison Force Arising from Solid Salt Bridge Formed after Drying of Liquid Bridge — *Y. Endo, Y. Kousaka and H. Onitsuka* 215
- Creep Failure Process for Fine Powder Beds by Tensile Loading — *H. Kamiya, M. Naito, J. Tsubaki and G. Jimbo* 223

- Information Articles 234

Explanation of the cover Photograph

Full 3D Simulation of Spouted Bed Using DEM

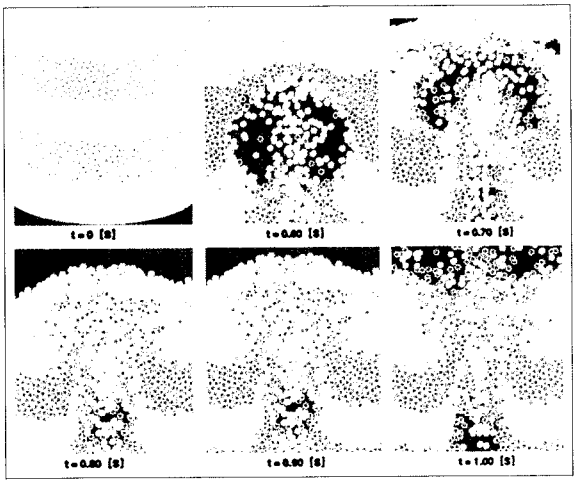

A full 3D discrete particle simulation was performed for a spouted bed. A air jet issus from the center of the bottom plate to the particle layer. The solid phase was obtained from the Lagrangian calculation; trajectories of individual particles were calculated using the classical Newtonian equations of motion. The particle-particle interaction due to contact forces was modeled by the DEM (discrete element method). The gas phase was assumed to be inviscid and described by local variables. The gas-particle interaction was taken into account. The boundary fitted coordinate method (BFC) was used to deal with three-dimensional structures of the flow field. Primary conditions are as follows.

Particle size = 4 mm,
Particle density = 2700 kg/m^3
Particle number = 30,000,
Vessel diameter = 120 mm,
Superficial air velocity = 1.8 m/s.

By courtesy of Professor Y. Tsuji,Dep. of Mechanical Engineering, Faculty of Engineering, Osaka University.

Review

Grinding Aids†

D. W. Fuerstenau
*Department of Materials Science and Mineral Engineering, University of California**

Abstract

The use of chemical additives for improving the efficiency of both wet and dry comminution is reviewed. Although such additives can affect breakage strength under general comminution conditions crack velocities are probably too great to involve adsorption effects. Additives in dry grinding systems appear to function by coating the particles and preventing reagglomeration. In wet grinding systems, their main influence on grinding is through their effect on slurry rheology. Such additives do not affect the specific energy for grinding but only regulate mill power draft and kinetics.

1. Introduction

The large tonnages of mineral raw materials comminuted annually, the low energy efficiency and high energy intensity of grinding operations in conventional tumbling mills together with the depletion of high-grade, coarse-grained ores over the years have all compelled researchers to find ways to improve the overall performance of grinding mills. Of the gross energy input to the mill, perhaps only 1 or 2 percent of it results in the production of new surface area. Most of the input energy ends up as heat, resulting from transmission losses, deformation and wear of crushing media and crushing surfaces, fruitless impacts or stresses, friction, kinetic energy, elastic and plastic deformation, and sound. During some comminution operations, reagglomeration of particles (an energy loss) or de-agglomeration (an energy gain) can occur. In some devices, the kinetic energy of the comminuted fragments might result in secondary breakage. Adding certain chemicals, which are often surface-active, to the mill feed in small quantities (0.1 percent of the feed solids) to improve mill throughput in both dry and wet grinding has been widely reported in the literature (1,2). In the cement grinding industry, grinding aids have now been regularly employed in plants for several decades. Although a large number and variety of chemicals are reported to be efficacious as grinding additives, for the most part their mechanisms have not been precisely delineated (1,2).

There are many reasons why the mechanisms by which these aids improve mill performance are not well understood. First, only in a few of the more recent studies reported has the energy expended for grinding been taken into account, even though it is well recognized that energy is a rational basis for the analysis of grinding results. In most of the studies, batch grinding experiments with and without additive were performed for a certain length of time, and the energy expended by the mill was assumed to be the same whether the additive was present or absent. This implies identical mill power in both cases. However, in wet grinding, the power drawn by the mill can be significantly influenced by the presence/absence of the additive, particularly in slurries at high solids content.

Second, the surface area of the ground product has generally been measured using air permeability methods. Changes in the specific surface of samples ground in the presence of an additive are very unsatisfactory indicators to deduce the effect of these aids if the surface area is measured by air permeametry. The additives are generally surface-active, and therefore give rise to dispersion/agglomeration effects with powders, which is the actual purpose for their use in industrial dry grinding systems, but the specific surface measured with air permeability methods on such dispersed/agglomerated samples can lead to erroneous inferences.

Under these circumstances, despite a large number of papers available on the subject, a coherent understanding of the mechanism(s) by which additives may improve the performance of tumbling mills has been elusive. Often the first explanation given for the action

* Berkeley, California 19720, USA
† Received 30 June, 1995

of a grinding aid has been that it reduces the breakage strength of the material being comminuted. However, in his paper on the physical aspects of comminution, Rumpf (3) showed from theoretical considerations that it is very unlikely that changes in the environment brought about by an additive would improve the efficiency of a grinding operation, measured in terms of energy. Perhaps, the most detailed research reported on additives is that of Klimpel and co-workers (4) on the use of polycarboxylates in wet grinding systems; their research clearly points to the action of those additives being the control of slurry rheology.

Comminution involves several subprocesses: 1) the transport of particles to the zone in the mill where they can be stressed, 2) loading or stressing of the particles such that they fracture, 3) prevention of reagglomeration of the fine fragments and 4) the removal of fine broken particles from the grinding zone. Grinding aids potentially can play a role in all four of the subprocesses that occur during comminution. The mechanisms involved in grinding aid action may include 1) the reduction of breakage energy, 2) embrittlement to reduce plastic deformation 3) the flocculation/dispersion of fines, 4) the prevention of reaggglomeration, and 5) control of slurry rheology. A useful objective for a grinding aid in ore milling would be to foster breakage along grain boundaries, thereby enhancing liberation. The overall objective of this paper is to review and discuss how various types of chemical additives might or might not affect comminution subprocesses and energy losses.

2. Crack Propagation and Fracture Energy

The production of fine particles involves the propagation of cracks when materials are stressed mechanically above their breakage strength. Both bulk and surface properties of a material determine the energy required for fracture. Any aspect of the chemical environment that can affect breakage energy and crack propagation could be considered to be a grinding aid.

The Griffith theory for the energy balance in crack extension states that a crack will propagate if the loss in elastic strain energy is greater than the increase in surface energy accompanying the formation of new surface. For a crack of length $2a$ inside a specimen, the fracture strength, σ_f, is given by (5):

$$\sigma_f = \frac{2Y\gamma^{1/2}}{\pi a} \tag{1}$$

where Y is the modulus of elasticity and γ is the surface free energy of the solid material. Often the Griffith criterion for fracture is written as:

$$\sigma_f = \frac{YG_c^{1/2}}{\pi a} \tag{2}$$

where G_c is the total work of fracture. Quite early on, fracture researchers recognized that plastic deformation might be occurring in the region around the crack tip so that the energy to form the crack surface may exceed the surface energy of the material. Thus, G_c may involve the energy required not only for the formation of new surface, but also for plastic deformation, chemical reactions, etc.

Controlled cleavage of solid materials has been quite widely used to determine the surface free energy of solids and the results show good agreement with calculated values and with the results from other kinds of measurements. Under controlled cleavage of brittle solids, all of the energy put into the system can be accounted for as either strain energy or surface energy (6). This would be the ultimate in the energy efficiency of comminution.

After detailed consideration of the energies involved in the controlled cleavage of quartz under various experimental environments, Parks (7) has analyzed how stages of water adsorption reduce the surface free energy of quartz. As discussed by him, the presence of water has a major effect on the surface energy of quartz, a phenomenon that must be taken into account when analyzing the results of experimentally fracturing quartz.

How much the surface free energy, γ, is reduced by adsorption is given by the Gibbs adsorption equation:

$$d\gamma = -\sum \Gamma_i d\mu_i \tag{3}$$

where μ_i is the adsorption density of species i and Γ_i is its chemical potential. Parks' estimates of the surface and interfacial free energies of quartz through consideration of its interaction with water are given in **Table 1**. The greatest reduction in the surface-free energy of quartz comes from the chemical reaction of water vapor molecules with ≡ Si- and ≡SiO- sites at the fracture surface to form surface silanol groups, that is ≡ SiOH surface sites.

Hammond and Ravitz (8) measured the tensile breaking load of annealed fused silica rods in various

Table 1 Estimated Surface and Interfacial Energies of Quartz (7)

Surface or Interface		Free Energy, mJ/m^2
γ_s	(quartz/vacuum)	>2000
γ_{sh}	(quartz/silanol surface)	480 – 690
γ_{sf}	(quartz/saturated water vapor)	406 – 458
γ_{sw}	(quartz/liquid water)	335 – 385

saturated vapors and found that the breaking load decreased in accordance with the reduction in surface tension brought about by the adsorption of the vapor. The Gibbs adsorption equation was used to calculate the lowering of the surface tension of the solid. **Table 2** summarizes their results. Although they baked the specimens at 800°C at 10^{-4} torr for 30 minutes, their results indicated that the surface free energy of the fused silica rods was 400 mJ/m^2, which is a rather low value.

In a study of the effect of dissolved surfactants on the stress required for the propagation of cracks in synthetic quartz crystals, Dunning et al. (9) found the mean values of the crack propagation stress in air (ambient humidity) to be 69.7 MPa, 60.5 MPa in liquid water, 48.6 MPa in 3×10^{-4} M dodecyltrimethylammonium bromide (DTAB) and 45.3 MPa in 1×10^{-3} M DTAB. Cationic organic surfactants, such as DTAB, strongly adsorb on silica from aqueous solutions. In addition, morphological studies showed that the cracks propagated in DTAB environments were often bifurcated. This work provides an indication that adsorption from aqueous solution can affect fracture behavior.

Table 2 Surface Energy Lowering and the Fracture Strength of Silica Rods in Various Saturated Vapors (8).

Saturated Vapor	Surface Free Energy Lowering mJ/m^2	Fracture Strength, MPa
Vacuum	0	91.1 ± 4.8
Dry benzene	52	93.9 ± 6.9
Butyl alcohol	85	82.2 ± 4.1
Propyl alcohol	110	66.3 ± 0.7
Water	244	55.2 ± 3.9
Water*	244	45.6 ± 4.8

(*This series of breakage tests was carried out after 100 minutes of exposure to water vapor, whereas all of the other results were for 10 minutes of exposure).

The results given in **Table 2** indicate that there are time effects involved in the action of an additive on breakage strength. Clearly, since the diffusion of molecules to the crack tip and possible chemical reaction require finite time, the environment can affect crack propagation only if the crack velocity is sufficiently low (as would be the case in controlled cleavage experiments). Schoenert (5) reported the results of crack velocity measurements in glass as a function of crack extension energy, G_c, under different environmental conditions. **Figure 1,** adapted from his paper, shows crack velocities as a function of G_c for glass in vacuum (10^{-4} and 10^{-6} torr), humid air and liquid water at room temperature (20 − 23° C). Clearly, water strongly influences and promotes crack propagation at slow rates. As an example, a crack propagates at a velocity of 10^{-4} cm/sec in high vacuum when G_c is 8.5 joule per m^2 whereas only 2.4 joule per m^2 is required in liquid water. **Figure 1** shows that at a crack velocity of about 0.05 cm per sec, the presence of water in the vapor has no effect on the system, that is the G_c value is not affected by water-vapor stress corrosion (the formation of surface silanols).

In dry grinding in ball mills, the loading time is less than 1 second and cracks will propagate faster than 10^{-1} cm/sec. Therefore, one must conclude that for dry grinding neither adsorption nor chemical reaction can influence crack propagation in a comminution mill. For wet grinding, however, crack velocities must be greater than 10 cm per sec before the influence of the environment becomes negligible.

3. The Concept of Surface Energy Reduction in Grinding Aid Action

Some of the studies summarized in the previous section showed that the amount of work involved in propagating a slow crack (that is in forming new crack surface) in a brittle material is related to the surface free energy of the material, and that the energy to propagate a crack can be reduced through adsorption at the surface.

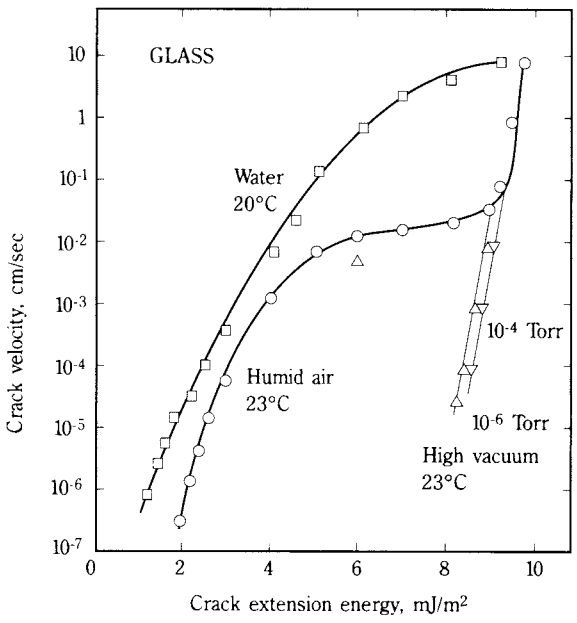

Fig. 1 Crack velocity in glass as a function of crack extension energy, Gc, in high vacuum, humid air, and liquid water (after Schoenert, Ref 5).

Since comminution involves the production of new surface, the amount of energy required to produce a given amount of surface should be reduced by decreasing the surface energy of the material being comminuted. This relatively intuitive mechanism was believed to be responsible for the improved efficiency of rock drilling, as suggested by Rehbinder and Kalinkovaskaya (10). Rose and Sullivan (11) extended this concept of adsorption-induced decrease in surface energy to explain the mechanism of grinding aids in tumbling mills. However, crack propagation velocities measured by Schoenert in dry systems are such that adsorption cannot take place rapidly enough to affect dry comminution. Others have also suggested that crack propagation velocities in impact breakage that occurs in grinding mills are much greater than the spreading velocities of the surfactant molecules by diffusion into the cracks. As indicated by the work of Locher and von Seebach (12), even vapors of a (liquid) grinding aid adsorbed on the solid surface cannot improve breakage efficiency by decreasing the surface energy of the solid. It is, therefore, very doubtful that adsorption-induced surface energy changes can be responsible for the mechanism of grinding aid action in dry systems.

Westwood and Goldheim (13) showed that adsorption of surfactants from solution can reduce the strength of materials only when plastic deformation is important in the process of fracture. According to them, the adsorption of the surface-active molecules or ions on the solid surface essentially blocks the motion of dislocations near the surface, rendering their motion under stress gradients very difficult. Material plasticity due to dislocation movement is thus greatly reduced and the solid is rendered brittle. This mechanism applied to tumbling mill grinding is also subject to criticism similar to the foregoing discussion on Rehbinder's effect, namely that the rate of dislocation movement is much lower than crack propagation rates in impact fracture. Locher and von Seebach (12) have also given experimental evidence indicative that Westwood's mechanism is probably inoperative.

It has been suggested that molecules of the grinding aid might penetrate deep into the tips of pre-existing cracks and exert pressure on the crack tips, aiding the fracture process. The role of this in impact fracture is, again, doubtful, since, as pointed out by Somasundaran (14), long-chain organic surfactants which would have limited diffusion owing to their larger size.

A further factor to be considered is that the environment may influence the level of strain energy in the particle when cracks begin to propagate but may not affect the amount of energy needed to achieve the desired level of size reduction. For example, in a study of the breakage of Pyrex glass cylinders, Sullivan and Fuerstenau (15) found that the relation between breakage energy, E, and product particle size could be expressed by:

$$E = CX_m^{-1} \tag{4}$$

where C is a constant and X_m is the Gaudin-Schuhmann size modulus of the product. Annealed specimens broke at a load of 9500 kg whereas unannealed specimens broke at a much lower load, namely at 4300 kg. However, the product from the annealed specimens was much finer and obeyed the same relation (Eq. 4). These results suggest that even if an adsorbed species lowers the initial breakage strength, the relation between specific energy and the size distribution of the product may not be altered.

4. Grinding Aids in Dry Systems

Historically, considerably more effort has been expended in developing grinding aids for dry grinding systems than for wet grinding systems with most of this work being oriented toward the cement industry, where huge amounts of cement clinker are dry ground in ball mills. Cement clinker is particularly difficult to grind, and the fine grinding of this material is one of the chief problems of that industry. The first commercial use of grinding aids in the cement industry came about 50 years ago. These grinding aids, which are generally organic liquids added in amounts usually not exceeding 0.25% by weight, are used to increase the product fineness at a given production rate or to increase the production rate at a given product size. The benefits of any grinding aid must outweigh its cost; furthermore, the grinding aid should have no detrimental effect on downstream processing or the finished product. Given these constraints, the industrial acceptance of grinding aids in the cement industry that took place over a period of 10 to 15 years must be considered relatively rapid.

Figure 2 shows a typical comparison between the grinding of cement clinker with and without a grinding aid. As recently reviewed (See Reference 17 for sources), 0.1% of di- or tri-ethanolamine increases the rate of clinker grinding by 22-29%, with glycerol and lower alcohols being less effective. A 25-50% increase in the production rate has been reported with glycol as the grinding aid. The use of

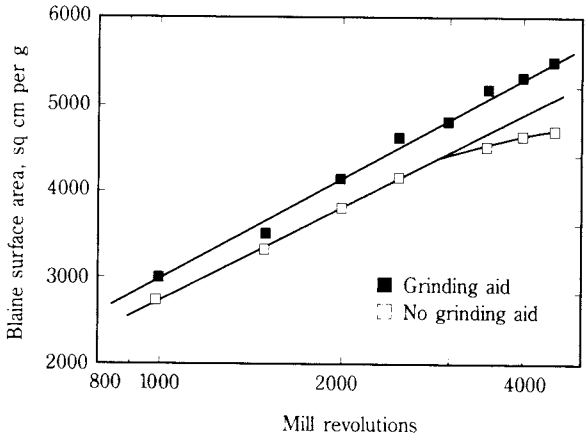

Fig. 2 A typical comparison between grinding of cement clinker with and without a grinding aid in a laboratory mill (after Ref. 16).

0.05% propylene glycol in pilot plant grinding tests showed that a 20% increase in production accompanied by a 10% decrease in energy costs is possible. The addition of as little as 0.01-0.05% of organo-silicones has been found to decrease grinding time by 70%. In addition to these, other additives have been shown to have grinding aid characteristics for grinding cement clinker, including resins, cod oil, kojic acid, carbon blacks, wool grease, calcium sulfate, urea, asphaltenes, etc. In general, experience has shown that polar grinding aids are more effective than nonpolar additives. The addition of hydrophilic surface-active substances such as calcium ligno-sulfonates during the comminution of cement clinker allows production of highly effective plasticized cements. In an analogous manner, it is possible to obtain hydrophobic cements by introducing hydrophobic-type additives (acidol-naphthenate soap or sodium abietate) during comminution. These additives comprise about 0.1% of the mass of the pulverized cement.

The effect of grinding aids on the grinding of materials other than cement clinker has also been reported. Some examples (See Ref. 17) include the use of wool grease in the grinding of gypsum, limestone, and quartz, the effect of hydrocarbons in the milling of aluminum powder, the use of silicones in the ball mill grinding of quartz; and the use of acetone, carbon tetrachloride, benzene and nitromethane in the vibratory milling grinding of glass, marble, and quartz.

In view of the inability of theories based on adsorption-induced improvement of the breakage or fracture subprocess to explain the action of grinding aids, it has been postulated by many researchers that their effect is in controlling the agglomeration and flow characteristics of material in the mill. The idea that grinding aids caused dry dispersion of material was suggested over 50 years ago when a considerable increase in dust was noticed in the early commercial uses of grinding aids in cement grinding (18). Observations like these over a period of time suggested that grinding aids coat the cement particles, shielding them from agglomerating forces and thereby preventing the particle from welding back together again. It has been argued that grinding aids readily satisfy the valence forces produced by material fracture (16, 19). Since grinding aids usually are polar substances, they can preferentially adsorb on specific sites where the breakage of electrovalent or covalent bonds result in residual electrical forces. By the same token, at least part of the improved efficiency in wet grinding over dry grinding may be attributed to the polar nature of water.

It is believed, therefore, that grinding aids which chemisorb on solid particles would most effectively reduce adhesive tendencies between particles and thereby improve grinding efficiency. Since adhesive forces are (particle-size) surface-area dependent, the relative improvement in grinding efficiency is greater, the finer the product size (12, 17). It should be noted that most of the surface area data were obtained by air permeability methods and this tends to magnify the benefits of grinding aids when assessing the results in terms of new surface.

At very fine grinds, the tendency of ground particles to coat the grinding media and mill liner becomes very pronounced and has long been considered to limit the effectiveness of the grinding process. There has been some diversity in opinion as to whether grinding aids are effective only in reducing ball and liner coating but, as Mardulier (16) points out, this can be considered as a special and extreme case of agglomeration.

5. Grinding in Liquids

As pointed out earlier, perhaps water itself can be considered a grinding aid because of the improved efficiency and mill capacity obtained with wet grinding relative to dry grinding. **Figure 3**, plotted from the results from Coghill and DeVaney (20) for the grinding of dolomite in a pilot-scale ball mill, clearly shows better grindability of the material over the entire range of mill holdups in wet grinding as compared to dry grinding. A variety of reasons have been put forth to explain this phenomenon. As discussed earlier, the effect of water is believed by some to

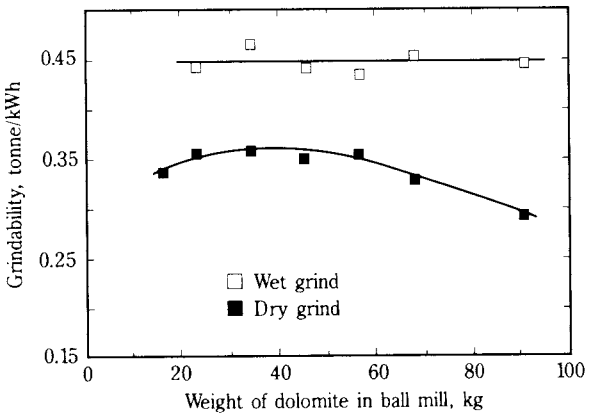

Fig. 3 Comparison between the grindability of dolomite when ground under wet and dry conditions as a function of holdup in a ball mill (data from Ref. 19).

be due to its polar nature and consequent ability to satisfy the surface residual electrical forces created upon fracture, thereby reducing adhesive tendencies between the ground particles (16). In liquid water, the surface energy (7) and the energy to propagate cracks is markedly reduced (5). Also, the cushioning effect of fine particles in wet grinding will be minimal because they become suspended in the liquid. This would lead to increased grinding action on the coarser particles, with improved grinding efficiency.

Meloy and Crabtree (21) proposed that the surface tension of the liquid enables particles to cling to balls and move into the zone of maximum grinding action. Their results indicate that particles are ground more rapidly in liquids of high surface tension. They also found that larger particles are ground more rapidly in a more viscous liquid, while smaller particles show the opposite effects. This they attributed to two competing phenomena: at higher viscosity, the coarser particles tend to be lifted into the grinding zone, while the cushioning effect is enhanced. This implies the existence of an optimum liquid viscosity for grinding. Similar results were reported by Schweyer in 1942 (22). Although grinding in organic liquids is economically prohibitive in most cases, these studies imply that to obtain a narrow size distribution in the product, a high viscosity liquid might be used as the grinding environment if the material to be ground has a high unit value. Kapur et al. in 1965 (23) showed that the specific gravity of the material with respect to the environment is important; if the material is less dense than the environment (the liquid in which it is ground), it tends to float away from the grinding zone in the mill, which reduces comminution. A detailed analysis of the role of fluid density on comminution was recently carried out (24). The study showed that with different liquid fluids the grinding path remains invariant even though the energy input is throttled significantly with increase in fluid density.

Although organic liquids tend to be economically impractical, it must be mentioned that many of them have been shown on a laboratory scale to provide more efficient grinding environments than water. Several workers observed that grinding in alcohols appears to be more efficient than grinding in water, an example being doubling the surface area per unit of expended energy for grinding quartz in alcohol. The results of Lin and Mitzmager (26) are rather interesting in that grinding in nonpolar carbon tetrachloride and methylcyclohexane actually decreased the rate of fine particle production somewhat compared to the corresponding rate in water. However, this decrease was not observed if only a small amount of water was dissolved in the organics, indicating that polar water molecules in such a system may be acting as a grinding aid.

6. Additives in Wet Grinding Systems

As with grinding aids in dry grinding systems, a fairly large number of investigations on the effectiveness of chemical additives for wet grinding have been reported in the literature mostly for laboratory-scale investigations.

In 1942, Szantho (27) demonstrated that Flotigam P (C12-C14 amine) in concentrations of up to 0.03% produced a 100% increase that in surface area of quartzite and limestone. As can be seen from the results given in **Figure 4**, the effectiveness of the grinding aid increases with increasing concentration to a maximum, beyond which further additions cause

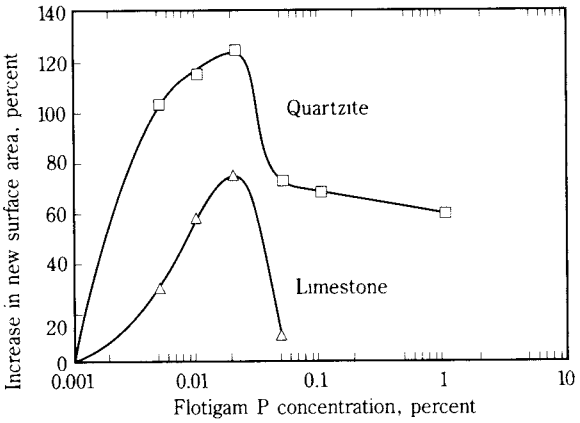

Fig. 4 Effect of a commercial flotation reagent (Flotigam P) on the grinding of quartzite and limestone in a rod mill. An optimum Flotigam P concentration of about 0.03% results in a maximum increase in product surface area (After Szantho, 27).

a decrease in the specific surface area of the products. As summarized (Ref. 17), some other reported examples of the beneficial effects of grinding aids in wet grinding include the work of Khodakov and Rehbinder (1961) on the ball milling of quartz; Kokolev et al. who found a four-fold decrease for the time of grinding alumina in the presence of about 0.005% organo-silicones; and Orlava et al. on the grinding of zircon and other minerals with 0.2% triethanolamine, giving a four-fold decrease in grinding time. In some cases (17, 27), the addition of organic liquids to a wet grinding system has been reported to decrease grinding efficiency.

There has also been considerable study of the effects of inorganic electrolytes on grinding performance (14, 17). Although there are some ambiguities, it can be generally concluded that some improvement in grinding results from the addition of an optimum electrolyte concentration and that dispersing agents improve wet comminution performance.

More recently, Somasundaran and El-Shall (28, 29) conducted a detailed experimental investigation of the application of both inorganic and organic additives to wet ball mill grinding, with details of ionic strength and pH control being given. In a study of the wet grinding of quartz in a laboratory ball mill, Somasundaran and El-Shall (29) found that the addition of dodecylammonium chloride (a cationic surfactant) can be either beneficial or detrimental to the grinding process, depending upon the pH and the concentration of amine. Using the change in the percentage of minus 200-mesh quartz produced as an index of grindability, they found that in neutral or alkaline solutions, the amine is beneficial to the process whereas under acidic conditions, the effects of amine additions are detrimental (29). Plots of their results, have the same general shape as curves showing the effect of pH and amine concentration on contact angles or flotation response of quartz in other words, significant effects occur upon amine adsorption.

In order to delineate what must be responsible for these complex effects, they also conducted single-impact breakage experiments, flocculation/dispersion studies, and measurements of suspension fluidity. The results given in **Figure 5(a)** and **5(b)** show how pH affects all of these properties of quartz in the presence of 10^{-3}M amine additions and 10^{-5}M $AlCl_3$, respectively. Both the amine and the aluminum chloride affect the grinding process because of their effect on primary breakage and pulp fluidity. The grindability index for $AlCl_3$ addition was the change in the production of minus 400-mesh particles. In the case of the $AlCl_3$ addition, improvement in the acidic pH range results from improved pulp fluidity as well as enhanced primary breakage; at pH 10 decreased pulp fluidity and enhanced dispersion retards grinding rate. Somasundaran and El-Shall (28) have summarized the explanation of their results for a

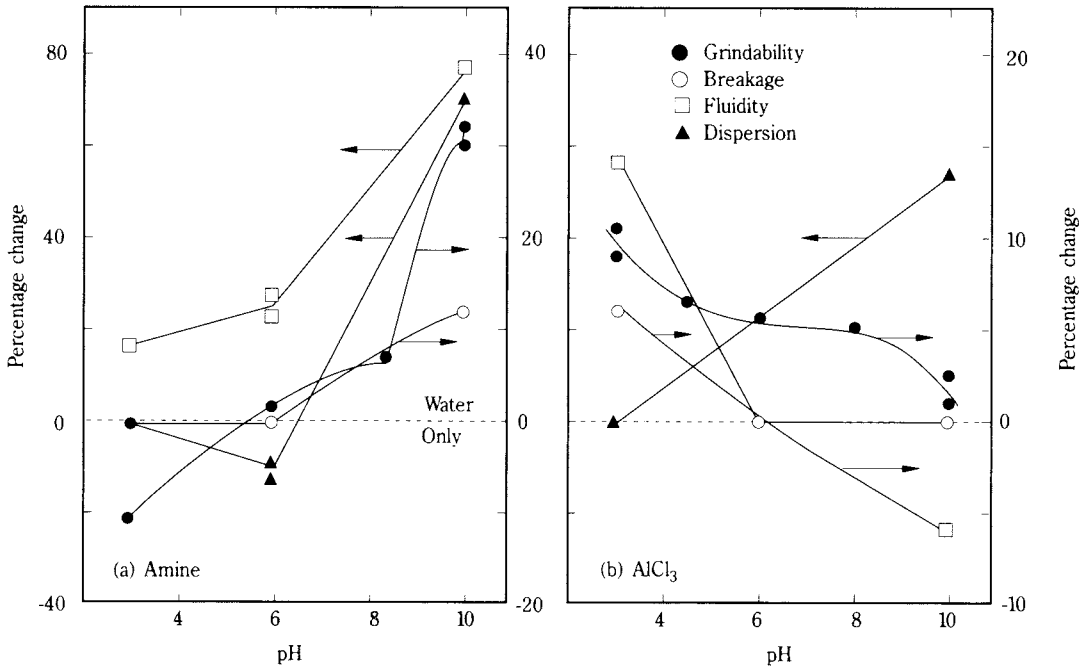

Fig. 5 (a) Effect of pH and 10^{-3}M dodecylammonium chloride on grindability, particle breakage, suspension fluidity, and degree of flocculation/dispersion of quartz.
(b) The same for 10^{-5}M aluminum chloride solutions (after 28).

number of additives and pH conditions (**Table 3**). The fluidity (rheology) and degree of dispersion of the suspension appears to have a major role in this system.

7. Polymeric Grinding Aids

Klimpel and coworkers (4, 30, 31) have written an extensive series of papers concerning the use of hydrophobic polymers as grinding aids, including not only extensive laboratory studies but also plant-scale applications. An example of the type of results that Klimpel and coworkers obtained for wet batch ball milling is given in **Figure 6**, which shows the production of minus 325-mesh taconite as a function of weight percent solids in the slurry. Without any grinding aid, the production of minus 325-mesh product falls off markedly as the slurry density increases above 80 percent solids. With the addition of the grinding aid, (a polycarboxylate designated as XFS 4272 by Dow Chemical Company) the production of minus 325-mesh product increased markedly. Grinding at such high pulp densities in the presence of 0.03 percent of the additive resulted in a higher than average mill torque, a more finely ground product and a pulp of lower viscosity.

From their extensive test work, Klimpel and coworkers conclude that significant advantages can be realized by using grinding aids if 1) the mill is operated in a region of percentage solids high enough so that a further increase produces a large slurry viscosity increase in the absence of the grinding aid, 2) the solids in the slurry have sufficient adsorption capacity for the grinding aid so that it can improve the slurry dispersion characteristics, and 3) the grinding aid has consistently good dispersion characteristics over the range of physicochemical conditions (such as slurry pH, intensity of mixing, etc.) encountered in practical operation of the mill.

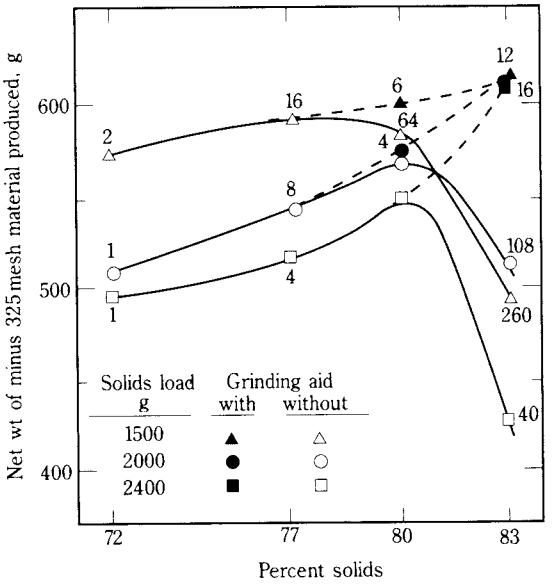

Fig. 6 The net amount of fines produced during grinding plotted against the percent solids in the pulp. The number beside the experimental points are the values for pulp viscosity in thousand centipoises (after Ref. 30).

As a consequence of increasing the solids content of a suspension, the rheological characteristics of a slurry may change from Newtonian to non-Newtonian. This transition is always accompanied by an increase in the viscosity of the suspension. There are three controllable factors which regulate the rheological properties of a pulp or slurry: 1) slurry density, 2) particle size distribution, and 3) chemical environment. Particle shape (which also has a major effect) cannot be controlled in comminution systems. As grinding proceeds, at a given solids concentration, the particle size distribution changes and the produc-

Table 3 Summary of the Various Conditions Leading to Enhancement or to a Reduction in the Rate of Grinding Quartz in Aqueous Systems (after Somasundaran and El-Shall, Ref. 28).

Enhanced Grinding		Reduced Grinding	
Condition	Possible Mechanism	Condition	Possible Mechanism
Water		Water	
low pulp density	higher pulp fluidity	higher pulp density	decreased pulp fluidity
acidic solution	better dispersion of particles	alkaline solution	decreased pulp fluidity
Aluminum Chloride		Calcium Chloride	
acidic solution	improved pulp fluidity and primary breakage	acidic solution	flocculation of particles
neutral solution	better dispersion of particles	neutral solution	decrease in pulp fluidity
Amine		Sodium Silicate	– –
alkaline solution	improved primary breakage and pulp fluidity balanced partly by increased flocculation.	Sodium Sulfate	
		all pH conditions	– –

tion of fresh surface adsorbs chemicals present in the system and, thus, slurry rheology can change with time. Recently, Velamakanni and Fuerstenau (32) conducted a detailed study of how polycarboxylate polymers affect the viscosity of suspensions of different minerals. The polymers used were polyacrylic acid (PAA), sodium polyacrylate (SPA) and Dow's XFS 4272 and the minerals tested included dolomite, hematite and quartz. The molecular weights of PAA and SPA were 5000 and XFS 4272 is 5000-10000. As can been seen by the results presented in **Figure 7**, the viscosity of a minus 65-mesh dolomite slurry (61 volume percent solids) was reduced at a critical additive dosage of 0.012 wt percent for SPA and 0.03 percent for XFS 4272. Because there must be adsorption before these effects can take place, there are solution (pH, ionic strength, contaminant ions) and mineral-specific (adsorption sites, surface charge) effects. Polymers which stabilize suspensions adsorb directly onto the particle surface and must be sufficiently charged that they induce electro-static repulsion between interacting particles. The polymer molecules must be large enough to prevent the particles from coming close enough together for the attractive forces to operate (steric stabilization) and must be highly charged to give rise to strong electrical repulsion.

The three polymers studied by Velamakanni and Fuerstenau (32) have different effects on the behavior of mineral suspensions. PAA had no effect on the viscosity of dolomite and hematite suspensions. This appears to be the result of pH (6.5 with PAA and 9.2 with SPA). At pH 9.2 the zeta potentials of the polymer-coated dolomite and hematite particles are sufficiently high that strong electrostatic repulsion between particles contributes to viscosity reduction. SPA and PAA do not adsorb on clean quartz, but over the pH range of 4 to 6 the viscosity of the suspension of quartz that had been ground in a steel mill is markedly reduced because of the strong PAA adsorption induced by Fe(III) activation.

Those polymers used in rheological studies on suspensions of dolomite, hematite and quartz were also tested for their efficacy as additives in grinding these same minerals. The polymer dosage required to enhance grinding was taken as the critical polymer concentration obtained from the rheological studies on suspensions. To ensure free-flowing slurries during grinding, a slight excess over the critical polymer concentration must be present. **Table 4** summarizes the final pH, the slurry viscosity, and the amount of fines produced after wet grinding the minerals with and without polymers. These results clearly show the relationship between the effect of the polymer and pH on the rheology of the mineral suspension and its effect on grinding kinetics.

Klimpel (33) has also demonstrated that polymeric additives can affect breakage kinetics. In ball milling 20 × 30 mesh coal at low solids concentrations (57.0 wt percent solids), the breakage rate follows first-order behavior in both the presence and absence of the grinding aid (**Figure 8**). When the solids concentration is increased to 72.3 wt percent, the grinding rates deviate from first-order behavior as grinding proceeds (**Figure 8b**) and the slurry becomes viscous. By adding the carboxylate polymer, the rate again becomes first order. The absolute rate of breakage with and without polymer at 57 wt percent solids was 125 grams per minute. At 72.3 wt percent solids, it was initially 120 grams per minute, dropping to 54 grams per minute as the slope of the breakage rate function decreased (**Figure 8b**). By adding the polymer under these conditions, the absolute breakage rate was increased to 134 grams per minute. Under these conditions, the development of a yield stress and high slurry viscosity causes the grinding kinetics to deviate from first order. The addition of the grinding aid eliminates the yield stress and reduces the viscosity. Klimpel (34) has also experimentally demonstrated that slurry viscosity affects the sharpness of classification in cyclones. Thus, reduction of

Table 4 The effect of polymeric additives on the viscosity of mineral slurries and on the production of minus 37 μm particles after wet ball milling (Ref 32).

	DOLOMITE			HEMATITE			QUARTZ		
Additive	pH	Slurry Condition	Prodn. <37 μm (%)	pH	Slurry Condition	Prodn. <37 μm (%)	pH	Slurry Condition	Prodn. <37 μm (%)
None	9.2	viscous	46	8.5	viscous	35	6.4	viscous	35
XFS 4272	9.5	free-flow	54	9.2	free-flow	50	9.2	viscous	22
SPA	9.5	free-flow	54	9.2	free-flow	50	9.2	viscous	21
PAA	6.5	viscous	31	4.8	viscous	33	4.3	free-flow	53

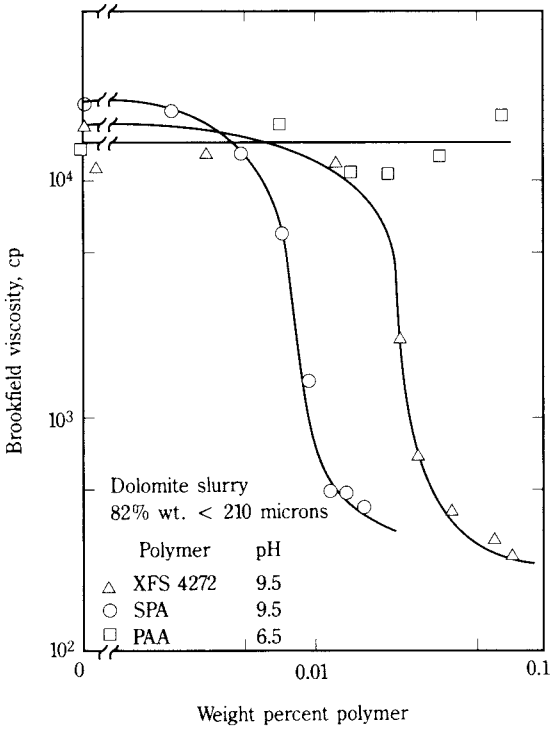

Fig. 7 The effect of polymer dosage on the apparent (Brookfield) viscosity of 82 wt % (61vol. %) dolomite suspensions. Dolomite is a minus 65 mesh ground product (after Ref. 32).

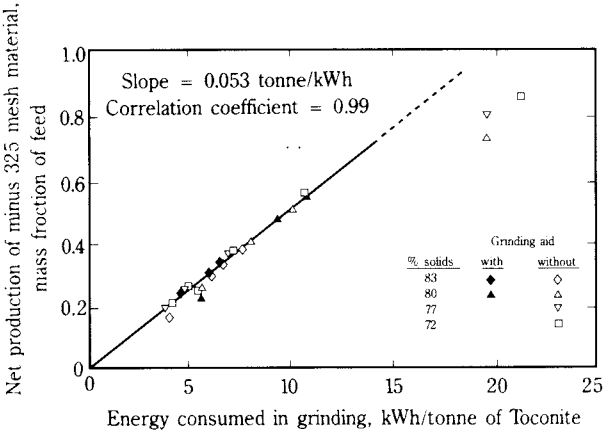

Fig. 9 Net production of minus 325-mesh taconite vs. the net energy expended for grinding (data taken from Katzer et al., Ref. 30).

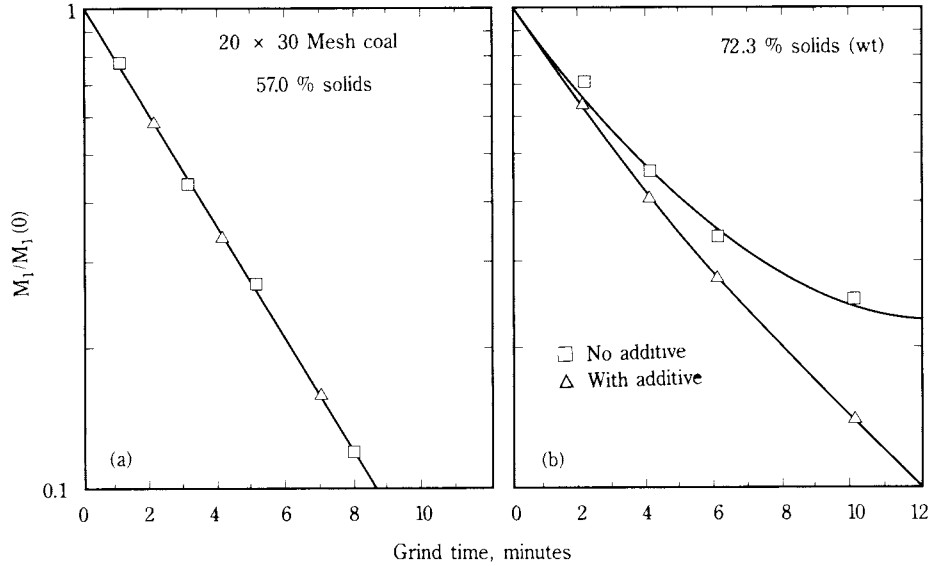

Fig. 8 Rate of feed size disappearance in the wet grinding of 20 × 30 mesh coal at (a) 57.0% solids and (b) 72.3% solids, with and without XFS 4272 grinding aid (Ref. 28).

slurry viscosity may have the added effect in wet comminution systems of improving the separation efficiency of the classification system.

Fuerstenau et al. (35) analyzed the results from Katzer et al. (**Figure 6**) in terms of the energy expended per unit mass of material being ground, that is in terms of specific energy. A plot of the mass fraction of minus 325-mesh material produced per kWh of energy expended results in a single straight line, the slope of which gives the tonnes of minus 325-mesh material produced per kilowatt-hour of energy expended (**Figure 9**). This convincingly suggests that

in terms of specific energy, there is little improvement in grinding in the presence of the grinding additive in this system.

To delineate what must be happening, Fuerstenau et al. (35) conducted 70-minute batch grinding tests in which the instantaneous mill torque was recorded continuously. In separate experiments, the viscosity of the pulp obtained after grinding was measured for different grind times. **Figure 10** presents a plot of the instantaneous torque drawn by the mill versus grinding time for the 82% dolomite slurry, with and without 0.03 wt percent grinding additive. As can be seen by the results given in **Figure 10**, the torque drawn by the milll is essentially the same up to about 25 minutes of grinding, irrespective of the presence or absence of the grinding additive. The important observation from the plots in **Figure 10** is that without the grinding aid, the torque drawn by the mill decreases rather sharply with grind time between 30 and 55 minutes. Further, during the time when the torque is decreasing, it fluctuates widely about the instantaneous mean value. Beyond about fifty minutes, again the torque remained constant (but at a significantly lower value) and the instantaneous fluctuations also dampened. In the presence of the additive, the trend is reversed, though it is not as dramatic as that in the absence of the additive.

Fuerstenau et al. (35) quantitatively explained how modifying the pulp viscosity by an additive alters the dynamics of grinding media inside the mill. In wet grinding, there is a critical pulp viscosity above which the grinding media "centrifuge" because the balls cannot be detached from the mill wall during the time of rotation. An estimate of this critical viscosity can be made by analyzing the forces acting on the grinding media (**Figure 10**). When the media "centrifuge" in a pulp with viscosity greater than the critical value, fewer balls cataract/cascade. The mill power decreases, and a correspondingly smaller amount of fines is generated. Certain additives are able to reduce pulp viscosity to a value less than the critical viscosity (about 4000-5000 centipoise) and provide conditions where the grinding balls do not centrifuge so that the mill draws more power and more fines are generated. Additives are ineffective at lower pulp densities because pulp viscosity is already less than the critical value.

In summary, for wet grinding at high solids concentrations, when improved grinding results from the presence of an additive, it is always accompanied by increased energy consumption. The results from Fuerstenau et al. (35) suggest that the main beneficial effect of a polymeric additive for grinding minerals is to permit full utilization of grinding media inside the mill through pulp viscosity reduction. When grinding results are analyzed in terms of specific energy expended for comminution, no beneficial effect is observed for the systems discussed.

Subsequently, Fuerstenau et al. (36) showed how slurry rheology can affect grinding behavior by causing changes in the split of the charge between the cascading and cataracting zones in the mill. In the absence of a dispersant, as the pulp thickens, there occurs an increasingly disproportionate split of the

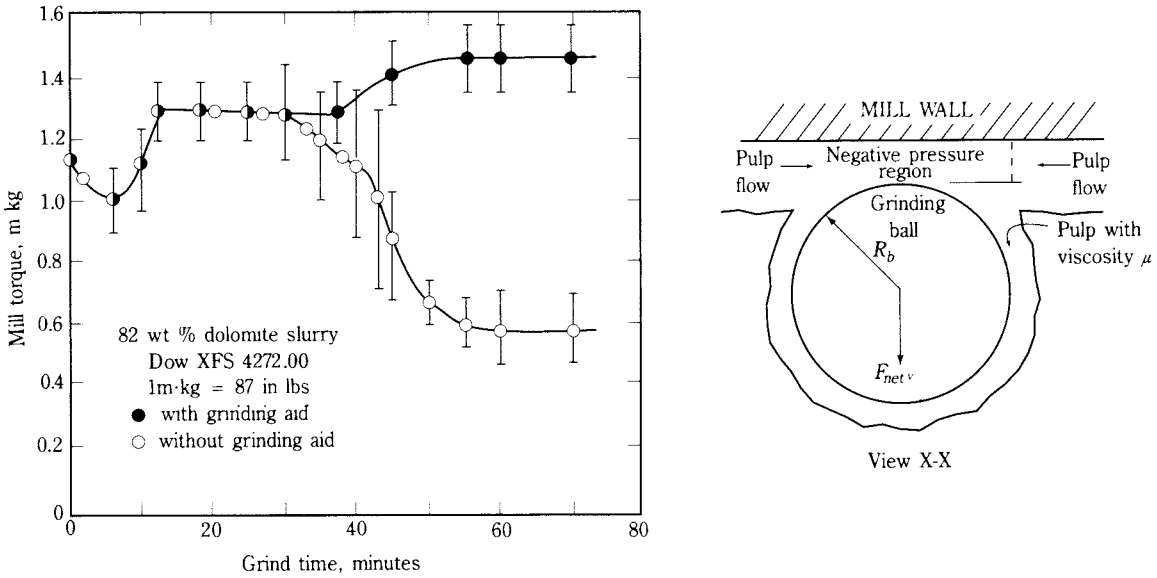

Fig. 10 Mill torque versus grind time for the wet grinding of minus 10-mesh dolomite feed slurry at 82% solids in the presence and absence of grinding aid XFS-4272. Also indicated are the instantaneous torque fluctuations. The attachment of a grinding ball to the mill shell by a viscous slurry is also shown schematically (after Ref. 35).

grinding charge between cascading and cataracting/centrifuging masses, resulting in a complex relationship between the instantaneous viscosity and mill torque. In the presence of dispersants, the partitioning of charge in a relatively fluid suspension occurs to a much lesser extent. A multi-torque mill model has been derived which tracks the overall mill torque as a function of changing viscosity of the pulp, permits estimation of the charge split between cascading and cataracting-centrifuging regimes, and explains the occurrence of a peak torque value at some intermediate stage. As a consequence, the grinding rate should be at its maximum when the torque peaks that is, when the slurry has acquired some pseudoplastic character, in line with the observations by Klimpel. The model also explains the shape of the curves given in **Figure 10**.

Kapur et al. (37) extended these concepts to a cascade-cataracting model for the power draft of tumbling mills and tested the model against published data. **Figure 11** shows both the experimental and model results for dolomite ground wet in a heavily loaded slurry (61 vol % solids) in a 254-mm diameter ball mill, with and without the addition of a grinding aid. Without additives, initially when particles are coarse and a viscous homogeneous pulp is yet to be formed, the mill charge moves at the mill speed in a cascading pattern. The amount of cataracting increases with grinding time as the solids become finer and the pulp thickens, while at the same time the torque goes through a maximum. The lower portion of **Figure 11** gives the results for the same

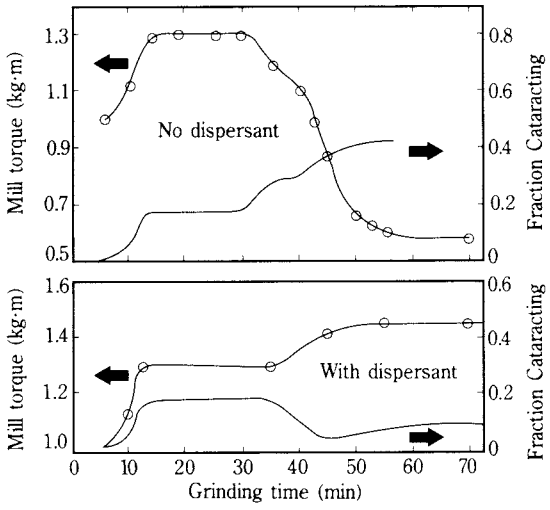

Fig. 11 Mill torque and fraction of charge load cataracting as a function of time when dolomite slurry is ground in a ball mill without an added dispersant [upper figure] and with sodium polyacrylate added as dispersant [lower figure] (after Ref. 37).

milling system but with the addition of sodium polyacrylate as a dispersant, which prevents the pulp from becoming excessively viscous. With the grinding aid, the fraction of material cataracting remains low and the torque high.

In Australia, Kapur et al. (38) investigated the use of polymeric dispersants in a continuous, closed-circuit, stirred ball mill grinding system to produce a target product of minus 10 μm from zinc sulfide flotation middlings. The dispersant used was Dispex at a dosage of 0.5 % by weight. With slurries at 50 % solids content, the performance with and without dispersant was the same. At 65 % solids, it was impossible to grind the material in the stirred ball mill without dispersant but with dispersant the system performs well. Since the power draw was found to be the same in both cases, adding the dispersant increased the production of fines by nearly 50%

Summary and Conclusions

In order to improve the efficiency of comminution systems, there has been a wide interest in the use of grinding aids. Dry grinding additives for cement have found extensive industrial application whereas wet grinding additives for rheology control are just now becoming important. The mechanism for their action appears to be quite well understood in some instances and unclear in others. Many of the observed results are clouded because surface areas were measured by air permeametry and the lack of energy measurements. In dry grinding, crack propagation appears to be too rapid for strength reduction by adsorption to occur. However, practical cement grinding aids appear to function by adsorbing on the external particle surface and thereby preventing reagglomeration. The influence of the liquid, particularly polar water, enhances grinding. Perhaps the most fully understood system involves more recent work on the use of polymers for rheology control in wet grinding mills. Rheology affects grinding kinetics and slurry transport.

The size distributions of the ground product are a function of the cumulative energy input only in normal grinding systems, even when the power drawn by the mill varies appreciably with milling conditions and/or grinding time. The implication is that the grinding rates are proportional to the mill torque and the latter can be used directly to monitor and analyze mill performance and the role of grinding aids, notwithstanding the fact that the slurry may undergo major changes in its rheological character. In plants

being operated at high slurry densities for maximum throughput, control of rheology is necessary so that the viscosity does not exceed the critical value. It is for this purpose that polymer grinding aids have their utility.

References

1) G.C. Lowrison, Crushing and Grinding, CRC Press, Inc., Cleveland, OH, 1979:60.
2) H. El-Shall and P. Somasundaran, Powder Technology, 1984, 38:275-293.
3) H. Rumpf, Powder Technology, 1973, 7:148-159.
4) R.R. Klimpel and W. Manfroy, I&EC Proc. Des. Dev., 1978, 17:518-523.
5) K. Schoenert, Trans. Soc. of Min. Engineers AIME, 1972, 252:21-26.
6) J.J. Gilman, J. Applied Physics, 1960, 31:2208.
7) G.A. Parks, J. Geophysical Research, 1984, 89:3997-4008
8) M.L. Hammond and S.F. Ravitz, J. Am. Ceramic Society, 1963, 46:329-332.
9) J.D. Dunning, W.L. Lewis and D.E. Dunn, J. Geophysical Research, 1980, 85:5344-5354.
10) P.A. Rehbinder and N.A. Kalinkovaskaya, J. Tech Phys. (USSR) 1932, 2:726-755
11) H.E. Rose and R.M.E. Sullivan, A Treatise on the Internal Mechanisms of Ball, Tube, and Rod Mills, Chem. Publishing Co., New York, 1958, 236.
12) F.W. Locher and H.M. von Seebach, Ind. Eng. Chem. Proc. Des. Dev., 1972, 11:190-197.
13) A.R.C. Westwood and D.L. Goldheim, J. Am. Ceramic Society, 1970, 142-147.
14) P. Somasundaran and I.J. Lin, I&EC Proc. Des. Dev., 1972, 11:310-331.
15) D.A. Sullivan and D.W. Fuerstenau, unpublished results.
16) F.J. Mardulier, ASTM Proceedings, 1961, 61: 1078-1093.
17) Comminution and Energy Consumption, Publication NMAB-364, National Academy Press, Washington, D.C., 1981, 206-223.
18) H.L. Kennedy and J.G. Mark, U.S. Patent 2, 141, 571 (1938).
19) D. Ocepek, and E. Eberl, 3rd European Comminution Symposium, Nuremberg, Dechema Monographien, 1976, 79:183-195.
20) W.H. Cohill and F.D. DeVaney, U.S. Bureau of Mines Tech. Paper No. 581, 1937
21) T.P. Meloy and D. Crabtree, 2nd European Symposium on Comminution, Amsterdam, 1966, Dechema Monographien, 1967, 57:405-426.
22) H.E. Schweyer, Ind. Eng. Chem., 1942, 34: 1060-1064.
23) P.C. Kapur, A.L. Mular and D.W. Fuerstenau, Canadian J. Chem. Eng.,1965, 43:119-124.
24) P.C. Kapur, L.M. Berlioz and D.W. Fuerstenau, Powder Technology, 1988, 54:217-224.
25) W.V. Engelhardt, Naturwissenschaften, 1946, 33: 195-203.
26) I.J. Lin and A. Mitzmager, AIME Trans., 1968, 241:412-420.
27) E. Szantho, Erzbergbau Metallhuetenw., 1942, 2:353-360.
28) P. Somasundaran and H. El-Shall, in Ultrafine Grinding and Separation of Industrial Minerals, S.G. Malghan, Ed., AIME, New York, 1983:21-35.
29) H. El-Shall and P. Somasundaran, Powder Technology, 1984, 38:267-273.
30) M. Katzer, R.R. Klimpel and J. Sewell, AIME Trans., 1981, 270:1471-1476.
31) R. R. Klimpel and R.H. Hansen, Minerals and Metallurgical Processing,1989, 6:35-43.
32) B.V. Velamakanni and D.W. Fuerstenau, in Flocculation in Biotechnology and Separation Systems, Y.A. Attia, Ed., Elsevier, Amsterdam, 1987: 211-223.
33) R. R. Klimpel, Powder Technology, 1982, 32: 267-277.
34) R.R. Klimpel, Powder Technology, 1982, 31: 255-262.
35) D.W. Fuerstenau, K.S. Venkataraman and B.V. Velamakanni, Int. J. Mineral Processing, 1985, 15:251-267.
36) D.W. Fuerstenau, P.C. Kapur and B.V. Velamakanni, Int. J. Mineral Processing, 1990, 28: 81-98.
37) P. C. Kapur, S. Ranjan and D.W. Fuerstenau, Int. J. Mineral Processing, 1992, 9-29(1992).
38) P. C. Kapur, T. W. Healy, P.J. Scales and D. V. Boger, Int. J. Mineral Processing, to be published 1995.

Author's short biography

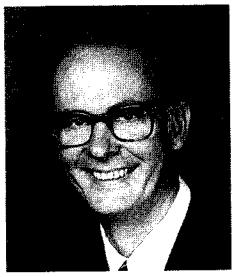

Douglas W. Fuerstenau

Field:

Mineral processing and extractive metallurgy; application of surface and colloid chemistry to mineral systems; fine particle technology; principles of comminution, flotation pelletizing; hydrometallurgy; extraction of metals from deep-sea manganese nodules; coal beneficiation (360 publications)

Education:

B.S. (Metallurgical Engineering), South Dakota School of Mines and Technology, 1949
M.S. (Mineral Engineering), Montana School of Mines, 1950
Sc.D. (Mineral Engineering), Massachusetts Institute of Technology, 1953.

Professional Experience:

Assistant Professor, Dept. of Metallurgy, Massachusetts Institute of Technology (1953-1956); Section Leader Metals Research Laboratories, Union Carbide Metals Co., Niagara Falls, New York, (1956-1958); Manager, Mineral Engineering Laboratory, Kaiser Aluminum and Chemical Corporation, Permanente, California. (1958-1959); Associate Professor, (1959-1962), Professor, 1962-1992), and Chairman, (1970-1978), Dept. of Materials Science and Mineral Engineering, Univ. of California, Berkeley; Guest Professor University of London, Imperial College (1966), University of Karlsruhe (1973), Technical University of Clausthal (1984); Director, California Mining and Mineral Resources Research Institute; P. Malozemoff Chair in Mineral Engineering (1987-1992); Professor Emeritus (1993-), Professor in the Graduate School (1994-)

Optimum Design for Fine and Ultrafine Grinding Mechanisms Using Grinding Media†

Tatsuo Tanaka*

1. Introduction

Ultrafine grinding in the submicron range has currently attracted attention in connection with the development of new ceramics and electronic materials, and quite a few investigators have reported experimental data of wet process milling using grinding media. As mills using grinding media, conventional ball mills, vibration mills, planetary mills, and stirred mills are typical machineries; special interests have been focused on ultrafine grinding using grinding balls smaller than 1 mm in diameter. Based on the experimental data presented recently in Japan including the classical data well known worldwide, a general form of the selection function applicable commonly to a wide range of particle sizes if possible for various kinds of grinding mills, and the optimum ball size to maximize the rate of grinding are first dealt with in this review.

The comminution kinetics is referred to in order for the design of the ultrafine grinding mechanism to be emphasized, in which the size distribution of the finished product can be discussed in relation to the particle size and the time required. The size distribution governs the properties of the ground product so that the size distribution should be adjusted to meet the requirement by setting up a closed circuit grinding system. Various modes of the closed circuit system are considered together with the basic characteristics of the resulting size distribution as well as the basic design procedures.

Furthermore, the improvement in the rate of grinding is considered from various points of view. One possibility involves composite balls of different sizes which have been declared in most text books on comminution to be ineffective. On the contrary, this review shows that a specific size distribution of the balls may lead to an remarkable improvement in the rate of milling. Finally, physicochemical consideration is also taken into account for the purpose of grinding rate promotion. Grinding aids can be used not only for improving the grinding rate but also for the modification of the finished surface of the ground products.

* 5-12, 2-27, Sumikawa, Minami-ku, Sapporo, Hokkaido 005, Japan
Tel. 011-583-1586
† Received 16 May, 1995

1.1 Rate of ultrafine grinding related to ball size

K. Tanaka et al[1,2] reported extensive experimental data of finely grinding $BaTiO_3$ to 1.9 micron by using a ball mill and a vibration mill, varying widely the ball diameter and the specific gravity, the ball filling degree, the rotating speed or vibrational conditions as well as the slurry concentration. Among them the effect of ball size on the rate of grinding is noteworthy. The rate of grinding calculated from the specific surface area increase per unit time measured with the BET method was expressed in the form of the following empirical equation.
For ball milling

$$R_{\alpha} r^{-0.741} exp\{-(0.738/r)\} \quad (1)$$

and for vibration milling the following is obtained

$$R_{\alpha} r^{-0.633} exp\{-(0.270/r)\} \quad (2)$$

where r is the radius of a ball ranging from 15 mm down to 0.2 mm.

On the other hand, Tashiro et al[3] conducted a ball milling speed of 220 rpm with zirconia balls ranging in three stages from 1 to 15 mm in diameter D. They proposed the following empirical equation under some theoretical assumptions:

$$R_{\alpha} D^{0.89} exp\{-0.896 (D/b)^{0.278}\} \quad (3)$$

wherein b is the size of particle and D is the ball diameter.

The formulae above are somewhat similar and it is of some interests to note that Eqs(1) through (3) were obtained by taking the rate of grinding as being the product of an increasing function and a decreasing function with increasing D (or r) although the resulting expressions are quite opposite. These works, however, are extremely important contributions because they derived a general form of the selection function applicable to grinding in the submicron range

in which, if dry process had been performed, a grinding limit would have been probable.

From these studies it is suggested[1] that the ultrafine grinding predominantly proceeds by compression and shearing at the contact points between colliding balls, not by the impact of balls dropping onto the powder bed. Thus, the rate of grinding or the selection function may be proportional to the following items: (1) total number of contact points between balls, (2) collision frequency of a ball with another, (3) volume of particle nipped at a contact point for grinding, (4) pressure acting on the particles nipped by balls, (5) probability that the stress applied on the particles exceeds the inherent strength for possible fracture. Each item can be formulated as follows (1) the total number of contact points is inversely proportional to the cube of a ball diameter under a constant ball filling degree, varying with J/D^3. (2) the collision frequency can be given as a function of v/D, where v is the speed of a colliding and the mean free path varies with D. (3) the volume nipped by two balls is calculated to be proportional to Db^2 (4) the stress created by hitting balls can be expressed by the force divided by the effective contact area between a ball and the nipped particle bed. The surface area is found to be proportional to Db and to the force $\rho D^3\alpha$ where ρ is the density of a ball and α is the acceleration following a collision. Thus, the stress is proportional to $D^2\rho\alpha/b$. (5) if the stress above is smaller than the strength required to crush the material then no grinding can be expected. For this purpose the following probability P should be multiplied:

$$P = exp\{-(b\sigma_{st}/\rho D^2\alpha)\} = exp\{-(D_m/D)^n\} \quad (4)$$

$$D_m = a\ function\ of\ (\sigma_{st}b/\rho\alpha) \quad (5)$$

α is unknown but the highest acceleration of a ball dropping onto a powder bed of the tightest packing was reported to be proportional to the hitting velocity, v. The exponent n in Eq (4) appears equal to 2 dimensionally but preferably can be adjusted from experimental data. D_m is the representative ball diameter for a given material to be nipped for possible fracture by overcoming the strength. The probability P is plotted against D/D_m in **Figure 1**, where D_m is D corresponding **Figure 1** to $P = 0.368$. Therefore, the rate of grinding can be expressed by the product of the items (1) through (5), divided by the total weight of the material in the mill, considering the frequency of the materials introduced into the comminution area. The total holdup W is proportional

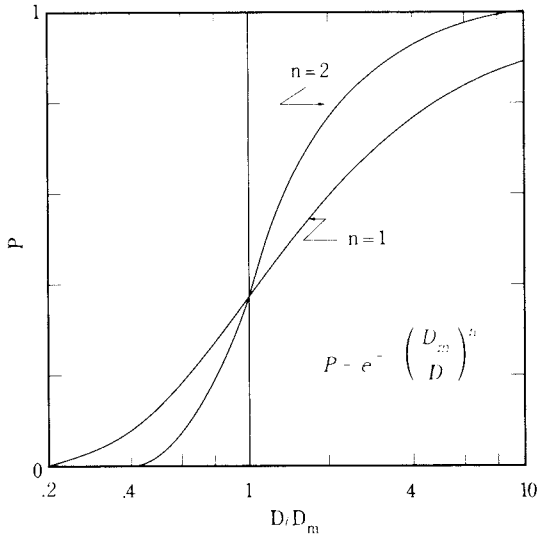

Fig. 1 Grinding probability vs. ball diameter divided by D_m

to JU, where U is the fractional filling of material per interstitial space among balls. Then we have

$$R\propto(v/D)(J/D^3)(Db^2)(\rho D^2v/b)exp\{-(D_m/D)^n\}/(JU) \quad (6)$$

or $$R\propto(v^2J\rho b/Df_c)exp\{-D_m/D)^n\} \quad (6')$$

where f_c is the fractional volume of the material inside the mill and equals JU. Compared with Eq(1) to (3), the derived formula(6′) looks like Eqs(1), (2) rather than Eq(3), as far as the effect of ball diameter on the rate R is concerned, the latter of which, however, involves b, being consistent with Eq(6′).

Differentiating the above equation with respect to D and putting the derivative equal to zero gives $D_{opt} = (1/n)^{-1/n}D_m$, wherein D_{opt} is the optimum diameter of the grinding balls and when $n=1$, $D_{opt} = D_m$, and when $n = 2$, $D_{opt} = 1.4\ D_m$. Therefore, if Eq(6′) is to be confirmed by experimental data, D_m becomes very important for determining the most efficient grinding condition for a given material.

2. Confirmation of the derived equation from various aspects

Current experimental data[5-14] including the classically well known grinding studies are listed in **Table 1**, in which the documentations are presented for ball mills, vibration mills, planetary mills and stirred mills. Most works here were carried out through a wet process and fortunately the selected data were obtained almost at the same hitting velocity, $v \fallingdotseq 1$ m/s, even with different types of mills of different sizes,

Table. 1 Published experimental conditions of various milling mechanisms for fine and ultrafine powder, using balls as the grinding media.

No	Authors and reference	Kind of mill, wet or dry	Operating conditions	Ball size and specific gravity	Hitting velocity, v (m/s)	Material crushed and size, b
1	Tanaka etal, 1)	Ball Mill, wet 20~50 % solid	D_M = 30cm, N = 58~105 r.p.m.	D = 0.4~30 mm, 2.7~7.8	0.9~1.6	$BaTiO_3$ 1.9 micron
2	ditto, 2)	Vibration, wet, 20~50 % solid	Amplitude = 3 ~7 mm, freq. = 23.5~28 Hz	D = 0.3~30mm, 2.7~7.8	0.5~1.3	$BaTiO_3$, 1.9 micron
3	Tashiro etal, 3)	Ball, wet, 4.3 vol %	D_M = 8 cm, N = 220 r.p.m	D = 1~15 mm, PSZ, 5.7	0.92	Pb (Zn, Nb, Fe, W)O_3 1.6 micron
4	Kelsall etal, 14)	Ball, continuous, wet, 66.7% solid	D_M = 12 inch, 60 r.p.m.	1/2~3/2 inch steel, 7.8/ composite	1	Calcite, 20~28 mesh, 8~10 mesh
5	Coghill & Devaney, 12)	Ball, wet,	D_M = 19 inch 50 r.p.m.	D = 0.62~2.75 inch ; 7.8	1.2	Dolomite, 0.01 ~0.07 inch,
6	Bradley, 5)	Planetary, wet, 67% solid	D_M = 6.35 cm, 4.2Hz, 8.3Hz, 16.6Hz	D = 6.4~19mm, steel, 7.8	0.84, 1.65, 3.3	Quartz, 2mm
7	Mankosa et-al, 6)	Stirred, wet, 43% solid	D_I = 10.2 cm, 200~350 r.p.m	D = 1~6mm, steel, 5mm glass, Composite	1.06~1.76// 1.6, 2.4, 3.2 mm. eq. wt.	Coal, 70micr-on.
8	Hashi etal, 7)	Stirred, wet, 30% solid	1.3 lit. Vessel	D = 1.6~2.5mm, & 0.5~0.7mm glass, 2.7	7.8	Calcite, 11.3 micron
9	Stadler etal, 11)	Stirred, wet, Visco = 1~ 500 mPas		D = 0.3~10mm steel, 7.5 glass, 2.7	14.5~19	Pigment, 15 micron
10	Kanda etal, 19)	Ball, wet, 200g/240cc water	D_M = 14 cm, 108 r.p.m.	Composite, 1.2mm, 7.8 & 20mm 3.6	1.58	Calcite, -20 mesh
11	Zhao, Jimbo, 10)	Planetary, dry,		1.2~8.4mm, 7.8/5.2mm, 3.6/1.5mm, 2.5		Quartz, 63~ 2000 micron
12	Kugimiya, 8)	Stirred, wet, 40 vol%	Vol = 1400cc	D = 0.4~10mm, PSZ, 5.7	15	Pb (Zn, Nb, Sn, Ti, Zr)O_3; 2.2 micron

so that we can cancel v temporarily in Eq(6′). First, Eq(6′) will be verified using the 4 kinds of mills data by varying the ball size to obtain the maximum value of R, the other variables remaining unchanged. Assuming D_m first then R is calculated from Eq(6′) as a function of D. **Figure 2** shows the calculated curve as compared with K.Tanaka's[1] wet ultrafine ballmilling data. A logarithmic plot reveals that a better coincidence can be brought to about $n=1$ rather than $n=2$, to be more parallel. D_m is 2 mm. Likewise, vibration milling data by Tanaka confirmed Eq(6′) where $D_m=1$ mm as shown in **Figure 3**. A similar trend was also found with the data of Coghill's ball mill fine grinding as shown in **Figure 4** where $n=1$ is still better than $n=2$.[12]

As in **Table 1** the materials used are quartz, calcite, coal, dolomite and some electronic materials like $BaTiO_3$, of which the strengths are not always clear except for calcite and quartz. Thus, it is assumed here that the strength of materials as well as the size dependence except for quartz are the same as those of calcite. The strength of some materials was reported in detail by Yashima[9] as a function of size in air and water, respectively. Evaluating D_m in this way

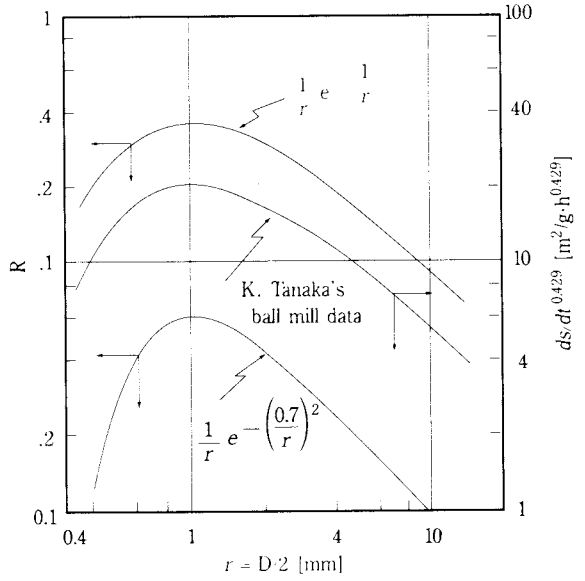

Fig. 2 Comparing the rate of ball milling by K. Tanaka with Eq(6′) in which $n=1$, 2 and $r_m=1$, 0.7 mm, respectively

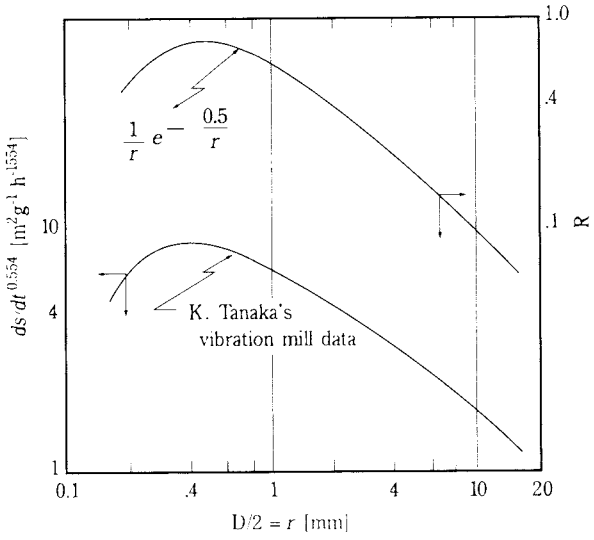

Fig. 3 Comparing the rate of vibration milling by K. Tanaka with Eq(6′) in which $n=1$, $r_m=0.5$mm

for each experiment in **Table 1**, an important correlation is found as shown in **Figure 5**, from which we have, regardless of the type of mills.[4]

$$D_m = 1.75 \times 10^{-1} (b/\rho) \sigma_{st}^{0.8} \qquad (7)$$

where *SI* units are used for ρ(kg/m^3) and σ_{st}(*Pa*) under $v=1$ – 2 m/s. Since $\sigma_{st} \propto b^{-q}$ where q nearly equals 0.5, Eq(7) becomes $D_{opt} \propto b^{0.6}$, which agrees with the conventional optimum ball size in relation to particle size.

Next, as an example for confirmation by varying b in Eq(6′), Zhao and Jimbo[10] 's planetary milling data are studied. The ball size was 8 mm with b

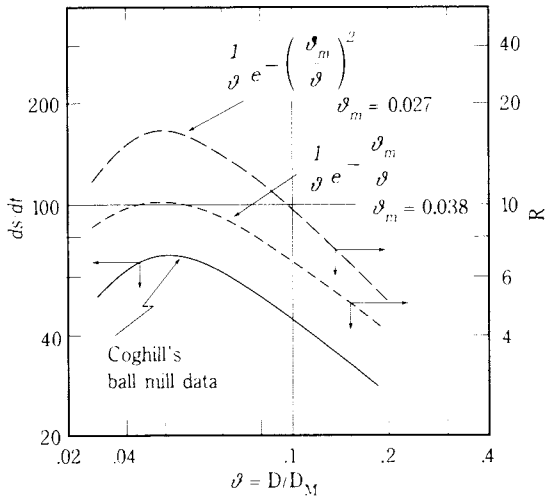

Fig. 4 Coghill's ball milling data with Eq(6′) in which abscissa ϑ is the ratio of D to D_M, the mill diameter

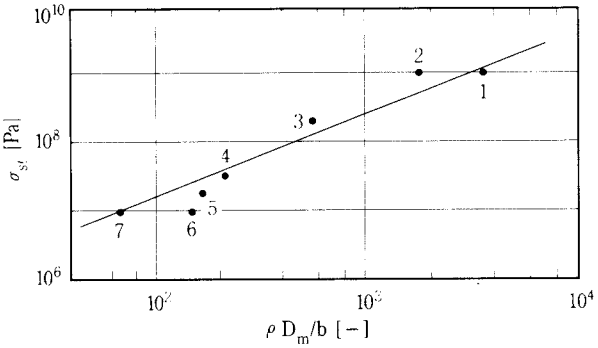

Fig. 5 Correlation between D_m, the optimum ball diameter, and other variables concerned

ranging from 60-2000 microns. Using an average value for b of some fractions together with ρ and σ_{st} gives D_m in Eq(7), which enables one to calculate R as depicted in **Figure 6**. The dotted curve was drawn by using a complex probability function, which appears to be almost proportionally coincident with Eq(6′).

The influence of the density of the balls on the rate of grinding should be almost linear in Eq(6′), whereas K.Tanaka[1,2] varying $\rho = (2.7-7.8) \times 10^3$ kg/m^3, supported this both for ball mills and vibration mills. Zhao et al[10] also recognized this effect in the planetary mill experiment, and Mankosa[6] pointed out that steel balls are clearly more efficient than glass balls with stirred mills at a lower speed of the impeller, $v=1.7$ m/s. It is very interesting, however, to note the latest report of Kugimiya[8] who stated that no effect of ball density had been recognized in the wet stirred milling with much higher rotating speed, e.g., $v=14$ m/s. This means that the 4th term in Eq(6) can be replaced by a constant shearing stress arising from the rotating

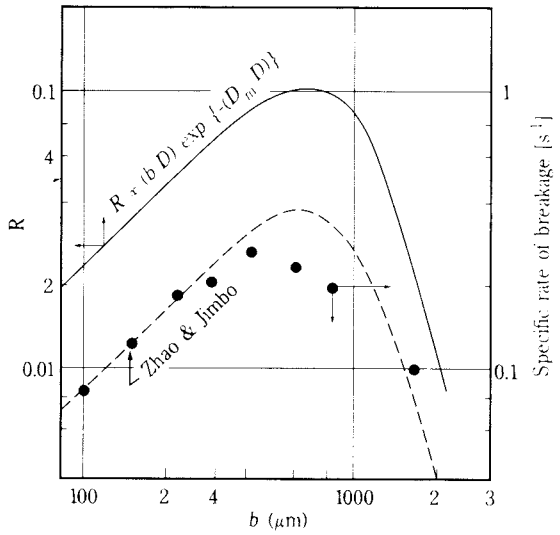

Fig. 6 Comparing the rate of milling by dry planetary mill by Zhao with Eq(6′) in terms of particle size crushed.

impellers, resulting in $R_x(b^2/D^3)$. In fact, Kugimiya[8] and Hashi[7]'s data for high speeds seem to confirm it in **Figure 7**, and more improvement would be expected with stirred mills for ultrafine grinding by varying the speed, because other types are more or less restricted in increasing the hitting speed freely due to their constructions and mechanisms.

As to the effect of J, the mill filling degree, in Eq(6′), Rose[13] stated that the rate of milling is approximately linear with J up to $J=50-60\%$ for ball mills and $J=80-90\%$ for vibration mills.[17] K.Tanaka[1] indicated that at $J=40$ and 60% the rate of grinding was the same for ball mills. Furthermore, they also did experiments of vibration milling, varying the slurry concentration[2] by holding a constant volume of water. This corresponds to the relation between R and f_c in order to check Eq(6′), which is depicted in **Figure 8**. Therefore, the comfirmation of Eq(6′) is reasonably satisfactory so far for the various terms concerned.

3. Kinetics of comminution and the selection function

The rate of grinding based on the specific surface increase per unit time has been dealt with in comparison with fine and ultrafine grinding mechanisms using balls as grinding media. On the other side, the particle size distribution of the finished product is also important as it influences the properties of the product. To discuss the size distribution in the lapse of time the kinetics of comminution is significant. Defining the selection function, $S(x, t)$ and the breakage function, $B(\gamma, x)$, a dynamic mass-size

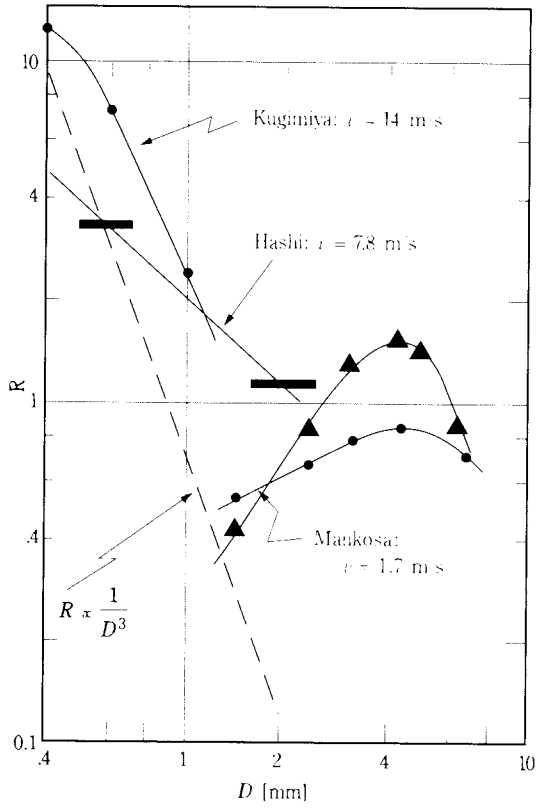

Fig. 7 Effect of colliding speed on the rate of wet stirred milling

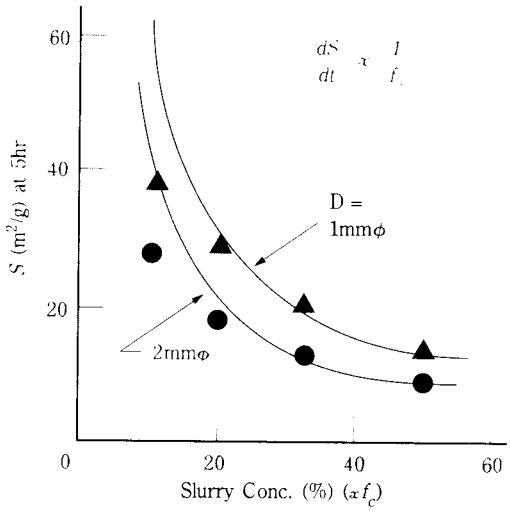

Fig. 8 Rate of vibration milling by K.Tanaka compared with Eq(6′) in terms of the fractional powder filling which is proportional to the slurry concentration

balance is taken, where agglomeration of fine particles is negligible, as

$$\partial^2 D(x,t)/\partial t\cdot\partial x = -(\partial D(x,t)/\partial x)S(x,t) + \int_x^{x_m} (\partial D(\gamma,t)/\partial\gamma)S(\gamma,t)(\partial B(\gamma,x)/\partial x)d\gamma \quad (8)$$

where $D(x, t)$ is the cumulative undersize, t the time, x the particle size, and γ is the size of a single particle to be broken. x_m is the maximum particle size present. Assuming $B(\gamma, x)=(x/\gamma)^m$, and $S(x, t)=Kx^n$, wherein K is the grinding rate constant and m, n are the exponents, respectively,[18] then Eq(8) can be analytically integrated into the following forms, $R(x, t)$ being the cumulative oversize:

When $m=n$, (mostly $n=1$)

$$R(x, t)=R(x, 0)exp(-Kx^n t) \quad (9)$$

When $m \neq n$, then

$$R(x, t) \fallingdotseq R(x, 0)exp\{-(\mu Kx^n t)^\nu\} \quad (9')$$

where μ and ν are determined from m/n, see **Figure 9**. Eq(9), (9′) have been accepted for many years as the Rosin-Rammler size distribution as a function of time and if the selection function $S(x, t)$ is replaced and is assumed to be proportional to R in Eq(6′), i.e. the particle size x is replaced by b in Eq(6′) in the range where R is proportional to b as in **Figure 6**, then the rate constant K can be regarded as a definite function of the various parameters involved. This might make it possible to regulate the size distribution of a product by adjusting the operating variables of the mills. Namely, where $R \propto b$ and $x(=b)$ are constant, $R \propto S(x, t) \propto K$. Then, we have from Eq(6′)

$$Sf_c \propto Kf_c \propto (v^2 J\rho/D)exp\{-(D_m/D)\} \quad (10)$$

This suggests a possible contribution of the operating variables of a mill to the rate constant K which controls the size distribution of a product. **Figure 10** represents the product of the experimental selection function of a ball mill by the fractional holdup f_c together with J and U, proposed by Shoji et al[20]. Eq(6′) indicates that Sf_c varies with J, but is independent of U, whereas **Figure 10** indicates a similar tendency.

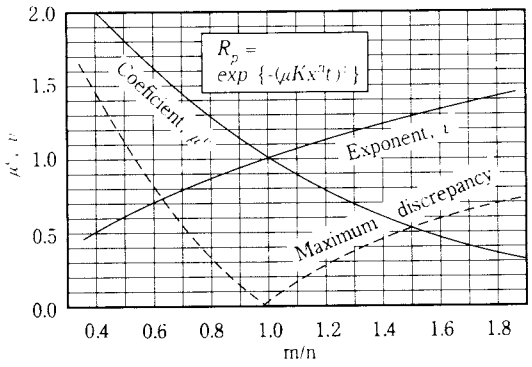

Fig. 9 μ and ν in relation to m/n as the result of analytical integration of Eq (8)

4. Size distribution controlled by various modes of closed circuit system

Size distribution can be regulated by adopting the closed circuit grinding system composed of a mill and a classifier as schematically shown in **Figure 11**. The theory has been dealt with elsewhere[21] regarding the case where both a clean cut classifier and a nonideal classifier are involved, and, a nomography was given for the former as in **Figure 12**, to readily obtain the necessary parameters for designing the circuit. The basic equations are

$$R_p(x/x_c^*)=(1+C1)exp\{-(x/x_c^*)^n/(1+C1)\}-C1 \quad (11)$$

$$(x_c/x_c^*)^n=(1+C1)ln\{1+(1/C1)\} \quad (12)$$

$$x_c^{*n}=F/KW \quad (13)$$

where R_p is the cumulative oversize of the product, $C1$ is the circulating load ratio (= mill return/product), x_c the cutoff size of the classifier, and x_c^* is the characteristic parting size when $C1$ tends to infinity. F is the feed to the circuit, W the holdup of particles in the mill and K is the grinding rate constant mentioned above. A mill design should be based on W in Eq(13) using K. Somewhat modified circuits have

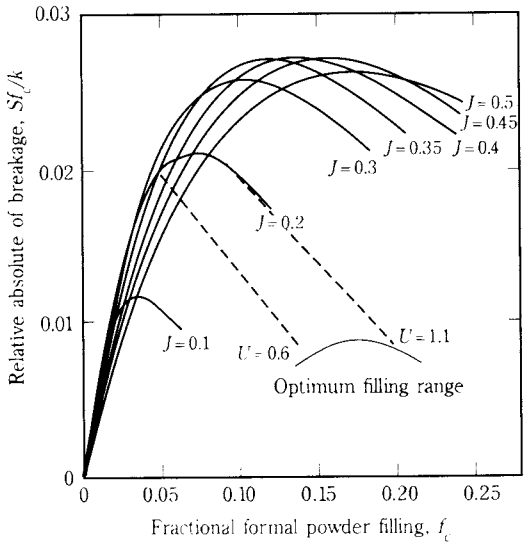

Fig. 10 Relationship between the selection function and the fractional powder filling in a ball mill, presented by Shoji et al

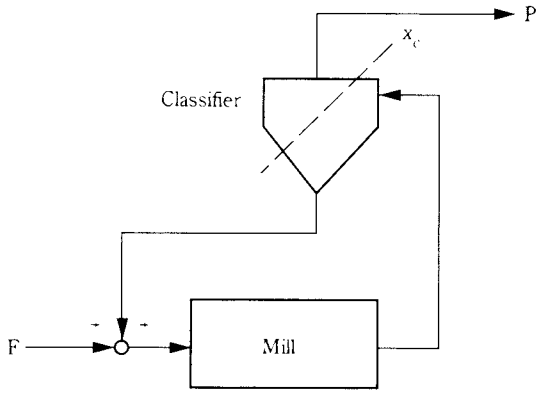

Fig. 11 Standard type of closed circuit grinding system

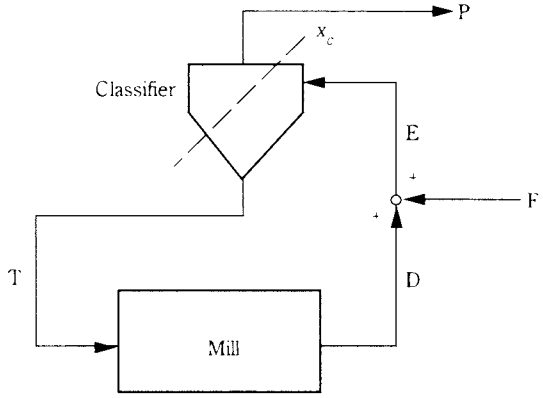

Fig. 13 Closed circuit grinding system of which feed location is different from the standard type

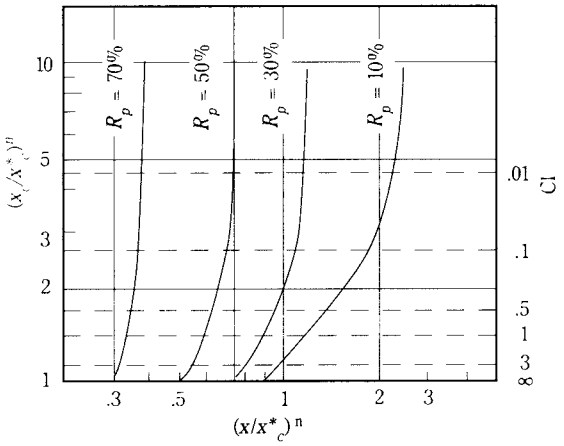

Fig. 12 Numerical relationship among $R_p(x/x_c^*)$, $(x/x_c^*)^n$, $(x_c/x_c^*)^n$ and $C1$ for the standard type

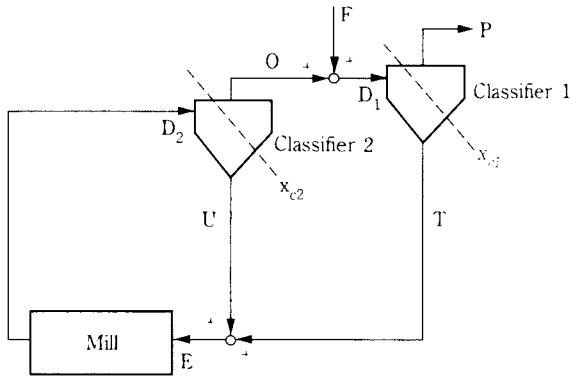

Fig. 14 Closed circuit system in which one mill and two classifiers are involved

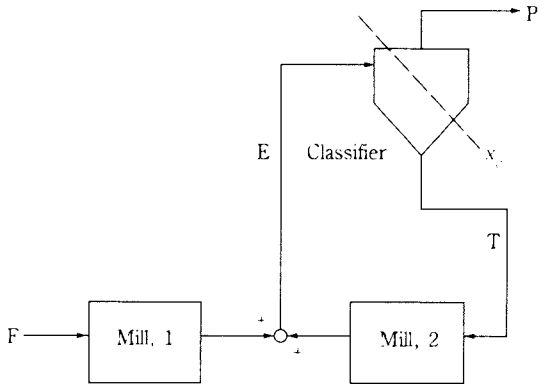

Fig. 15 Closed circuit system in which two mills and one classifier are involved (Type 1)

been considered in industry as in **Figures 13** and **14**,[22] the characteristics of them are that the feed materials are first introduced into a classifier before entering a mill. The latter uses two classifiers. As a result of the analysis of these circuits, the nomograph in **Figure 12** can be used as it stands, except that $C1 = 1 + "C1"$ for **Figure 13** and $C1_1(1 + C1_2) = 1 + "C1"$ for **Figure 14**, where "$C1$" is the value of $C1$ derived from **Figure 12** to fulfill the same design requirement with the use of a standard scheme as shown in **Figure 11**. The suffixes 1, 2 denote the number of the classifiers indicated, resp. Generally, the product of $C1$ added by 1 means an advantage in the grinding capacity. On the other hand, two other schemes of closed circuit grinding systems are introduced in **Figures 15** and **16**, both of which are featured by using two mills and one classifier. The analysis of those circuits provides another nomograph to find out the necessary parameters for the design of those schemes (Type 1 and Type 2, respectively) as shown in **Figure 17**. **Figure 18** illustrates the calculated size distribution of the product with each scheme as well as the circulating load. It should be emphasized here that $C1$ being infinity appears

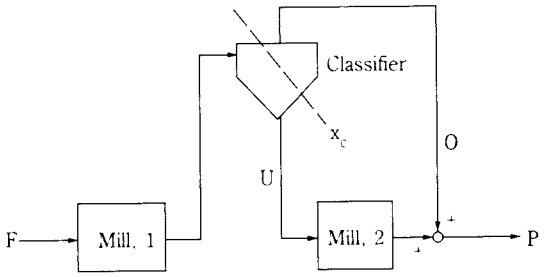

Fig. 16 Closed circuit system in which two mills and one classifier are involved (Type 2)

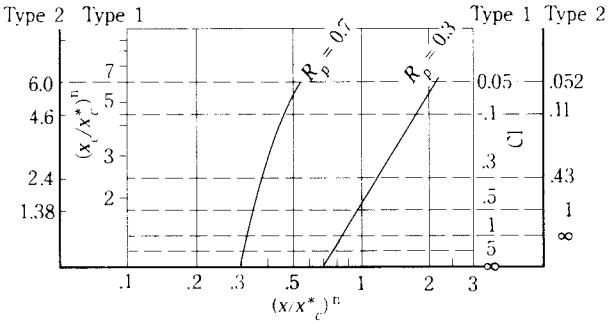

Fig. 17 Numerical relationship among $R_p(x/x_c^*)^n$, $(x/x_c^*)^n$, $(x_c/x_c^*)^n$ and Cl for the Type 1 and Type 2

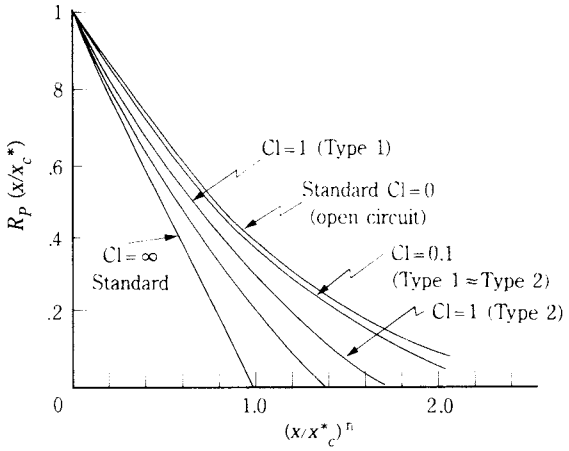

Fig. 18 Calculated size distribution of product of various schemes of closed circuit with various circulating load ratios using clean cut classifiers

impossible in a real closed circuit but this is practically realized in a mill of an air swept system, for example. This corresponds to the mechanism where only fine particles producing smaller than x_c should instantaneously be discharged from the mill, the theory of which was reported by Ouchiyama et al.[23]

5. Possibility for increasing the rate of grinding

Now let's come back to the rate of grinding affected by the size of the grinding media. In view of the most experimental data in the past we feel that the size of balls was uniform and very few studies dealt with composite balls. Some books on comminution[15, 16] stated that the exponent q should be nearly 3 in the Gaudin-Schuhmann expression, $P(D) \propto D^q$, where $P(D)$ is the cumulative undersize weight distribution with respect to ball size D. Based on this equation, the number frequency $f(D)$ becomes

$$f(D) = D^{q-4} / \int_{D_s}^{D_l} D^{q-4} dD \tag{14}$$

The average ball diameter $\overline{D}$ is therefore given by

$$\overline{D} = \int_{D_s}^{D_l} Df(D)dD = D_1 \{(q-3)(1-k^{q-2})/(q-2)(1-k^{q-3})\} \tag{15}$$

where $k = D_S/D_l$, the ratio of the smallest size, D_S, to the largest one, D_l. $\overline{D}$ can be used in items (2) through (5) mentioned in the 1st section. Next, regarding item(1) we can use the Ouchiyama et al's formula for the number of contact points of a random assemblage, C_T.[24]

$$C_T = 16(1-\mathcal{E})\ N\ \{3+(\overline{D^2}/\overline{D}^2)\}/4 \tag{16}$$

where $\mathcal{E}$ is the porosity for a single size ball, N the total number of balls and $\overline{D^2}$ is the average square diameter. They are expressed by using K, q, D_l and W', the total weight of balls, respectively, as

$$N = (6W'/\pi\rho D_l^3)\{q(1-k^{q-3})/(q-3)(1-k^q)\} \tag{17}$$

$$\overline{D^2} = \int_{D_s}^{D_l} D^2 f(D)dD = D_l^2(q-3)(1-k^{q-1})/(q-1)(1-k^{q-3}) \tag{18}$$

Substituting Eq(15) through(18) into Eq(6′) we have the rate of grinding at constant b and f_c as well as $P=1$ for the case of a composite ball size.

$$R \propto (W'/D_l)(q/1-k^q)[3\{(q-3)/(1-k^{q-3})\} \cdot \{(1-k^{q-2})/(q-2)\}^2 + (1-k^{q-1})/(q-1)]/4 \tag{19}$$

Setting the ratio of W'/D_l to be unity, R is computed as a function of q and k and given in **Figure 19**. It is at once noted that as q tends to be small R is likely to increase, so that the larger size distribution of the balls appears to be preferable.

Only three runs of experiments listed in table 1,

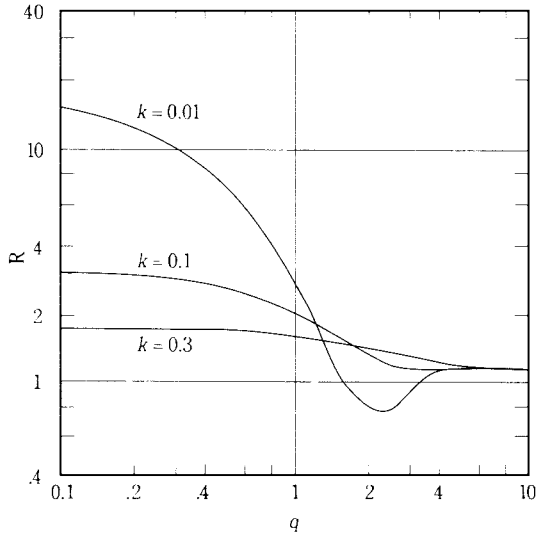

Fig. 19 Calculated improvement of grinding rate by using the composite ball size of various size distributions.

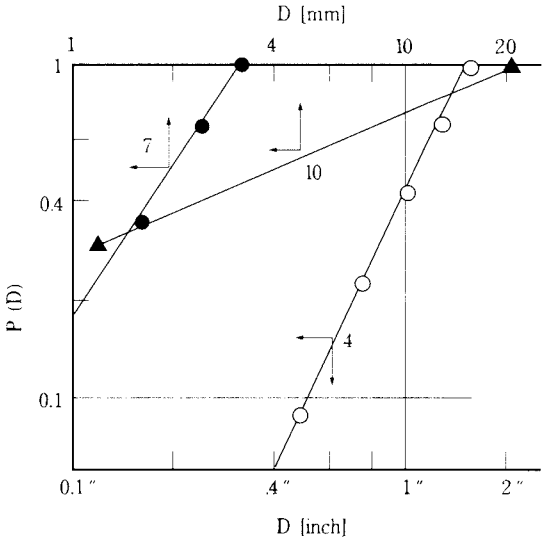

Fig. 20 Gaudin-Schuhman plot of ball size distribution, to determine q

i.e. Kelsall (5 components), Mankosa (3 components) and Kanda (2 components) were compared with uniform sized media. Based on the documents q and k are available for all experiments to calculate R from Eq(19). See **Figure 20**. The net increase of the grinding rate can be calculated from $R(P/P_1)$ -1, where P and P_1 correspond to D and D_1 resp., in Eq(4). The calculation resulted in 7% as compared with the 8% increase obtained with experimental data given by Kelsall,[4] whereas 21% was obtained compared with 23% for the reported Mankosa's[7] experiment. Finally, Kanda reported ultrafine grinding of calcite in a ball mill with a mixture of steel balls of $D=1.2$ mm and alumina balls of $D=20$ mm at a number ratio of 1000:1, the total weight being 2 kg compared to the single size of alumina balls of $D=20$ mm, the total weight being 2 kg.[19] From **Figure 20**, the necessary parameters are obtained as $q=0.5$ and $k=0.06$, which yield $R=3.2$ from Eq(19). The experimental data demonstrated that the grinding rate was 3 times that obtained with single sized balls, indicating an outstanding increase and a satisfactory agreement with the calculation. In **Figure 19** we see that R never change too much with q greater than 3. This does not contradict the experience which has been stated in textbooks which indicate composite balls were not effective.

It can be concluded that for fine and ultrafine grinding considerable improvements may still be expected by selecting appropriate grinding mechanisms as well as operating variables as described above. Moreover, an emphasis should be put upon the physicochemical devises that make it possible to increase the rate of grinding. The strength of a material σ_{st} is given by

$$\sigma_{st} \doteqdot \sqrt{Y\lambda/c} \tag{20}$$

where Y is the Young's modules, λ the surface energy and c is the crack length. Wet process and addition of some surfactants serve as reducing λ by adsorption effect on the solid surface, leading to a decrease in the strength, σ_{st}. These additives are called grinding aids which have been noted for use to modify a fresh surface exposed to grinding, taking advantage of the reactivity. This assists fine particles to be well dispersed, resulting in better grinding efficiency. It has been reported that about a 20 time improvement was secured in the rate of grinding. Cryogenic grinding is also an application of physical chemistry, which reduces the toughness $\sqrt{Y\lambda}$ to assist crushing.

Conclusion

Contribution of various parameters regarding grinding mechanisms using balls was reviewed theoretically and compared with current experimental data of fine and ultrafine grinding in the submicron range. An important correlation was obtained between the optimum ball size and density, and the size and the strength of a material regardless of the kind of machinery. The comminution kinetics was discussed not only in relation to the rate constant as a function of these parameters for design procedure, but also for the adjustment of particle size of the product by varying the closed circuit grinding schemes. A new

proposal for the size distribution of balls has been made for securing the improvement of the rate of grinding, although it appears generally pessimistic in text books. Other various trials are to be considered from different aspects of comminution techniques.

Nomenclature

$B(\gamma, x)$	: breakage function	[−]
b	: particle size of material	[mm]
C_T	: total number of contact points	
c	: crack length	[m]
$C1$	: circulating load ratio	[−]
D	: ball diameter	[mm]
$\overline{D}$	: average ball diameter	[mm]
$\overline{D^2}$	: average square diameter	[mm]
D_1	: impeller diameter	[mm]
D_M	: ball mill diameter	[mm]
D_m	: representative ball diameter	[mm]
D_{opt}	: optimum ball diameter	[mm]
D_l, D_s	: max. and min. ball diameter	[mm]
$D(x, t)$	: Cumulative undersize of particles	[mm]
F	: feed to the circuit	[kg/s]
$f(D)$	: frequency ball size distribution	[1/mm]
f_c	: fractional volume of holdup	[−]
J	: mill filling degree	[−]
K	: grinding rate constant	[1/s.mm^n]
$P(D)$	: cumulative undersize of ball size distribution	[wt] [−]
q	: exponent	
$R(x, t)$	: cumulative oversize of particles	[−]
R_p	: R(x) of product	[−]
R	: rate of grinding	[m^2/kg.s, 1/s]
r	: radius of ball	[mm]
$S(x, t)$	: selection function	[1/s]
S	: specific surface	[m^2/kg]
t	: time	[s]
U	: fractional holdup per interstice of balls	[−]
v	: hitting speed	[m/s]
W	: holdup of materials in a mill	[kg]
W'	: total weight of balls	[kg]
x	: particle size	[mm]
x_c	: classifier cut size	[mm]
x_c^*	: characteristic cutsize	[mm]
Y	: Young's modulus	[Pa]
α	: acceleration due to collision	[m/s^2]
γ	: particle size to be broken	[mm]
k	: ratio of min. to max. diameter of ball	[−]
m	: exponent	
N	: total number of balls	[−]
n	: exponent	
P	: crushing probability	[−]
P_1	: P for $D = D_1$	[−]
λ	: surface energy	[J/m^2]
$\mathcal{E}$	: porosity of balls	[−]
ρ	: density of ball	[kg/m^3]
σ_{st}	: :breakage strength	[Pa]
ζ	: shearing stress	[Pa]
μ, ν	: parameters determined from m/n	

References

1) Tanaka, K.et al: J.Soc.Mat.Sci. Japan 35, 54 (1986); 36, 29 (1987)
2) Tanaka, K.et al: J.Ceramic.Soc., Japan, 95, 579 (1987)
3) Tashiro, S.and H.Igarashi: ibid., 98, 1082 (1990)
4) Tanaka, T.: J.Soc.Powder Tech., Japan, 31, 25 (1994)
5) Bradley, A.A.: Dechem.Mono.Zerklein.Symp.Cannes, B69, 1292, S.781 (1971)
6) Mankosa, M.J.et al: Powder techn., 49, 75 (1986)
7) Hashi, Y. and M.Kusunoki: 24th Symp. Text 135 (1989)
8) Kugimiya, K.: Micromeritics, 36, 177 (1992)
9) Yashima, S. and F, Saitoh: J. Soc. Powder techn., Japan, 16, 714 (1979)
10) Zhao, Q. and G. Jimbo: ibid., 25, 603 (1988)
11) Stadler, R.et al: Chem. Ing. tech., 62, 907 (1990)
12) Coghill, W.H. and F.D.Devaney: U.S.Bur.Mines, Tech. Paper, 581 (1937)
13) Rose, H.E. and R.M.E.Sullivan: Ball, Tube, Rod Mills, P.158, Constable (1958)
14) Kelsall, D.F.et al: Powder Techn., 1, 291 (1967/8)
15) Slegten, J.A.: Sympo/Zerklein.Frankfurt a/M, S355 (1962)
16) Beke, B: Process of Fine Grinding. p89, Akademiai Kiado (1981)
17) Rose, H.E. and R.M.E.Sullivan: Vibration Mills, p.99, Constable (1961)
18) Nakajima, Y. and T.Tanaka: IEC, Proc.Des.Dev. 12, 23 (1973)
19) Kanda, Y. et al: J.Soc.Powder Tech. Japan, 26, 406 (1989)
20) Shoji, K. and L.G.Austin: Powder Techn., 31, 121 (1982)
21) Furuya, M.et al: IEC., Proc.Des. Dev., 10, 449 (1971); 12, 18 (1973)
22) Tanaka, T.: J.Soc.Powder Tech. Japan, 31, 333 (1994)
23) Ouchiyama, N.et al: IEC.Proc.Des. Dev., 15, 471 (1976)
24) Ouchiyama, N. and T.Tanaka: IEC, Fundamental, 19, 338 (1980)

Author's short biography

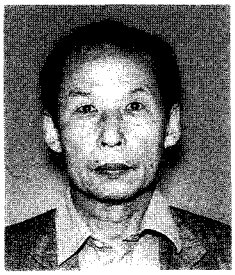

Tatsuo Tanaka

Tatsuo Tanaka is a graduate in Chemical Engineering from Kyoto University, where he received Doctor's degree in 1957. He studied as a Fulbrighter in 1958 through 1960 at the University of Minnesota. After working at Kanazawa University he was appointed in 1962 to be Professor of Chemical Engineering at Hokkaido University where he taught and conducted research until his retirement in 1990. His research interests are mainly concerned with the kinetics theory of particulate processes, particularly in comminution, tumbling granulation, solid- solid reaction, spontaneous ignition as well as dust explosion. For those works he was awarded by the Japan Society for Chemical Engineers in 1988 and the Society of Powder Technology, Japan, in 1989. He experienced visiting professors in Taiwan and Australia in the past. Now he is assigned Professor Emeritus, Hokkaido University, and currently once in a while he enjoys giving lectures upon the domestic and international requests.

Review

Ultrasonic Particle Sizing†

P. Khatchikian[1], U. Riebel[1], U. Kräuter[2]
[1]*Institute of Mechanical Process Engineering, Technical University Cottbus**
[2]*Institut of Mechanical Process Engineering and Mechanics University Karlsruhe***

Abstract

The measurement of particle size distributions and particle concentrations is an important task in laboratories and in technical processes that deal with suspensions. Especially the instruments designed for on-line applications in production processes mostly evaluate the interactions of light with the suspended particles, viz. extinction, scattering and diffraction. While the interaction of particles with ultrasonics is essentially the same as with light, the application of ultrasonics offers special technical advantages, which are due to the extremely broad range of wavelengths and the coherent detection of ultrasonic waves. Ultrasonic spectrometry makes possible the on-line measurement of the particle size distribution and particle concentration in suspensions at concentrations of up to 30% by volume without diluting the suspension. This paper is intended to introduce the reader to the fundamentals of ultrasonic particle sizing and to explain present efforts in this field. In the last section, some successful realizations of ultrasonic particle sizing instruments are presented.

1. Introduction

Multiphase systems, especially those consisting of solid particles dispersed in a liquid, are encountered in many technical processes. Knowledge of the dispersion state of these systems is desired in most cases, whether to evaluate product quality, to optimize the efficiency of the following processing units or to operate closed-loop process-control devices. The last-mentioned case seems to be the most challenging for the technology of measurement, since fast on-line systems have to be provided. The information on the dispersion state is basically required in terms of particle concentration and particle size distribution (PSD).

A number of highly developed instruments based on light extinction, scattering or diffraction measurement are available for laboratory use, but a succesful application in on-line control is problematic for various reasons: Due to multiple-scattering problems, the solids concentration is restricted to values much lower than those encountered in typical processes. Diluting the suspension before measuring is impracticable, since it increases the total cost of the system considerably and because dilution can cause changes in the dispersion state, esp. with sensitive particles such as soluble crystals, fragile flocs, etc. Further, the wavelenth of the available light sources is restricted to a discrete value (when using lasers) or to the rather narrow range of visible light, together with the adjacent regions of ultraviolet and infrared, which spans just about a decade in terms of wavelength. As a consequence, the wavelength of radiation used with optical systems cannot be adapted to the particle sizes in order to achieve a certain particle-wave interaction behaviour.

Ultrasonic waves exhibit many parallels to light, but there are important differences in practical use:

- The frequency (and thus the wavelength) is variable over a wide range.
- Ultrasonics penetrate almost any material, making measurements in coloured and even opaque media possible. Dynamic ranges of up to 100 dB can be achieved.
- Ultrasonic receivers are coherence-selective detectors and hence have a low sensivity for scattered and multiply scattered waves.
- The different mechanisms of particle-wave interaction allow different approaches for an ultrasonic-based measurement system.
- Since lenses, etc. are not needed, mechanical stability is a minor problem.

Overall, ultrasonics offer enough interesting properties to justify the development of ultrasonic-based

* P.O. Box 10 13 44, D-03013 Cottbus, Germany
** D-76128 Karlsruhe, Germany
† Received 29 May, 1995

measurement systems for the monitoring of particle size distribution and concentration. In fact, this has led to the development of commercially built on-line and in-situ PSD analysers on the base of frequency-dependent extinction measurements that cover a broad range of particle sizes and can cope with extremely high particle concentrations.

This paper is intended to introduce the reader to the fundamentals of particle size analysis by means of ultrasonic waves and to review some successful realizations of particle size analysers. First, the different mechanisms of interaction between particle and wave are surveyed to provide a fundamental understanding of ultrasonic extinction and related phenomena. Then, the history of ultrasonic particle sizing from the early beginnings to the present state is reviewed. The focus is on developments that have already gained practical relevance.

2. Particle-wave interactions[1)]

The physical background of ultrasonic particle sizing is complicated, as a variety of different mechanisms of interaction between particles and waves are superimposed and hence interfere with each other. The interaction of ultrasonic waves with suspended particles manifests itself a) in backscattering of the ultrasonic wave, b) in an extinction of the wave and c) in an influence on the wave propagation velocity (**Figure 1**).

As is subsequently shown, the influence of suspended particles on wave propagation velocity is extremely dependent on material properties such as the fluid viscosity, particle and fluid densities and compressibilities. Hence, gaining information on the particle system by measuring the wave propagation velocity is problematic and has not yet been applied to the analysis of particle size distributions successfully. On the other hand, the velocity of sound in suspensions can be measured very precisely with an adequate technical setup, as shown below; so this approach should not be excluded from the first.

Nevertheless, this paper is focused on the discussion of extinction, which is much better investigated. In the following section, the different interaction mechanisms are discussed in detail to offer a more comprehensive understanding of ultrasonic extinction and the possibilities of applying it to particle size measurements.

At low particle concentrations, the Bouguer-Lambert-Beer Law (BLBL) is valid for the formal description of ultrasonic extinction. This law is derived from an

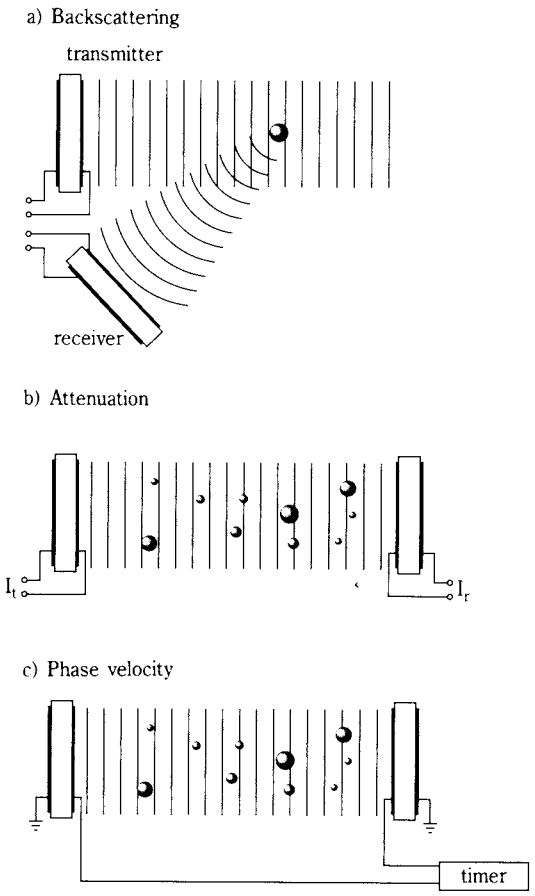

Fig. 1 Principles of particle detection: Backscattering, extinction, phase velocity.

intensity balance for an infinitesimally thin layer of suspension:

$$dI = -I\alpha_{Ext,DS} \cdot \Delta z \tag{1}$$

where $\alpha_{Ext,DS}$ is the extinction coefficient of the disperse system. By integration, this leads to an expression for the transmission T

$$T = I/I_0 = \exp\{-\alpha_{Ext,DS} \cdot \Delta z\} \tag{2}$$

and the extinction E

$$E = -\ln I/I_0 = \alpha_{Ext,DS} \cdot \Delta z \tag{3}$$

In both cases, I_0 and I are the radiation intensities transmitted in the absence and presence of particles, respectively, and Δz is the pathlength.

From the physical point of view, it is most appropriate to express the particle concentration in terms of the particle projectional area per unit fluid volume:

$$C_{PA} = \frac{\text{particle projectional area}}{\text{suspension volume}} \tag{4}$$

and to describe the intensity of particle-wave interaction in terms of the extinction efficiency K:

$$K = \frac{\text{extinction cross-section}}{\text{particle projectional area}} \tag{5}$$

With that, the extinction coefficient of the disperse system can be interpreted as the product of the particle extinction efficiency with the particle projectional area concentration:

$$\alpha_{Ext,DS} = K \cdot C_{PA} \tag{6}$$

For practical purposes, it can be more useful to describe $\alpha_{Ext,DS}$ in terms of the volume-related particle extinction coefficient, α_{Ext}, and the particle volume concentration, C_V:

$$\alpha_{Ext,DS} = \alpha_{Ext} \cdot C_V \tag{7}$$

Of course, both interpretations should lead to consistent results, which is expressed by the equality:

$$\alpha_{Ext} = \frac{\text{extinction cross-section}}{\text{particle volume}} = \frac{1.5}{x} K \tag{8}$$

With α_{Ext}, the BLBL can be written as:

$$-ln \frac{I}{I_0} = \alpha_{Ext} C_v \Delta z \tag{9}$$

As with light, the predominant parameter in ultrasonic particle-wave interaction is the relationship between particle size x and wavelength λ, conventionally expressed by the particle size parameter

$$\sigma = \frac{\pi x}{\lambda} = \frac{\pi x f}{c_F} \tag{10}$$

c_F: phase velocity in the fluid.

It can be shown that the different mechanisms of particle-wave interaction causing extinction are related to certain regimes of the particle size parameter σ. Therefore, it is useful to describe the extinction behaviour of suspended particles in terms of the extinction efficiency K as a function of σ for the entire parameter range. As a typical example of the behaviour of solid particles, **Figure 2** illustrates the extinction efficiency of glass beads suspended in water. With large particle size parameters ($\sigma > 1$), scattering is the predominant interaction mechanism and only one parameter, σ, is required to trace the extinction function in this range. With small particle size parameters (Rayleigh range, $\sigma < 1$) however, entrainment is the dominant interaction mechanism and K possesses a pronounced dependence on both the particle size parameter and the particle size itself. Further, K may vary by several orders of magnitude depending on the particle and fluid densities and the fluid viscosity.

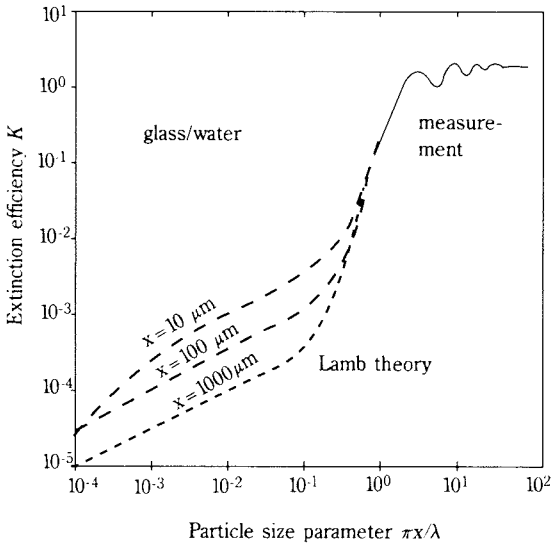

Fig. 2 Extinction efficiency K of glass beads suspended in water as a function of the particle size parameter σ[1].

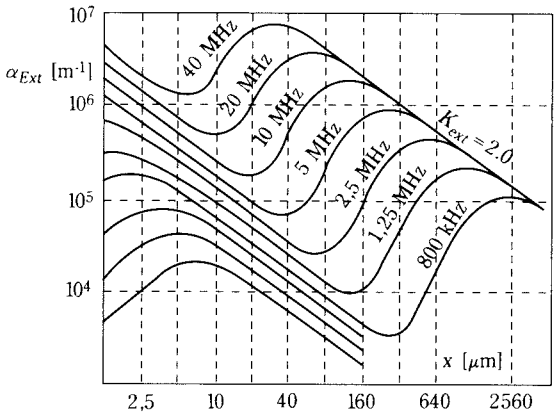

Fig. 3 Extinction coefficient α_{Ext} as a function of particle size and frequency.

Values of α_{Ext} calculated with a formula by *Lamb* and *Wolters* demonstrate the dependence of extinction on the frequency f and the particle size x (**Figure 3**). With particles of 40μm, for example, extinction at 40 MHz exceeds the value at 5 MHz by two orders of magnitude. Only for high frequencies and particle sizes do the curves coincide, since K is constant in this domain.

2.1 Mechanisms of particle-wave interaction

Going into more detail, the interaction of suspended particles with ultrasonics may be understood as being an additive superposition of the three principal interaction mechanisms depicted in **Figure 4**, viz., entrainment, scattering and resonance. Driven by pressure gradients and viscous drag forces, a suspended particle will participate in the translational movement of the surrounding fluid, but with a different amplitude and with a certain phase-lag[2,3]. For ultrasonic frequencies below a certain transition frequency f_t, the entrainment is dominated by viscous drag forces. Particle and fluid translational amplitudes tend to be equal and the phase-lag becomes very small; therefore, this regime is referred to as the regime of perfect

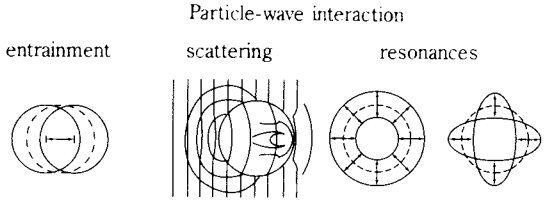

Fig. 4 Mechanisms of particle-wave interaction[1].

entrainment. The suspension as a whole may be regarded as a continuum with respect to ultrasonic propagation. As a consequence, ultrasonic extinction is very low, but the wave propagation velocity in the suspension, c_{Susp}, may differ considerably from the wave propagation velocity in the pure suspending fluid, c_F . An approximate value is calculated as

$$c_{Susp} = \frac{1}{\sqrt{\varkappa_{Susp}\,\rho_{Susp}}} \tag{11}$$

where

$$\varkappa_{Susp} = C_V \varkappa_p + (1 - C_V)\varkappa_F$$

$$\rho_{Susp} = C_V \rho_p + (1 - C_V)\rho_F \tag{12}$$

Depending on particle and fluid properties, the ultrasonic velocity can be increased or reduced by the presence of particles. For solid and liquid particles, the velocity changes to be expected are comparable to the velocity changes caused by moderate temperature variations.

The transition frequency f_t itself depends on the hydrodynamic properties of the suspending fluid and on the size of the particles. According to *Skudrzyk*[2], f_t is calculated as

$$f_t = \frac{6\eta_F}{\pi \rho_F x^2} \tag{13}$$

For frequencies above f_t and particle sizes still small compared with the wavelength, the translational movement of particles is dominated by pressure gradients and the relation of particle amplitude to fluid amplitude depends only on the particle and fluid densities. This interaction regime is therefore characterized as that of partial entrainment. With particles that are large in comparison with the wavelength, entrainment is of only marginal importance as the average of the hydrodynamic forces acting on the surface of a large particle is small compared with inertia and the particle remains stationary, interacting only by scattering.

Resonances may be excited in all deformable particles. Resonances include oscillations of the particle volume (monopole resonance) and oscillations of the particle shape (dipole and multipole resonances). A special case of great practical interest is the monopole resonance of gas bubbles, which has been intensively investigated. The approximate frequency of resonance is calculated as

$$f_{Res} = \frac{1}{\pi x}\sqrt{\frac{3\chi p}{\rho_F}} \tag{14}$$

which corresponds to the particle size parameter of resonance:

$$\sigma_{Res} = \frac{1}{c_F}\sqrt{\frac{3\chi p}{\rho_F}} \tag{15}$$

For air bubbles in water at ambient pressure, values of about $\sigma_{Res} = 0.014$ are obtained. The monopole resonance of gas bubbles is combined with extremely high extinction efficiencies ($K_{Res} = 100-400$) and with significant changes in the wave propagation velocity[4,5,6,7] (**Figures 5** and **6**).

For small particle size parameters (ca. $\sigma<0.1$), the extinction behaviour of particles can be treated analytically, including scattering and the effect of translational particle-wave interactions[3]. The validity of the obtained equation was investigated experimentally by *Wolters*[9] and was found to give reasonable results in the case of rather dense particles ($\rho_p = 2.5$ g/cm^3, ($\rho_F = 1.0$ g/cm^3), whereas in the case of a low density difference between particle and fluid, the experimental values were considerably higher than those predicted.

In the range of higher particle size parameters, more elaborate theories must be applied in order to calculate the scattering cross-sections. Based on the work of

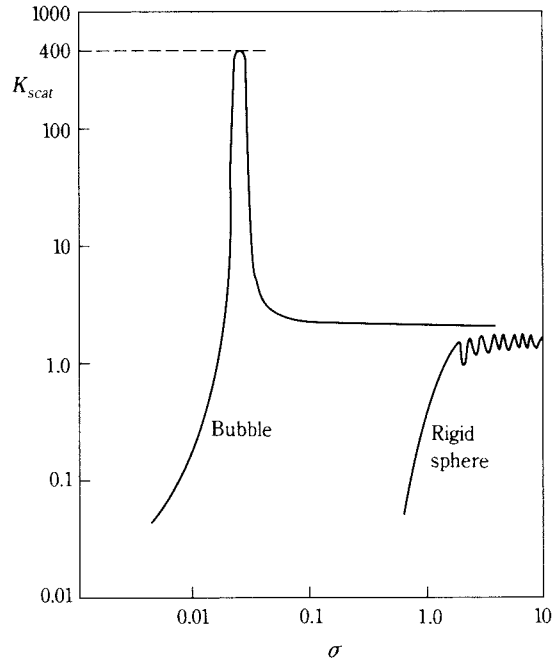

Fig. 5 Ratio of the total scattering cross-section to geometrical cross-section K as a function of the particle size parameter σ for a bubble and for a rigid sphere[8] (schematic graph).

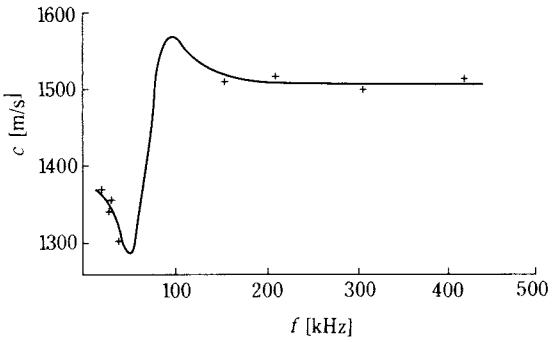

Fig. 6 Measured and calculated phase velocity c as a function of the frequency near resonance[4].

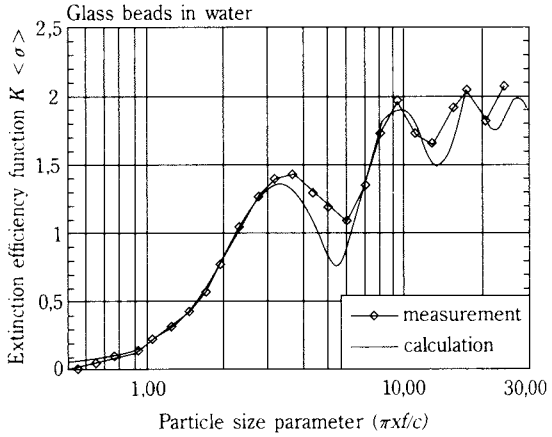

Fig. 7 Calculated and measured extinction efficiency function in the range of $\sigma > 1$[12].

Hay and *Mercer*[10] and *Faran, Jr*[11], *Kräuter*[12] calculated the extinction efficiency function $K(\sigma)$ analytically and compared it with measured values (**Figure 7**). The two curves show good agreement, although some assumptions are inherent in the calculation: The viscosity of the fluid, absorption in the particles and heat transfer in the system have to be negligible. In other cases, where these conditions are fulfilled less strictly, rather important discrepancies may occur between calculations and experimental results.

Attempts to calculate the velocity of sound in suspensions are known for low particle size parameters ($\sigma < 1$)[13,14]. These theories predict a constant value of phase velocity for $\sigma < 0.001$ (according to Eq. (11), perfect entrainment) and a rise from that particle size parameter on to the end of validity around $\sigma = 1$. The exact shape of the curves depends on the material data, viz. the viscosity of the fluid and the densities and compressibilities of both the solid and the liquid phase. Experimental results[12] with particle size parameters of ca. $\sigma = 0.005$ to 0.1 confirm the theories to some degree. Measurements of the ultrasonic phase velocity in a broad range of the particle size parameter are presented in **Figure 8**. For low values of σ, the phase velocity rises with σ as predicted by the theories. In the range of medium particle size parameters, an oscillation of c can be observed that obviously passes into the value of the pure suspending fluid when σ reaches infinity. The similarity to the extinction efficiency function (**Figure 2**) in the range of high values of σ is quite remarkable.

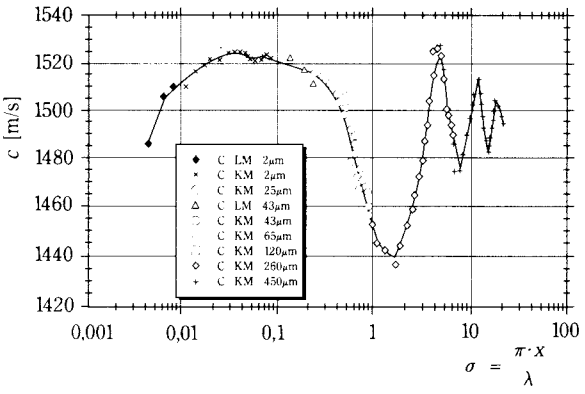

Fig. 8 Measured phase velocity of ultrasound as a function of the particle size parameter σ for glass beads of $x = 2\mu m$ to $450\mu m$ suspended in water[12].

3. Particle-particle interactions; extinction in Concentrated Suspensions[15,16]

A major advantage of ultrasonics compared to light is the possibility of making measurements in highly

concentrated suspensions. This section deals with the phenomena due to particle-particle interactions that occur in suspensions with increasing particle concentration. The significance of this discussion is due to the fact that so far, the evaluation of ultrasonic extinction measurements is ultimately based on the Bouguer-Lambert-Beer law of extinction, while the validity of this law is limited to low particle concentration[15]. In view of the technical possibilities to measure with particle concentrations of up to $C_V = 0.4$ and more, it seems necessary to provide a basic understanding of particle-particle interactions. The most important interparticulate interactions which are discussed here are steric interactions, dependent scattering and multiple scattering.

- The fact that particles have a certain spatial extension and act as physical entities is the cause of steric interactions. Material bodies cannot interpenetrate, and so contact forces arise upon approach of two particles. Therefore, a particle cannot occupy any given place in the system and the arrangement of particles in a concentrated suspension is not random any more; instead, steric interactions will lead to the establishment of short-range order. This effect has to be taken into account for particle concentrations exceeding $C_V = 0.05$. Steric interactions are found to be prevalent within a wide range of concentration and particle size parameters, which is of interest regarding ultrasonic extinction measurements. Therefore, much of the authors' efforts have been focused on modeling steric interactions to understand their effect on extinction[12,15,16]. At present, the effect of steric interactions on extinction is well understood for the range of large particle size parameters ($\pi x/\lambda > 1$) and can be quantified by an extinction equation, which remains valid up to $C_V = 0.4$, approximately. Steric interactions lead to an increase of extinction compared to the values expected from BLBL. The effect is noticeable from about $C_V = 0.05$ onwards and becomes very significant (factor of 2 and more) with higher concentrations. In the range of smaller particle size parameters, the effects from steric interactions are masked by effects from dependent scattering.
- Dependent scattering denotes scattering processes where the mechanism of particle-wave interaction itself is modified by the presence of neighbouring particles. Two or more particles form a complex with scattering properties differing from those of an arrangement of single, independent scatterers. The physical conditions for dependent scattering are given when the interparticle clearance a is inferior to the wavelength of the radiation, thus allowing an intense, mutual coupling of wave fields within and in the vicinity of neighbouring particles. In general, dependent scattering leads to a decrease of extinction. The condition for the onset of dependent scattering is $a/\lambda \leq 0.3$. From that, an expression for a critical concentration $C_{V,crit}$ can be derived that exhibits a strong influence of particle size: At a given volume concentration, dependent scattering is more likely to occur with small particles.
- Multiple scattering is the most commonly known mechanism of particle-particle interaction. The mechanism of multiple scattering implies that radiation undergoes interaction with different particles consecutively, i.e. radiation scattered by a first particle is scattered by a second particle and so forth. Multiple scattering does not imply that the mechanism of interaction between particle and wave is modified in any way. When multiply scattered radiation is received, the extinction is reduced below the correct value. Since multiple scattering in random media is a statistical process, multiply scattered radiation is characterized by a distribution of optical path lengths. Compared with radiation passing directly from the emitter to the receiver, there is a loss of coherence (if there was any before) and a broadening of the angular distribution of radiation. Multiple scattering is a major problem with optical extinction systems, whereas ultrasonic receivers are very little sensitive to incoherent radiation, as long as they are much larger than the wavelength. The amplitudes of scattered (spherical) waves or of multiply scattered waves are averaged to zero over the receiver plane (see **Figure 9**). With properly designed equipment, ultrasonic extinction or velocity measurements will in general not be affected by multiple scattering, except for the very highest concentrations.

Because different physical mechanisms are responsible for the different particle-particle interactions, conditions are found where one or the other interaction mechanism is dominant. **Figure 10** gives a map of the $\pi x/\lambda - C_V -$ plane with an outline of the regions in which steric interactions and dependent scattering, respectively, are to be expected. The curves are calculated with the mentioned criterion for the onset of dependent scattering and the 5% vol. limit for steric interactions. With an ultrasonic extinction measurement setup as described in[16], it is possible to distinguish between the coherent and the incoherent part of the received radiation. The results of an extinction measurement in a highly concentrated suspension obtained with this instrument are presented in

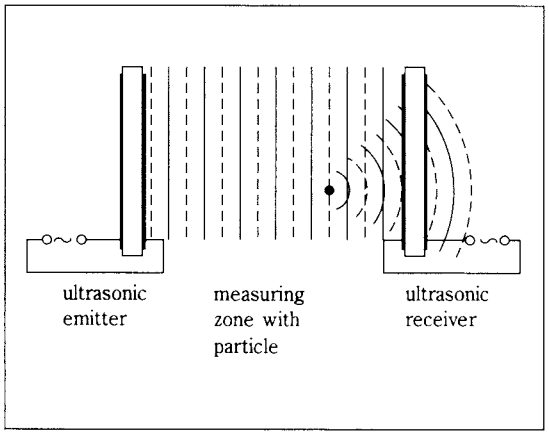

Fig. 9 The (coherent) plane wave is detected, the amplitude due to the sphere-wave is averaged to zero in the receiver.

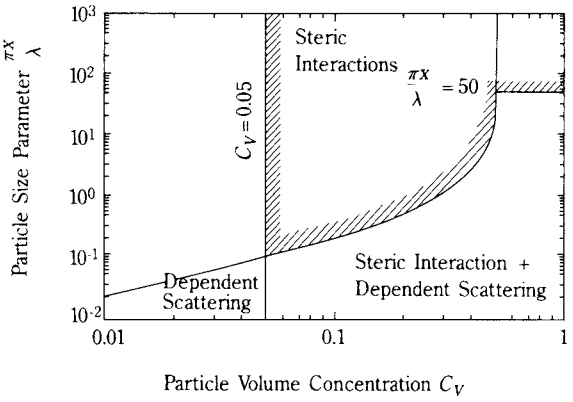

Fig. 10 Steric interactions versus dependent scattering in the $\pi x/\lambda - C_V$ plane.

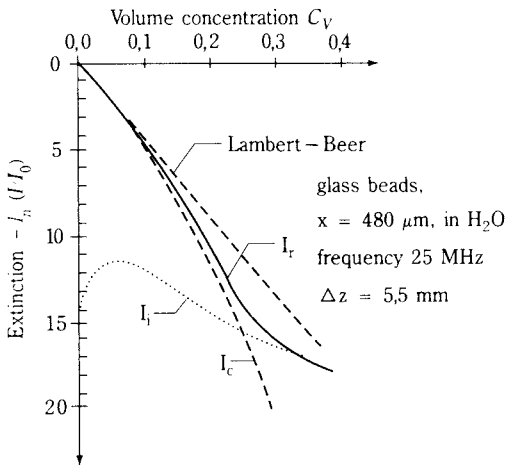

Fig. 11 Coherent (I_c) and incoherent (I_i) component of the received intensity (I_r).

Figure 11. For low concentrations, the measured extinction is in accordance with the Lambert-Beer value, since the coherent part of intensity exceeds the incoherent part and steric interactions are not significant. From a concentration of approx. 10% by volume onwards, steric interactions cause progressively higher extinctions than according to BLBL. With even higher concentrations, the influence of multiple scattering becomes apparent; this is due to the fact that the coherent part of the intensity decays faster with rising concentration than the incoherent one. In the example shown here, disturbances from multiple scattering are evident from particle concentrations of approx. 15% by volume onwards; however, with an appropriate design of the measurement system, it is possible to shift this limit to volume concentrations of about 35%.

4. Technical approaches to ultrasonic particle Sizing

Technical systems of ultrasonic particle sizing have developed only quite recently, with the availability of both fast electronic circuits for the generation and detection of ultrasound and sufficiently fast computers for the deconvolution of the spectral extinction or velocity data. In the following, a short survey of technical applications will be given, with special attention to those systems which have already gained some practical importance or which have been important for the historical development.

4.1 Measuring in gas-liquid systems

One might think that gas-bubbles in liquid systems should not be subject to a powder and particle-magazine, but since these systems exhibit unique interactions with ultrasonic waves, they are interesting enough for this paper. Gas bubbles are of practical importance in the chemical and food industry, fishery, ocean navigation, and so on. As with solid particles, there are three approaches to bubble detection[8,17] (**Figure 1**):

- A very effective scattering of sound when the bubble is insonified at or near its natural frequency. Backscattering at variable frequency can be measured to determine the number of bubbles.
- The absorption and scattering causes extremely high attenuation of the sound wave, especially near the frequency of resonance (see **Figure 5**). For frequencies above the resonance, the extinction efficiency of bubbles is $K = 2$, independent of the bubble size. This effect may be used for the measurement of interfacial areas in gas-liquid systems[18].

- The compressibility of the bubble depends on the frequency, and so the wave propagation velocity in the suspension is a function of the frequency, too. **Figure 6** shows this phenomenon. The difference between the speed of sound in the bubbly liquid and the value in the pure liquid can be used to calculate the volume concentration.

Medwin[8,17),1977] performed in-situ experiments in sea-water with two different setups:

– In the pulse-echo technique, a short sinusoidal wave train is sent out and reflected at a steel-plate. The same transducer receives the reflected echoes. From the damping of the echoes, the scatter along the path can be obtained, the exponential attenuation of the echo patterns in sea compared to that of pure water provides the excess absorption and, finally, the time between the echoes gives information on the local speed of propagation. The latter could not be evaluated in Medwin's experiments, since the pulse-echo technique was unable to measure the dispersion of sound speed accurately enough, but the extinction cross-section and the scattering cross-section were determined as a function of the frequency. Further, the number of bubbles in a given radius increment per unit volume of water was calculated directly, assuming that only the resonating bubbles will give a significant contribution to extinction.

– No reflections are utilized with the continuous wave technique, but two hydrophones separated by a certain distance on a line in the direction of sound propagation receive the waves instead. The speed of sound can be determined very easily by comparison of the phases in the two signals. Since it is not a plain sine-wave that is used, but a composition of sine-waves with up to 32 harmonics, a more sophisticated signal interpretation including a FFT analysis has to be employed in order to determine the attenuation. The attenuation can then be used to calculate the volume fraction of bubbles in the range of $x \ldots x + \Delta x$ and, from that, the bubble density distribution function.

Gazanhes, et al.[4),1984] have done theoretical and experimental work on the behaviour of the phase velocity and the absorption in bubbly water as a function of frequency. For their experiments, they used a Gauß-distributed bubble collective with a mean diameter of 100 μm and a bubble volume concentration of up to 10^{-4}. With an ultrasonic transmitter and a receiver in the dispersion, the ultrasonic resonance spectrum was measured in the frequency range of 15 kHz to 500 kHz. The authors were able to determine the mean bubble diameter and the standard deviation of the Gauß distribution.

4.2 Measuring in solid-liquid systems

Measurement systems for bubbles are mostly operated in the range of bubble resonance frequency, which allows a rather direct determination of the bubble size spectrum. In solid-liquid systems, such pronounced particle resonance frequencies do not exist. Instead, the sizing of solid particles relies on spectral extinction measurements covering a broad frequency range, so that every particle size class runs through at least two regimes of particle-wave interaction with different slopes in the extinction efficiency function. In this way, it is guaranteed that the system of linear equations relating the spectrum of extinctions measured at various frequencies to the spectrum of particle concentrations in the various particle size classes can be solved unambiguously. In solid-liquid systems, distinct changes in the slope occur around particle size parameters of $\sigma \approx 10^{-4} \ldots 10^{-2}$ (transition from total to partial entrainment, Eq. (13)) and around $\sigma = 1 \ldots 10$, and both regimes are utilized for measurements. Hence it is useful to distinguish between low-frequency and high-frequency approaches to ultrasonic particle sizing, owing to the specific advantages and problems of the respective regimes:

$\sigma \ll 1$:
- Low frequencies are easier to handle
- The low extinctions associated with low particle size parameters make measurements in highly concentrated suspensions possible

$\sigma \geq 1$:
- Dependent scattering effects are almost non-existent
- Material properties have less influence on the extinction efficiency than in the range $\sigma \ll 1$
- Gas bubbles in the suspension do not necessarily cause measurement errors; their effect can be eliminated

4.2.1 Low-frequency approaches

Urick[19)1948], and others investigated the extinction of ultrasonics at a single, relatively low frequency. The author found a definite relation between particle concentration and measured extinction up to high concentrations, and so the applications mainly proposed were monitoring of the solids concentration, with the other phase properties and the particle size distribution being constant.

Fritsche[20),1968] measured the absorption coefficient of ultrasound in industrial suspensions of $(NH_4)_2SO_4$

crystals at 0.8 MHz and 4 MHz with crystals from about 10μm to 1000μm. His goal was to determine the crystal concentration. The author found the absorption coefficient to rise linearly with concentration, the gradient depending on the frequency and particle size. He concluded that ultrasonic attenuation measurements are a suitable means of concentration determination in crystal suspensions, as long as the particle size distribution remains constant during operation so that calibration excludes all effects of particle size on absorption.

Two different frequencies, transmitted and received by two separate pairs of transducers, are used with the ARMCO − Autometrics PSM 100 which is based on a patent by *Cushman, et.al.*[21),1973]. A change of particle concentration will lead to changes of the extinction which are proportional for both frequencies, while a change of the particle size distribution causes different changes in the extinction at the two frequencies. The concentration of the suspension is then calculated from the sum of the measured extinctions, their difference provides one single point of the particle size distribution curve. For this, the PSM technique can only be applied when the PSD is monomodal, of a known type and uniquely defined by a single point. Results obtained with the PSM are published in[22)]. Detailed technical data on the instrument are not known, but it seems evident that the system operates in a frequency range where extinction is dominated by the mechanism of entrainment ($x \ll \lambda$). In this range, the analysis relies very much on exact information on the material data of particles and fluid (density, compressibility and viscosity). Further, air bubbles in the suspension lead to substantial changes in attenuation. The problem can be solved by removing the air with a device that utilizes a combination of centrifugal force and reduced pressure, but this increases the cost of the overall system considerably. The PSM is capable of measuring distributions with mean sizes ranging from 40 μm to 100 μm at solids concentrations of up to ca. 25% by volume[22)]. The rather high concentration limit is due to the low frequencies used and the low extinction associated with these. The instrument is employed in the control of grinding circuits in the preparation of minerals.

Alba and *Herbst*[23)] developed the PROASSIST SDE-21 as an extension to the PSM. Five frequencies in the range of 1 MHz to 6 MHz are used to give an estimate of the particle size distribution in 5 intervals with an update every 30 seconds. Just as with the PSM, the SDE-21 relies on an expression for the attenuation $\alpha(x,f)$ in a monosized dispersion with particle size parameters of $\sigma \leq 1$[22)]. Assuming the total extinction to be a weighted average of the attenuations contributed by each particle size fraction, the Lambert-Beer equation is taken in a discretizised, integral form for the mathematical deconvolution of the measured extinctions. The measurable range of mean sizes is equal to that of the PSM; in the case of both, the electronics and transducer configuration do not allow measurements over 10 MHz. The simple mathematical model employed is only approximately valid and empirical data are still required to provide accurate size information. Even though the SDE-21 system estimates five fractions, it cannot handle broad or narrow distributions due to the inversion mathematics it employs for deconvolution.[22)]

Pfau[24),1974] investigated the effeciency of flocculation with a Doppler system, measuring both the frequency shift and the intensity of backscattered ultrasonic waves. He found that either the mean particle size or the particle concentration in a suspension can be determined from the measured intensity, as long as one of these two parameters is known and constant. Experiments with 5 MHz ultrasonics in suspensions of particles ranging from about x = 20μm to 80μm ($\sigma < 1$) and constant concentrations of 1% vol. showed a linear rise of the received intensity with particle size. The opposite case (constant particle size and variable concentration) brought linear results, too.

Boxman, Scott and *Jochen*[25),1995] report on a prototype in-line ultrasonic cell for measuring particle size distributions in dilute (<4% vol.) slurries of submicron particles. In their effort to develop a high-concentration ultrasonic PSD-analyser, the authors are working on a model of ultrasonic attenuation that can cope with the effects occurring at higher concentrations, whereat they focus on multiple scattering. Further, measurements of attenuation spectra in the frequency range of 2 MHz to 50 MHz at concentrations of 0.5% to 40% (vol.) were performed that exhibit the expected deviations from linearity from approx. 5% onwards. Attempts to extract PSD information by inverting the measured ultrasonic spectra were only partially successful, as the authors report. They suggest to resign from deconvoluting and to consider the attenuation spectrum as being a good representation of the actual sample.

4.2.2 High-frequency approaches

Horak[26),1977] was interested in the physiological properties of blood, e.g. the aggregation of red blood cells as a function of the stirring rate in a sample. He has performed measurements of the ultrasonic

attenuation spectra within a frequency range of 4 MHz to 50 MHz in human blood and in suspensions of polystyrene spheres in water. Due to the relatively high frequencies and particle sizes of up to 300μm, it was possible to investigate the attenuation behaviour with particle size parameters of $\sigma >> 1$. The slope of the change in attenuation around $\sigma \approx 1$ turned out to be a measure of the variation of the particle diameters in the suspension. The spread of the PSD could thus be determined by this slope, and the average particle size by the frequency at which the change in attenuation took place. The author has suggested using attenuation measurements to extend Doppler systems as they are used in medicine. These devices analyse, for example, the flow rate of blood in a vessel by evaluating the frequency shift of reflected ultrasonic waves; information on the aggregation of the red blood cells was obtained by attenuation measurement.

Riebel and *Löffler*[1)1989], have developed an on-line particle size and concentration monitor based on the measurement of ultrasonic extinction in suspensions at M different frequencies f_i in a relatively broad range from ca. 0.5 MHz to 100 MHz. In spite of the technological difficulties, high-frequency ultrasonics were chosen because extinction is less dependent on particle shape and material properties in the domain of high particle size parameters ($\sigma > 1$). Contrary to pulse-echo systems, for example, the suspension is insonified continuously; therefore only very low intensities are needed and sensitive particle structures like agglomerates are not destroyed so easily.

For the mathematical deconvolution of the measurements, the Lambert-Beer equation for the extinction from a particle size distribution

$$-ln\left(\frac{I}{I_0}\right)_{f_i} = \Delta z C_{PA} \int_{x_{min}}^{x_{max}} K(f_i, x)\, q_2(x)\, dx \qquad (16)$$

is approximated by the discretizised version

$$-\frac{1}{\Delta z}\, ln\left(\frac{I}{I_0}\right)_{f_i} = C_{PA} \sum_j K(f_i, x_j)\, q_{2,j} \Delta x_j \qquad (17)$$

for discrete particle size intervals j, $j = 1 \ldots N$. With M different measuring frequencies f_i, a set of linear equations is obtained which is expressed as

$$m = K\, g \qquad (18)$$

where m = vector of measured extinction values,

$-\frac{1}{\Delta z}\, ln\left(\frac{I}{I_0}\right)$;

g = vector of particle size distribution, $C_{PA}\, q_2(x)\, dx$;
K = matrix of extinction coefficients.

The values of $K(f_i, x_j)$ are taken from measured $K(\sigma)$ functions and are stored in the system software. As with most indirect methods of measurement, for example laser diffraction spectroscopy[27)], the results obtained from a direct inversion of Eq. (18):

$$g = K^{-1} m \qquad (19)$$

tend to be unstable and very sensitive to minute measurement errors; special inversion algorithms have to be applied. In the course of the authors' work, several different deconvolution algorithms were tested by means of experiments and computer simulations. Their performance can be evaluated in terms of the behaviour with very narrow, very broad or polymodal particle size distributions, very high concentrations, different solid/liquid systems, and so on. The algorithm implemented finally can be regarded as a successful compromise, since the system can handle any given PSD.

Kräuter and *Riebel*[28)] have recently introduced an interesting alternative to the usual deconvolution techniques. They employed a neural network to estimate particle size distributions from measured extinctions. No knowledge whatsoever of particle-wave interaction, etc. is required, but the network has to be trained with data from measurements or from reliable simulations. Dependent on the desired output quality, the number of necessary training steps can exceed 2000. Experiments with monomodal particle size distributions and concentrations of up to 20% by volume brought results comparable to those of standard inversion methods.

A commercial version of the above-mentioned development is the OPUS (On-line Particle size analysis by Ultrasonic Spectrometry) system offered by SYMPATEC, which has found applications for the on-line-control of solid-liquid systems (emulsion polymerization, crystallization) in the chemical industries. At the present stage of development, the OPUS allows measurements of concentrations and particle size distributions of any type in a range from ca. 2 μm to 3000 μm at concentrations of up to 25% – 30% by volume. As a result of the high frequencies used with the system, gas bubbles appear as particles in the uppermost particle size interval, and so the influence of gas bubbles in the suspension can be eliminated

quite easily. A complete measurement takes approx. 20 seconds. **Figures 12** to **14** show some results obtained with the OPUS. **Figure 12** gives an impression of the ability of ultrasonic particle sizing to cope with extremely high particle concentrations and low density contrasts ($\varrho_{polystyrene}$ = 1.06 g/cm^3). The variance in the measured PSDs is due to the high-concentration effects discussed in section 3, viz. steric interactions and dependent scattering. Measurements with smaller and more dense particles yield no concentration dependence at all (**Figure 13**). For comparison purposes, a measurement obtained with laser diffraction analysis is shown here. The deviation can be explained by the different equivalent diameters the two systems give; equal results can only be expected for ideal spheres. Very small particles are not the preferred domain of the OPUS, but particles as small as 1μm in diameter can be analysed without problem (**Figure 14**).

Recently, *Pendse* and *Sharma*[29),1993] introduced the Pen Kem 8000, an ultrasonic PSD estimator designed especially for slurries of inorganic, submicron particles. Similar to the OPUS, the system measures ultrasonic attenuation spectra at several frequencies in the range of 1 MHz to 100 MHz, but, as far as it is evident from the author's contribution, the mathematical deconvolution technique and the physical model of particle-wave interaction employed differ considerably. Only the viscous energy dissipation due to the relative motion of particle and fluid is taken into account, restricting the validity of the model to low particle size parameters and high density contrasts ($\Delta\varrho/\varrho_F \gg 1$). The authors report on results from measurements in titanium dioxide slurries with concentrations of 3.5% and 42% by volume and particle sizes from ca. 0.1μm to 10μm. A PSD estimate takes about 10 minutes.

5. Conclusion

Of the various possibilities to detect and size particles by means of ultrasound, the extinction methods appear to be the most feasible from the technical point of view. A variety of technical solutions, ranging from ultrasonic extinction measurements at a single frequency and measurements at two frequencies to spectrometric extinction measurements with a multitude of measuring frequencies has developed during the past two decades. While the technical details differ greatly, a common feature of ultrasonic extinction measurement appears to be the ability to

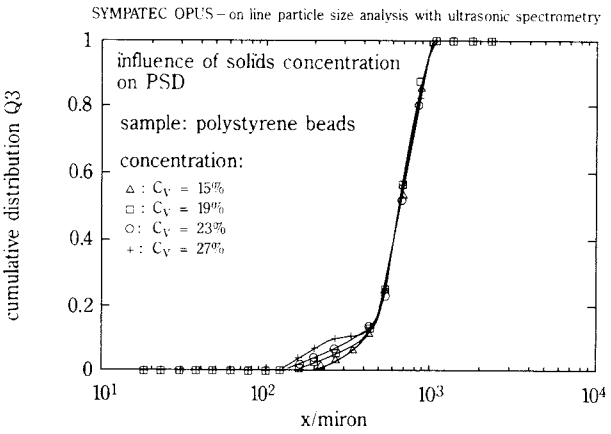

Fig. 12 Particle size distributions of polystyrene beads ($\varrho_{polystyrene}$ = 1.06 g/cm^3) in water measured with the OPUS. The effect of steric interactions and dependent scattering causes concentration-dependent deviations in a certain particle size range.

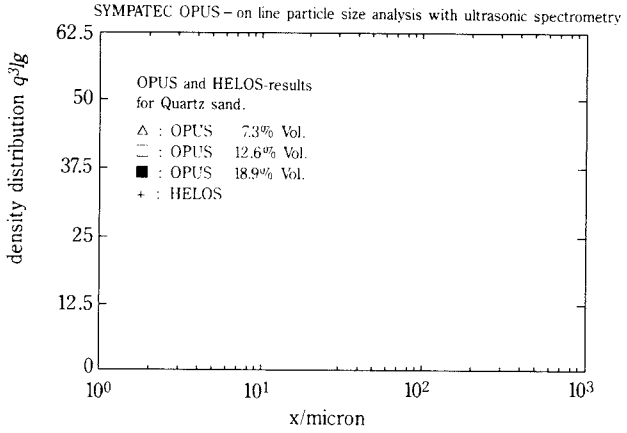

Fig. 13 Measured PSDs for suspensions of quartz sand in water. The deviations from laser diffraction measurement are due to the different equivalent diameters with the two systems.

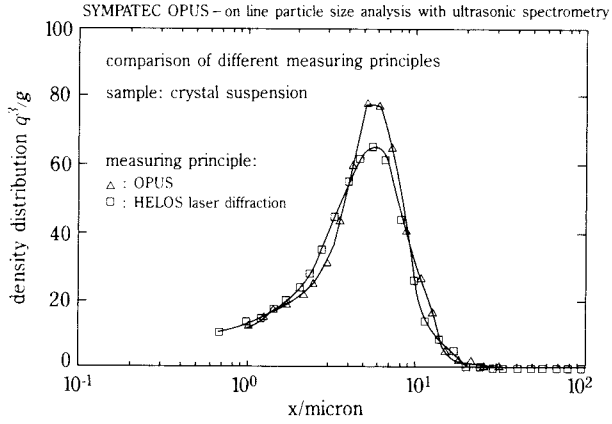

Fig. 14 PSD of zeolite crystals ranging from x = 1μm to 100μm measured with the OPUS and with laser diffraction for comparison.

measure in highly concentrated suspensions, which offers unequalled prospects for applications in on-line measurement and process control.

Symbols

C_{PA}	particle projectional area concentration	[m^{-1}]
C_V	volume concentration	[−]
c	sonic velocity	[m s^{-1}]
f	frequency	[s^{-1}]
I	ultrasonic intensity	[kg s^{-2}]
K	extinction efficiency	[−]
p	pressure	[kg m^{-1} s^{-2}]
q_2	particle area density distribution	[m^{-1}]
x	particle diameter	[m]
z	length	[m]
α	extinction coefficient	[m^{-1}]
χ	ratio of specific heats of gas at constant pressure and constant volume	[−]
η	dynamic viscosity	[kg m^{-1} s^{-1}]
$\varkappa$	compressibility	[m s^2 kg^{-1}]
λ	wavelength	[m]
ρ	specific density	[kg m^{-3}]
σ	particle size parameter ($=\pi x/\lambda$)	[−]

Indices:

0	value in pure suspending fluid
DS	disperse system
Ext	extinction
F	fluid
P	particle
PA	projectional area
Res	resonant
Scat	scattering
Susp	suspension
V	volume

Operators:

Δ	discrete difference

References

1) Riebel U., Löffler F.: The Fundamentals of Particle Size Analysis by Means of Ultrasonic Spectrometry, Part. Part. Syst. Charact. 6 (1989), 135-143
2) Skudrzyk E.: The Foundations of Acoustics, Springer, Berlin (1971)
3) Lamb H.: Hydrodynamics, Cambridge University press,(1945), 6th Ed.
4) Gazanhes C., Arzeliès P., Léandre J.: Propagation acoustique dans un milieu diphasique eau-bulles d'air. Application à la caractérisation d'un milieu diphasique par voie acoustique, Acustica 55 (1984), 113-122
5) Sage K.A., George J., Überall H.: Multiple Resonances in Sound Scattering from Gas Bubbles in a Liquid, Journ. Acoust. Soc. America 65 (1979) 6, 1413-1554
6) Minnaert M.: On Musical Air Bubbles and the Sound of Running Water, Philosophical Magazine 16 (1933), 235-248
7) Meyer E., Skudrzyk E.: Über die akustischen Eigenschaften von Gasblasenschleiern in Wasser, Acustica 3 (1953), 434-440
8) Medwin H.: Counting bubbles acoustically: a review, Ultrasonics 15 (1977) 1, 7-13
9) Wolters K.: Über die Ultraschall-Extinktion in Suspensionen und ihre Anwendung zur Messung niedriger Partikelkonzentrationen, Thesis RWTH Aachen, (1961)
10) Hay A.E., Mercer D.G.: On the theory of sound scattering and viscous absorption in aqueous suspensions at medium and short wavelengths, J. Acoust. Soc. Am. 78 (1985) 5, 1761-1771
11) Faran J. Jr.: Sound Scattering by Solid Cylinders and Spheres, J. Acoust. Soc. Am., 23 (1951) 4, 405-418
12) Riebel U., Kräuter U., Khatchikian P.: Unpublished work.
13) Gregor W., Rumpf H.: Velocity of Sound in Two-Phase-Media, Int. J. Multiphase Flow 1 (1975), 753-769
14) Atkinson C.M., Kytömaa H.K.: Acoustic Wave Speed and Attenuation in Suspensions, Int. J. Multiphase Flow 18 (1992) 4, 577-592
15) Riebel U., Kräuter U.: Extinction of Radiations in Sterically Interacting Systems of Monodisperse Spheres; Part 1: Theory, Part. Part. Syst. Charact. 11 (1994), 212-221
16) Kräuter U., Riebel U.: Extinction of Radiation in Sterically Interacting Systems of Monodisperse Spheres; Part 2: Experimental Results, Part. Part. Syst. Charact. 12 (1995), in press
17) Medwin H.: Acoustical determinations of bubble-size spectra, J. Acoust. Soc. Am., 62 (1977) 4, 1041-1044
18) Stravs A.A., von Stockar U.: Measurement of Interfacial Areas in Gas-Liquid Dispersions by Ultrasonic Pulse-Transmission, Chem. Eng. Sci., 40 (1985) 7, 1169-1175
19) Urick R.J.: The Absorption of Sound in Suspen-

sions of Irregular Particles, J. Acoust. Soc. Am. 20 (1948), 283-289
20) Fritsche K.: Zur Eignung von Ultraschallabsorptionsmessungen für die Konzentrationsbestimmung an technischen Ammonsulphatsuspensionen, Chem. Technik 20 (1968) 7, 419-421
21) Cushman Ch.R., Anderson V., Hale J.: Particle Size and Percent Solids Monitor, U.S. Pat. no. 3,779,070 (1973)
22) Allen T.: Particle Size Measurement, Chapman & Hall, 4. ed. (1990)
23) Herbst J.A., Alba J.: A new System for On-line Measurement of Multipoint Size Distributions and Solids Concentrations in Slurries, Proassist Company, Salt Lake City, USA
24) Pfau B.: Simultane Geschwindigkeits-, Konzentrations- oder Partikelgrößenmessung mit Ultraschall in Zweiphasenströmungen, Verfahrenstechnik 8 (1974) 2
25) Boxman A., Scott D.M., Jochen C.E.: Measuring Particle Size and Concentration Using Ultrasonics, 6th Europ. Sympos. Part. Charact. (PARTEC), (1995), Preprints
26) Horak G.: Real-Time Ultrasonic-Spectroscopy in Suspensions, Acustica 37 (1977) 1, 11-20
27) Heuer M., Leschonski K.: Results Obtained with a New Instrument for the Measurement of Particle Size Distributions from Diffraction Patterns, Part. Charact. 2 (1985), 7-13
28) Kräuter U., Riebel U.: Neural Network Recognition of Particle Size Distributions Measured by Ultrasonic Spectroscopy, 6th Europ. Sympos. Part. Charact. (PARTEC), (1995), Preprints
29) Pendse H.P., Sharma A.: Particle Size Distribution Analysis of Industrial Colloidal Slurries Using Ultrasonic Spectroscopy, Part. Part. Syst. Charact. 10 (1993), 229-233

Author's short biography

Ulrich Riebel

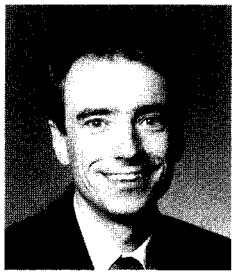

Professor Ulrich Riebel received his doctoral degree in 1988 with a thesis on ultrasonic particle sizing at the University of Karlsruhe (TH), where he had worked as a research assistant of Prof. Friedrich Löffler at the Institute for Mechanical Process Engineering and Mechanics ("Institut für Mechanische Verfahrenstechnik und Mechanik"). After having worked with the Sympatec Company in 1989/90, he went back to Friedrich Löffler's institute as a senior scientist. Since July of 1994 Ulrich Riebel holds the Chair of Particle Technology at the University of Cottbus. His main research interests are particle sizing by means of ultrasound and light especially in highly concentrated suspensions, dust separation and interparticulate forces in crystal suspensions.

Peter Khatchikian

The author studied chemical engineering at the University of Karlsruhe (TH) and received his diploma in 1994. Since July of 1994 he is research assistant of Ulrich Riebel at the University of Cottbus. Peter Khatchikian's main research interests are the development of new methods in ultrasonic particle sizing and the statistics of signals in extinction measurement.

Udo Kräuter

Udo Kräuter received his diploma in chemical engineering from the University of Karlsruhe (TH) in 1990. Since then he is research assistant of Ulrich Riebel. Udo Kräuter works on several problems that deal with ultrasonic particle sizing, e.g. wave propagation in highly concentrated suspensions. He is also interested in the statistics of transmission signals in light extinction measurement.

Review

Nanostructures: The Next Generation of High Performance Bulk Materials and Coatings†

B.H. Kear
Department of Mechanics and Materials Science
*Rutgers University**
P.R. Strutt
Precision Manufacturing Center
*University of Connecticut***

Abstract

This paper presents an overview of recent research performed at Rutgers University and the University of Connecticut on the synthesis and processing of nanostructured materials. Highlights of this collaborative research program include: (1) synthesis of carbide strengthened steel and hard cermet powders from aqueous solution precursors, (2) synthesis of ceramic powders and ceramic matrix composites from metalorganic precursors, (3) densification of powder compacts by liquid phase sintering, (4) formation of high quality coatings by thermal spraying, and (5) demonstration of superior hardness and wear resistance in bulk cermet materials and coatings.

Nanostructured bulk materials with designed multifunctional coatings present unprecedented opportunities for advances in materials properties and performance for a broad range of structural applications.

1. Introduction

For generations, materials with fine-scale microstructures have been recognized to exhibit remarkable and technologically attractive properties. In the past few years, interest has been growing in a new class of materials that are composed of ultrafine grains or particles (1). A feature of such 'nanostructured' materials is the high fraction of atoms that reside at grain or particle boundaries. Although much of today's research in the nanomaterials field is focussed on the synthesis and processing of bulk materials, there is also growing interest in the preparation of coatings.

Research on nanostructured materials (hereafter n-materials) has been a major activity at Rutgers University and the University of Connecticut since the late 1980's. Progress has been made in the synthesis of (1) n-metal powders by the Aqueous Solution Reaction method, (2) n-cermet powders by the Spray Conversion Processing method, and (3) n-ceramic powders by the Chemical Vapor Condensation method. Advances have also been made in the consolidation of n-powders by solid and liquid phase sintering methods (for bulk materials) and by thermal spraying (for coatings), while preserving the desirable nanostructures.

In what follows, we will describe highlights of this research, with the emphasis on synthesis and processing methods and the characteristics of the resulting nanostructured materials. One example will be cited that illustrates the performance advantages to be gained by substituting 'nanograined' material for conventional 'micrograined' material in a cutting tool application.

2. Nanostructured metals and alloys

Carbide strengthened steels are widely used for gears, bearings and shafts in gas turbine engines, because of their good resistance to tempering, wear and rolling contact fatigue. In the fully hardened condition, such steels contain a fine dispersion of $M_{23}C_6$, M_2C or MC carbide particles in a martensitic matrix. Some of the carbide particles, however, can be as large as several microns in diameter, in which case they can act as favorable sites for crack initiation in fatigue. To circumvent this problem, an attempt is now being made to develop an *n*-M50 steel, a prototype carbide strengthened steel, in which the dispersed carbide phase is of uniform nanoscale dimensions. The anticipated superior strength, wear resistance and fracture toughness of the *n*-M50 steel

* Piscataway, NJ 08855-0909 U.S.A
** Storrs, CT 06269-5119 U.S.A
† Received 16 June, 1995

is expected to significantly enhance its properties and performance.

An Aqueous Solution Reaction (ASR) method has been developed to synthesize *n*-M50 steel powder (2). The synthesis involves three steps: (1) preparation of an aqueous solution of mixed metal (*Fe, Cr, Mo* and *V*) chlorides using de-ionized and *de*-oxygenated water, (2) reductive decomposition of the starting solution with sodium trialkyl-borohydride to obtain a colloidal solution of the metallic constituents, and (3) after filtering, washing and drying, gas phase carburization under controlled carbon and oxygen activity conditions to form the desired nanodispersion of carbide phase in a metallic matrix. A similar procedure has been used to synthesize *n*-Cr_3C_2/Ni powders for use in thermal spraying of corrosion resistant hard coatings (3) (see section 6). In both cases, separation of the sodium chloride from the colloidal solution is carried out by repeated washing in a centrifuge. A small amount of an organic passivation agent, such as a solution of paraffin in hexane, which is added to the final wash, provides protection of the high surface area powder against spontaneous combustion when dried and exposed to air.

Procedures for the low temperature consolidation of the as-synthesized *n*-M50 powders are being investigated.

3. Nanostructured ceramics

Silicon-base ceramics, such as *SiC* and *Si3N4*, are useful materials for many engineering applications, such as highly stressed components in heat engines, grinding wheels and wear parts, because of their excellent high temperature mechanical strength and good oxidation resistance. Silicon carbide is also useful because of its favorable electrical resistance (heating elements) and thermal conductivity (substrate materials). A limitation of today's processing of these materials is the very high sintering temperature and pressure needed for powder consolidation, which is a consequence of their covalent bonding. Sintering aids can be used, but they frequently degrade properties. An alternative approach is to take advantage of the lower sintering temperatures characteristic of nanostructured powders. This was the approach adopted in our research.

Inert Gas Condensation (IGC) is the most versatile process in use today for synthesizing experimental quantities of nanostructured powders (1). A feature of the process is its ability to generate non-agglomerated *n*-powders, which are sinterable at relatively low temperatures. In IGC processing, **Figure 1(a)**, an evaporative source is used to generate the powder particles, which are convectively transported to and collected on a cold substrate. The nanoparticles develop in a thermalizing zone just above the evaporative source, due to interactions between the hot vapor species and the much colder inert gas atoms (typically 1-20 mbar pressure) in the chamber. Ceramic powders are usually produced by a two-stage process: evaporation of a metal source, or a metal suboxide of high vapor pressure, followed by slow oxidation to develop the desired n-ceramic powder particles.

Recently, we have modified a conventional IGC processing unit for the purpose of synthesizing

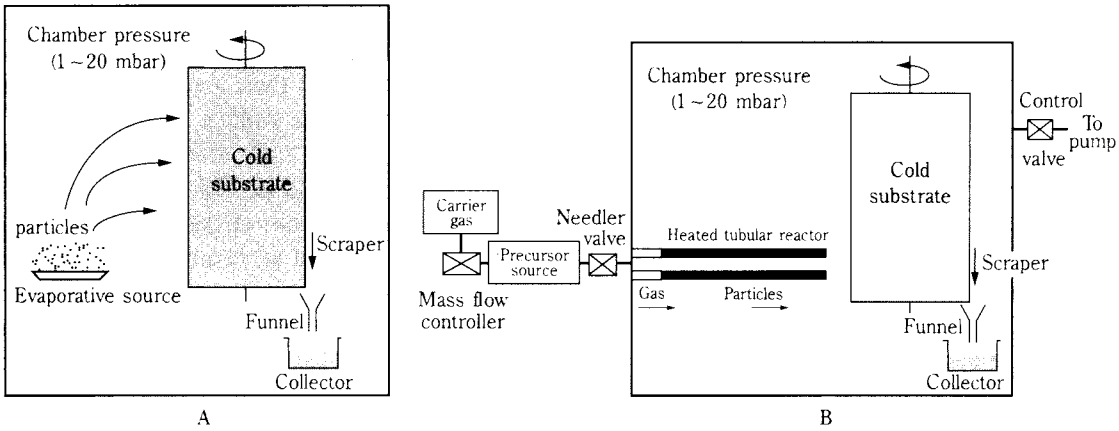

Fig. 1 Schematic representation of (a) inert gas condensation (IGC) process, and (b) chemical vapor condensation (CVC) process

n-ceramic powders from metalorganic precursors. In this new Chemical Vapor Condensation (CVC) process (4,5), Figure 1(b), the original evaporative heating source is replaced by a hot-wall tubular reactor, which decomposes the precursor/carrier gas to form a continuous stream of clusters or nanoparticles exiting from the reactor tube. Critical to the success of CVC processing are: (1) a low concentration of precursor in the carrier gas, (2) rapid expansion of the gas stream through the uniformly heated tubular reactor, (3) rapid quenching of the gas phase nucleated clusters or nanoparticles as they exit from the reactor tube, and (4) a low pressure in the reaction chamber. The resulting *n*-ceramic powder particles are non-agglomerated, as in the IGC process, and display low temperature sinterability, as well as other useful characteristics as infiltrants (see section 5.). Non-agglomerated *n*-TiO_2 and *n*-ZrO_2 powders produced by the CVC method can be sintered to theoretical density at temperatures as low as 0.4 Tm. This is in contrast to the ultrafine powders produced by conventional ambient pressure combustion flame and arc-plasma powder processing methods, which yield cemented aggregates that can be consolidated only at much higher sintering temperatures.

The CVC process has been used to synthesize *n*-powders of a variety of ceramic materials, which cannot easily be produced by the IGC process, because of their high melting points and/or low vapor pressures. Examples are *n*-SiCxNy powders, for which there are many suitable organosilicon precursors, such as hexamethyl-disilazane (HMDS). In a particular case, the actual composition of the resulting powder is strongly influenced by the choice of carrier gas. Thus, HMDS/H_2O, HMDS/H_2 and HMDS/NH_3 give *n*-ceramic powders with compositions close to SiO_2, SiC and Si_3N_4, respectively.

Consider the CVC synthesis of Si-rich powders from HMDS/He, in which the temperature of the tubular reactor is varied over the range 1100-1400 C in 100 C steps. With the flow rate of He fixed at 8.55×10^{-3} mole/min, the HMDS concentration in the gas stream is about 16.4 mole % at ambient temperature. Under these conditions, about 2 grams of amorphous *n*-SiCxNy powder is collected in several minutes. Relevant data on powder characteristics and compositions are presented in **Tables 1** and **2**. The average particle size from TEM ranges from 6-10 nm, with the smallest particle size corresponding to the highest reaction temperature. The density of the particles increases with decomposition temperature, indicating a higher degree of precursor pyrolysis at the highest temperature. A noteworthy feature is the unexpectedly large amount of oxygen in the powders, which decreases with increasing pyrolysis temperature. In contrast, the concentration of carbon and nitrogen in the powders increases with pyrolysis temperature. The atomic ratios of the constituent elements of the powders are clearly at variance with the atomic ratios in the original HMDS precursor. Furthermore, there is substantially more carbon in the product powders than that of stoichiometric SiC. In all cases, annealing the amorphous powders at 1600 C in flowing high purity argon for 2 hours causes crystallization to

Table 1 Some Important Characteristics of As-synthesized N-SiCxNy Powders

Sample name	Reactor Temp. (C)	Powder Density* (q/cm^3)	Powder appearance	Surface area** (M^2/g)	Particle size from BET (nm)	Particle size from TEM (NM)
S−1	1100	2,614	brown	568	4	10
S−2	1200	2,737	dark-brown	555	4	10
S−3	1300	2,781	brown-black	360	6	8
S−4	1400	2,783	jet-black	272	8	6

* measured by pycnometry using He gas
**measured by single point BET adsorption

Table 2 Chemical of As-synthesized Amorphous n-$SiCxNyO_2$ Powders, as Determined by Rutherford Backscattering Spectroscopy

Sample name	Experimental Condition	SiCxNyOz X	Y	Z
HMDS	as-received precursor	3.00	0.50	0.00
S−1	synthesis at 1100C	1.26	0.35	0.61
S−2	synthesis at 1200C	1.35	0.40	0.47
S−3	synthesis at 1300C	1.45	0.48	0.29
S−4	synthesis at 1400C	1.51	0.49	0.28
A−1	annealing at 1600C	1.00	0.00	0.00

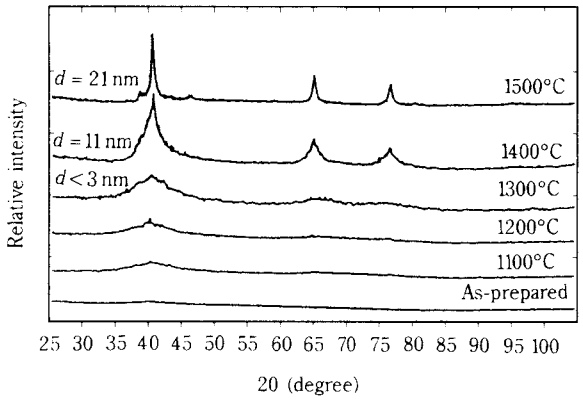

Fig. 2 XRD patterns of as-synthesized amorphous n-SiCxNy powders after annealing in flowing argon

essentially phase pure SiC. The crystallization process is initiated at about 1100-1200 C and is essentially complete at 1400 C, **Figure 2**.

4. Nanostructured cermets

Ceramic/metal composites (cermets) are the materials of choice for cutting tools, drill bits and wear parts. Typically, such materials are produced by mechanical mixing of powders of the constituent phases, followed by cold compaction and liquid phase sintering. This limits the attainable structural scale of the composite material to about 0.3 microns, so-called 'micrograined' cermets. Recently, a new chemical process, called Spray Conversion Processing (SCP), has been introduced, which is capable of synthesizing 'nanograined' cermets (6), **Figure 3**. The new process involves three steps: (1) preparation of an aqueous solution mixture of salts of the constituent elements, (2) spray drying of the starting solution to form an homogeneous precursor powder, and (3) fluid bed conversion (reduction and carburization) of the precursor powder to the desired *n*-cermet powder.

For several years, Rutgers University has been conducting research on the preparation and consolidation of *n*-WC/Co powders (7). Concurrently, a tribology group at Stevens Institute of Technology has been evaluating their friction and wear properties(8). More recently, the University of Connecticut has established a complementary research activity on thermal spraying of *n*-WC/Co and other cermet powders (see section 6). Highlights of this tripartite collaborative research program include: (1) synthesis of *n*-WC/Co powders with WC grain size controllable down to about 50 nm, (2) densification of powder compacts by liquid phase sintering in vacuum or hydrogen, (3) mitigation of WC grain growth during liquid phase sintering by the use of potent grain growth inhibitor carbide phases, such as VC or Cr_3C_2, (4) demonstration of hardness in fully sintered nanograined WC/Co (with inhibitor carbide phase) that is twice that of conventional micrograined material, (5) confirmation of enhanced wear resistance and cutting performance in sintered materials of high hardness, and (6) demonstration of the feasibility of thermal spraying *n*-WC/Co powders.

Recent research has shown that incipient melting in VC- and Cr_3C_2-doped WC/Co alloys occurs at temperatures about 250 C below the melting point of the undoped alloy (9). Moreover, we have found that these alloys can be deformed in the semi-solid state, provided that the volume fraction of the dispersed carbide phase does not exceed about 75%. Such 'semi-solid forming' is not a new concept. Several processes were introduced in the 1970's, based on pioneering work done at MIT. The desired structure is produced by cooling a molten alloy to form a slurry, which is mechanically stirred to break-up the dendrites. The roughly spherical morphology of the granular structure of the semi-solid alloy leads to a low shear strength, even with a relatively high solid fraction, which permits the semi-solid to be shaped in a die. In Rheocasting, a slurry is produced in a mixer and delivered directly into a die. In Thixocasting, a billet having the required microstructure is first cast and, at a later time, a slug cut from the billet is heated to the semi-solid state and forged in a die. The present semi-solid processing method differs from the MIT method in several respects: (1) a slurry is formed by heating a powder mixture into the semi-solid region of the phase diagram, (2) no mechanical stirring is required to obtain the desired semi-solid state, with a roughly spherical grain or particle morphology, and (3) an ultrafine structure is obtained by utilizing a nanocomposite powder produced from a chemical precursor.

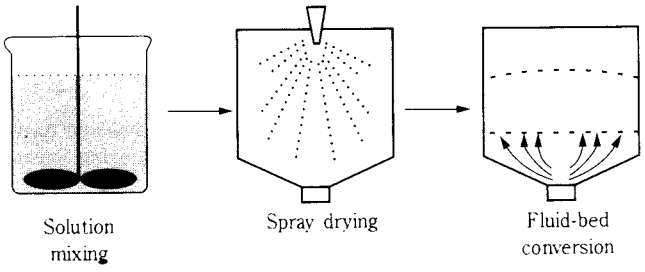

Fig. 3 Schematic diagram of scaleable process for the preparation of nanostructured powders, starting from aqueous solution precursors

Currently, we are investigating semi-solid forming of Cr_3C_2-doped *n*-WC/Co alloys, because of the unusually low melting point of the Co-rich eutectic liquid phase. An interesting aspect is the effect of subsequent directional solidification of the eutectic liquid phase, which is confined to narrow channels between the WC phase in the bicontinuous structure. The possibility exists of being able to generate a single crystal Co-rich matrix that is isotropically reinforced with a rigid network of nanograined WC phase.

In tests performed on VC-doped *n*-WC/Co materials, the measured hardness increases with VC concentration up to a maximum of 2190 VHN at 0.8 wt.% VC(7), **Figure 4**. These data correlate with a reduced mean free path for the cobalt binder phase (i.e. reduced WC grain size), as determined by magnetic coercivity measurements (also confirmed by TEM). This is striking evidence for the potency of VC as a WC grain growth inhibitor in liquid phase sintering of *n*-WC/Co alloys. Recent measurements show that nanograined materials possess superior hardness at all compositions. The relatively high hardness (>1850 VHN) at high Co content (>10 wt% Co) raises interesting questions about the prospects of being able to achieve improved hardness in *n*-WC/Co without sacrificing fracture resistance. We are investigating the relationship between hardness and fracture resistance, including both transverse rupture strength and fracture toughness, in fully sintered *n*-WC/Co, with varying amounts (3-30 wt%) of the ductilizing Co phase.

Another interesting observation has been the striking difference in response of micrograined and nanograined materials to a scratch test (8), **Figure 5**. The micrograined material shows evidence for combined plastic deformation and fracture of the WC

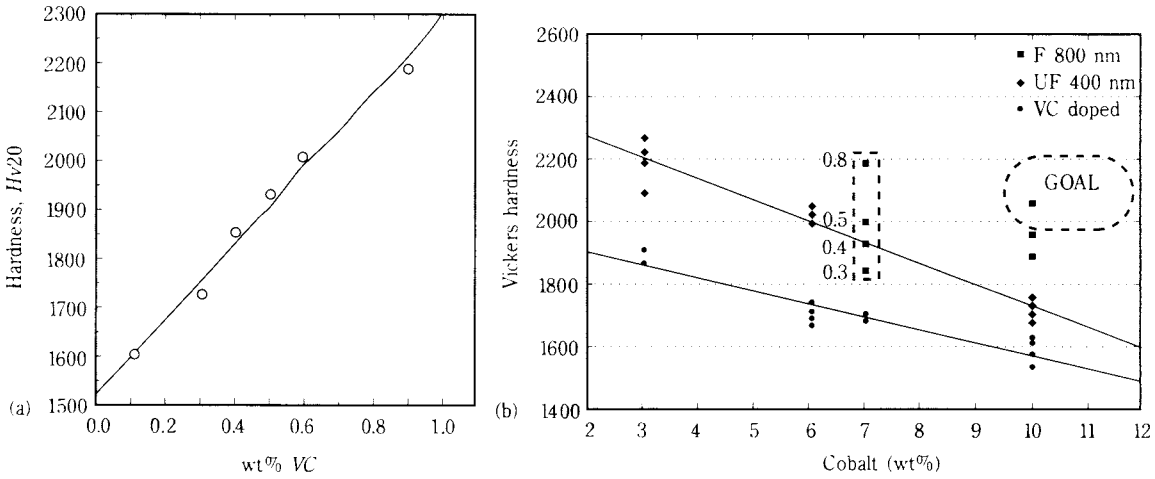

Fig. 4 (a) Hardness vs. wt.% VC (grain growth inhibitor) in WC/7 wt.% Co alloys, (b) hardness vs. wt.% Co binder phase in WC/Co alloys, comparing data for conventional "micrograined" and "nanograined" materials

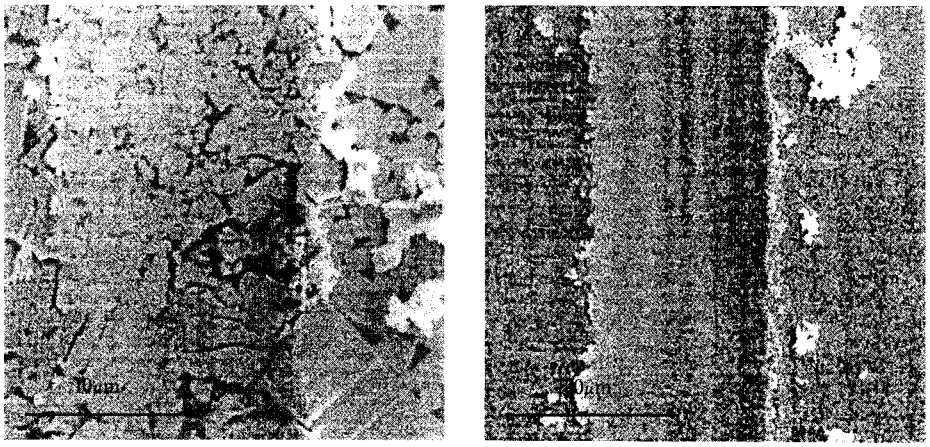

Fig. 5 Comparison of response of (a) micrograined, and (b) nanograined WC/Co samples to a scratch test (100 gm load, using a diamond indentor)

grains, whereas the nanograined material yields by pure plastic deformation, despite its high hardness. Evidence for superior abrasive wear resistance of *n*-WC/Co, as well as for improved cutting performance of *n*-WC/Co drill bits has been obtained (10).

Using SCP technology, Nanodyne Inc. is producing industrial-scale quantities of *n*-WC/Co powders, with compositions extending over the range of commercial interest (3-25 wt% Co). Advances are also being made by several companies in the fabrication of cutting tools, drill bits and wear parts.

5. Nanostructured composites

Ceramic matrix composites (CMC's) are the materials of choice for high temperature structural applications in the next generation of high performance gas turbine and internal combustion engines. Typically, CMC's are fabricated in three steps: (1) the fibers are woven into the desired 2-D or 3-D structures, (2) the woven structures are infiltrated with ceramic matrix powders, and (3) the composite preforms are consolidated by high temperature sintering. Because of the relatively large particle size and the extent of particle agglomeration in commercially available ceramic powders, it is difficult to completely infiltrate the interconnected pores in the woven structures. Thus, the resulting sintered composites can contain many flaws. In addition, because of the high temperature required for sintering, severe fiber-matrix reaction and even fiber damage often occurs. Recent research has shown that these problems can be overcome by utilizing IGC- or CVC-synthesized *n*-ceramic powders as matrix infiltrants, because of the ease with which a nanoparticle slurry can be infiltrated into a woven

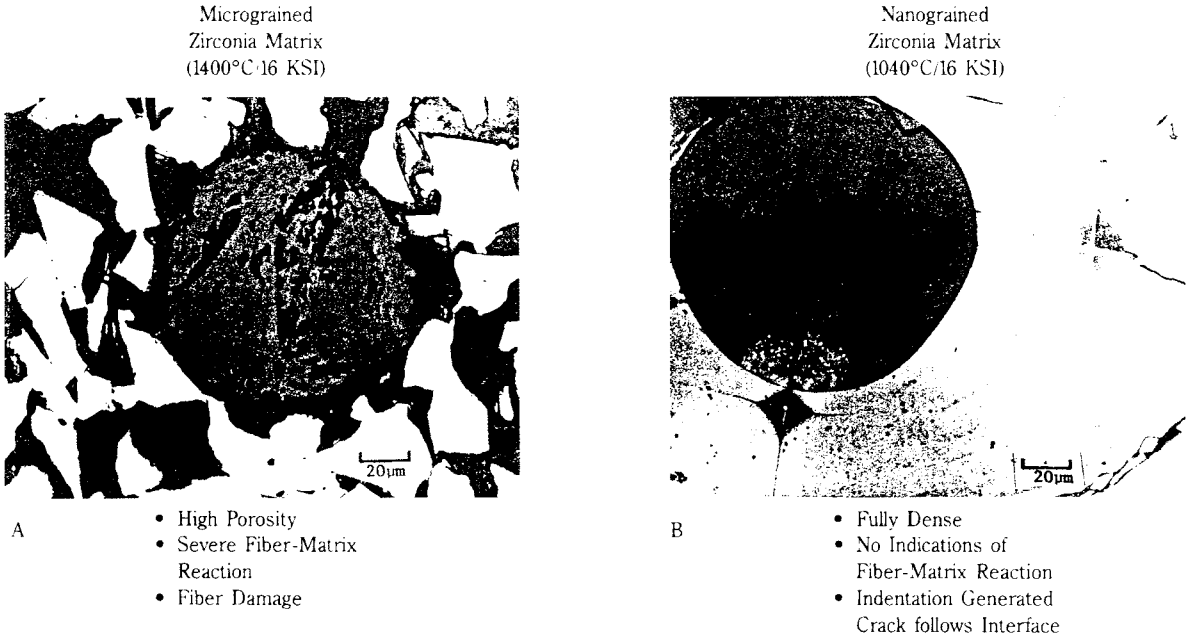

Fig. 6 Comparison of sinterability of (a) micrograined, and (b) nanograined ZrO_2 matrix in an Al_2O_3 fiber-reinforced composite

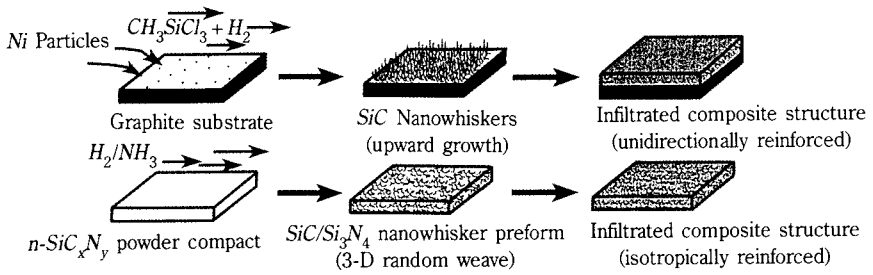

Fig. 7 Schematic diagrams showing two different approaches for synthesizing whisker-reinforced ceramic matrix composites; (a) unidirectionally reinforced, (b) isotropically reinforced

pre-form and its lower sintering temperature.

A recent test performed on an Al_2O_3-fiber weave infiltrated with 'nanograined' ZrO_2 powder has demonstrated the feasibility of both low temperature sintering and ideal infiltration of the fibrous structure (11), **Figure 6**. A fully dense composite was achieved at 1040 C/16 ksi, with no indications of fiber-matrix reaction. In contrast, the fibrous material infiltrated with conventional 'micrograined' ZrO_2 powder, and sintered at 1400 C/16 ksi, showed high porosity and severe fiber-matrix reaction, as well as gross fiber damage. Another interesting feature displayed by the nanograined-matrix composite was that cracks initiated by microhardness indentations tended to follow fiber-matrix interfaces. In other words, the fiber-matrix interfaces appeared to be acting as effective crack blunters. The possibility of enhancing fracture toughness by this mechanism is being explored.

Looking ahead, an interesting extension of this technology would be to fabricate nanostructured whisker-reinforced CMC's entirely from metalorganic precursors. Two options have recently emerged from our research, **Figure 7**. Using trichloromethyl-silane as precursor compound and a nanodispersed nickel catalyst on a graphite support, the feasibility of growing SiC nanowhiskers at practical growth rates of several mm/hr at temperatures of 1100-1400 C has been demonstrated.(12) Whisker growth occurs by the so-called vapor-liquid-solid (VLS) mechanism, where the silicon source gas reacts with the Ni nanoparticles to form a liquid Ni/Si eutectic; thereafter, whisker growth occurs by transport of the silicon through the liquid droplet to the growing whisker at its base, **Figure 8**. Because this is in effect a growth-from-the-melt process, a typical SiC whisker displays a high degree of crystalline perfection and exceptionally high strength. Recently, we have also

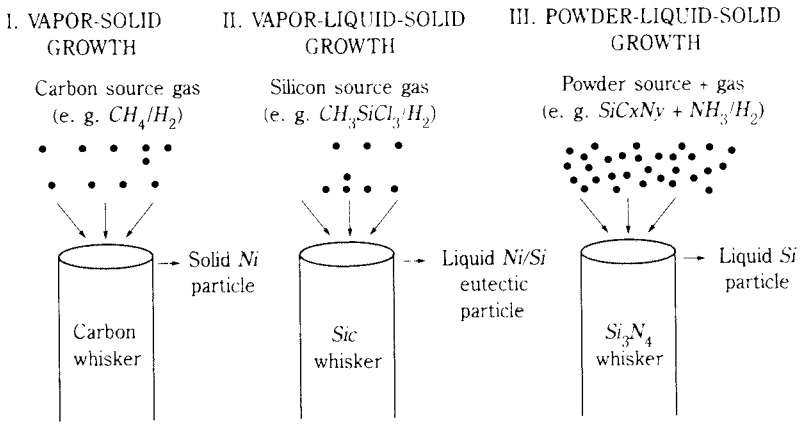

Fig. 8 Illustration of three types of whisker growth mechanism

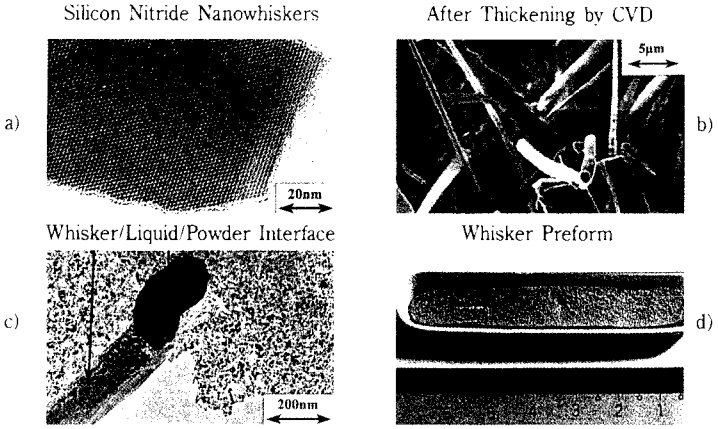

Fig. 9 (a) HREM image of as-synthesized Si_3N_4 whisker, (b) whiskers after thickening by CVD, (c) evidence for powder liquid-solid whisker growth mechanism, and (d) whisker pre-form

discovered that CVC-synthesized *n*-SiCxNy powders, prepared by thermal decomposition of hexamethyldisilazane, can also be transformed into nanowhiskers by a simple heat treatment in a reactive gas stream (5). Thus, heating the n-powders in flowing H_2 at 1200 C yields SiC whiskers, whereas heating in flowing NH_3/H_2 gives Si_3N_4 whiskers. Rapid growth of the whiskers occurs by two different mechanisms: by a new powder-liquid-solid (PLS) growth mechanism and by the more familiar VLS growth mechanism, **Figure 8**. An interesting feature of the thermochemical conversion of the *n*-powders into whiskers is the formation of a three-dimensional random weave, which replicates the shape of the original powder bed from which it is derived. In fact, the whisker pre-form, which is both strong and resilient, can be removed intact from its container, say a ceramic crucible, **Figure 9**, and used for subsequent processing. We are now attempting to infiltrate whisker pre-forms with nanoparticle slurries in order to investigate the possibilities for *n*-CMC sheet fabrication, **Figure 7**.

As an extension of this work, we have also initiated research on *n*-MMC's and *n*-PMC's. The feasibility of processing *n*-MMCs by electro-chemical infiltration of whisker pre-forms has been demonstrated, using electroless nickel plating as the means to infiltrate the woven structures (13). The hardness and wear behavior of the electrochemically infiltrated material has shown a several fold increase over the value of the bulk matrix. Research in *n*-PMC's is still in its infancy, but a novel approach to composite fabrication has been successfully tested.

6. Nanostructured coatings

Thermal spraying is a widely used industrial process for applying protective coatings to materials surfaces. An attractive feature of the process is its ability to produce coatings, ranging in thickness from 25 microns to several millimeters, of almost any desired material. Historically, thermal spray deposition of metal, ceramic and composite coatings was developed for applications in aircraft gas turbine engines. During the past ten years, the range of applications has rapidly expanded into other areas, including land-based gas turbines, diesel engines, automobiles, surgical implants and wear parts.

In thermal spraying, powders are fed into a combustion flame or plasma arc spray gun, where they are rapidly accelerated by the high velocity gas stream exiting from the gun nozzle, **Figure 10**. During the short residence time in the flame or plasma, the particles are rapidly heated to form a spray of partially or completely melted droplets. The large impact forces created as these particles arrive at the substrate surface promotes strong particle-substrate adhesion and the formation of a dense coating. Even so, problems arise from the inability to reproducibly control coating composition, structure and grain morphology, presence of residual porosity, and technical difficulties associated with delivering powder at a uniform rate to the thermal spray gun. Furthermore, it appears that there is no possibility using existing technology to further refine the coating structure, which is the most direct route to enhance properties and performance, nor for that matter can the powder delivery problem be easily resolved. To overcome these limitations, we have been investigating the use of nanostructured powder feed, delivered to the gun in the form of a slurry or generated in-situ from a metalorganic precursor (14). Some progress has already been made, but more work is needed to realize the full potential of uniform and continuous delivery of nanoparticle powders to the thermal spray gun.

Recent research at the University of Connecticut has demonstrated the feasibility of thermal spraying of *n*-WC/Co powders, prepared by SCP technology (see section 4). A procedure has also been devised to reprocess as-synthesized powders into sprayable powder agglomerates, suitable for use in standard powder feed systems, irrespective of whether they have been prepared by chemical or physical methods. Important differences in the thermal spraying of 'micrograined' and 'nanograined' WC/Co powders can be appreciated from **Figure 11**. Micrograined particles experience surface melting only, which contrasts with homogeneous or bulk melting of nanograined particles. Thus, when the particles impinge on the substrate, the semi-solid nanograined particles flow more freely, thereby forming a much denser coating, which has a completely uniform nanocomposite structure. Because of the rapid kinetics of WC nanograin dissolution in the liquid Co, the relative amounts of these two phases can be predicted using the equilibrium phase diagram. Thus, a controlling factor is the degree of superheat above the pseudo-binary eutectic in the WC-Co system. The higher the particle superheat the lower its viscosity, and hence the higher the deformation rate when it collides with the substrate. Under appropriate conditions, the semi-solid particles should display thixotropic behavior, i.e. the dynamic viscosity should decrease with increasing shear rate. The turbulent flow created in the impacting particles should be

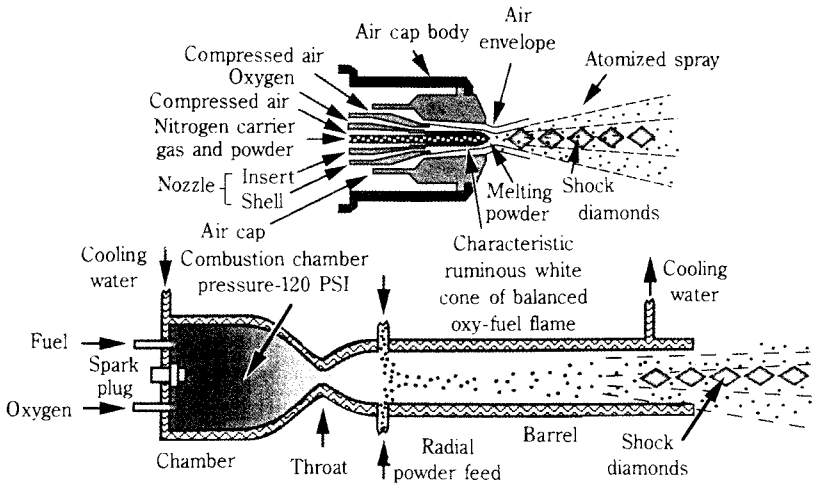

Fig. 10 Schematic diagram of two types of HVOF gun, (a) low pressure throat type (Metro Diamond Jet) and (b) high pressure chamber type (Hobart Tafa JP-5000)

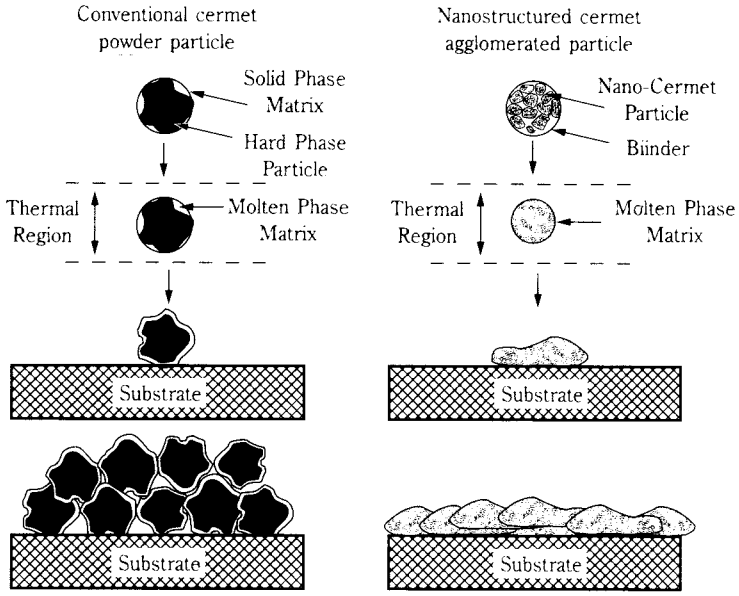

Fig. 11 Comparison of thermal spray deposition of conventional and nanostructured WC/Co powders

useful in disintegrating particle agglomerates and thus promoting structural homogeneity in the deposited coating.

Tests have shown a much higher hardness in the nanograined composite coating, provided that precautions are taken to avoid decarburization in the flame or plasma. One method of accomplishing this is to use low pressure plasma spraying, where the powder particles are naturally protected from oxidation in the plasma flame. High density coatings, with reproducible high hardness values, can be achieved by this means.

In high cobalt alloys, the resulting 'splat-quenched' coating consists of nanodispersed WC grains in an amorphous Co-rich matrix phase(15). The problem of decarburization in thermal spraying of WC/Co powders is less acute in high velocity oxy-fuel (HVOF) spraying, because of the lower particle temperatures and shorter particle residence times, compared with plasma spraying.

Important recent innovations in HVOF and plasma spraying have been the introduction of (1) yttria stabilized zirconia (YSZ) thermal barrier coatings,

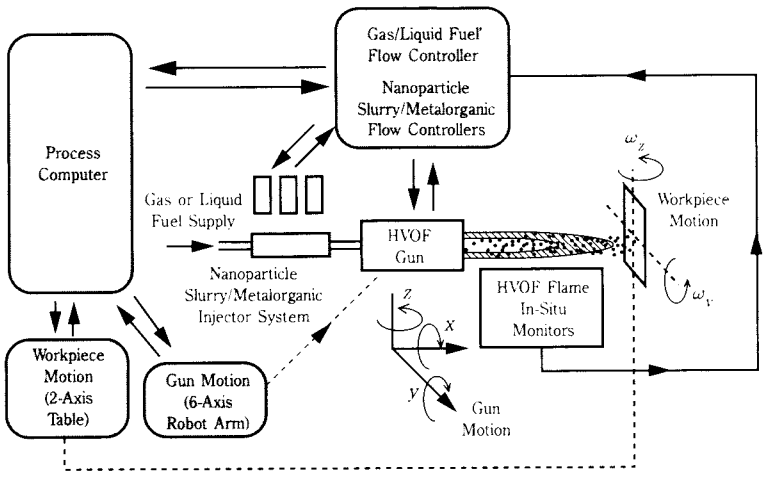

Fig. 12 Intelligent processing of nanostructured coatings using an HVOF thermal spray system

either as an overlay coating on an MCrAlY bond coat or as a continuously graded composite coating, and (2) Cr_3C_2/Ni hard coatings that display hot corrosion resistance superior to that of conventional WC/Co. We have been investigating the use of nanostructured powders of these materials, prepared by ASR and CVC methods (see sections 2 and 3), as feedstocks in thermal spraying. Preliminary work has underscored the need to develop improved means of delivering the nceramic powders to the combustion flame or plasma. Our research is leading us towards the use of nanoparticle slurry feeds, formed by ultrasonic dispersal of the as-synthesized powders, and delivered directly to the spray guns. A multiple source nanoparticle delivery system is now being developed in order to generate multilayer or continuously graded coating structures. The coatings will be designed to minimize thermal expansion mismatch stresses between the different layers, which is a prerequisite to enhance resistance to coating spallation under thermal cycling conditions.

7. Future perspective

Looking ahead, it is clear that whatever the processing route selected to produce a specific nanostructured bulk material or coating, property optimization will require in-situ monitoring and feed-back control. Anticipating this need, an effort has been initiated to probe the environment in which the materials processing occurs.

Currently, attention is focussed on the mechanisms involved in thermal spray deposition of nanostructured coatings, using the high velocity oxy-fuel (HVOF) method. The overall sensing and control system envisioned for an HVOF system is shown schematically in **Figure 12**. The use of diagnostic techniques is required to establish (1) the spatial and velocity distributions of the particles in the combustion flame, (2) the temperature profile and nature of thechemical reactions occurring in the flame, and (3) the characteristics of the splat quenching phenomena as the particles impinge on the substrate. A convenient method for determining spatial and velocity distributions of in-flight particles is by thermal imaging or laser strobe illumination, whereas spectral sensors may be used to establish the nature of the chemical reactions occurring in the flame, which is a critical factor in spray deposition of coatings of n-WC/Co and other materials. A powerful technique for detailed investigation of combustion phenomena is laser-induced fluorescence, which may be used to determine the nature of chemical species in the high velocity gas stream, and to provide data on the shock front associated with the gas stream. As can readily be appreciated, the entire thermal history of the nanoparticles while in transit in the HVOF flame largely determines the structure of the resulting deposited coating.

Experimental data obtained from the various imaging and flame analysis methods will be used to validate computer simulations of the HVOF process. Global diagnostics of such variables as gas and particle flow rates, gas pressure, stand-off distance (gun to substrate), and substrate temperature will be correlated with coating structure and morphology. This information will be benchmarked with the simulations, leading to reduced or derived process simulators required for intelligent control algorithms and system development. It is anticipated that these studies will provide the basis for the design and construction of a production thermal spray unit, with real-time process control. A feature of this unit will be multi-axis robotic

control of the thermal spray gun, which will permit uniform deposition of shape conformal coatings on complex parts in a highly reproducible manner. This is critically important in high volume production of coatings, where detailed inspection of individual components is not possible.

A successful initiative in thermal spraying will lead quite naturally to a consideration of other opportunities for modeling, numerical simulation and diagnostics, particularly in the area of vapor phase synthesis of nanostructured powders from metalorganic precursors.

9. References

1) H. Gleiter, Progress in Materials Science, 33 (1990).
2) K.E. Gonsalves, T.D. Xiao, G.M. Chow and C.C. Law, Nanostruct. Mater. 4, 130 (1994).
3) T.D. Xiao and P.R. Strutt, University of Connecticut, unpublished research (1994).
4) W. Chang, G. Skandan, H. Hahn, S.C. Danforth and B.H. Kear, Nanostruct. Mater.4, 345 (1994).
5) W. Chang, G.Skandan, S.C. Danforth, B.H. Kear and H. Hahn, Nanostruct. Mater. 4, 507 (1994).
6) L.E. McCandlish, B.H. Kear and B.K. Kim, Mater. Sci. and Tech. 6, 953 (1990).
7) B.H. Kear and L.E. McCandlish, Nanostruct. Mater. 3, 19 (1993).
8) T.E. Fischer, Stevens Institute of Technology, unpublished research (1994).
9) R.K. Sadangi,B.H. Kear and L.E. McCandlish, to be published (1994).
10) Z. Fang, J.W. Eason, J.M. Reed and S.E. Tindle, Proc. IPC Printed Circuits Expo, IPC, Lincolnwood, IL (1994).
11) S. Bose, Pratt & Whitney, East Hartford, CT, unpublished research (1994).
12) B. Gallois, Stevens Institute of Technology, unpublished research, (1994).
13) K. Sheppard, Stevens Institute of Technology, unpublished research (1994).
14) R.F. Boland, P.R. Strutt and B.H. Kear, US Patent Application (1994).
15) L.E. McCandlish, B.H. Kear, B.K. Kim and L. Wu, Protective Coatings: Processing and Characterization, ed. R.M. Yazici, The Metallurgical Society, Warrendale, PA (1990).

Author's short biography

Bernard H. Kear

Professor and Chairman

Deparment of Mechanics and Materials Science

Rutgers University, Piscataway, NJ 08854

Bernard H. Kear received his B.Sc., Ph.D. and D.Sc. degrees in Materials Science and Engineering from the University of Birmingham, England, From 1958-63 he was with the Franklin Institute in Philadephia where he studied the effects of long-range ordering on the plastic properties of crystals. From 1963-81 he was with the Pratt & Whitney Division of United Technologies Corporation where he investigated the interrelationships between structure/properties/processing in superalloys, participated in the development of single crystal turbine blade technology, and spearheaded the development of laser surface modification treatments. From 1981-86 was Scientific Advisor at Exxon's Corporate Research Center, where he conducted research in chemical vapor deposition and its applicability to large scale in-situ surface modification of reactor vessels and the up-grading of the surface properties of steel structures. In 1986 he assumed his present position as State of New Jersey Professor of Materials Science and Technology. Presently, he is Chairman of the Department of Mechanics and Materials Science. His current research activities are focused on chemical vapor deposition of ceramics, chemical synthesis of nanostructured composite materials, and MOCVD synthesis of high Tc superconductors. Kear has published .00 technical papers, has edited 9 books in the field of materials, and has been granted 30 patents. He was awarded the Mathewson Gold Medal of TMS-AIME in 1971, and the Howe Medal of ASM in 1970. He was elected to the National Academy of Engineering in 1979. From 1983, he served as a member of the National Materials Advisory Board and was Chairman from 1986-1989. Currently, he is co-editor of the journal Nanostructured Materials.

Group Report

Comparative Study of Particle Size Analyses Using Common Samples†

Hideo Yamamoto and Tatsushi Matsuyama
*Department of Engineering, Soka University**

1. Introduction

The particle size is one of the most essential factors representing properties of powder or its system. Indeed, various instruments for particle size analysis based on various principles have been developed and used. The progresses are remarkable today in application of new principles, enhancement of performance, and rapid and simple measurement with introductions of laser, computer technology and the latest sensors. High-tech machines are coming onto the market one after the other, and more than 50 models are presently available; each of them gives reproductive data rapidly and easily only if you load a sample and press a button.

Traditional problems of particle size analysis are still unsolved in spite of these progresses in apparatuses. For example, if you compare the results of particle size measurements obtained by different principle or methods, they often do not give good agreement. This tendency seems to reside in the background of the diversification of the measuring principles and instrument models. One of the major factors is that the definition of a particle size obtained varies with each principle of measurement. The actual measured quantities are physical or geometrical quantities depending on the size of a particle; they are e.g., areas, volumes, sedimentation velocities, or the intensity distributions of scattered light. Based on these measurements, the particle size is always represented by a diameter, having dimension of length, of a spherical particle which gives the same observed quantity. This may be a natural reason of incoincidence in measured particle sizes except for spherical particles. Furthermore, the users face to a problem that the incoindidences are observed in not only the results based on different principles, but also in the results measured by different models based on the same principle, or measured by different machines of the same model. It is hence important to compare various models mutually and to investigate the causes of the differences in the measured results.

The Society of Powder Technology, Japan, has been repeatedly tackling this problem. As early as 1961, the first "Particle Size Analysis Working Group" was organized, and joint measurements with various instruments using common samples were performed[1]. Later, commercial models had been diversified by applying new principles and introducing new sensors and computers. In 1983, the second "Particle Size Analysis Working Group" was organized and joint measurement was projected. A comparative study on the various principles and instruments was performed comprehensively using seven common samples, and had given a great achievement[2]. These common samples were, except for one kind, particles in the micron order or larger size, and the measurement of the particles in the sub-micron region was regarded little. The rapid progress in the material sciences and engineerings requires today the strict particle size analysis in the region of sub-micron, and many corresponding models have been developed.

The "Sub-Micron Particle Size Analysis Working Group" was organized as the third working group, and the principles and instruments have been studied in detail for more than four years since 1989. Following the tradition, the group's main activities were the joint measurements using common samples (six types). Based on these measurements, the agreements between the results given by different models were studied including theoretical discussions on the principles. The summary of the activities of the past four years and part of the achievements are reported here. The details are compiled and published in a book "Particle Size Analysis and Technology" (ed. The Society of Powder Technology, Japan, published by Nikkan Kogyo Shinbunsha; 1994). It should be read if interested.

2. Organization, activities, tested models

The working group was finally made up of 64 members from 22 universities and public research institutes, 15 user companies, and 14 makers and dealers.

* 1-236 Tangi-cho, Hachioji, Tokyo 192, JAPAN
Tel. & Fax: +81/426-91-9454

† This report was originally printed in *J. Soc. Powder Technology, Japan.* **32**, 117 (1995) in Japanese, before being partially translated into English with the permission of the editorial committee of the Soc. Powder Technology, Japan.

The working group was organized into three classes as managing committee, small working groups and general meeting. The specific joint measurements were carried out by the small working groups with each principle. All members were, therefore, divided into ten small working groups shown in **Table 1** (duplicate participation accepted). To classify the principle and method of measurement, various criteria would be available, and ten groups as shown in **Table 1** were decided for the sake of convenience based on a certain viewpoint.

Each SMALL WORKING GROUP was chaired by the small group manager, and commercial models using the same principle were comparatively studied. Specifically, six common samples were jointly measured using the *engaged models* listed in **Table 1**. On the basis of the results, the theoretical and mechanical problems of the method and agreement among models were closely investigated. Each small group included makers or dealers engaged in the development or sale of the test model, and the features, problems, and handling cautions of the instrument from the aspect of both hardware and software were explained in discussions. They also participated in the joint measurement, and submitted their recommending optimum record. Their data and the other users' data were also compared. Based on these joint measurements, problems and noticed points in the measurement were studied for each model.

The MANAGING COMMITTEE consisted of the small working group managers and the persons in charge of study on sample preparation. The committee selected the common samples, measured and circulated the basic properties of the particles, and studied the sample preparation method. Discussions on comparison of *different measuring principles* were mainly performed here based on the data reported by the small groups.

At the GENERAL MEETING, specific reports by the small working groups and a comprehensive report by the managing committee were made, and the further specified study was carried out on the basis of their results. These studies disclosed some problems, and gave some solving method to be achieved theoretically or technically. These discussions were fed back into subsequent joint measurements.

3. Properties of common samples and sample preparation condition

3.1 Properties of common sample

Six kinds of powder were used as the common

Table 1 Classification into the small working groups and tested models

Measuring principle	Small group manager	Tested models
Centrifugal sedimentation light extinction method	K. Suzuki (National Industrial Research Institute, Nagoya)	CAPA700 (Horiba) SA-CP4L, SA-CP3 (L), SA-CP2 (Shimadzu) SKA5000, MPS-Z (Seishin enterprize) BI-DCP (Brookhaven)
Sedimentation X-ray absorption method	S. Edno (National Institutie for Resources and Environment)	SediGraph 5100, SediGraph 5000D (Micromeritics) BI-XDC (Brookhaven)
Laser diffraction and scattering method	H. Takano (Doshisha Univ.)	HELOS (Sympatec) HR-850 (B) (Alcatel) LA-500, LA-700 (Horiba) LS130 (Coulter) MasterSizer (Malbern) MICROTRAC MKII SRA, SPA, FRA, (Reeds & Northrup) SALD-1100, SALD-2000 (Shimadzu) SK-PRO 7000S, LMS-24 (Seishin enterprize)
Optical blockage method	F. Ikazaki (National Institute of Materials and Chemical Research)	CIS-1 (Galai)
Electrical sensing zone method	H. Yamamoto (Soka Univ.)	Multisizer (Coulter)
Photon correlation method	M. Nakayama (Kokushikan Univ.)	AUTOSIZER (Malbern)
Chromatography	Y. Mori (Doshisha Univ.)	Unavailable in the market, house-made
Gas phase method	C. Kanaoka (Kanazawa Univ.)	DMA, Cascade impacter
Centrifugal sedimentation weight method	T. Yokoyama (Hosokawa micron Co.)	Differential pressure method Unbalance method,
Image analysis method	S. Endo (National Institutie for Resources and Environment)	IP-1000 (Asahi Chemical Industry) LuzexF LA555 (Pierce)

Note: Present positions of small group managers are shown

samples: they are abrasives WA #10000 and WA #8000, iron oxide (Fe_2O_3: α-hematite), and three types of monodispersed spherical silica particles with mean particle size of about 0.5, 0.9, and 1.4 μm. **Table 2** shows measured values of particle density, refraction index, and ζ-potential of the samples. The measuring conditions for each property are also shown in the table. In the joint measurements, these properties were used as common conditions. Properties considered as suitable for a certain model (e.g., refraction index) were also determined for each model if necessary, and the measurement using such the values was executed again.

3.2 Sample preparation conditions

The sample preparation methods and their conditions were given the most regard in the joint measurement of the common samples. Of course, there is an adequate method of preparing samples for each principle and apparatus. Here, however, the following common conditions of the minimum limits were set to study the agreements between principles and between models. The small working groups took measurements in both specified common conditions and optimum conditions for each principle and instrument.

i) WA #10000, WA #8000, and iron oxide

dispersion medium: 0.05 wt% aqueous solution of sodium hexametaphosphate

mother liquor concentration: Not particularly specified. Sample prepared as an appropriate particle concentration for each instrument from the beginning.

dispersion condition: Dispersion for 20 minutes in an ultrasonic bath. The power of ultrasonic waves is not specified.

ii) SP5H (0.5 μm spherical silica particles)

dispersion medium: 0.05 wt% aqueous solution of sodium pyrophosphate.

mother liquor concentration: particle concentration of 0.1 wt% (5 wt% for X-ray method). It was diluted to optimum concentration for each instrument before measurement.

dispersion condition: Dispersion for 15 minutes in 300 W ultrasonic bath. Here, the sample container (beaker) was placed at the resonance point of the ultrasonic bath.

iii) SP9H, SP14H (0.9, 1.4 μm spherical silica particles)

dispersion medium: 0.025 wt% aqueous solution of sodium pyrophosphate.

mother liquor concentration: particle concentration of 0.1 wt% (5 wt% for X-ray method). It was diluted to optimum concentration for each instrument before measurement.

dispersion condition: Dispersion for 15 minutes in 300 to 600 W ultrasonic bath. Here, the sample container (beaker) was placed at the resonance point of the ultrasonic bath.

The sample preparation condition i) was determined in the first days of this study, when the effects or the prepared amount of sample, hysteresis before measurement, and power of ultrasonic wave on the dispersion state of the sample were not known sufficiently, and therefore, the condition setting was somewhat ambiguous. Afterwards, as the working group activities were advanced and the informations were accumulated, the effects of the concentration of the mother liquor and the processing history and duration before measurements had been revealed. The search methods such as optimum dispersion operating point in the ultrasonic bath were also clarified, and hence, the conditions were set strictly for the measurements of silica particles. The relevant informations are also available in the book ''Particle Size Analysis and Technology''.[3)]

Table 2 Basic properties of the common samples

	Abrasive		Iron oxide	Spherical silica particles		
	WA #10000	WA #8000	(Fe_2O_3)	SP5H (0.5 μm)	SP9H (0.9 μm)	SP14H (1.4 μm)
Particle density[1)] (x10^3 kg/m^3)	3.74	3.27	5.01	1.95	2.25	2.25
Refraction index (real number portion only)	1.73	1.76	2.4. or more (difficult to measure)	1.44	1.45	1.45
ζ-potential	-67.9[a)]	-80.2[a)]	-74.8[a)]	-89.9[b)]	-91.6[c)]	-95.0[c)]

1) Mean of three measurements by auto-pycnometer 1320 (Micromertics; air replacement method)
2) Measured at RIMS (Kyoto Fission Track Co.)
3) Measured with model 501 of PEN KEM (electrophoresis method)
a) In 0.05 wt.% aqueos solution of sodium hexametaphosphate
b) In 0.05 wt.% aqueous solution of sodium pyrophosphate
c) In 0.025 wt.% aqueous solution of sodium pyrophosphate

4. Results of measurements

There are numerous concepts regarding the method of comparison of the results, but, the results were summarized basically for the following principle in this report.

1) Results are summarized into one diagram for each sample and each principle of measurement, and the different models and instruments were comparatively studied.
2) The meaning of particle size obtained with each principle is basically classified into the follows:
   a) particle size by geometrical characteristics,
   b) particle size by dynamic characteristics, and
   c) particle size by optical characteristics.

Accordingly, the electrical sensing zone method, optical blockage method, image analysis method were divided into group (a), all of the sedimentation method including centrifugal light extinction method, X-ray absorption method, and centrifugal sedimentation weight method were divided into group (b), and Laser diffraction and scattering method and photon correlation method were also divided into group (c).

Because of limited pages in this paper, all data cannot be introduced. Please refer to the original paper[4] for details.

4.1 WA#10000

Figure 1 summarizes the results of geometrical characteristic measurement methods, that is, the optical blockage method (dotted line), the electrical sensing zone method (solid line), and image analysis method (single dot chain line). In this case, the lower measurement limits of the optical blockage method and the electrical sensing zone method are 0.40 and 0.47 μm, respectively, and existences of the smaller particles are neglected; therefore, the results indicate rather larger particle size distributions, so these results should be regarded as only reference data. On the other hand, the image analysis method seems to miss the larger particles, because the number of particles measured was less than a thousand. The difference seen between the results of two models is suspected to be due to preparation method of sample images. In general, the scale shown on the sample image obtained with an electron microscope has an error of several percent, and it was found that there might be an error of nearly ten percent between sample images taken with different electron microscopes. Hereinafter, therefore, in the comparative study of image analysis, common sample images printed on the same scale from the negative taken with the same electron microscope were used.

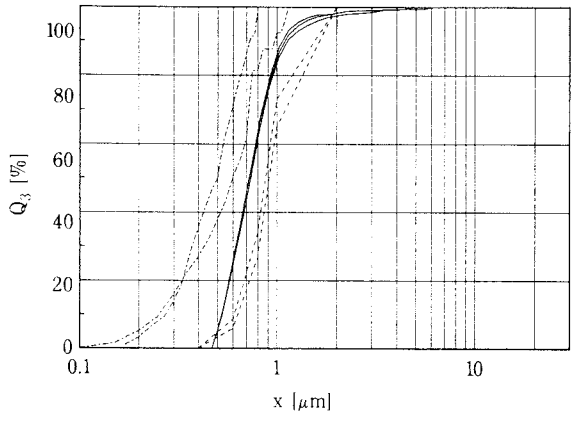

Fig. 1 Results of WA#10000 by the electrical sensing zone method (solid line: 6 results), the optical blockage method (dotted line: 2 results), and image analysis method (single dot chain line: 2 results)

Figure 2 compares two commercial models of centrifugal sedimentation light extinction method made by the same maker. The solid line shows the higher (later) model. The results of the higher model show four different measurement modes (three acceleration modes and one constant speed mode), and considerable differences are noted. The rightmost solid line, which indicates the result of the constant speed mode, shows the result of the larger particle size distribution compared to results of the other modes (acceleration). Here, it should be noticeable that the disturbance of the sample liquid occurs due to the convection or the like during the acceleration period until the rotating speed becomes constant. On the other hand, the results are also different depending on the models, but the model difference alone could not be blamed because the operators and places of measurement were different.

Figure 3 shows the results obtained with two models of X-ray absorption method. The solid line

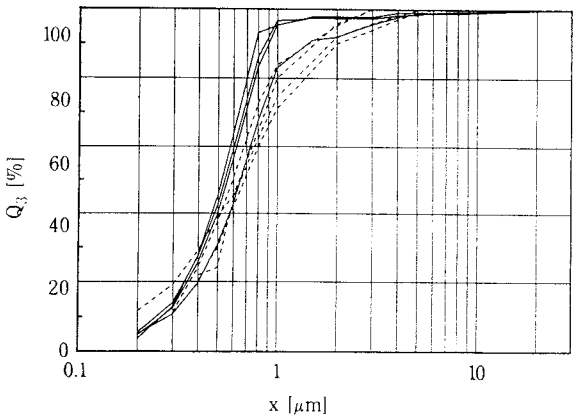

Fig. 2 Results of WA#10000 by centrifugal sedimentation light extinction method (2 models of the same maker)

indicates the higher model, and here six results obtained by different operators (and different instruments) are shown. Although there is a slight difference at the fine particle size, the reproductivity is extremely excellent. A slight variation due to difference of model was also noted.

Figure 4 summarizes the results of dynamic characteristics (sedimentation). A difference arises depending on what is used to measure the successive change of the sedimentation amount of the particles. The solid line denotes the optimum data* of three models (of three different makers) of centrifugal sedimentation light extinction method. The difference in the results would show the appearance of the difference in the correction method of the extinction coefficient proposed by each makers because this sample contains many sub-micron particles. A major weakpoint of the light extinction method is that the correction of the extinction coefficient for sub-micron order particle is necessary. This is because that the size of particle is similar to or lower than the wavelength of visible light (0.38 to 0.78 μm). By contrast, the X-ray absorption method (dotted line) dose not require correction of the extinction coefficient as does the light extinction method. Hence, the difference between two dotted lines (different models) seems to be due to the difference in the instrument construction and data processing software. It is noticeable here that the weight method (differential pressure method, unbalance method) in the process of development coincides well with the X-ray absorption method.

Figure 5 shows the results of the laser diffraction and scattering method. Fourteen results obtained with seven models are shown. The dotted lines indicate the results of incomplete dispersion.** Since the data of WA#10000 correspond to the oldest measurement of the working group, the refractive index of the specified common conditions could not be entered at some instruments, which allowed only the fixed value.*** Therefore, in spite of the same principle, a large difference was found in the results, which seems to be largely influenced by the input of refractive index because of the sample having many particles in the sub-micron region, aside from the difference in the instruments construction and analysis software. The result marked with a circle is a characteristic result of this model, although noted in other samples.

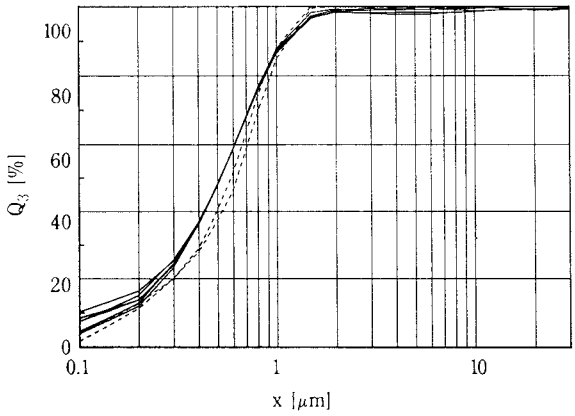

Fig. 3 Results of WA#10000 by X-ray absorption method (2 models)

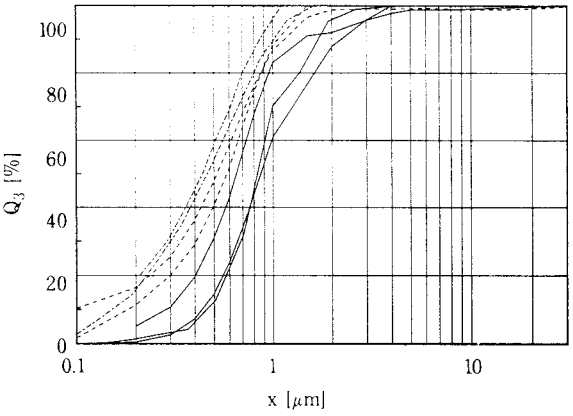

Fig. 4 Comparison of WA#10000 on various sedimentation methods (light extinction with 3 models: solid line, X-ray method with 2 models: dotted line, weight method with 2 models: single dot chain line)

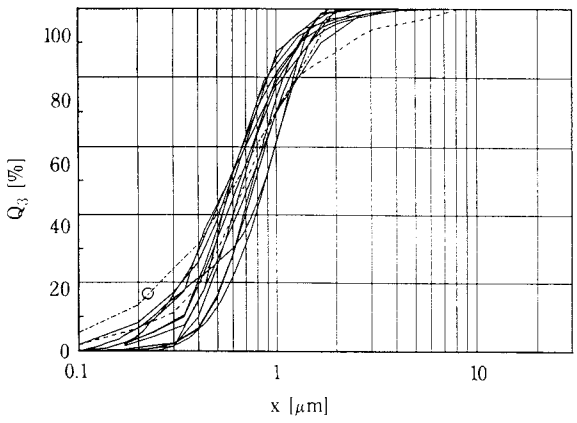

Fig. 5 Results of WA#10000 by lasesr diffraction and scattering method (7 models, 14 results)

* Results of measurements in the optimum conditions of the instruments proposed by the supplier of the instrument, regardless of the common conditions.

** The power and irradiation time of the ultrasonic bath used by this operator were 300 W and 20 min, conforming to the common condition, however, this operator also reported similar data indicating incomplete dispersion with other principles and samples. This seems to be caused by the fact that the bath power was not in a rated state or the resonance point could not be found.

*** Afterwards, with the running of the common measurements, the instruments and softwares were improved, and the instrument constants came to be available for each model.

4.2 WA#8000

Figure 6 shows the results of the optical blockage method (solid line) and the electrical sensing zone method (dotted line). Distributions of this sample were within the measuring range of these instruments. The repeatability of the electrical sensing zone method is extremely excellent. Difference in the results of the optical blockage method was probably due to instrumental errors and difference in sample concentration.

Figure 7 shows the results of the centrifugal sedimentation light extinction method (dotted line) and X-ray absorption method. It could be considered that there was a difference in the strict sense; however, in comparison to the results of WA#10000, it is reasonable to regard that these results coincided with each other. This is due to absence of the sub-micron particles; accordingly, this sample gives no difference due to the correction of the extinction coefficient. The difference in maximum and minimum diameter seems to be owing to the instrument construction and operating conditions.

In **Figure 8**, the results of the centrifugal sedimentation weight method (dotted line) are overlapped on **Figure 7**. These good coincidences with the results of the light and X-ray method make a expectation of the practical use of this method.

Figure 9 shows the results of the laser diffraction and scattering method. The figure shows 26 results obtained with 7 models. Although not clear in the figure, the reproductivity is superior with the same model. There is, however, a difference at the fine particle size, and a slight difference is noted depending on the models. Besides, as compared with other principles of the measurement, all models provided larger values with a significant difference. The cause of this is unknown.

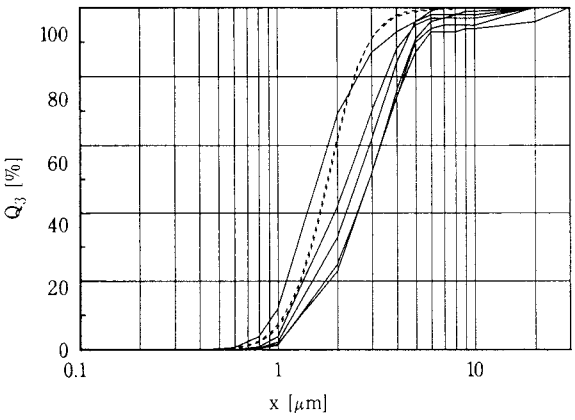

Fig. 6 Results of WA#8000 by the electrical sensing zone method (dotted line: 2 results) and the optical blockage method (solid line: 6 results)

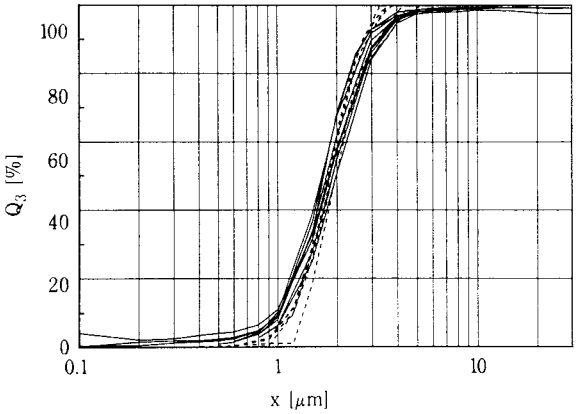

Fig. 7 Results of WA#8000 by sedimentation method (light extinction with 1 model, 7 results: dotted line, X-ray absorption with 2 models, 9 results: solid line)

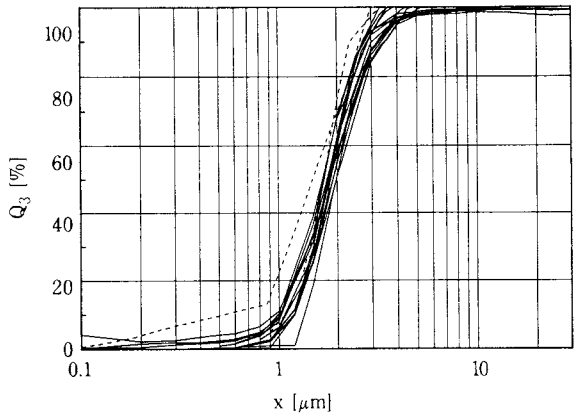

Fig. 8 An overlap of weight method (dotted line) onto Fig. 7

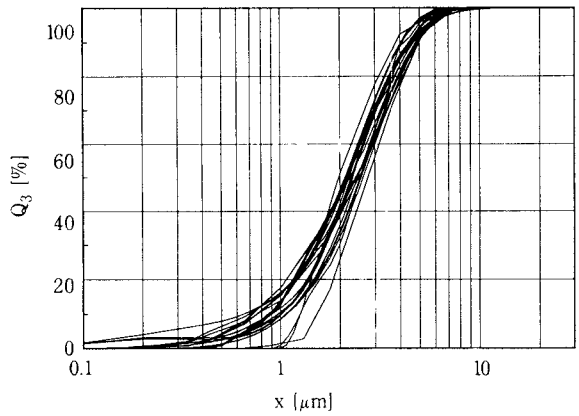

Fig. 9 Results of WA#8000 by laser diffraction and scatering method (7 models, 26 results)

4.4 SP5H (monodispersed silica spherical particles of around 0.5 μm)

Figure 10 shows the results of the image analysis method (solid line, 3 models) and the electrical sensing zone method. With the electrical sensing zone method, the lower limit of measurement was 0.52 μm, therefore, this should be regarded as an only reference data. The result of the image analysis method shows

a very narrow distribution. A slight difference at the fine particle size is due to a difference in the image processing and conversion method into the diameter of the corresponding circle. Although the same sample images were used, the number of particles extracted to analysis was slightly different.

Figure 11 shows the results of the centrifugal sedimentation light extinction method (4 models, 6 results). The data indicated by the solid line and the closer (2 models) were corrected with the extinction coefficient, while other three results indicated by dotted line were not corrected; they caused some differences. The dotted line shows three results obtained with one model, and two lines from the right indicate the rotating speed of 3000 and 5000 rpm in its order. The lower rotating speed causes the greater centrifugal dilution effect (see chapters 4 and 5 of "Particle Size Analysis and Technology"[3]), and the results show as if non-existent large particles were present. The other dotted line shows the result after correction of the data at 5000 rpm with respect to the centrifugal dilution effect. The enhancement of the larger particles distribution has been successfully corrected. In the case of the sample having a wide distribution, it seems that the centrifugal dilution effect is less obvious. On the other hand, in the case of a narrow distribution as in this sample, the correction is necessary because it appears so significant that it cannot be ignored. The single dot chain line on the right side shows the result obtained with the model using a line start method (without correction of extinction coefficient). The line start (simultaneous sedimentation) method maintains the sample particles at a certain sedimentation liquid surface, and allows them to sediment centrifugally at time $t = 0$ simultaneously. Therefore, as far as the successive changes of particle concentration of the same measuring surface are observed, no correction on the centrifugal dilution effect is necessary, because the sedimentation distance is identical and, therefore, that effect is the same for all particles of any size. Accordingly, it coincided well with the result of the light extinction method when the correction for the centrifugal dilution effect (the leftmost dotted line) was introduced.

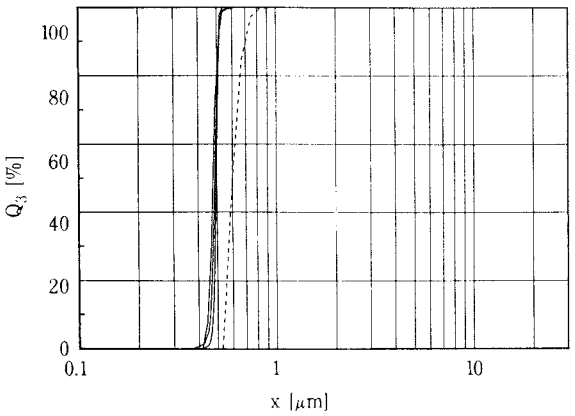

Fig. 10 Results of silica particles (SP5H) by electrical sensing zone method (dotted line: reference data) and image analysis (solid line: 3 models)

Figure 12 shows the results of the X-ray absorption method. The solid line shows the results of the same model (gravitational sedimentation), while the operator (instrument) was different. The long tail on the coarse particle side is due to poor dispersion. The dotted line represents the data of the model used for centrifugal sedimentation. From this point of time, the model using the centrifugal sedimentation comes to be available for the X-ray absorption method.

Figure 13 shows the results of the laser diffraction and scattering method (solid line: 5 models and 7 results) and photon correlation method (dotted line). There are considerable differences as from narrow to wide distributions depending on the models. In

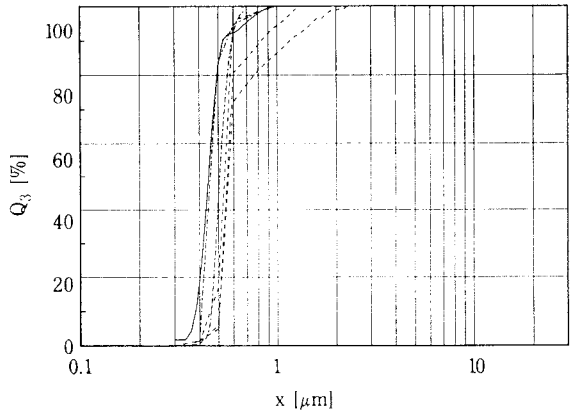

Fig. 11 Results of silica particles (SP5H) centrifugal sedimentation light extinction method (4 models, 6 results)

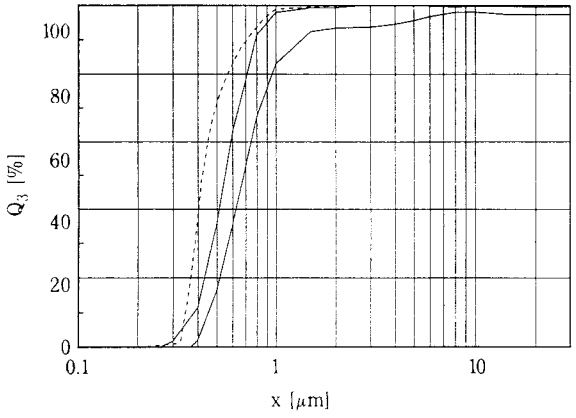

Fig. 12 Results of silica particles (SP5H) by X-ray absorption method (2 models, 3 resuls)

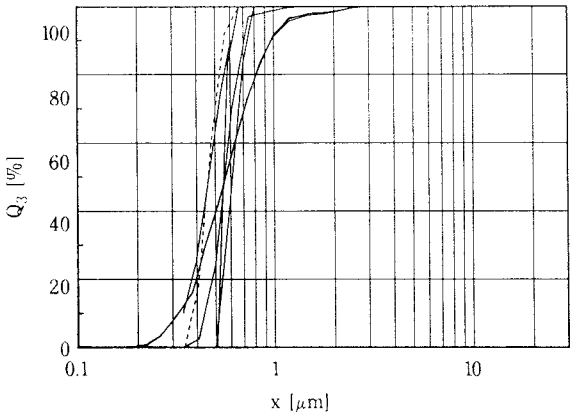

Fig. 13 Results of silica particles (SP5H) by laser diffraction and scattering method (solid line: 5 models, 7 results) and photon correlation method (dotted line)

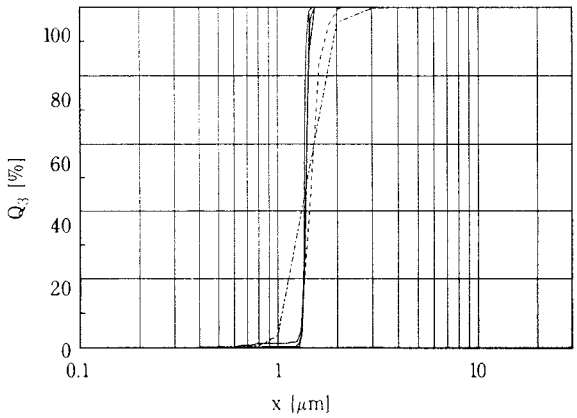

Fig. 14 Comarison of silica particles (SP14H) by the optical blockage method (single dot chain lilne), electrical sensing zone method (dooted line), and image analysis method (solid line: 3 models)

general, if the refraction index is adjusted to the measured value or reported value, a considerable difference appears in the results depending on the models. This is because that the refraction index of the measured or reported value is not an optimum for each instrument, but each instrument has its own optimum value. The photon correlation method (dotted line) provides a narrow distribution and the mode diameter is close to 0.5 μm. This fact suggests that the photon correlation method is very useful for monodispersed samples under sub-micron size. In the present study of the working group, the data of the photon correlation method could not be accumulated sufficiently, but this method is expected to be used widely for the measurement of sub-micron samples in the future, and it is necessary to investigate this method closely in the near future.

4.6 SP14H (monodispersed silica spherical particles of around 1.4 μm)

Figure 14 shows the results of the image analysis method (solid line: 3 models, 3 results), the electrical sensing zone method (dotted line) and the optical blockage method (single dot chain line). Both the electrical sensing zone method and the optical blockage method cover the size distribution of the sample particles in their measuring range. The optical blockage method gave results with broad distribution in comparing to others. The electrical sensing zone method (dotted line) gave results coinciding with results of the image analysis method, but gave a tail in the coarse range. This is caused by the phenomenon that the particles do not pass through the center of the aperture (here, we called it "wall vicinity pass effect"). The electrical field strength in the cross section of the aperture is not uniform. As the strength near the wall is relatively larger than it at the center, a particle passing near the wall is observed as a somewhat larger particle (see chapter 11 of "Particle Size Analysis and Technology"[3] for detail).

Figure 15 shows the results of the centrifugal sedimentation light extinction method (5 models, 8 results). Here again, the distribution of the larger particles was enhanced in the results of the model not corrected for the centrifugal sedimentation dilution effect. The dotted line represents the result of the line start method. It is observed as a narrow distribution very close to the results of the image analysis method shown in **Figure 14**.

Figure 16 shows the results of the X-ray absorption method (2 models, 5 results). The gravitational sedimentation method (solid line) gave a wide distribution. The results of the centrifugal sedimentation model (dotted line) indicated a narrow distribution, and they nearly coincided with the dotted line in the previous figure. These models were made by the same maker. In the case of that the same maker supplies models based on different principles, the results are often incoincident, which should be taken into consideration.

Figure 17 compares the results of all sedimentation methods. The single dot chain line represents the results of weight methods. A considerable difference is noted depending on the measured physical quantity.

Figure 18 shows the results of the laser diffraction and scattering method (9 models, 12 results), and photon correlation method (dotted line: 1 model). The results of the laser diffraction and scattering method were considerably different as in the cases of other silica particle samples. The photon correlation method

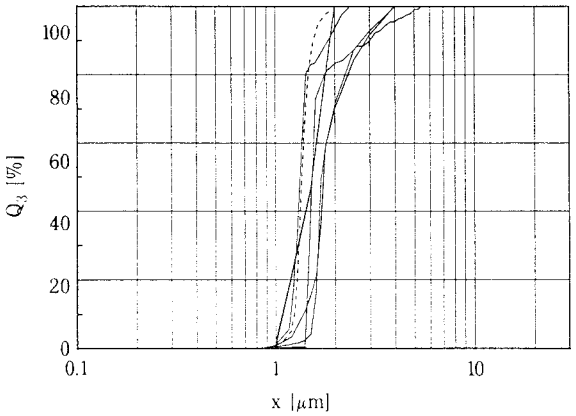

Fig. 15 Results of silica particles (SP14H) by centrifugal sedimentation light extinction method (5 models, 8 results)

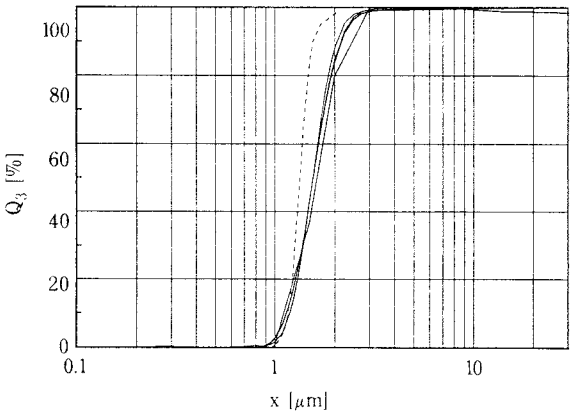

Fig. 16 Results of silica particles (SP14H) by X-ray absorption method (2 models, 5 results)

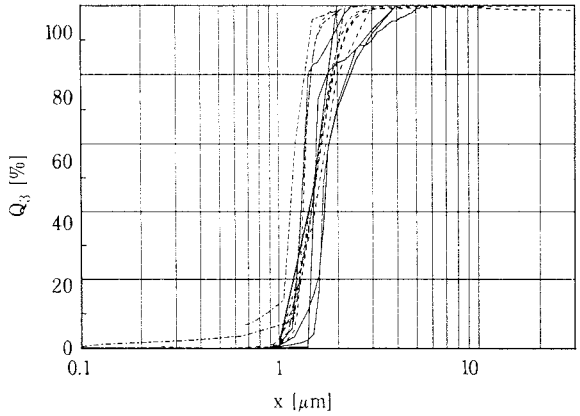

Fig. 17 Results of silica particles (SP14H) by various sedimentation methods (single dot chain line: by weight method)

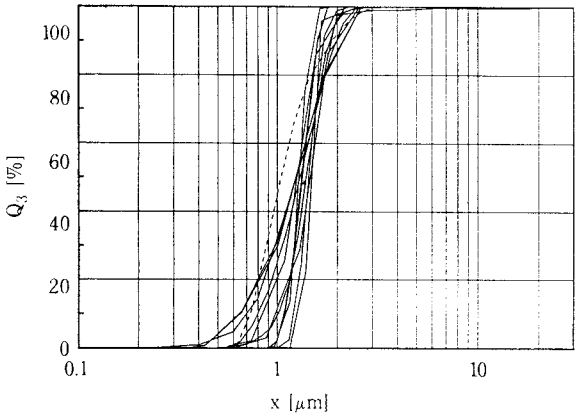

Fig. 18 Results of silica particles (SP14H) by laser diffraction and scattering method (solid line: 9 models, 12 results) and photon correlation method (dotted line: 1 result)

gave results as the smaller particles. The upper measurement limit of the photon correlation method seems to be about 1 μm.

5. Conclusions

Unfortunately, all data cannot be introduced within the limited number of pages of this paper. For details see the original paper.[4] From the limited data disclosed here, it may be at least understood that agreement of the results is not sufficient for principles, models and instruments. The cause is not sufficiently discussed herein. The details should be discussed by the readers themselves who are well versed in the features of the principles and apparatuses of these measurements.

Anyway, the apparatuses will continue to progress, and the progress will perform more and more in the automation and simplification of the operation and of data processing. Accordingly, the skill of the operator will be less required, and factors causing the error will decrease drastically. As the results, the process will be automated from measurement to data processing, requiring no human help, and the intervention of human will decrease more and more. Ultimately, the instrument may present the data while man could not know how the process is performed. In order not to be ruled by the data, the user is asked to be wise and clever, and is requested to understand the principle and features of the instruments. We shall be pleased if the achievements of our working group studies are of any help to the readers for correct measurements and evaluations depending on the purpose, by making the best use of the features of individual instruments.

The author acknowledges here to the members of the sub-micron particle size measurement working group of the Society of Powder Technology, Japan, for their enthusiastically participating into the joint measurements and discussion on the data to obtain useful informations.

The monodispersed silica particles used as the common samples were kindly supplied by the Chemical Engineering Research Institute of Tokuyama Co., and the refractive index of particles was measured with the cooperation of Kyoto Fission Track Co. The

author and the members of the working group are also here make a grateful acknowledgment for their kindly cooperations.

References

1) The Society of Powder Technology, Japan (ed.): "Particle Size Analysis and Technology", pp.329-339, Nikkan Kogyo Shinbunsha (1975)
2) The Society of Powder Technology, Japan: Particle size measurement seminar text "General comparative study of recent measuring methods of particle size distribution", (Tokyo; 1987)
3) The Society of Powder Technology, Japan (ed.): "Particle Size Analysis and Technology", Nikkan Kogyo Shinbunsha (1994)
4) Yamamoto, H., J. Soc. Pow. Tech., Japan, 32 (1995) 117

Author's short biography

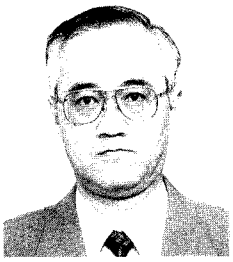

Hideo Yamamoto

Hideo Yamamoto was born in 1943 in Tokyo and graduated from the Department of Chemical Engineering, the University of Tokyo, in 1967. He received the Dr. Eng. degree from the University of Tokyo, in 1979.
He joined the Department of Chemical Engineering, University of Tokyo in 1976, and in 1989 to become an Associate Professor at the Institute of Industrial Science, University of Tokyo. He was a Visiting Researcher at Delft University of Technology, in The Netherlands, from 1984 to 1986. He joined the Department of Bioengineering at Soka University, as a Professor in 1991.
His field is particle technology and applied electrostatics. His current researches are particles separation from gases, fine powder dispersion in gas, particle size analysis, production and application of ultra fine particles, triboelectric charging of polymer particles, high temperature electrostatic precipitation, electrostatic formation of ceramic membrane, chemical reaction in surface corona plasma, and electrostatically handling of biomaterials.

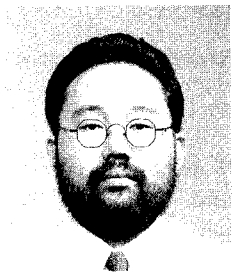

Tatsushi Matsuyama

Tatsushi Matsuyama was born in 1964 in Kanagawa, Japan, and grew in Nagano in his early days. He graduated from the Department of Chemical Engineering, the University of Tokyo, in 1987. He received the Ph.D. degree from the University of Tokyo, in 1995.
He joined the Department of Bioengineering, Soka University, as an Associate Researcher in 1992, and in 1995 to become a lecturer. His field at present is particle technology and applied electrostatics. His current researches involves contact charging of polymer particle and metal plate, and to calculate the potential distribution around the dielectric particle located near a conducting plane.

Dispersants in Stirred Ball Mill Grinding †

Y. Wang and E. Forssberg
*Division of Mineral Processing, Luleå University of Technology,**

Abstract

The influence of chemical dispersants on the milling of dolomite was examined using a stirred ball mill. The effective degree of grinding was found to depend on the aggregation/dispersion state or the viscosity of the slurry, which can be controlled by the amount of dispersants and by the solids content. It has been indicated that a more viscous slurry should be preferred in the grinding operation to improve the grinding rate and specific energy input. The beneficial effect of the periodic addition of the polymeric dispersants on the grinding efficiency was quite pronounced at a 70% by wt. solids slurry. In addition, the size distribution of the product becomes steeper in the cases of periodic polymer addition. Viscosity control in the ultrafine grinding of dolomite is important from the viewpoints of grinding efficiency and specific energy input. The results were obtained from carefully conducted experiments.

1. Introduction

In recent years, some success with the use of chemicals in mineral comminution has been achieved. This approach to improve the grinding efficiency is rather attractive since the chemicals can be employed in the existing equipment and the benefits are obvious from the viewpoint of energy saving and size reduction. However, the mechanisms in such a treatment are still poorly understood, especially for wet fine grinding. The addition of chemical dispersants into the slurry being ground is believed to enhance grinding efficiency either by modifying the rheological properties of the slurry or by assisting the fracture process itself. The latter theory given by Rehbinder (1932) is often rejected because of the large difference in the velocity of a propagating crack and that of diffusing molecules. The Rehbinder chemomechanical effects (i.e., the reduction of effective hardness of solids by surfactants) are restricted to the immediate vicinity of a propagating crack tip (Carter, Henshall and Wakeman, 1991). On the other hand, the importance of slurry viscosity in wet fine grinding has been emphasised (Clarke and Kitchener, 1968; Klimpel et al., 1982, 1983, 1984; El-Shall and Somasundaran, 1984; Laapas, Lahtinen and Lukkarinen, 1984; Kawatra and Eisele, 1988; Fuerstenau et al., 1985, 1987, 1990; Gao and Forssberg, 1993). Klimpel et al. (1982, 1983) showed that chemicals can be selected which effectively control the slurry rheology and give higher grinding rates than are possible without chemical addition. The mechanism involves the two factors which lead to optimum breakage rates. The first factor is the tendency of higher slurry densities towards a limit to give somewhat higher breakage rates; the second factor is the decrease of breakage rates caused by an excessively high slurry viscosity. The function of a grinding additive is to allow the use of higher slurry densities with reduction of the associated effect of higher viscosity, that is, maintaining a pseudo-plastic rheological character without excessive yield. These results were later confirmed by Fuerstenau and his associates (1990). They explained qualitatively the critical viscosity concept by a mathematical model of the processes which occur in a ball mill. Recently, Gao and Forssberg (1993) analysed the rheological properties of the dolomite slurries which were produced with a polymeric dispersant in a stirred ball mill. They found that the grinding efficiency depends on the fluidity of the slurry.

With regard to the identification of suitable viscosity control chemicals, a number of necessary conditions must be established. Klimpel et al. (1983) identified that most of the effective chemicals were low molecular weight, water-soluble polymers, *NaOH* or *KOH*, and well-known inorganic dispersants such as sodium silicates, sodium polyphosphate, etc. The required conditions are described simply as follows: a) the chemical must adsorb over enough of the solid surface available in the mineral being ground so as to affect slurry viscosity; *b*) the slurry viscosity must be high

* S-971 87, Luleå, Sweden
† Recceived 20 April, 1995

enough that use of the chemical can help to reduce or control the slurry viscosity; *c*) the chemical must be consistent in its ability to lower the viscosity as a function of varying chemical concentration, *pH*, water quality and amount of shear present; *d*) the chemical must be non-toxic and degradable; *e*) the chemical must not adversely affect downstream operations; *f*) the use of chemicals must be economically viable in grinding.

When ultrafine grinding is undertaken, effects occur which are not present in coarse grinding. These include very high viscosity of the slurry, aggregation and agglomeration of fine particles, cushioning effects, etc., which adversely affect the fine grinding operations. It is evident that very fine grinding can cause aggregation and agglomeration of the minerals. Chemical dispersants may prevent the formation of these strong agglomerates by keeping the particles well dispersed and/or preventing fusion of particle surfaces. The addition of dispersants in the ultrafine grinding of minerals is thus necessary, especially to the industrial and/or clay minerals. Handling otherwise becomes impossible due to very poor fluidity of the slurry being ground, which results in a grinding rate which is rather low, although the operation is possible with a diluted slurry. Also, it is important to realise that conclusions from experiments on the effect of the chemicals will depend on the properties of the minerals to be ground.

The literature reveals that chemical dispersants may influence fine grinding by changing the state of aggregation or dispersion of fine materials, hence altering the viscosity of the slurry being ground. This may, in turn, influence the grinding by a mechanical rather than chemical effect. The objective of the present study is therefore to investigate the ultrafine grinding of dolomite in a stirred ball mill by using various chemicals to control the viscosity of the slurry being ground.

2. Experimental work

2-1 Mineral used

Ground dolomite (size: 0-70 μm; specific gravity: 2.85 g/cm^3) supplied by Ernström Mineral *AB*, Sweden, was used as the experimental material. **Figure 1** shows the particle size distribution of this material sample, in which the mean particle size or d_{50} is 12.0 μm. Its specific surface area is about 2.00 m^{2}g^{-1}. The chemical characteristics of the sample are shown in **Table 1**.

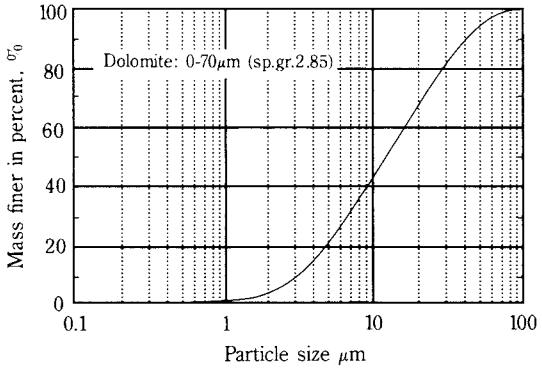

Fig. 1 Particle size distribution of the sample

Table 1: The chemical properties of the dolomite sample

Assay	*CaO*	*MgO*	Fe_2O_3	Al_2O_3	SiO_2	LOI
Content, %	28.7	21.7	0.4	0.8	6.3	42.2

2-2 Chemical reagents

Five different chemicals were investigated as possible dispersants for the wet ultrafine grinding of dolomite. These chemical dispersants may be desirable in the products (coating or filler) for the pigment and paper industries. They involve

a) organic polymeric reagents:
   - Dispex *CP* (sodium salt of an acrylic copolymer);
   - Dispex *N*40 (sodium salt of a polycarboxylic acid);
   - *DP*6-3437 (sodium salt of polymer);

b) inorganic reagents:
   - Calgon (sodium hexametaphosphate);
   - *TSPOP* (Tetrasodiumpyrophosphate, $Na_4P_2O_7$).

The organic polymeric chemicals were supplied by AB CDM, Sweden. Dispex *CP* and DP6-3437 are recently developed pigment dispersants for aqueous systems. The three organic dispersants all are low molecular weight (molecular weight <6500), anionic, water-soluble polymers. They are stable over a wide range of *pH* and temperature. Dispex *N*40 and Dispex *CP* are both effective over a *pH* range of 5-14 and up to a temperature of 373K. The organic dispersants produce a stabilising and dispersing effect by means of the most fundamental and economic process possible. The process involves ionisation in water to produce a sodium cation together with a polyanion. Worthy of note is that an excessively long hydrocarbon chain of a polymer may eventually lead to particle flocculation, but the polymers of lower molecular weight are commonly used as dispersants (Laskowski and Pugh, 1992). A mixture of sodium salts of cyclic hexametaphosphoric acid constitutes a commercially

produced inorganic dispersant under the trade name of Calgon. Tetrasodiumpyrophosphate (*TSPOP*) is also an inorganic dispersing reagent. These two anionic dispersants have an affinity for the mineral surface and adsorb either electrostatically or by hydrogen bonding. They are miscible with water in all proportions. The Calgon and *TSPOP* used in this investigation were purchased from *KEBO AB*, Sweden. The amount of the dispersant used is determined as % by weight dry dispersant/dry mineral material.

2-3 Grinding mill and studies

A stirred ball grinding mill, manufactured by Draiswerke *GmbH*, Germany, was employed for the grinding tests. A diagrammatic representation of the mill in continuous mode is shown in **Figure 2**. The grinding was carried out in a 150-mm-diameter by 420-mm-long stainless chamber equipped with seven 120-mm diameter discs. The discs rotate at 1818 rpm or 11.4 m sec^{-1} peripheral speed (measured by Digital Hand Tachometer HT-446, ONO SOKKI Co., Ltd, Japan). The flowrate of the slurry was 1.5 litres per minute, which was controlled by a slurry pump. The product material for each pass was discharged through two specially designed screen cartridges inserted at the end of the grinding chamber. Beads of zircom, $ZrSiO_2$ with a specific gravity of 3.7 g/cm^3 and 1.6-2.5 mm in size were employed as the grinding media. The bead load was 70 percent by volume. Cooling water was used both to prevent a rise in temperature during the grinding operation as well as a sealing system.

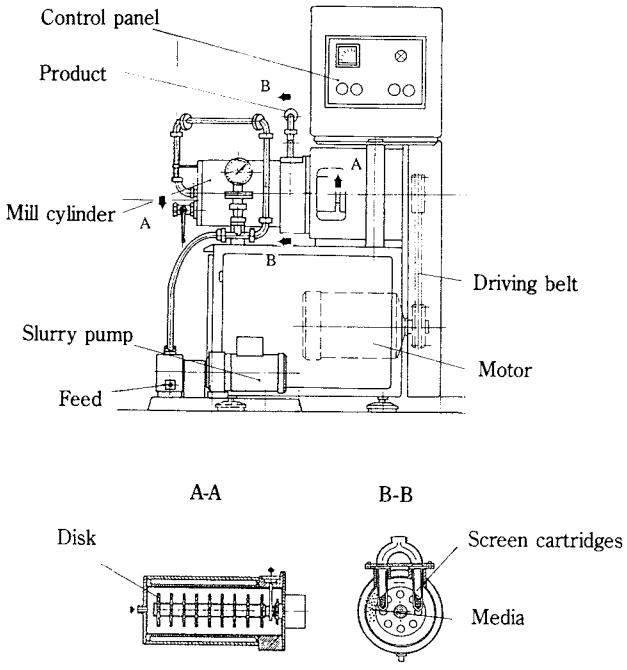

Fig. 2 The Drais stirred ball mill used in the investigation.

In this investigation, the grinding tests were performed using 60%, 70% and 75% solids by weight (or 34.5%, 45.0% and 51.3% by volume) slurries. For each test, 40 kg of powdered dolomite was mixed with water to prepare the slurry in the presence of a certain chemical dispersant. The slurry was fed at first through the mill for 10 minutes to obtain the determined solids concentration. The remaining slurry was then used for the investigation. During each experiment the mill runs at 9 or 11 passes. A small amount of slurry sample was removed from each of the two passes. The samples were analysed separately for viscosity, particle size and specific surface area.

2-4 Measurements

Particle size distribution: Particle size distribution analysis was carried out using an X-ray Sedimentometer SediGraph 5100D, manufactured by the Micromeritics Co., Ltd., U.S.A.. The particle size range varied between 0.5 μm and 100 μm. The slurry was sampled for each measurement. The particles in the sample were deagglomerated by means of ultrasonic waves and an aqueous solution of Calgon (0.1 % concen.) prior to the analysis.

Specific surface area (B.E.T. method): The specific surface area was measured by the Flow Sorb II 2300 (Micromeritics Co., Ltd., U.S.A.). A representative amount of sample was taken from the previously deagglomerated and homogenised sample and allowed to dry in an oven at 353K (80°C) in order to remove the residual moisture in the sample before the measurement.

Viscosity: Brookfield rotational viscometers (Brookfield Engineering Lab. Inc., U.S.A.) have been successfully applied to analyse the rheology of mineral suspensions (Howard, 1985). The measurements reported in this study were made with a Brookfield rotational digital viscometer Model DV-II with its disc spindle number 3 rotating in a 600 ml beaker in the presence of the spindle guard. The Brookfield viscosity, η (poise), is determined by:

$$\eta = \frac{\sigma}{\gamma} \tag{1}$$

where γ is the shear rate related to the speed, sec^{-1}, σ is the shear stress, dynes cm^{-2}. In Eq. (1), γ takes into account the parameters of the spindle surface area over which the torque is acting and the torque itself. The shear rate is determined by the angular rotational speed (rpm) and the gap between the

spindle and the outer boundary or the beaker wall. As is known, the majority of semi-solids such as mineral slurries which either are found in nature or are man-made, are non-Newtonian. Non-Newtonian materials are dependent on shear rate. Measurements at different rotational speeds with the same or different spindles will result in different calculated viscosities. The information for characterising the non-Newtonian materials is shown in **Figure 3**.

The slurry of dolomite with a certain chemical used in the beaker was placed in a constant temperature (295K) bath and agitated for 30 minutes. The temperature of the slurry was maintained to within 1K. Agitation was then stopped and the Brookfield spindle, also maintained at the temperature of measurement, was immersed in the slurry and three readings were taken at each spindle speed; the mean value was used. The rotation speeds used in this measurement were 100, 20, 10, 5, 2.5, 1, 0.5 rpm. A non-toxic silicone fluid (5000 cP at 298K) was used as a Brookfield viscosity standard for checking the calibration of the viscometer used.

Energy consumption: A Micro VIP electrical meter (manufactured by ELCONTROL Co., Italy) was connected to the main power supply in order to measure the energy consumption of the mill. The print-out of the measured results is available at intervals of 5 minutes set up in advance. The active power (kW) and the active energy consumption (kWh) were determined. In this study, the active power and the energy consumption (kWh) were recorded by taking the power factor into account. Three consecutive readings were taken for each grinding pass. In order to evaluate the net energy consumption of the Drais mill, the mass specific energy input, E_m (kWh/t), is determined by (Stehr and Weyand, 1990):

$$E_m = \frac{P - P_0}{M_p \times C} \tag{2}$$

where P is the active power draft of rotor, P_o is the idle power draft (without grinding media and ground material), M_p is the mass flowrate of the slurry suspension, and C is the solids concentration.

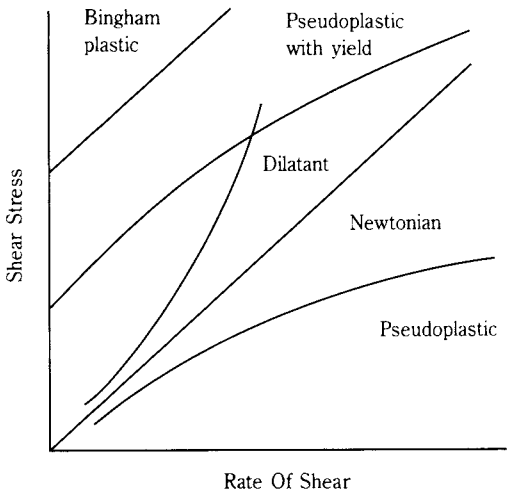

Fig. 3 Shear stress versus shear rate curves for time-independent non-Newtonian slurries (Kimpel, 1984)

3. Results and discussion

3-1 Different chemicals

Figure 4 shows the effect of specific energy input (E_m) on the median diameter (d_{50}) as well as on the specific surface area (S) in the presence of various organic and inorganic chemical additives. It is clear that the organic dispersants effect a more favourable grinding action than the inorganic ones. The difference is more pronounced at the fine ends. This may be due to their different adsorption mechanisms at the solid/liquid interface, such as ion exchange, ion pairing, hydrogen-bonding, hydrophobic bonding, van der Waals interaction, etc. It is known that polyphosphates have an affinity for the particle surface and can adsorb either electrostatically or by the hydrogen bonding, or by forming strong covalent bonds with a number of metallic cations (Conley, 1974). The amphipathic nature of the polymeric dispersants impart their characteristics mostly through steric effects as opposed to electrostatic causes. Although these mechanisms are not exactly clear, it is believed that different chemical additives produce different aggregation/dispersion states of the slurry. Thus, the grinding performance is affected to varying degrees by friction and impact between the particles.

Besides this, among the organic dispersants, Dispex *N*40 gives a superior performance in the grinding efficiency compared with Dispex *CP* (see **Figure 4**). This difference may be partly attributed to the dispersing characteristics of these polymers. As mentioned earlier, Dispex *CP* is a sodium salt of an acrylic copolymer, while Dispex *N*40 is a sodium salt of a homopolymer. The multiple ionic groups in these two polymers can impart high surface charges to the particles onto which they adsorb. When the tendency to adsorb on the surface of a solid particle of an individual functional group attached to the backbone of the polymer is low, the number of such groups in the macromolecule must be large enough so that the total adsorption energy of the molecule

is sufficient to anchor it firmly to the particle surface. Homopolymers, consequently, are not as versatile as copolymers. Copolymers of monomers with different structural characteristics yield products that can adsorb strongly to a wider variety of substrates. Thus, acrylic acid copolymerized with longer-chain monomers can increase the binding energy of the dispersing agent to the particle surface (Buscall and Corner, 1986). Furthermore, some measurements at Allied Colloid Ltd., U.K. have confirmed that the amounts of Dispex *CP* are more sensitive to the modification of the slurry viscosity than those of Dispex *N*40. This means that a more viscous slurry controlled with Dispex *N*40 can achieve better grinding efficiency at the same level of additives.

On the other hand, for a polymetric dispersant, chemisorption between the $-COO^-$ of the polymer and the Ca^{2+} and Mg^{2+} of the dolomite surface may occur. This may contribute to the dispersion of the particles due to the formation of the adsorption layers. The influence of the adsorbed layers on the particle size could be negligible due to their small thicknesses (Tadros, 1982).

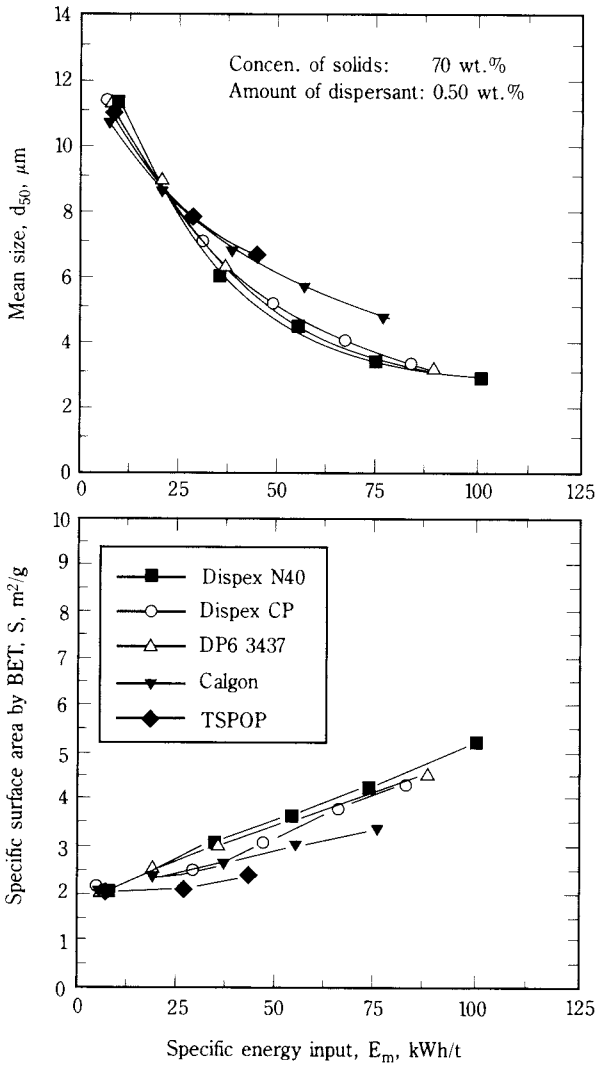

Fig. 4 Mean size as well as specific surface area vs. specific energy input during ultrafine grinding with different chemical dispersants at a slurry density of 70% solids by weight.

For the design of a polymeric dispersant, what is often required is not a totally deflocculated system but rather one in which there is a controlled amount of weak flocculation, for example, to give the desired rheological properties (Vincent and Whittington 1982). The polymeric dispersants used met this requirement.

3-2 Amounts of the chemicals

It is well known that it is necessary to admix dispersant additives into the dense slurry being ground in the stirred ball mill. The amount of the dispersant is an important and critical factor in the operation. **Figure 5** shows the relationship of the specific energy input (E_m) to the specific surface area (S) at different amounts of the three polymeric dispersants. It is interesting to note that the grinding energy efficiency increases when the amount of dispersants drops. It is also visible that the ultrafine grinding of dolomite is enhanced at a lower amount of these polymers. The enhancement and the increased fineness can be obtained by controlling the rheology of the slurry being ground, which is adjusted with an appropriate amount of the dispersant additives. Note that this study did not involve any grinding results without dispersants. This is because the handling became impossible due to the very poor fluidity of the slurry being ground at the high solids contents investigated.

The Brookfield viscosites of the samples taken from each pass with different amounts of Dispex *N*40 are shown in **Figure 6**. In this Figure, the Brookfield viscosities did not change with the number of passes at more than 1.00 wt.% of this polymeric dispersant. This illustrates that the presence of different amounts of the additives transforms the slurry through different types of rheologies, and the large addition of the dispersant obviously increases the fluidity of the slurry to such an extent that the probability of breakage is decreased. Furthermore, the higher the pass number, the finer the particle size. The rheological behaviour of mineral dispersion depends on the particle size. This means that the finer particle slurry presents the higher viscosity. However, the application of an excessive amount of the polymer overcomes such a dependence. When adding the dispersant into the slurry, the interactions between the particles are

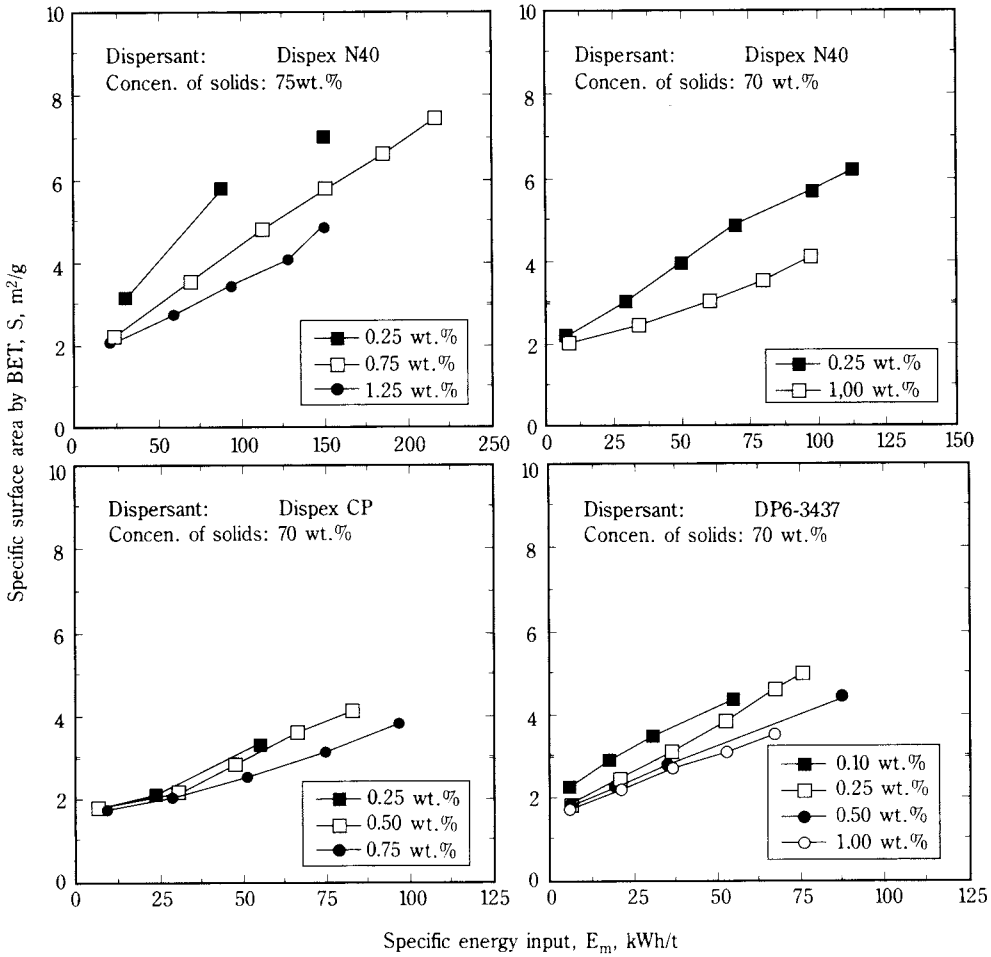

Fig. 5 Specific surface area vs. specific energy input during ultrafine grinding with different amounts of the polymeric dispersants at a slurry density of 70% or 75% solids by weight.

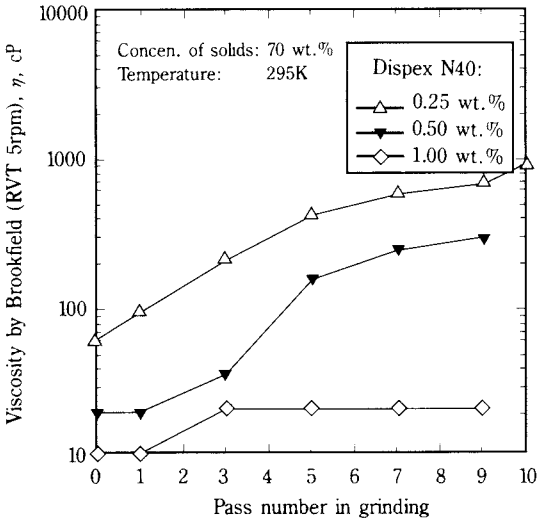

Fig. 6 Variation in slurry viscosity during grinding process at different amounts of Dispex N40 and a slurry density of 70% solids by weight.

weakened and are finally broken as soon as repulsion between the particles predominates. Consequently, the results of dispersion is a reduction of the yield stress, which finally disappears, whereupon the slurry system obtains the character of a rather freely flowing fluid. The flow behaviour of the aggregated suspension is of the Bingham type. In the measurements of the slurry rheology at low shear rates (Gao and Forssberg, 1993), with more than 1.00 wt.% Dispex N40, the slurry rheology was transformed from Bingham plastic to dilatant. However, since the rheological behaviour of the slurry at very high shear rates in the mill is rather complex, it is difficult to distinguish which rheological state is desirable for effective milling operation. The pseudo-plastic shear thinning without excessive yield may be a likely state, as suggested by Klimpel et al. (1983).

In a concentrated slurry with large additions of dispersants, the particles are not subjected to the forces of attraction. They are free to move as individuals. The reason for this may be the adsorption of

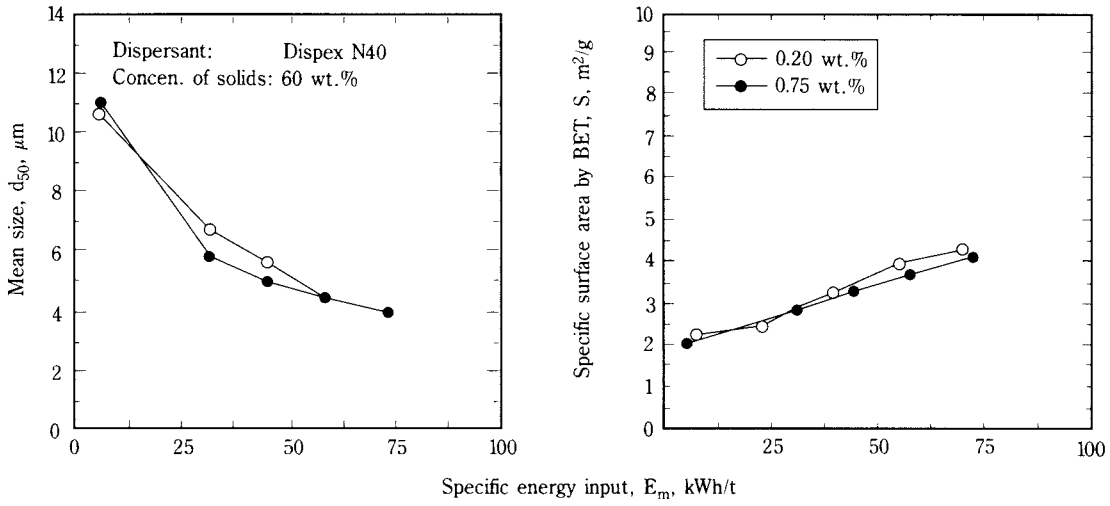

Fig. 7 Mean size as well as specific surface area vs. specific energy input during ultrafine grinding with different amounts of Dispex N40 at a slurry density of 60% solids by weight.

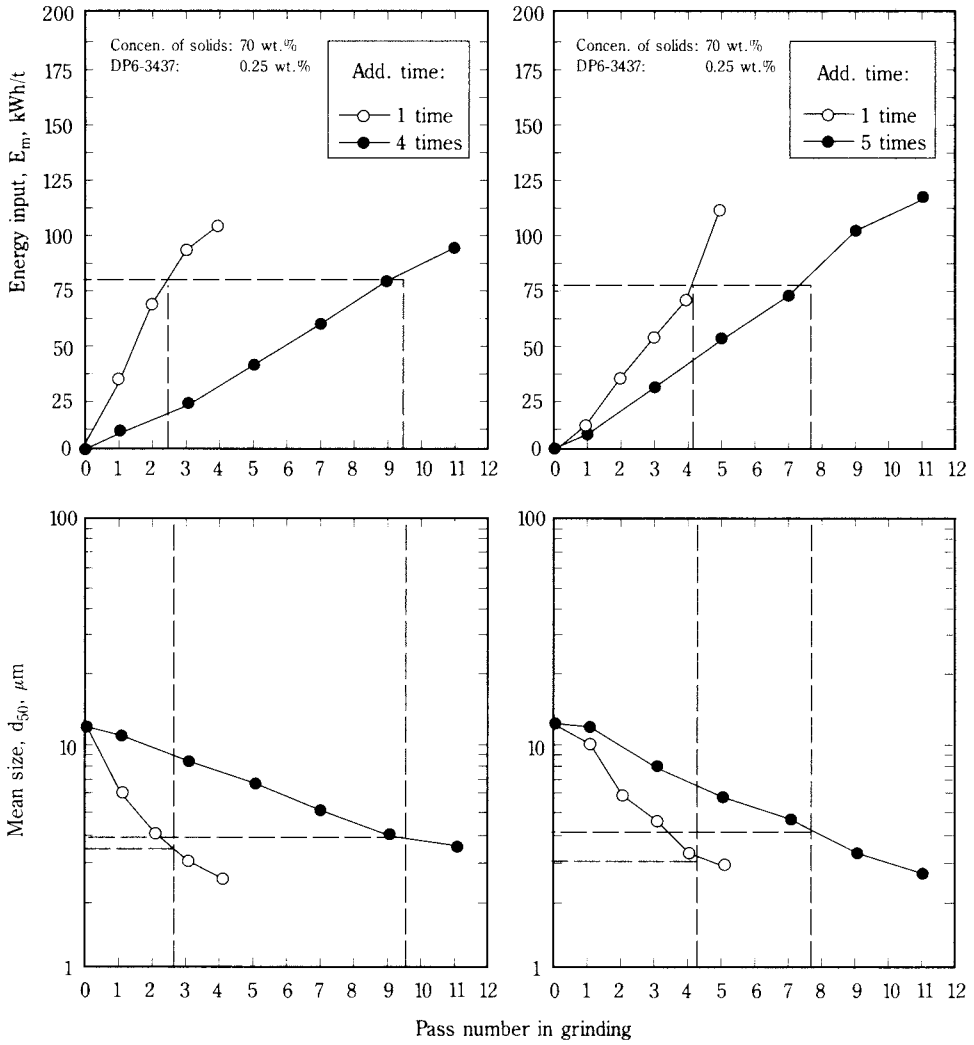

Fig. 8 Energy-size reduction relationships produced by periodic or instantaneous addition of the polymeric dispersants at a slurry concentration of 70 wt. %.

the anionic molecule on *Ca* and *Mg* ions sites of dolomite at higher *pH*. This leads to a strong electrostatic repulsion between the particles, which subsequently results in a reduction in the slurry viscosity at a higher addition of the dispersant. It was suggested (Fuerstenau et al., 1990) that the role of polymeric dispersants might be restricted to keeping the slurry viscosity low and the energy input high when milling a dolomite in a ball mill. From the results obtained, it seems that a properly viscous slurry is desirable for ultrafine grinding from the specific energy input point of view.

The amount of the polymeric dispersants is also related to the slurry density, as shown in **Figure 5**. However, at lower solids content (see **Figure 7**), this relationship appears to be insignificant. The fluidity or the viscosity of the slurry being ground shows little change at various amounts of the polymer. Conversely, at higher solid content, say more than 70% solids by weight (or 45% solids by volume), the grinding efficiency depends on the amount of polymeric additives.

3-3 Method of introducing the chemicals

As discussed above, using a smaller amount of dispersant can lower the specific energy consumption (kWh/t) for the ultrafine grinding of dolomite in a stirred ball mill. Therefore, periodic addition of the dispersant into the slurry being ground during the process can be beneficial from the viewpoint of improving the grinding energy efficiency. **Figure 8** shows the results of the energy-size reduction with periodic or instantaneous additions of Dispex *N*40 or DP6-3437, respectively. It is visible that the periodic addition leads to an increased grinding rate and a decreased specific energy input (kWh/t). This procedure makes the viscosity of the slurry suitable for the attrition and impact of the particles. The control of the viscosity of slurry thus becomes a critical factor in such an operation. Excessively high viscosities make handling impossible due to the poor fluidity of the slurry without or with only very small amounts of the additives. Too low a viscosity gives a reduced grinding rate and an increased specific energy input. The periodic addition may optimize the yield stress of the slurry until the final product is achieved. In addition, the results in **Figure 9** indicate that a steeper size distribution of the product can be obtained by the periodic addition of the polymeric chemicals.

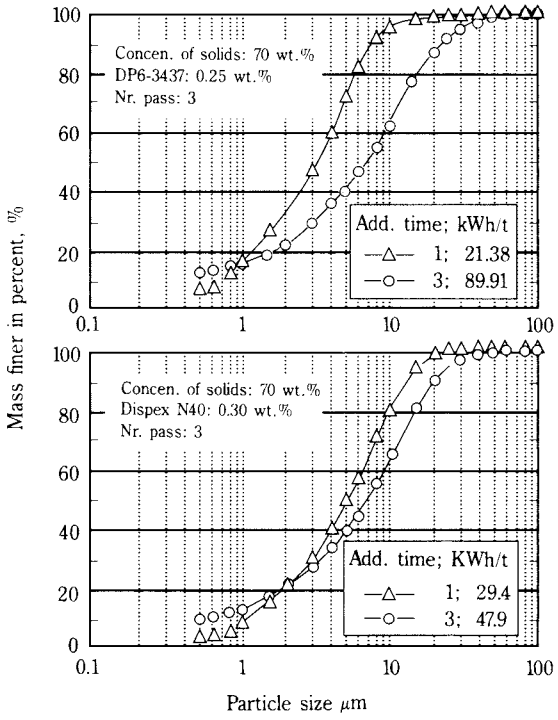

Fig. 9 Product size distributions obtained by periodic or instantaneous addition of the polymeric dispersants at a slurry concentration of 70 wt.%.

3-4 Solids concentration

Although it is possible to carry out ultrafine grinding at diluted slurries without any dispersant additives, the handling is impossible at high solid densities due to the poor fluidity of the slurry. The effect of grinding chemicals with respect to the solids content is shown in **Figure 10**. The dependence of specific surface area (S) on the specific energy input (E_m) is illustrated in relation to the results for various solid contents with the dispersants. With the lower dispersant additives, the grinding was efficient at the higher slurry density. At low slurry densities, the particles are not close enough together for appreciable attrition to occur. Most of the breakage is by impact. At higher slurry densities, the particles tend to be close enough for suitable friction and impact. **Figure 11** shows that the denser the slurry, the higher the slurry viscosity. This phenomenon illustrates that the slurry fluidity varies with the slurry density. For the cases of higher solid contents, the appropriate viscosity or fluidity of the slurry being ground leads to an increase in the grinding efficiency. However, no enhancement occurs at an excessive amount of the additive (see **Figure 12**).

As discussed above, at a dense slurry with reasonable addition of the polymer, the particles were subjected to surface repulsive forces due to the adsorption of the polymer chains. At a high rate of shear in the mill, the shearing process may become so rapid that the particles are no longer able to move around freely. They are piled up in front of moving particles and

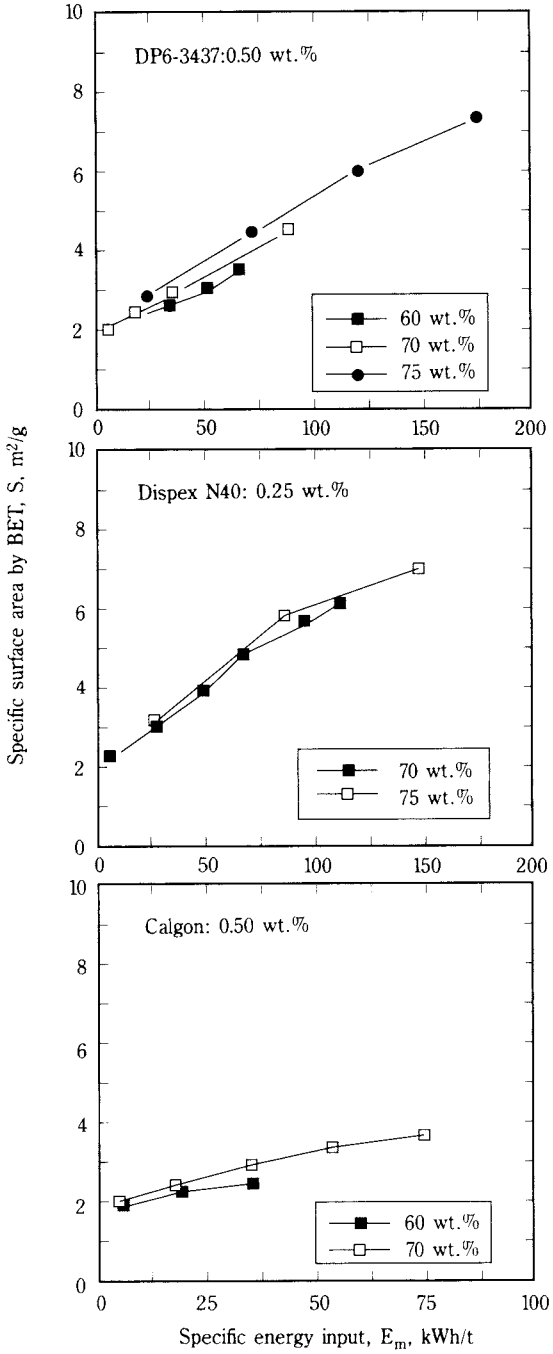

Fig. 10 Specific surface area vs. specific energy input during ultrafine grinding with different solids concentrations of dolomite in the presence of the chemical dispersants.

create a properly viscous slurry, which favours such a grinding operation. The dispersant additive has a critical effect on the solid contents in the grinding operation. The critical solid concentration, under the operating conditions in this study, can be exceeded beyond the point where the dispersant is effective.

It can be concluded that at relatively low solids concentrations, e.g. less than 60 percent solid by

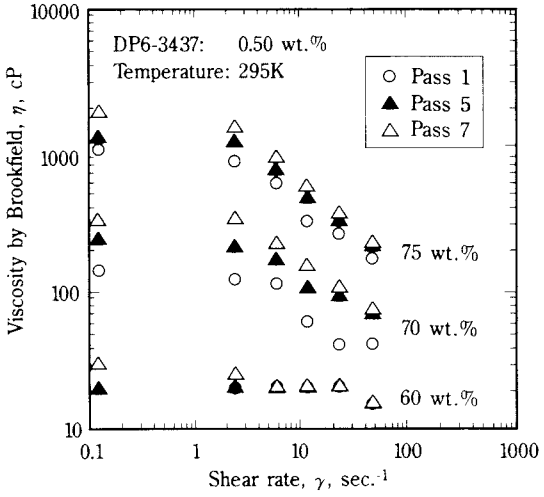

Fig. 11 Variation in slurry viscosity during grinding process at different solids concentrations in the presence of 0.50 wt.% DP6-3437.

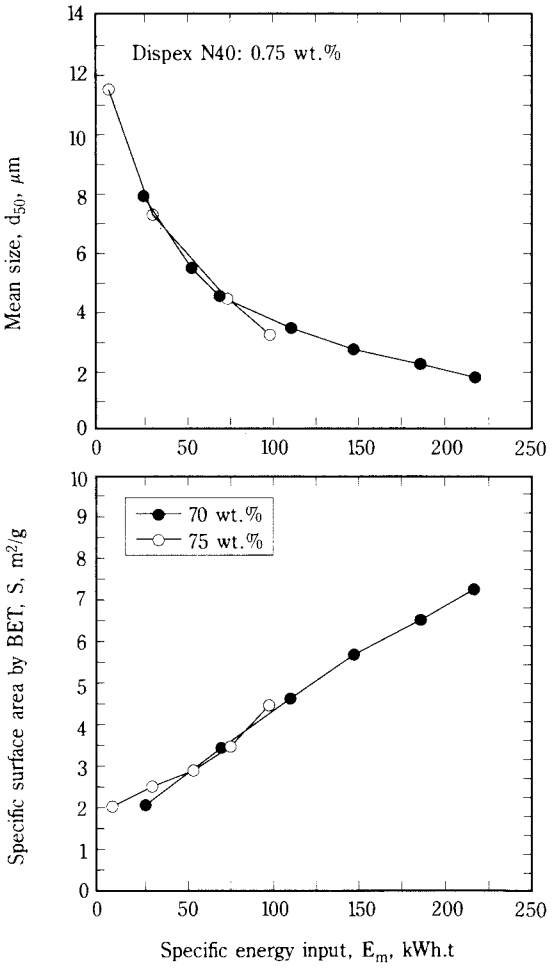

Fig. 12 Mean size as well as specific surface area vs. specific energy input during ultrafine grinding with different solids concentrations of dolomite in the presence of 0.75 wt.% Dispex N40.

weight (or 34.5 percent solid by volume), the apparent viscosity changes insignificantly, especially at higher additives of the dispersants. At higher solids contents the rheological character of the slurry undergoes a qualitative change, which is reflected in a significant increase in the apparent viscosity. Beyond a certain solid concentration, the viscosity rises steeply and, concurrently, the grinding rates drop. The addition of polymeric dispersants may deflocculate the aggregates, and as a consequence, the suspension can accommodate more solids before exceeding the critical limit. The degree of size reduction achieved is a unique function of cumulative energy expended per unit mass of solids at the appropriate amount of polymeric dispersants. Thus, the effectiveness of the grinding chemicals resides in the enhancement of throughput, provided, of course, the slurries are dense enough.

The suite of fragments produced by breakage of a given size without further fragment rebreakage is termed primary breakage distribution. This function is represented by $b_{i,j}$ – the fraction of just broken j material that falls into smaller size interval i. $B_{i,j}$ represents the same information put on a cumulative basis of material broken from size j to size i or smaller:

$$B_{i,j} = \sum_{k=n}^{i} b_{k,j} \tag{3}$$

It has been indicated that the measured $B_{i,j}$ values for breakage in high solids contents have a relatively finer primary fragment distribution than for lower solids contents (Klimpel, 1983).

The experimental results have shown that the change in the slurry consistency caused by adding the chemicals significantly affects the energy consumption per unit ton of dry material ground in the stirred ball mill. It can be recognised that successful grinding demands a properly viscous slurry. This means that the specific energy input utilisation is improved at higher solids content and at lower dispersant additive levels. These results are in contrast to the situation in grinding metallic ores in tumbling mills. This may be caused partly to the difference in mill design and the material being ground.

4. Conclusions

Addition of dispersants into the dolomite slurries ground in a stirred ball mill is necessary; this at least produces an increase in the grinding rate.

The milling efficiencies have been shown to be influenced by the aggregation/dispersion state of the particles in the slurry. The slurry flow behaviour is easily affected by the addition of the chemicals. The polymeric dispersants have a superior effect on the grinding action, as compared with the inorganic chemicals. Experimental results show that the effective ultrafine grinding requires properly viscous slurry conditions controlled at a smaller amount of the additive and at a higher solid content. In this context, too low a viscosity gives a decreased grinding rate and an increased specific energy input. Too high a viscosity adversely affects the milling operation. The viscosity of the slurry during the ultrafine grinding may control the rates of surface enhancement and size reduction.

It is indicated that the periodic addition of the polymeric dispersant into the ground slurry during the process can improve the grinding rate as well as the specific energy efficiency. By adding the polymers periodically, the product size distribution obtained becomes steeper.

Acknowledgements

This work was a part of the European Commission Project entitled "Ultrafine Grinding, Delamination & Characterisation of Minerals" (*BRE2 CT94-1023 GRINDELA*). The authors are extremely grateful to the *EC* and the Swedish Mineral Processing Research Foundation (*MinFo*) for supporting this work. They are also indebted to the *AB CDM*, Sweden, for supplying the polymeric chemicals and the corresponding information, and to the Ernström Mineral *AB*, Sweden, for providing the dolomite sample.

References

1) Rehbinder, P. A. and Kalinkovskaya, N.: Reduction in stability of the surface layer of a solid by the adsorption of surface acting substances, J. Tech. Phys. USSR, 2, pp. 726-755, (1932).
2) Carter, G.M.; Henshall, J. L. and Wakeman, R.J.: Influence of surfactants on the mechanical properties and comminution of wet-milled calcite, Powder Technology, 65, pp. 403-410, (1991).
3) Clarke, B. and Kitchener, J.A.: The influence of pulp viscosity on fine grinding in a ball mill, British Chemical Engineering, Vol. 13, No. 7,pp. 991-995, (1968).
4) Klimpel, R.R. and Austin, L.G.: Chemical additives for wet grinding of minerals, Powder Technology, 31,pp. 239-253, (1982).
5) Klimpel, R. R.: Slurry rheology influence on the performance of mineral/coal grinding circuits; Part 2. Min. Eng., 35,pp. 21-26 (1983).

6) El-shall, H. and Somassundaran, P.: Mechanisms of grinding modification by chemical additives: organic reagents, Powder Technol., 38, pp. 267-273, (1984).
7) Klimpel, R.R.: Influence of material breakage properties and associated slurry rheology on breakage rates in wet grinding of coal/ores in tumbling media mills,Reagents in the mineral industry, IMM, Ed. M. J. Jones and R. Oblatt, pp 265-269, (1984).
8) Laapas, H.; Lahtinen, U. R. and Lukkarinen, T.: Effect of surfactants in fine grinding, Reagents in the mineral industry, IMM, Ed. M. J. Jones and R. Oblatt,pp 13-17, (1984).
9) Kawatra, S.K. and Eisele, T.C.: Rheological effects in grinding circuits, Inter. J. Miner. Process., 20, pp 251-259, (1988).
10) Fuerstenau, D.W.; Venkataraman, K.S. and Velamakanni, B.V.: Effect of chemical additives on the dynamics of grinding media in wet ball mill grinding, Inter. J. Miner. Process., 15, pp. 251-267, (1985).
11) Velamakanni, B.V. and Fuerstenau, D.W.: The influence of polymeric additives on the rheology of dense slurries, Flocculation in biotechnology and Separation Systems, Ed. Y.A. Attia, Elsevier, Amsterdam, pp.211-223, (1987).
12) Fuerstenau, D. W.; Kapur, P. C. and Velamakanni B.: A multi-torque model for the effects of dispersants and slurry viscosity on ball milling, Intern. J. Miner. Process., 28, pp. 81-98, (1990).
13) Gao, M. W. and Forssberg, E.: The influence of slurry rheology on ultrafine grinding in a stirred ball mill, XVIII Inter. Miner. Process. Congr. Sydney, Australia, pp 237-244, (1993).
14) Laskowski, J. S. and Pugh, R. J.: Dispersions stability and dispersing agents, in Colloid Chemistry in Mineral Processing, Chapter 4, Elsevier, pp. 115-171, (1992).
15) Howard, D. W.: Modern developments in viscometers, in Ceramic Engineering and Science Proceedings, The American Ceramic Society, Vol. 6., No. 11-12,pp. 1395-1405, (1985).
16) Stehr, N. and Weyand, C.: Control system for agitated media mills, 7th European symposium of comminution,Part 2, Ed. K. Schönert, Ljubljana, pp. 681-695, (1990).
17) Conley, R.F.: J. Paint Techno. 46, pp. 51-56, (1974).
18) Buscall, R. and Corner, T.: Colloids Surf., 17, pp. 39-44, (1986).
19) Allied Colloids Ltd., Technical and processing data for DISPEX CP, pigment dispersant for aqueous systems, (1994).
20) Vincent, B. and Whittington, S. G.: Polymers at interfaces and in dispersed systems, Surface and Colloid Science, Ed. E. Matijevic, Vol. 12, Plenum Press,pp. 1-108, (1982).

Author's short biography

Yanmin Wang

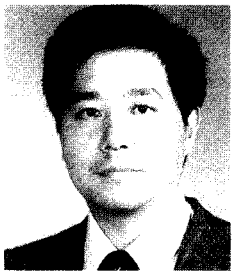

Dr. Yanmin Wang graduated from the North-Eastern University, China (1980). He obtained his doctor degree from the Luleå University of Technology (LUT), Sweden, in 1993. He is presently a research scientist in the Chemical & Metallurgical Engineering Department at LUT, and is in charge of several research studies on comminution/classification and physical separation.

Eric Forssberg

Born 1943. PhD in mineral processing 1973, Royal Institute of Technology, Stockholm, Sweden; Professor of mineral processing 1974, Luleå University of Technology, Sweden; Dean Faculty of Engineering 1980-1990; Chairman International Scientific Committee and Steering Committee of the International Mineral Processing Congress (IMPC) 1985; Member of the Royal Swedish Academy of Engineering Sciences: Member of the Russian Federation Academy of Natural Sciences; Chairman European Chapter of the International Comminution Research Association (ICRA), 1993; Chairman Working Party Comminution and Classification, European Federation of Chemical Engineering, 1995.

Characterization of Nanocrystalline Oxide Powders Prepared by CO_2 Laser Evaporation†

E. Müller, Ch. Oestreich, and U. Popp
*Freiberg University of Mining and Technology**
G. Michel, G. Staupendahl, and K.-H. Henneberg
*Friedrich Schiller University***

Abstract

Today, a world-wide interest exists in producing nanosized ceramic powders. One of the suitable techniques is based on the evaporation of solid primary materials by lasers. Although this technique has been known for nearly two decades, the literature has hitherto only rarely reported effective powder yields (a few grams per hour). We produced nanocrystalline zirconia and alumina powders by evaporation of oxides in the focus of a CO_2 laser (transversal flow of the CO_2 gas; P_L = 0.75 ... 4 kW) and by recondensation of the oxides in a carrier gas stream (air, oxygen, argon). Most experiments were carried out in the continuous wave (cw) mode, but earlier ones were also done by means of a pulsed laser (pw). The powder yield depends strongly on the laser power, on the focusing and on the velocity of the moving oxide target. Maximum yields of more than 100 g h^{-1} were attained.

The zirconia and alumina powders so prepared consisted of nearly spherical particles with diameters in the range of 10 to 100 nm. The particle distribution can be controlled by the parameters of the formation process. Features of the crystal phases and of the chemical composition of the produced powders are reported.

1. Introduction

Nowadays, there is a world-wide trend in the development of technologies for producing nanosized ceramic powders. Considering only the 3rd Conference of the European Ceramic Society (Sept. 1993, Madrid, Spain), we find eight contributions [1a-g] concerning the preparation and special properties of such powders. There are, however, slight differences in the interpretation of the term "nanosized".

The potential advantages and applications of such nanosized powders result from the extremely small dimensions of the particles and thus the extremely high surface. The densification rate $d\varrho/dt$ and the strain rate $d\mathcal{E}/dt$, depend very strongly on the grain size d during a ceramic sintering process. Assuming a relationship of the form d^{-p} with p in the range of 2 to 4, it is to be supposed that $d\varrho/dt$ and $d\mathcal{E}/dt$ will increase by factors of the order of 10^8 and 10^6, respectively, if the grain size diminishes from 1 μm to 10 nm [2].

This means that the sinter temperatures can decrease significantly. In this way, a co-firing of such ceramic materials with a second component of a lower heat stability such as reinforcement fibres may become possible. In addition, such nanocrystalline ceramics can possess unusual properties such as superplasticity or machinability [3]. A stabilization of metastable crystalline phases may be another consequence of the extremely small particle sizes [4] which can also lead to unusual ceramic properties.

Today, a lot of different techniques for producing manosized powders are under development. In addition to routes in the fluid phase such as sol-gel [1a], precipitation [5], hydrothermal [6] processes, gas-phase processes are tested or optimized for the prepartion of such powders. One type of such gas-phase technique which is similar to the process discussed here is the so-called (inert) gas condensation technique. By using usually UHV equipment, solid materials are evaporated in an inert or reactive atmosphere originally by means of heat [2, 7], today also by sputtering with noble gas ions [8] or by an electron beam [9, 10]. The vapour recondenses in the gas phase and deposits on cooled surfaces. In order to produce nanosized oxide particles in this way, frequently the metal or one of its suboxides is used as starting materials

* D-09596 Freiberg, Germany
** Jena, D-07743 Jena, Germany
† Received 10 May, 1995

for the evaporation because of their higher vapour pressure in comparison with the stoichiometric oxide. However, in this case, the powder has to be reoxidized which can lead to coarsening or agglomeration of the nanosized particles. In principle, extremely fine particles with a maximum size of 10 nm are achievable in this way but the powder production rates are typically confined to a few hundred milligrams per hour.

Other promising gas-phase techniques for producing nanosized powders are plasma-chemical methods with different kinds of plasma excitation such as a d.c.arc [1c] or microwaves [1b]. In this case, gaseous primary materials are frequently needed. The production rates are significantly higher (several grams to several hundred grams per hour) than in the case of the gas condensation technique, but the size distribution functions become distinctly wider and extend to the range higher than 100 nm.

At present, many groups use the laser-assisted chemical vapour precipitation (LCVP) technique to prepare nanosized powders [1d-f, 11-14]. Although the same energy source, a laser, is used as in the technique described in this paper, there are important differences. In the former case, the laser is used to activate a chemical gas-phase reaction. Therefore, expensive gaseous primary materials are generally needed. Predominantly, the technique is used for producing non-oxide powders such as silicon carbide, silicon nitride or mixtures thereof. Very fine particles with diameters in the range of a few nanometers to a few tens of nanometers are obtained, but often the powders are inhomogeneous in their atomic structure and composition.

The most fully developed technique to produce nanosized powders in the gas phase is that of pyrolysis of metal halides in an oxyhydrogen flame. The method became known as the AEROSIL® technique [15], since the most important nanosized material prepared by this technique is highly dispersed silica, which today is used industrially on a large scale for producing paintings and lacquers, reinforced polymers and rubbers, cosmetics and pharmaceuticals and catalysts. The technique is also used today for producing nano-sized alumina, titania, and zirconia.

Many of the particles are connected by interparticular solid bridges due to the heat treatment of the powders necessary to remove the HCl which is formed during the reaction and which is adsorbed onto the particle surfaces. Also, most of these powders show a very strong tendency to agglomerate due to the high content of surface hydroxyl groups which result from the preparation conditions. Although these powders are cheap and easily available, there is little application of such powders in the field of advanced ceramics.

Within the context of all these gas-phase techniques, we want to discuss the advantages and disadvantages of the method of laser evaporation which we apply for producing nanocrystalline oxide powders. The method is distinguished by the possibility of using a solid material such as coarse powders, sintered ceramics or ceramic waste as the starting material. This material is evaporated in the focus of a laser beam, and the vapour recondenses in the stream of an inert (or reactive) carrier gas. This method was first described two decades ago by Kato [16], and in the meantime, Mordike and co-workers [17-18] have been engaged in this field. They applied this method for producing nanosized oxide particles by evaporating not only intrinsic oxides in an inert atmosphere, but also metals in an oxidizing atmosphere. To date, the advantages of the method, the possibility of producing extremely pure nanosized powders with size distributions which are controllable by the parameters of the evaporation process, were outweighed by the disadvantage of very low powder production rates. Mordike et al. applied Nd: YAG laser (400 W average power) and achieved rates of 3 to 4 g h^{-1} as best results for alumina and zirconia.

The aim of this research is to show how this rate can be increased by investigating correlations between laser parameters, the powder yield, the energetic efficiency as well as the particle characteristics. Our researches are not yet finished, and our paper has the character of a status report.

2. Experiments and results

2.1 The experimental set-up

In order to achieve high vaporization rates for oxide materials we chose a CO_2 laser, because the wavelength of the emitted laser beam (λ = 10.6 μm) is absorbed by oxides to a very high degree (in comparison with that of a Nd: YAG laser). For this purpose, a transverse flow CO_2 laser GTL 480 [19] was available. It is characterized in the cw operation mode by the following parameters:

- laser output power: 1...4kW
- diameter of the laser beam: 40 mm
- electro-optical efficiency: 11 %
- total electrical supply 70 kW

(for resistance stabilized discharge)

Due to the resonator configuration, the laser can be operated using a so-called Q-switch (quality switch) by applying a high-speed chopper disk which is mount-

ed in the focal plane of an intracavity telescope [20]. The pulses have typical lengths of $\tau \approx 120$ ns FWHM (full width at half maximum) and power peaks of nearly 100 kW at repetition rates of a few kHz. The averaged power can be varied by up to 1 kW as a function of the pulse tail.

The majority of the experiments were carried out in the cw mode, but early results using the pw mode conditions will also be reported. **Figure 1** shows a schematic of the evaporation chamber which works usually with normal air, but oxygen or argon were also used. The laser beam enters through the opening *E* and is focused onto the surface of the oxide sample in the sample holder *D*. As oxide samples, we used coarse powders of different particle sizes ($d_{50} > 1\mu$m) as well as sintered oxide ceramics of zirconia and alumina. In most of the experiments, we applied a coarse powder of unstabilized zirconia as primary material.

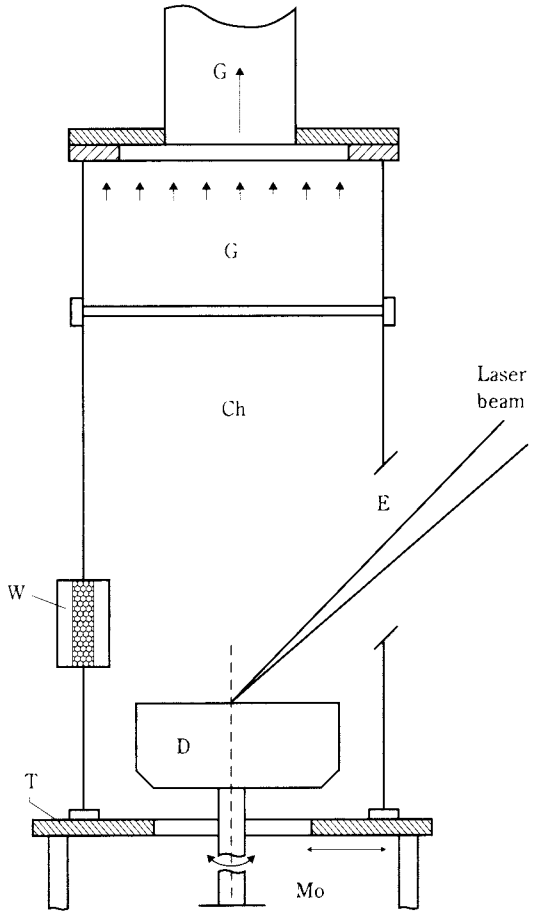

Fig. 1 Schematic of the evaporation chamber
(Ch: chamber; D: drum with oxide material; E: opening for the laser beam entering; G: gas stream produced by suctions; Mo: motor; T: table; W: window)

During evaporation, the laser beam has to be moved on the sample surface in a well-defined manner in order to avoid the formation of deep craters and to ensure reproducible evaporation conditions. The movement is a superposition of translation and rotation and is caused by a controllable motor *Mo*.

The oxide vapour recondenses in the atmosphere above the sample. Due to the very narrow region at high temperature which is created by the laser, the nuclei migrate quickly to cooler regions of the reactor and the particle growth is stopped. The particles are transported by a carrier gas stream *G* which is caused by a pump at the end of the apparatus for all experiments in air. Whenever we used argon or oxygen atmospheres, the carrier gas stream is defined by the flow rate of the gases that stream in. In those cases, we used a modified evaporation chamber with a window for the incident laser beam and an additional gas inlet. The particles are collected by depositing on collision tins in a horizontal glass tube of about 2 m in length.

2.2 The powder yield

When applying this technique, the vaporization rates reported in the literature [18] are in the order of only a few grams per hour. Therefore, we investigated the process parameters which significantly influence the vaporization rate and the powder yield, respectively, with the intention of increasing them.

The vaporization rate depends strongly on the position of the focal plane of the laser relative to the oxide target surface. We obtained the optimum energy input and thus the highest powder yield when the focal plane coincided with the surface of the oxide sample. The laser beam was focused by means of a spherical mirror of focal length $f = 150$ cm which created a focussed area of $A_F = 0.0078$ cm^2.

The dependence of the vaporization rate, *dm/dt*, of unstabilized coarse zirconia powder on the laser intensity, I, operating in the cw mode is shown **Figure 2**. A drastic increase of the vaporization rate

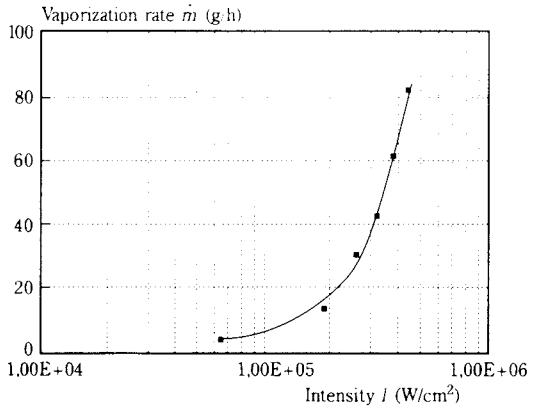

Fig. 2 Vaporization rate *dm/dt* of zirconia as a function of laser intensity

is observed in the range of intensity from about $6 \cdot 10^4$ W cm^{-2} ($dm/dt = 4$ g h^{-1}) to $4.5 \cdot 10^5$ W cm^{-2} ($dm/dt =$ 83 g h^{-1}). The necessary energy coupling may be explained by multiple reflection in the vapour channel and by the formation of a laser-induced plasma in the channel [21]. At an intensity of $4.5 \cdot 10^5$ W cm^{-2}, there is no indication of a limit to the vaporization rate. The experimental feasibilities were limited by the maximum power of the available laser.

In the experiments described so far, the oxide target was rotated relative to the laser beam at about 0.75 r.p.m. This must be mentioned because it was noticed that significant changes in the yield of powder can be achieved by varying this target velocity. However, the correlation is complex because the yield is determined also by the laser intensity. This complex behaviour is illustrated in **Figure 3**. It shows the dependence of the rate of vaporization of zirconia on the median linear velocity of the oxide target, relative to the laser beam for three different laser intensities. Only in the case of the highest intensity ($4.2 \cdot 10^5$ W cm^{-2}) can an increase of *dm/dt* be observed for velocities higher than 20 cm s^{-1}. This condition gave the best powder yield of about 130 g zirconia powder per hour at a velocity of 28 cm s^{-1}. This powder yield value is higher by a factor of about 40 than the corresponding one previously reported in [18].

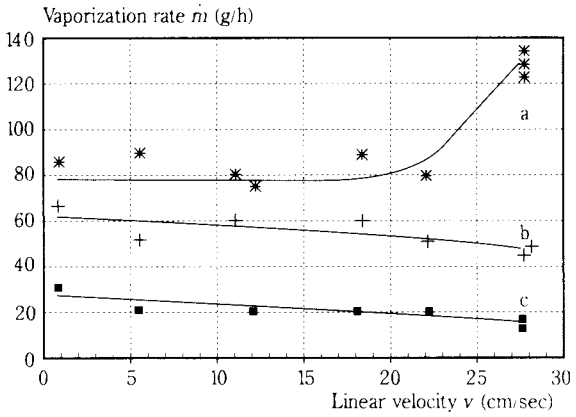

Fig. 3 Vaporization rate *dm/dt* of zirconia as a function of the velocity of the oxide target relative to the laser beam for various laser intensities (a: $I = 4.2 \cdot 10^5$ W cm^{-2}; b: $I = 3.1 \cdot 10^5$ W cm^{-2}; c: $I = 2.1 \cdot 10^5$ W cm^{-2})

In this way, we produced amounts of 0.5 kg of zirconia powders from selected samples.

2.3 The energetic efficiency

By using the powder yield value of 130 g h^{-1}, we can estimate the energy which is necessary to produce 1 g of ZrO_2; if we take into consideration the applied intensity $I = 4.2 \cdot 10^5$ W cm^{-2} as well as the focal area $A_F = 0.0078$ cm^2. The laser power factor of P_L was 3.276 kW. It follows that 3.276 kWh of energy is necessary to produce 130 g of ultrafine zirconia powder or, in other words, an efficiency of about 40 g ZrO_2/kWh was achieved.

This value is higher by a factor of 2.5 than the corresponding reported value [18]. Moreover, in comparison with the efficiency factors of other gas-phase processes for producing nanosized oxides [10], this result is one of the best and is exceeded significantly only by the flame pyrolysis technique (>100 g/kWh). A comparable value of the efficiency can be estimated from data which is reported [1c] for the synthesis of nanosized alumina/silica powders by a plasma chemical route. A plasma power of 104 kW was used to convert 5 kg of oxide per hour which corresponds to an efficiency factor of 48 g h^{-1}.

The calculated energy necessary to prepare 1 g of nanosized zirconia ($2.5 \cdot 10^{-2}$ kWh g^{-1} = 90 kJ g^{-1}) taking into account that (see 2.1.) the mean electro-optical efficiency of a CO_2 laser is 11%, seems to be 2 to 3 orders of magnitude higher than that which is necessary to prepare powders by mechanical grinding. However, it is well known that the mass specific energy for grinding depends strongly on the particle size achieved. Usually, energy factors in the order of 1 kJ g^{-1} correspond to grain sizes of a few micrometers.

Weichert [22], for instance, investigated the dependencies of the mean specific breakage energy on the particle size. His results for glass spheres of sizes in the range from 10 μm to 10 mm, can be extrapolated to fictitious particles of 10 mm. This dependence is characterized by a straight line a double logarithmic representation. Thus a fictitious mass specific energy of about 1000 kJ g^{-1} is obtained for preparing an oxide powder with a mean particle size of 10 nm by means of grinding. Although such a powder cannot be prepared in this way, this extrapolation suggests that the mass specific energies needed for laser evaporation are not unacceptably high for the particle size obtained.

2.4 The particle size and shape

Zirconia particles of typical size and shape produced by laser evaporation are shown in **Figure 4**. The micrograph was taken by TEM (Philips CM 30). The powder was prepared with a laser power of 3.0 kW and a focussed area of 0.0078 cm^2. The carrier gas was air and the sample rotated at a speed of 0.75 r.p.m. The vaporization rate achieved was 65 g h^{-1}.

It is seen that the powder consists of particles in the range from 10 to 100 nm. The particles are almost spherical in shape which is typical of powders from gas-phase processes. This zirconia sample has a specific surface area determined by BET, S_{BET} of 18.9 $m^2\ g^{-1}$. The cumulative size distribution by volume Q_3 is distinguished by $d_{10} = 32$ nm, $d_{50} = 58$ nm and $d_{90} = 111$ nm.

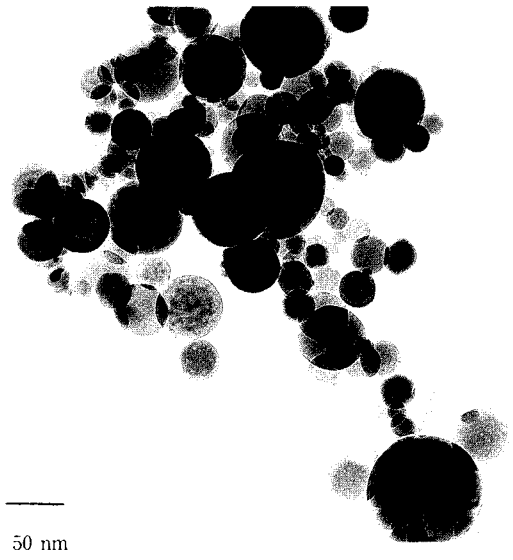

Fig. 4 TEM micrograph of particles of unstabilized zirconia prepared by laser evaporation

The particle size distribution functions were determined by measuring the sizes of at least 1000 particles from electron micrographs. For example, **Figure 5** shows the cumulative size distributions by number (Q_0) and by volume (Q_3) for another sample of unstabilized zirconia ($P_L = 2.7$ kW, $A_F = 0.0078$ cm^2, $S_{BET} = 16$ $m^2\ g^{-1}$, $dm/dt = 44$ g h^{-1}). From this figure, a value of d_{50} (Q_3) = 66 nm results.

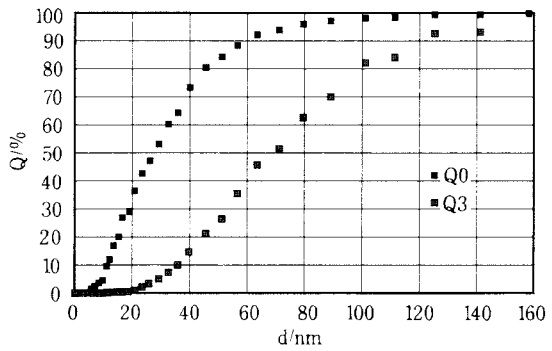

Fig. 5 Cumulative particle size distributions of a prepared zirconia powder (Q_0: by number, Q_3: by volume)

There are various parameters of the evaporation process that influence the particle size distribution. We investigated the following ones:

- the laser power, P_L
- the area of the laser focus, A_F
- the speed of the target relative to the laser beam
- the velocity of the carrier gas stream
- mode of operation of the laser
- the pulse length and the repetition rate in the case of the pw mode.

Figure 6 illustrates the influence of P_L and A_F on the surface area of the powders produced. It is obvious that the dependence on the power at a fixed focal area is only weak. Conversely, there is a significant dependence on the focal area at constant power. We interpret this behaviour in the following manner: If the laser power increases on a fixed focal area, the amount of evaporated oxide, i.e. the oxide vapour pressure above the sample surface, will increase. Simultaneously, the temperature of that vapour will also increase. Nucleation of new oxide particles (or droplets in the first state of their development) from the vapour requires a supersaturated vapour. However, since the supersaturation of a vapour is proportional to the oxide vapour pressure but decreases if the temperature increases, the degree of supersaturation must not be allowed to change significantly by increasing the laser power at a fixed focus area and, in this way, the conditions for nucleation and particle growth may remain comparable independently of P_L.

A change of the focal area at constant power changes P_L, the volume of the intrinsic process zone and – with that, the supersaturation as well as the temperature gradient of this zone – is changed. A decrease of the focal area at a fixed laser power causes an increase of the supersaturation and consequently of the nucleation rate. However, the process zone is

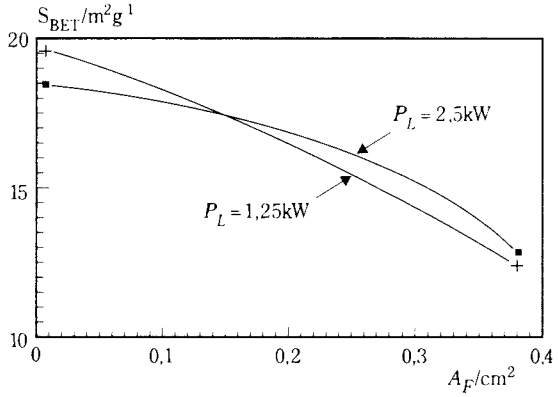

Fig. 6 The specific surface area S_{BET} of zirconia as a function of the area of the laser focus, A_F for two laser P_L

smaller so that the growth time of the particles is reduced. Consequently, a larger quantity by smaller particles develop.

Another essential factor which influences the particle size distribution is the mode of operation of the laser. The experiments reported so far utilised the cw mode. **Figure 7** illustrates the influence of the operating mode on the cumulative distributions, Q_0, of the particle size of unstabilized zirconia. The laser intensity used for preparing sample 30 under cw conditions ($1.3 \cdot 10^5$ W cm^{-2}) was almost the same as the averaged intensity applied in the pw mode for producing sample 33A, (pulse lengths: 120 ns; repetition rate: 3.5 kHz; peak power about 100 kW). Significant differences in the size distribution of these samples can be seen. The d_{50} values are 20 nm and 13.5 nm respectively, and the d_{90} values are 47 nm and 32 nm. The surface area values are 19 m^2 g^{-1} for sample 30 and 30 m^2 g^{-1} for sample 33A. Obviously, the growth time of the particles is curtailed or interrupted by the pulse mode so that smaller particles form.

We have also obtained comparatively high values of surface area of 30 m^2 g^{-1} and more in the case of the cw mode provided that we also used a higher velocity (about 5 m s^{-1}) of the carrier gas stream. These experiments are still in progress and a further increase of the surface area is expected by combining the pw mode of operation with gas streams of higher velocity.

First attempts to convert these ultrafine powders into sintered ceramics were successful, and we observed a significant decrease in the required sinter temperature. It can be shown by dilatometry that the densification process is complete at a temperature of approx. 1200°C, whereas 1500°C and more is usually needed to sinter most of the commercially available zirconia powders.

Similar particle sizes were obtained by evaporation of mixtures of zirconia and alumina and of pure alumina, respectively, at process conditions used for zirconia. **Figure 8** shows the number density distribution of a powder we produced from the evaporation of transformation-toughened ceramics consisting of alumina with 6 weight % ZrO_2 and 0.375 weight % Y_2O_3 ($I = 2.6 \cdot 10^5$ W cm^{-2}). By comparing the broadening of the BRAGG peaks of alumina as well as of zirconia, we conclude that there are no significant differences in the particle sizes of either component. This mixed powder of alumina and stabilized zirconia is characterized by a specific surface area $S_{BET} = 44$ m^2 g^{-1}, whereas pure alumina powders produced by laser evaporation show surface areas in the range of 50 to 60 m^2 g^{-1}.

2.5 Analysis of the crystal phases and the chemical composition of the powders

The nanosized powders prepared were studied by means of X-ray diffraction. In each case, crystalline phases were detected without indication of the existence of a significant amorphous portion. For instance, **Figure 9** shows the diffraction patterns of three unstabilized zirconia powders, prepared at the same intensity ($I = 6.6 \cdot 10^4$ W cm^{-2}), but in different atmospheres (air, oxygen, argon).

These investigations with different atmospheres in

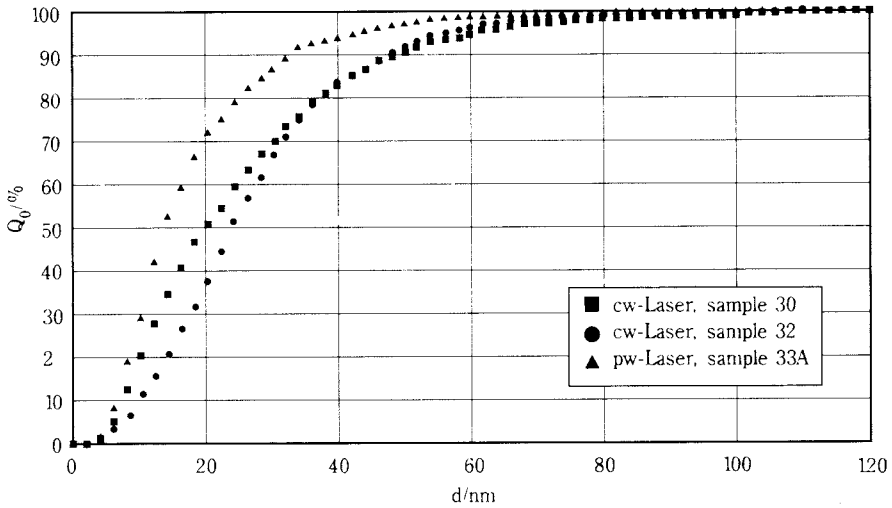

Fig. 7 Cumulative particle size distribution by number for three zirconia samples prepared under different laser conditions (sample 30: cw, $I = 1.3 \cdot 10^5$ W cm^{-2}; sample 32: cw, $I = 6.7 \cdot 10^4$ W cm^{-2}; sample 33A: pw, $I_{av} = 1.2 \cdot 10^5$ W cm^{-2})

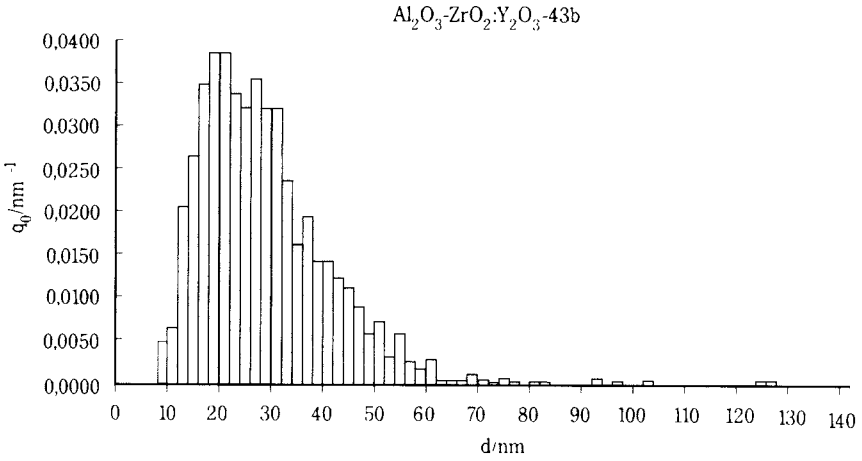

Fig. 8 Number density distribution q_0 of a powder produced by evaporating transformation-toughened ceramics (alumina with partially stabilized zirconia)

the evaporation chamber were carried out in order to exclude their possible influence on the crystallinity of the unstabilized zirconia, since it had been noticed that the tetragonal phase component, x_T, was surprisingly high. This component can be estimated by the intensity ratio of the tetragonal (101) peak to the sum of the corresponding monoclinic ones $\{(1\,1\,\bar{1}) + (1\,1\,1)\}$. Thus:

$$x_T = I_T(101)/\{I_M(11\bar{1}) + I_T(101) + I_M(111)\}.$$

Dependent upon the preparation conditions, x_T has values of 0.5 to over 0.9, although the monoclinic modification is stable at room temperature. Similar results have been reported previously [17, 18, 23].

Certainly, it is known [4] that the tetragonal modification can be stabilized by controlling the particle size. Garvie and Goss [4] discuss that phenomenon from thermodynamic considerations and conclude from the theory as well as from experimental results that zirconia particles with diameters of less than 10 nm should exist in the tetragonal form at room temperature. Lee et al. [23] rely on these thermodynamic arguments to explain the high content of tetragonal particles in their laser-evaporated zirconia powders. However, in contrast to [4], we found tetragonal ZrO_2 particles with diameters of more than 100 nm [24].

Some experiments were repeated with a different atmosphere in order to test wether a possible non-stoichiometry of the oxide or an incorporation of nitrogen into the oxide lattice during vapour recondensation in air was being the culprits in hindering transformation from tetragonal→monoclinic during the cooling process. However, the results in **Figure 9** show that the intensity ratios remain unchanged if the atmosphere is varied while keeping the process conditions constant. In this case, we found a tetragonal part of about 55% independent of the atmosphere (air, oxygen, argon) employed. Thus, we have to conclude in agreement with Heuer and Rühle [25] that this martensitic t→m transformation is kinetically dominated. We suppose that the delay in formation of monoclinic nuclei is due to the extremely short process time as well as to the very regular particle shapes in which structure defects, acting as possible nucleation centres, are rare. This hypothesis is supported by the observation that the amount of tetragonal zirconia can be decreased significantly, to less than 20%, by applying an additional tempering treatment for 30 min at 600°C, in the course of which S_{BET} does not decrease significantly. This means that in spite of their small size, the majority of the zirconia particles tend to transform into the monoclinic form, but that during the process there is insufficient time to complete the transformation during the process.

In the case of alumina, also, particles of the most stable form (α-Al_2O_3) are not obtained. We found a mixture of γ-and δ-Al_2O_3 about one-third γ-and two-thirds δ-alumina, although the powder is formed at temperatures significantly above the transformation temperature of α-alumina of approx. 1200°C. An almost identical diffraction pattern of alumina can be observed for powders prepared by the AEROSIL® technique [15]. In that case, too, the particle formation

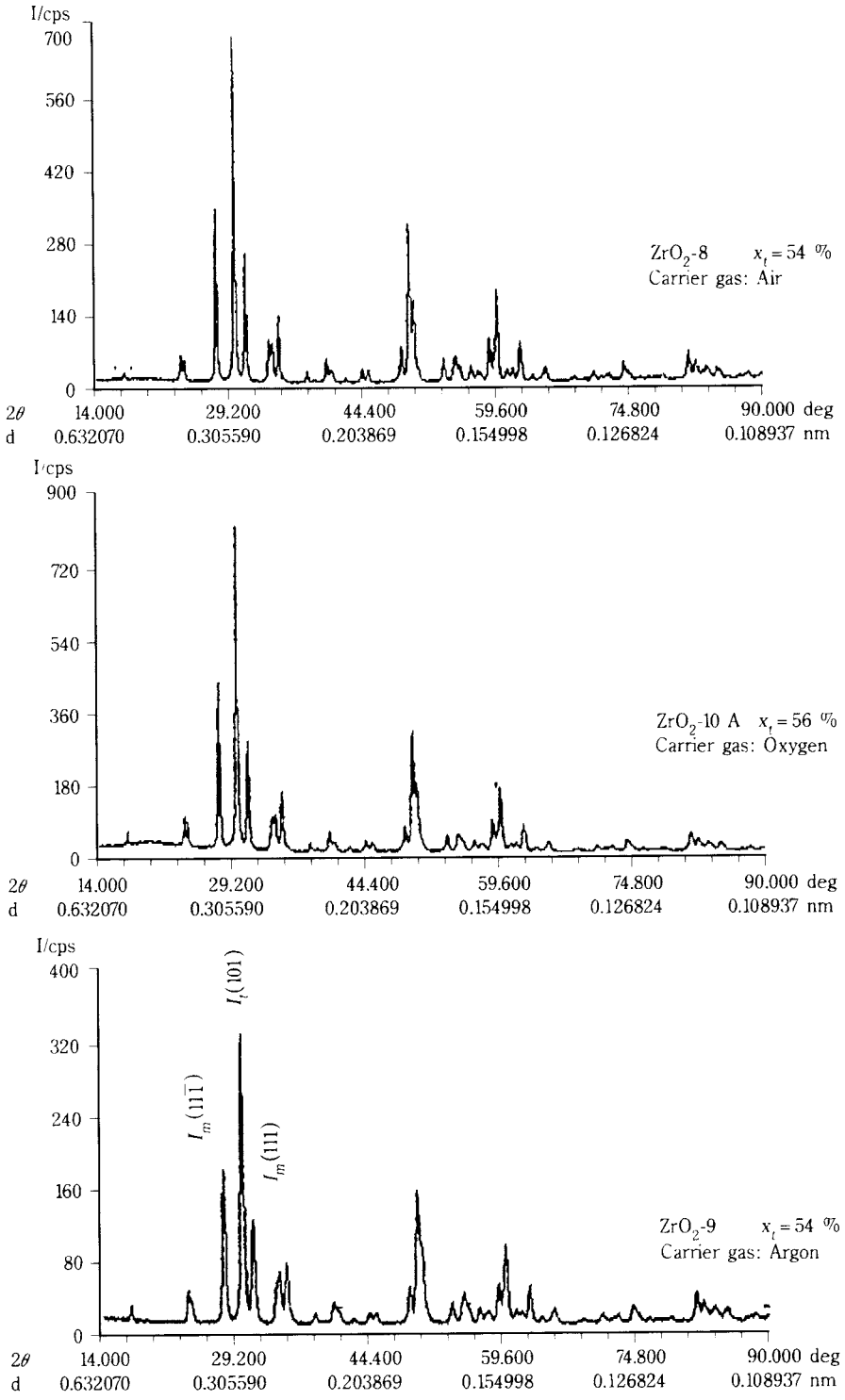

Fig. 9 XRD patterns of zirconia samples prepared under different atmosphere (ZrO_2-8: air; ZrO_2-9: argon; ZrO_2-10A: oxygen)

takes place at temperatures greater than 1200°C. Investigation of this transformation process is still in progress.

By means of ICP optical emission spectroscopy (GBC Integra XM), it was possible to confirm that the powder preparation technique discussed here is an extremely clean process that does not contribute impurities during the powder formation. In the case of alumina as well as of unstabilized zirconia, no differences in the chemical composition of the starting material and the prepared powders were observed. However, when evaporating ZrO_2 stabilized by CaO, MgO or Y_2O_3, clear composition changes are observed. The prepared powders are enriched and the

residual material is depleted in stabilizers which have lower boiling points than zirconia ($T_B = 4300°C$). Examples are magnesia ($T_B = 3600°C$) and calcium oxide ($T_B = 2850°C$). Conversely, the content of yttria ($T_B = \sim 5000°C$) is slightly reduced in the prepared powder. In the case of the evaporated mixture of alumina ($T_B = 2980°C$) and zirconia, an enrichment of alumina is also found in the resultant powder. In future, we will try to diminish or avoid such effects by using a pulsed laser instead of a continuous one, since it is possible that a shortening of the process time will hinder the achievement of a local thermodynamic equilibrium.

3. Conclusions

The aim of this paper is to show that the technique of evaporating solid oxide materials in the focus of a laser is a competitive method for producing nanosized oxide powders in comparison with other gas-phase processes. It has been shown that this technique permits distinctly higher evaporation rates (in the order of 100 g ZrO_2 h^{-1}) and better energy efficiency (40 g ZrO_2 kWh^{-1}) than hitherto reported in the literature.

Evaporation rates and particle size distribution can be controlled over a wide range by adjusting various process parameters such as the laser intensity, the movement of the oxide target relative to the laser beam, the velocity of the carrier gas stream, and the mode of operation of the laser. The nanosized powders prepared have diameters in the range of 10 to 100 nm. The powders have specific surface areas up to 30 m^2 g^{-1} (ZrO_2) and 60 m^2 g^{-1} (Al_2O_3), respectively. A further increase of these values seems to be possible.

The nanosized oxide powder prepared by laser evaporation are crystalline, but the existence of metastable modifications is obviously typical in such powders. Changes in the chemical composition are possible during the evaporation and recondensation of multi-component oxides, by applying the cw mode of operation of the laser.

List of symbols

A_F	laser focal area	[cm^2]
d	particle diameter	[nm]
f	laser focal length	[cm]
I	laser intensity	[W cm^{-2}]
I_M	intensity of a monoclinic BRAGG peak	[s^{-1}]
I_T	intensity of a tetragonal BRAGG peak	[s^{-1}]
m	mass	[g]
p	exponent	[ ]
P_L	laser output power	[kW]
Q_0	cumulative size distribution by number	[ ]
q_0	number density distribution	[nm^{-1}]
Q_3	cumulative size distribution by volume	[ ]
r.p.m.	rotations per minute	[min^{-1}]
S_{BET}	surface area determined by the BET method	[m^2g^{-1}]
T	temperature	[°C]
T_B	boiling point	[°C]
t	time	[s]
x_T	tetragonal part of zirconia	[ ]
ε	mechanical strain	[ ]
λ	laser wave length	[μm]
ϱ	density	[g cm^{-3}]
τ	laser pulse length	[ns]

Acknowledgments

The authors are grateful to the Deutsche Forschungsgemeinschaft and to the Fonds der Chemischen Industrie Deutschlands for their financial support of this research.

References

1) Proceedings of the Third European Ceramic Society Conference. (Eds.: P. Duran, J.F. Fernandez) Faenza Editrice Iberica, Castellón de la Plana (Spain) 1993

1a) Marquis, P.M.: Sol based processing for high performance ceramics. p.1-8

1b) Vollath, D.; Sickafus, K.E.: A continuous process to produce nanophased ceramic powders. p.9-14

1c) Chang, K.; Qafssoui, F.; Hiboux, S.; Ageorges, H.; Baronnet, J.M.; Williams, J.K.; Iddles, D.M.: Synthesis of nanometer size ceramic powders in a d.c. transferred arc plasma furnace. p.15-20

1d) Boulanger, L.; Herlin, N.; Luce, M.; Cauchetier, M.; Tougne, P.; Hommel, H.; Legrand, A.P.: Evolution of the structure of nanometric SiC laser formed powders. p.21-26

1e) Lihrmann, J.-M.: Processing of laser formed, nanosized powders. p.27-32

1f) Herlin, N.; Luce, M.; Musset, E.; Cauchetier, M.: Production of nanocomposite Si/C/N preceramic powders by laser pyrolysis of hexamethyldisilazane. p.33-88

1g) Michel, D.; Mazerolles, L.; Gaffet, E.: Nanocrystalline oxide powders prepared by ballmilling. p.255-260

2) Hahn, H.: Microstructure and properties of nanostructured oxides. Nanostruct. Mater. 2 (1993) 251-265.

3) Niihara, K.: New design concept of structural ceramics - ceramic nanocomposites. J. Ceram. Soc. Jpn. Intern. Ed. **99** (1991) 945-952
4) Garvie, R.C.; Goss, M.F.: Intrinsic size dependence of the phase transformation temperature in zirconia microcrystals. J. Mater. Sci. **21** (1986) 1253-1257
5) Lerot, L.; Legrand, F.; De Bruycker, P.: Chemical control in precipitation of spherical zirconia particles. J.Mater. Sci. **26** (1991) 2353-2358
6) Pyda, W.; Haberko, K.; Bucko: Hydrothermal crystallization of zirconia and zirconia solid solutions. J. Am. Ceram. Soc. **74** (1991) 2622-2629
7) Chang, W.; Cosandey, F.; Hahn, H.: Electron microscopy study of phase transformations in nanostructured yttriumoxide. Nanostruct. Mater. **2** (1993) 29-35
8) Averback, R.S.; Höfler, H.J.; Hahn, H.: Sintering and grain growth in nanocrystalline ceramics. Nanostruct. Mater. **1** (1992) 173-178
9) Eastman, J.A.; Thompson, L.J.; Marshall, D.J.: Synthesis of nanophase materials by electron beam evaporation. Nanostruct. Mater. **2** (1993) 377-382
10) Günther, B.; Kumpmann, A.: Ultrafine oxide powders prepared by inert gas evaporation. Nanostruct. Mater. **1** (1992) 27-30
11) Ning. X.G.; Ye, H.Q.; Liang, Y.; Zheng, F.: Structural characterization of ultrafine SiC powder made from laser-heated vapour-phase reactions. J. Mater. Sci. Lett. **11** (1992) 59-62
12) Borsella, E.; Botti, S.; Alexandrescu, R.; Morjan, I.; Dikonimos-Makris, T.; Giorgi, R.; Martelli, S.: Nanocomposite ceramic powder production by laser-induced gas-phase reactions. Mater. Sci. Engineer. **A168** (1993) 177-181
13) Georghiu, A.; Sénémaud, C.; Rouler, H.; Dufour, G.; Moreno, T.; Bodeur, S.: Atomic configurations and local order in laser-synthesized Si, Si-N, Si-C, and Si-C-N nanometric powders, as studied by x-ray-induced photoelectron spectroscopy and extended x-ray-absorption fine-structure analysis. J.Appl. Phys. **71** (1992) 4118-4127
14) Strutt, P.R.; Gonsalves, K.E.; Xiao, T.D.: Synthesis of polymerized preceramic nanoparticle powders by laser irradiation of metalorganic precursors. Nanostruct. Mater. **1** (1992) 21-25
15) Ettlinger, M.: Hochdisperse Metalloxide nach dem AEROSIL®-Verfahren. Degussa Schriftenreihe Pigmente, Nr. 56, Frankfurt 1989
16) Kato, M.: Preparation of ultrafine particles of refractory oxides by gas evaporation method. Japan J. Appl. Phys. **15** (1976) 757-760
17) Lee, H.-Y.; Riehemann, W.; Mordike, B.L.: Sintering of nanocrystalline ZrO_2 and zirconia toughened alumina (ZTA). J. Europ. Ceram. Soc. **10** (1992) 245-253
18) Lee, H.-Y.; Riehemann, W.; Mordike, B.L.: Charakterisierung von laserzerstäubten nanoskaligen Oxidpulvern. Z. Metallkd. **84** (1993) 79-84
19) Triebel, W.; Ose, E.; Michel, G.; Petrich, A.: Experimental and theoretical investigation of a transverse flow CO_2-laser. Proceed. SPIE **1031** (1988) 41-47
20) Triebel, W.; Michel, G.; Linke, P.: Generation of high-peak power kHz repetition rate pulses in a cw discharge transverse flow CO_2 laser by Q-switching technique. J. Phys. D: Appl. Phys. **25** (1992) 1293-1297
21) Beck, M.; Dausinger, F.; Hügel, H.: Study of energy coupling at deep laser welding. Laser und Optoelektronik **21** (1989) 80-84
22) Weichert, R.: Theoretical prediction of energy consumption and particle size distribution in grinding and drilling of brittle materials. Part. Part. Syst. Charact. **8** (1991) 55-62
23) Lee, H-Y.; Riehemann, W.; Mordike, B.L.: Sintern von nanokristallinem ZrO_2. In: Verstärkung keramischer Werkstoffe (Ed.: N. Claussen), DGM Verlag Oberursel 1992 pp. 211-224
24) Oestreich, Ch.; Müller, E.; Schreiber, G.; Michel, G.; Henneberg, K.-H.: Diffraction studies on the size dependence of the t→m transformation of zirconia. Fresenius' J. Anal. Chem. **349** (1994) 155-157
25) Heuer, A.H.; Rühle, M.: On the nucleation of the martensitic transformation in zirconia (ZrO_2). Acta metall. **33** (1985) 2101-2112

Author's short biography

Uta Popp

Uta Popp got a diploma in inorganic-nonmetallic materials at the Freiberg University of Mining and Technology (TU) in July 1985.
Since 1986 she is working as a research assistant at the Institute of Ceramic Materials of the Freiberg University of Mining and Technology with emphasis on joining and synthesis of technical ceramics.

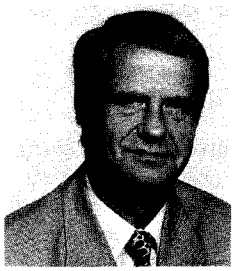

Eberhard Müller

Eberhard Müller received a diploma in physics in 1966 from the Friedrich Schiller University of Jena. He got his doctor degree in 1970 at the same university in the field of crystal structure analysis by X-ray diffraction. In the following time he was engaged in structure analysis of surfaces and interfaces by electron diffraction as well as in theoretical investigations on the stability of surface structures. 1986 he defended his "Doctor of Science" thesis on the structure chemistry of crystalline interfaces.

1986 – 1989 he was occupied with the preparation and characterization of highly dispersed oxides and with theoretical calculations of the surface energy of small particles. After a sabbatical at the Department of Material Engineering of the Federal University of São Carlos in Brazil (crystallization of glasses) he changed to the Freiberg University of Mining and Technology in 1990 and got a professorship on inorganic composites. Since that time he is engaged in the field of nanocrystalline ceramic powders as well as of ceramic fibres.

Christiane Oestreich

From 1975 to 1980 she studied physics. Since 1980 she works at the Technical University of Freiberg. Mrs. Oestreich obtained a doctorate in physics to luminescence of semiconductor materials in 1986.
Since 1987 she is a research assistant in the department of material science. There she started with joining of ceramics. Her recent fields of research are physical vapour deposition and investigations of ultrafine ceramic powders by transmission electron microscopy.

Günter Michel

Günter Michel was born in Eisenach, Thüringen, Germany, on September 16, 1948. He received the degree of diploma in physics from the University of Jena "Friedrich Schiller" in September 1972 in the area of quantum electronics. His dissertation concerned the characterization of perturbed arcs in turbulent axial gas flow.
From 1973 to 1991 he worked at the Physical-Technical-Institute, Jena, where he did research in the area of gas discharges and laser physics.
In 1992 he transferred to the Technical-Institute of the University of Jena. His present interests include High Power CO_2-Lasers and their applications.

Author's short biography

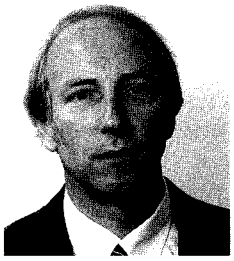

Gisbert Staupendahl

Gisbert Staupendahl was born in Querfurt, Germany, on April 14, 1945. He received the diploma in Physics from the Physical Institute of the Friedrich Schiller University Jena. The graduation and the qualification for a lectureship he received from the same university in 1973 and 1981, respectively. In these years his research interests have included nonlinear optical effects in semiconductors, optical bistability and the development of high-power CO_2 lasers.

From 1982 to 1987 he has been with the Feinmechanische Werke Halle, Germany, where he was engaged in the research and development of CO_2 lasers for industrial applications.

Since 1987 he is a lecturer at the Technical Institute of the Friedrich Schiller University Jena. His present interests include the modulation of intense CO_2 laser radiation and the interaction of this radiation with matter.

Karl-Heinz Henneberg

After terminating his training as a precision mechanic (1964), firstly Karl-Heinz Henneberg studied control engineering (1967-70) and later he recieved a diploma in engineering for the construction of scientific instruments (1974) from the Friedrich Schiller University of Jena. Since 1974 he has been engaged in the field of research and development at the Institute of Physical Chemistry of the University of Jena. Topics in this field are the projecting and construction of devices for the preparation and characterization of highly dispersed and/or porous substances, specially oxides.

Relationships Between Surface Areas of Red Tropical Soils Measured by Different Methods†

H. C. Ferreira and G. A. Neves
*Department of Materials Engineering Federal University of Paraíba**
T. H. Topper
*Department of Civil Engineering University of Waterloo***

Abstract

A variety of tests are currently used to determine surface area in different branches of engineering and industry. This paper analyzes the relationships between these tests based on the results obtained by each test for a group of nine red tropical soils collected in the north east of Brazil. The ethylene glycol monoethyl ether (EGME) method that showed a good correlation with direct measurement of particle size by electron microscopy, is taken as a base for the graphical representation of results. Conversion factors between the tests and the EGME test and the standard deviation of the conversion factors are calculated.

The results show that test procedures can be divided into three groups in terms of increasing spread in the test results - polar molecules and direct measurement tests with a spread of less than 15%, methylene blue and BET tests with a spread of about 30% and Blaine, Fisher and granulometric tests with a spread of about 50% when plotted against EGME data. It is noted that the test methods that gave a larger spread are used in industry and process control, because they may be performed quickly at a modest cost. The more accurate methods are slower and in some cases more expensive.

1. Introduction

Surface area is used in the engineering practice to correlate the size of particles of granular materials with other engineering properties. These correlations can be used as a measure of associated properties and as a control parameter in a wide variety of engineering processes.

At present, a variety of methods using different physical and chemical principles are used to measure surface area in different industries. Each of these methods has evolved in response to the need to control a specific process or evaluate a specific product. Unfortunately, the surface area values obtained using these different methods vary widely. In some cases (Ferreira and Brito, 1984) there even seems to be little or no correlation between the values given by different methods.

The various granulometric methods of calculating surface area (arithmetic mean diameter, geometric mean diameter and Mellor's mean diameter) which use grain sizes determined by sedimentation are no longer in use for the control of engineering processes. However, the grain size curves are still used to classify soils. The precision and repeatability of surface areas calculated by these methods is not adequate for most engineering applications.

The Blaine (Blaine, 1943) and the Fisher (Carman, 1939) air permeability methods, both compare the time required for a given volume of air to pass through a cylindrical sample of the compacted material with the time taken for the same volume of air to pass through a sample of known surface area.

The Blaine method is used to measure the fineness of Portland and other cements. Fisher's method is used to determine the fineness of metal powders and oxides. Both methods are quick giving results in about five minutes per test. This allows continuous monitoring of industrial processes. However the precision of these methods is low. The Fisher method which uses more sophisticated and expensive equipment than the Blaine method is somewhat more precise.

* 58109-970 Campina Grande, PB – Brazil
Tel. – 0055 83 333 1000 – Ext. 146
Fax – 0055 83 333 1080
** Waterloo, Ontario, Canada
Tel. – 001 519 885 1211
Fax – 001 519 888 6197
† Received 12 June, 1995

The Hang and Brindley (1970) method based on the adsorption of methylene blue dye has for some time been used to control the fineness of raw materials in the ceramics industry and has recently been utilized to characterize soils in soil mechanics applications (Casanova, 1986). This method is quick, taking about one half hour per test, but its precision and repeatability are low.

The adsorption of polar molecules of ethylene glycol, glycerol and ethylene glycol monoethyl ether (EGME) (Bower and Gschwend, 1952) is the traditional method for measuring surface area in soils and agricultural studies. This method is characterized by a relatively high degree of precision and repeatability, but is slow and time consuming making it unsuitable for such applications as process control where a rapid feedback is required.

The classic BET method for measuring surface area (Brunauer, Emmett and Teller, 1938)is based on the adsorption of gaseous hydrogen and nitrogen. It is widely used in the chemical industry and materials technology. Its precision and repeatability are good. Each test requires about two hours, a reasonable time for most purposes, but perhaps somewhat slow for a process control. Another disadvantage of this method for industrial applications is that the equipment required for the tests is relatively expensive.

Direct measurements of particle sizes using transmission or scanning microscopy gives very accurate determinations of particle cross section areas. The former does not allow a direct measurement of particle thickness. The latter, at least in theory, allows particle thickness to be determined by changing the sample orientation. However, for materials with unregulated crystalography, it is difficult to separate the particles in the photographic images. This method, although potentially very accurate, is used mainly in research. It is one of the slowest methods for measuring surface area and requires very expensive electron microscopes.

This paper analyzes the degree to which the results of the surface area measurements obtained by different methods can be related with each other. The model materials used in this study were samples of fines fractions of a group of red tropical soils collected in three states in the north east of Brazil. Data obtained by the EGME method which demonstrated good correlations with other measurements using polar molecules, as well as with direct measurements have been used as a base for graphical presentations of data obtained by other methods.

2. Materials and Experimental Procedures

Soil Samples – The red tropical soils from the north east of Brazil used in this investigation were taken from samples stored in the soils laboratory, Solos II, of the Civil Engineering Department, Centre of Science and Technology of the Federal University of Paraíba. The samples were collected from locations in the States of Maranhão, Paraíba and Piaui and identified by the abbreviations BUPI, CAPI, PDMA, VGMA, SLMA, JPPB, TEPB, ARPB and CTPB. A detailed description of the samples and their location of origin is available in Ferreira and Brito (1981).

Sample Preparation – In order to increase the clay fraction the wet soil samples were screened through the ABNT n°200 (0.074 mm) screen. Then they were air dried under the incandescent bulbs that accelerated the drying process by raising the material temperature to about 50°C. The dry samples were comminuted by a porcelene pestle, screened through the ABNT n°200 (0.074 mm) screen and dried in an oven to a constant mass. These specially prepared samples were used in the various procedures for measuring the surface area as it is described below.

Granulometric Method – Surface areas were derived from granulometric analysis by sedimentation performed by Lima (1983) using the method of BS1377 (1975) commonly called the densimeter method. The calculations of surface area were conducted in accordance with Singer and Singer (1975) and gave numerical values in m^2/g accurate up to 0.01 m^2/g.

Blaine's Method – Surface areas were determined using the Blaine permeameter in accordance with MB – 348 of ABNT (1966). The standard used was the cement sample obtained from the Brazilian Portland Cement Association which had a surface area of 0.342 m^2/g and a specific mass of 3.21 g/cm^3. Values of surface area in m^2/g were calculated to an accuracy of 0.01 m^2/g.

Fisher's Method – Fisher model 95 permeameter and a reference sample having a surface area of 0.3030 m^2/g and a specific mass of 3.15 g/cm^3 obtained from the National Bureau of Standards ''NBS'' were used in the surface area determination. The methods used are those described by Neves (1989) and the numerical values of surface area in m^2/g were calculated to an accuracy of 0.01 m^2/g.

Methylene Blue Method – The methodology described by Chen et al (1974) was applied in the surface area determination using methylene blue. A conversion factor of 7.8043 based on molecules of methylene blue having a face area of 130$Å^2$ as suggested by

Hang and Brindley (1970) was used in the equations for the calculation of surface area, where surface area is a product of cation exchange capacity by the conversion factor. Surface areas were calculated in m^2/g to an accuracy of 0.01 m^2/g.

Adsorption of Polar Molecules Method – The determination of surface area using polarized molecules was performed in accordance with the methodology of Diamond and Kintner (1968) for glycerol, that of Carter et al (1965) for ethylene glycol monoethyl ether (EGME) and that of Bower and Gschwend (1952) for ethylene glycol. A detailed description of these methods and their application is also available in Guedes and Ferreira (1992). As with the other methods the surface areas for these cases were calculated in m^2/g to an accuracy of 0.01 m^2/g.

The BET method – The surface areas of the fines fraction of the red tropical soil samples were determined using the methodology described by Brito and Ferreira (1984). This method, which for the first time was described by Brunauer, Emmett and Teller in 1938, gives numerical values of surface area in m^2/g to the nearest 0.01 m^2/g.

Direct measurement – Surface areas were determined from measurements based on a planimeter of cross sectional areas in images taken in a transmission electron microscope (TEM). A description of the details of the measurement and calculation procedures is available in Conciani and Ferreira (1988). The TEM procedure used did not allow the accurate measurements of the particle thickness and evaluation of the surface area was made assuming a series of thicknesses within the range reported in the literature for this class of materials. The thicknesses chosen were D/3, D/5, D/10 and D/15 where D is the mean diameter of the cross sectional area examined. The surface areas were calculated in m^2/g accurate to within 0.01 m^2/g.

3. Results and Discussion

The results of the surface area determinations for the fines fraction of the various red tropical soils samples are given in **Table I**. The statistical correlations based on the assumption of a linear relationship between the various surface area measurements are given in **Table II** for those cases where the coefficient of correlation was greater than 0.70. The best correlations are between the three methods using polar molecules of EGME, ethylene glycol and glycerol, all of which gave a coefficient above 0.96 at a significance level of 0.002%. Also, as it may be seen from **Table I**, the numerical values given by the three methods are similar. **Figure 1** gives values of surface area of ethylene glycol and glycerol plotted against those for EGME. With the exception of one test result all the data obtained is lined up at the equal values of the dependent and independent variables. In the exceptional case, the ethylene glycol and glycerol data are positioned close to each other. This is consistent with the slightly higher coefficient of correlation between these two test methods compared with the EGME results. The factor correlating the results of determinations by these three methods is approximately equal to one (1.05 for ethylene glycol and 1.02 for glycerol); the standard deviation of the factor is 12% of the mean value for ethylene glycol and 8% of the mean value for glycerol.

Because the EGME method is not as time consuming as very slow (but accurate) polar methods, it was used as a base to plot the data obtained by the other methods. **Figure 2** displays data obtained by

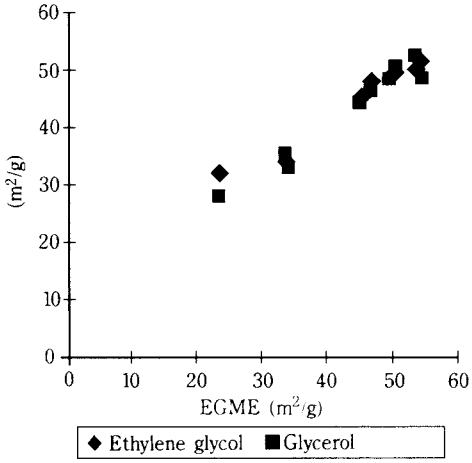

Fig. 1 Surface Areas Determined by Ethylene Glycol and Glycerol Techniques Versus Those Determined by EGME Technique.

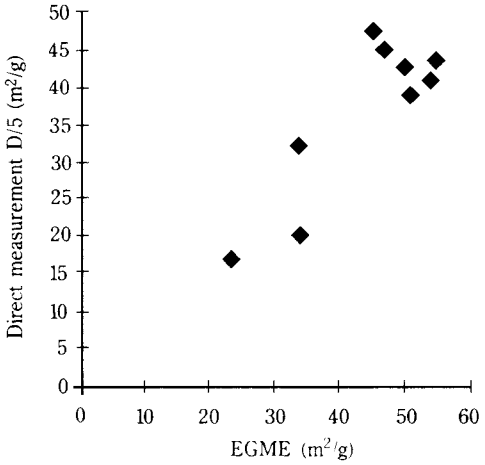

Fig. 2 Surface Areas Determined by Direct Measurement (D/5) Versus Those Determined by EGME Technique.

Table I Surfaces Area of the Fines Fraction of Red Tropical Soils from the Northeast of Brazil.

Samples	Methods of Testing to Determine the Surface Area (m^2/g)													
	Granulometric Methods			Blaine Cement Standard 0,34 m^2/g	Fisher NBS Standard 0,3030 m^2/g	Methylene Blue Molecule of 130A^{02}	EGME Molecule of 52A^{02}	Ethylene Glycol	Glycerol	BET	Direct Measurement			
	Mellor Mean Diameter	Arithmetic Mean Diameter	Geometric Mean Diameter								C = D/3	C = D/5	C = D/10	C = D/15
BUPI	0.08	0.09	0.10	0.70	0.50	20.29	33.54	33.87	33.54	14.92	16.03	20.66	32.70	77.28
CAPI	0.08	0.09	0.10	1.05	0.85	21.85	46.15	48.39	46.77	22.22	32.47	45.30	77.10	110.21
PDMA	0.09	0.11	0.12	1.29	1.23	39.02	33.22	34.14	35.30	25.18	9.17	32.39	55.02	78.01
VGMA	0.08	0.10	0.11	0.68	0.50	40.58	49.20	49.68	49.24	25.23	29.00	43.09	69.48	98.61
SLMA	0.07	0.08	0.10	0.78	0.77	15.61	23.08	32.26	28.24	21.48	12.39	17.32	29.71	42.11
JPPB	0.08	0.09	0.10	1.90	1.32	26.53	50.00	50.97	51.18	34.95	28.27	39.62	67.72	96.16
TEPB	0.10	0.12	0.13	1.14	0.92	48.39	53.15	50.32	52.95	39.12	29.96	41.49	71.92	101.96
ARPB	0.06	0.06	0.07	1.05	0.81	24.97	44.76	46.13	44.83	42.64	34.05	47.55	82.79	114.67
CTPB	0.09	0.11	0.12	1.48	0.82	29.66	53.85	51.94	49.42	28.73	31.11	43.66	74.61	105.88

Table II Linear Correlation Between the Various Surface Areas of Fines Fraction of Red Tropical Soils from the North East of Brazil.

VARIABLE Y	VARIABLE X	LINEAR EQUATION y = ax + b	COEFFICIENT OF CORRELATION (R)	SIGNIFICANCE LEVEL (%)
EGME	GLYCEROL	y = -8.29 + 1.18x	0.98	0.001
ETHYLENE GLYCOL	GLYCEROL	y = 4.65 + 0.91x	0.97	0.001
EGME	ETHYLENE GLYCOL	y = -11.98 + 1.24x	0.96	0.002
D/3	ETHYLENE GLYCOL	y = -21.74 + 1.05x	0.92	0.049
D/15	EGME	y = 11.27 + 1.87x	0.88	0.187
D/5	ETHYLENE GLYCOL	y = -14.73 + 1.16x	0.88	0.214
D/5	GLYCEROL	y = -10.24 + 1.08x	0.87	0.204
D/5	EGME	y = -1.78 + 0.90x	0.86	0.239
D/3	GLYCEROL	y = -15.39 + 0.92x	0.86	0.268
D/3	EGME	y = -8.34 + 0.77x	0.86	0.267
D/10	ETHYLENE GLYCOL	y = -16.01 + 1.79x	0.86	0.266
D/15	GLYCEROL	y = -2.43 + 2.16x	0.85	0.398
D/10	GLYCEROL	y = -7.32 + 1.62x	0.84	0.468
D/15	ETHYLENE GLYCOL	y = -8.99 + 2.28x	0.83	0.557
D/10	EGME	y = 6.45 + 1.32x	0.82	0.684
FISHER	BLAINE	y = 0.20 + 0.59x	0.85	0.383
METHYLENE BLUE	ARITHMETIC MEAN	y = -11.39 + 434.62x	0.73	1.310
BET	DIAMETER D/10	y = 4.34 + 0.37x	0.72	2.970

direct measurement assuming the thickness of the soils particles is equal to one fifth of their diameter (D/5). **Table I** shows the D/5 results give the closest numerical values to those obtained by the polar molecules methods. The spread of the results relatively, to the linear curve is small. The factor relating D/5 direct measurement and the EGME results is 0.85 and the standard deviation of this factor is 16% of the mean value. Interpolation of the data obtained for the various ratio values of the thickness-to-diameter indicates that the ratio of D/6.3 will result in a correlation factor of one between direct measurement and the EGME data. If the average thickness of particle can be determined precisely when using scanning microscopy, the direct measurement can offer a promising standard which can be used as a reference for calibration of surface area measurement by other techniques. Although it does not account for surface topography the spread due to this factor should be small compared to that observed with other techniques. The main advantage of the method is the fact that it doesn't depend on the many assumptions required by other techniques.

Figure 3 presents a plot of data obtained by the methylene blue and BET methods versus the EGME data. The spread of the data is approximately ± 30% in relation to central line. The same central line and the spread region can be used to characterize results obtained by both methods, but the individual data points for these two methods show no tendency

to converge indicating that their correlation with each other is no better than that of each of them with the EGME results. The factors relating the methylene blue and BET methods to EGME are 0.70 and 0.67 respectively with standard deviations of 33% and 28% of the mean values accordingly.

Figures 4 and **5** give values of surface area obtained by the Blaine and Fisher methods plotted against the EGME data. The spread is about 40% and 50% correspondingly. The factors relating Blaine and Fisher measurements to those of the EGME method are 0.03 and 0.02 respectively. The standard deviations are 33% and 50% for the mean values. It should be noted that the numerical values obtained by these methods are much smaller than those given by the other methods. **Figure 6** represents a plot of the Blaine surface area measurements versus those obtained by the Fisher method. The correlation factor is 1.31 (Blaine value = 1.31 × Fisher value) and the standard deviation of the factor is 18% for the mean value. The spread of about ±25% is somewhat smaller in magnitude than that of data for each of these methods plotted against the EGME method.

The surface area values obtained by the Mellor calculation based on the granulometric data is plotted versus EGME data in **Figure 7**. The factor relating the Mellor values to the EGME values is 0.002. The standard derivation of the factor is 30% for the mean value. The data on the graph exhibits a spread of about ± 40% in relation to the mean curve. A similar but slightly greater spread was obtained when the geometric mean diameter was calculated from the granulometric data and plotted versus the EGME

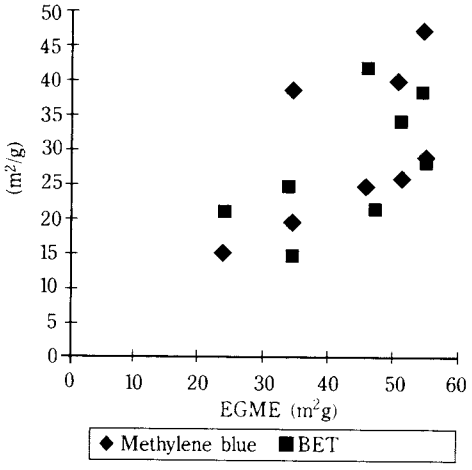

Fig. 3 Surface Areas Determined by Methylene Blue and BET Techniques Versus Those Determined by EGME Technique.

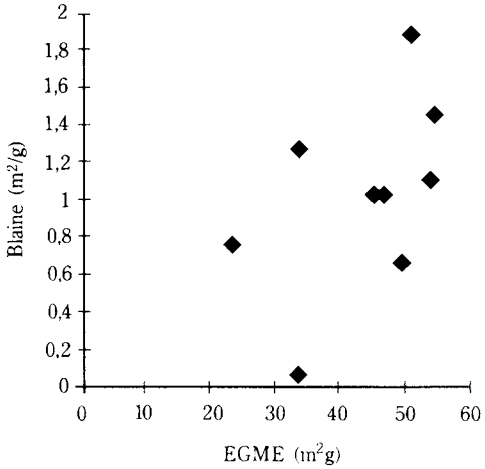

Fig. 4 Surface Areas Determined by Blaine Technique Versus Those Determined by EGME Technique.

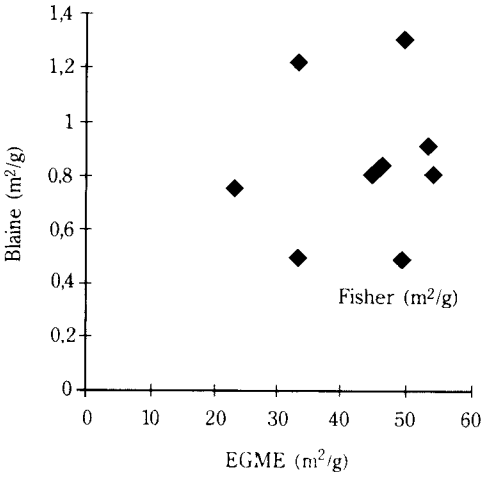

Fig. 5 Surface Areas Determined by Fisher Technique Versus Those Determined by EGME Technique.

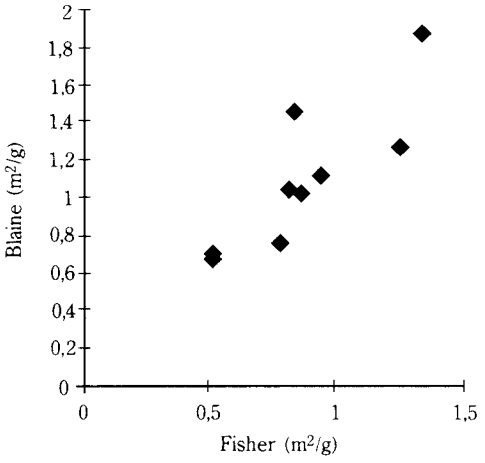

Fig. 6 Surface Areas Determined by Blaine Technique Versus Those Determined by Fisher Technique.

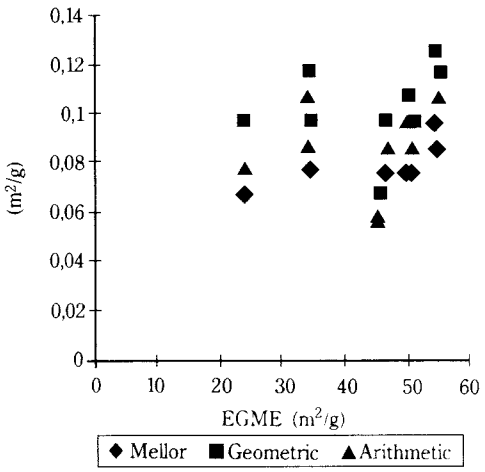

Fig. 7 Surface Areas Determined by Granulometric Methods Techniques Versus Those Determined by EGME Technique.

values. Visual analysis of the data, however, can bring one to the conclusion that there is little or no correlation between the Mellor and the EGME data.

Data obtained by the polar molecules methods not only have demonstrated nearly identical results for the samples tested (with coefficient of correlations among them greater than 96%)find they correlate very well with the physically meaningful direct measurement data (with the correlation coefficient of approximately 87% for D/5) which can be further improved by using the thickness-to-diameter ratio equal to D/6.3. Data for the EGME method was taken as a basis for the graphical comparisons. These comparisons show that the methods of determining surface area can be divided into three groups in terms of increasing dispersion of the data in the graphs and presumably decreasing precision of the method. The first group includes the polar molecules and direct measurement techniques, the second – the adsorption of methylene blue and BET methods and the third – the Blaine and Fisher methods and the granulometric methods.

The degree of spread of data observed in the BET versus the EGME plot and a relatively poor correlation between the BET and the data obtained by polar molecules methods were unexpected since both the BET and the polar molecules methods are based on the isotherms of adsorption.

The methods currently used in the control of industrial processes, namely the Blaine, Fisher and the methylene blue (which are utilized in the production of cement, metaland ceramic powders) are among those that showed the greatest spread of data in the graphical plots. However, replacing them with a more accurate method such as one of the polar molecules methods would significantly increase the cost and time consumed for testing. The present results do not seem to confirm the supposition that the BET method, which is intermediate in terms of testing time is much more accurate than the Blaine and Fisher methods.

The very slow and expensive direct measurement techniques are promising for the scientific applications.

4. Conclusions

(1) The three polar molecule methods of measuring surface area using EGME, ethylene glycol and glycerol gave almost identical surface area values for all of the samples.

(2) The direct measurement by electron microscopy technique gives results that, for an appropriate thickness assumption, are almost the same as the results given by the polar molecules methods.

(3) The spread of the results for the methylene blue and BET methods, when plotted against EGME data, is significantly greater than for the polar molecules or direct measurement techniques. The Blaine, Fisher and granulometric methods show still a greater spread.

References

1) A.B.N.T., (Brazilian Association for Technical Standards) Determination of the Fineness of Portland Cement Using an Air Permeability Apparatus, MB – 348, 1966.

2) Blaine, R.L., A Simplified Air Permeability Fineness Apparatus, A.S.T.M. Bulletin, 1943.

3) Bower, C.A. and Gschwend, F.B., Ethylene Glycol Retention by Soils as a Measure of Surface Area and Interlayer Swelling, Soils Science Society Proceed., Vol. 16, 342 to 345, 1952.

4) Brito, L.P., The characterization of Powders by Means of Surface Areas Applied to the Lateritic Soils of the Northeast Region of Brazil, Masters Thesis, Department of Chemical Engineering, Federal University of Paraíba, Paraíba, Brazil, 1984.

5) Brunauer, S., Emmett, P.H. and Teler, E., Adsorption of Gases in Multimolecular Layers, J. Amer. Chem. Soc., 60, 309, 1938.

6) B.S.I., Methods of Testing Soils for Civil Engineering Purposes, BS – 1377, Test 2 (A), London 1975.

7) Carman, P.C., Determination of Specific Surface of Powders, J. of the Soc. of Chem. Ind., 58(1), 1 (1939).
8) Carter, D.M., Heilman, M.D. and Gonzales, C.L., Ethylene Glycol Ether for Determining Surface Areas of Silicate Minerals, Soil Science 100 (5), 356 (1965).
9) Casanova, F.J., The Methylene Blue Test as Used in the Characterization of Lateritic Soils, Proceedings of the 21st Annual Meeting of the Brazilian Association of Pavements, Vol. II, 227, 1986.
10) Chen, T.J., Souza Santos, P., Ferreira. H.C., Calil, S.F., Zandonadi, A.R. and Campos L.M. Determination of the Cation Exchange Capacity and Surface Area of Some Clays and Ceramic Brazilian Kaolins by Methylene Blue and Correlation With Some Technical Properties , Cerâmica 20 (79), 32 (1974).
11) Conciani, W. and Ferreira H.C., The Determination of the Surface Area of the Fines Fraction of Lateritic Soils by Direct Measurement, Proceeding of the 23st Annual Meeting of the Brazilian Association of Pavements, Vol. I, 33, 1988.
12) Ferreira H.C. and Brito L.P., The Determination of the Surface Area of the Fines Fraction of Lateritic Soils of the Northeast of Brazil, Cerâmica 30 (171), 69 (1984).
13) Guedes, L.M.M. and Ferreira H.C., The Determination of the Surface Area of the Fines Fraction of Lateritic Soils of the Northeast Region by the Adsorption of Polar Molecules, Proceeding of 10th Brazilian Meeting of Science and Materials Engineering 181, Águas de Lindoia, São Paulo, 1992.
14) Hang P.T. and Brindley, G.W., Methylene Blue Adsorption by Clay Minerals: Determination of Surface Areas and Cation Exchange Capacities, Clay and Clay Minerals 18, 203 to 212, (1970).
15) Kinter E.B. and Diamond, D., Gravimetric Determination of Monolyer Glycol Complexes of Clay Minerals, NAS, NRC, Conference of Clay Minerals, Pub., 566, 318 to 347, 1968.
16) Lima, R.C., Granulometry of Lateritic Soils: Methodology, Effect of Thermal and Mechanical Energy and their Relationships with Chemical and Mineral Composition, Masters Thesis, Civil Engineering Department, Center of Science and Technology, Federal University of Paraíba, Campina Grande, PB, Brazil, 1983.
17) Neves G.A., The Influence of Surface Area on the Pozzolanic Activity of the Lime-Lateritic Soil System, Masters Thesis, Chemical Engineering Department, Center of Science and Technology, Federal University of Paraíba, Campina Grande, PB, Brazil, 1989.
18) Singer, F. and Singer, S., Industrial Ceramics, Chapman & Hall LTD., London, 1971.

Author's short biography

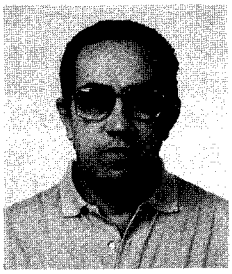

Heber Carlos Ferreira

Professor Heber Carlos Ferreira graduated in Civil Engineering at the Politechnical School of Federal University of Paraíba, and got his M.Sc. and Dr. Eng. degrees in Materials Engineering at the Politechnical School of São Paulo University. At present, he is working with soil mineralogy, clay technology and conventional ceramic materials and lectures in three different Engineering Departments (Materials, Chemical and Civil) of the Federal University of Paraíba. Up to now he has published 135 papers and supervised 38 master thesis.

Timothy Hamilton Topper

Professor T.H. Topper received a PhD in Engineering from Cambridge University in 1962 and since has worked in the Civil Engineering Department at the University of Waterloo in Waterloo, Canada. Since 1975 he has been also involved in collaborative research with the Federal University of Paraíba Center for Science and Technology in Campina Grande, Brazil. His principal area of research is in materials with a special interest in fatigue.

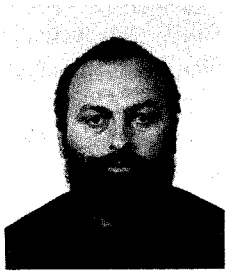

Gelmires de Araújo Neves

Gelmires de Araújo Neves graduated in Mining Engineering and M.Sc. in Materials Engineering at the Federal University of Paraíba. At present, he is working with clay technology and conventional ceramic materials and lectures in two different Engineering Departments (Materials and Civil) of the Federal University of Paraíba. Up to now he has published 25 papers.

Investigation of the Behaviour of Cohesive Powder in the Biaxial Tester†

H. Feise and J. Schwedes
Technical University Braunschweig
*Institute of Mechanical Powder Processing**

Abstract

The results from experiments with cohesive limestone powder in a Biaxial Tester are presented. The biaxial tester allows a plane homogeneous deformation and measurement of the complete stress-strain states. It was found that proportional strain paths lead to associated proportional stress paths. Strain paths with a sharp bend lead to asymptotic stress paths. Under pure shear deformation, the limestone exhibits steady-state flow in the critical state. The critical state stress was found to be a function of the volumetric strain, i.e. the porosity, but not of the consolidation procedure.

The Cam-Clay model of Roscoe has been extended to include the cohesion exhibited by many fine powders. The cohesive strength is represented by an isotropic tensile stress measure, used to shift the yield curves into the tensile regime. Significant cohesive strength can only be achieved in fairly dense packings.

1. Introduction

Advances in bulk solids handling and silo technology have always been based on an increased understanding of the bulk solids mechanical behaviour. Janssen [1] introduced the notions of wall friction and lateral stress ratio in 1895 to calculate the stresses in the bin and the loads on the bin walls. In 1964, Jenike [2] made use of the concepts of yield locus, effective yield locus and internal friction to perform his investigations on the stresses in a hopper during discharge. More recently, several workers [3, 4, 5] applied the finite element method and constitutive models from soil mechanics to silo problems.

One major obstacle to the use of advanced constitutive models has been the lack of relevant experimental data for the materials and loading situations encountered in silo technology. Nearly all investigations have been done on soils such as sand or clay and stress levels of about 1000 kPa. Experiments at lower stress levels have been performed, e.g. by Maltby [6], Haaker [7], and Luong [8].

In this paper, experiments with a fine, cohesive limestone powder ($x_{50} \approx 5\ \mu m$) in a true biaxial tester specifically designed for small stresses will be reported. The results gathered from the biaxial tests have been utilized to extend the Cam-Clay model to cohesive bulk solids.

2. The Biaxial Tester

The Biaxial Tester is one of several devices available to investigate the mechanical behaviour of the bulk solids. In contrast to the shear testers more common in silo technology, the Biaxial Tester allows measurement of the complete stress-strain state in the sample; a fact which predestines the results from the biaxial tester for use with advanced constitutive models. **Figure 1** shows the biaxial tester of the

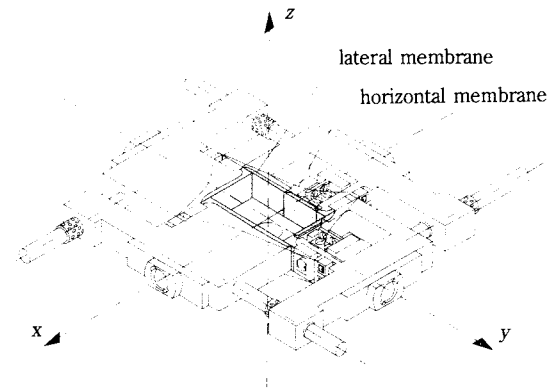

Fig. 1 True Biaxial Tester [9]

* Volkmaroder Str. 4-5, D-38104 Braunschweig, Germany
† Paper presented at 3rd European Symposium "Storage and Flow of Particulate Solids" (Jannsen Centennial), PARTEC, Nürnberg, Germany, 21-23 March 1, 1995

Institut für Mechanische Verfahrenstechnik of the Technische Universität Braunschweig. The material sample in the centre of the device is brick shaped. Its vertical (z) faces are covered by a top and a bottom plate.

In the horizontal directions (x and y), the sample is constrained by four steel platens (1 to 4). These platens are supported in such a fashion that each pair (1-3 or 2-4) can be moved without changing the distance of the other pair. The application of silica grease to the loading platens keeps the transmitted shear stresses to a minimum ($\mu \leq 0.02$) such that the measured normal stresses can be considered principal stresses. In all experiments the deformation of the sample has been prescribed and the resulting stresses have been measured.

The way of conducting experiments in the biaxial tester ensures that no shear strains or shear stresses can develop on the x, y and z planes. All measured normal stresses and strains must therefore be principal stresses or principal strains. This means that the experimental results can be fully described in the principal space. The line linking all measured strain states in the principal strain space is referred to as "Strain path". Similarly, a "Stress path" is defined in the principal stress space. As the biaxial tester allows deformations in the x-y plane only, the strain path must lie completely in the $\varepsilon_x - \varepsilon_y$ plane. The stress path, however, is a general three-dimensional curve in the $\sigma_x - \sigma_y - \sigma_z$ plane. For convenience, the diagrams will nevertheless be limited to two dimensions.

3. Experiments with Fine Limestone Powder

3.1 Proportional Strain Paths

Experiments with a linear strain path belong to the simplest deformations possible in the biaxial tester. The experiment starts with $\underline{\varepsilon} = \underline{0}$ and progresses with a constant deformation rate in the x and y directions. As the ratio of $\dot{\varepsilon}_y/\dot{\varepsilon}_x$ remains constant, these strain paths are referred to as proportional strain paths. For proportional strain paths, the ratio $\dot{\varepsilon}_y/\dot{\varepsilon}_x$ equals the ratio $\varepsilon_y/\varepsilon_x$ therefore in **Figure 2** the $\varepsilon_y/\varepsilon_x$ ratio is used to characterize the depicted strain paths [9]. The resulting stress path is also linear and proportional. For each strain path, the measured stress paths from two independent experiments are shown. One can see clearly that to each direction of the strain path, a distinct direction of the stress path can be correlated. These paths are therefore called "associated stress and strain path", their directions "associated directions".

3.2 Asymptotic Stress Paths

In **Figure 3**, results from experiments are shown where the strain path shows a sharp bend. In the first part of the experiment the sample was consolidated with $\varepsilon_y/\varepsilon_x$. After 10 to 15% of volume change, the y platens were stopped and deformation commenced in the x direction (curve $C_0 \ldots C_2$). The measured stress paths are made up of two parts as well. Initially, the stress paths follow the associated direction already known from **Figure 2**. After the change in the respective strain path, however, σ_y decreases rapidly and the stress paths finally evolve parallel to the stress path A2, which is associated to the strain path with $\varepsilon_y/\varepsilon_x = 0$. The ordering of the stress paths $C_0 \ldots C_2$ with respect to A2 follows the amount of volume change during the first part of the strain path. This behaviour is called "asymptotic behaviour" and was first investigated with sand, where the influence of the initial straining proved to be negligible.

3.3 Pure Shearing

The investigation of the material behaviour in pure shearing is especially important since the interpretation of the standard Jenike and ring shear tests depends on the concepts of pure shearing and steadystate flow. All deformations without volume change will be considered "pure shear" deformations. In the biaxial tester, this requires $\dot{\varepsilon}_y/\dot{\varepsilon}_x = -1$ and means that the sample always has to be consolidated before it can be subjected to a pure shear loading.

Figure 4 shows the stress and strain paths of six experiments with pure shear loading. Starting from the same initial density, the samples were subjected to consolidation up to two stress levels under three initial path directions. One can see that the stress paths initially follow the directions known from **Figure 2**. As soon as the shear part of the strain path begins, the stresses decrease down to some stationary level. Subsequent shearing results in scatter around this point but no significant change in stress. This behaviour – deformation without change in volume and stress – is considered "Steady-State Flow" in silo technology. From **Figure 4**, one can also see the influence of the loading history. While six different consolidation paths have been used, only two levels of steady-state flow arise. Stress paths which belong to strain paths with the same level of volumetric strain end at the same steady-state stress level.

Further experiments showed that all steady-state stresses lie on a line through the origin, the "critical state line" [10].

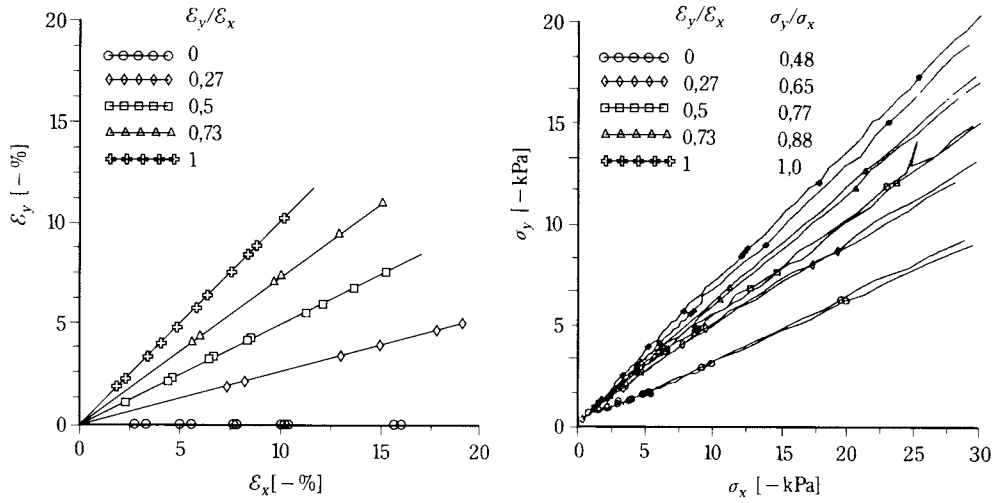

Fig. 2 Consolidation under proportional deformation

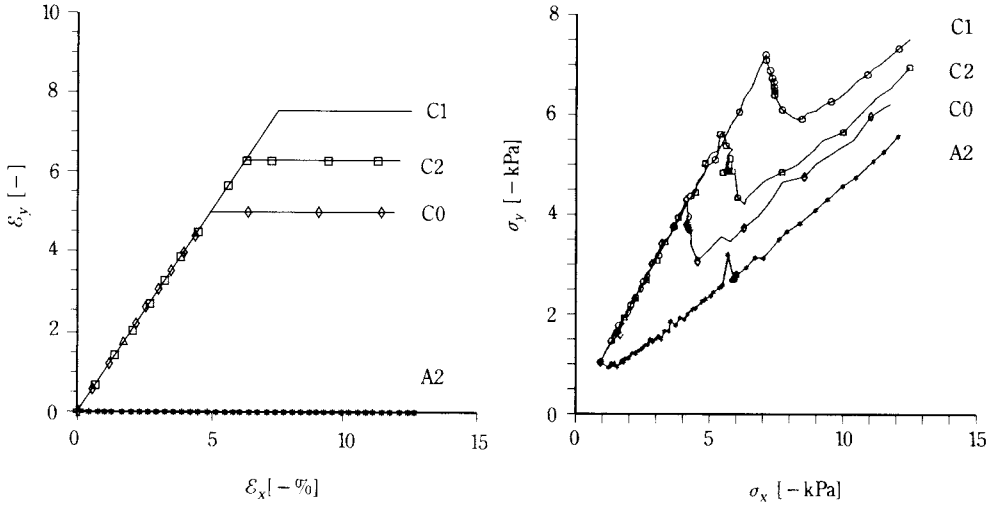

Fig. 3 Asymptotic behaviour

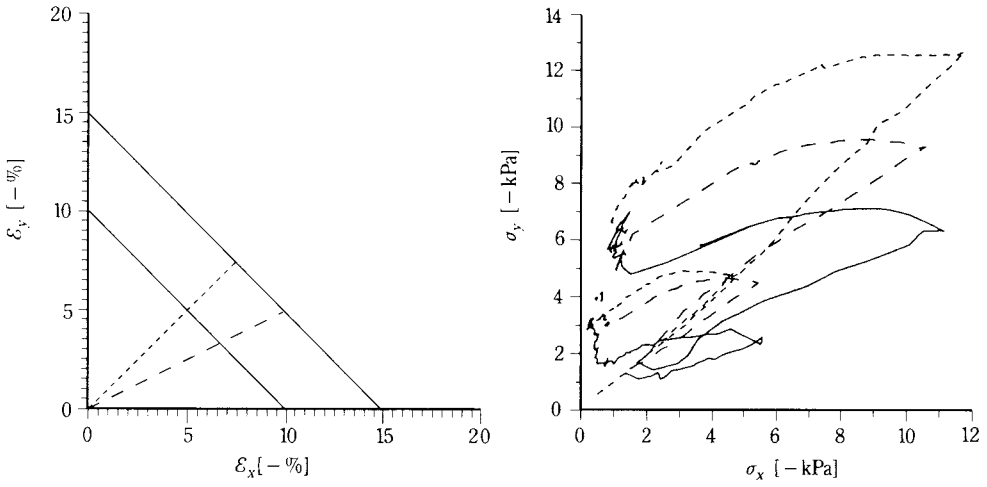

Fig. 4 Material response under shear loading

4. Cam-Clay for Cohesive Bulk Solids

The constitutive model of Roscoe [11], commonly referred to as Cam-Clay Model, is based on the observation of steady-state flow and the concept of the critical state line.

The Cam-Clay Model was initially derived from Triaxial tests of cohesionless soils only. It involves a yield curve in $s-\sigma_m$ space, where s is the deviatoric stress (a general shear stress measure) and σ_m is the hydrostatic pressure. For each bulk density (or porosity) a separate yield curve exists. **Figure 5** shows a typical Cam-Clay yield curve. The curve shows the maximum deviatoric stress s the material can sustain under a given hydrostatic pressure σ_m. This means that only stress states are permissible which lie either on or under the yield curve. One can see that the maximum sustainable deviatoric stress is associated with the intersection of the critical state line and the yield curve. It cannot sustain any deviatoric stress if the hydrostatic pressure becomes negative; i.e. the model is not defined for tensile stress states.

The experiments with the biaxial tester at the TU Braunschweig were performed with a very fine limestone powder which exhibits cohesion. Thus the original version of the Cam-Clay model is not applicable here. Nowak [10] has therefore extended the Cam-Clay model to include cohesion. Following the ideas of Höhl [5], it was assumed that any compressive deformation induces a small cohesive strength into the bulk solid. This cohesive strength originates from development of a small tensile strength, measurable by the isotropic tensile stress σ_t sustainable by the material. σ_t will be referred to as the isotropic tensile strength of the material. A saturation function ensures that the cohesive strength of the material cannot grow beyond all bounds.

The introduction of the cohesive strength into the Cam-Clay model leads to a shift of the left-hand part of the yield curve while the overall shape remains, see **Figure 6**. The point of no shear strength, which in **Figure 4** was associated with $\sigma_m = 0$, has now moved into the tensile regime to the point $\sigma_m = \sigma_t$.

In the Cam-Clay model, each yield curve belongs to a specific porosity n, which in turn leads to a specific stress state on the critical state line. Using these two pieces of information, one can calculate the isotropic tensile strength σ_t belonging to a certain porosity. **Figure 7** shows the isotropic strength σ_t plotted against the porosity n for the limestone powder used. It can be seen that the cohesive strength represented by σ_t remains fairly low for a porosity greater than 0.6 and that it changes rapidly for porosities between 0.5 and 0.6.

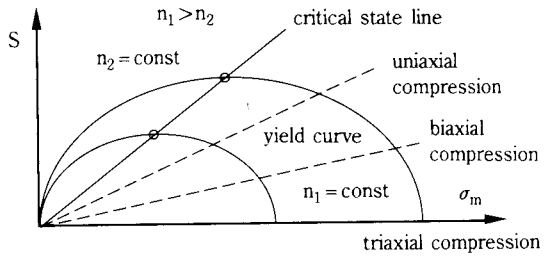

Fig. 5 Yield curve of the Cam-Clay model (schematically) [10]

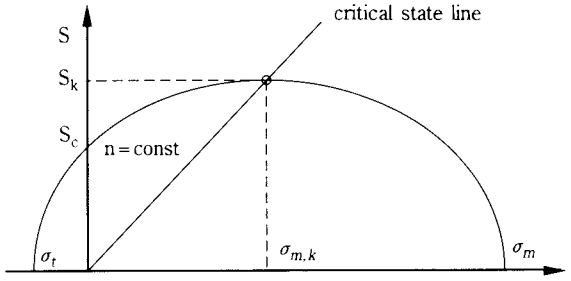

Fig. 6 Extended Cam-Clay model [10]

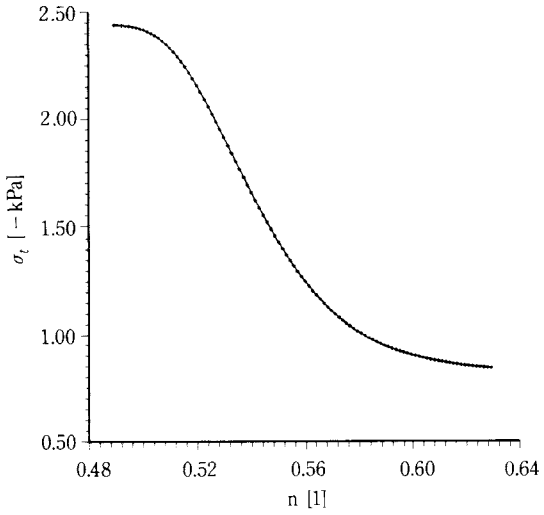

Fig. 7 Isotropic tensile strength of limestone according to extended Cam-Clay model

5. Symbols

n	[1]	porosity
s	[kPa]	deviatoric stress
		$s = \sqrt{(\sigma_1-\sigma_m)^2+(\sigma_2-\sigma_m)^2+(\sigma_3-\sigma_m)^2}$
x_{50}	[μm]	mean particle diameter
$\underline{\epsilon}$	[1]	strain tensor
$\varepsilon_x \ldots \varepsilon_y$	[1]	normal strains
$\dot{\varepsilon}_y \ldots \dot{\varepsilon}_x$	[1/s]	strain rates

μ	[1]	friction coefficient ($\mu = \tau/\sigma$)
σ	[kPa]	normal stress
$\sigma_1 \ldots \sigma_3$	[kPa]	principal stresses
σ_m	[kPa]	hydrostatic pressure ($\sigma_m = 1/3\ (\sigma_1 + \sigma_2 + \sigma_3)$)
σ_t	[kPa]	isotropic tensile strength
τ	[kPa]	shear stress

6. References

1) H.A. Janssen: Versuche über Getreidedruck in Silozellen; Zeitschrift des Vereins deutscher Ingenieure 39 (1985) 35, 1045-1049
2) A.W. Jenike: Storage and Flow of Solids, Bull No. 123, Utah Eng. Exp. Station, University of Utah, USA (1964)
3) U. Häussler, J. Eibl: Numerical Investigations on Discharging Silos; Journal of Engineering Mechanics 110 (1984) 6, 957-971
4) C. Lyle: Spannungsfelder in Silos mit starren, koaxialen Einbauten, PhD-thesis, TU Braunschweig, Germany (1992)
5) H.W. Höhl; J. Schwedes: Extension of elastoplastic constitutive models with respect to cohesive bulk solids, Powder Technol. 70 (1992) 1, 31-42
6) L.P. Maltby: Investigations of the Behaviour of Powders under and after consolidation, Proc. Intern. Symp. Reliable Flow of Particulate Solids II, Oslo, Norway, Aug. 1993, EFChE Publ. Ser. No. 96, 307-333
7) G. Haaker, F.C.J. Rademacher: Direkte Messung der Fließeigenschaften von Schüttgütern mit einem abgeändertem Triaxial-Gerät; Aufbereitungstechnik 11 (1983), 647-655
8) M.P. Luong: Flow Characteristics of Granular Bulk Materials, Part. Part. Syst. Charact. (1993) 10, 79-85
9) M. Nowak, J. Schwedes: An investigation on the pure shearing of cohesive limestone with the true biaxial shear tester, Chem. Eng. Tech. 15 (1992) 5, 295-299
10) M. Nowak: Spannungs-/Dehnungsverhalten von Kalkstein in der Zweiaxialbox, PhD-thesis, TU Braunschweig, Germany (1994)
11) A.N. Schofield, C.P. Wroth: Critical State Soil Mechnics, McGraw-Hill (1968)

Author's short biography

Dipl.-Ing. Hermann Josef Feise

Born 04.01.1964 in Adlum, Hildesheim, Germany
Education:
Graduate from Gymnasium Josephinum, Hildesheim in 1983 Study of Mechanical Engineering at:
- Technische Universität Braunschweig, Braunschweig, Germany 1984 – 1987
- University of Waterloo, Waterloo, Canada, 1987 – 1988
- Technische Universität Braunschweig, Braunschweig, Germany 1988 – 1990

Professional work: research assistant at the Institut für Mechanische Verfahrenstechnik der Technischen Universität Braunschweig in the area of Mechanical Process Engineering since 1990
research area: Modelling of the Mechanical Behaviour of Bulk Solids

Dr.-Ing. Jörg Schwedes

Born 1938 in Berlin
Study of mechanical and chemical engineering at the Technical Unviersities of Karlsruhe and Munich
Dipl.-Ing. 1964 at Karlsruhe
Dr.-Ing. 1971 at Karlsruhe (Prof. Rumpf) with a thesis on the shear properties of slightly compressed cohesive granular materials.
1971 – 1976 with Bayer AG at Leverkusen as head of a research group working in the field of mechanical process engineering.
since 1976 Professor and Director of the Institute of Mechanical Process Engineering, Technical University of Braunschweig.
main research activities:
- mechanics of bulk solids (measurement of flow properties, silo design, development and application of constitutive laws for bulk solids, instationary flow of gases in bulk solids, flow promoting devices, handling of contaminated soils)
- comminution (wet grinding in agitated ball mills, vibratory milling, grinding of micro-organisms, particle classification in the μm-range)

about 130 publications
1982 – 1984: Vicepresident of the Technical University of Braunschweig
1989 – 1991: Dean of the Faculty of Mechnical Engineering
since 1991: consultancy with Dr. Schulze on bulk solids technology

An Experimental Study of the Wear at Hopper Walls*†

G.D. Corder
*JK Tech, JKMRC Commercial Division**
R.B. Thorpe
*University of Cambridge, Dept. of Chemical Engineering***

Abstract

In this paper we describe experiments in which the equivalent of 100 tonnes of abrasive sand have been passed through a pilot-scale wedge-shaped hopper of half angle 10° and outlet width 1 cm. The walls were then cut up and the change in wall thickness accurately measured. The rate of wear was found to be greatest at the outlet. In interpreting these results, we used the simple abrasive model for wear recommended by Johanson and Royal [1]. In this model, the rate of wear is simply proportional to both the force on a particle pressing on the wall and the speed with which it scrapes down that wall. In order to calculate these parameters, we used a measurement of the velocity in a granular material at the wall of the hopper and a prediction for the stress which is a modification of the well-known method of Janssen. The constant of proportionality (the wear coefficient) for the model was measured in a pin-on-disc experiment. A prediction for the wear profile was thus obtained which shows reasonable (within a factor of two) agreement with experiment. The apparent success of the pin-on-disc method of measuring the wear coefficient suggests that it can be used instead of the more expensive methods advocated by others.

1. Introduction

The flow of hard and abrasive materials from storage vessels such as hoppers and silos causes wear to the walls of the vessel. This wear is concentrated near the outlet. The rate of wear is greater in mass flow silos which are designed for the uniform flow desirable for other reasons. It is useful to be able to predict the wear profile and the rate of wear so that the silo can be reinforced with thicker walls where necessary. This problem has received little attention in the scientific and engineering literature. In a paper published in 1982, Johanson and Royal [1] give general guidelines on the matter which form the basis of advice they will give as part of a design package offered by the company of consultants for whom they work. The paper is short on scientific reasoning and gives no specific experimental results. The methodology used by Johanson and Royal is based on the simple abrasive model for wear. In this model, the rate of wear, dq/dt, is simply proportional to both the force on a particle pressing on the wall and the speed, v_w, with which it scrapes down that wall. Or in terms of an average contact stress between the particles and the wall:

$$dq/dt = C\sigma_w v_w \quad (1)$$

Johanson and Royal use the well-known in-house methods of Jenike and Johanson Inc. to predict the stress and velocity at the wall. Despite the implication of flow, Johanson and Royal use the static stress profile without any argued justification. No measurements of wear from silos or hoppers are reported.

In order to complete their prediction of the wear profile down the walls of a silo, Johanson and Royal require an empirical constant of proportionality. This is obtained from their patented wear tester which consists of a full-pitch screw feeder that forces the granular material to be stored in the silo onto a rotating disc made of the material from which the silo walls are to be made. The speed of the disc and the normal force exerted on it by the granular material are recorded. The temperature of the material is monitored to ensure that it does not become too hot. After the tester has been run for an appropriate time, the disc of wall material is removed and the amount of wear is measured. This straightforwardly gives a value for the constant C in equation 1.

Another contribution to the study of the wear at hopper and silo walls originates from a group based

* Isles Road Indooroopilly, Queensland 4068, Australia
** Pembroke Street, Cambridge CB2 3RA, U.K.
† Received 12 June, 1995

at the University of Newcastle in Australia. The simple wear model is again commended [2] and used to predict wear profiles, albeit with a warning that it may be only approximately correct. In a more recent publication [3], a linear wear test apparatus is proposed as an alternative to the Johanson and Royal tester. The linear wear tester consists of a conveyor belt onto which the appropriate bulk solid is fed from a hopper. A sample of wall material is then placed on top of the material on the belt and the sample is anchored to a load cell which is used to measure the shear force needed to hold the sample in position. The sample is then weighted to apply a normal force to the sample. The conveyor belt is then started and the belt speed measured. After a suitable length of time, the sample is removed and the amount of wear measured. A full set of tests was conducted in which the relation between the amount of wear, applied normal stress, belt velocity and time was obtained. In each case, a linear relation was measured which is in accordance with the simple model of abrasive wear (eqn. 1). Results of tests where 2-mm beach sand was used to wear polyethene (UHMW), mild steel and 304 stainless steel and bauxite was used to wear mild steel, bisalloy 360 and bisalloy 500 are reported. The results give the following values of C (as defined in eqn. 1) in the order listed in the previous sentence: 0.044, 0.047, 0.020, 0.53, 0.36, 0.35 TPa^{-1}. No measurements of *in situ* wear from hoppers or silos are reported.

We have also previously published some of the results of our research into the wear at hopper walls [4, 5, 6]. The work reported in the first two publications concerned experiments in which three kinds of sand were driven by air pressure through conical nozzles made from perspex and brass. The wear profiles were reasonably consistent with the simple model of abrasive wear (eqn. 1). Values for C for the wear of perspex were reported erroneously but later corrected [6] to: 3.5 TPa^{-1} for an angular sand of 218 μm, 2.4 TPa^{-1} for the sand used in the experiments reported in this paper, and 1.8 TPa^{-1} for a sub-rounded sand of 165 μm particle size. The values for C from wear of brass were also incorrectly reported by the same factor, i.e. they should be 1.25, 0.5 and 0.35 TPa^{-1}, respectively, for the three sands. Further details of the work reported in the two papers [4, 5] and some of the work reported below is to be found in the PhD thesis [6].

2. Experimental apparatus

A relatively large wedge-shaped hopper (**Figure 1**) with perspex walls inclined at an angle (α) of 10° to the vertical was used in gravity flow experiments to measure the rate of wear of such walls by sand. The width of the slot outlet was 1 cm and its breadth was 20 cm. The sand used was Chelford 60 which is a common silica-based sand of medium angularity supplied by British Industrial Sand Ltd. The sand has a solid density of 2460 kg/m^3 and a bulk density, ρ, of 1550 kg/m^3. The volume-surface mean particle size is 211 μm. The sand has an angle of internal friction of 31° and an angle of wall friction against perspex of 20°.

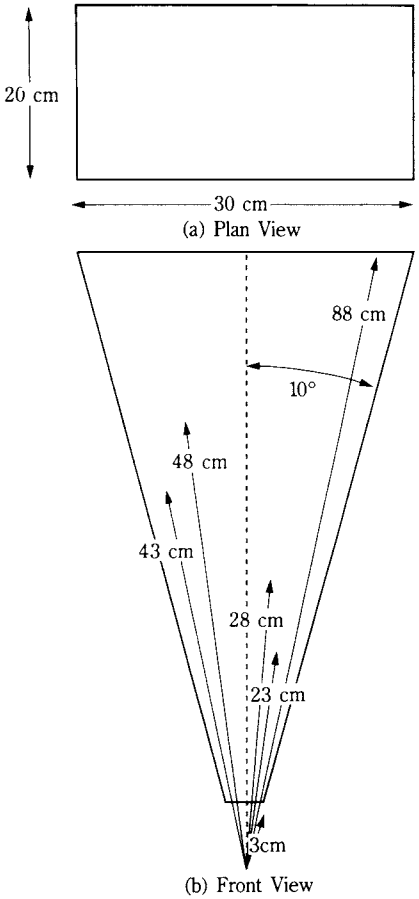

Fig. 1 Schematic diagram of the test hopper

In the experiment for which results are reported below, the sand was allowed to flow through the apparatus under the influence of gravitational forces for the equivalent of 24 hours continuous running. This was achieved by recycling the sand periodically whilst ensuring that the level of the sand in the test hopper was always the same: further details are to be found in Corder [6]. The mass flow rate, W, varied slightly but was nearly constant at 1 ± 0.1 kg/s.

In a separate experiment, we asked a colleague in the Materials Science Department in Cambridge to use his wear apparatus to measure a value of C for perspex as worn by sand. In Mercer's experiment [9], a pin of perspex was worn by a rotating piece of sandpaper at a stress of 60 kPa and a speed of 0.63 m/s. We understand that the pin-on-disc experiment is a common and cheap method of measuring wear rates when materials are being assessed for their resistance to abrasion. The value of C was determined to be 93 TPa^{-1}, which for some time we thought to be unrealistically high – mainly because the value of C from our nozzle experiments [5, 6] was much lower at 2.4 TPa^{-1}. However, the results outlined below lead us to believe that the air-driven nozzle experiments are not directly comparable to wear at the walls of a hopper in gravity flow. They do, however, remain relevant to wear during the discharge from pressurised systems.

3. Results

During operation, the speed of particle movement was measured by following the progress of dark grains down the walls. The resulting velocities are plotted against radial distance from the virtual apex of the hopper, r, in **Figure 2**. Also included in this figure are the velocities calculated by assuming that there is no profile of velocity across the hopper (i.e. the speed in the centre is the same as that at the wall), i.e. from the equation of mass continuity:

$$v = \frac{W}{2\rho\alpha r b} \tag{2}$$

The other line in **Figure 2** is the more realistic best fit line which passes through the origin. This line is marked as semi-theoretical because the careful measurements of velocity profiles in hoppers of Cleaver and Nedderman [7] and their theoretical developments [8] more than justify such an epithet. It can be seen that the velocity at the walls is roughly a third that predicted from eqn. 2.

The perspex walls were removed from the apparatus and the thickness measured by means of a micrometre gauge. The results for the right-hand wall are shown in **Figure 3**: The thickness was measured in four places at each radial position at 2.5, 7.5, 12.5 and 17.5 cm from the front vertical wall of the hopper. It can be seen that the wear was uniform across the hopper with a roughly linear vertical variation: the greatest wear is at the outlet. The equivalent result for the left-hand wall is given in **Figure 4**. The differences between **Figure 3** and **Figure 4** are reassuringly minor given that the two walls are in symmetrical orientation to one another.

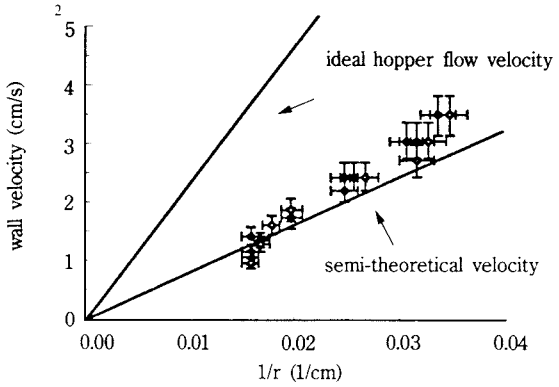

Fig. 2 Velocities measured at the wall of the hopper: the ideal velocity is given by equation 2 and the semi-theoretical velocity by multiplying equation 2 by a factor of about 1/3 to give a good fit to the data.

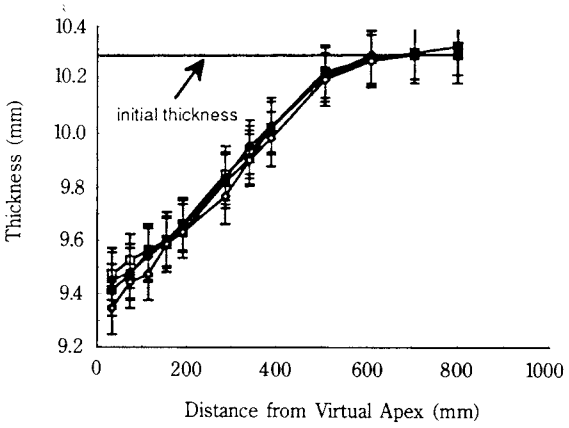

Fig. 3 Measured wear at right-hand wall

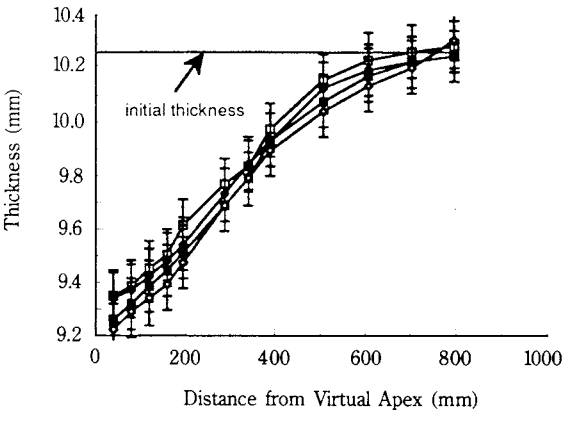

Fig. 4 Measured wear at left-hand wall

4. Theoretical prediction for conical hoppers

There is an extensive literature on the prediction of stress profiles in hoppers. These predictions can de divided into static and dynamic predictions. The static predictions assume that the material in the hopper is not moving and are generally speaking more sophisticated. The dynamic predictions include acceleration terms in a force-momentum balance which is used to predict both the mass flow rate of material and, as a consequence, the stress profile. It is usual to supply a lower boundary condition for the stress, and this has traditionally been that the stress falls to zero at the position of the outlet slot. A simple version of this approach is described by Thorpe [12] for a conical hopper.

The first theoretical prediction we present here is for the gravity flow of Chelford 60 sand through a 30° conical brass nozzle identical in size (outlet diameter of 2.24 mm) to that used in the experiments described by Corder and Thorpe [5]. When the predicted stress is multiplied by the velocity of the particles at the wall from a prediction based on a continuity equation analogous to equation 2, the result may be inserted in equation 1. By using the value of C reported for the nozzle experiments of Corder and Thorpe [5] of 0.5 TPa^{-1}, equation 1 was integrated with respect to time to give the shape of the wall of the hopper. The resulting positions for the right-hand wall after 10 and 20 years are given in **Figure 5**. It is helpful in understanding **Figure 5** to note that the prediction after 0 years represents the position of the wall prior to any wear taking place. Corder [6] gives further details of how these predictions were obtained and how the stress and velocity profiles were adjusted as the position of the wall changed.

These results suggest that there should be little or no wear at the outlet. This is hardly surprising

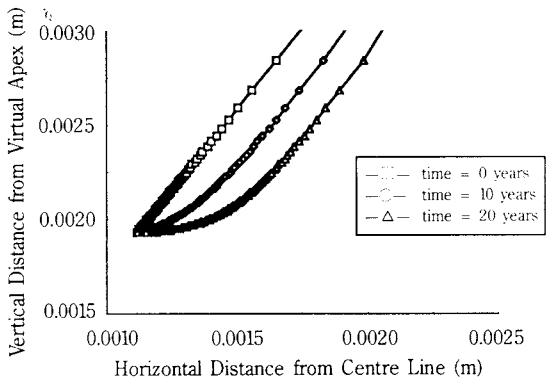

Fig. 5 Predicted positions of the wall after various wear times for a 2D hopper (zero stress at outlet)

since the stress has been set to be zero at the outlet and as a result, the rate of wear given by eqn. 1 is zero. Such a shape is most unrealistic – as has been previously pointed out [4].

As was noted in the introduction, those who have published predictions for wear in hoppers have always used the value for stress obtained from a static analysis. This is fundamentally unsatisfactory because it does not make any allowance for the effect of acceleration – an effect which has been established in physics for three centuries. However, there has been speculation in the literature that the zero stress boundary condition at the outlet is in error [9, 10]. In order to avoid the highly complex approaches taken by some theoreticians on this matter, we have stuck to our simple one-dimensional model and set the stress at the outlet at such a value as makes the prediction of the flow rate from the hopper match the experimentally determined value. (The experimental value is usually 10-25% less than the value predicted from theories [12].) This approach is in part justified by the good agreement between predictions using the same approach and experiment reported by Corder [6] for the air-assisted wear of nozzles by sand. This stress at the outlet (i.e that which correctly predicts the flow rate of the sand from the nozzle) lies between zero and the value which is obtained from a static analysis. Although our approach is somewhat speculative, we regard it as being better founded on fundamental understanding than any previous approach to the prediction of the wear at the walls of a hopper.

The stress profile generated in the manner indicated above was then substituted into equation 1 to obtain the rate of wear. This rate was integrated to obtain a prediction of the position of the wall after 10 and 20 years. These predictions are plotted in **Figure 6**, and are much more realistic than those generated by the fully dynamic method (i.e. those in **Figure 5**) with the wear being approximately uniform all the way up the hopper. However, this result of uniform wear is not in agreement with the predictions put forward in previous papers [1, 3, 4] which predict that the wear should be inversely proportional to the distance from the virtual apex (i.e., r). The reason for the difference lies in the details of the stress profile near the outlet, which we have already pointed out is neither fully dynamic nor static (as assumed in the previous papers). This is a significant result in that the rate of wear is greatest near the outlet where the difference between our prediction and that of others is greatest.

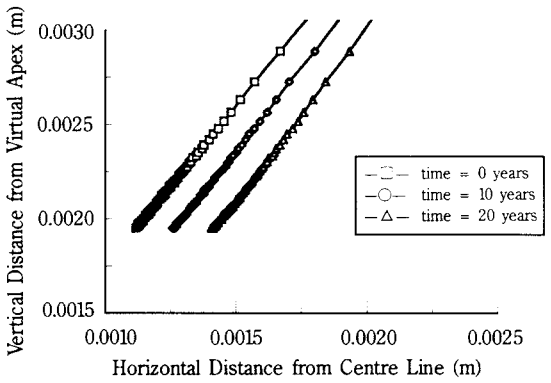

Fig. 6 Predicted positions of the wall after various wear times for a 2D hopper (non-zero stress at outlet)

5. Theoretical prediction for wedge-shaped Hoppers

The above result (of constant wear at all heights) for the wear of the walls of a conical hopper was predicted on very simple grounds by both ourselves [4] and others [1, 2, 3] for flow through the different geometry of a wedge-shaped hopper such as the one used in the experiments reported here. However, comparison with the experimental wear profiles (**Figure 3**) shows that although the prediction (of uniform wear) is better than that which would be obtained by using a stress profile with a zero value at the outlet (compare **Figure 5**), the wear obtained in the experiment is linear with distance from the outlet rather than uniform (i.e. the result of the previous simple prediction).

One of the main reasons why the wear profile is not constant is that the hopper is not infinite in breadth, b. This in turn affects the stress profile in that the shear stresses, τ_w, generated on the front and back walls support the material and so reduce the vertical normal stress, σ_{zz}, assumed to be a constant over the top and bottom of the slice. This effect is variable because the fraction of the perimeter which is front and back wall as opposed to inclined perspex wall decreases from over a half towards the top of the experimental hopper to nearly zero at the outlet. The simplest way to account for this changing influence is to use the method of differential slices commonly attributed to Janssen. This approach involves a one-dimensional force balance in the vertical (z) direction over a differential slice with vertical sides: a diagram of the elemental slice used in this analysis is given in **Figure 7**. Because no momentum terms are involved this will lead to a static stress prediction. The resulting differential equation is:

$$\frac{d\sigma_{zz}}{dz} + \rho g = \frac{2\tau_w}{b} + \frac{\tau_{yz}}{z\tan\alpha} \tag{3}$$

Taking the usual assumption of passive failure for the flow of a granular material in a converging duct, it is possible to relate the shear stresses to the normal stress and thus obtain an ordinary differential equation in σ_{zz} and z only. This equation can be numerically integrated to give a stress profile, which when combined with the wall velocity and substituted into equation 1 using Mercer's coefficient, gives a new prediction of the wear rate, and this in turn on integration with respect to time gives the wear profile shown in **Figure 8**. Also shown in the graph are the

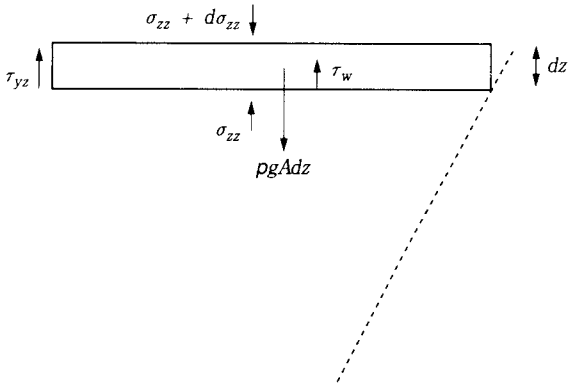

Fig. 7 The differential slice used to obtain eqn. 3 showing the forces and stresses acting on the element.

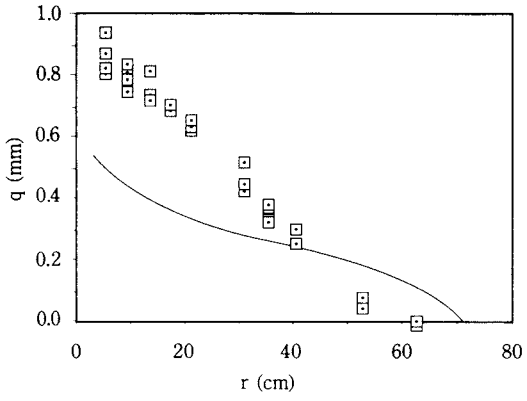

Fig. 8 Comparison of experimental wear (⊡) with the passive prediction of wear (–)

experimental results from the left-hand wall – this time plotted without error bars. The prediction is clearly better than that of a constant wear rate, i.e. a constant value of q.

For a reason which will become obvious, the wear profile prediction is plotted in **Figure 9** in the same way as above but with one difference. The difference

is that instead of passive failure of the granular material, active failure has been assumed throughout. The prediction is clearly further from the data and the shape of the curve is less like the shape of the data. In **Figure 10**, the experimental wear from both the left and right-hand walls are compared with the passive prediction of wear, but this time all three curves are normalised such that they agree on the amount of wear at the outlet: this is equivalent to using a value for C in eqn. 1 that is about 50% higher than the value measured by Mercer. The agreement between prediction and experiment close to the outlet is encouragingly good. Reasons why agreement is not obtained further up the hopper are given in the next section.

The close agreement between the wear predicted by using Mercer's pin-on-disc value for the wear coefficient C in equation 1 suggests that this simple and cheap method may be an acceptable method for generating prediction of wear rates. This would be of benefit since it would obviate the need to use the more complex wear testers advocated by other authors [1, 3].

5. Discussion

It is possible that the velocity of the sand at the walls close to the outlet is not well predicted by any simple modification of eqn. 2. For example, it is plausible that the velocity of the particles at the wall near the outlet is greater than the value we have assumed in that the velocity distribution there is more uniform across the hopper. This would lead to an increase in velocity of up to threefold giving greater wear than predicted at the outlet. (It is worthy of note that the data plotted in **Figure 2** are, for reasons of experimental difficulty, no closer to the outlet than 0.25 m.) This explanation, however, seems unlikely when it is noted from **Figure 8** and **10** that the discrepancy between prediction and measurement seems to occur in a region 0.25 to 0.6 m around the outlet where measurements of velocity at the wall have been obtained.

The stress within a static granular material is understood to range between two limits. These limits are called active and passive. It is common to assume that the material towards the top surface in a silo is at or close to the active limit. This is because the material will have fallen into the silo from a filling device and such a movement is that typically associated with active failure. However, close to the outlet the material is assumed to be in passive failure.

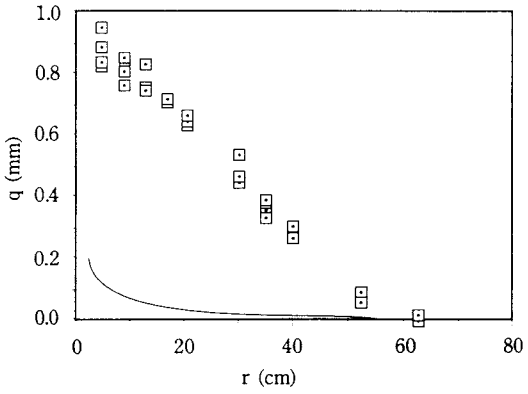

Fig. 9 Comparison of experimental wear (⊡) with the active prediction of wear (−)

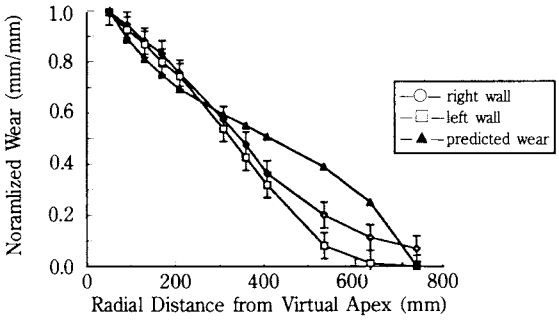

Fig. 10 Measured wear compared with the normalised prediction from the Janssen style analysis, both having been normalised

This is because it either is or has at some time been flowing through the hopper towards the outlet. This is a converging flow in which the walls have to push the material inwards; an action which is typically associated with passive failure. As a consequence, in some region within the hopper or silo there must be a transition from active to passive failure. If the transition is sudden it can give rise to large jumps in the horizontal normal stress as is illustrated in **Figure 11**. This phenomenon is known as the switch stress and is allowed for in the various national and international design codes for silos. However, the transition need not be sudden and, in the case of a hopper (as opposed to a conical-cylindrical silo)

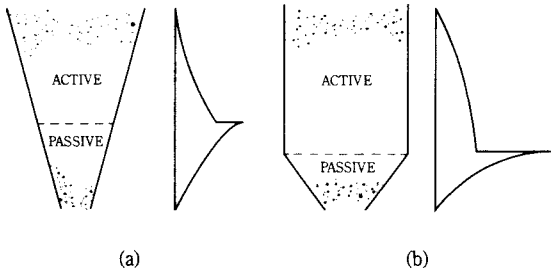

Fig. 11 Stress profiles in silos and hoppers

such as the one used in the experiments reported here, the position of the switch is not fixed but can wander with time. This means that the time average normal stress on the inclined wall of the hopper will lie somewhere inbetween active and passive, being close to active towards the top of the material and almost certainly passive at the outlet. In **Figure 12**, we have plotted both the active and passive predictions for the wear profile for our hopper. Superimposed are three example sudden "switches" between active and passive. If there were to be a switch across a horizontal plane which did not move with time, it is clear that an unusual wear pattern would result. If on the other hand, the switch plane were to move around with time and/or change its orientation from the horizontal or become curved or, more likely, the switch from active to passive failure were to occur more gradually over a region representing as much as a half of the height of the hopper [13], the resulting wear profile would be for q to be small for high values of r (corresponding to the active limit) and then to rise up to join the passive curve as the outlet was approached. Reference to **Figure 10** reveals that this is precisely the kind of wear profile we have measured in our experiments.

It is thus not possible to reject the hypothesis advocated previously by several authors [1, 3, 4, 5] that the wear of hopper and silo walls is consistent with the simple wear model (eqn. 1). However, since a full understanding of the stress and velocity profiles is required for any prediction of wear to be accurate, some uncertainty remains over both the accuracy of any prediction of wear based on the simple model of wear and over that full validity of the model itself.

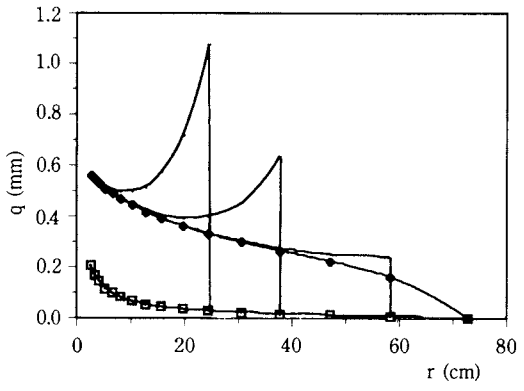

Fig. 12 Comparison of experimental wear with predicted wear, with the switch between active (□) and passive (◆) zones at various heights within the hopper

6. Conclusions

1) The wear caused by sand flowing under the influence of gravity to the walls of a hopper seems to match within reasonable limits the predictions of the simple model of abrasive wear advocated by several authors.
2) It is important (and not necessarily straightforward) to measure or be able to predict both the velocity of the particles at the wall and the normal stress on the wall.
3) The experimental wear profiles suggest that the stress at the wall is more accurately represented neither by the values usually associated with a static analysis nor by those associated with assuming a zero stress at the outlet. This is an interesting clue for those interested in modelling in detail the flow of material in the region of the outlet.
4) Wear in a wedge-shaped hopper is greatest at the outlet and this is not in agreement with the predictions of previous papers published on the wear at hopper walls.
5) It may be possible to measure the wear coefficient for gravity flow using a very simple and cheap pin-on-disc experiment. This would be a great saving in time and effort over the tests suggested by other authors.

Acknowledgements

The authors wish to acknowledge the financial support of the Shell group of companies through their Thornton Research Centre.

Nomenclature

A Area of top of elemental slice (m^2)
b Breadth of the wedge-shaped hopper in the x direction (out of paper in all figures) (m)
C Wear coefficient: constant of proportionality in equation 1 (Pa^{-1})
g Acceleration due to gravity (m/s^2)
q Reduction in the thickness of the wall (m)
r Distance from the virtual apex of the hopper ("radial co-ordinate") (m)
t Time (s)
v_w Velocity of the particles at the wall (m/s)
W Mass flow rate of sand (kg/s)
z Vertical distance above a reference plane (i.e. the Cartesian co-ordinate) (m)
α Half angle of the hopper
ρ Bulk density of sand (kg/m^3)

σ_w Stress on and at the wall (Pa)
σ_{zz} Average normal stress on a vertical plane (Pa)
τ_w Shear stress on the front and back walls (Pa)
τ_{yz} Shear stress on a vertical plane very close to the inclined walls of the hopper (Pa)

References

1) Johanson, J.R. and Royal, T.A.: Measuring and use of wear properties for predicting life of bulk materials equipment, *Bulk Solids Handling*, **2** (1982), 3, 517-523.
2) Roberts, A.W.; Ooms, M. and Scott, O.J.: Surface friction and wear in the storage, gravity flow and handling of bulk solids, *Proc. War on Wear* (1984), Nottingham, UK (Inst. Mech. Eng.)
3) Roberts, A.W. and Wiche, S.J.: Prediction of lining wear life of bins and chutes in bulk solids handling operations, *Tribology Int.* (1993), **26**, 5, 345-352
4) Corder, G.D. and Thorpe, R.B.: Wear at hopper walls, Chapter 4.3 of "Tribology in Particulate Flow" (1987), Eds. B.J. Briscoe and M.J. Adams, Adam Hilger, Bristol.
5) Corder, G.D. and Thorpe, R.B.: The abrasive wear of hopper walls, *Proc. Antiwear,* 20-22 September 1988, London (Institute of Metals)
6) Corder, G.D.: The failure properties and abrasive behaviour of sand in hoppers, Ph.D. Thesis, University of Cambridge (1988), UK.
7) Cleaver, J.A.S. and Nedderman, R.M.: The measurement of velocity distributions in conical hoppers, *Chem. Engng. Sci.* (1993), **48**, 3703-3710
8) Cleaver, J.A.S. and Nedderman, R.M.: Theoretical prediction of stress and velocity profiles in conical hoppers, *Chem. Engng. Sci.* (1993), **48**, 3693-3702
9) Mercer, A.P.: *Private communication,* 1985.
10) Kaza, K.R. and Jackson, R.: Boundary conditions for a granular material flowing out of a hopper or bin, *Chem. Eng. Sci.* (1984), **39**, 915-916
11) Ravi Prakash, J. and Kesava Rao, K.: Steady compressible flow of cohesionless granular materials through a wedge-shaped bunker, *J. Fluid Mech.* (1991), 225, 21-80
12) Thorpe, R.B.: Air-augmented flow of granular materials through orifices, Ph.D. Thesis, University of Cambridge (1984), UK.
13) Nedderman, R.M.: Statics and kinematics of granular materials, (1992), Cambridge University Press, UK.

Author's short biography

Dr. Glen David Corder

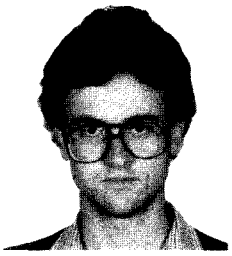

In 1982, Glen Corder obtained first-class honours in chemical engineering from the University of Queensland in Australia, going on to obtain a masters degree in control engineering from the same university. He then went to the University of Cambridge in the United Kingdom and obtained his doctorate in chemical engineering in 1988. He then took up a job with KBC Process Automation in the UK before returning to Australia in 1992 to take up his present employment with JK Tech, and works on the analysis of particle grinding and classification plant.

Dr. Rex Barry Thorpe

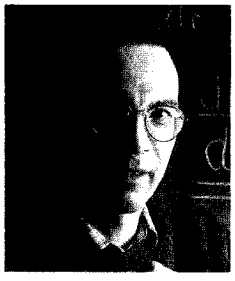

In 1979, Rex Thorpe obtained first-class honours in chemical engineering from the University of Cambridge, UK. He went on to take the fourth year of the course in Cambridge to obtain a Master of Engineering degree. After undertaking a doctoral course and obtaining his PhD degree in 1984, he worked as a designer of oil and gas production platforms for Brown and Root (UK) Ltd. He then returned to Cambridge as a lecturer in the Department of Chemical Engineering. His research interests cover a number of topics in powder and multiphase flow.

Investigations into Fine Grinding*

J. Dodds[1], Ch. Frances[2], P. Guigon[3], A. Thomas[4]
[1]*LSGC-CNRS-ENSIC, 1 rue Granville, 54001 Nancy, France*
[2]*ENSIGC, 18 Chemin de la Loge, 31078 Toulouse, France*
[3]*UTC, Dept Ginie Chimique, B.P.649 60206 Compiegne, France*
[4]*LEM-ENSG, BP 40, 54500 Vandoeuvre, France*

Abstract

This paper presents four different studies from the French national research project that deal with the fine grinding of hydrargillite. These include pilot plant tests of dry grinding in an air jet mill and wet grinding in a stirred bead mill. Two other more fundamental studies are concerned with determining fragmentation schemes in fine grinding. The first investigation concerns theoretical predictions of breakage of complex agglomerate crystals such as hydrargillite, plus image-analysis-based methods of identifying different types of particle morphology. Finally, single-particle impact fragmentation is studied in a specially designed apparatus which allows observation of particle impacts on a target at up to 300 m/s. This has led to the identification of different regimes of breakage that affect complex crystals such as hydrargillite.

1. Introduction

It has been estimated that a considerable amount of the total world energy consumption is used for industrial particle size reduction processes. Metallurgical industries are based on mineral ores which necessarily pass through crushing and grinding operations. The materials used in the building industry all require a size reduction process at some stage or other. Furthermore, comminution theory is not well developed and the design of industrial plant is made on the basis of laboratory tests which are difficult to extrapolate, resulting in expensive over-sizing of equipment, thus adding to their inherent energy inefficiency. Finally, there is a lack of fundamental knowledge of fragmentation mechanisms that makes it impossible to predict product quality (particle size distribution, particle shape, physical properties) – all factors which are very important when fine grinding is used to produce special high-value products such as ceramics, pharmaceuticals, fillers, and pigments, etc.

For all these reasons, a co-ordinated research action has been set up in France to study modelling and design methods required for the production of fine powders with controlled properties, well-defined particle size distributions, and also to improve process energy efficiency. Four research teams are working on different aspects of the problem with the overall objective of extending knowledge and developing a methodology for modelling fine grinding operations. All of the teams are working with the same material, hydrargillite; $Al(OH)_3$. The programme includes pilot plant tests with two types of mill : An Alpine 100 AFG opposed jet mill (in Nancy), and a Drais Perl-Mill V/H stirred bead mill (in Toulouse). In parallel, there is a more fundamental study of fragmentation mechanisms in the high-velocity impact of jets of particles being carried out in Compiegne. Finally, the team in Vandoeuvre is examining theoretical fragmentation schemes and developing methods for characterising the debris.

* Received 12 June, 1995

2. Theoretical Aspects

2.1 Batch grinding

Batch grinding is generally described on the basis of the breakage (B_{ij}) and selection functions (S_i) which represent the distribution of particle sizes resulting from the breakage of a mother particle and the aptitude of that particle to break, respectively. We thus have the well-known equation for batch grinding in cumulative form:

$$\frac{\partial R(x,t)}{\partial t} = -S(x,t)R(x,t) + \int_x^\infty \frac{\partial (S(y)B(x,y))}{\partial y} R(y,t)dy \qquad (1)$$

where $R(x,t) = \int_x^\infty m(y,t)dy$

The general analytical solution to the integro-differential equation of batch grinding comprises a convergent series of iterated kernels. This solution is complicated and has found no practical application, leading workers to develop analytical solutions based on simplified representations of the selection and breakage functions. Kapur [2] in particular has shown that the grinding equation has a similarity solution when the breakage rate function is a power law and the breakage distribution function is self-similar, i.e. in cumulative form it is:

$$B(x,y) = B(x/y) \tag{2}$$

The interesting aspect of this solution is that the distributions generated at different times collapse into a single curve when they are plotted as a function of dimensionless particle size $x/\mu_1(t)$ where $\mu_1(t)$ is the first moment of the particle size distribution. Kapur has shown that the first moment, median or any other quantile size are all proportional to one another and that any characteristic length could be used instead of μ_1. When the size spectra of material being ground in a mill is self-similar, the mechanism of size reduction probably remains constant during the operation, and extrapolation in time or any other operating variable becomes easy.

Particle size is normally measured with instruments giving distributions in size classes, and it is often more convenient to use equation (1) in terms of discrete size classes as follows:

$$\frac{dR_i}{dt} = -S_i R_i(t) + \sum_{j=1}^{i-1} (S_{j+1}B_{i,j+1} - S_j B_{ij}) R_j(t) \tag{3}$$

where $R_i(t) = \sum_{j=1}^{i-1} m_j(t)$ and $B_{i,j} = \sum_{k=j+1}^{i} b_{k,j}$

$m_i(t)$ = the mass fraction of particles in size class i. S_i = the probability of breakage of particles of class i. b_{ij} = mass fraction of particles of class j which break to end in size class i.

This formalism was established over 25 years ago [1] and many methods have been developed to determine the breakage and selection functions, in particular by means of experiments with monoclass sieve cuts. Unfortunately, it is difficult to prepare narrow sieve fractions in the particle size range covered by fine and ultrafine grinding, i.e. <50 μm, and there are also difficulties in reconciling instrumental particle size analysis methods (Coulter Counter, Laser diffraction, etc.) with sieve sizing. These problems can be avoided by using the method proposed by Kapur [2-4], who gave an approximate solution of equation 3 in terms of two parameters G_i and H_i, which are themselves functions of the functions $B_{i,j}$ and S_i.

$$R_i(t) = R_i(0) \exp\left(G_i t + H_i \frac{t^2}{2}\right) \tag{4}$$

Equation (4) proposed by Kapur derives from an infinite series stopped at order 2, but by noting that $R_i(t) = R(x_i,t)$, this may be generalized to any order p in terms of the particle size distribution at time t, with respect to the initial particle size distribution [4]:

$$\frac{R(x,t)}{R(x,0)} = \exp\left(\sum_{k=1}^{p} K^{(k)}(x) \frac{t^k}{k!}\right) \tag{5}$$

where $K_i^{(k)} = \sum_{j=1}^{i-1} (S_{j+1}B_{i,j+1} - S_j B_{i,j})(G_j - G_i)^{k-1} \frac{R_j(0)}{R_i(0)}$

(for $k>1$)

Taking this expression to any given order, it is possible to obtain a mathematical representation of the evolution of the particle size distribution during batch grinding to any degree of precision.

2.2 Continuous grinding

In the case of a continuous grinding process, the relation between the feed and product particle size distributions will depend both on the grinding kinetics and on the time the material spends in the mill. If the solids move through the mill in plug flow, a mean residence time can be used in equation (5), but in general, the existence of a distribution of residence times (E(t)) must be taken into account. To a first approximation, which will be relaxed later on, it may be assumed that the residence time distribution is independent of particle size. Thus the change in particle size distribution between the inlet ($R_e(x)$) and the outlet ($R_s(x)$) of a continuous grinding process is given by the following:

$$\frac{R_s(x)}{R_e(x)} = \int_0^\infty \exp\left(\sum_{k=1}^{p} K^{(k)}(x) \frac{t^k}{k!}\right) E(t)dt \tag{6}$$

Thus in addition to the representation of the kinetics it is also necessary to have an expression for the residence time distribution in the mill.

3. Stirred bead mill

3.1 Batch experiments

Figure 1 shows a schematic diagram of a stirred bead mill (Dyno-mill KDL) where the grinding medium consists of small beads which are violently stirred by the four stirrer discs. The particles to be ground are pumped through the mill as a slurry and ground by the mechanical action of the moving beads. Experiments have been performed to determine the change in particle size distribution of hydrargillite with time during grinding in a stirred bead mill. An example of the results is shown in **Figure 2**. For this run, the initial size distribution can be well described by a Rosin-Rammler-type equation:

$$R(x,0) = exp\left[-\left(\frac{x}{20.9}\right)^{1.1}\right] \tag{7}$$

These results can also be represented as shown in **Figure 3**, i.e. in terms of the variation of the mass fraction less than a certain particle size as a function

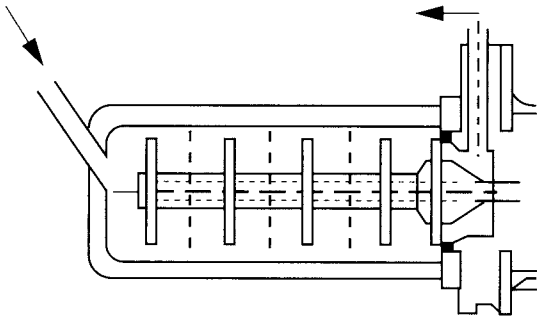

Fig. 1 A stirred bead mill

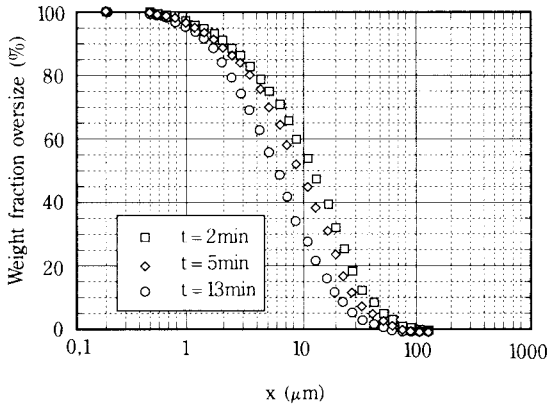

Fig. 2 Change in particle size distribution in batch grinding with a stirred bead mill

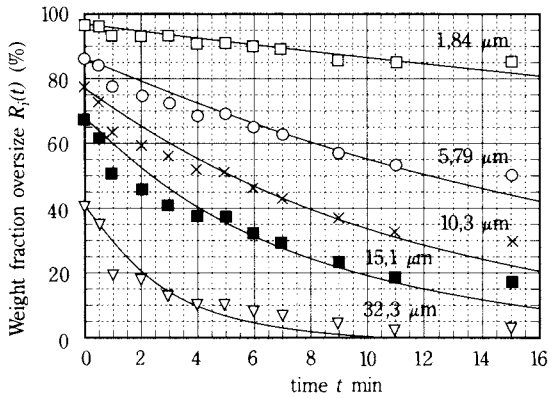

Fig. 3 Change in $R(x_i,t)$ with time for 5 different values of x_i

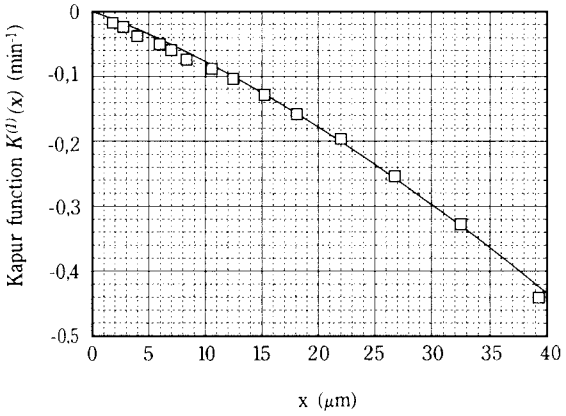

Fig. 4 The function $K(x)$ used in figure 2 and its fit to an exponential

of grinding time. Equation (5), taken to order 1, is now used to obtain a mathematical representation of the grinding kinetics. The lines in **Figure 3** show the result using values of the coefficient $K(x)$ as shown in **Figure 4**. Batch grinding kinetics can therefore be represented as follows:

$$\frac{R(x,t)}{R(x,0)} = exp(K(x)t) \tag{8}$$

where $K(x) = -kx^a$ with $k = 0.0037$ and $a = 1.29$

It can easily be demonstrated that this equation is self-similar as is illustrated in **Figure 5**. Here, the cumulative size distributions are given as a function of the characteristic size $x/x_{63.2}$ using $x_{63.2}$ as the particle size corresponding to 63.2% of particles smaller than $x_{63.2}$.

These results can be compared with other experiments in a 1-litre batch ball mill, and **Figure 6** shows the evolution of the particle size in a typical run. For this experiment, the operating conditions were chosen to be similar to those commonly used in actual practice (mill speed =75 % of critical, 15 mm stainless steel balls, 20 % volume filling, 40 % powder filling, slurry density 50 %). The initial particle size was between 100 and 125 μm, and preliminary experiments – reported elsewhere [7] – established that these conditions would lead to minimum fineness. **Figure 6** clearly shows that the size distributions exhibit self-

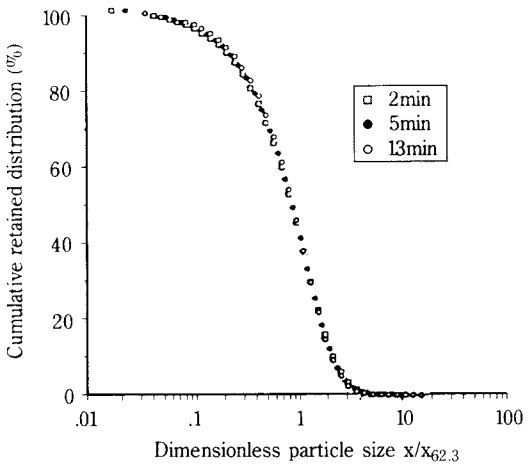

Fig. 5 Self-similar particle size distribution (stirred bead mill)

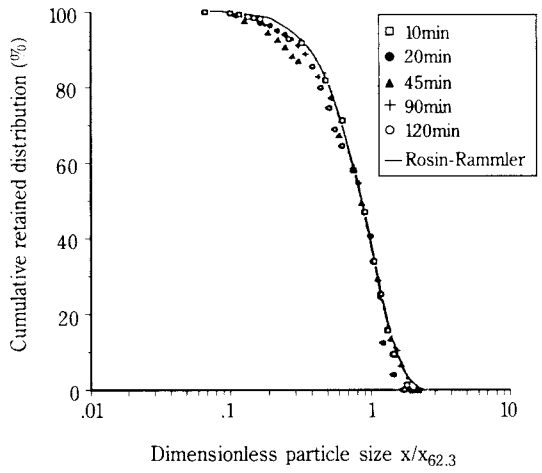

Fig. 6 Self-similar particle size distribution (ball mill)

similarity even after relatively short grinding times. Applying the Rosin-Rammler equation to these results leads to the following expression for the batch grinding kinetics in the ball mill:

$$R(x,t) = exp\left[-\left(\frac{x}{x_{63.2}(t)}\right)^2\right] \tag{9}$$

In batch grinding, the characteristic particle size decreases as a function of the time of grinding, and Kapur has shown that it varies with time as in the Walker general energy-size equation:

$$\frac{dx_{63.2}(t)}{dt} = -Cx^e_{63.2}(t) \tag{10}$$

Integrating this with the initial conditions $R(x,t) = R(x,0)$ leads to an equation similar to equation (8). It was found that the experimental results could be correlated by the following equation:

$$R(x,t) = R(x,0)exp(-2.4\cdot10^{-5}x^2t) \tag{11}$$

Even though the two equations – (8) and (11) – for the batch grinding kinetics differ by an order of magnitude, the self-preserving character of the particle size distributions is demonstrated in both cases.

3.2 Continuous grinding

3.2.1 Mass transport in a stirred bead mill

In order to characterise the transport of particles through a stirred bead mill, the standard grinding chamber of a Drais Perl Mill was replaced by a chamber which allows samples to be withdrawn from inside the mill. The mill is thus divided into five compartments numbered C1 to C5 as shown in **Figure 7**. Slurry samples can be taken by means of a syringe in each compartment – either near the centre at the stirrer shaft or from the periphery at the mill wall. An example of the change in particle size distribution within the mill during continuous grinding of hydrargillite is shown in **Figure 8**. This shows that the particle size decreases linearly between the inlet and the outlet of the mill, and shows no evidence of classification by size in the mill. However, comparison of the size distributions of particles taken at the mill axis and at the wall (**Figure 9**) does demonstrate radial classification by the action of centrifugal force.

3.2.2 Residence time distribution

As indicated above, if a continuous grinding process is to be treated, it is necessary to know the residence time distribution. As a first approximation, the radial classification of the particles may be neglected and the mill simulated as a series of stirred cells of volume defined by the separation between the stirrer discs.

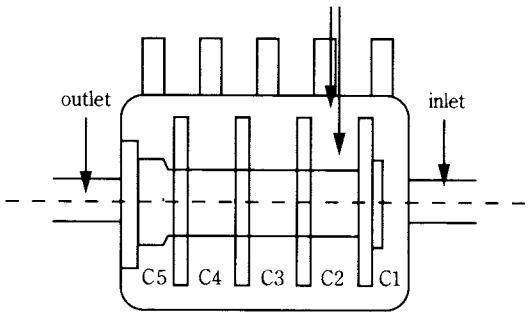

Fig. 7 Drais Perl Mill showing sample points

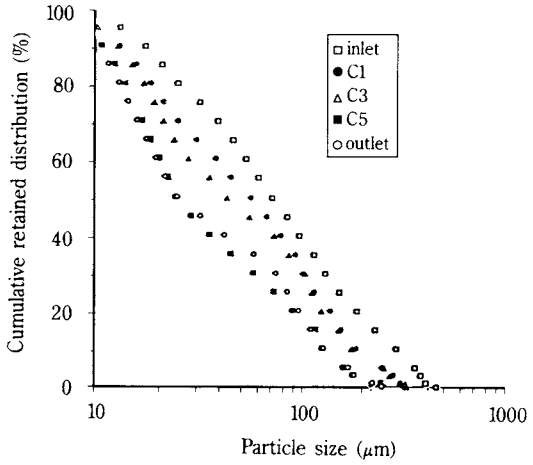

Fig. 8 Evolution of the particle size distributions between the inlet and the outlet of the mill

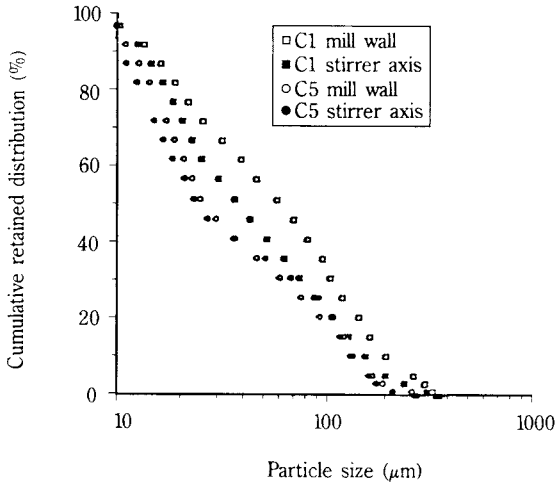

Fig. 9 Comparison of the particle size distributions for samples taken at the mill wall and near the stirrer axis

The only adjustable factor here being the inter-cell recycle factor. Thus, the assumption that solids move through the mill in the same way as the carrier fluid allows the use of tracer experiments on the liquid to determine the residence time distribution. Such experiments have been presented elsewhere together with the transfer function of the model [6]. Combining equation (6) with the expression for the batch grinding kinetics (8) leads to:

$$\frac{R_{out}(x)}{R_{in}(x)} = \int_0^\infty exp(-kx^a \cdot t_s) E(t_s) dt_s \tag{12}$$

This particular case can be identified as the Laplace transformation of the function $E(t_s)$ and may therefore be written as:

$$\frac{R_{out}(x)}{R_{in}(x)} = L(E(kx^a)) \tag{13}$$

Knowledge of the transfer function of the flow model in the mill can then be used in equation (13) to predict the output particle size distribution as a function of the input size distribution. **Figure 10** shows an example of experimental results compared with three theoretical predictions where the stirred bead mill is considered to be (1) in plug flow, (2) a perfectly mixed stage, and (3) where the transfer function established experimentally [6] is used.

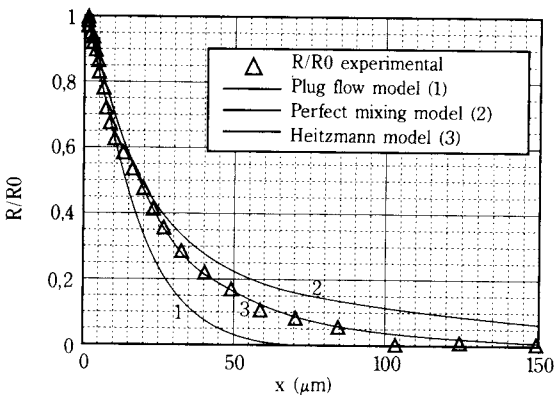

Fig. 10 Comparison between the particle size distributions in continuous grinding and predictions using three models of flow in the mill

4. Opposed jet mill

An Alpine 100 AFG opposed jet mill with its integrated 50 ATP turbo-classifier was used. In this type of mill, the particles contained in the hopper are introduced into the grinding chamber by a screw feeder

and are broken by their impact on one another under the action of three jets of compressed air. The particles are then swept upwards to the turbo-classifier where they are either allowed to exit from the mill or are returned to the grinding section. The size separation is controlled by the rotational speed of the classifying wheel. This type of mill can therefore be represented by the flow sheet shown in **Figue 11**.

All the flows shown in **Figure 11**, other than the feed and the product, are internal in the mill and cannot be directly measured. However, as will be shown later, it is possible to make independent measurements on the grinding section and on the classification section. Such information can then be coupled by mass balance over the grinding circuit to link the feed and product particle size distributions:

$$R_0(x) = \frac{1}{I_p(x)} R(x) + \left[\frac{1-I_p(x)}{I_p(x)}\right] \int_0^x \left[\frac{\Gamma(x)}{1-\Gamma(x)}\right] \cdot \frac{dR}{dx} dx + \left[\frac{1-I_p(x)}{I_p(x)}\right]\left[\frac{E_T}{1-E_T}\right] \tag{14}$$

In this equation, $I_p(x)$ is the batch grinding kinetics coupled with the residence time distribution, $\Gamma(x)$ is the grade efficiency curve of the classifier, and E_T is the total efficiency of the classifier under the conditions of use. It is possible to eliminate E_T from this equation, but the result is far too complicated to be of use.

4.1 Grinding kinetics in a 100 AFG opposed jet mill

In an Alpine 100 AFG mill, it is not possible to make independent measurements of the particle size distribution of the material leaving the grinding section and entering the classifying section. However, short and quasi batch grinding experiments can be performed by loading the mill with a quantity of powder equal to the hold-up in continuous operation, setting the classifier to maximum speed to retain particles in the mill, and operating it under the same conditions of air pressure and flow rate as in continuous operation. Sampling at different intervals gives the time variation of the cumulative oversize distribution. An example of such results and their correlation to the Kapur approximation is shown in **Figures 12** to **14** where:

$$K^{(1)}(x) = ax \frac{1}{1 + (x/\gamma)^{\beta}} \tag{15}$$

where

$a = 3.8 \cdot 10^{-4}\ \mu m^{-1}\ s^{-1}$, $\gamma = 106.4\ \mu m$, $\beta = 2.8$

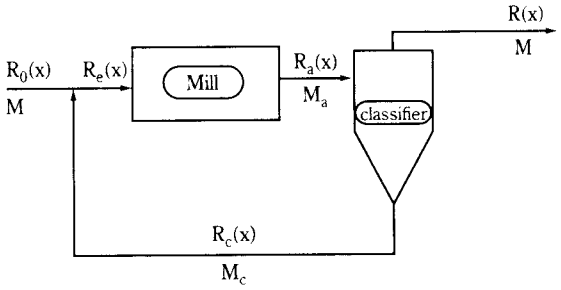

Fig. 11 Flow sheet of an air jet mill showing the grinding and classifying sections

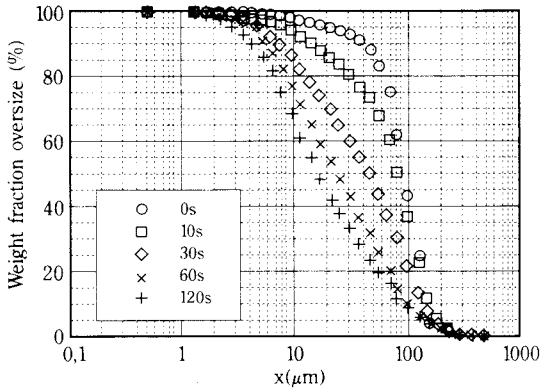

Fig. 12 Change in particle size distribution in quasi batch grinding in an air jet mill

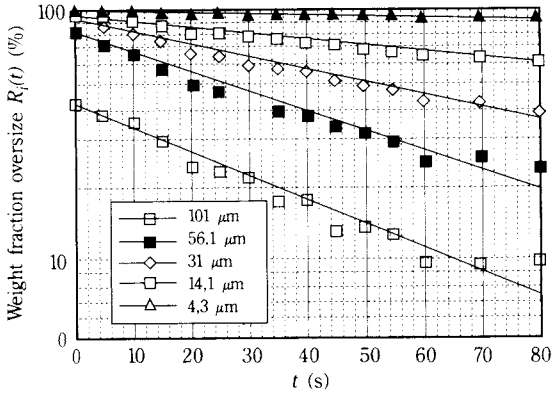

Fig. 13 Fit of the results in figure 12 by a first order Kapur function

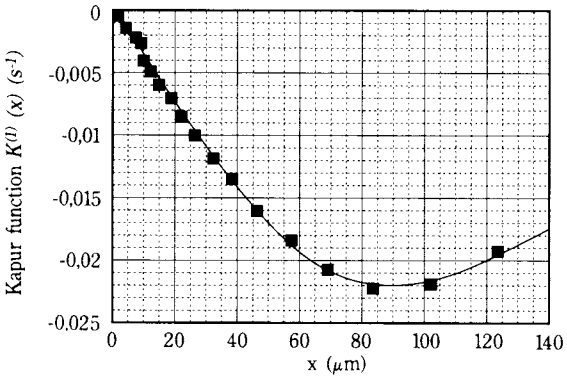

Fig. 14 The function $K(x)$ used in figure 13 and its fit to an exponential

This analysis is only valid for times less than 80 sec, which will be shown later to be adequate for effective residence times in continuous operation.

4.2 Classification in a 100 AFG opposed jet mill

The opposed jet mill can be converted to a 50 ATP classifier by removing the air jet section and replacing it with an air inlet section. This then allows independent determination of the characteristics of the classifier, and in particular determination of the grade efficiency curve $\Gamma(x)$ and total efficiency E_T for substitution in equation (14). An example of the result is given in **Figure 15**.

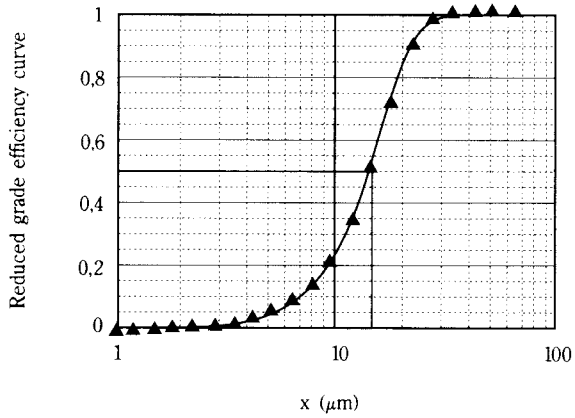

Fig. 15 Reduced grade efficiency curve

4.3 Residence time distribution and overall operation of an opposed jet mill

The only remaining factor is the residence time distribution in the mill. The practical difficulties involved in making tracer measurements have been circumvented by numerical testing of flow models of the mill. The simplest version which gives an adequate representation of the results is shown in **Figure 16**. As can be seen, this assumes an active grinding zone of 50 cm^3 included in the convergence of the 3 jets, followed by a plug flow transfer zone leading to and coming from the classifying section. Combination of these three elements (batch grinding kinetics, classification and residence time distribution), leads to a prediction of the overall action of the air jet shown in **Figure 17** as compared with the experimental results in continuous grinding. It should be noted that this corresponds to a mean residence time of about 13 seconds, well within the limits of validity of the batch grinding equation (15).

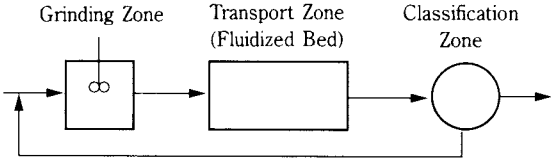

Fig. 16 Flow model for residence time distribution in an air jet mill

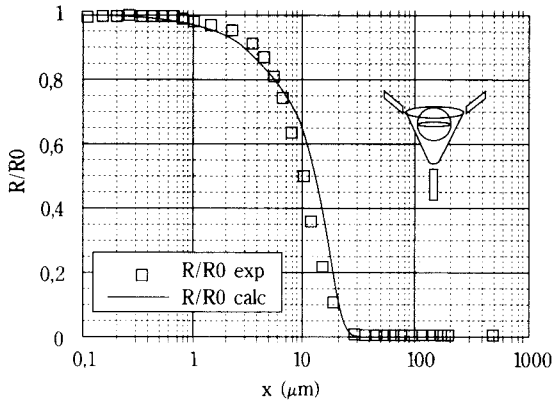

Fig. 17 Comparison between experimental and computed (eq. 14) particle size distribution in continuous grinding in an air jet mill

5. Study of fragmentation mechanisms

Another separate part of the programme concerns a fundamental study of the fragmentation of particles in high-velocity impacts with the aim of gaining insight into the elementary processes occurring in an air jet mill and eventually a better understanding of the role of particle morphology. Two different aspects of this have been examined: an experimental apparatus has been built to observe high-velocity impacts (up to 300 m/s), and a theoretical study has been made to provide means of characterising debris and fragmentation routes for $Al(OH)_3$.

5.1 Fragmentation scheme for $Al(OH)_3$

SEM examination of particles of hydrargillite (**Figure 18**) leads to the proposed fragmentation scheme shown in **Figure 19**. In this, the original particles (shown at top left) can be broken down to the ultimate debris (bottom right) by several routes involving different mechanisms: rupture of grain joints, chipping, cleavage and grinding. The practical question raised is: Can the different routes occurring in a given grinding mill be determined and provide the grinding "signature" of a mill?

A given type of particle is situated in the fragmentation scheme by two parameters: particle size and particle morphology. The first of these can be determined by standard particle size analysis, for example, by laser diffraction. The second can be determined by image analysis using a sufficiently discriminating

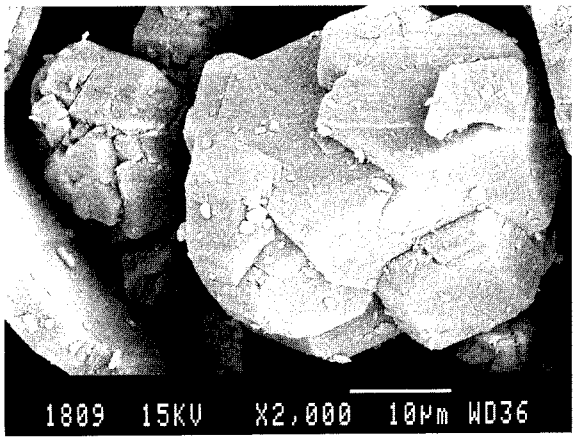

Fig. 18 SEM photo of a particle of hydrargillite

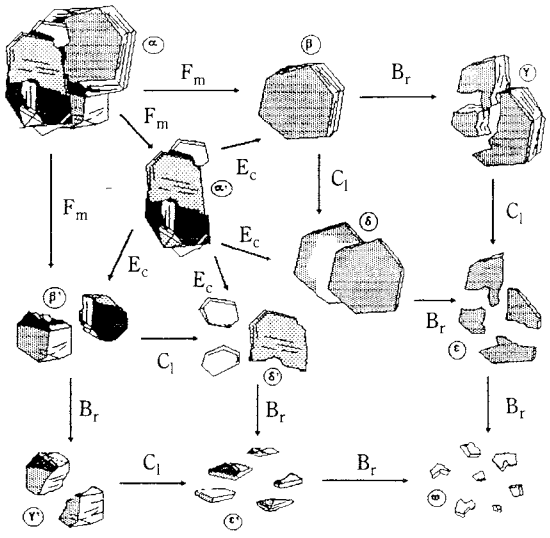

Fig. 19 Proposed theoretical fragmentation scheme for hydrargillite: F_m, rupture of joints; E_c, chipping; C_l, cleavage; B_r, ultimate grinding

definition of particle morphology. The first method tried was fractal analysis by the Richardson-Mandelbrot method. This gave information on the detailed structure of particle contours, but presented problems of interpretation as soon as the scale of observation was close to the scale of the details used for discrimination.

Another method for characterising the morphology of ground material under development is based on the Hausdorff space or distance. In this, the contour of an irregular particle (A) is compared with a reference shape (R) in terms of the minimum distances between the real contour and the reference contour. The maximum of the minima from the reference to the particle is called the Hausdorff distance (H). The minima of the minima from the particle to reference is called the morphological distance (D).

$$H(A,R) = Max\{d(A,R), d(R,A)\} \quad \text{Hausdorff distance}$$

$$D(A,R) = Min\{d(A,R), d(R,A)\} \quad \text{Morphological distance}$$

These two values allow any given particle to be represented in a $\{H,D\}$ diagram. An example of these diagrams applied to debris of hydrargillite is shown in **Figure 20**. In addition, these characteristics can be used to define other morphological parameters such as: anisotropy, sinuosity, or roughness, and changes in these can be given as trajectories on the $\{H,D\}$, as are also shown in **Figure 20**, giving the results of simulations of changes in ideal systems. Finally, **Figure 21** shows the results of the Hausdorff morphological analysis applied to hydrargillite subjected to 0, 10, 20, and 30 seconds grinding in an air jet mill.

6. Experimental study of high velocity impacts

6.1 Experimental equipment

Experimental equipment has been built to study the fracture of particles accelerated in a jet of air and impacting on a target [9]. As shown in **Figure 22**, it includes an air solids mixing unit, an accelerating nozzle, and a chamber containing the orientable target plate plus a cyclone/filter system for recovering the particles. The energy supplied to the particles is determined from the velocity of the particles, which is measured by two different techniques: an optical correlation method (Vector probe), and by video recording using a high-shutter-speed camera. This equipment allows experiments at velocities from 10 to 300 m/sec at solid loadings from 0.001 to 3.

A preliminary study of the hydrodynamics of the jets showed that the particles do not follow the lines of gas flow near the impact zone if the criterion λ is greater than 1 [8], where λ is given by:

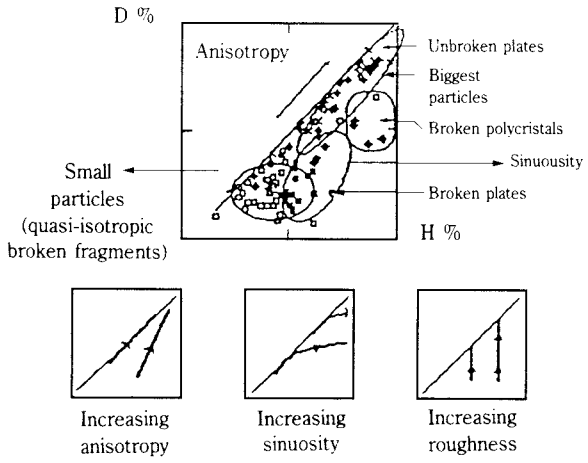

Fig. 20 Particle morphology in the Hausdorff space

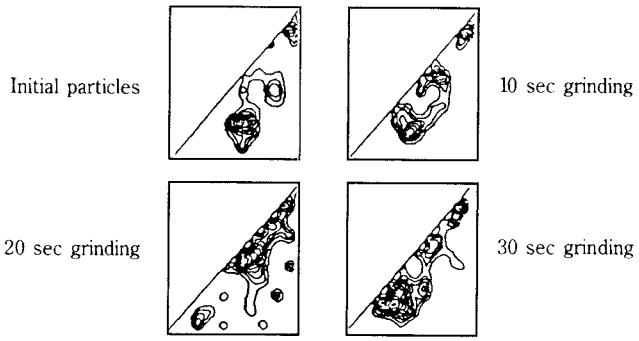

Fig. 21 Changes in morphology by air jet milling shown in the Hausdorff space

$$\lambda = \frac{\rho_s d_p^2 Re_p \; CdU_g}{432 \mu_f H} \tag{16}$$

This limits the use of very small particles, but in all the experiments reported here λ was always greater than 10.

It was further established that particle-particle interactions in the nozzle are minimised, and the results are comparable with single-particle impacts with very dilute jets which have a solids to air flow rate ratio of less than 0.1. However, the jet system has the advantage that a great number of particles are used and the results are statistically significant with respect to particle-particle variability.

By adding a second particle jet system, the equipment can be further extended for the study of double jet impacts.

6.2 Methodology

The experimental parameters are the air and the solids flow rates, W_j, and W_s, respectively, and the type of solid. Several different target materials and orientations have been used, but the discussion here will be limited to experiments with a silicon carbide target set at 90° to the incident jet. The particle size distribution is measured before and after impact by sieving or with a laser diffraction instrument and related to the impact velocity V_s or the specific energy $E_s = \rho_s V_s^2/2$. Several methods have been used to characterise the fragmentation (particle diameter or

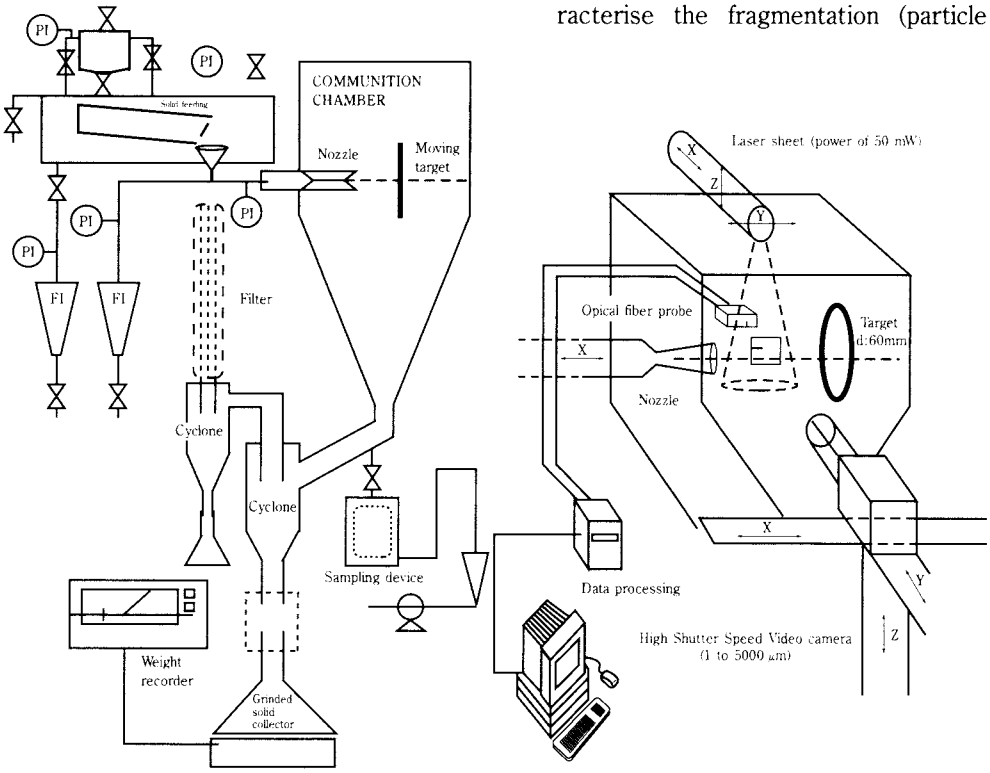

Fig. 22 Apparatus for high-velocity impact experiments with the associated velocimetry systems

particle surface criteria, the amount of fines created, population balance methods), but here, only the size reduction ratio d_i/d_f will be considered.

6.3 Experimental results

Here, we report a selection of the results for 5 different types of particle: 3 inorganic powders (glass beads $d_i = 129\mu m$, sand $d_i = 90\text{-}125\mu m$, hydrargillite $d_i = 93\mu m$) and 2 polymers (polyamide P11 $d_i = 123\mu m$, polymethylmethacrylate PMMA $d_i = 173\mu m$).

6.3.1 Inorganic particles

Figure 23 shows the results obtained with the glass beads; they are similar to those obtained with sand. That is, after a threshold value there is a progressive increase in d_i/d_f with particle velocity or with energy. The variation is linear with kinetic energy, meaning that the size reduction ratio varies with the square of the velocity of the particles. The existence of a threshold shows that in the low energy domain, the particles undergo plastic deformation on impact without breaking. It seems that this depends exclusively on the nature of the material, the particle size, and on the nature and surface state of the target, regardless of the fragmentation criterion that is used.

Figure 24 shows the effects of impacts on two particle sizes of hydrargillite. The smaller size is obtained by sieving the debris after impact of the larger size. It can be seen that in addition to a threshold value, there is a change in slope for the larger particles at a critical value of impact energy. This discontinuity is evidence of a change in impact behaviour corresponding to two fragmentation mechanisms. Reference to **Figure 19** indicates that the first mechanism would seem to correspond to rupture by chipping or splitting of the grain joints of the hydrargillite where the weakest bonds are broken to produce smaller aggregates. The second mechanism would seem to correspond to cleavage of the particles and their destruction by grinding. The reduction in slope indicates that this second type of rupture is harder to produce.

Figure 24 also compares the behaviour of the initial hydrargillite particles (particle size 93 μm) with those of 37 μm particles obtained after a single impact at 15 kJ/kg. It can be seen that the smaller particles show a linear variation in size reduction ratio with impact energy and a slope identical to that of the second regime of the initial hydrargillite. Reasoning in terms of the total overall specific energy supplied to the particles in the two impacts (i.e. adding 15 KJ/kg) shows that the curve for the second impact is in line with the other results. This observation only holds

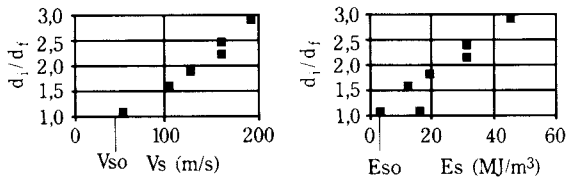

Fig. 23 Influence of particle velocity or impact energy on the size reduction ratio for glass beads

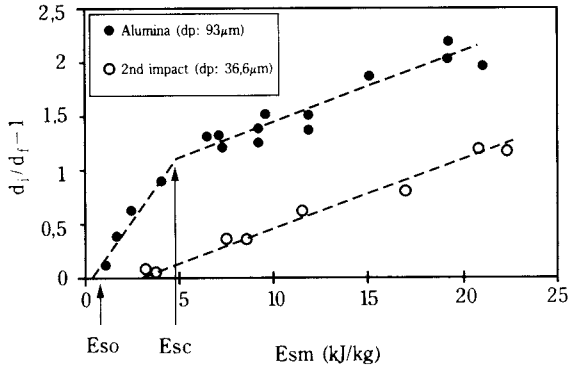

Fig. 24 Influence of impact energy on the size reduction ratio for 935m and 375m hydrargillite

true for two impacts.

Further experiments with four different sieve cuts of hydrargillite allow us to plot the variation of the threshold energy (E_{so}) and critical impact energy (E_{sc}) as defined in **Figure 24** as a function of the particle size. The diagram shows 4 fragmentation zones corresponding to different mechanisms (**Figure 25**). All impacts below the Eso frontier are "pseudo-elastic". There is no significant reduction in particle size. The E_{sc} frontier indicates a limiting diameter of $\approx$ 40 μm, corresponding to the maximum size of

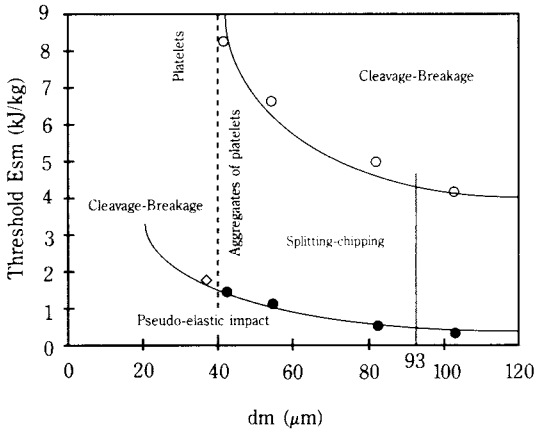

Fig. 25 Diagram of the fracture modes for hydrargillite

tablets. Smaller particle sizes can only be produced by cleavage-grinding to fragment the tablets. Particles of a size greater than 40 μm seem to be associations or aggregates of tablets which will give two types of fracture according to the kinetic energy of impact. Between E_{so} and E_{sc} there is rupture by chipping-splitting to give smaller associations of tablets. For energies greater than E_{sc}, the tablets are broken by cleavage-grinding to give thinner tablets or fragments of tablets. The different zones roughly correspond to the theoretical scheme shown in **Figure 19**.

6.3.2 Organic particles

The experiments with organic particles demonstrate the difference in behaviour on impact between a semi-crystalline polymer (polyamide P11) and an amorphous polymer (PMMA). On the one hand, the semi-crystalline polyamide particles are easily broken and there is a significant size reduction ratio which, just as for sand and glass, varies in a linear fashion with the square of the impact velocity. And on the other hand, it is impossible to break the amorphous polymer PMMA with one impact. SEM observation shows that the particles are flattened at the point of impact and it seems that this plastic deformation engenders fissures which develop sufficiently over 5 and more impacts to lead to rupture.

7. Conclusion

A method of macroscopic modelling to predict the particle size distribution of product from continuous fine grinding has been developed and tested on two different types of mill: a stirred bead mill and an opposed air jet mill. This has been further extended to the case of a grinding circuit formed by an air jet mill with an integral classifier by combining batch grinding kinetics, a solids flow model, and the grade efficiency curve of the classifier.

A more fundamental investigation of fragmentation mechanisms in fine grinding of hydrargillite has led to the development of several methods of characterising debris morphology so as to identify fragmentation routes. Single-particle fragmentation experiments have identified at least two regimes of fracture of the hydrargillite which depend on impact energy.

Future work will attempt to combine these different approaches with the aim of finding a means of operating fine grinding processes to produce not only particles of a given size distribution, but also of a controlled particle morphology.

Acknowledgements

This research is financially supported by ''CNRS'' and the ''Agence de l'Environnement et de la Maîtrise de l'Energie'' (ADEME) and by a complementary grant from IFPRI.

Nomenclature

a	constant	(−)
$B(x, y)$	breakage function related to size x and y	(−)
B_{ij}	breakage function related to class i and j	(−)
D	Morphological distance	(m)
d_f	final mean diameter	(m)
d_i	initial mean diameter	(m)
$E(t)$	residence time distribution function	(s^{-1})
E_s	specific energy	(J/m^3)
E_{s0}	threshold specific energy	(J/m^3)
E_{sm}	mass specific energy	(kJ/kg)
E_t	total efficiency of the classifier	(−)
G_i	Kapur function, eq. (4)	(s^{-1})
H	Hausdorff distance	(m)
H_i	Kapur function, eq. (4)	(s^{-2})
$I_p(x)$	batch grinding kinetics coupled with residence time distribution	(−)
$K_i^{(k)}$	Kapur function related to class i	(s^{-k})
$m(y, t)$	mass fraction for particle of size y, batch operation	(−)
$R(x, t)$	cumulative size distribution at time t, batch operation	(−)
R_i	cumulative size distribution related to size i	(−)
$S(y)$	selection function related to size y	(s^{-1})
S_i	selection function related to class i	(s^{-1})
t	time	(s)
V_s	particle velocity	(m/s)
V_{s0}	threshold particle velocity	(m/s)
x	particle size	(m)
y	particle size	(m)
$\Gamma(x)$	grade efficiency curve of the classifier	(−)
λ	inertia number, eq.(16)	(−)
$\mu_1(t)$	first moment of the particle size distribution	(m)

indice

e	inlet
i	class
s	outlet

References

[1] Epstein, B.: Logarithmic-normal distribution in breakage of solids, Ind. Eng. Chem., 40, 1948, 2289.

[2] Kapur, P.C.: Kinetics of batch grinding – part A: Reduction of the grinding equation, Trans. Soc. Min.Eng. AIME, 247, 1970, 299-303 – part B: An approximate solution to the grinding equation, Trans. Soc.Min.Eng. AIME, 247, 1970, 309-313.

[3] Kapur, P.C.; Agrawal, P.K.: Approximate solutions to discretized batch grinding equation, Chem. Eng. Sci., 25, 1970, 1111-1113.

[4] Kapur, P.C.: Self preserving size spectra of comminuted particles, Chem. Eng. Sci., 27, 1972, 425-431.

[5] Berthiaux, H.: Modélisation du broyage fin dans un broyeur à jets d'air et à lit fluidisé – Etude du couple broyeur – selecteur, Doctorate Thesis, INPL Nancy France 1994.

[6] Varinot, C.; Berthiaux, D.; Heitzmann, D.; Dodds J.: Entropie 188/189, 1995, 71-75.

[7] Frances, C.; Laguerie, C.: Industrie Minérale, Mines et Carrières, Les techniques Vol. I, 1995, 93-98

[8] Laitone, J.A.: Aerodynamic effects in the erosion process, 4th Int. Tribology Conf., Paisley 1979, 239-246.

[9] Mebtoul M.; Large, J.F.; Guigon, P.: High-velocity impact of particles on a target – an experimental study, 8th European Symp. on Comminution, Stockholm 1994, Vol. 1, 90-101.

Author's short biography

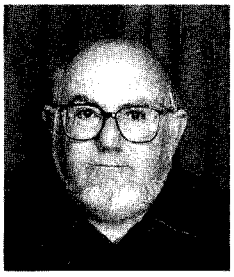

John Dodds

John Dodds was awarded a degree in Chemical Engineering at Loughborough University of Technology (UK) in 1965 and a PhD from the same university in 1968 for work on the structure of particle packings and dewatering filter cakes. He then moved to work in France at the Laboratoire des Sciences du Génie Chimique, (Chemical Engineering Science Laboratory) in Nancy. His work there has covered: Ion exchange and adsorption processes, transport and capture of colloids in porous meda involving colloid characterisation by Hydrodynamic Chromatography and Field Flow Fractionation as well as deep bed and membrane filtration processes. He now leads a team in Particle Techonology working in packing models of porous media, instrumental methods for particle size analysis and fine grinding and classification processes. He is the author of over 200 papers and presentations at international conferences and the co-author of the book "Physics of Granular Media".

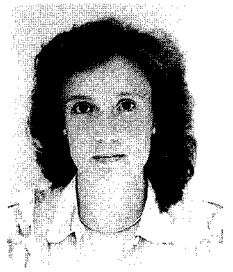

Christine Frances

Christine Frances was born in 1965. She graduated from the Ecole Nationale Supérieure de Génie Chimique of Toulouse in 1988. She obtained the Doctor degree of the Institut National Polytechnique de Toulouse (France) in the field of crystallization. Since 1992 she is a researcher of CNRS (National Center of Research) in the field of comminution.

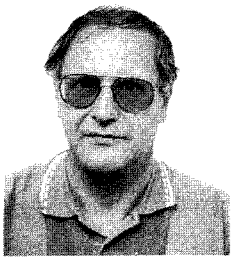

Pierre Guigon

Pierre Guigon is a Chemical Engineer from ENSIGC Toulouse-France (1971). Master of Engineering Science, UWO London Ontario, (canada) 1974., Docteur Ingénieur, UTC Compiègne (France) 1976, Docteur es Science, UTC Compiègne (France) 1987. He is professor of Chemical Engineering at the University of Compiègne. His research is in the field of particle suspensions (fluidization, pneumatic transport) and particle technology (comminution and agglomeration).

Alain Thomas

Alain Thomas was born in 1942. He graduate d from the Ecole Nationale Supérieure de Géologie de Nancy in 1966. Docteur es Science, Institut National Polytechnique de Lorraine in 1975. His reseach is in the field of modelisation of mineral structures related with comminution.

Air Entrainment and Dust Generation from a Falling Stream of Bulk Material†

Paul Cooper and Peter C Arnold
Department of Mechanical Engineering
*University of Wollongong**

Abstract

Bulk materials handling operations involving falling streams of the bulk material are common throughout industry. Proper design of any fugitive dust control system servicing such operations requires knowledge of the behaviour of the free-falling stream in terms of the air entrained by the falling material and the concentration of dust liberated. In this paper results of experiments on alumina powder free-falling from a hopper are presented. It was found that the material stream initially contracts in cross-section as it accelerates and a boundary layer of dusty air develops around the core stream of bulk material. Results of air entrainment per unit mass of parent material are also given. The authors describe a simple analytical model of the complex air entrainment process by treating the falling stream of material as a negatively buoyant plume of dusty air fully miscible with the ambient air. The experimental data are successfully correlated using this approach. The plume model provides a more realistic description for the situation considered here than previous theoretical treatments based on air movement induced by isolated particles independently falling through quiescent air.

1. Introduction

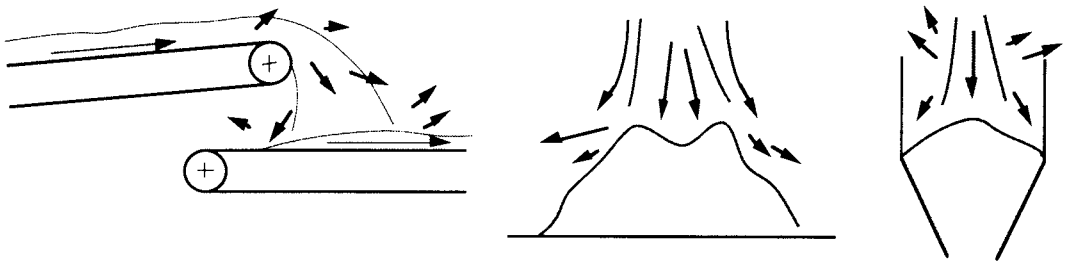

Fig. 1. Schematic of typical bulk material handling operations involving air entrainment and fugitive dust generation from falling streams of material.

Dust generation from materials handling operations has been a significant issue for many years for industrial processes as diverse as mining and food processing. However, in recent times control of dust emissions has become of increasing concern as worker exposure limits and plant emission controls have become more stringent and as recovery of valuable product previously lost in fugitive dust is seen as economically important. The cost of cleaning up plant affected by fugitive dust can be enormous. In the UK, for example, it has been estimated that annual costs to industry of dust, mess and spillage from materials handling operations is of the order of US$300 million p.a. at 1987 prices (Wilkinson *et al*, 1989).

In a great many bulk material handling operations the material concerned undergoes a freefall and subsequent impact either on a solid surface or on the top of bulk material as in the examples of conveyor transfers and silo filling (see **Figure 1**). This paper deals with some of the fundamental fluid dynamic processes involved in dust generation and air movement when this type of freefall operation occurs. In all types of handling operation fugitive dust is liberated the bulk material by the process

* Wollongong NSW 2522 AUSTRALIA
† Received 15 June, 1995

known as "pulvation" where the aerodynamic forces acting on individual dust particles are greater than the forces acting to maintain the cohesiveness of the bulk material. The theoretical treatment of pulvation in common freefall operations has been very limited in past literature and little quantitative data is available to designers of industrial ventilation systems on the quantity of dust liberated for a given process and bulk material or on the nature of air movement that carries away the dust.

There are several mechanisms by which dust is liberated from the parent material during operations involving freefall. In these situations all the bulk material becomes airborne and in so doing accelerates downwards and expands, entraining air and liberating fugitive dust. The flow phenomena are complex and parameters of prime importance to the design of any dust control system that is applied to control of dust include:

- air entrainment volume (and hence the required air extraction rate by an industrial ventilation system)
- dust concentration in the contaminated air
- location of the extraction point to minimise dust loading.

A schematic example of the situation of interest here is shown in **Figure 2** where a falling stream of dusty material impacts on a stockpile. Fugitive dust control is effected by surrounding the process with an enclosure (this may be the silo or bin for the material concerned). To prevent dust escaping from the entry to the container, sufficient air must be extracted by the dust collection system to match the air influx in the stream of material (entrained air) and the air displaced by the entering solid particles (displaced air). To ensure the dust control system is designed properly, therefore, we need to know the amount of *air entrained* by the free-falling material. Here only the region where the material is free-falling is of concern.

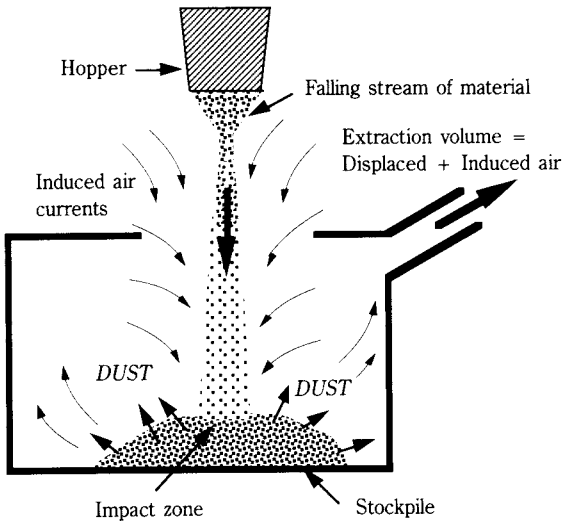

Fig. 2. Schematic of a dust control system operating on a container being filled by a falling stream of material

When considering *dust generation* there are two principal physical mechanisms whereby dust leaves the bulk material and is carried away from the stockpile by air currents: i) dust is liberated during the free-fall of the parent material; ii) the falling stream impacts on the stockpile releasing the entrained air which causes pulvation of fugitive dust from the stockpile.

A great deal of research has been carried out on methods by which the "dustiness" of a given material may be determined. The general approach has been to develop a particular type of apparatus which generates dust in a repeatable manner either by dropping a known mass of the parent material in a single charge (e.g. Heitbrink *et al*, 1992) or by agitating the material under steady state conditions in a sealed chamber, for example. However, the "dustiness" of a material determined by these methods may not be quantitatively useful when a designer is concerned with a dust generation process that differs significantly from the dustiness test used. In the view of the present authors the most appropriate direction of research in this area is to determine dust generation from a given industrial process by considering both the characteristics of the bulk material and dynamics specific to the process concerned.

Previous fundamental research on the air entrainment and dust liberation processes from falling streams of material is limited to a very few studies. Hemeon (1962), for example, developed a means of predicting air entrainment based on the air movement induced by a single particle falling through quiescent air. As we discuss below, this approach has several limitations when used to model a falling stream of bulk material where the vast majority of particles do *not* behave as if they are falling through quiescent air. Very little else by way of quantitative guidance is available in the literature to the designer seeking to predict the air entrainment and dust loading on an industrial ventilation system venting an enclosure such as that shown in **Figure 2**. The Industrial Ventilation Manual (ACGIH, 1986), for example, gives recommended extraction rates for conveyor transfer enclosures but contains little advice as to the effect of

material properties on either the required extract volumes or dust loading. To quote the Industrial Ventilation Manual on conveyor belt ventilation design (Figure VS-50-20) "Note: Dry, very dusty materials may require exhaust flow rates 1.5 to 2.0 times stated values". This clearly illustrates the qualitative nature of the published design criteria. The Industrial Ventilation Manual provides useful practical guidance on issues such as the clearance between belt loads and sealing skirting but gives no information on the likely behaviour of the bulk material and dusty air within the enclosure.

More recently Plinke *et al.* (1991) have performed an extensive experimental study of dust generation from falling streams of sand, cement, flour and limestone. They reported correlation of the measured dust generation as a fraction of total parent material flow rate in terms of parameters including, drop height, mass flow rate, particle size and moisture content.

The aim of our research at the University of Wollongong is to develop a theoretical model of the processes of dust generation and air entrainment to enable air entrainment and dust loading to be determined as a function of the properties of the bulk material (particle size distribution, particle density, etc) and the material handling process parameters (such as drop height and mass flow rate). The major focus of the work reported in this paper is on our progress toward quantification of the air entrainment in a falling stream of dusty bulk material.

2. Experimental Apparatus

A laboratory-scale experimental rig was built to carry out fundamental research on the type of situation shown in **Figure 2** where a continuous stream of material enters a container through an opening in the upper surface and fugitive dust is prevented from escaping by extracting air through a second opening in the container. The experimental apparatus is shown schematically in **Figures 3** and **4** and is described in detail by Smithers (1994). A double hopper arrangement was used to generate a falling stream of material with constant mass flow rate. The entire hopper system was suspended from a frame so that the mass flow rate of material could be measured directly by means of load cells attached to the suspension cables. An open-top, glass-sided enclosure, 1.0m square in plan and 0.8m tall, was used as the observation chamber to allow visual observation and filming of the particulate and fluid dynamic processes.

The mass flow of material was controlled by varying

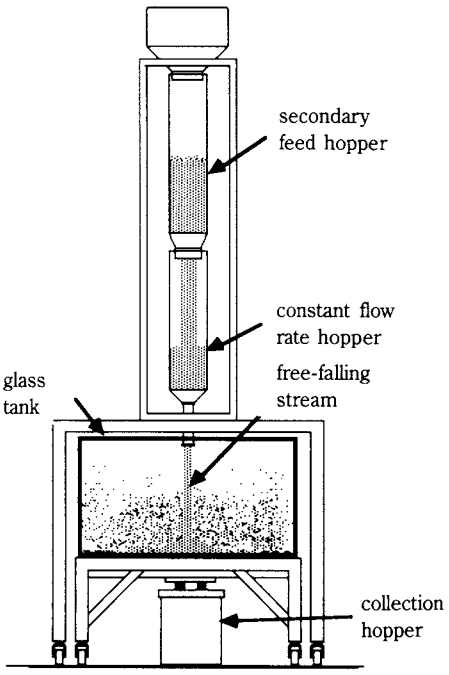

Fig. 3. Experimental apparatus for measurement of dust generation and air entrainment.

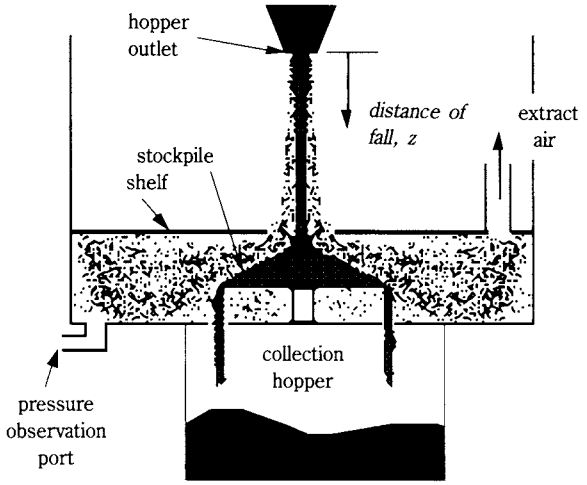

Fig. 4. Details of experimental apparatus for measurement of air entrainment.

the outlet diameter of the lower hopper. To ensure a constant drop height during the course of an experiment, stockpile height was maintained by means of a disc suspended above the chamber floor onto which

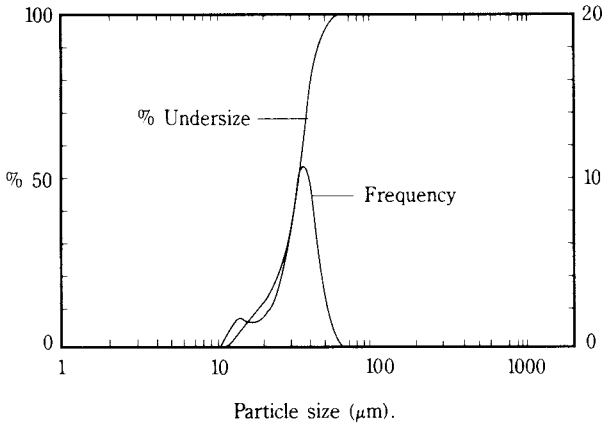

Fig. 5. Particle size distribution for alumina parent bulk material.

the material impacted. Excess material flowed off the stockpile into a collection bin below the observation chamber through an annular outlet as shown in **Figure 3**. The material used for the experimental work reported here was alumina. The bulk material particle size distribution was determined using a Malvern^{TM} Series 2600 laser particle sizing system and is shown in **Figure 5**.

To determine the amount of air entrained in the falling material stream a shelf was placed in the observation chamber as shown in **Figure 4**. The falling stream of material passed through a 57mm diameter hole in the enclosure shelf which was located 40mm above the top of the stockpile. Air was then extracted from the region under the shelf until there was no static pressure difference between this region and outside. An extremely sensitive means of detecting when internal and external pressures were equal was provided through smoke being introduced into a small "pressure observation port" in the floor of the observation chamber. Smoke movement either in or out of the port then indicated an imbalance between internal and external pressures. The air extraction volume was measured by means of a rotameter.

3. Experimental Results

3.1 Cross Sectional Area of Falling Stream of Dusty Material

The experimental apparatus was designed for investigation of a steady state flow of material with as little disturbance to the stream on leaving the hopper as possible. The flow was generally observed to be steady with occasional disturbances lasting a fraction of a second as flow in the hopper outlet adjusted to internal inhomogeneities. Contrary to some comments in the literature, the cross-sectional area of the falling stream of material was actually found to *decrease* upon exiting the hopper outlet much as a viscous liquid stream diameter decreases upon release from an opening in a horizontal surface. Due to the turbulent air flow around the stream of material a "boundary layer" of dust-laden air developed around the main core region and this did increase in cross-section with increasing drop height. This "boundary layer" was the region of quiescent air affected by the downward motion of the material core stream and was limited in extent. Using smoke injected into the enclosure as a means of fluid flow visualisation,

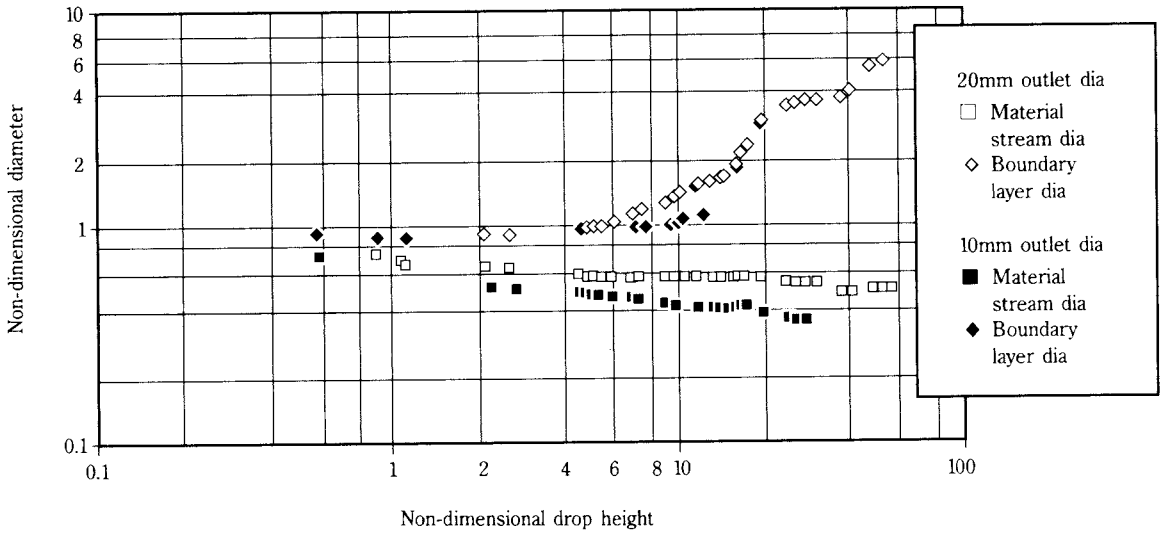

Fig. 6. Diameters of core bulk material stream and dust laden boundary layer for stream of alumina normalised against hopper outlet diameters of 10mm and 20mm (Woodall, 1993).

the diameter of the boundary layer was estimated (Woodall, 1993). As the distance, z, through which the material stream fell increased, so the turbulent motion of air and smaller particles led to a blurring of the interface between the falling stream and the "boundary layer". However, the boundary of the main core of bulk material remained distinct over the drop heights investigated to date (i.e. up to 830mm). Quantitative experimental results of the variation of material stream and boundary layer cross-section with drop height are shown in **Figure 6** where drop height and the diameters of the core stream of material and of the boundary layer are non-dimensionalised with respect to the hopper outlet diameter.

3.2 Dust Generation from the Falling Stream

Two distinct dust generation mechanisms were observed as described above: i) dust liberation within the falling stream and ii) dust liberation as the falling stream impacted on the stockpile. To determine how dust generation in this first region is related to drop height and particle size a MetOne^{TM} dust particle counter was used to measure the dust concentration in the experimental enclosure above the shelf. The data shown in **Figure 7** are necessarily qualitative in nature since it was not possible to sample isokinetically due to difficulties in matching local air flow rates in the experimental chamber to the air sampling extraction rate. However, the data presented provide a useful insight into the way in which dust generation is affected by both drop height and dust particle size. Further research into this aspect of the problem is ongoing.

3.3 Air Entrainment by the Falling Stream of Material

A number of experiments were carried out to determine the dependence of air entrainment on drop height and mass flow rate of the alumina. The influence of drop height on air entrainment is clearly very important in design of materials handling operations such as conveyor transfers. Air entrainment flow rates, Q_{ent}, per unit mass flow, $\dot{m}$, of the parent bulk material are shown in **Figure 8** for a constant hopper outlet diameter of 10mm. Here Q_{ent} is the total air flow extracted from beneath the shelf of **Figure 4** less the volume flow of the parent material. The results from twelve individual experiments are presented in **Figure 8** and air entrainment, Q_{ent}, is seen to be proportional to drop height raised to the power 1.8.

The relationship between air entrainment per unit mass flow to actual mass flow is important in determining the validity of any theoretical model of the entrainment process. Our experiments confirmed the fact that more air is entrained as the mass flow rate of the bulk material increases. However, the amount of air entrained per unit mass of material, $Q_{ent}/(\dot{m})$, decreases with increasing mass flow rate as shown in **Figure 9.** This is an important finding as this indicates that as the bulk material mass flow rate increases, so the air entrainment by each individual particle decreases. This result demonstrates that air entrainment models based on the behaviour of individual particles in quiescent air cannot model the influence of bulk material mass flow rate on entrainment satisfactorily.

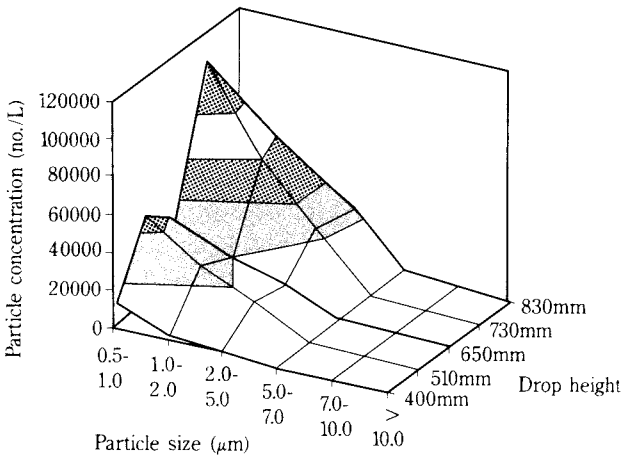

Fig. 7. Alumina dust concentration measured above shelf for ϕ10mm hopper outlet.

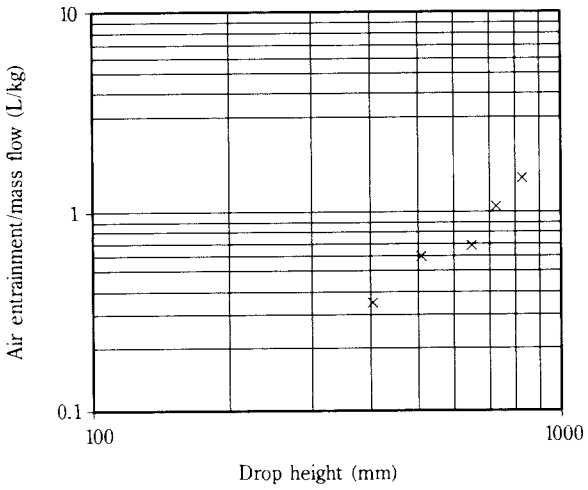

Fig. 8. Air entrainment normalised to parent bulk material (alumina) flow rate versus drop height for ϕ10mm hopper outlet.

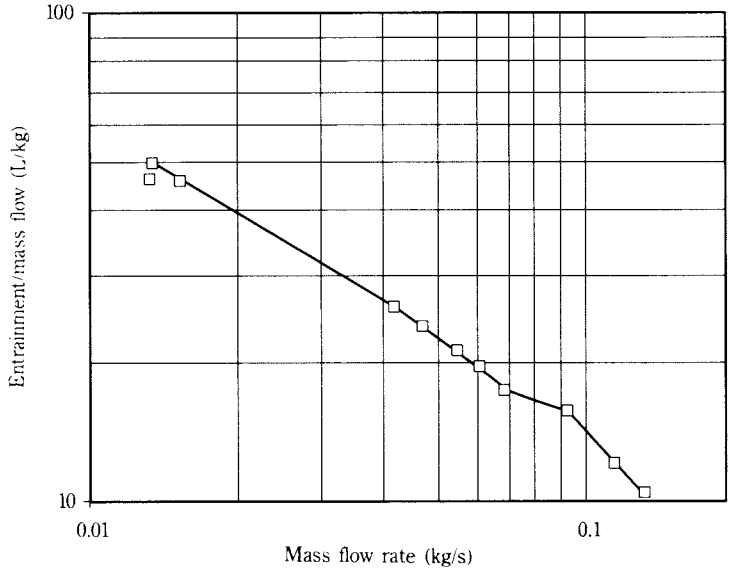

Fig. 9. Air entrainment normalised with respect to parent material flow rate for constant drop height, z = 650mm.

4. Analytical Models of Air Entrainment

The movement of individual particles within the falling stream of any bulk material will be extremely complex. The motion of an individual particle in quiescent air is in itself a complex phenomenon where drag on the particle changes as the particle accelerates and if the particle is sufficiently massive it will attain a velocity such that turbulent flow is induced in its wake. One might therefore visualise the air and particle motion in a falling stream of many particles of different sizes to be influenced by both the macroscopic flow field induced by the material falling under the influence of gravity and by the small scale turbulent motion induced by the motion of individual particles.

The first attempt to model this complex situation with regard to prediction of air entrainment by the falling stream was reported by Hemeon (1962). Hemeon's method of predicting the air volume entrained in a falling stream of material is based on the following assumption.

work done by drag forces of a falling particle accelerated from rest to terminal velocity in quiescent air	=	work needed to accelerate the entrained air from rest to entrained velocity

For a continuous stream of falling material, the drag forces were assumed to be a multiple of that arising from a single particle falling through quiescent air. Hemeon's theory essentially treated the stream of bulk material as behaving in the same way as multiple single particles and has been used to predict the volumetric flowrate of air, Q_{ind}, induced by a stream of material of cross-section area, A. In SI units this flow rate may be shown to be (Smithers, 1994):

$$Q_{ind} = \frac{0.66\ g\ \dot{m}\ (h\ A)^2}{d_p \rho_p}^{1/3} \qquad (1)$$

Where d_p and p_p are the particle diameter in metres and density in kg/m^3, respectively, g is the gravitational acceleration constant, $\dot{m}$ is bulk material mass flow rate in kg/s and h is the drop height in metres. (Note that several major assumptions are made in the course of the derivation of equation (1) in regard to the drag on the particles in the ambient air). The value of Q_{ind} obtained is then modified by an arbitrary factor to account for the fact that the material stream does not behave as individual particles falling through quiescent air. Hemeon's model has also been used by others such as Morrison (1971) and Tooker (1992) to predict the air flow through an opening induced by a falling stream of material.

While the approach adopted by Hemeon has been quoted in the literature many times there are several problems associated with this model of the air entrainment process which include: a) a continuous stream of material certainly does not behave in the

same way as individual particles falling independently through quiescent air – particles will reach much higher velocities than if acting individually in quiescent air, turbulent wakes downstream of the individual particles will increase turbulence levels and influence the motion of particles following, etc; b) most bulk materials have a wide range of particle sizes and yet a single value of d_p must be chosen in equation (1); c) there is no way of determining the cross section of the stream, A, at a given point unless the process is already in place and observable.

The theoretical approach adopted by the present authors is to treat the falling stream as a collection of particles. The behaviour of the stream is actually dependent on many factors but as a first approximation one may take it to posses characteristics from two extremes, firstly, where the stream is made up of very massive particles that fall vertically under the influence of gravity alone as shown in **Figure 10a** (negligible drag forces) and, secondly, where the stream is made up of extremely fine particles with no cohesion that fall in a plume as shown in **Figure 10b** which is analogous to the way in which a miscible plume of buoyant hot air rises from a smoke stack.

Consider first the extreme situation shown in **Figure 10a** where a bulk material of massive particles falls from a hopper. A steady flow might be regarded as falling with very little drag force acting on the majority of the particles in the stream and that all particles accelerate at a rate equal to the gravitational constant, g. If one assumes that the momentum of the entrained air is negligible compared to that of the solid particles within the stream and that the slip velocity between the air and particles is very small, then the air entrained may be calculated simply according to the principle of conservation of volume; i.e. the entrained air volume flow rate must be equal to the cross-sectional area of the stream multiplied by the difference in velocity at the end of the drop-height in question and at the start of free-fall. The entrained air volumetric flow rate, Q_{ent}, is then given by:

$$Q_{ent} = ((V_0^2 + 2gh)^{1/2} - V_0) A_0 \qquad (2)$$

where V_0 and A_0 are the bulk material velocity and cross-sectional area at the start of free-fall, respectively, g is gravitational acceleration and h is the drop height.

The second and opposite extreme is the case of a stream of very fine powder falling from the outlet of a hopper. If the particles are extremely small and not cohesive in any way, their terminal velocity will be very small compared to any induced air velocities and the resulting flow would develop as a miscible plume from a source of negative buoyancy (see **Figure 10b**). The volumetric flow in a plume of positively or negatively buoyant fluid miscible with ambient fluid may be determined using well known plume flow equations, such as those developed by Morton et al (1956). The plume may be modelled using the "entrainment assumption" which may be

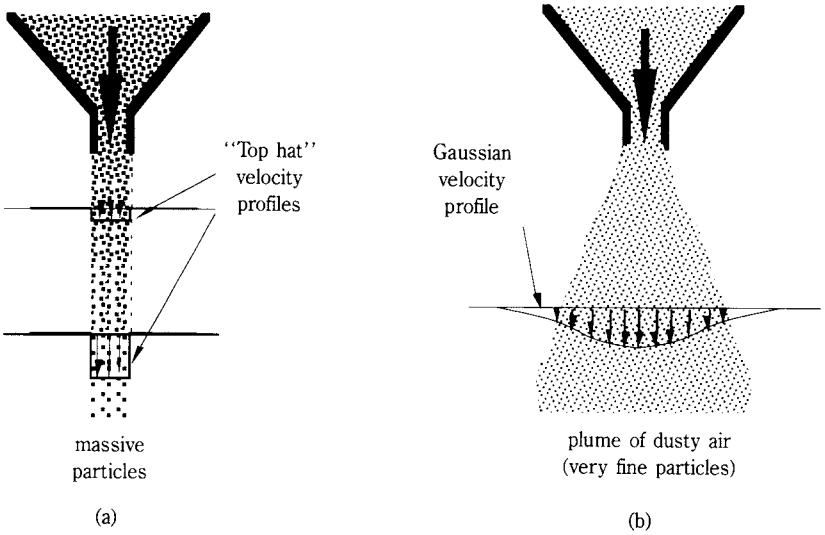

Fig. 10. Two possible extremes of free-falling particle stream behaviour: a) large particles falling vertically under gravitational forces alone b) extremely fine particles acting as a miscible plume.

summarised by stating that the horizontal velocity of ambient air drawn into the plume at a given cross-section is directly proportional to the mean vertical velocity of fluid within the plume. The constant of proportionality is known as the "entrainment constant", α. Solution of the governing equations for mass, momentum and density may be solved analytically. The volumetric flow rate, Q_{plume}, at a given distance h from the point source (theoretically with zero mass and momentum flux) is given by the relation:

$$Q_{plume} = C B^{1/3} h^{5/3} \tag{3}$$

where C is constant (usually of the order 0.1 for miscible plumes) related to the entrainment constant, α, and B is the buoyancy flux. In the situation considered here, where the fluid surrounding the plume is not significantly stratified, B is constant throughout the vertical plume development and is defined as volumetric flow, Q, multiplied by reduced gravity $g' = g(\rho\text{-}\rho_\infty)/\rho_0$ where ρ is the mean density of the plume, ρ_∞ is the density of the ambient fluid and ρ_0 is a reference density).

Thus, there are several ways in which the air entrainment by a stream of falling bulk material might be approximately modelled. Three such simple analytical models described above may be summarised as: the individual particle model (Hemeon); the massive particle model; the miscible plume model.

5. Discussion

The behaviour of the stream of bulk material leaving the hopper described in section 3.1 above indicates that the majority of the parent material falls in a stream that may in fact have a cross sectional area less than that of the hopper outlet. However, the existence of a "boundary layer" of dusty (negatively buoyant) air around this core stream indicates that air is induced to flow over a considerably wider cross section than the material stream itself. It seems likely then that from the point of view of air entrainment the stream would indeed show characteristics applicable to both the massive particle and miscible plume models.

The quantitative air entrainment results presented in **Figures 8** and **9** provide a means of assessing the validity of the three models of air entrainment outlined above. As one would intuitively expect, the amount of air entrained by a falling stream of material increases with increasing drop height as indicated in **Figure 8**. All three models predict this in a qualitative sense. Also it is clear that as the total mass flow rate of the parent material increases so the interaction of each particle with the ambient air is lessened in the average and the air entrained per unit mass of parent material will decrease. We have also found this to be the case experimentally as shown in **Figure 9** and we now demonstrate that the experimental data presented here goes someway to demonstrating that the plume analysis of air entrainment provides the best air entrainment model to date.

Assuming that air entrainment, Q_{ent}, per unit mass flow rate of parent material mass, $\dot{m}$, is related to drop height, h, and material mass flow rate, $\dot{m}$, by the relationship:

$$(Q_{ent}/\dot{m}) \approx k\,(\dot{m})^m \times h^n \tag{4}$$

(where m, n and k are empirically determined constants), the three entrainment models described above in equations (1), (2) and (3) then lead to values of the exponents m and n as shown in **Table 1**. The experimental values of the exponents have been derived from our data presented in **Figures 8** and **9**. Clearly from this qualitative examination of the theoretical and experimental data, the plume model matches observations better than either Hemeon's approach or the simple large particle model.

The utility of the plume model is demonstrated even more clearly when it is used as a predictive tool. The air entrainment volume data for all the experiments in the present study have been correlated using equation (3) and an entrainment constant of 0.031. **Figure 11** shows a plot of air entrainment predicted using equation (3) for each set of experimental conditions, h and $\dot{m}$, against the measured values of $(Q_{ent}/\dot{m})$ in units of L/kg. The data spread is relatively small and the correlation holds over more than an order of magnitude of variation in $(Q_{ent}/\dot{m})$. This lends weight to our belief that application of the plume model may be extended to cover larger scale industrial situations and with appropriate calibration the model could be used as a design tool.

Table 1. Theoretical and experimental values of exponents used for determining air entrainment volume per unit mass of parent material.

Theoretical Model	Exponents m	n
Hemeon	−0.67	0.67
Large particle model	−1.0 (near to source)	0.5 (far from source)
Plume model	−0.67	1.67
Experimental results	−0.65	1.8

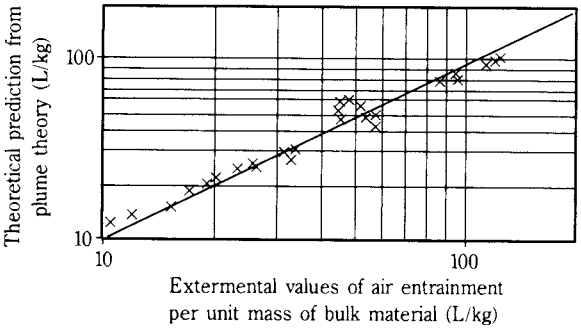

Fig. 11. Air entrainment predicted from simple plume theory against measured values (entrainment constant = 0.031).

The fluid dynamics analysis of conventional miscible fluid plume flow assumes either gaussian or "top-hat" velocity and density profiles across the plume at any cross-section. The velocity profile across a falling stream of bulk material is not known, however, the fact that the plume model works in the application here is not a surprise and adds to the ubiquitous success of the "entrainment assumption" in situations as diverse as volcanic eruptions, laboratory experiments and oceanographic phenomena. The entrainment constant that best correlates our data here is 0.031. However, since this is an empirical constant further research is required to determine whether the constant is widely applicable to materials handling applications or whether it is a strong function of parameters such as particle size distribution and mass flow.

Moreover, the authors are cognisant of the fact that a large number of factors affect air entrainment which they have not dealt with here explicitly, due to lack of space. Clearly the manner in which a falling stream of material becomes airborne is important. In our research to date we have been concerned with the fundamental flow processes involved and have chosen a simple method of releasing the parent bulk material. In many practical situations the material becomes airborne with a considerable initial momentum, possibly in a horizontal direction as is the case with conveyor transfers. Similarly, the influence of nearby solid objects and boundaries may influence air flow around the falling stream and hence affect entrainment volume. These matters are currently under investigation at the University of Wollongong.

Designers of fugitive dust control enclosures involving falling streams of materials should be aware of the mechanisms by which air is entrained and dust liberated from the free-falling material and the way in which air de-entrains upon impact with the stockpile carrying significant quantities of dust with it. Knowledge of these mechanisms allows the designer to predict more accurately the best positions for extract air removal from an enclosure to minimise the dust loading on the air cleaning system. To facilitate development of a theoretical model for accurate prediction of air entrainment and dust generation, further research is necessary to model the various two-phase flow phenomena involved, to model the influence of bulk material properties on dust generation and air entrainment and to test the theoretical models using full-scale plant.

6. Conclusions

Air entrainment and dust generation by falling streams of bulk materials is important in the design of many fugitive dust control systems. Currently there is little quantitative data available in the literature to guide the designer of such systems. In this paper experimental results have been presented for air entrainment and dust generation by a stream of alumina falling under steady state conditions from a small hopper.

The experimental results have demonstrated the following: the cross sectional area of the stream of bulk material decreases with increasing drop over the heights investigated in the present study – a boundary layer of dusty air of increasing cross section develops with increasing drop height; air entrainment per unit mass flow of parent material is proportional to $Z^{1.8}$, where Z is distance from the hopper outlet; the air entrainment per unit mass flow of parent material decreases with increasing mass flow.

Three simple analytical models of the air entrainment process have been discussed: the single particle model of Hemeon; the massive particle model; and the miscible plume model. The miscible plume model is based on the plume equations commonly used in environmental fluid dynamics and has been shown here to provide the best correlation of the experimental air entrainment data.

Nomenclature

A = cross sectional area of falling stream [A]
B = buoyancy flux [m^4/s^3]
d_p = particle diameter [m]
C = constant in equation (3)
g = gravitational acceleration constant [m/s^2]
g' = reduced gravity $g(\rho-\rho_\infty)/\rho_0$ [m/s^2]
h = drop height [m]
Q = volume flow rate [m^3/s]

Q_{ent} = volume flow of entrained air [m^3/s]
V_0 = Velocity of bulk material leaving hopper [m/s]
α = entrainment constant
ρ = mean density of plume [kg/m^3]
ρ_p = particle density [kg/m^3]
ρ_∞ = density of ambient fluid [kg/m^3]
ρ_0 = reference density [kg/m^3]

References

1) ACGIH, American Conference of Governmental Industrial Hygienists, Industrial Ventilation – A Manual of Recommended Practice, 19th Ed (1986).
2) Heitbrink, W.A., P.A. Baron and K. Willeke: Am. Ind. Hyg. Assoc. J., **53**(10), 617-624 (1992).
3) Hemeon, W.D.L., Plant and process ventilation, Industrial Press, N.Y (1962).
4) Morrison, J. N.: Trans. Soc. Mining Engineers, AIME, March 1971, 47-53 (1971).
5) Morton, B., G.I. Taylor and J.S. Turner: Proc. Royal Soc. London, Series A, 234A, 1-22 (1956).
6) Plinke, M.A.E., D. Leith, D.B. Holstein, and M.G. Boundy: Am. Ind. Hyg. Assoc. J., **52**(12), 521-528 (1991).
7) Smithers, T, "Generation of dust from a falling stream of material", BE honours thesis, Dept. Mechanical Engineering, University of Wollongong (1994).
8) Tooker, G.E.: Bulk Solids Handling, vol. 12, no. 2, 227-232 (1992).
9) Wilkinson, H.N., A.R. Reed, and H. Wright: Bulk Solids Handling, 9, 93-97 (1989).
10) Woodall, I. "Investigation of various dust generation Mechanisms as a means of controlling industrial pollution", BE honours thesis, Dept. Mechanical Engineering, University of Wollongong (1993).

Author's short biography

Dr. Paul Cooper

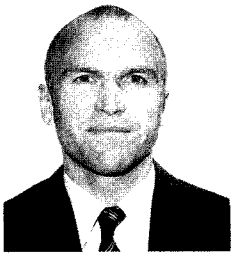

Dr. Cooper is a Senior Lecturer with the Deparetment of Mechanical Engineering at the University of Wollongong. He received his BSc, MSc and PhD degrees from Imperial College (UK) and has been working in the areas of industrial ventilation and air conditioning for the past five years. His main research interests are in the fields of dust and fume control, duct network design, hot process fume control, scale modelling of fluid flows and natural convection processes.

Prof. Peter Arnold

Professor Peter Arnold is Professor of Materials Handling and Processing, Department of Mechanical Engineering at the University of Wollongong and is Director of the Bulk Materials Handling Centre. In 1991 he was awarded the degree of Doctor of Science by the University of Wollongong and in 1993 was elected a Fellow of the Australian Academy of Technological Sciences and Engineering for his significant contributions to the science and technology of bulk solids handling. Professor Arnold is on the Editorial Boards for the journals Bulk Solids Handling, Powder Handling and Processing, Powder Technology as well as KONA. He is a foundation member, and currently Deputy Chairman of the Institution of Engineers, Australia, National Committee on Bulk Materials Handling.

Constitutive Model for Dry Cohesive Powders with Application to Powder Compaction †

V. M. Puri, M.A. Tripodi and H.B. Manbeck
Agricultural and Biological Engineering Department
The Pennsylvania State University
G. L. Messing
Materials Science and Engineering Department
The Particulate Materials Center
The Pennsylvania State University

Abstract

Continuum theory-based constitutive models suitable for simulating the load response of dry cohesive powders have been critically reviewed. Based on a set of criteria, three candidate models for further investigation have been identified: Cam clay, Adachi and Oka model, and Krizek et al.'s endochronic theory based model. Since the modified Cam clay model is the foundation of many advanced constitutive models, it was chosen and applied to compaction load response of a dry cohesive powder (wheat flour). The constitutive equation parameters were determined using four types of conventional triaxial tests: drained, undrained, mean effective stress and isotropic tests. Based on these tests, the three Cam clay parameters for wheat flour were: 2.1 (slope of critical state line), 0.130 (loading index) and 0.022 (unloading index). Low pressure uniaxial compaction tests were performed with the powder in a thin-walled aluminum column. A finite element model (FEM), with the modified Cam clay constitutive model for dry cohesive powder's response, was used to predict the compression behavior. The FEM calculated values compared favorably with measured wall strains. The FEM predicted stress distribution in the powder mass identified troublesome regions with large shear stresses and tensile stresses.

1. Introduction

The handling and processing of powders (e.g. agricultural, ceramic, pharmaceutical, metal and mineral) constitutes a large volume, high value-added industry. Pressed products are often fabricated from a mixture of powders and additives. After mixing and granulation, powders are transported to a processing stage where they may be tabletted as medicines, pressed into shapes for use in manufacturing industry, or pelletized as feed. All phases of the powder industry, namely, storage, handling, and processing are operations that require precise knowledge of the behavior of powder systems to achieve the desired control. To model the behavior, powder mechanics must be understood and defined, yet the mechanics are most complex. Particular difficulties arise when attempts are made to predict the mechanical behavior of cohesive bulk solids that are under externally applied loads. For example, a cohesive powder in storage will form aggregates and clusters, resulting in irregular flow. For highly precise manufacturing operations, as the making of precision components, expensive medicines, or when exact percentages of ingredients are needed to ensure product quality, flow deviations may result in significant economic loss. Therefore, it is desirable to design equipment that processes the bulk solid in a known, predictable manner. For this capability, knowledge of the load-deformation behavior of powder systems is essential.

For near net shaping of advanced materials, compacting powders in a die is a preferred method because no liquids are involved during forming, organic binders and lubricants comprise only a small fraction of the total solids, i.e. ~10 vol%. The binders and lubricants are easily removed prior to densification (i.e. sintering), and high production rates of net shaped components are achieved. For example, ceramic ferrites, capacitors, metal gears, carbide cutting tools, and small, complex-shaped electronic components are manufactured by die pressing. For these applications dimensional precision, uniformity of pressed density, freedom from defects and pressed surface finish are critical measures of quality.

† Received 16 June, 1995

Because ceramic particles are <1 μm diameter and elastic, the powder is combined with organic polymers (i.e., binders) to form free-flowing >100 μm granules. Pressing pressures typically range up to 100 MPa but are often limited to lower pressures to reduce die wall wear by the abrasive ceramic powders. Deformation of the binder-ceramic granules is regulated by adjusting the polymer properties and content. In this manner, the elastoplastic ceramic powder is changed to a viscoelastic or viscoplastic material during pressing [1, 2].

Despite the extensive utilization of die pressing, there are few detailed studies about the powder mechanics involved in the manufacture of high quality components by pressing. The literature that is available is mostly focused on empirical relations between pressed density and pressure. These empirical relations are system specific and provide little fundamental insight about factors controlling the above measures of component quality. Recently, constitutive and finite element modeling have been successfully applied to metal powder pressing. However, only a very limited number of the reported studies have measured the elastoplastic or viscoelastic or elasto-viscoplastic constitutive model parameters and validated the finite element models for the same powder under compression. Nevertheless, it is this approach that will enable a complete understanding of the mechanics of powder pressing.

2. Literature Review

An objective of this paper is to first review potential models for their suitability for describing ceramic powder compaction.

Because a vast number of models exist, we outline the essential categories of constitutive models and then focus specifically on models for load-deformation behavior of cohesive powders. In the second part of the paper, we discuss the utilization of the Cam clay model for low pressure consolidation of wheat flour. By this example, we demonstrate the testing approach required for characterizing the compaction of a constrained powder. Finally the Cam clay model and the measured parameters are combined into a fourth-generation FEM model. The results of this FEM simulation are reviewed and the relevance of this approach to ceramic powder compaction discussed.

An engineering approach to predicting the mechanical behavior of powders is to develop a constitutive model, and then predict how the powder will deform or flow under load. Constitutive models are important because they allow a designer to quantitatively predict material behavior, then produce an effective design based on calculated numbers. Models can be divided into two groups: empirical and rational. Empirical models are developed by taking experimental data of a material under specific loading conditions and then statistically determining the equations that will closely match the data. Rational models apply physical laws to describe the stress-strain behavior of the material. These models are based on either microscopic or macroscopic scale parameters. Microscopic models consider each particle in a bulk solid as a distinct entity and then predict stress-strain behavior based on a distribution of interparticle forces. Macroscopic (continuum) models treat the bulk solid as a continuum or interacting continua and describe load-deformation characteristics of the material as a whole.

Each type of model has positive attributes. Empirical models accurately reflect the data on which they are based and are more easily obtained. Microscopic models consider force reactions on each particle and thus are very sound with respect to obeying laws of momentum and energy. Rational macroscopic models are usually easier to understand than microscopic models. They also satisfy, on the average, the mass, momentum, and energy equations, and can be quite accurate if the model assumptions are reasonable.

There are several empirical models in existence, a popular one being Kondner's model [3], which represents axial stress as a hyperbolic function of axial strain. Kondner's model, being consistent with other empirical models, produces good results for clay under axial loading. But for all of these models, as examples, Kuno and Okada [4] and Saleeb and Chen [5], only a specific loading condition can be predicted, and load-deformation behavior is not physically explained by actual material properties or by the laws of mechanics.

A large research initiative has been underway since the early 1980s to model the stress-strain behavior of granular materials at the microscopic level, focusing on particle-particle interactions and using the resultant of these interactions to predict the behavior of each particle and then the whole assembly of particles. Behavior at that level is a function of, among other factors, particle geometry, surface characteristics, friction forces, and material hardness. Most models treat particles as smooth spheres or cylinders to allow for a feasible prediction of particle contacts. Due to the very large number of particles in a given volume and complexity of these behavioral equations,

no comprehensive models have been developed to date. Microscopic models are still significant as they do provide important insights into the behavior of particulate materials.

Rational models for bulk solids need to initially include whether the material is cohesive or cohesionless. As mentioned, cohesion adds difficulty to a model. The majority of cohesionless macroscopic models have been developed for sand [6-8]. Two of these models have been verified for wheat en masse [9, 10]. Clay soil is the predominant cohesive bulk material that has been modeled. Early models date back many years [11] with subsequent models increasing in sophistication [12].

The application of continuum models developed for clay soils, which are typically in the saturated state, to powders that contain relatively low levels of free water may be questioned. Most soil models use effective stresses, which are the principal stresses minus the pore liquid pressure, to predict behavior. In this sense the particle matrix in the soil responds to the applied load, a condition similar to what would be expected in a dry powder. A second point is that soils are considered bulk solids, as are powders, grains, and granulated products, and hence many researchers agree that theories derived for soils are assumed to be valid for any bulk solid.

Early plasticity models made use of the Mohr-Coulomb criterion [12], which defined the yield locus of material. The yield locus is still very applicable to industrial needs, as illustrated by the widespread use of the Jenike flow function in hopper design [13]. But yield loci curves are restrictive in the sense that their construction is dependent solely upon maximum and minimum principal stresses that induce yielding or flow of the material; i.e., stress-path information and the influence of the intermediate principal stress (σ_2) are not considered in their formulation. These limitations are serious since load-deformation of bulk solids is known to be a function of path and σ_2. Models using the Mohr-Coulomb criterion are herein termed ''limit-state''.

The Drucker-Prager criterion [14], similar to the Mohr-Coulomb criterion, is a widely used plasticity theory to describe failure. Drucker-Prager defined a plastic yield surface in terms of three principal stresses, with elastic strain states inside the yield surface and plastic strain states on the yield surface; thus, the material is considered elastic-perfectly plastic. A state of stress outside the yield surface is unstable. A major shortcoming of the Drucker-Prager model is that failure is predicted during a volume increase (dilatancy), whereas many clays fail during densification (contractancy).

The critical-state concept [15] was introduced to soil modeling and states that a bulk material reaches a volume after which additional loading produces flow with no further volumetric change. In other words, when a bulk solid is loaded, particles rearrange, deform, fuse, and fracture, causing the volume to either decrease or increase. Decreasing volume means strain-hardening and increasing volume means strain-softening. In either case, the bulk solid reaches a stress state at which additional load may change the shape of a given mass but not its volume. This state is the critical state characterized by a critical void ratio or critical density. Before reaching the critical state, the bulk solid undergoes continuous yield states; hardening (or softening) after each yield state. There are limitations to this theory, which include the assumptions of isotropic hardening and associative flow; i.e., yield function is the same as the potential function (the function that describes the plastic potential surface, the surface normal to the plastic flow vector).

Another type of continuum constitutive model, different from the plasticity models, is the endochronic theory [16]. The endochronic theory considers stress-strain behavior in terms of a thermodynamic process instead of a mechanical process, as considered by plasticity theory. Viscoplasticity now becomes a function of internal state variables of which intrinsic time is one [17]. The state of the material depends upon past strain history through an internal clock.

Constitutive models developed specifically for powders were generally aimed at defining a flow function. Flow functions became popular after the work of Jenike [13], and as a result many gravity-flow hopper designs rely on the Jenike data charts. It is much more difficult to design hoppers through which cohesive powders flow because the conventional shear tests, such as Jenike, direct shear, and Peschl, do not adequately predict the tendency of the powder to aggregate and arch. In constitutive modeling, cohesion is an extremely difficult phenomenon to describe mathematically. Consequently, much research effort has concentrated on quantifying cohesion. Matchett [18] and Molerus [19] each explain cohesion as the sum of interparticle friction forces. Although their methodologies were different (Molerus used particle contacts and Matchett used the concept of friction bonds across a sphere plane) they employed the same basic principles, that is, they explain cohesion as interparticle attractive forces, then use a distribution

of forces over the material mass, and finally sum the distribution to get a single cohesion parameter. The cohesion parameter could then be used in the constitutive equations to predict a yield locus.

Both rational and empirical constitutive models have been presented and under rational models, microscopic and continuum models have been introduced. In a review of all model types, the rational continuum-type models are most attractive. A powerful continuum model has the potential to predict accurately powder behavior under a variety of loading conditions with a reasonable amount of testing and computation.

2.1 Discussion of models

A literature review of the key models for describing the load response of cohesive particulate materials identified two models that possess the most attributes crucial for the development of a generalized particulate mechanics model, namely: path-dependency, physically meaningful parameters, three-dimensional anisotropic capability, time-dependency, the capability to predict cyclic loading response, and the application of the model to an industrial setting. These attributes were first used as criteria for selecting models for preliminary review. Once a preliminary screening was done, the attributes mentioned were again used to rank the reviewed models in terms of their appropriateness for further testing of dry cohesive powders [20].

2.1.1 Modified Cam clay model

The review of continuum modeling reveals that a major distinction can be made between how models predict failure in powder systems. The limit-state models [21-23] were inadequate since they do not provide the required stress-path information.

Among the stress-path dependent models discussed, most [24-30, 31, 32, 33, 34] were based on the Cam clay model [15]. The Cam clay model was the first to use the critical state theory to describe yield criterion and hardening. The critical state concept [12] was used by Roscoe et al. [35] as an attempt to describe yielding of soils during triaxial tests. Roscoe et al. [35] relied upon earlier works of Hvorslev [36] and Gilbert [37].

The Cam clay model used three critical-state parameters: M (slope of critical-state line); λ (slope of loading path); and $\varkappa$ (slope of unloading path). Parameters e_o (initial void ratio), p_c (hardening parameter) and N (consolidation parameter) are also used in the elastoplastic constitutive equations. All parameters are derived from conventional triaxial tests. Based on numerous observations from implementation of the original model, a "modified" Cam clay model was formulated in which the original theory was intact except for the definition of dissipated work during plastic strain. Subsequently, the modified Cam clay model [12] redefined the flow function, which in effect altered the shape of the yield surface. Hereafter, only the modified Cam clay model will be considered. This model assumes the associative flow rule, i.e. the direction of the yield vector coincides with the direction of the plastic strain vector.

The modified Cam clay flow rule is given as:

$$\delta\varepsilon_s^p / \delta\varepsilon_v^p = (M^2 - \eta^2)/2\eta \tag{1}$$

where $\delta\varepsilon$ represents differential strain, superscript p means plastic state, subscripts s and v refer to shear and volumetric states, respectively, and η is the ratio between mean effective stress p' and the deviatoric stress q. For triaxial loading conditions, $q = \sigma_1 - \sigma_3$, where σ_1 and σ_3 represent principal stresses. The flow rule can be integrated to give the equation of the yield locus [12]:

$$q^2 + M^2 p'^2 = M^2 p' p_c \tag{2}$$

where p_c is, in effect, the size of the yield locus at critical state. A volume-pressure relationship has the following form [38]:

$$V = N - \lambda \ln (p) \tag{3}$$

where V represents specific volume defined as $1+e$, and e represents the voids ratio. The combination of Eqs. (2) and (3) gives a representation of the modified Cam clay yield surface in stress-space with axies of p', q and V.

Given the definition of the yield surface in stress-space, the movement of material's stress state can be predicted using constitutive equations. The derivation of these equations from the flow rule, the yield surface and the definition of plastic work is given in detail in several sources [12, 38, 39], and will not be repeated here. The strain components during flow are separated into elastic volumetric, plastic volumetric and plastic shear strains (elastic shear strains are assumed to be negligible). The constitutive equations are then defined by the following:

$$\delta\varepsilon_v^e = \lambda / V [\delta p' / p' + (1 - \varkappa/\lambda) 2\eta\delta\eta / (M^2 - \eta^2)] \tag{4}$$

$$\delta\varepsilon_v^p = (\lambda - \varkappa) / V [\delta p' / p' + 2\eta\delta\eta / (M^2 + \eta^2)] \tag{5}$$

$$\delta\varepsilon_s^p = (\lambda-\varkappa)/V[\delta p'/p' + 2\,\eta\delta\eta/(M^2-\eta^2)]\cdot \cdot(2\eta/(M^2-\eta^2)) \quad (6)$$

Elastic strains are denoted by the superscript e. Eqs. (4)-(6), therefore, represent the relationship of stress to strain in a given particulate material and allow one to predict successive stress states on a material given the constitutive parameters, the initial conditions of the material, and the loading conditions imposed on the material.

2.1.2 Adachi and Oka rheological model

The assumptions made in the development of Cam clay model were limiting: flow was considered associative; hardening was isotropic; plastic behavior was time-independent; intermediate principal stress was not relevant. Subsequent models removed one or more of the limitations to make the Cam clay model more general. Among the modified Cam clay models presented, only the one presented by Adachi and Oka [40] considered all of these limitations and, more importantly, defined the constitutive parameters in a lucid, physically analogous manner. This model will, therefore, be discussed in sufficient detail; that is, (1) the constitutive equation will be shown and the parameters explained; (2) any tests performed to determine parameters and validate the model will be discussed; and (3) a critique will be given of the model as used by the authors. For the sake of consistency, the original notation used by the authors will be used in this paper.

Adachi and Oka [40] defined the two yield functions in their model: static (f_s) and dynamic (f_d). The static yield function helps determine material parameters, and the dynamic function is used to define the stress-strain relation. Function, f_s, is the yield function described by the critical state theory and has the following equation:

$$f_s = \sqrt{2}J_2^{(s)}/M^*\sigma_m'^{(s)} + \ln \sigma_m'^{(s)} \quad (7)$$

where J_2 is the second invariant of deviatoric stress tensor, M^* is a critical index parameter, and σ_m' is mean effective stress. Superscript (s) denotes the static equilibrium state. Function f_d is the same as Eq (7) except that the dynamic state of stress is used. Yield functions were derived on the assumption of associative flow and the material being isotropic (anisotropy is mentioned as an appendix to the model [40]). The constitutive equation for the strain rate tensor during dynamic equilibrium of normally consolidated clay is expressed as:

$$\mathcal{E}_{ij}(t) = s_{ij}(t)/2G + [\varkappa/3(1+e)](\sigma_m'(t)/\sigma_m')\delta_{ij} + ((1/M^*)\sigma_m')\Phi(F)\{s_{ij}/[\sqrt{(2J_2)}]\} + ((1/3M^*)\sigma_m')\Phi(F)\{M^* - [\sqrt{(2J_2)}]/\sigma_m'\}\delta_{ij} \quad (8)$$

where

$$\Phi(F) = c_o \exp\,[m'\ln(\sigma_{my}'^{(d)}/(\sigma_{my}'^{(s)})]$$

Parameters c_o and m' are time-dependent material properties, G is shear modulus, $\varkappa$ is swelling index, e is void ratio, s_{ij} is deviatoric stress, δ_{ij} is the Kronecker delta, $\sigma_{my}'^{(d)}$ is a dynamic hardening parameter, and $\sigma_{my}'^{(s)}$ is a static hardening parameter. Plastic volumetric strain is related to $\sigma_{my}'^{(s)}$ through the compression index λ. On a practical level, Eq. (8) can be separated into parts and each term evaluated. The first term of Eq. (8) accounts for elastic deviatoric strain due to the presence of elastic shear modulus and the deviatoric stress tensor. The second term accounts for plastic volumetric strain since $\varkappa$ is a volumetric parameter and the Kronecker delta (S_{ij}) means only the volumetric stress components (σ_{11}, σ_{22}, σ_{33}) are non-zero. The rest of the terms account for the plastic deviatoric strain.

Determination of parameters follows a well defined procedure, and all values are obtained using the triaxial test. Parameters, λ, $\varkappa$, and e are obtained from consolidation and swelling tests. Shear modulus G and index M^* are obtained from triaxial compression tests, as was done in the Cam clay model. Parameter m' is found by taking the linear slope of the stress ratio (q/σ_m' where q = deviatoric stress = $\sigma_1' - \sigma_3'$) versus log $\mathcal{E}(t)$ for axisymmetric triaxial compression tests. For m', M^* must be known and $\mathcal{E}^{(e)}(t)$ (elastic strain rate) is neglected. Parameters c_o and $\sigma_{my}'^{(s)}$ can be combined into one parameter, C, during plastic strain. Combining two parameters into one decreases the sensitivity of the equation, but is simpler to evaluate. Parameter C is determined using triaxial compression tests and plotting $\mathcal{E}^p(t)$ (plastic strain rate) versus q where $\mathcal{E}^e(t)$ is neglected and m', M^*, λ e, and $\varkappa$ are as previously determined. An anisotropic consolidation parameter was discussed briefly by Adachi and Oka [40]. But more investigation is required to determine the potential of this parameter to represent the non-isotropic response of particulate materials.

Typical parameter values for Fukakosa clay, determined from triaxial compression and hydrostatic tests, are shown in **Table 1**. A plot of effective stress path for measured and predicted values at strain rate $\mathcal{E}(t)$ = 0.0082%/min is shown in **Figure 1**. A

Table. 1. Parameter values for Fukakosa clay [40]

Parameter	Value
λ	0.1
$\varkappa$	0.02
M^*	1.22
m'	28.8
e_o	0.72
G°	363 kPa
C	1.96×10^{-9} 1/s

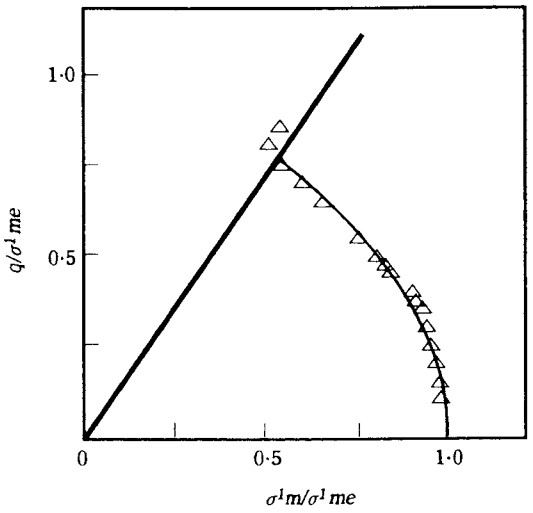

Fig. 1. Effective stress-path for Fukakosa clay at a strain rate of 0.0082%/min [40]. Symbols indicate actual data, the curve is predicted behavior, and the line is the critical state line. q/σ'_{me} is normalized deviatoric stress and σ'_m / σ'_{me} is normalized effective stress.

plot of normalized deviatoric stress versus strain for measured and predicted values at the same strain rate are shown in **Figure 2**. These plots illustrate the capability of the model to predict accurately behavior of clay under typical triaxial loading conditions. The original plots given by Adachi and Oka included the same information explained above for two strain rates: 0.0082%/min and 0.0835%/min. The second strain rate (0.0835%/min) has been omitted to show clearly the close agreement Adachi and Oka found between the model and measured data. The higher strain data shows an increase in deviatoric and volumetric strain as strain rate is increased. The authors acknowledge that this effect is implied by the constitutive equations [Eq (8)].

The constitutive model was applied in a two-dimensional consolidation analysis of a clay foundation during the construction of an embankment [33]. A finite element mesh was generated that replicated the clay embankment. Using the elasto-plastic constitutive equations of Adachi and Oka [40] excess pore pressure versus total vertical stress and lateral

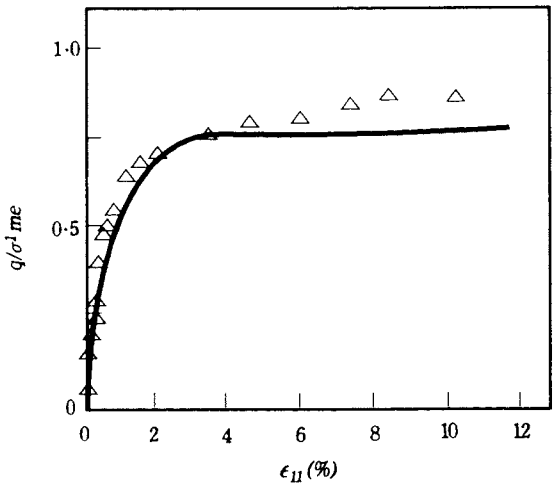

Fig. 2. Stress-strain relation for Fukakosa clay at a strain rate of 0.0082%/min [40]. Symbols indicate actual data and the curve is predicted behavior. q/σ'_{me} is normalized deviatoric stress and ε_{11} is the axial strain

displacement versus foundation settlement could be numerically calculated for the toe of the embankment via the finite element model. The FEM results were compared to an empirical model generated from actual field data. The FEM predicted a pore water pressure/vertical stress ratio of 0.75 for the first 33 days of consolidation and a ratio of 1.0 from 33 to 100 days, which almost exactly matched the empirical results. Similarly, the FEM predicted lateral displacements in the first 33 days of consolidation exactly matched the empirical displacements. The observed FEM displacements at 100 days consolidation were within 10%.

Adachi and Oka's [40] elastoplastic model has several advantages. First, the plastic strain increment is a function of time; therefore, creep phenomenon can be predicted, and the model, most likely, can predict cyclic loading with some adjustments. Second, the model has the potential to include material anisotropy. Furthermore, the parameters used in the model (λ, $\varkappa$, e, G, M^*, m', *and* C) have an easily understandable physical representation. An apparent shortcoming, however, is that of all the model parameters, $\varkappa$ alone seems to be able to account for cohesion. To explain, the unloading index $\varkappa$ is determined from the void ratio e versus log p (mean pressure) plots during the unloading cycle of consolidation. Since elastic strains after compression are plotted versus applied load, cohesive forces will have a tendency to keep the particles together and to resist any observed recovery to the original volume. No other parameter directly includes cohesive forces.

A final consideration is that all testing by Adachi and Oka [40] was mainly on saturated clays. The issue of water content has been mentioned as a concern, since the powders in question will generally not have high water contents. In a drained compression test, the capillary force from the pore water will tend to pull the particles together, thus functioning as a cohesive force. This would be equivalent to the interparticle cohesive forces, such as van der Waals and chemical forces, generated in a dry powder. For comparable undrained tests, void ratio change will have to be incorporated in the constitutive equations. The fact that Trassoras et al. [41] effectively used a clay model for tungsten-carbide powder is encouraging.

2.1.3 Krizek et al. endochronic model

Another model, namely the endochronic model developed by Krizek et al. [42] and used by Ansal et al. [43] is also a promising candidate. The model of Krizek et al. [42] focused on five important points: (1) recoverable and irrecoverable strains as soon as loading begins, (2) deformation is a function of stress history and strain rate, (3) volumetric stress components cannot be neglected, (4) normal strain has components due to volumetric and hydrostatic stresses and shear strain only due to shear stress, and (5) shear and bulk moduli vary with time (thus, they are functions of plastic strain, strain rate, and change in volumetric strain due to friction). The model assumes that the material's resistance to shear stress is a first-order function of effective normal stress and interparticle distance. For consistency, notation and symbols used by the authors will be followed.

The constitutive equations for the model are based on two state variables, intrinsic time (Z) and a densification/dilatancy measure (λ). The intrinsic time increment, dZ, is a function of ζ (rearrangement measure), t (time), Z_1 and τ_1 (both material constants). Rearrangement measure ζ is determined from a coupled hardening/softening function (F). Determination of strain is a two-part process. The first part, which is a function of deviatoric stress, is to determine λ, which is a function of another densification/dilatancy function (L). Since λ neglects hydrostatic stress, strain includes bulk modulus (K) in the formulation for volumetric strain. The constitutive equations can be written as:

$$d\varepsilon_{ij}^{d} = ds_{ij}/2G + s_{ij}dZ/2G$$

$$d\varepsilon_{ii}^{v} = d\sigma_{ii}'/3K + d\lambda$$

where

$$dZ = f[\zeta(F),\ t,\ Z_1,\ \tau_1]$$

$$d\lambda = f(L) \tag{9}$$

and ds_{ij} is incremental shear stress tensor, $d\varepsilon_{ij}$ is incremental strain tensor, $d\sigma_{ii}'$ is incremental effective volumetric stress, G is shear modulus, $d\lambda$ is the increment of λ, and superscripts d and v mean deviatoric and volumetric, respectively.

To determine the internal variables Z and λ in Eq. (9), ξ, F and L have to be calculated from 14 constants: α_1, α_2, α_3, α_4, β_1, β_2, C_1, C_2, C_3, C_4, C_5, τ_1, τ_2, and Z_1. These are all determined using data of cycling, constant strain rate tests on clay isotropically consolidated under different effective stresses. A trial and error procedure was used to vary the parameters to reproduce these data curves. Parameter values were computed by Krizek, et al. [42] for New Field clay and are given in **Table 2**. These values were then used to obtain the predicted curve of axial strain versus number of cycles shown in **Figure 3**, and also for the predicted curve of pore pressure versus number of cycles shown in **Figure 4**. The close agreement of predicted and measured values show the ability of the model to handle cyclic loading of clay.

The endochronic model of Krizek et al. [42] has many attributes. Model predictions correlate well with observed stress-strain behavior. The constitutive equations are time-dependent since time is internal to the equation. Increases of pore pressure and axial strain owing to cyclic loading were predicted with fair accuracy. A major drawback of the model is that none of the parameters can be directly linked to cohesion since the parameters do not have any simple physical representation. Also, the method the authors used to determine parameters is not clear at this point, except that a statistical approach was used

Table 2. Parameter values for New Field clay [42]

Parameter	Value
Z_1	0.0155
α_1	4
α_2	25
α_3	10
α_4	0.75
β_1	15
β_2	2
C_1	2.2
C_2	1500
C_3	0.25
C_4	4500
C_5	35,000

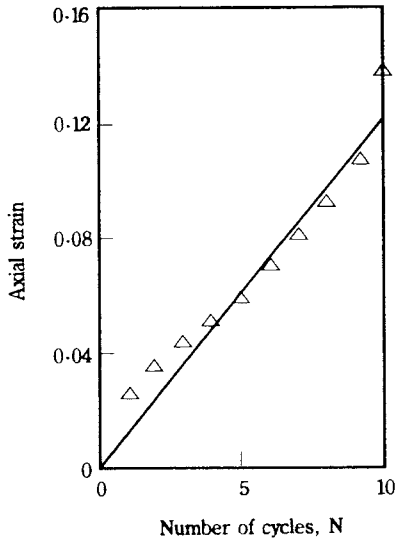

Fig. 3. Axial strain of New Field clay for constant strain-rate cyclic test [42]. Symbols indicate actual data and the curve is predicted behavior.

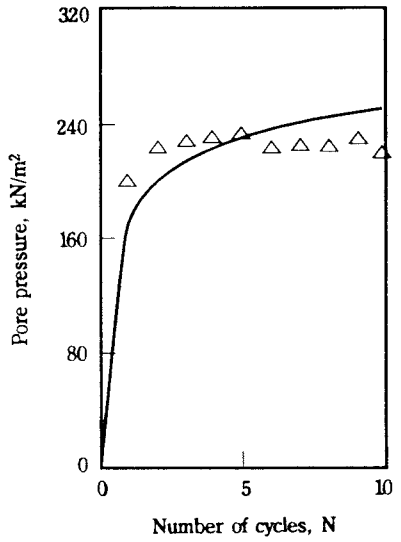

Fig. 4. Pore pressure of New Field clay at constant strain-rate [42]. Symbols indicate actual data and the curve is predicted behavior.

to determine the parameter values.

Both of the endochronic theory based models discussed in detail [42, 43] have the potential to predict the load response of selected food and agricultural products over a limited load range. References are cited [9, 10] where sand models were used for wheat. Feda [44] has published yield loci data on wheat, sugar, and lentils, and these fall in a form consistent with sands and clays. Finally, triaxial testing of sugar and flour show experimental trends similar to clays [45]. All of these results encourage further exploration of the models reviewed as candidates to be applied to food and agricultural materials.

The Cam clay model is a basic soil model upon which many other constitutive models are based. It provides adequate results for predicting soil behavior in conventional triaxial tests as well as in consolidation analysis and for determining foundation strengths. In addition, the model is relatively easy to use and understand. For these reasons, the Cam clay model was a logical starting point for application of soil models to dry cohesive powders under compaction.

3. Experimental Procedure

The modified Cam clay model requires the following tests for parameter determination [12]:

(1) Three conventional triaxial compression (CTC) tests, with the pore line ported to atmosphere, each at different confining pressures. These tests are referred to as drained tests.

(2) Three constant volume, triaxial compression tests, each at different confining pressures. These tests are referred to as undrained tests.

(3) Three constant mean effective stress (MES), triaxial compression tests, each at different mean effective stresses. The tests are referred to as MES tests.

(4) One hydrostatic triaxial compression (HTC) test with three unloading-reloading cycles. This test is referred to as the isotropic or HTC test.

Since all tests were designed for soils, particularly in saturated states, confining pressures are meant to be applied using a liquid medium. Given that dry powders are typically in unsaturated states and have low moisture contents when compared to saturated soils, it was considered more appropriate to use air as the pressurizing medium, as performed by Zhang et al. [46] and Bock et al. [47]. Specimen pore pressure was recorded and converted into corresponding volumetric change in specimen pore space. A schematic of the conventional triaxial tester used in this study is shown in **Figure 5.**

Drained tests are fairly straightforward in analysis and procedure. The triaxial specimen is axially compressed along the longitudinal axis via the Instron crosshead, which moves at a constant displacement rate and houses the load cell. Movement of the load cell was accurate to within 10^{-2} mm, which is within 10^{-4}% of the specimen height and sufficiently accurate for this investigation. A constant confining pressure is applied in the chamber (σ_3 = constant). Confining pressure was measured by a transducer (Omega model PX612-100GV, accurate to 0.7 kPa). Pore air is ported to the atmosphere, thus draining the specimen. To measure the volumetric change for the

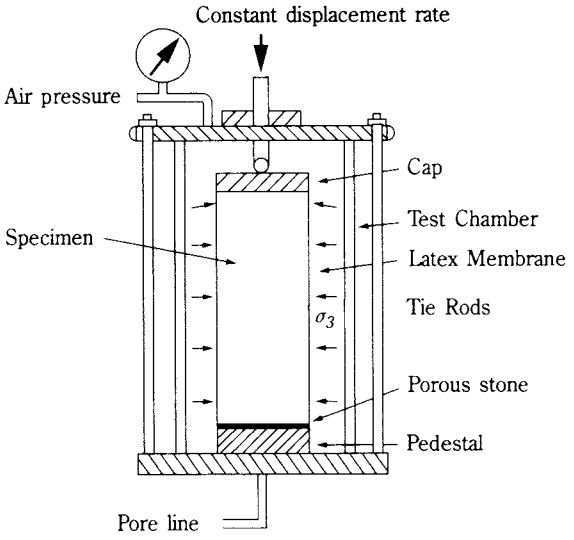

Fig. 5. Schematic of the triaxial testing apparatus.

drained tests, the pore line was ported to atmosphere after certain increments of pore pressure (0.5 kPa) accumulated. These increments were then summed at the end of each test. Drained tests were run at three confining pressures, as shown in **Table 3**.

Undrained tests posed particular problems, since, by definition, they are constant-volume tests. For dry, compressible powders, constant volume is not possible, since there are no saturated states as with soils. For undrained tests, the best that could be done was to close the pore line to have constant-mass tests, and monitor the pore pressure change. Confining pressures used for the undrained tests are shown in **Table 3**.

The mean effective stress (MES), p', is defined as:

$$p' = (\sigma_1 + \sigma_2 + \sigma_3 - 3u)/3$$

which becomes for triaxial conditions:

$$p' = (\sigma_1 + 2\sigma_3 - 3u)/3 \qquad (10)$$

where u is the fluid pressure developed in the pore spaces of the powder. For the MES tests, the effective stress was held constant by altering the confining pressure, σ_3, in proportion to the increase in σ_1 supplied by the crosshead and the change in pore pressure. The mean pressures tested are shown in **Table 3**.

Table 3. Treatment of triaxial tests

Test type	Conditions
Drained	σ_3 = 24, 34 and 45 kPa
Undrained	σ_3 = 24, 34 and 45 kPa
MES	initial σ_3 = 104, 138 and 172 kPa
Isotropic	3 cycles: 21-34, 21-48 and 21-76 kPa

4. Finite Element Model

The FEM used was the fourth generation model in a series of useful models [48-51]. There are three components of the discretized system: 1) the stored material; 2) the structure (wall) surrounding the material; and 3) the interface between wall and material.

It is important to note that the global stiffness matrix, $[K]$, depended upon the strain and stress states of the elements. Strain and stress were likewise dependent upon the displacements of the nodes of the elements. In effect, $[K]$ was a function of global displacement vector $\{U\}$, more adequately expressed as $[K(\{U\})]$, and was non-linear. For the compaction cylinder, surcharge pressure, applied to the top of the powder mass, was divided into incremental pressures. Element force vectors $\{f\}$, were determined for an increment of pressure for each powder element, then inserted into the global vector $\{F\}$. Finally, an iterative routine was used to solve for $\{U\}$, (**Figure 6**) to converge the residual of the vector sum $[K]\{U\}-\{F\}$ below a tolerance value. If the residual was below tolerance, then a solution for $\{U\}$ was assumed and the program proceeded to the next pressure increment. If, however, the residual was not below tolerance, $\{U\}$ was changed (which also changed $[K]$) with the aim of reducing the residual below the tolerance. The number of iterations needed for convergence, in general, was less than seven, and so the maximum number of iterations was set to 50. If 50 iterations were exceeded, the program quit, meaning a force balance could not be reached. The solution routine was repeated for each pressure increment. A detailed discussion of element stiffness matrices, element property matrices, i.e., wall, powder and interfaces, is reported by Tripodi et al. [52].

Because a compressible powder was modeled (wheat flour), large deformations had to be accounted for during compaction. Deformations of 30% of the original height of the powder compact were expected. Such large deformations would result in nonsense terms generated for total strains (greater than 100%) if a domain change was not incorporated into the FEM. In order to simulate the compaction test in the FEM, four guiding rules were followed: i) incremental strain was calculated for all elements, and, if the total became too great ($>0.2\%$), the nodes were released from the fixed locations and the geometry allowed to adjust to the strain; ii) the entire mesh was reconfigured when the criterion in step (i) required it; iii) once a mesh (domain) change occurred, initial

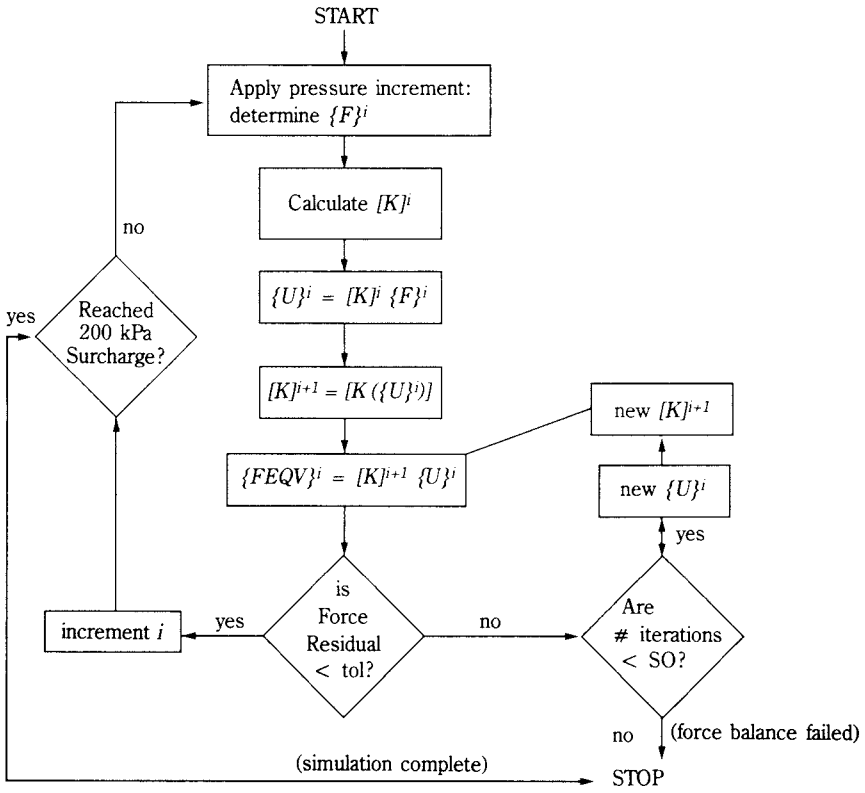

Fig. 6. Flow chart of the solution routine for the finite element model.

stress and strain states, as well as voids ratios, were calculated for the new mesh; and, iv) stress and strain information was stored for all domains used. Based on these guiding rules, the FEM checked all powder element vertical strains (ε_{zz}) to see if any exceeded a level of 0.2% strain. Once a mesh change had been implemented, element stresses, strains and centroid coordinates were stored. Since the FEM was the type of model that applied incremental loads to the top boundary, vertical displacements for the top layer nodes were different. These vertical displacements for nodes at the top layer of the mesh were averaged to find a single value for vertical domain change. A radial domain change was subsequently calculated using the radial displacements of the wall elements. Once radial and vertical changes were calculated, the dimensions of the domain were adjusted and a new mesh configured to represent the powder mass. For the new mesh, any differences in nodal displacements at the top loading boundary were corrected by nullifying all initial displacements.

5. Compaction Cylinder Tests

It was important to test the constitutive models in an application that reflected common industrial applications. To achieve this aim, a compaction cylinder was constructed that used an INSTRON loading device to axially compress a flour sample prepared in an aluminum cylinder. A 60.6 mm diameter × 121 mm height, 1 mm wall thickness, aluminum cylinder was built. This cylinder was instrumented with 45° rosette strain gages (Micromeasurements, Model # CEA-13-125UT-350). These rosettes provided strain measurements in three orientations – hoop, 45°, and vertical – for the cylinder at each location. Gages were arranged vertically in three strips and attached to the cylinder at 120° spacing. Along each strip, rosettes were attached at three levels: TOP level at 89 mm from cylinder base, MIDDLE level at 57 mm from base, and BOTTOM level at 25 cm from the base. A schematic of the test cylinder with dimensions and gage locations is shown in

Figure 7. Axial load, crosshead displacement and strain values for each gage were recorded as the powder sample was axially strained at an initial strain rate of $\dot{\varepsilon}(t)$ = 0.0825% per min.

6. Test Results and Comparison with Finite Element Modeling

6.1 Compaction test results

The Cam clay model was developed with the goal of predicting failure in soil masses due to foundation or embankment loads; typical applications of soils. For these conditions, water can seep through the soil mass, and soil particles rearrange and settle in reaction to the applied loads. Loads may become quite large, and the soil matrix experiences elastic stress states followed by elastic-plastic states. Finally, if loads become too great, the material fails in shear and yields. Yielding continues until the critical state is reached. Stress-strain predictions under these conditions can be readily handled.

Under the compaction loading, however, there were different constraints put on the particulate material. The particulate mass was confined in all directions by the cylinder wall and the cylinder floor. These constraints forced the material to stiffen during loading. The Cam clay model does not accommodate an increase in stiffness, nor does it allow any dependence of its parameters on stress. As shown in **Table 4**, all parameters are fixed values determined from specified triaxial tests [53] and do not vary with applied stress levels. Compaction loading, unlike triaxial loading, stiffened the wheat flour during strain, and the simple definition of some parameters, particularly the elastic parameters, were insufficient at high stress levels.

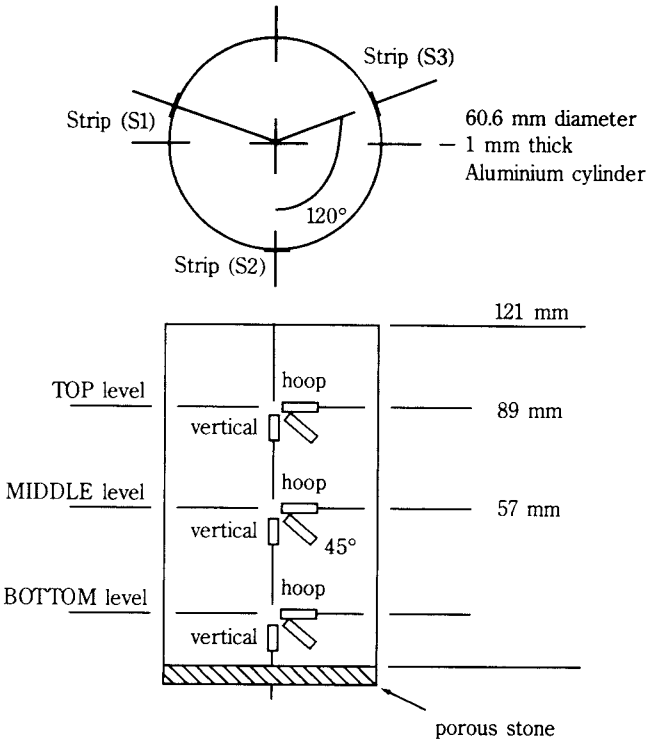

Fig. 7. Schematic of compaction cylinder with strain gages

6.1.1 Dependence of Cam clay parameters on stress path and pressure

All of the Cam clay parameters were determined using the set of triaxial tests shown in **Table 3**. The confining pressures and mean effective stresses used for these tests were chosen based on test experience using wheat flour. By definition, Cam clay parameters do not vary with applied stress, and the pressure levels used to determine the parameters were considered adequate. It was shown in the data used to determine material parameters [53] that parameter values changed at different pressure levels, but mean values were chosen to predict load curves, with good results.

However, chosen pressure levels, and the consequent parameter values that were determined, had a significant impact on the FEM termination level. For example, parameter M was changed from the value of 2.1, calculated using the triaxial data, to a lower value of 1.1, the lower value meaning an increase in strength in the material. The FEM simulated stress states to the desired level of 200 kPa. Originally, for $M=2.1$, the FEM terminated at a pressure level of 46.2 kPa. Thus a stiffer material resulted in the FEM running to a higher pressure. Similar results occurred when altering λ, $\varkappa$, and p_c, as well as for elastic parameters E and K. If calculated parameter values were altered in ways that stiffened the material, the FEM simulated powder response greater than

Table 4. Modified Cam-clay parameters for wheat flour [53].

Parameter	Value
Critical state	
λ	0.13
$\varkappa$	0.022
M	2.1
Elastic	
E	4.9 MPa
K	4.2 MPa
Initial	
e_0	1.06
p_c	45 kPa

the base value of 46.2 kPa. Likewise, softening the material caused a quicker program termination. Inspection of the stress states and property matrices during these numerous FEM simulations made it clear that one or more elements had reached a critical state. Elements at the critical state cannot accept more load. But the powder mass, being restrained by the aluminum cylinder, increased stress in the powder mass, which attempted to stiffen the material. A force balance was not reached, and the program terminated. Note that it would require only one element to reach the critical state and create a force imbalance, causing program termination.

Vertical strains in the compaction cylinder, predicted using the Cam clay model in the 4th generation FEM, agreed well with average measured values for surcharge pressures between 0 and 59.4 kPa surcharge [52]. However, predicted hoop strains in the compaction cylinder were somewhat satisfactory only for the BOTTOM level of strain gages [52].

6.2 Predicted stress distribution in the powder compact

The mesh used for all FEM simulations, showing respective element numbers, is illustrated in **Figure 8**. Mesh size (number of elements) was determined by running preliminary analyses on the FEM. The smallest mesh size (least number of elements) was chosen that provided the desired predictive capabilities.

Figures 9 and **10** give the horizontal-plane and vertical-plane stress distributions, respectively, in the compaction cylinder using the FEM simulation, and for a surcharge pressure of 20 kPa. Horizontal-plane stress distributions are given with respect to sections cut in the compaction cylinder at planes corresponding to the TOP, MIDDLE and BOTTOM gage locations. In Figure 8, TOP and BOTTOM planes correspond, respectively, to the elements at the 87.2 mm and 21.5 mm heights displayed. The MIDDLE plane corresponds a level between the 47.6 mm and 60.8 mm heights in **Figure 8**. In effect, the horizontal-plane stress distributions show hoop and vertical stresses as they varied moving outward from powder mass center to the wall, along the TOP, MIDDLE and BOTTOM planes. For labeling purposes, hoop-direction stress for the TOP level will be termed T, H; vertical-direction stresses for the TOP level will be T, V; MIDDLE hoop-direction stresses will be M, H; MIDDLE vertical-direction stresses will be M, V; BOTTOM hoop-direction stresses will be B, H; and BOTTOM vertical-direction stresses will be B, V. With regard to the FEM output, all stresses were applied at element centers in the finite element

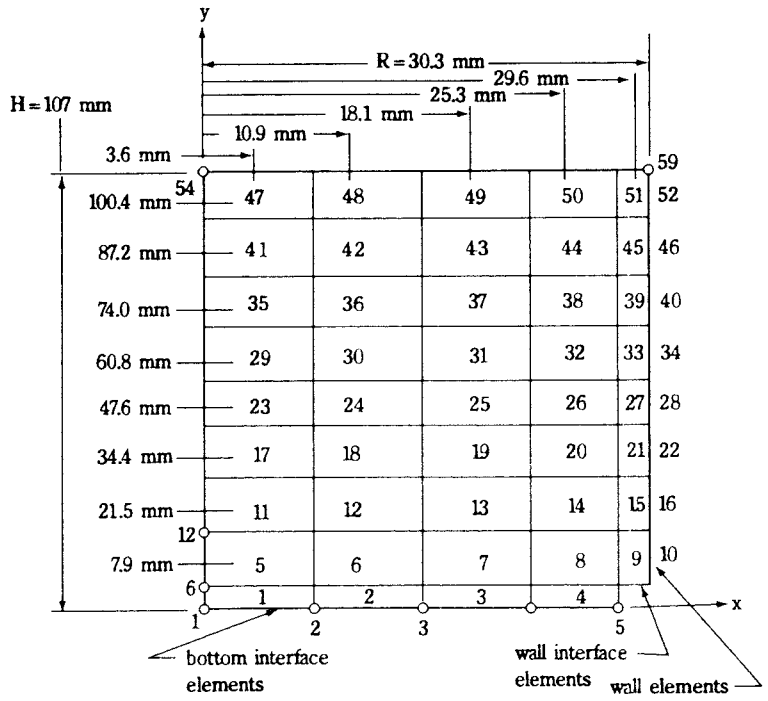

Fig. 8. Finite element mesh, with element numbers and initial dimensions (not to scale).

mesh. Therefore, locations of the element centers form the abscissa of the plot in **Figure 9**. Stress points at the element centers are linearly connected to approximate the distribution between the distinct elements.

Vertical-plane distributions are given with respect to section cuts along planes parallel to the cylinder centerline. These planes correspond to the radial values of 3.6 mm and 25.3 mm shown in **Figure 8**. These radii refer to the powder elements along the centerline of the compaction cylinder (3.6 mm) and the elements nearest the wall interface (25.3 mm). In effect, vertical-plane distributions show how powder stresses varied throughout the depth of the compaction cylinder. Again, stresses were applied at element centers; the locations form the ordinate of **Figure 10**. For labeling purposes, vertical-plane distributions for hoop-direction stresses near powder mass center will be termed C,H; vertical-direction stresses near center will be C,V; hoop-direction stresses near wall will be W,H; and vertical-direction stresses near wall will be W,V.

Vertical stress distributions at TOP and MIDDLE (**Figure 10**) were in agreement with the findings of Thompson [54]. Actually, Thompson proposed a parabolic stress distribution for a ram-on-compact. It is apparent that if stresses of T,V (**Figure 10**) were curve-fit, a parabolic curve would be appropriate. At BOTTOM, vertical and hoop stresses were essentially zero since most of the load was taken out by the walls at BOTTOM. In Figure 10, hoop stresses at the wall tell an involved story. From 60 mm above cylinder base to the top loading boundary, hoop stresses at the wall are tensile. More comprehensive visual aids regarding the distribution of stresses in the powder mass are given in **Figures 11** and **12**. Two directions of stresses are illustrated, shear (rz) and hoop ($\Theta\Theta$), in **Figures 11** and **12**, respectively. Contour lines, i.e. constant stress lines, are given in intervals of 2 kPa. **Figure 11** illustrates how predicted shear stresses in the powder mass accumulated near the intersection of the loading boundary and the retaining wall, which is also the intersection of the powder-wall interface and the top of the powder mass. The interface friction component pulls greatest at the area of load concentration (top of the powder mass) and causes the greatest distortion of powder elements (high shear stresses) near the wall. The result was a reversal in direction of hoop stresses, from compressive to tensile stresses near the wall of the cylinder (**Figure 12**).

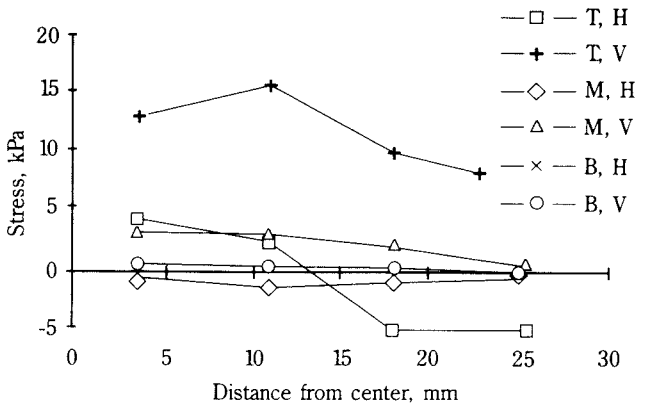

Fig. 9. FEM predicted Horizontal-plane stress distributions at 20 kPa pressure.

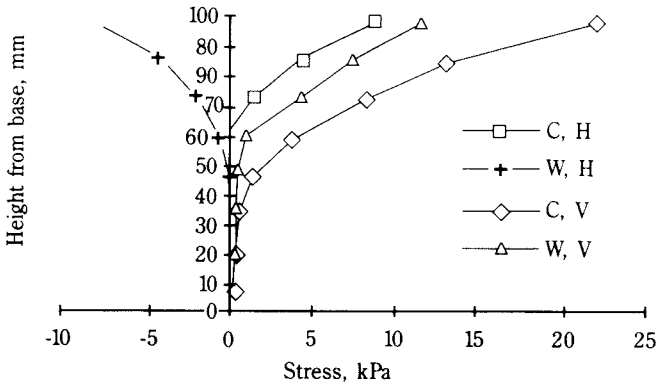

Fig. 10. FEM predicted Vertical-plane stress distributions at 20 kPa pressure.

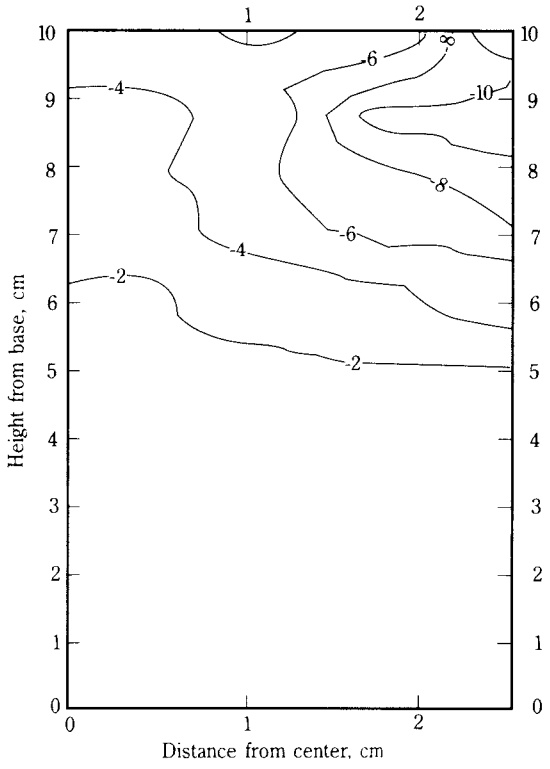

Fig. 11. FEM generated Iso-shear stress contours at 20 kPa pressure.

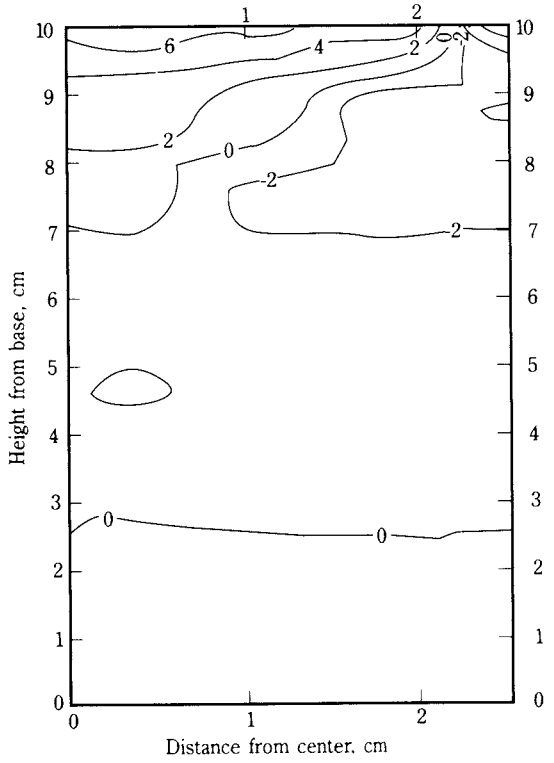

Fig. 12. FEM generated Iso-hoop stress contours at 20 kPa pressure.

7. Conclusions

This study has shown that the Cam clay model is adequate for predicting the powder's stress state for low loading conditions. However, for the high loading conditions characteristic of ceramic compaction, pharmaceutical tabletting, or pelletizing modifications in the model will be required to adequately handle the characteristic large deformations, and high shear and tensile stresses of these processes. Another problem identified by these studies is that constitutive parameters are not constant over a wide range of loading conditions. Also, the prediction capability of the FEM is sensitive to definition of the powder-wall interface elements. However, by identifying these issues, it appears that the Cam-clay model can be applied to higher stress situations once the necessary modifications are incorporated into the testing program (i.e. constitutive parameter determination) and the model refined and expanded.

Acknowledgments

This research was funded by the E. I. du Pont de Nemours and Company, Wilmington, DE, the Particulate Materials Center at the Pennsylvania State University, and by the Pennsylvania Agricultural Experimental Station. Wheat flour was supplied by the Kellogg's Company.

References

1) S.J. Lukasiewicz and S.J. Reed. Am. Ceram. Soc. Bull. (1978) 57:798-805.
2) C.W. Nies and G.L. Messing.J. Am. Ceram. Soc. (1984) 67:301-304.
3) R.L. Kondner.J. of Soil Mechanics and Foundations Division, ASCE, SM1 (1963), 115-143.
4) H. Kuno and J. Okada.Powder Technol., (1982), 33: 73-79.
5) A.F. Saleeb and W. F. Chen, (1980) New York, ASCE.
6) P.V. Lade. J. of Soils and Structures, (1977), 13:1019-1035.
7) J. Ghaboussi and H. Momen. Modeling and analysis of cyclic behavior of sands. In: Pande, G.N., Zienkewicz, O. C. (eds). Soil mechanics-transient and cyclic loads. New York, NY, John Wiley, 1982.
8) R.R. Young. Ph. D. Dissertation, The University of California, Berkeley, California, (1982).
9) Q. Zhang, V.M. Puri and H.B. Manbeck. Transactions of the ASAE, (1986), 29(6):1739-1746.
10) Y.Li, V.M. Puri and H. B. Manbeck. Transactions of the ASAE, (1990), 33(6):1984-1985.
11) K. Terzaghi and R.B. Peck. Soil Mechanics in engineering practice. (1948), New York, John Wiley.
12) C.S. Desai and H.J. Siriwardane. Constitutive laws for engineering materials with emphasis on geologic materials, (1984) Prentice-Hall, Inc., Englewood Cliffs, NJ.
13) A.W. Jenike. Bulletin 123, (1964) Utah Engineering Experimental Station, University of Utah, Salt Lake City, UT.
14) D.C. Drucker and W. Prager. Quarterly of Applied Mathematics, (1952), 10(2):157-165.
15) A.N. Schofield and C.P. Wroth. Critical-state soil mechanics. (1968) London: McGraw-Hill.
16) Z.P. Bazant, A. M. Ansal and R.J. Krizek. Endochronic model for soils. In: Pande, G. N.: Zienkewicz, O.C. (eds). Soil mechanics-transient and cyclic loads. (1982) New York, John Wiley.
17) P. Peryzna.Advances in Applied Mechanics, New York, Academic Press, (1971), 2:313-354.
18) A.J. Matchett. Powder Technol., (1987), 51: 167-178.
19) O. Molerus. Powder Technol., (1978), 20:161-175.
20) M.A. Tripodi, V.M. Puri, H. B. Manbeck and

G.L. Messing. J. Ag. Engrg. Res., (1992), 53:1-21.
21) P.T. Stainforth and R.C. Ashley. Powder Technol., (1973), 7:215-243.
22) M.D. Ashton, D.C.-H., R. Farley and F.H.H. Valentin. Rheologica Acta, BA and 4, Heft 3, (1965), pp. 206-218.
23) O. Molerus. Powder Technol., (1975), 12:259-275.
24) R. Nova. Symposium on Geotechnical Aspects of Coastal and Offshore Structures, Bangkok, December 1981, p. 47-59.
25) M.J. Pender. A model for the cyclic loading of over-consolidated soil. In: Pande, G.N.: Zienkewicz, O.C. (eds). Soil mechanics – transient and cyclic loads (1982), New York, John Wiley.
26) Y.F. Dafalias, L.R. Herrman, and A. Anandarajah. International Conference on Recent Advances in Geotechnical Earthquake Engineering and Soil Dynamics (1981), 1:139-144.
27) Y.F. Dafalias, L.R. Herrman and J. DeNatale. Limit equilibrium, plasticity and generalized stress-strain in geotechnical engineering (1981), New York, ASCE.
28) A. Anandarajah. NUMETA 85, Numerical methods in engineering: theory and application (1985), Rotterdam. A.A. Balkema, p.455-464.
29) J.P. Carter, J.R. Booker, and C.P. Wroth. A critical state soil model for cyclic loading. In: Pande, G.N.; Zienkewicz, O.C. (eds). Soil mechanics-transient and cyclic loads (1982), New York, John Wiley, p.219-252.
30) J.H. Prevost. Proceedings of the NATO Advanced Study Institute, Lisbon, Portugal (1982), pp.79-101.
31) D.J. Naylor. International Journal for Numerical Methods in Engineering (1985), 21:1187-1204.
32) H. Hirai. Soils and Foundations, 1989, 29(3):14-24.
33) F. Oka, T. Adachi, and Y. Okano. International Journal for Numerical and Analytical Methods in Geomechanics (1986), 10:1-16.
34) M. Matsui. Soils and Foundations (1988), 28(4): 19-37.
35) K.H. Roscoe, A.N. Schofield and C.P. Wroth, Geotechnique (1958) 8 22-43.
36) M. Hvorslev, Ingeniorvidensk. Skri. Ser., A (1937) No. 45.
37) G.D. Gilbert. Ph. D. Thesis, London University, UK, 1954.
38) A.M. Britto and M.J. Gunn. Critical State Soil Mechanics Via Finite Elements (1987), Ellis Hardwood Limited, Chichester.
39) D.M. Wood. Soil Behavior and Critical State Soil Mechanics, (1990) Cambridge University Press, Cambridge, UK.
40) T. Adachi and F. Oka. Soils and Foundations (1982), 22(4):57-70.
41) J. Trasorras, T.M. Krauss, and B.L. Ferguson. Advances in Powder Metallurgy, Volume 1. American Powder Metallurgy Institute, Princeton, NJ, (1989).
42) R.J. Krizek, A.M. Ansal and Z.P. Bazant. Proceedings of the ASCE Geotechnical Engineering Division, Special Conference Earthquake Engineering and Soil Dynamics (1978), 1:557-568.
43) A.M. Ansal, Z.P. Bazant, and R.J. Krizek. Prediction of soil behavior by endochronic theory. In: Yong, R.K.; Ko, H.-Y. (eds). Limit equilibrium, plasticity and generalized stress-strain in geotechnical engineering (1980), New York, ASCE.
44) J. Feda. Mechanics of particulate materials. Amsterdam, The Netherlands (1982), Elsevier.
45) S. Kamath, V. M. Puri, H. B. Manbeck and R. Hogg. Powder Technol., 76 (1993) 277-289.
46) Q. Zhang, V.M. Puri and H.B. Manbeck, Transactions of the ASAE, 29 (1986) 1739-1746.
47) R. Bock, V.M. Puri and H.B. Manbeck. Transactions of the ASAE, 32 (1989) 1701-1708.
48) Q. Zhang, V.M. Puri and H.B. Manbeck. Transactions of the ASAE, 30 (1987) 1797-1806.
49) V.M. Puri and H.B. Manbeck. ASAE Paper No. 91-4076 (1991), ASAE, St. Joseph, MI.
50) Q. Zhang. Ph. D. Dissertation, The Pennsylvania State University, University Park, PA. 1987.
51) Y.Li, V.M. Puri, and H.B. Manbeck. Transactions of the ASAE, 34 (1991) 2207-2215.
52) M.A. Tripodi, V.M. Puri, H.B. Manbeck and G.L. Messing. Powder Technol., (1995) (In press)
53) M.A. Tripodi, V.M. Puri, H.B. Manbeck and G.L. Messing. Powder Technol., 80 (1994) 35-43.
54) R.A. Thompson. Ceramic Bulletin, 60 (1981) 237-251.

Author's short biography

Virendra M. Puri

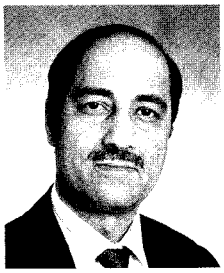

Dr. Virendra M. Puri is Professor of Agricultural and Biological Engineering at the Pennsylvania State University. Professor Puri is also the research thrust leader of Powder Storage, Flow and Handling group of the Particulate Materials Center. Dr. Puri received his B.S. from Indian Institute of Technology and M.S. and Ph.D. from the University of Delaware in Mechanical Engineering. Professor Puri's research interests include: measurement of fundamental engineering properties of powders, development and validation of constitutive models, and use of numerical methods to model flow and compaction behavior of powders. He has served as the chairman of the Bulk Solids Storage Systems Committee of the American Society of Agricultural Engineers. Dr. Puri regularly offers a post-graduate course in the area of powder mechanics and a hands-on industrial short course. Professor Puri has received several teaching and research awards.

Michael A. Tripodi

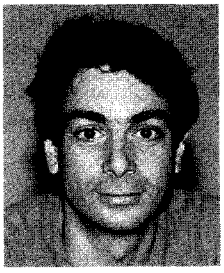

Dr. Michael A. Tripodi received his B.S. in Mechanical Engineering from Clarkson University. Dr. Tripodi received his M.S. in Agricultural Engineering from the Virginia Polytechnic Institute. He completed his Ph.D. in Agricultural Engineering and Biological Engineering from Penn State in 1994.

H.B. Manbeck

Dr. H.B. Manbeck is Professor of Agricultural Engineering in the Agricultural and Biological Engineering Department at the Pennsylvania State University. He earned the B.S. and M.S. Degree in Agricultural Engineering from the Pennsylvania State University and the Ph.D. from Oklahoma State University. He has held faculty positions at the University of Georgia, Ohio State University and has been at Penn State since 1980. He has conducted research on constitutive behavior of bulk solids and loads, especially thermal loads, in bulk solids storage structures since 1969. He is currently involved in cooperative research efforts between the Particulate Materials Center and the Agricultural and Biological Engineering Department at Penn State to develop rational models to predict stress states in bulk solids systems.

Gary L. Messing

Dr. Gary L. Messing is Professor of Ceramic Science and Engineering and Director of the Particulate Materials Center at The Pennsylvania State University. Dr. Messing received his B.S. in ceramic engineering from the New York State College of Ceramics at Alfred University and his Ph.D. in materials science and engineering at the University of Florida. He was a research scientist for two years at Battelle Columbus Laboratory before joining the Materials Science and Engineering Department faculty at Penn State. Dr. Messing is coorganizer of the International Powder Processing Conference series with H. Hausner and S. Hirano, and Editor of the Journal of the American Ceramic Society, and has served as Chairman of the Basic Science Division. Professor Messing received the Wilson Research Award at Penn State in 1992, a 1993 Richard M. Fulrath Pacific Award (U.S. recipient), and is a Fellow of the American Ceramic Society.

Ball Charge Dynamics in a Planetary Mill†

B. K. Mishra*
*Comminution Center University of Utah**
Salt Lake City UT 84112, U.S.A.

Abstract

Planetary mills are gaining importance in the area of ultrafine grinding. The charge motion inside the mill is complex and previous works have considered force balance on a single particle for motion analysis. The inherent difficulties of single particle force balance are avoided in the multiparticle numerical scheme called the discrete element method (DEM) presented here. Many interesting motion patterns develop as the operating parameters such as percent critical speed, ball load, etc., are varied. The application of the DEM code for the qualitative analysis of the charge motion is demonstrated.

1. Introduction

The concept of the planetary ball mill is not new; however, with the ever-increasing need to produce large volumes of ultrafine powder for ceramic applications, research interest has expanded since 1971. Planetary mills operate in a high-intensity acceleration field. This strong acceleration field is due to the movement of the ball mill itself about a center of gyration. In order to achieve this, the ball mill is situated on a gyration shaft that revolves about a center. Strong centrifugal forces are generated within the mill by the rotation of the shaft that give rise to higher grinding rates. In comparison to conventional ball mills, the power input per kilogram of balls in a planetary mill can be 10 to 100 times higher.

The planetary mill generates very high stresses compared to a ball mill and consequently offers better breakage kinetics and ultrafine comminution. These qualities are exploited in a mill called the high-intensity nutating mill, which is a centrifugal mill situated on a nutating axis [7]. In the 1970s, the planetary mill was thought of as a compact grinding mill in underground mining operations. Bradley et al. [2] described the development of a large-scale mill for mineral ore grinding. Since then much has been done to gain a better understanding of these mills [4, 8, 12, 17].

The dynamics of the charge inside any particulate material processing equipment is complex and difficult to characterize in terms of operating and design variables. It is particularly difficult in the case of a planetary mill. Joisel [9] analyzed the motion of balls in a planetary mill and provided a graphical scheme for constructing trajectories of the balls. Bradley [1] dealt with the same problem by proposing a rotating gravitational field and derived a relation for the critical gear ratio of a planetary mill. Hoyer [6] derived an analytical model of particle trajectory as a function of mill operating conditions. In this study, the predicted shape of the charge was found to be in excellent agreement with photographic evidence of the charge in motion. Schmidt and Korber [14] used the familiar force balance as well as dimensionless numbers to classify ball charge motion in a centrifugal mill. In a recent paper, Raasch [13] gives an analytical solution to the cataracting motion of balls, which interestingly leads to the impact velocity of grinding balls on the mill shell.

In all of the past works the motion of the ball charge is analyzed by a force balance on a single ball. Hoyer's work also takes the same approach and hence uses a single arbitrary parameter to arrive at predictions.

A description of the planetary mill and the underlying theory dealing with the dynamics of the charge is essential before a new model is presented. What follows here is a description of the mill in similar terms as developed by Hoyer [6]. **Figure 1** shows a configuration of the planetary mill where a ball mill rotates about a primary axis. Here D is the mill diameter and G is the diameter of rotation of the mill axis, also known as the gyration axis. Let R be the ratio of the speed of rotation of the mill axis to

* Asst. Professor, Dept. of Matls. & Met. Engg., I.I.T. Kanpur, Kanpur 208016, INDIA.
** Manuscript of lectures presented at the USBM Generic Mineral Technology Center for Comminution, Department of Metallurgical Engineering, University of Utah, Salt Lake City, Utah.
† Received 27 June, 1995.

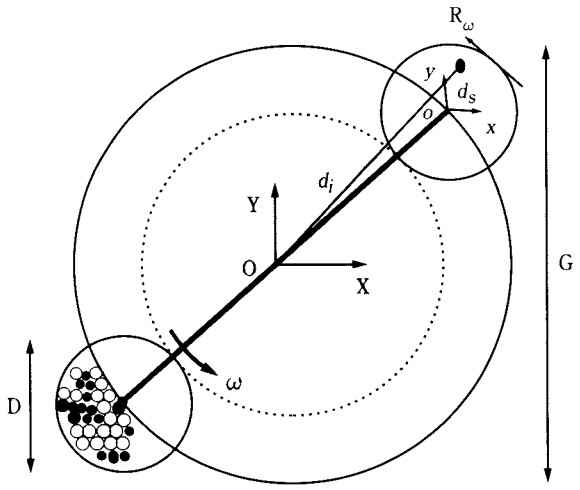

Fig. 1. Description of a planetary mill:The gyratory shaft O-o rotates about O and the mill rotates about o.

the speed of the rotation of the mill about its center. Then, if the shaft rotates at an angular velocity of ω, the mill rotates at $R\omega$ on the shaft, and therefore $(R+1)\omega$ relative to the earth. A negative value of R indicates that the mill and the shaft rotate in opposite directions. With this background, the analysis of the mechanics of a planetary mill with the discrete element method (DEM) is shown here. The analysis of charge motion is essentially a multi-body collision problem that is amenable to DEM analysis. DEM allows one to do parametric studies by varying the physical as well as the material properties. The purpose of this paper is to show that this numerical model accurately reproduces the qualitative behavior of the ball charge under different operating conditions and hence establishes it as a tool for future analysis.

2. Discrete Element Method

Primarily, the discrete element method is a scheme to simulate any problem dealing with the behavior of discontinuous particle systems. Mineral processing systems invariably deal with particulate materials of varying nature. Quantitative models characterizing these processing units often treat the particulate system as a continuum for mathematical simplicity. On the other hand, DEM allows modeling of hundreds of thousands of particles individually at the cost of significant computational work; it is this computational requirement that limits its acceptance. Nevertheless, DEM results are more reliable and give better insight to the micro-mechanical processes occurring at the particulate level.

The discrete element analysis starts with a description of elements or entities comprising the physical system. In a two-dimensional representation of a simple system such as tumbling mills, these elements could be simply line-type or disc-type or both. More complex systems are modeled using superquadric elements to study spatial behavior of particulates in three dimensions. Regardless of dimensions, first a numerical scheme is needed to detect contact between elements or entities. After establishing the contact for any given element and its relative displacement, the force balance equations of DEM are solved next. These are the translational and rotational equations of motion, and a contact deformational equation. In the case of damping, additional terms defining the damping behavior of the material may be incorporated into the contact deformational equation. These equations are presented below in their most compact form,

$$[M]\ddot{x} + [C]\dot{x} + [K]x_i = \{f\} \tag{1}$$

where x is the displacement, $[M]$, $[C]$, and $[K]$ are the mass, damping, and stiffness matrix, and f is the applied load. Integration of this equation for x is done by the explicit central difference time-marching scheme. Details of the computational procedure are given in the Appendix in accordance with the pioneering work of Cundall and Strack [3].

The main calculation is done under a time-increment loop, and since DEM analyses require tens of thousands of time steps, an efficient contact detection algorithm is mandatory. Once one element's contacts with other elements are established, the next task is to compute the relative velocity between the contacting elements. From the relative motion of neighboring elements and the interaction relationships, contact forces between these elements are computed. These contact forces are then computed for all of the neighboring contacts and are summed for each element. Applied forces resulting from environmental conditions such as buoyancy, drag, or adhesive forces are also computed for each element. By stepping in time, the motion of the elements is computed from the dynamic equilibrium equation. The entire solution procedure is repeated for the next time step after updating the coordinates and potential neighboring contacts for each element.

A natural application of DEM is for the motion of spherical steel balls in tumbling mills. Here the motion is imparted to balls by the movement of the

mill shell itself. The DEM technique has been well exploited for impact energy spectra, power, and dynamic porosity predictions in laboratory, pilot-scale, and industrial-size ball mills [10, 11]. Yokoyama et al. [15, 16], in their comprehensive treatment of vibration milling by DEM, showed that the breakage rate of glass particles increases linearly with the collision frequency of balls in the mill. The unmeasurable quantities such as impact energy spectra, ball-wall impact forces, collision frequency, etc., make the DEM technique unique against the background of traditional models.

In the DEM formulation of a planetary mill, some additional forces come into play, and hence the force balance is modified as follows. The acceleration on any given particle is found by

$$\sum F_i = m\ddot{x}_i = ac_i = ao_i \qquad i = 1,2 \tag{2}$$

where aci and aoi are Coriolis and centrifugal acceleration, respectively, and m is the mass of a ball. In reference to **Figure 1**, the position of any ball in one coordinate system can be changed to another coordinate system by simple transformation, and therefore it is easy to compute the acceleration of any given ball at a known position. The individual accelerations are computed as follows: The Coriolis acceleration is,

$$ac_i = 2d_s R\omega^2 \cdot e1_i \qquad i = 1,2 \tag{3}$$

and the centrifugal acceleration due to the gyrating shaft is

$$ao_i = dl\omega^2 \cdot e2_i \qquad i = 1,2 \tag{4}$$

Here $e1_i$ and $e2_i$ are the component of the unit vectors from the respective centers of motion to any ball under consideration. With these modifications to the generalized force balance equations shown in the Appendix, DEM produces the correct charge motion.

The concept of critical speed is also needed in the simulation of planetary mills. The acceleration field exhibits a maximum and minimum value at some locations within the mill. The critical speed corresponds to a condition where the absolute centrifugal acceleration due to the rotation of the mill about its own axis is so high that all the balls tend to lie against the shell throughout a cycle. Under the centrifuging conditions, it can be shown that

$$N_c = \frac{1 + R}{\sqrt{G/D}} \tag{5}$$

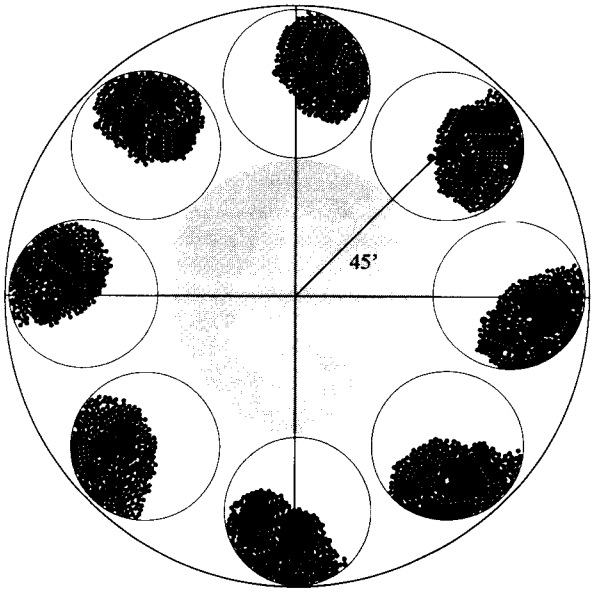

Fig. 2. Charge motion inside a planetary mill; R = −1.

where N_c is the fractional critical speed. Depending on the value of R, the term $\frac{1+R}{\sqrt{G/D}}$ could be positive or negative. It should be pointed out that there is a range of R over which the mill can be operated without centrifuging.

3. Numerical Results

In this numerical study, a 10 cm diameter mill situated on a 60 cm gyration shaft is simulated to study the charge during one revolution of the gyration shaft. This mill is loaded with 400 balls of 3-mm diameter, which fills the mill to 50% including charge porosity. For this mill it is found that the ratio of mill speed to gyration shaft speed, R, must lie within the range of −3.513 to 1.513. During one revolution, snapshots were taken at equal intervals of time, and the result of the simulation for $R = -1$ is shown in **Figure 2.** Here the mill rotates in a clockwise direction, and accordingly the shaft rotates in the opposite direction. It is seen from this figure that the charge within the mill is displaced in the direction of motion of the mill, which is the most common feature of charge dynamics in planetary mills.

In previous theoretical analyses [6, 13], the point of departure of a ball from the wall has been chosen arbitrarily, because in such single-particle theories it is not known whether other particles would be pressing against the particle in question. The con-

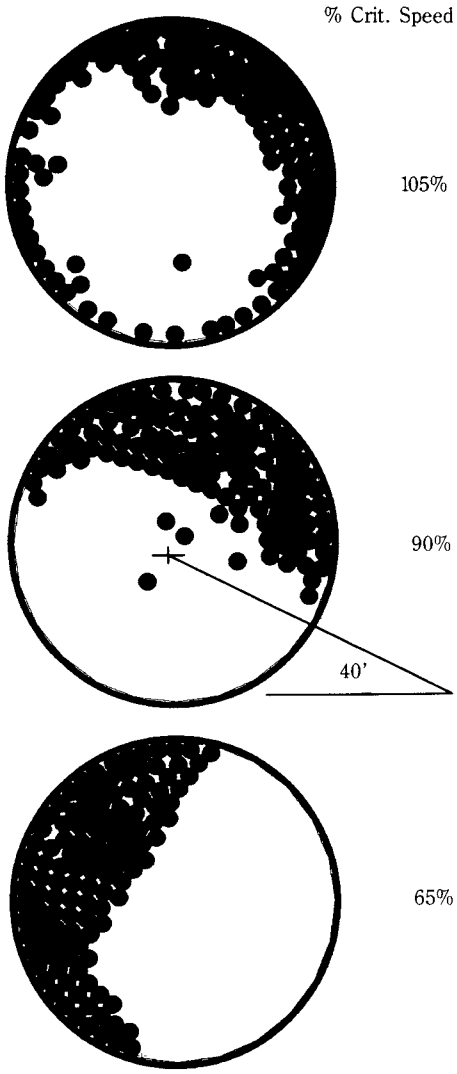

Fig. 3. Variation of charge profile with percent critical speed.

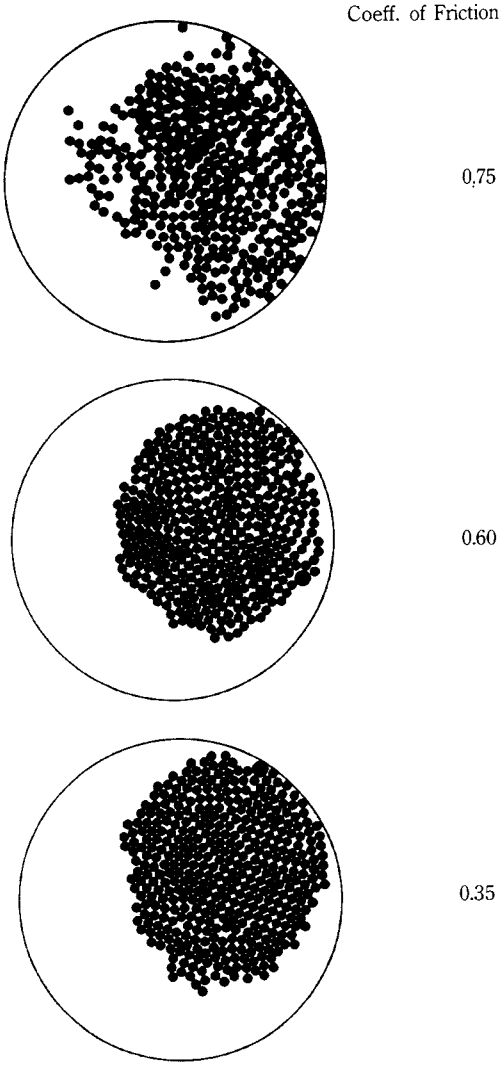

Fig. 4. Effect of the coefficient of friction on the charge profile.

venience of DEM in resolving such questions speaks for the power of such direct simulation schemes. It should be noted that DEM makes no assumptions in this regard except for setting ball-to-ball and ball-to-wall contact properties.

The motion of the charge is shown to vary with the relative speed of the mill in relation to the speed of the gyration shaft. In another simulation, the same mill that rests on a gyrating shaft of 60 cm is simulated. **Figure 3** shows three snapshots of charge motion at three critical speeds. In these simulations the gyrating shaft speed is kept at 33 rad/sec, while the mill speed is varied to attain 65%, 90%, or 105% of the critical speed. All these snapshots correspond to the same location of the mill in reference to the center of gyration. At 65% critical speed the motion is fully cascading, and at 90% cascading and cataracting is seen. Finally, at 105% the ball charge is fully centrifuged. Once again simplified analysis could not model cascading motion because of the complexity of inter-particle effects.

The profile of the charge in motion is also a strong function of the coefficient of friction. The effect of the coefficient of friction on charge motion and power draw has been neglected in almost all milling problems, and the planetary mill is no exception. In this

model the coefficient of friction is introduced at the contact points between sliding surfaces. The shear force at the contact is set to a maximum value if sliding occurs, and this maximum is μF_n where μ is the coefficient of friction. **Figure 4** shows the effect of the coefficient of friction on the overall motion of the charge at a fixed value of R. It is seen that not only does the charge profile change with the coefficient of friction, it also tends to become loose. As mentioned earlier, the highlight of the DEM simulation is that it predicts the frequency of collisions as a function of energy of individual collisions, called an impact energy spectrum.

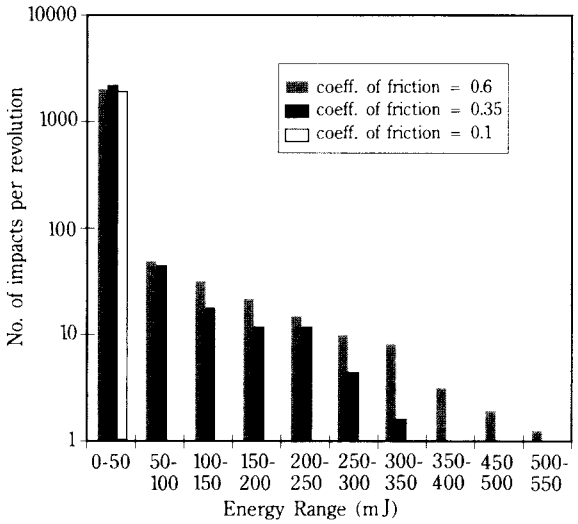

Fig. 5. Energy distribution in a planetary mill for three values of the coefficient of friction.

Figure 5 shows such a spectrum for the planetary mill. This energy is a dissipative energy due to damping and sliding at the contact point of collisions. It is seen from this figure that for $\mu = 0.4$ all the impacts are within an energy range of 0 to 50 mJ. When μ is increased to 0.6, an energy spectrum develops between 0 to 500 mJ. Here, in addition to low-energy impacts, more and more high-energy impacts occur; however, the energy dissipated due to sliding is much reduced. In this analysis it is found that more than 50% of the energy spent is due to sliding of layers of balls over one another. This intense sliding is the cause of temperature increase during grinding.

The ball filling has a direct bearing on the efficiency of grinding, as in other mills. However, in a planetary mill, unstable charge motion results when the ball filling is below a certain value, which in turn is a function of G/D [6]. This idea is best illustrated in **Figure 6.** In this figure, simulation results at fractional ball fillings of 0.75, 0.5, and 0.25 are shown. It

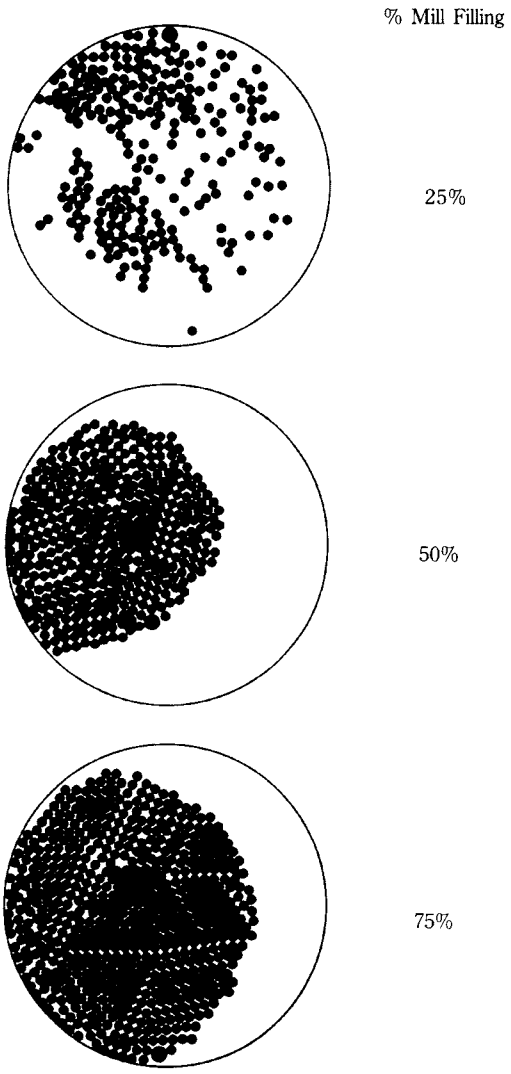

Fig. 6. Effect of ball filling on charge motion; R = −1.

is seen from the figure that the charge motion begins to collapse as the filling is decreased. For a complete understanding of this aspect, more careful simulations under different operating conditions with a greater number of particles are needed. Finally, it must be pointed out that the simulation results compare very well with the photographic results provided by Hoyer [6].

Summary

A numerical tool known as the discrete element method is used to analyze the complex dynamics of the charge within the planetary mill. A planetary mill

consisting of a 10-cm diameter mill connected to a 60-cm gyrating shaft is simulated. The following observations were made under different operating conditions.

- The charge profile is a strong function of percent critical speed. There is a window of operation established for the above planetary mill, $1.513 > R > -3.513$, above which the charge centrifuges, and thus different combinations of mill speed and shaft speed may be used to control power draw and breakage rate.
- The coefficient of friction plays an important role in the analysis of the charge. In the analytical formulations found in the literature to predict trajectories of balls and shape of the charge, this aspect has often been neglected. Here it is shown that charge tends to loosen when the coefficient of friction is high. Also, there is an increase in high-energy impacts with an increase in the coefficient of friction. The fraction of energy spent in sliding of balls ranges from 70 to 50% as the coefficient of friction is changed.
- The effect of mill filling is shown by analyzing the profile of the charge. With a decrease in the mill filling the charge appears to collapse. However, more careful study is needed to analyze this effect.

From the above results, the utility of the DEM technique to analyze the mechanics of a planetary mill is established.

Acknowledgement

The author wishes to thank Dr. Raj K. Rajamani for useful discussions and for the computer facilities to carry out this research. This research has been supported by the Department of the Interior's Mineral Institute Program administered by the U.S. Bureau of Mines through the Generic Mineral Technology Center for Comminution under grant number G1135249.

References

1. A. A. Bradley, *Some principles of centrifugal milling.* Preprint of the 3rd European symposium on comminution, 1971.
2. A. A. Bradley, A. J. Freemantle, and P. J. Lloyd, *Developments in centrifugal milling,* J. of South African Inst. of Min. and Metall. (1975), p. 78.
3. P. A. Cundall and O. D. L. Strack, *A discrete numerical model for granular assemblies,* Geotechnique, 29 (1979). p. 47.
4. R. L. Gamblin, *Centrifugal grinding and mixing apparatus.* U.S. Patent Appl. No. 427, 815, 1989.
5. R. W. Hockney and J. W. Eastwood, in Computer simulations using particles, McGraw-Hill Int'l Book Co., New York, 1981.
6. D. I. Hoyer, *Particle trajectories and charge shape in centrifugal milling.* Int. Conf. on Recent Advances in Mineral Sciences and Technology, Mintek, South Africa, 1984.
7. D. I. Hoyer and G. M. Boyes, *The high intensity nutating mills — a batch milling simulation,* Minerals Engineering, 3 (1990), p. 35.
8. G. Jimbo, *A new energy law of comminution for the ultrafine range.* Proc. of Particle Technology Forum, Denver, Colorado, U.S.A., 1994.
9. A. Joisel, *Planetary mills,* Rev. Mater. Constr. Trav. Publics No. 493 (1956), p. 234.
10. B. K. Mmishra and R. K. Rajamani, *Motion analysis in tumbling mills by the discrete element method,* KONA Powder and Particle (1990), p. 92.
11. —, *Simulation of charge motion in ball mills. Part 2: Numerical simulations,* Int. J. Miner. Process. (1994), p. 187.
12. K. J. Nilsen, *Milling of ceramic powders in a centrifugal barrel mass finisher (planetary centrifugal ball mill).* Proc. of Particle Technology Forum, Denver, Colorado, U.S.A., 1994.
13. J. Rraasch, *Trajectories and impact velocities of grinding bodies in planetary ball mills,* Chem. Eng. Technol., 15 (1992), p. 245.
14. P. Schmidt and R. Korber, *Planetary mills,* Aufbereitungs Technik, 32 (1991), p. 659.
15. T. Yokoyama, K. Tamura, and G. Jimbo, *A numerical analysis of the movement of balls in a vibration mill,* Int. Chem. Eng., 34 (1994), p. 611.
16. T. Yokoyama, K. Tamura, H. Usui, and G. Jimbo, *Numerical analysis of balls in a vibration mill in relation with its grinding rate,* KONA (1993), p. 179.
17. Q. Zhao, *Mechanism of fine grinding in a planetary mill,* PhD thesis, Nagoya University, Japan, 1989.

Appendix

The basic equations that are solved in DEM consist of translational and rotational equations of motion and a contact deformational equation. For a multibody collision-type problem, the contact detection and the contact interaction relationships constitute the major part of the computational need. The main calculation is done under a time-increment loop. Since DEM analyses require tens of thousands of time steps,

an efficient algorithm to detect contact is required. Once one element's contacts are established, the next task is to compute the relative velocity between the contacting elements. From the relative motion of neighboring elements and the interaction relationships, contact forces between these elements are computed. These contact forces are then determined for all of the neighboring contacts and are summed for each element. Applied forces resulting from boundary conditions such as buoyancy, drag, and adhesive forces are added to the force sum for each element. By stepping in time, the motion of the elements is computed from the dynamic equilibrium equation. The entire solution procedure is repeated for the next time after updating the coordinates and potential neighboring contacts for each element. Each of these individual steps are discussed below.

Decomposition of Contact Motion

The DEM code works with individual particles with normal and shear contact springs and dashpots. **Figure 7** shows two discs i and j are in contact; the discs have center coordinates (x_i,y_i) and (x_j,y_j), and radii r_i and r_j, respectively. Let the discs have translational and rotational velocities $(\dot{x}_i,\dot{y}_i,\dot{\theta}_i)$ and $(\dot{x}_j,\dot{y}_j,\dot{\theta}_j)$. The contact force determination is done by a series of calculations as outlined below. With the above terminology, the relative velocity of the discs can be found by defining the unit normal vector $\mu 1$ as

$$\vec{\mu}_1 = \cos\alpha\ \vec{x} + \sin\alpha\ \vec{y} \tag{6}$$

Here $\vec{x}$ and $\vec{y}$ are the unit vectors in the x and y directions, respectively. The unit tangential vector $\vec{\mu}_2$ from i to j is obtained by a clockwise rotation of $\vec{\mu}_1$ by 90 degrees. Therefore, the relative velocity of disc i with respect to j is

$$\vec{V}_r = [dv_x - \sin\alpha\cdot(\Omega)]\ \vec{x} + [dv_y + \cos\alpha\cdot(\Omega)]\ \vec{y} \tag{7}$$

where $dv_x = \dot{x}_i - \dot{x}_j$, $dv_y = \dot{y}_i - \dot{y}_j$ and $\Omega\ \dot{\theta}_i r_i + \dot{\theta}_j r_j$. The relative velocity is resolved in the normal and tangential directions.

Force Update

The interaction of balls at contact points is modeled as shown in **Figure 7.** A set of spring and dashpot in both normal and shear direction is employed. Knowing the incremental forces for the current time step, the force update for the next time step is done as follows:

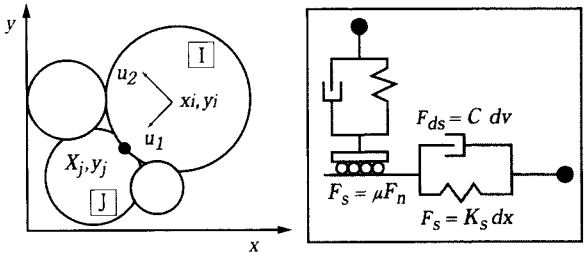

Fig. 7. Representation of a contact by a pair of spring and dashpot.

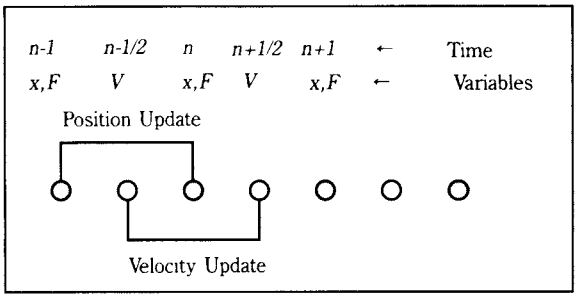

Fig. 8. Integration scheme for velocity and position update.

$$F_n(i+1) = F(i) + K_n\ \vec{V}_r\cdot\vec{u}_1\ \Delta t + \beta_n K_n\ \vec{V}_r\cdot\vec{u}_1 \tag{8}$$

and

$$F_s(i+1) = F(i) + K_s\ \vec{V}_r\cdot\vec{u}_2\ \Delta t + \beta_s K_s\ \vec{V}_r\cdot\vec{u}_2 \tag{9}$$

wheret Dt is the incremental time; K_n and K_s are the stiffness of the springs in the normal and tangential directions, respectively; and β_n and β_s are Rayleigh proportional damping constants for the normal and tangential dashpots.

The total shear force due to the spring is compared with the frictional force acting at the contact. The maximum of shear force that can exist at the contact is given by

$$F_{fr} = \mu \times F_n \tag{10}$$

where μ is the coefficient of friction. If $|F_s| > F_{fr}$, then slip is presumed to exist. In this case, the total contact force is calculated by setting the shear force to the maximum and the shear damping force to zero.

Integration Procedure

The contact forces acting on ball i from all contacts are summed, and the resulting total force is resolved in the global directions. Similarly the net moment acting on the body is determined. This force and moment can then be used to estimate the translational

and rotational accelerations. By integration of this acceleration, the velocity and displacement of the disc may be estimated.

A leapfrog integration scheme that uses a constant step is implemented. As shown in Fig. 8, the velocity of the disc is estimated at time step $n + 1/2$ by knowing the acceleration at the n^{th} time step:

$$V_x(n + 1/2) = V_x(n - 1/2) + \frac{d^2x_i}{dt^2} \Delta t \tag{11}$$

$$V_y(n + 1/2) = V_y(n - 1/2) + \frac{d^2y_i}{dt^2} \Delta t \tag{12}$$

Then the displacement of the disc is found by a further integration:

$$x(n + 1) = x(n) + V_x(n + 1/2)\,\Delta t \tag{13}$$

$$y(n + 1) = y(n) + V_y(n + 1/2)\,\Delta t \tag{14}$$

$$\theta(n + 1) = \theta(n) + \dot{\theta}\,(n + 1/2)\,\Delta t \tag{15}$$

The details of this integration procedure are best described by Hockney and Eastwood [5].

Once the new locations of the discs are obtained, the incremental contact velocities are computed by following the procedure outlined above; the new contact forces are found and the cycle is repeated. In the presence of damping force, the above integration scheme is modified by approximating the velocity as an average velocity as done in a central difference scheme.

Author's short biography

B.K. Mishra

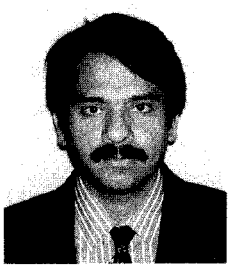

B.K. Mishra has a B.S. (1981) from REC Rourkela, India, and Ph.D (1991) from University of Utah. Prior to graduate study he was working as a project manager with Indian Metals. After two years of post-doctoral work at the comminution center of the University of Utah, he joined Indian Institute of Technology, Kanpur as assistant professor. He has been awarded with a research grant fro the Govt. of India to study the stratification problem in jig bed. His research interests are in crushing, grinding, classification, and minerals beneficiation. He is also engaged in research that deals with discrete element simulation of mineral processing problems.

Contamination and Sinterability of Planetary-milled Alumina†

Osami Abe
*Dept. of Mater. Sci., Faculty of Eng., Ibaraki Univ.,**

Abstract

Contamination of planetary milled alumina powder has been studied and correlated to sinterability. Ground powders contain Si and N contaminations derived from the grinding media and mill pot made of Si_3N_4. Strong shear stress generated during planetary milling induces a mechanochemical reaction of worn-out Si_3N_4 with H_2O contained in methanol used as a liquid medium forming hydrated SiO_2 and provides an amorphous layer consisting of Si_3N_4, hydrated SiO_2 and Al_2O_3 on the surface of alumina particles. This suggests a possibility of applying planetary milling to surface modification of ceramic powders despite the problem of contamination. The surface layer containing the contaminations results in the formation of a mullite phase at the grain boundary during sintering. The low diffusion coefficient of mullite degrades sinterability even at a contamination as low as 400 ppm-Si. When the contamination increases to 0.5 mass%-Si, irregular grain growth and the formation of closed pores take place, suggesting the degradation of mechanical properties.

1. Introduction

Grinding and mixing using mills are the fundamental unit operations for the fabrication of high performance ceramics in which fine particle size of starting powders is an inevitable requirement. Fine ceramic powders have been produced by so called "build-up" processes such as sol-gel processes, gas-phase reactions, and coprecipitation methods and "break-down" processes using mills. Ultra-fine particle size and high purity providing excellent sinterability and optimal development of microstructure are the reason why the "build-up" powders are becoming attractive despite the low productivity and high manufacturing cost[1,2]. The grinding limit ranging over a few micrometers in ball mills, vibration mills and other conventional mills is inadequate for the requirement of high-performance ceramics.

In such situation, planetary ball milling, which is a kind of media agitation milling, has a high efficiency in producing fine powders with a size comparable to "build-up" ones as described in previous papers[3-5]. The peculiarity of this type of mills is the high speed grinding due to the high shear stress generated between grinding media in an elevated centrifugal field. It is supposed that the powder particles ground by planetary milling suffer crystallographic damages on their surface and internally during grinding to "sub-micron" particle size. The contamination through the wear of the grinding media and mill-pot wall also increased in relation with the efficient size reduction. For the application of planetary milling to ceramics, it is necessary to characterize the ground powders in relation to sinterability and microstructural development.

In the present paper, alumina powders with various amounts of contaminations have been prepared by a planetary mill treatment of a "build-up" powder under conditions providing few changes in specific surface area and the characterized powder properties are correlated to sintering behavior.

2. Experimental procedure

High-purity α-alumina powder (Taimei Chemicals, TM-DAR, 15.7 m^2g^{-1}, purity: 99.99%) was used as the starting powder. This powder was prepared by thermal decomposition of $NH_4AlO(OH)HCO_3$[6,7]. A planetary ball mill (Kurimoto Tekko-Syo) was used for grinding[3-5]. Weighed alumina powder (30.00 g) was encapsulated into a Si_3N_4 pot (480 cm^3) shown in **Figure 1(A)** with Si_3N_4 balls (ϕ 3) and distilled

* 4-12-1 Nakanarusawa, Hitachi 316, JAPAN

† This report was originally printed in *J. Soc. Powder Technology, Japan.* **30**, 548 (1993) in Japanese, before being translated into English with the permission of the editorial committee of the Soc. Powder Technology, Japan.

methanol (water content: 0.11%). The pot was completely filled with methanol so as to prevent further size reduction of the powder and to emphasize the influence of contamination on sintering behavior. After the mill-treatment for 60 min at the conditions listed in **Table 1**, the methanol was evaporated at 80°C during stirring and the powder was further dried in an oven at 120°C. The obtained powders were granulated through a 60 mesh Nylon sieve. The temperature increase in the mill-pot was measured using the assembly shown in **Figure 1 (B)**. The wear amount of the balls was measured as the mass loss of washed and dried balls before and after the mill-treatment. For the measurement of temperature and wear amount, alumina powder was not fed into the pot.

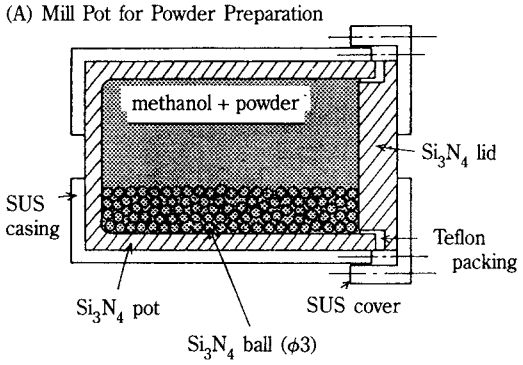

Fig. 1 Schematic drawing of mill pot assembly.

Table 1 Operating condition of planetary mill

	V_f (%)	F_{rev} (Hz)	F_{rot}/F_{rev} ratio
2A	26.3	2.92	2.0
2B	26.3	5.83	2.0
2C	26.3	8.33	2.0
5A	52.6	2.92	2.0
5B	52.6	5.83	2.0
5C	52.6	8.33	2.0

Specific surface area (S_{BET}) was measured by a N_2 adsorption BET method. Contamination was evaluated by measuring the amounts of silicon (C_{Si}), nitrogen (C_N), and carbon (C_C) in the ground powders. A part of the powder was decomposed in fused Na_2CO_3 at 1000°C and dissolved into 1 mol dm^3 HNO_3 for the measurement of C_{Si} by ICP spectrometry. C_N was obtained by a thermal extraction method (Leco, TC-136), where the powder (20 mg) in a tin capsule was thermally decomposed with a Ni flax and the resultant N_2 gas was determined by a thermal conductivity detector using He as a carrier gas. The carbon contamination, which was possibly caused by the decomposition of methanol, was measured by a combustion method (Leco, WC-12). The lattice distortion was estimated from the half-value width of X-ray diffraction peaks (Rigaku-Denki, RAD-B, CuKα, 40 kV, 100 mA). The surface property of the particles was estimated by FTIR (Perkin Elmer, 1760X, NaCl disk technique) and ESCA (Shimadzu-Seisakusyo, CR-6B).

Sintering was performed with the use of a dilatometer (Rigaku-Denki, DRC-1, heating rate: 5 K min^{-1}). The powder (5 g) was pre-pressed to the size of 10 × 15 × 42 mm and cold-isostatically pressed at 300 MPa for the measurement of temperature dependence of shrinkage by dilatometry[8,9]. The microstructure of the sintered materials (1600°C, 10 min) was observed by scanning electron microscopy (SEM, JEOL, JSM-330A).

3. Results and discussion

3.1 Wear of grinding media and temperature increase of liquid medium

The wear amount (ΔW) of the balls and the temperature (T) inside the pot during the planetary mill treatment are shown in **Figure 2**. A marked increase in ΔW and T was observed in the early stage of the treatment within 10 min and it stabilized within 10-50 min. It is considered that the rapid increase in ΔW and T at the initial stage is caused by the friction

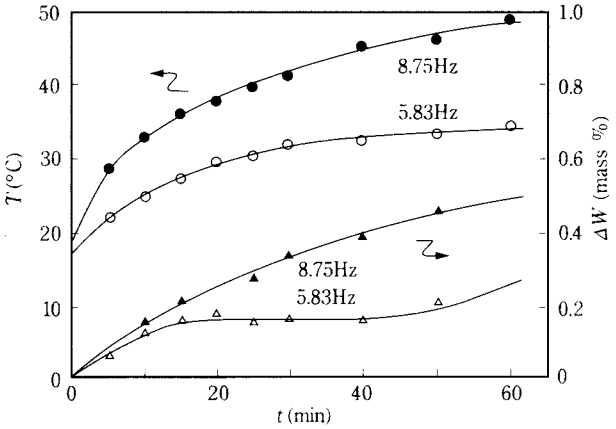

Fig. 2 Temperature (T) increase and wear amount of balls (ΔW) during planetary mill treatment; V_f = 26.3%, in methanol.

among balls and between balls and mill-pot wall because an adiabatic condition can be assumed in the pot. With further increase in treatment time (t), the intrusion of heat from the machine body and radiation from the pot become apparent and a heat equilibrium must be attained for the heat generated by friction (Q) and these non-adiabatic factors. At a low revolution frequency (F_{rev}) of 5.83 Hz, the heat equilibrium must be attained at a relatively early stage of the treatment showing a stabilized increase in ΔW and T, while the continuously increasing ΔW and T was observed at t = 10-50 min for a high F_{rev} of 8.33 Hz.

The Q value resulting from the temperature increase of methanol (400 cm^3, C_P[10]: 2.55 $JK^{-1}g^{-1}$), Si_3N_4 balls (250 g, C_P[11] = 0.714 $JK^{-1}g^{-1}$), and the 1/4 volume of Si_3N_4 mill pot (1200 g) was calculated as 8.2 kJ for F_{rev} = 5.83 Hz and 15.0 kJ for F_{rev} = 8.33 Hz at t = 5 min assuming an adiabatic condition and a temperature gradient decreasing from the inner to the outer side of the mill-pot inversely proportional to the 2nd power of the pot radius. The uncertainty of the latter assumption corresponding to the temperature increase of the 1/4 volume of the mill-pot to T would be diminished by the lower C_P of Si_3N_4 than that of methanol. A similar trial using distilled water (C_P[12]: 4.715 $JK^{-1}g^{-1}$) instead of methanol indicated 7.9 kJ for Q at F_{rev} = 5.83 Hz, showing a relatively good agreement with 8.2 kJ for methanol. The heat generation at t = 5 min was equivalent to the average work of 27-50W. The obtained Q value corresponding to 1 − 5% of the overall driving power (1 − 2 kW[5]) in this operating condition is reasonable for this type of mill. Powder particles punched between balls receive a considerable stress from the swaying motion of the balls during planetary milling.

3.2 Contamination of mill-treated powders

The characteristics of mill-treated powders are listed in **Table 2**. S_{BET} was almost unchanged by the mill-treatment; less than 20.1 $m^2 g^{-1}$ for 5C under the most severe grinding condition. The carbon content increased from 52 ppm to 93-74 ppm. However,

Table 2 Characteristics of mill-treatd powder

	S_{BET} ($m^2 g^{-1}$)	d_{eq} (μm)	C_{Si} (mass%)	C_N (mass%)	C_C (ppm)	C_N/C_{Si}
Orig.	15.7	0.096	N.D.	N.D	52.7	
2A	15.7	0.096	0.0.58	0.026	56.3	0.45
2B	18.6	0.081	0.16$_9$	0.024	63.3	0.14
2C	16.9	0.089	0.22$_0$	0.067	93.3	0.30
5A	15.7	0.096	0.045	0.027	59.2	0.60
5B	18.1	0.083	0.083	0.053	66.9	0.27
5C	20.1	0.075	0.56$_9$	0.14$_8$	74.1	0.26

C_C was at a very low level meaning little decomposition of methanol during the mill-treatment. Higher Si and N contamination (C_{Si} and C_N) was observed for higher fractional ball filling (V_f) and for higher F_{rev}. The ratio C_N/C_{Si} was lower than 0.67 for the stoichiometry of Si_3N_4, indicating that a part of the Si_3N_4 was mechanochemically oxidized by H_2O contained in the methanol. The amounts of Si_3N_4 and SiO_2 as an oxidation product were obtained from the C_{Si} and C_N and plotted against F_{rev} as shown in **Figure 3**. For V_f = 52.3%, both amounts of Si_3N_4 and SiO_2 increased with the increase in F_{rev}. In contrast, for V_f = 26.3%, only the amount of Si_3N_4 increased with increasing F_{rev}, and almost the same amount of SiO_2 was obtained at F_{rev} = 5.83 and 8.33 Hz. It was considered that the SiO_2 formed through the following mechanochemical oxidation (1) and dehydration (2).

$$Si_3N_4 + 12H_2O = 2Si(OH)_4 + 4NH_3 \quad \text{(during grinding)} \quad (1)$$

$$Si(OH)_4 = SiO_2 + 2H_2O \quad \text{(during drying)} \quad (2)$$

The overall amount of SiO_2 formed possibly from the content of H_2O in methanol was evaluated as 1.21 mass% (V_f = 26.3%) and 0.91 mass% (V_f = 52.6%). The observed values shown in **Figure 3** were lower than the evaluated values. Especially for V_f = 26.3%, the SiO_2 content showed a limit around 0.2 mass% at F_{rev} > 5.83Hz with a reduced increase in C_{Si} as shown in **Figure 4**. This may be caused by the consumption of H_2O for the surface oxidation of the Si_3N_4 balls in addition to the oxidation of worn-out Si_3N_4 to form a Si-$(OH)_x$ protective coating layer on

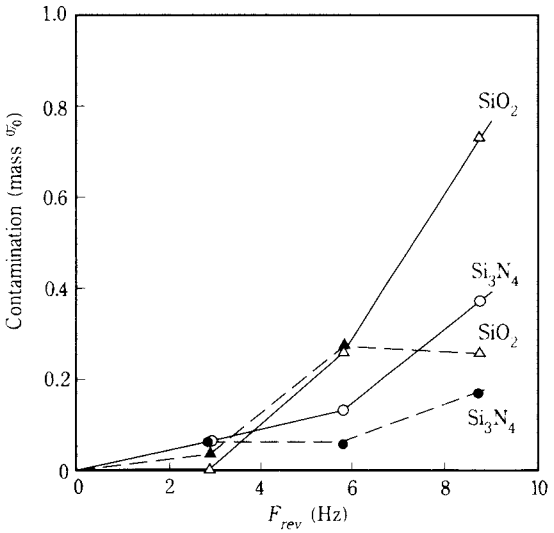

Fig. 3 Contamination of Al_2O_3 powder as a function of revolution frequency (F_{rev}); V_f = 26.3%: Si_3N_4 (•), SiO_2 (▲), V_f = 52.6%: Si_3N_4 (○), SiO_2 (△).

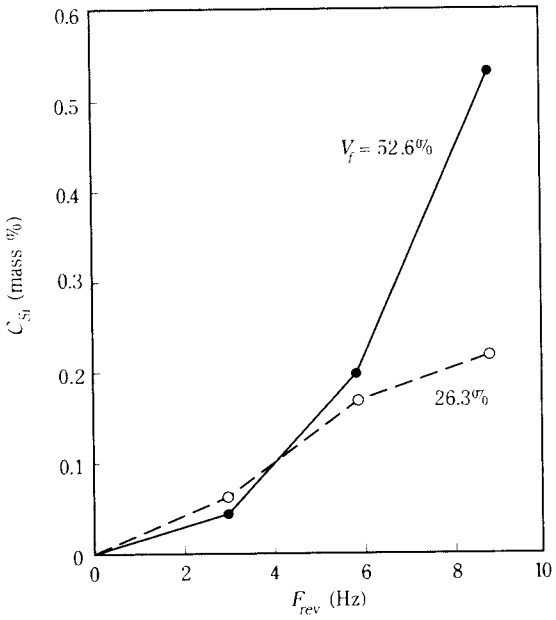

Fig. 4 Dependence of silicon contamination (C_{Si}) on revolution frequency (F_{rev}).

the surface of the Si_3N_4 balls preventing significant abrasion of the grinding media. For $F_{rev} = 52.6\%$, the strong friction among balls would tear off the protective coating and increase the abrasion of the grinding media at high F_{rev}. In this case, the SiO_2 content in ground products markedly increased as shown in **Figureg 3**.

For a further study of the possibility of protective layer formation, the ΔW and T measurements were performed for a liquid media containing 2 or 5 mol% H_2O. **Figure 5** shows the effect of 2 mol% H_2O addition on ΔW and T in comparison with distilled methanol and distilled water as the liquid media, where alumina powder was not fed. The T for 2 mol% H_2O indicated intermediate values between methanol and water. In contrast, the 2 mol% H_2O addition resulted in a markedly reduced ΔW (little

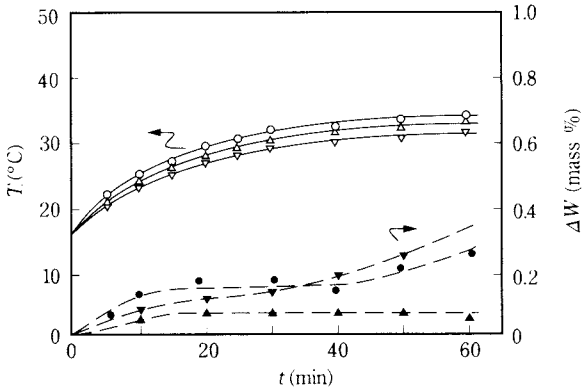

Fig. 5 Influence of water content in liquid medium on temperature (T) and wear amount of balls (ΔW); methanol (○, ●), water (▽, ▼), 2mol% water-methanol (△, ▲).

increase in ΔW at $t > 20$ min) supporting the above-mentioned discussion. The addition of 5 mol% H_2O indicated the same result as that of 2 mol%. Although the formation of Si-$(OH)_x$ layer was expected on the ball surface in water, no protection effect was observed. This suggests a dispersion of the oxidation product into water with high polarity rather than clinging on the ball surface as in methanol with low polarity.

3.3 Characteristics of mill-treated powders

The interplanar spacing (d) and half-value width (w) of X-ray diffraction peaks showing crystallographic imperfection are listed in **Table 3**. A slight increase in d and w from JCPDS data was observed for the mill-treated powders. However, the degree of the increase was almost comparable to that for a ball-milled powder and was insufficient for characterizing the imperfection. This may be due to the smaller particle size (d_{eq} = 0.075-0.096 μm in **Table 2**) than the penetration depth of X-ray into oxides (several μm)[13], where the resulting d and w indicate an average imperfection of the particles. The possibility of deformed or modified surface is still unclear.

Table 3 Interplanar spacing (d/nm) and half value width (w/deg. in parentheses) of X-ray diffraction peaks

	Miller indices			
	(024)	(116)	(124)	(030)
JCPDS (10-173)	0.1740	0.1601	0.1404	0.1374
Orig.	0.1741_5 (0.169)	0.1602_8 (0.169)	0.1405_7 (0.173)	0.1374_6 (0.174)
2A	0.1742_0 (0.170)	0.1603_1 (0.179)	0.1405_7 (0.181)	0.1374_9 (0.180)
2B	0.1742_1 (0.175)	0.1603_2 (0.176)	0.1406_6 (0.184)	0.1374_9 (0.183)
2C	0.1741_8 (0.174)	0.1603_0 (0.181)	0.1405_6 (0.185)	0.1374_8 (0.186)
5A	0.1741_6 (0.172)	0.1602_7 (0.178)	0.1405_6 (0.176)	0.1374_7 (0.176)
5B	0.1741_8 (0.175)	0.1602_9 (0.180)	0.1405_6 (0.183)	0.1374_8 (0.184)
5C	0.1741_9 (0.175)	0.1603_0 (0.180)	0.1405_6 (0.185)	0.1374_8 (0.187)
$Al_2O_3 + SiO_2$	0.1741_8 (0.171)	0.1602_7 (0.182)	0.1405_7 (0.187)	0.1374_7 (0.188)

The surface of powder particles was studied by FTIR and ESCA. **Figure 6** shows the IR spectra of mill-treated powders compared with a reference mixture of Al_2O_3 and SiO_2 (C_{Si} = 0.5 mass%). The reference mixture showed characteristic absorption at 600 − 900 cm^{-1} (Al-O) and around 1100 cm^{-1} (Si-O). The absorption of Si-N was observed at the same range as that of Al-O. The powders 2A and 5A with the smallest C_{Si} showed little absorption for Si-O. The powders 2B, 2C, and 5B (C_{Si} = 0.2 mass%)

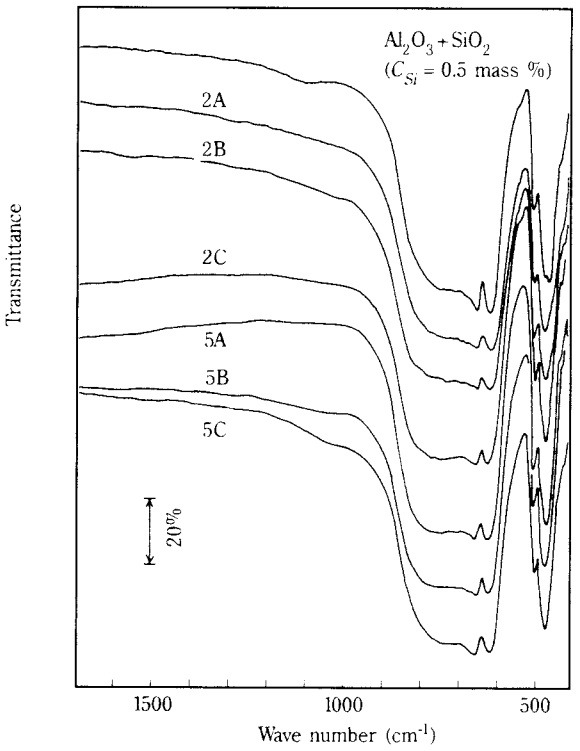

Fig. 6 Infrared spectra of milled powders; $Al_2O_3+SiO_2$ denotes ball milled oxides.

indicated a small absorption at 950 – 1100 cm^{-1}. An evident absorption at 1050 cm^{-1} was observed for 5C with the highest C_{Si}. However, the wave number did not agree with 1100 cm^{-1} for Si-O or with the expanded absorption at 750–1050 cm^{-1} for Si-N.

Figure 7 shows the ESCA spectra for Si (2p) of the mill-treated powders. The powders 5A and 5B showed peaks at 103.8 and 102.2eV corresponding to SiO_2 and Si_3N_4, respectively. The other powders, especially 5C, showed peaks at 103.0eV reported for many silicates instead of 102.2eV. There were two explanations for the peak at 103.0eV; silicate formation and a combination of two peaks for SiO_2 and Si_3N_4. For the latter case, the powder 5C containing 0.74 mass% SiO_2 and 0.37 mass% Si_3N_4 as contaminations in **Figure 3** should indicate a signal intensity of about 60% that of the reference mixture (C_{Si} = 0.5 mass%, that was 1.17 mass% SiO_2). However, the observed signal intensity for 5C (24% of the reference) was quite lower than the estimated value. Then, it was considered that the silicate-like amorphous surface layer was formed from hydrated SiO_2, Al_2O_3 and perhaps worn-out Si_3N_4 by the strong shear stress applied to powder particles during planetary milling despite the fact that no X-ray diffraction peaks appeared except α-Al_2O_3. This feature of the mill-treated powders suggested the possibility of applying planetary milling to ceramic powders for surface modification.

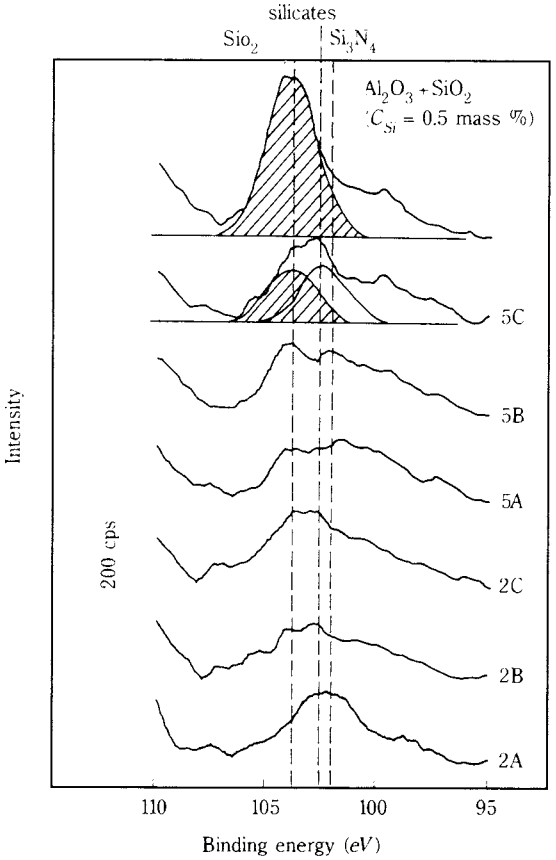

Fig. 7 ESCA spectra for Si (2p) of mill-treated powders; $Al_2O_3+SiO_2$ denotes ball milled oxides.

3.4 Sintering behavior and microstructure of sintered materials

The sinterability of mill-treated powders was estimated from the temperature dependence of shrinkage ($\Delta L/L_o$) during sintering. Shrinkage of the untreated powder (Orig.) started at 1000°C, progressed markedly above 1100°C, and ended at 1400°C. A higher temperature was required for the shrinkage of mill-treated powders with higher C_{Si}. The shrinkage at 1300°C was of the order of Orig. >5A >2A>2B, 5B>2C>5C which agreed with the order of C_{Si}. In addition, the powders 2B, 5B, 2C, and 5C showed a two-step shrinkage below and above 1400°C. **Figure 8** shows the iso-shrinkage diagram, where the temperatures corresponding to 2 to 16% shrinkage are plotted as a function of C_{Si}. In **Figure 8.**, the expanded distance between the plots means a difficulty of shrinkage, that is poor sinterability. It was noted from **Figure 8** that a very low C_{Si} at 0.045 mass% (5A) markedly degraded sinterability. For example, the temperature required for 5A to densify up to 90% (shrinkage: 14%) increased by more than 100°C to 1410°C. The shrinkage diagram for $C_{Si}<0.2$ mass% showed little degradation of sinterability up to 10% shrinkage (82% of the theoretical density) but severe

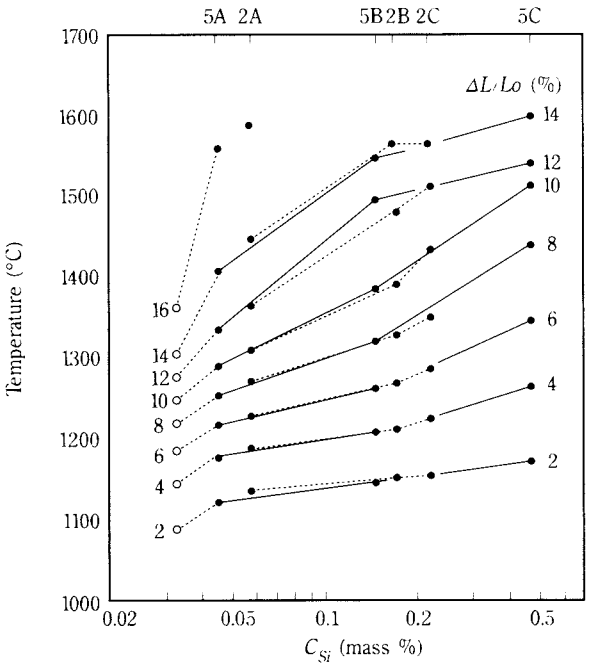

Fig. 8 Iso-shrinkage diagram for densification of Al_2O_3 as a function of Si-contamination (C_{Si}); dashed lines ($V_f = 26.3\%$) solid lines ($V_f = 52.6\%$).

degradation above 1400°C. The diagram at $C_{Si} > 0.2$ mass% showed a delayed shrinkage from 2% to 10%, a little enhancement at 10−12%, and the termination of densification at 90-92% at 1600°C. The Si-contamination existing on the surface of alumina particles is the reason why such small amount of contamination markedly disturb sintering.

Figure 9 shows the X-ray powder diffraction profiles of the materials sintered at 1600°C for 10 min. The formation of an increased amount of mullite phase ($2Al_2O_3 \cdot 3SiO_2$) was observed for the sintered materials containing an increased amount of Si-contamination. The mullite phase started to form at 1500°C without formation of intermediates such as spinel phase. Silicon nitride contained in the mill-treated powder was oxidized during sintering in air[14]. The direct formation of mullite phase is a typical feature of the syntheses from homogeneous mixture of fine constituents such as spray pyrolyzes[15, 16] in contrast to the formation of metastable intermediate phases during ordinary syntheses from coarse powders. The formation of no intermediates from the mill-treated powders supported the discussion on the formation of the modified surface layer on the powder particles. The degradation of sinterability of the mill-treated powders was related to the formation of the mullite phase with low diffusion coefficient[17] at the grain boundary derived from the surface layer. Although mullite was not identified at 1500°C by X-ray diffractometry, it was considered that the amorphous surface layer consisting of well-mixed fine SiO_2 and Al_2O_3 disturbs the material transport as well as the intergranular mullite phase.

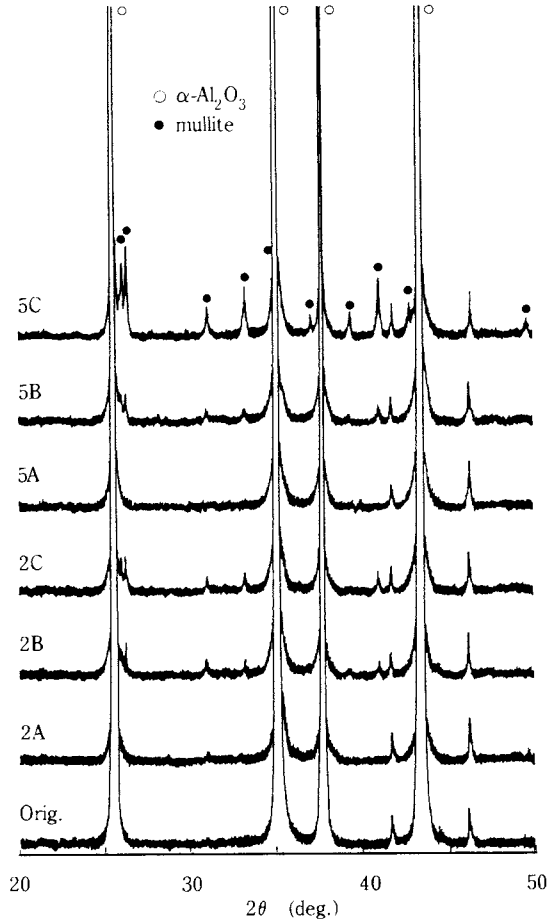

Fig. 9 X-ray diffraction profiles for sintered materials (1600°C, 10 min).

The mullite phase existing at the grain boundaries disturbs the boundary migration and grain growth in addition to densification. **Figure 10** shows the microstructure of sintered materials (1600°C, 10 min). The sintered untreated powder (Original) consisted of grains with a size of 1−5 μm and a small aspect ratio. The large grain size was due to the higher sintering temperature than the temperature suitable for this powder. A marked reduction of grain size was observed for the mill-treated powders even for 2A and 5A with $C_{Si} < 0.058$ mass% accompanied with an increase in aspect ratio to 2−3. The density of these materials attained 97−98% of the theoretical density. The high density and few residual pore-defects suggested little degradation of mechanical properties. The microstructure of sintered materials from 2C and 5C with high C_{Si} were characterized by a high aspect ratio of more than 3 and evident pore-

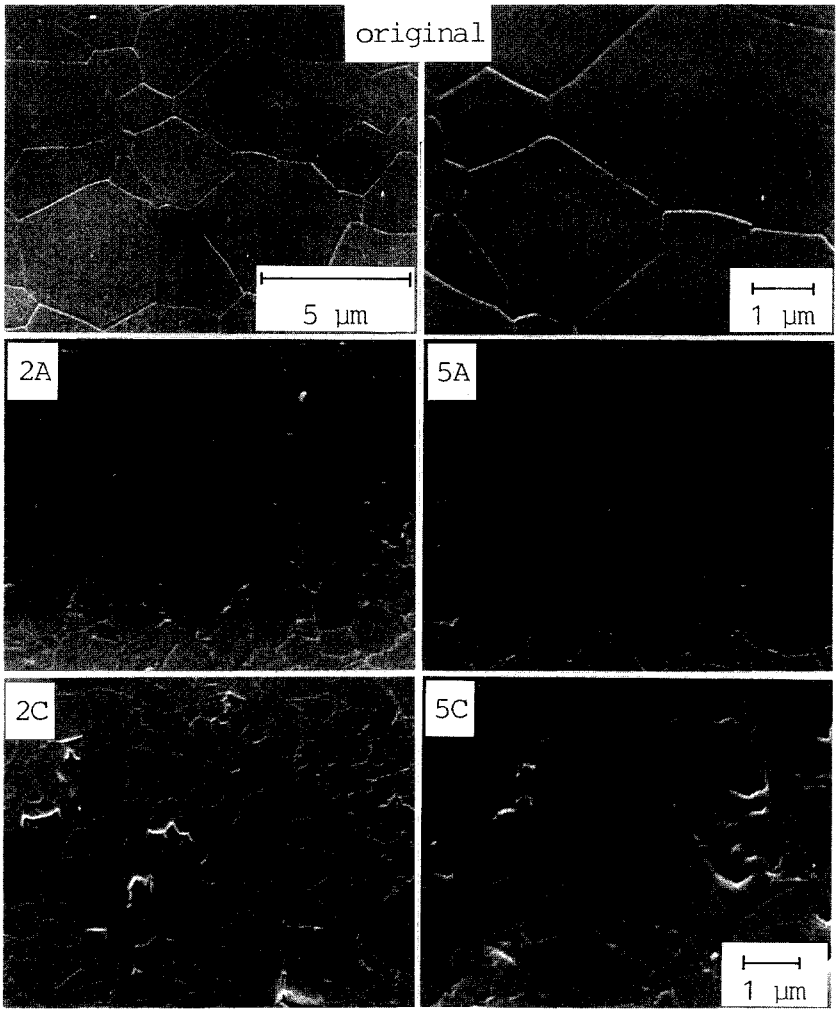

Fig. 10 Microstructure of sintered materials

defects. The low density of about 90% and the defects due to irregular grain growth suggested the degradation of strength. Mullite particles were not identified in the microstructure. However, the irregular grain growth induced by the quite fine mullite particles existing in the boundary was believed to be derived from the residual pores and the increase in aspect ratio.

4. Conclusion

Alumina powders with various amounts of contamination were prepared by a planetary mill treatment in methanol at an operating condition providing little change in the specific surface area so as to emphasize the influence of contamination on sintering behavior. The mill-treated powders contained Si and N contaminations derived from the grinding media and mill-pot wall made of Si_3N_4. A part of worn-out Si_3N_4 is mechanochemically oxidized by H_2O contained in methanol forming hydrated SiO_2. The contaminations form an amorphous reaction layer on the surface of alumina particles due to the high shear stress generated during planetary mill treatment. The formation of surface layer suggested the possibility of applying mill-treatment for surface modification. The contaminations disturb densification during sintering by forming a mullite phase with low diffusion coefficient even at a quite low contamination of 400 ppm-Si. Dense sintered materials can be obtained from powders with Si-contamination less than 0.2 mass%. However, a contamination higher than 0.2 mass% induces irregular grain growth providing sintered materials with low density containing residual pore-defects suggesting degradation of mechanical strength.

Acknowledgement

The author wish to thank Mr. K.Kaneko of Kurimoto-Tekko-Sho and Dr. A.Tsuge and Dr. Y.Kuwahara of National Industrial Research Institute of Nagoya for their helpful assistance.

Nomenclature

C_C	: carbon content	(mass%)
C_N	: nitrogen content	(mass%)
C_{Si}	: silicon content	(mass%)

C_p	:	heat capacity	($JK^{-1}g^{-1}$)
d	:	interplannar spacing	(nm)
d_{eq}	:	BET equivalent particle size	(μm)
F_{rev}	:	revolution frequency	(Hz)
F_{rot}	:	rotation frequency	(Hz)
Q	:	heat generated by friction during milling	(kJ)
S_{BET}	:	BET specific surface area	(m^2g^{-1})
T	:	temperature	(°C)
t	:	milling time	(min)
V_f	:	fractoinal ball filling	(%)
w	:	half value width of X-ray diffraction peak	(deg.)
$\Delta L/L_o$	:	shrinkage	(%)
ΔW	:	wear amount of balls	(%)

References

1) Kuwahara, Y.: "Kinousei-Funtai", Ed. by S.Toyama, p.173, Shinzansya-Scitech (1991).
2) Abe, O.: Powder Sci. & Engineering, 22, 61 (1990).
3) Yokoyama, T., T. Taniyama, G.Jimbo and Q.Zhao: J. Soc. Powder Technol., Japan, 28, 751 (1991).
4) Yokoyama, T., T. Kubota and G.Jimbo: J. Soc. Powder Technol., Japan, 29, 102 (1992).
5) Zhao, Q.: Doctoral Thesis (Nagoya Univ.), p.104 (1989).
6) Kato, S., T. Iga, S.Hatano and Y. Izawa : Yogyo-Kyokai-Shi, 84, 215 (1976).
7) Kato, S., T. Iga, S. Hatano and Y. Izawa, Yogyo-Kyokai-Shi, 84, 255 (1976).
8) Abe, O.: Seramikkusu-Ronbunshi, 98, 591 (1990).
9) Abe, O.: Seramikkusu-Ronbunshi, 100, 1196 (1992).
10) Chem. Soc. Japan, "Kagaku-Binran, Kisohen II", and Ed., p.902, Maruzen (1975).
11) Chem. Soc. Japan, "Kagaku-Binran, Kisohen II", and Ed., p.890, Maruzen (1975).
12) Chem. Soc. Japan, "Kagaku-Binran, Kisohen II", and Ed., p.892, Maruzen (1975).
13) Cullity, B.D.: "Element of X-ray Diffraction", 2nd. Ed. (Japanese Trans.), p.266 (1992).
14) Abe, O.: Preprint for 36th. Annual Meeting of GIRIN, p.93 (1984).
15) Kanzaki, S., H. Tabata, K. Kumazawa and S. Ohta: J. Am. Ceram. Soc., 68, C6 (1985).
16) Kumazawa, T. S. Kanzaki, J. Asaumi, O. Abe and H. Tabata, Yogyo-Kyokai-Shi, 94, 485 (1986).
17) Hoffman, D. W., R. Roy and S. Komarneli: J. Am. Ceram. Soc. Bull., 52, 620 (1985).

Author's short biography

Osami Abe is associate professor of materials science and engineering at Ibaraki University. He graduated the doctor course of Tokyo Institute of Technology, and also earned his doctorate in engineering in 1983. He started his professional career on materials science, specializing in ceramic science and powder technology at Government Industrial Research Institute, Nagoya (now National Industrial Research Institute of Nagoya), MITI in 1983. He moved to Ibaraki University in 1991.

Simultaneous process of Granulation, Grinding and Separation in a Continuous Tumbling Conical Granulator† – On the Shape Evaluation of the Granules and Granulating Conditions –

Masunori Sugimoto, Naoko Yokota and Hiroaki Miyanaga

*Department of Materials Science and Engineering, Faculty of Engineering, Toyama University**

Abstract

Small and spherical granules were made from $CaCO_3$-powder by the simultaneous process of granulation, grinding and separation in a continuous rotating conical vessel. The shape characteristics of the granules were evaluated by a pair of shape indices : ϕ is a measure of sphericity, and ζ is that of surface roughness. ϕ, ζ and granule size χ were plotted on three-dimensional graphs for various operating conditions of the granulator.

The result was that the increase in rotation speed of the vessel n was found to be more effective in obtaining smaller and spherical granules with smooth surface. The increase in ball charge B and feed ratio W produced small and non-spherical granules. Longer residence time $\bar{\theta}$ produced more spherical granules with smooth surface with $\bar{\chi}$ remaining unchanged.

1. Introduction

Recently, a new method for manufacturing fine powders including ultra-fine particles has been developed, and such fine powders are beginning to be widely used as powdery materials. Under the present circumstances, various problems associated with powder-technological operation of such powders are pointed out[1], and it is suggested, as one of the solutions to the problems, to make very small spherical granules from such materials that can be easily handled. We evaluated very small granules formed by a simultaneous process of granulation, grinding and separation in a single conical rotary vessel[2,3] by means of a pair of shape indices discussed in our previous report[4]. Additionally, based on such evaluation, the effects of the simultaneous granulating conditions on the shape characteristics of the granules were investigated, taking the size of a particle produced into consideration in the present paper.

† This report was originally printed in *J. Soc. Powder Technology, Japan*. **30**, 563 (1993) in Japanese, before being translated into English with the permission of the editorial committee of the Soc. Powder Technology, Japan.

* Gofuku, Toyama-shi 930, Japan
TEL. 0764-41-1271 Ext. 2782

2. Experimental

Experimental apparatus: An instrument similar to that described in our previous report[3] was used. A flow sheet of the granulation process using the instrument is shown in **Figure 1**. A conical vessel (length: 300 mm, smaller and larger end diameter: 123 and 243 mm ϕ) representing the main body of the instrument was fixed to a rotary cylinder, an outlet orifice-type weir of 93 mm of inner diameter was placed in a smaller diameter end of the vessel, and a scraper was attached in the vicinity of inner wall of the vessel. A table feeder 1 and an electric vibratory conveying

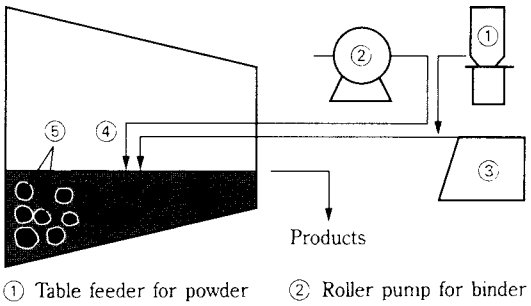

① Table feeder for powder ② Roller pump for binder
③ Vibratory conveyer ④ Nozzle
⑤ Grinding media

Fig. 1 Flow sheet for a simultaneous operation of granulation, grinding and separation by using a single tumbling conical granulator

feeder 3 were employed for a continuous supply of powder material, and a roller pump 2 and nozzle 4 were used for a continuous supply of binder. The ceramic balls (density = 2.4×10^3 kg/m^3) of 30 mm and 16 mm in diameter were mixed at the same weight, and used as a grinding medium. A conical vessel was kept at an inclination of 2° toward the smaller diameter end with a rotary cylinder.

Experimental materials: Calcium carbonate powders (50% particle size $\bar{\chi}_f \simeq 6 \times 10^{-3}$ mm) commercially available were employed as a powder material, and water as a binder.

Method of experiment: After the ceramic balls as a grinding medium were loaded at a predetermined quantity, the vessel was set to a given rotational speed. Calcium carbonate powder representing the powdery material was continuously supplied to the central part of the vessel at a constant feed rate, and water as a binder was continuously fed in drops to the material supply location through a nozzle. In the vessel, granulation, grinding and separation were simultaneously achieved, and after the discharge characteristics of granular particles obtained from the outlet at the smaller diameter end of the vessel became constant,[*1] the granular particles discharged were sampled three times in total at an interval of 10 min, and regarded as final products. The final products were analyzed for particle size by means of a small analytical screen (6.6 cm in diameter of screen container) after drying. As a result of the particle size analysis, it was confirmed that the particle size characteristics of these final products were also constant.

Further, fifty particles were randomly sampled from each group of granular particles having different size ranges, respectively, and their shapes were characterized by means of an image processing analyzer (LUZEX II, Nireco).

Breakage and/or change in shape of the granular particles due to the drying method and manual analysis using the small screen that were employed in the experiment were not observed, because small moist calcium carbonate granules obtained by using water as a binder in the granulating process were relatively hard and the granular particles after drying were harder.

Experimental conditions are shown in **Table 1**.

Table 1 Experimental Conditions

Feed rate of powder	F (kg·min^{-1})	$(3.5 \sim 30) \times 10^{-3}$
Feed rate of binder	G (kg·min^{-1})	$(4.0 \sim 31) \times 10^{-4}$
Feed ratio (= G/F)	W(−)	0.03 ~ 0.158
Average residence time	θ (min)	19 ~ 129
Weight of balls	B (kg)	0.2 ~ 0.8
Speed of rotation	n (min^{-1})	17 ~ 70

3. Experimental Results and Discussion

3.1 Evaluation and indicating method of shape of granular particles

A representative example of images of granular particles (particle size ≲ 1 mm with all particles) is shown in **Figure 2**. In the study, the image of a particle was approximated by an elliptic image with concaves and convexes as shown in **Figure 3**, and the shape of a granular particle was evaluated by the definition of two shape indices[4]. The indices are defined, respectively, as follows.

(I) Sphericity ϕ: a macroscopic shape index based on the deformation (change in shape) of an ellipse approximating the image of a particle to a circle

$$\phi = \frac{\text{Heywood diameter } (d_H) \text{ of the image of a particle}}{\text{Major axis } (D_e) \text{ of an ellipse (E)}} \quad (1)$$

(II) Smoothness ζ: a shape index focusing on convexes, concaves, projections and the like in the profile of the image of a particle

$$\zeta = \frac{\text{Circumferential length } (P_e) \text{ of an ellipse (E)}}{\text{Circumferential length } (P_p) \text{ of the image of a particle}} \quad (2)$$

In the definition above, the ellipse (E) is identical to a particle in an image area and the ratio of major to minor axes. In **Figure 2**, images representative of granular particles obtained are positioned in relation to the shape indices on coordinates of the sphericity ϕ and smoothness ζ [*2]. From the figure, the image of a particle close to 1.0 in both ϕ and ζ values is a smoother circle, and it was recognized by a microscope that such granular particle was smoother in a surface and more spherical. On the other hand, it was observed that a particle showing an image smaller in both ϕ and ζ values ($\phi \simeq 0.75$, $\zeta \simeq 0.85$) was a non-spherical particle having concaves and convexes in a surface thereof. Thus, these two shape indices ϕ and ζ were employed, as they were regarded to be effective for evaluating the shape characteristics of a granular particle. Additionally, in the study, the sphericity ϕ was plotted on the X-axis, smoothness ζ on the Y-axis and particle size χ on the Z-axis, so that a relation between the shape characteristics (ϕ, ζ) and particle size (χ) of all granular particles collected can be simultaneously observed. In order to magnify change

*1) In the present experiments, at least three times or more of the average residence time after discharge of the granular particles began, and it was confirmed that the discharge characteristics were sufficiently constant.

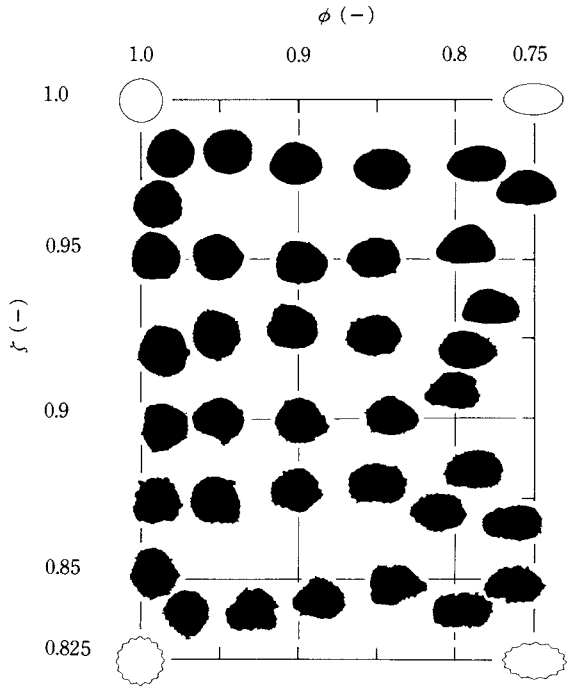

Fig. 2 Images of granules and their shape evaluation by a pair of shape indices ϕ, ζ, as a measure of sphericity and of surface roughness, respectively

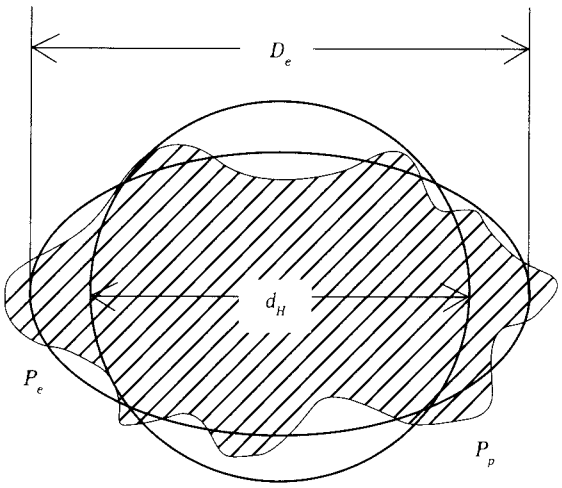

Fig. 3 An ellipse model of a granule image (The ellipse has the same area and ratio of breadth to length as the granule image)

in shape to a change in particle size, the granular particle size χ is shown in a logarithmic scale. Further, in the study, the ϕ, ζ and χ values of fifty granular particles of five different representative particle sizes (screening particle size χ = 0.13 (circle), 0.23 (solid rectangle), 0.39 (×), 0.55 (solid circle), 0.93 (rectangle)) were plotted in all cases, and a distribution of sizes of all granular particles (products) collected was also shown. Based on the above, the effects of the operating conditions on the relation between the shape characteristics and the size of granular particles are examined below.

3.2 Effects of average residence time ($\bar{\theta}$) of particles

Figure 4 shows the effects of average residence time of particles on the relation between the shape indices ϕ, ζ and the size χ of granular particles collected as a final product. It is recognized from the figure that the effects of average residence time $\bar{\theta}$ on the distribution of particle sizes is insignificant, but the effects of $\bar{\theta}$ on the relative variation of shape and size of particles are relatively high. In other words, whatever the value of $\bar{\theta}$ is, both values of ϕ, ζ of particles of different sizes generally tend to decrease as χ is reduced. In addition, it is found that a variation of the values of ϕ, ζ is significant when the residence time is relatively short at $\bar{\theta}$ = 19 min (a), but the variation of the values ϕ, ζ is reduced as the residence time is increased to $\bar{\theta}$ = 56 min (b), 129 min (c), and both average values tend to approach 1.0, respectively. Specifically, when the average residence time of particles is at $\bar{\theta}$ = 129 min (c), the variation of the values ϕ, ζ is reduced for a group of granular particles of $\chi \gtrsim 0.3$ mm, and it is observed that granular particles become smoother and more spherical, as the granulation time $\bar{\theta}$ is increased.

Figure 5 shows a relation between average sphericity $\bar{\phi}$, average smoothness $\bar{\zeta}$ and average particle size $\bar{\chi}$ with $\bar{\theta}$ calculated by the following formulae for all granular particles (products).

$$\bar{\phi} = \Sigma F(\chi_i) \cdot \phi_i \tag{3}$$

$$\bar{\zeta} = \Sigma F(\chi_i) \cdot \zeta_i \tag{4}$$

$$\bar{\chi} = \Sigma F(\chi_i) \cdot \chi_i \tag{5}$$

In the above formula, $F(\chi_i)$ is a weight fraction (−) of a group of granular particles at $\chi = \chi_i$ of particle size in the granular products, and ϕ_i, ζ_i are average shape indices (−) for a group of granular particles at $\chi = \chi_i$.

It is also observed from the figure that $\bar{\chi}$ remains almost unchanged with changes in $\bar{\theta}$, while $\bar{\phi}$ and $\bar{\zeta}$ approach 1.0 as $\bar{\theta}$ is increased, supporting the result of **Figure 4**. It is considered to be because the total number of cascading flows (∝ product of n and $\bar{\theta}$) of

*2) **Figure 2** shows the relation between the shape characteristics and ϕ, ζ calculated from Eqs. (1), (2) for granular particles that were obtained in the study. In the figure, in order to minimize the error variation of ϕ, ζ due to a difference in size of individual particle images, images of particles magnified approximately to the same size through a microscope were input to an image analyzer, and the ϕ and ζ values were calculated for the particle images.

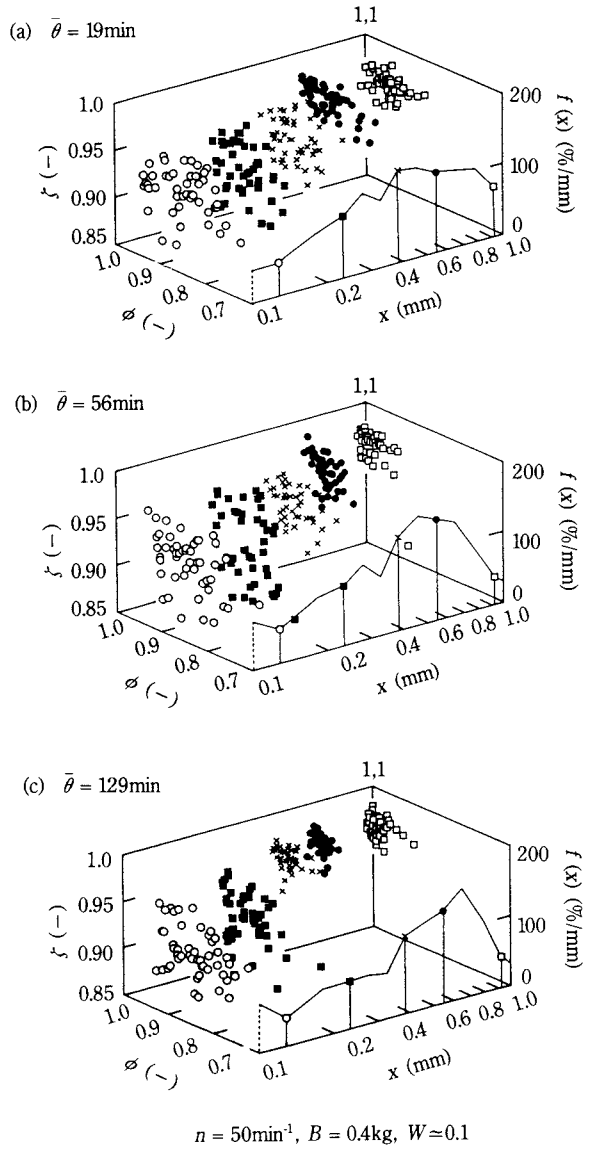

n = 50min^{-1}, B = 0.4kg, $W \simeq 0.1$

Fig. 4 Three-dimensional plots of the granule shape indices ϕ, ζ and size χ along with product size distribution curve (−・−) for various average residence time $\bar{\theta}$ (Keys: (granule size χ = 0.13 (○), 0.23 (■), 0.39 (X), 0.55 (●), 0.93 mm (□))

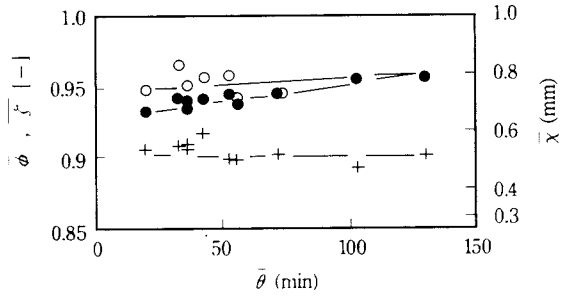

n = 50min^{-1}, B = 0.4kg, $W \simeq 0.1$

Key ●:ϕ ○:ζ +:$\bar{x}$

Fig. 5 Effect of residence time ($\bar{\theta}$) on granule shape ($\bar{\phi}$, $\bar{\zeta}$) and size ($\bar{\chi}$)

the granular particles through the vessel is increased, and rounding effects are enhanced.

3.3 Effects of a loading quantity (*B*) of the ceramic balls and rotational speed (*n*) of the vessel

Figures 6 and **7** are comparisons of the effects of a loading quantity B of the ceramic balls and rotational speed n of the vessel on the shape characteristics ϕ, ζ of particles of the final products with particle size reduction effect. Both B and n are representative operating factors dominating the reduction in size of the granular particles. It is found from the comparison of particle size distributions in the figures that an increase of either B or n enhances the grinding effect and reduction in size of the granular particles. However, their (B, n) effects on the shape characteristics of particles are considerably different.

Figure 6 is a comparison of the changes in size of granular particles and particle shape characteristics with an increase of the loading quantity of balls between B = 0.2 kg (a) and B = 0.8 kg (b). The shape indices ϕ and ζ of the latter (b) vary more widely in the entire range of particle sizes than those of the former (a), and their values are lower. Specifically, variation of the shape indices is significant in a range of larger particle sizes. It means that a reduction in size of the granular particles with an increase of the loading quantity of balls enhances the reduction in smoothness and sphericity of the granular particles over the entire size range.

Figure 7 is a comparison of the changes in size and shape characteristics of granular particles with an increase of the rotational speed n of the vessel between n = 17 min^{-1} (a) and n = 70 min^{-1} (b). At n = 17 min^{-1}, both ϕ, ζ significantly vary in the entire range of particle sizes. Specifically, variation of ϕ, ζ of granular particles of larger sizes is significant. It indicates that the consolidation and rounding effect of granular particles obtained are reduced, and many non-spherical granular particles having concaves and convexes in a surface thereof are produced, because the rotational speed n of the vessel is low. On the contrary, at n = 70 min^{-1}, variation of ϕ, ζ is generally reduced, and it is specifically recognized that variation of ζ becomes small for a group of granular particles of larger sizes. Further, the average values of both ϕ and ζ are closer to 1.0 in comparison with those for smaller sizes. In other words, it is found that a reduction in size of the granular particles with an increase of the rotational speed n of the vessel enhances the increase of smoothness and sphericity of the particles as well.

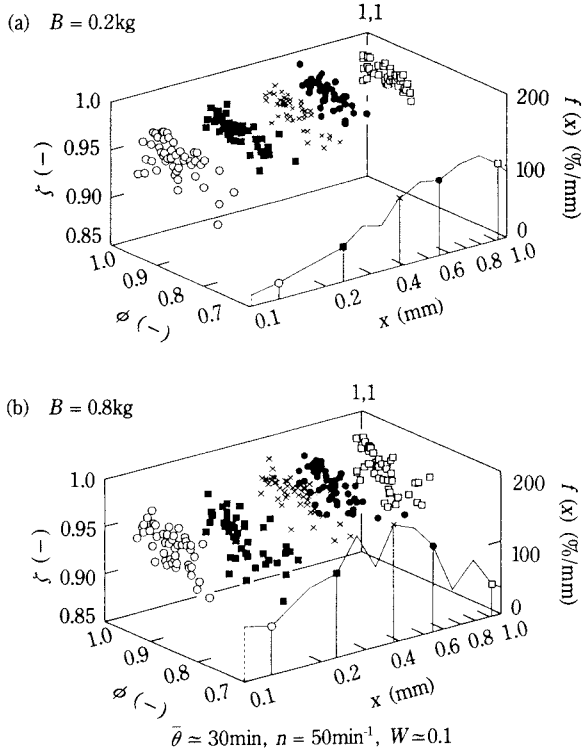

Fig. 6 Three-dimensional plots of the granule shape indices ϕ, ζ and size χ along with product size distribution curve (− · −) for ball charge $B = 0.2$kg (a) and 0.8kg (b) (Keys: same as Fig. 4)

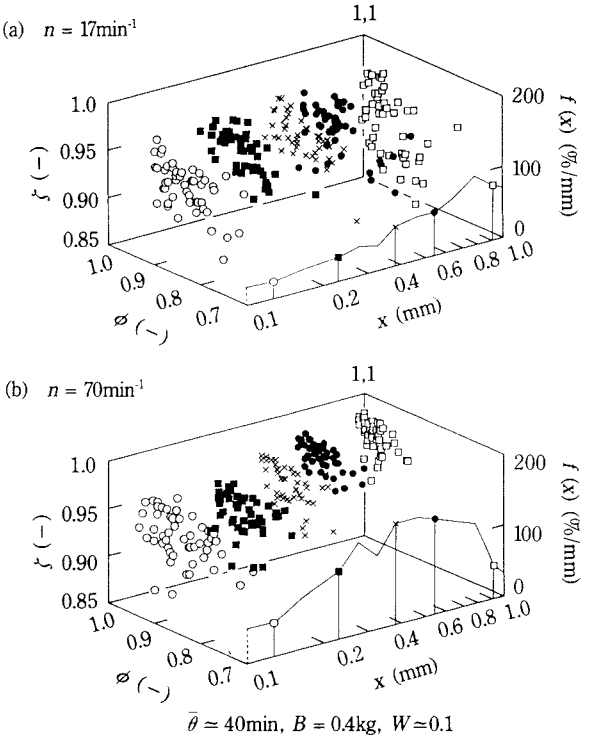

Fig. 7 Three-dimensional plots of the granule shape indices ϕ, ζ and size χ along with product size distribution curve (− · −) for rotation speed $n = 17$ min^{-1} (a) and 70 min^{-1} (b) (Keys: same as Fig. 4)

In **Figures 8** and **9**, the relations of $\bar{\phi}$, $\bar{\zeta}$ and $\bar{\chi}$ with the loading quantity B of ceramic balls and rotational speed n of the vessel are summarized. In **Figure 8**, $\bar{\phi}$, $\bar{\zeta}$ and $\bar{\chi}$ tend to decrease as the loading quantity B of ceramic balls is increased. On the contrary, in **Figure 9** $\bar{\chi}$ decreases as the rotational speed n of the vessel is increased, while both $\bar{\phi}$, and $\bar{\zeta}$ tend to increase within a low rotational speed region ($n <$ 50 min^{-1}), and to be almost constant within a high rotational speed region ($n \geq 50$ min^{-1}). As a result, an increase of either the loading quantity of ceramic balls or the rotational speed of the vessel increases the grinding energy and enhances the reduction in size of the granular particles. However, their effects on the particle shape characteristics are substantially different. The former promotes the reduction of smoothness and sphericity of the granular particles, while the latter enhances the increase of their smoothness and sphericity. It is considered to be because the grinding effect is increased in comparison with the rounding effect due to the increase of the loading quantity of ceramic balls that form the grinding medium. On the other hand, it is considered that the grinding and rounding effects are promoted by an increase in rotational speed of the vessel because the number of grinding and cascading flows of granular particles in unit time increases. Therefore, in order to obtain smooth spherical granules of small size, it is considered to be more effective to increase

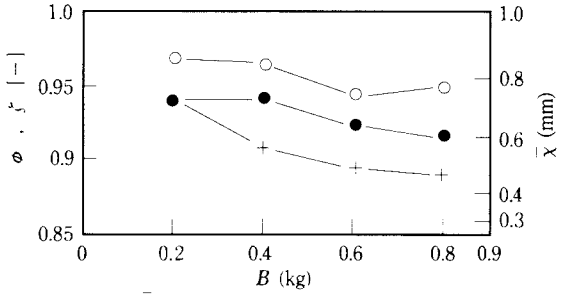

Fig. 8 Effect of ball charge B on the Granule shapes ($\bar{\phi}$, $\bar{\zeta}$) and size ($\bar{\chi}$)

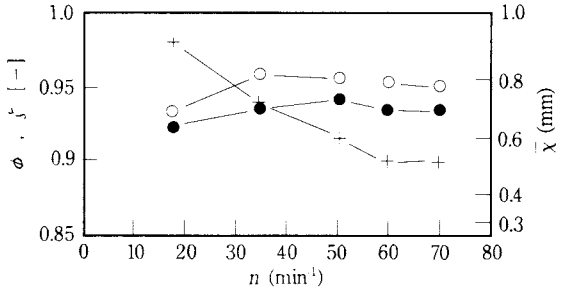

Fig. 9 Effect of rotation speed of the vessel on the granule shapes ($\bar{\phi}$, $\bar{\zeta}$) and size ($\bar{\chi}$)

the rotational speed of the vessel rather than the loading quantity of ceramic balls that form the grinding medium.

3.4 Effect of the feed ratio (W) of binder to material

Figure 10 shows the effect of the feed ratio W (−) of binder to material on a relation between the particle shape characteristics (ϕ, ζ) and the size χ of granular particles. The result of the experiment when W = 0.03 is shown in **Figure 10** (a), and that at W = 0.158 in **Figure 10** (b) for comparison. In the case when W is relatively lower (W = 0.03), the size χ of granular particles is generally larger. Variation of ϕ and ζ of particles of different sizes is relatively minor except for those with a smaller value of χ, and the values of ϕ and ζ are closer to 1.0. On the other hand, in the case when W is relatively higher (W = 0.158), in comparison with the case of W = 0.03, although the size of granular particles is generally small, variation of the ϕ and ζ values is significant, and both ϕ and ζ are at a low value. As a result, it is found that a reduction in size, smoothness and sphericity of granular particles is simultaneously enhanced by an increase of W. A relation between them is discussed below on the basis of the granulation process model proposed in our previous report[3].

In **Figure 11**, a granulation process model of a simultaneous operation of granulation, grinding and separation in a single rotary conical vessel is shown. In the model, the interior of the vessel is divided into three imaginary areas. Fine powder (raw material) fed into the central part of the vessel (granulation zone B) is granulated with binder. By segregation effects of particles in a rotary conical vessel, the smaller particles out of all granules segregate toward the smaller diameter end (rounding zone C) in the vessel, while the larger ones (coarse granules) toward the larger diameter end (grinding zone A) and are ground into small ones. The average size of small spherical granules segregating to the rounding zone C and collected at the discharge end of the vessel is shown by $\bar{\chi}_S$, the average shape indices of the granules $\bar{\phi}_S$, $\bar{\zeta}_S$ and those of small granules collected at the discharge end of the vessel through the zone B and C, after coarse granules (average size $\bar{\chi}_L$) segregating to the grinding zone A are finely ground are shown by $\bar{\chi}_G$, $\bar{\phi}_G$, $\bar{\zeta}_G$. Those of all granules (final products) collected from the outlet at the smaller diameter end are indicated by $\bar{\chi}$, $\bar{\phi}$, $\bar{\zeta}$. Now, assuming that all coarse granules of $\bar{\chi}_L$ are ground and collected as very small granules having a particle size $\bar{\chi}_G$ and average shape indices $\bar{\phi}_G$, $\bar{\zeta}_G$, the following formulae are obtained.

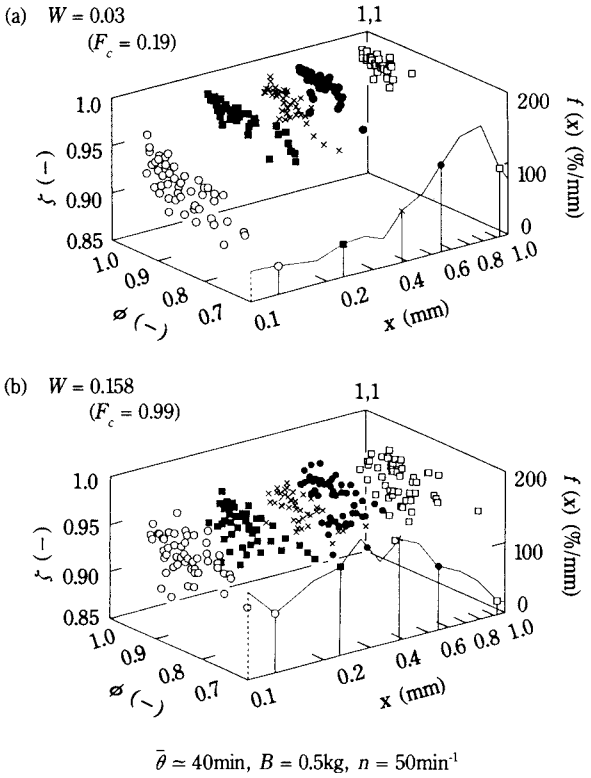

$\bar{\theta}$ ≃ 40min, B = 0.5kg, n = 50min^{-1}

Fig. 10 Three-dimensional plots of the granule shape indices ϕ, ζ and size χ along with product size distribution curve (−・−) for feed ratios W=0.03 (a) and 0.158 (b) (Keys: same as Fig. 4)

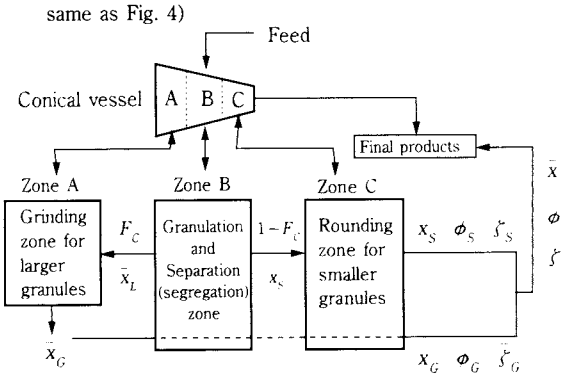

x_S, ϕ_S, ζ_S : Average size and shape indices of the granules discharged from the outlet after segregating toward the rounding zone (C) without grinding, respectively

x_G, ϕ_G, ζ_G : Average size and shape indices of the granules ground at the grinding zone (A) and discharged from the outlet, respectively

$\bar{x}$, $\bar{\phi}$, $\bar{\zeta}$: Average size and shape indices of the final product, respectively

F_C : Fraction of the larger granules (x_L) segregating toward the grinding zone (A) to total ones

Fig. 11 A continuous granulation process model for the simultaneous operation of granulation, grinding and separation in a tumbling conical granulator

$$\bar{\chi} = (1 - F_c) \cdot \bar{\chi}_s + F_c \cdot \bar{\chi}_G \quad (6)$$

$$\bar{\phi} = (1 - F_c) \cdot \bar{\phi}_s + F_c \cdot \bar{\phi}_G \quad (7)$$

$$\bar{\zeta} = (1 - F_c) \cdot \bar{\zeta}_s + F_c \cdot \bar{\zeta}_G \quad (8)$$

In the formulae, F_c is a fraction (−) of granules segregating toward the grinding zone (A) to total ones, and is obtained by the following formula.[3)]

$$F_c = W/W^* \qquad (0 < F_c < 1) \quad (9)$$

W^* is the upper limit (= 0.16) of W that allows granulation by the simultaneous process described in the report.

If Eqs. (6), (7) and (8) are changed to a dimensionless form by dividing them by $\bar{\chi}_s$, $\bar{\phi}_s$, $\bar{\zeta}_s$, the following formulae are obtained.

$$\frac{\bar{\chi}}{\bar{\chi}_s} = 1 - \left(1 - \frac{\bar{\chi}_G}{\bar{\chi}_s}\right) \cdot F_c \quad (10)$$

$$\frac{\bar{\phi}}{\bar{\phi}_s} = 1 - \left(1 - \frac{\bar{\phi}_G}{\bar{\phi}_s}\right) \cdot F_c \qquad (\bar{\phi}_G/\bar{\phi}_s \leq 1.0) \quad (11)$$

$$\frac{\bar{\zeta}}{\bar{\zeta}_s} = 1 - \left(1 - \frac{\bar{\zeta}_G}{\bar{\zeta}_s}\right) \cdot F_c \qquad (\bar{\zeta}_G/\bar{\zeta}_s \leq 1.0) \quad (12)$$

In the above formulae, it can be considered that the shape characteristics $\bar{\phi}_G$, $\bar{\zeta}_G$ of granular particles ground are lower than the shape characteristics $\bar{\phi}_s$, $\bar{\zeta}_s$ of those segregating toward the smaller diameter side without grinding, and such relations as $\bar{\phi}_G/\bar{\phi}_s < 1.0$, $\bar{\zeta}_G/\bar{\zeta}_s < 1.0$ may be assumed. Thus, it is appreciated from Eqs. (11) and (12) that the values of $\bar{\phi}/\bar{\phi}_s$, $\bar{\zeta}/\bar{\zeta}_s$ are reduced as F_C is increased. In other words, it is predicted that an increase of W enhances the reduction in smoothness and sphericity of granular particles (final product). In Eq. (10) concerning size characteristics, as discussed in our previous report[3)], $\bar{\chi}$ decreases as W is increased, when the grinding effect is high ($\bar{\chi}_G/\bar{\chi}_s < 1.0$).

According to the granulation process model above, the result of **Figure 10** (a) corresponds to such case when the fraction of granular particles segregating toward the grinding zone A, out of all granular particles produced in the granulation zone B, is at F_C = 0.19 (W = 0.03). In such case, about 20% of all granular particles are transferred to the grinding zone for size reduction, and simultaneously reduced in smoothness and sphericity, while about 80% of the granular particles directly segregate to the rounding zone C, and are rounded therein. They are simultaneously collected from the discharge part at the smaller diameter end. As a result, it is considered that smooth and spherical particles that have not been subjected to grinding occupy about 80% of all granular particles. The result of **Figure 10** (b) corresponds to such case when the fraction of granular particles segregating toward the grinding zone A is at F_C = 0.99 (W = 0.158). In such case, most granular particles (about 99%) once segregate to the grinding zone A, are ground to a smaller size therein, and thereafter are collected from the discharge part at the smaller diameter end. As a result, it is considered that most granular particles are non-smooth, non-spherical ground granules, regardless of the particle size, because most of them are subjected to grinding.

Figure 12 shows a relation between the average values of $\bar{\phi}$, $\bar{\zeta}$ and $\bar{\chi}$ and the feed ratio W of binder to raw material. From the figure, both $\bar{\phi}$ and $\bar{\zeta}$ decrease as W is increased. Such tendency is consistent with the result predicted from the granulation process model above. It is supposed that the reduction of $\bar{\chi}$ following an increase of W is because $\bar{\chi}_G/\bar{\chi}_s <$ 1.0. Accordingly, it is recognized that the amount of particles ground is increased in conjunction with the increase of the fraction F_C of granules segregating, as the ratio of binder to raw material is increased, and the reduction of smoothness and sphericity of granular particles is enhanced simultaneously with a reduction of their size.

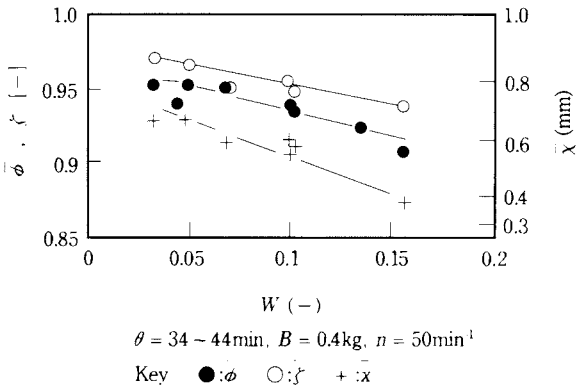

Fig. 12 Effect of feed ratio of binder to powder W on the granule shapes ($\bar{\phi}$, $\bar{\zeta}$) and size ($\bar{\chi}$)

4. Conclusion

We evaluated the shape characteristics of granular particles by a pair of shape indices, and their effects of the operating conditions on particle shape were investigated by showing the shape indices in a three-dimensional graph together with particle sizes. As a result, it was found that (a) an increase in the average residence time of the particles increases the total number of cascading flows of particles passing through

the continuous granulator, and enhances the increase in smoothness and sphericity of the particles; (b) an increase of the loading quantity of the grinding medium increases the grinding effect, and enhances the reduction in size, smoothness and sphericity of the particles; (c) an increase in rotational speed of the vessel increases the grinding and rounding effects, and enhances the reduction in size and the increase in smoothness and sphericity of the particles; and (d) an increase of the ratio of binder to raw material increases the quantity of particles ground in the grinding zone A, enhances the reduction in smoothness and sphericity of the granular particles, and simultaneously promotes the reduction in size of the granular particles, when the grinding effect is high.

Nomenclature

B	:	weight of balls charged	(kg)
D_e	:	major axis of equivalent ellipse model (E) of a projection having the same area and elongation as that of a granule	(mm)
d_H	:	Heywood diameter of granule projection	(mm)
F	:	feed rate of powder	(kg·min^{-1})
F_c	:	fraction of granules segregating to the grinding zone (A)	(−)
$F(\chi_i)$	:	weight fraction of granules having size χ_i to total granules	(−)
$f(\chi)$	:	particle size distribution function	(%·mm^{-1})
G	:	feed rate of binder	(kg·min^{-1})
H	:	total hold up	(kg)
n	:	speed of rotation	(min^{-1})
P_e	:	perimeter of equivalent ellipse model (E)	(mm)
P_p	:	perimeter of granule projection	(mm)
W	:	feed ratio of binder to powder	(−)
W^*	:	critical feed ratio of binder to powder corresponding to upper limit of the ratio required for forming granules	(−)
χ	:	granule size	(mm)
χ_i	:	granule size	(mm)
χ_f	:	average size of powder	(mm)
$\bar{\chi}_G$, $\bar{\chi}_L$, $\bar{\chi}_S$	:	average size of granules (see Fig. 11)	(mm)
$\bar{\chi}$	:	average size of the final product	(mm)
ϕ, $\bar{\phi}$	:	shape index of granule as a measure of sphericity (see Eq. (1)) and mean value, respectivley	(−)
ζ, $\bar{\zeta}$	:	shape index of granule as a measure of surface roughness (see Eq. (2)) and mean value, respectively	(−)
$\bar{\theta}$	:	average residence time ($=H/(F+G)$)	(min)

Subscripts

G, L, S	:	denote value of granule having size χ = χ_G, χ_L, χ_S, respectively

References

1) Sekiguchi, I.: J. Soc. Powder Technol., Japan, 26, 586 (1989)
2) Sugimoto, M., N. Yokota and H. Kawamoto: J. Chem. Eng., Japan, 23, 244 (1990)
3) Sugimoto, M., N. Yokota and M. Sugihara: J. Soc. Powder Technol., Japan, 27, 590 (1990)
4) Sugimoto, M., N. Yokota and H. Nakazawa: J. Soc. Powder Technol., Japan, 26, 624 (1989)

Author's short biography

Masunori Sugimoto

Dr. Masunori Sugimoto is Professor of Chemical Engineering Department (1979 – 1990) at Toyama University and of Materials Science and Engineering Department since 1990. His major research interests are solid mixing and segregation, particle shape characterization and their separation, and particle design with granulation. His current research interests are development of a continuous granulation process by simultaneous operation of granulation, grinding and separation using segregation behavior of particles passing through a rotating vessel.

Naoko Yokota

Naoko Yokota received her BE and ME degree from Department of Industrial Chemistry at Toyama University in 1986. After graduating, she worked at Department of Chemical Engineering, Toyoma University (1986 – 1993) as a Research Assistant under the direction of Prof. M. Sugimoto. Her major interests are particle shape analysis and characterization by computer operation.

Hiroaki Miyanaga

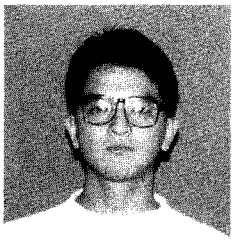

Hiroaki Miyanaga received his BE and ME degree from Department of Chemical Engineering at Toyama University in 1993. After graduating, he works at the Fujisawa Pharmaceutical Co. Ltd. as a research staff. His major interests are research and development of new technologies for granule properties and control.

An XPS Study on the Interaction at the Fe_3O_4/SiO_2 Boundary on the Surface of Composite Microspheres Prepared via a Shear-Compressive Mechanical Route†

Isao Saito and Mamoru Senna
*Faculty of Science and Technology, Keio University**

Abstract

Composite microspheres of polystyrene or silica coated with a double layer of Fe_3O_4/SiO_2 were prepared via mechanical routes using a shear − compressing type machine, specially designed for the purpose of surface coating. The binding energy of $Fe_{2p3/2}$ measured by XPS increased, while that of Si_{2p} decreased after composite formation. These synchronized shifts increased with increasing intensity of mechanical stress. After heat treatments, chemical interaction during mechanical treatment at the Fe_3O_4/SiO_2 interlayer in a composite particle was verified. The fine structure of the interlayer boundary was also examined in detail by electron microscopy.

1. Introduction

Formation or synthesis of composite particles via mechanical routes is increasingly studied with the development of hard wares for those purposes[1-6]. Apart from the relatively simple procedure not involving the use of any solvents, the mechanochemical effects at the interfaces of the host/guest or between a multiple of guests are unique for the synthesis via a mechanical route[7]. This kind of mechanochemical effects is not always particularly significant immediately after mechanical treatment, but often turns out to be important after subsequent thermal treatments. In other words, precursors of the products are formed due to mechanochemical effects, leading to a promotion of the subsequent solid state reactions on heating[8,9]. However, using spherical particles of tens of micrometers as host particles in the case of complex formation by a shear-centrifuge apparatus, the combination for the mechanochemical solid state reaction is quite restricted.

Double-layered composites can circumvent this limitation. During double coating, the reaction elements are successively attached on the surface, i.e., by coating the second component on the particles already coated with the first component. Since the choice of the first and the second components is almost unlimited, eventually every kind of solid state reaction can be induced in the confined area of the composite particles.

In contrast to the conventional reaction mixture, where the contact points of dissimilar particles are distributed throughout the mass of the reactant mixture, the contact points of the dissimilar particles are restricted to the interlayer boundaries in the case of a double-layered composite. This enables, for one thing, elucidation of the chemical interaction from the topochemical point of view, and for the other, preparation of a composite where the extent of chemical interaction at the interface is brought under control.

The purpose of the present study is to elucidate the chemical interaction at the boundary of two different guest layers with detailed structure development of fine structure.

2. Experimental methods

2.1 Preparation of composite particles

A commercial apparatus for fabricating complex particles following the principle of shear-compression (Ang-Mill Mechanofusion System, AM-15F, Hosokawa Micron) was used for the preparation of double layered composite particles. The materials employed as host and guest particles are listed in **Table 1**. The operational conditions are summarized in **Table 2**. The net operation time excludes the time for acceleration

Table 1 Starting materials

Abbreviation	Material	Manufacturer	Trade name	Av. particle size (μm)
Sb	Silica	San-ai Chem.	No.1061	9.3
P	Polystyrene	Soken Chem.	SGP-70C	15.6
Sa	Silica	Degussa	Aerosil 200	0.014
F	Magnetite	Toda Kogyo	SSP-9115	0.011

* 3-14-1 Hiyoshi, Kohoku-ku, Yokohama 223 JAPAN

† This report was originally printed in *J. Soc. Powder Technology, Japan.* **31**, 18 (1994) in Japanese, before being translated into English with the permission of the editorial committee of the Soc. Powder Technology, Japan.

Table 2 **Composite particles and their preparation conditions**

Symbol	Host (g)	Guest (g)	Net operation time (min)	Number of revolution (rpm)
F·Sb-1	Sb/54.75	F/0.36	30	1200
F·Sb-2	Sb/54.75	F/0.36	60	1200
F·Sb-3	Sb/54.75	F/0.36	30	2400
F·Sb-4	Sb/54.75	F/0.36	60	2400
Sa·P-1	P/23.67	Sa/5.87	30	1200
F·Sa·P-1	Sa·P-1/29.47	F/0.18	30	1200
F·Sa·P-2	Sa·P-1/29.47	F/0.18	60	1200
F·Sa·P-3	Sa·P-1/29.47	F/0.18	30	2400
F·Sa·P-4	Sa·P-1/29.47	F/0.18	60	2400

and deceleration for the initiation and termination of the machine operation.

2.2 Structural characterizatoin

Transmission electron microscopy (TEM) was predominantly used for this purpose. An ultrathin specimen sliced by an ultramicrotome was subjected to local elemental analysis by using an energy dispersive spectrometer (EDS), installed in a transmission electron microscope (TEM) with an electron beam of 25nm. 5 to 7 points along the diametral direction were chosen to determine the atomic ratio of *Fe/Si* to determine the distribution of the iron transfered from the second guest, magnetite, in the first guest, SiO_2. Distribution of *Fe* and *Si* was further elucidated by an electron probe microanalyzer (EPMA).

2.3 Chemical interaction

Two methods were used to evaluate the extent of chemical interaction between the host and guest particles or between two guest species. The extent of dissolution of iron was estimated. The sample containing nominally 3.0mg *Fe* in total, was put into 100cm^3 1N aqueous solution of HCl. Concentration of *Fe* was analyzed by a phenanthroline method.

For the purpose of examining the direct chemical interaction between magnetite and silica, X-ray photoelectron spectroscopy (XPS) was employed and it observed whether and to what extent the chemical shift of Fe_{2p} and Si_{2p} peaks took place. A 0.05g composite sample was pelletized in a mold of 11mm in diameter under 400MPa. With the aid of a calibration reference to the $Au_{4f7/2}$ signal at 83.8eV, the maximum possible error of the chemical shift was reduced to less than ±0.1eV.

3. Results and discussion

3.1 Surface structure of the composite particles

The BET specific surface area of the host silica beads was 155m^{2}g^{-1}. The surface of the composite sample Sb-1, where guest silica beads were top-coated by magnetite of ca. 0.3 μm, magnetite microparticles were smoothed with increasing net operation time and rate of revolution of the machine. This tallies well with the results obtained by Naito *et al*[10] which indicated that the apparent specific surface area of the composite decreases with increasing stress and duration.

On the surface of silica microspheres (Sa)-coating on the polystyrene host particles, Sa·P-1, silica particles were densely deposited, as shown in **Figure 1 (a)**. The top coat, Fe_3O_4, was also visible on the magnetite/silica double-coated polystyrene, F·Sa·P-1, as shown in **Figure 1 (b)**. With increasing rate of revolution during coating, the surface roughness increased, as shown in **Figures 1 (c)** and **(d)** for samples F·Sa·P-3 and 4, respectively. This kind of surface roughening by severe stress during coating was already suggested previously, when the substrate host particles are relatively deformable[7].

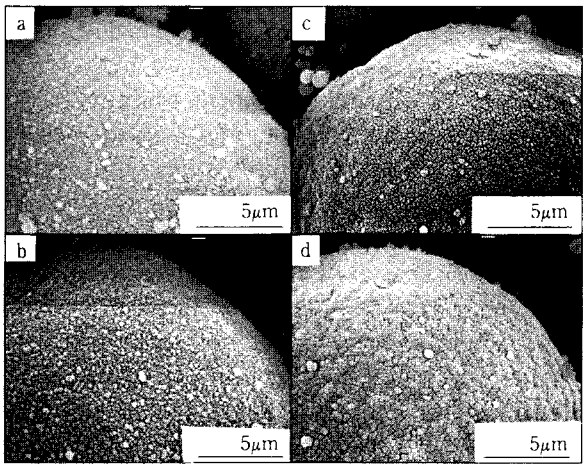

Fig. 1 Scanning electron micrographs of the composite microspheres: a: Sa·P-1; b: F·Sa·P-2; c: F·Sa·P-3; d: F·Sa·P-4.

3.2 Cross-sectional structure

The cross-section of the doubly coated composite particles, F·Sa·P-1 was subjected to EPMA line analysis. As shown in **Figure 2**, a distinct existence of two different species, *Si* and *Fe*, is detected.

In order to analyze the structure of the guest layer and the mechanism of such complex formation, further analysis was also carried out by transmission electron microscope (TEM). As shown in **Figures 3 (a)** and **(b)**, a double-layer as a whole was uniform in thickness, ca. 3 μm, in the case of the sample F·Sa·P-1. The thickness cannot be considered as being representative of the entire composite particles, since there is no guarantee of being cut through an equator. For the samples F·Sa·P-3 and F·Sa·P-4, two different

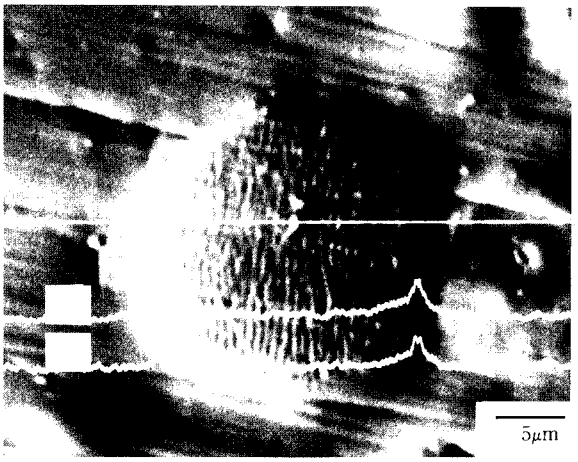

Fig. 2 EPMA line analysis of the F·Sa·P-1 cross-section

sections of the guest layer were obtained, i.e., with a relatively uniform thickness and a wavy layer with varying thickness, in accordance with the surface observation by SEM, shown in **Figure 1**.

Energy dispersive spectrometry was carried out with a beam spot diameter of 25nm to obtain the local elemental composition of the guest layer. Variation of the atomic ratio, *Fe/Si* along the thickness of the guest layer is shown in **Figire 4**. *Fe* is concentrated on the outermost layer for samples F·Sa·P-1 and F·Sa·P-2. In contrast, the maximum value of *Fe* concentration was found 0.27 μm inward from the outermost surface for the sample F·Sa·P-4, which was subjected to severer stressing during preparation. The thin dark layer shown in **Figure 3** (**f**) corresponds to this magnetite deposits. This indicates that the migration of the outermost layer during coating is also possible when the rate of revolution during the shear compression is high enough. In other words, the first and second guest species are partly mixed during mechanical stressing. It is to be noted that the thin dark layer is not a continuous circle. *Fe* maximum at the outermost surface was also observed depending on the spot, where local elemental analysis was carried out.

The bulk temperature of the specimen never exceeded 67°C, so that the migration of iron-containing species by thermal diffusion is not conceivable, even if the local temperature were considerably higher than the observed mean temperature. Rather, it is more likely that some parts of the second guest layer have been destroyed, detached together with a part of the first layer and reattached somewhere else. This also explains the discontinuity of the dark layer with enriched iron mentioned above. When the shear-compression stress is large enough, this kind of fall-off and reattachment must have been repeated.

3.3 Dissolution of guest species from composite guest layer

The extent of dissolution of iron-containing species was evaluated and is shown in **Figure 5**. The vertical

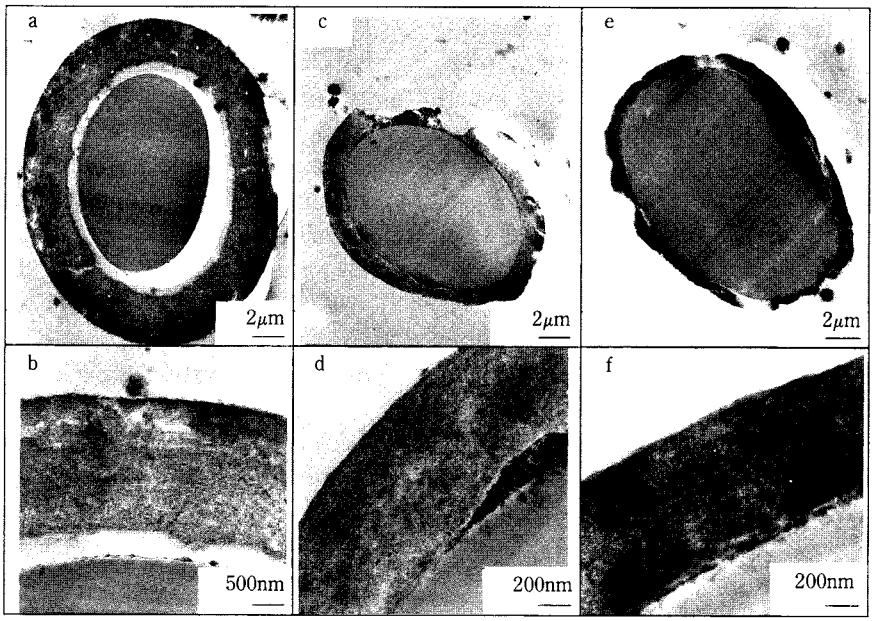

Fig. 3 Transmission electron micrographs of thin slices of the composite microspheres: a and b : F·Sa·P-1; c and d : F·Sa·P-2; e and f : F·Sa·P-4

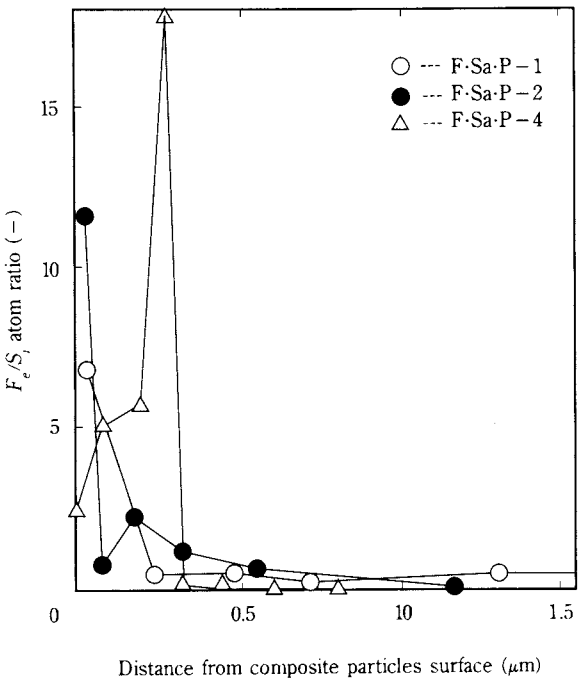

Fig. 4 Variation of the local atomic ratio, *Fe/Si* with the distance from the composite particle surface

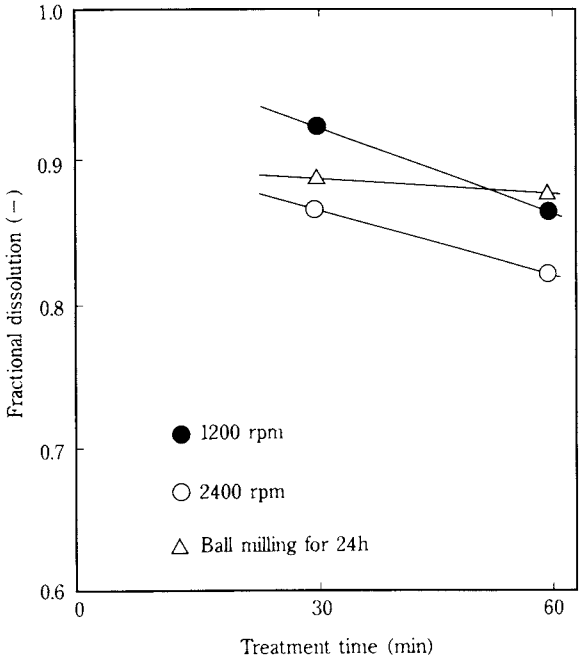

Fig. 5 Variation of fractional dissolution of *Fe* with net operation time for composite preparation

axis in **Figure 5** denotes the fractional dissolution, with respect to the total iron content calculated from the overall concentration of magnetite in the overall composite particles. The lower fractional dissolution means the larger fraction of magnetite remaining in the composite, in spite of the immersion of the sample into 1N HCl at 30°C for 48h, where bare magnetite can be completely dissolved. As shown in **Figure 5**, the fractional dissolution was smaller at a higher rate of revolution and longer retention time. One of the reasons for incomplete dissolution is obviously the geometrical factor, i.e., some part of magnetite was buried in the first guest layer, silica, preventing its contact with the acidic solution.

We have therefore tried to crush the guest layer in a ball mill in the presence of HCl solution and let it dissolve *in situ*. As shown by triangles in **Figure 5**, the fractional dissolution increased to some extent with additional ball milling *in situ*. Nevertheless, the fractional dissolution never reached unity. This might suggest that magnetite was chemically stabilized by virtue of mechanochemical reaction, although persisting geometrical factors, i.e., hard coating of magnetite particles by silica microspheres are not to be ruled out.

3.4 Chemical shift of XPS spectra

In order to examine directly whether and to what extent silica and magnetite mechanochemically interacted, X-ray photoelectron spectroscopy was carried out. The binding energies of inner electrons, Fe_{2p}, Fe_{3p} and Si_{2p} were examined. As shown in **Figure 6**, the binding energy of Fe_{2p} is shifted consistently toward a higher energy compared to that of the intact magnetite, 710.8eV, for the series of *F·Sb* samples, where magnetite was coated directly on the host silica beads. A similar tendency is also observed for the series of *F·Sa-P*, i.e., silica/magnetite double layered composite, coated on polystyrene beads, although the extent of the chemical shift was smaller than that for *F·Sb*, as shown in **Figure 7**. The binding energies of Fe_{3p} (not shown in the figure) showed a similar behavior.

As for the binding energy of Si_{2p}, the extent of chemical shift is much smaller, due mainly to its larger amount compared with magnetite. Nevertheless, the chemical shift in the direction opposite to that of the case of Fe_{2p}, i.e., toward the lower energy side, was observed, as shown in **Figures 8** and **9**.

3.5 Chemical interaction between guests or guest and host

From the chemical shifts of XPS spectra as well as the depression of iron dissolution, chemical interaction between magnetite and silica during a complex formation by shear-compression stressing has been indicated. Similar phenomena were reported for the chemical shift of V_{2p} electrons toward higher energy as a result of interaction with silica for supported catalyst of V_2O_5[11,12].

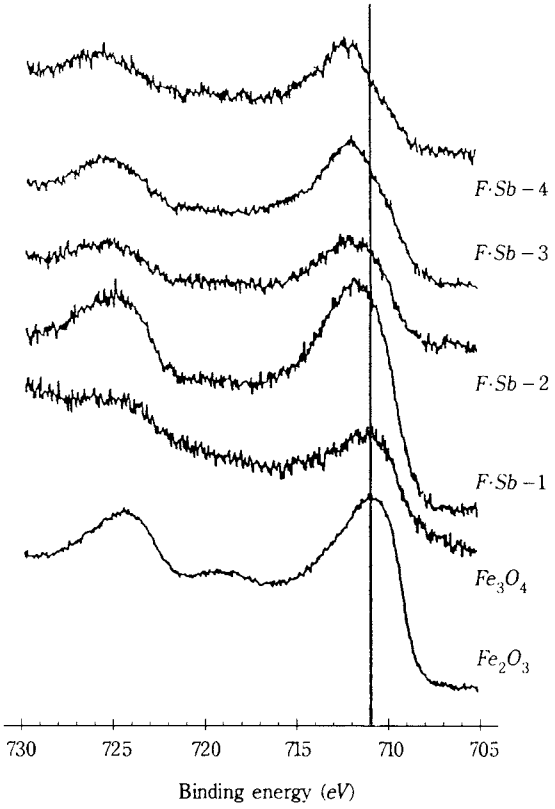

Fig. 6 Fe_{2p} XPS profiles for F·Sb composites. Vertical line corresponds to $Fe_{2p3/2}$ for untreated magnetite.

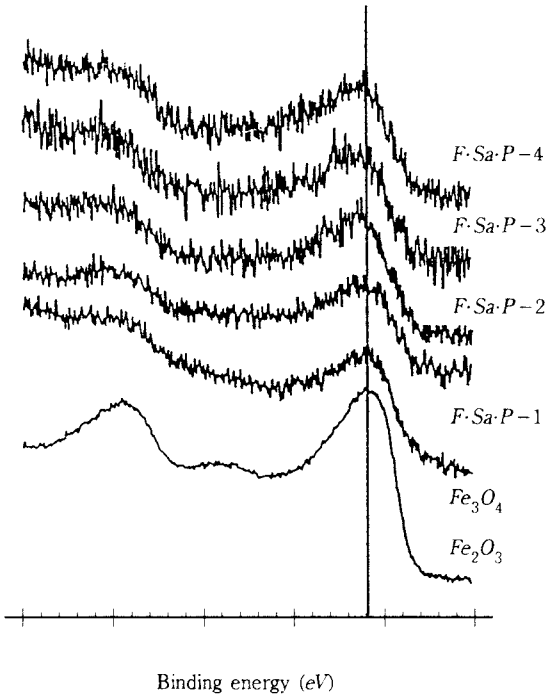

Fig. 7 Fe_{2p} XPS profiles for F·Sa·P composites with double guest layers. Vertical line corresponds to $Fe_{2p3/2}$ for untreated magnetite.

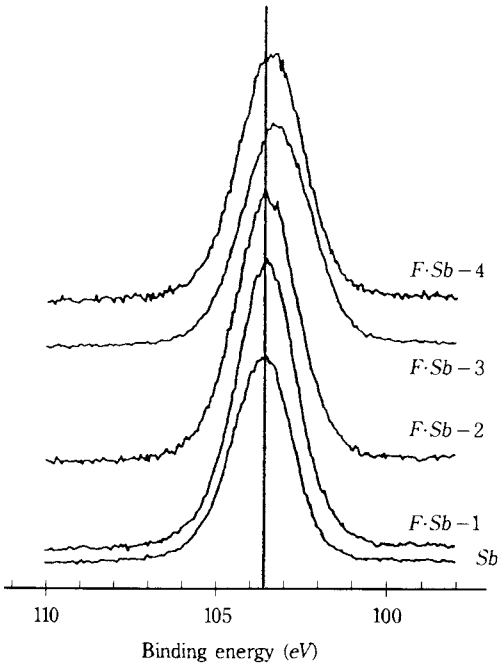

Fig. 8 Si_{2p} XPS profiles F·Sb composites. Vertical line corresponds to Si_{2p} for untreated silica.

The chemical shift of Fe_{2p}, Fe_{3p} can also take place by a simple oxidation from its ferrous state to a ferric state. Therefore, we examined the XPS peaks for hematite, obtained by calcining magnetite in air at 1100°C, with and without the coexistence of silica. As shown in **Figure 10**, commercial hematite and calcined magnetite without silica show the same chemical shift. However, when magnetite was calcined with silica microspheres (Silica a) and silica beads (Silica b), the chemical shifts observed were still higher by 0.4eV and 0.3eV, respectively. The chemical shifts to a value higher than the highest possible oxidation number of *Fe*, i.e. 3, can only be explained by a chemical interaction with silica. When incipient chemical bonding *Fe-O-Si* is formed at the magnetite/silica interface, the electron density of silica is increased due to the higher electron affinity of *Si* than that of *Fe*, leading to a decrease in the binding energy of the electrons bound to silicon atoms. The reverse is the case for iron, i.e., the interaction with silicon brings about a decrease in the electron density, causing an increase in the binding energy. These are exactly what we observed in **Figures 6** through **9**.

Incipient chemical interaction or reaction during mechanical treatment can be explained by a mechanical diffusion, where migration of the atoms takes place at the contact point due to local plastic deformation, i.e., microscopic diffusion through the surface defects[13].

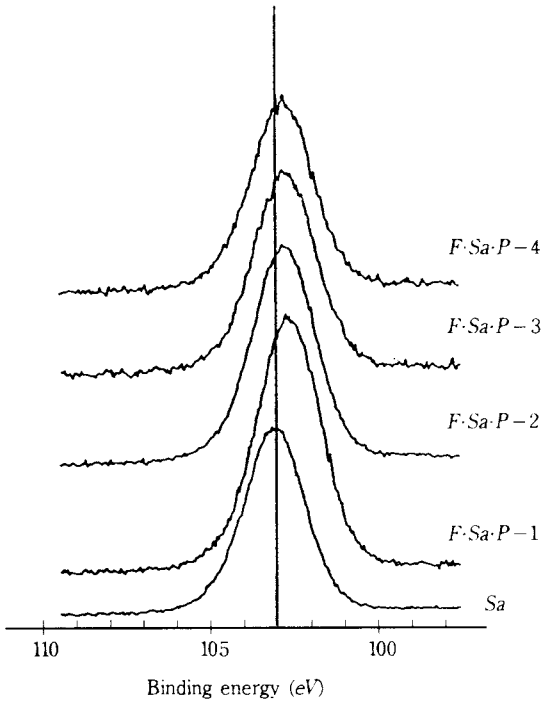

Fig. 9 Si_{2p} XPS profiles for F·Sa·P composites with double guest layers. Vertical line corresponds to Si_{2p} for untreated silica.

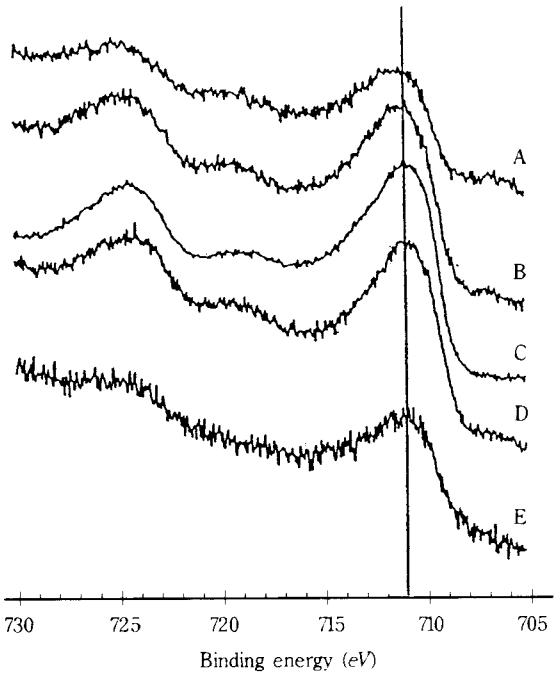

Fig. 10 Fe_{2p} XPS profiles for the samples after heating at 1100°C. Starting materials A: simple mixture of magnetite and silica (*Sa*); B: simple mixture of magnetite and silica beads (*Sb*) ; C: hematite without heating; D: magnetite; E: magnetite without heating. Vertical line corresponds to Fe_{2p} for untreated magnetite.

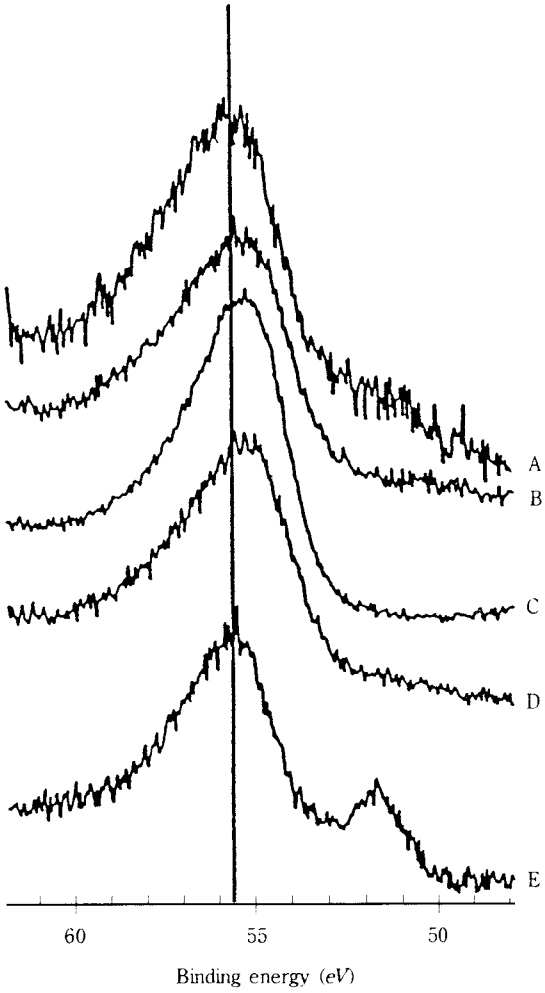

Fig. 11 Fe_{3p} XPS profiles for the samples after heating at 1100°C. Starting materials A: simple mixture of magnetite and silica (*Sa*) ; B: simple mixture of magnetite and silica beads (*Sb*); C: hematite without heating; D: magnetite; E: magnetite without heating. Vertical line corresponds to Fe_{3p} for untreated magnetite.

Formation of *Fe-O-Si* chemical bonding during mechanical treatment shown above is compatible with the change in the dissolution behavior. The formation of *Fe-O-Si* bonds provides the precursor of ferrosilicon compounds, in which iron is much stabler than in a simple iron oxide.

The effects shown above may not be caused exclusively by mechanical stress but by the result of combined thermo-mechanical effects. However, the dominant role is a mechanochemical one, since the XPS chemical shift of the mechanically treated samples was larger than that of the thermally treated ones.

4. Conclusion

With increasing rate of revolution during preparation of doubly coated spheres via a shear-compression mechanical route, a part of the second guest, magnetite, migrates into the first guest layer, silica, with simultaneous chemical interaction as confirmed by a retarded dissolution and, among others, by chemical shift of XPS analyses.

Acknowledgement

Financial support by Hosokawa Research Foundation of Powder Technology is sincerely appreciated.

References

1) Yokoyama, T., K. Urayama, M. Naito and T. Yokoyama: Kona, 5, 59 (1987)
2) Ono, K.: Kagakusouchi, 31, 40 (1989)
3) Alonso, M., M. Satoh and K. Miyanami: Powder Technol., 59, 45 (1989)
4) Tanno, K., T. Yokoyama and K. Urayama:J. Soc. Powd, Technol. Jpn., 27, 153 (1990)
5) Higashi, M., K. Terashita and K. Miyanami: Zairyou, 40, 417 (1991)
6) Kaga, H., Y. Taya, I. Shimotsuke and H. Katayama: Funtai oyobi Funmatsuyakin, 39, 546 (1992)
7) Mizota, K., S. Fujiwara and M. Senna: Mat. Sci. Eng., B10, 139 (1991)
8) Liao, J. and M. Senna: Thermochim. Acta., 197, 295 (1992)
9) Liao, J. and M. Senna: Thermochim. Acta., 210, 89 (1992)
10) Naito, M., M. Yoshikawa, T. Tanaka and H. Kondou: J. Soc. Powder Technol. Jpn., 29, 434 (1992)
11) Horvath, B., J. Strutz, J. Geyer-Lippman and E. G. Horvath: Z. Anorg. Allg. Chem., 483, 181 (1981)
12) Dillen and J. W. Geus: Appl. Catal., 40, 255 (1988)
13) Isobe, T., S. Komatsubara and M. Senna: J. Non-Cryst. Solid., 150, 144 (1992)

Author's short biography

Mamoru Senna, PhD

Graduated from Keio University, Graduate School in 1970, with a promotion to PhD. He has been a visiting scientist from 1972 to 1974 in Technische Hochschule Aachen and from 1980 to 1981 in Technische Universität in Karlsruhe. Since 1988, he is a professor in the Department of Applied Chemistry, Faculty of Science and Technology, Keio Universisty. Enhancement of reactivity of solids by mechanical and irradiational strategy, including soft-mechanochemical synthesis center his research interests.

Simultaneous Measurement of Particle Size and Electrostatic Charge by using the Laser Doppler Method †

Noriyoshi Kaya, Hiroyuki Tsujimoto, Shuji Sasabe,
*Department of Technological Development, Hosokawa Micron Co., Ltd.**
Shinchi Yoshikawa and M.K. Mazumder
*Univ. of Arkansas at Little Rock, College of Sci. and Eng. Technology***

1. Introduction

The electrostatic photography using toner particles is widely used by copiers, facsimile machines and laser printers. In the electrostatic development process, the electrostatic characteristics of toner particles have been extensively studied and measured due to their importance in determining the quality of finished print.

In the field of aerosols, on the other hand, since the behavior of aerosol particle also depends highly on the electrostatisticity of particles, many methods for measuring electrostatic charges have been studied. One of our authors proposed that the particle size and charge can be measured by applying one of the methods employed in the field of aerosols to toner particles[1]. When the toner particles are introduced into a detection area with electric and acoustic field simultaneously formed therein, the velocity of the particle is measured by the Laser Doppler method, and the particle size and electrostatic charge are calculated from the measured data[2]. The measurements of toner particles have confirmed the proposal and an instrument applied this method has been devised.

In this paper, this method of measurement is explained, and presented some applied examples for evaluating of the electrostatic characteristics of toner particles, as well as examples of recent measurements of mono-component toners with a modified toner feeding apparatus.

2. Principle of measurement

When charged particles vertically fall through acoustic and electric fields, as shown in **Figure 1**, the horizontal behavior of the particles is expressed by:

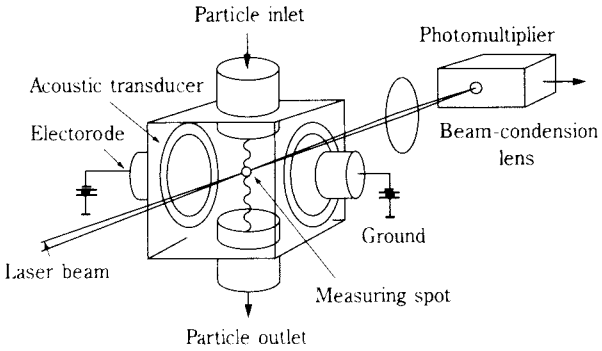

Fig. 1 Behavior of a particle subjected to acoustic and electric fields in a measurement cell

$$m_p \frac{dv_p}{d_t} + \frac{3\pi\eta D_p}{C_m}(v_p - u_g \sin \omega t) = qE \qquad (1)$$

where m_p: mass of particle (kg), v_p: velocity of particle (m/s), η: viscosity of air (Pa·s), ω: angular velocity of sound (rad/s), D_p: particle size (m), u_g:amplitude of sound (m), C_m: Cunningham's correction factor, q: charge of particle (C), E: electric field strength (V/m). By solving Eq. (1) at τ_p: relaxation time of particle $= m_p C_m / 3\pi\eta D_p$, generally, we obtain

$$v_p = \frac{u_g}{\sqrt{(1+\tau_p^2\omega^2)}} \sin(\omega t - \phi) + \exp\left(-\frac{t}{\tau_p}\right) \sin\phi + kqE\left\{1 - \exp\left(-\frac{t}{\tau_p}\right)\right\} \qquad (2)$$

where ϕ is the angle of phase lag (rad), and enters in the following relation with the relaxation time τ_p (s).

$$\tau_p\omega = \tan\phi \qquad D_p = \left(\frac{18\eta\tan\phi}{\rho_\rho C_m \omega}\right)^{0.5} \qquad (3)$$

In the above formula, ρ_ρ is the density of particles (kg/m^3), k = $C_m/3\pi\eta D_p$. Thus, the particle size D_p (m) can be obtained from Eq. (3), if the phase

* 1-9 Shoudai-Tajika, Hirakata, Osaka 573 Japan
** ETAS 575-2801 South Univ., Little Rock Arkansas 722204 USA
† This report was originally printed in *J. Soc. Powder Technology, Japan.* **31**, 202 (1994) in Japanese, before being translated into English with the permission of the editorial committee of the Soc. Powder Technology, Japan.

lag ϕ caused by a reference sound signal and actual vibration of the particle is known.In Eq. (3), at C_m = 1.0, ϱ_p = 1000 (kg/m^3), D_p is generally an aerodynamic particle size D_{pa}.

As Cunningham's correction factor C_m becomes $C_m \fallingdotseq 1$, where particle size is larger than 1.2 μm or more, most of the toner particles with a diameter less than 25 μm are calculated using C_m = 1. In the Laser Doppler method[3], a beat frequency Δf (Hz) generated by a laser beams applied from two directions to an object moving at a velocity v (m/s) is

$$\nabla f = \frac{2v \sin\theta \cos\psi}{\lambda} \tag{4}$$

where θ: half crossing angle of laser beams (rad), λ: wave length of laser (m), ψ: inclination of movement of particle in the direction of two crossing beams (rad). In the apparatus, since the inclination ψ seem to be that p_{si} = 0, and the crossing angle 2θ and wavelength λ of the laser beams are constant, when the position of optical elements are fixed, from Eq. (4), the beat frequency Δf is proportional to the velocity of particles v_p reduced from Eq. (4).

Separating the particle velocity v_p into 2 velocity components, v_a and v_e, from Eq. (2). The v_a is a particle velocity component into the acoustic field in the steady state and the v_e is the moving velocity in the electric field formed by parallel plate electrodes with an applied voltage V, and the distance between the plates being L.

Thus the beat frequencies Δf_a and Δf_e are respectively defined by,

$$\Delta f_a \propto \frac{u_g}{\sqrt{(1+\tau_p^2\omega^2)}} \sin(\omega t - \phi) \tag{5}$$

$$\Delta f_e \propto \frac{C_m}{3\pi\eta D_p} q\left(\frac{V}{L}\right) \tag{6}$$

A beat frequency actually measured at the velocity v_p of particles is a combination of Eqs. (5) and (6), a signal with an offset ϕ in relation to an acoustic reference signal is obtained by subjecting the beat frequency to FM demodulation at a frequency of acoustic oscillation, and the particles size D_p can be obtained by using Eq. (3). Regarding the quantity of charge, the velocity v_e of the movement is obtained by the beat frequency counted, and then input into a computer along with the particle size D_p and voltage V applied to the electrodes, and the quantity q of charge of the particles can be obtained by calculating Eq. (6).

3. Measuring apparatus

An optical measurement system and signal processing by the laser Doppler method are explained in **Figure 2**, and a block diagram of the entire apparatus is shown in **Figure 3**.

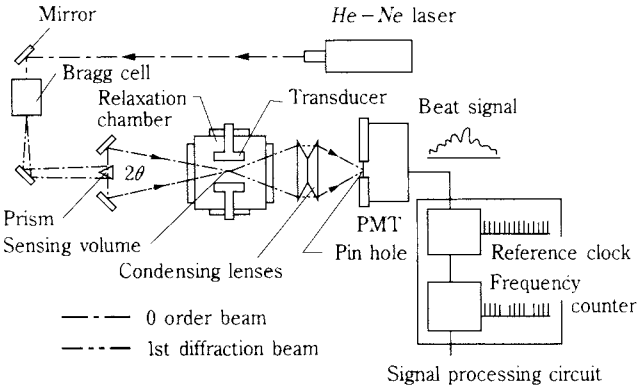

Fig. 2 Optical system and signal processing by the laser Doppler method

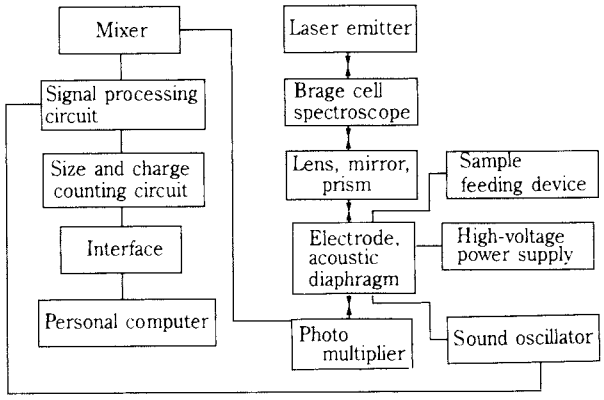

Fig. 3 Block diagram of measurement apparatus

A speaker acting as an electrode is attached to the side surface of the measurement cell, and acoustic oscillation of 1 kHz is used. The electrode on the opposite side is given an opposite polarity, so that the positive and negative voltages are applied evenly to the grounded frame of the apparatus.

Test particles introduced through a sample hole fall downward into the measurement cell, where they are shifted by the acoustic and electric fields. A laser beam is split by a Bragg Cell and the two resulting beams are then modulated to a frequency of 41 MHz, later intersecting each other in the center of a detecting area at a crossing angle of 6°. Here, the velocity of the particle shifted by the electrodes and acoustic oscillation is measured by a photomultiplier using the Laser Doppler method. The signal includes a beat frequency Δf proportional to the velocity v_p, and is electrically measured by separating the oscillating

velocity of the particles induced by acoustic oscillation from the velocity of movement induced by electric charge. From Eq. (5), the beat frequency Δf_a of the particles induced by acoustic oscillation shows a fluctuating sine wave at a frequency of 1 kHz. When the particle is oscillated to a frequency identical to the acoustic oscillation of 1 kHz, a periodic signal of sine wave length with a delay corresponding to the phase lag ϕ can be obtained. Then, by measuring the phase lag, the particle size can be obtained. Additionally, the beat frequency Δf_e caused by the movement of the particles due to electrostatic charging corresponds to a deviation from 41 MHz, and the velocity v_p of the movement is obtained by measuring the frequency. Then the particle size D_p and quantity of charge q can be obtained from Eqs. (5) and (6). In **Figures 4** and **5**, a relationship between the particle size and quantity of particle charge can be obtained by applying an electrically simulated signal of the particle to the circuit with a signal generator,

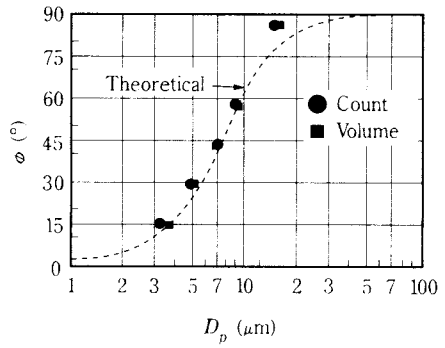

Fig. 4 Relation between phase difference and particle size

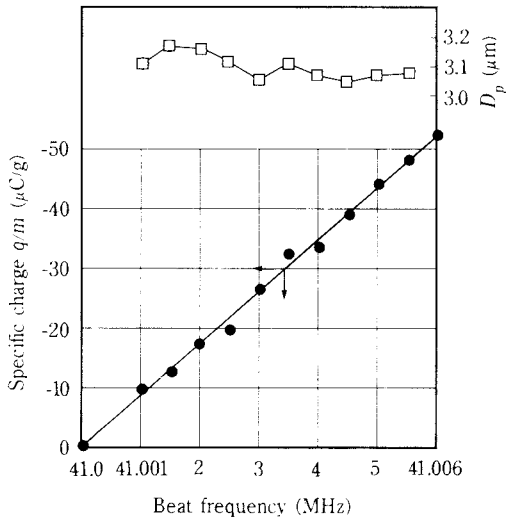

Fig. 5 Relation between quantity of charge and frequency

and assuming that the applied voltage is 100 V for testing the accuracy of the circuit. In **Figure 4**, a "Theoretical" curve is calculated by Eq. (3) and round and square marks were obtained by applying the simulated signals with a phase delay varied by the signal generator to the circuit. The mean particle size based on the particle count and based on the volume is reffered to as Count and Volume, respectively. Although ideally the mean particle sizes based on the count and volume coincide with each other, and are consistent with the theoretical formula, they do not perfectly coincide due to errors which are derived from the signal generator, measurement circuit and computer.

It is required to charge the test particles before measurement. To achieve the charging, in the case of a two-component toner, the toner is mixed with carrier particles and loaded into the feeding device, where they are subjected to a jet of nitrogen gas. The carrier particles are held in place by an electromagnet, allowing only the toner particles to fall through the measurement area. In the case of a mono-component toner, a feeder utilizing the charging mechanism of copying machines is employed for the measurement as described below. To measure particle charges when using the feeding device, the pressure of the nitrogen gas, angle and position of the nozzle affect the falling direction of the particles. Additionally, the atomospheric conditions of charging the test particles, such as the temperature and humidity in the measurement area, can also significantly affect the measurement. It is very important to consider such conditions with sufficient care.

After entering the measurement area, the particles are affected by the acoustic and electric fields, and biased in the horizontal direction as they fall. Then the beat frequency of the horizontal velocity is measured. In the modified apparatus, the beat frequency measurements are sent to the computer, interrupting any program operating at the time, and the distribution of particle size and the specific particle charge distribution are displayed on the computer screen in real time. After a predetermined number of particles are measured, the screen display is terminated and you can analyze the particle charge characteristics by using a particle size distribution, particle charge distribution and/or a three-dimensional distribution of particle size and charge.

4. Example of measurement and its evaluation

An example of a three-dimensional display of a measurement result is shown in **Figure 6**. It is

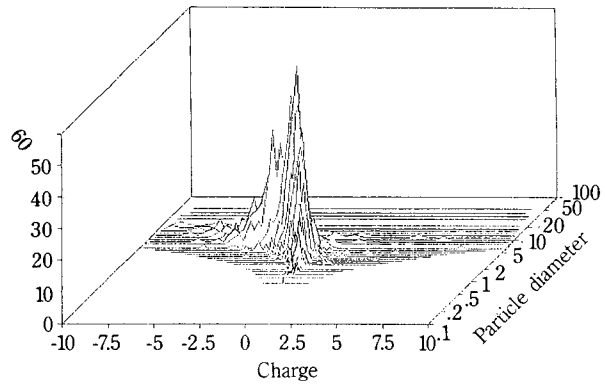

Fig. 6 Three-dimensional representation illustrating simultaneous measurement of quantity of charge and particle size

recognized in the figure that more particles are negatively charged, and the particle sizes range from 1 μm to 17 or 18 μm. Various studies on particle size and charging have been reported by using toner particles up to now[4]. As an example of these studies, three types of test samples, all having different charges characteristics, are compared in **Figure 7**. In the figure, D-1 is negatively charged and D-2 is positively charged, and although these samples have different polarities, both provide the same fine copy quality. It can be observed that the quantity of charge corresponds to the second power of the particle size in test sample D-1 and D-2. However such a relationship can not be observed in test sample D-3, because of poor charge characteristics.

On the right side of **Figure 7**, the actual quantity of particle charge of the test samples is shown, and it can be seen that the charge quantities are distributed relatively in a higher range.

Figure 8 shows the charge quntities of two-component toner in relation to the qualities of the carriers. The same two-component toners were charged by agitating them with two types of carriers (new and used), and measured for evaluating the carrier effects on charging toners. With the used carrier, it is clear that charge quality of toner was generally poor; although some coarse particles have a high charge, the distribution curve is located closer to a neutral point 0. This may be due to the amount of wear and breakage of toner which occurs during long-term use, and in the event that any toner particles become attached to the carrier surface. This surface contamination can not give sufficient charge to the toner. In fact, we observed, using a microscope, that the used carrier was contaminated by pieces of ground toner fused to its surface. Accordingly, we consider the toner to be insufficiently charged when the carrier surface is contaminated with grounded toner particles because the friction charge level is too low.

Recently, mono-component toners which do not contain carriers, are being used in more and more copying machines and laser printers to reduce the size of the apparatus. This type of toner cannot be charged as easily as a conventional two-component toner and accurate measurement of mono-component toner charges have been difficult. However we have

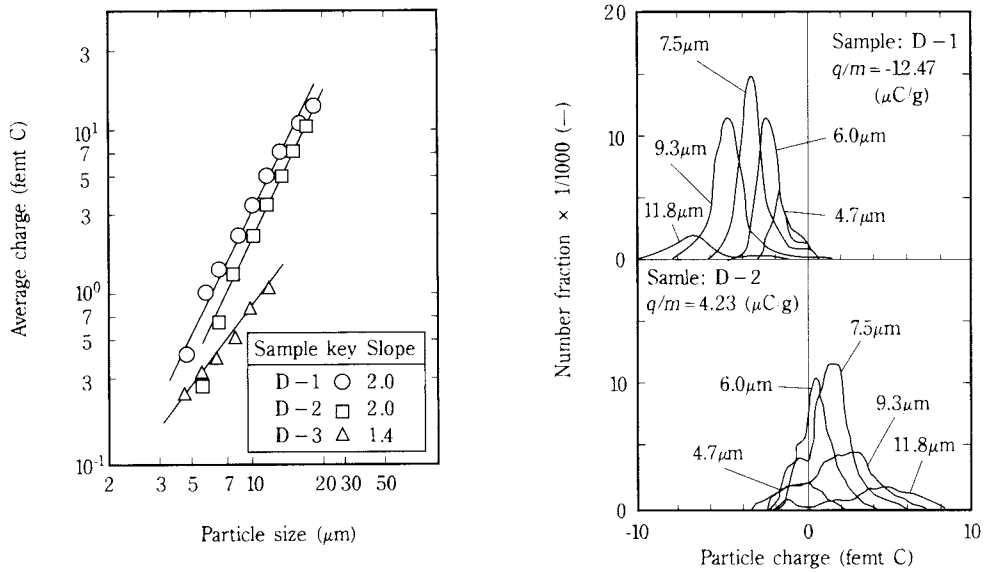

Fig. 7 Comparison of measurement of charge characteristics

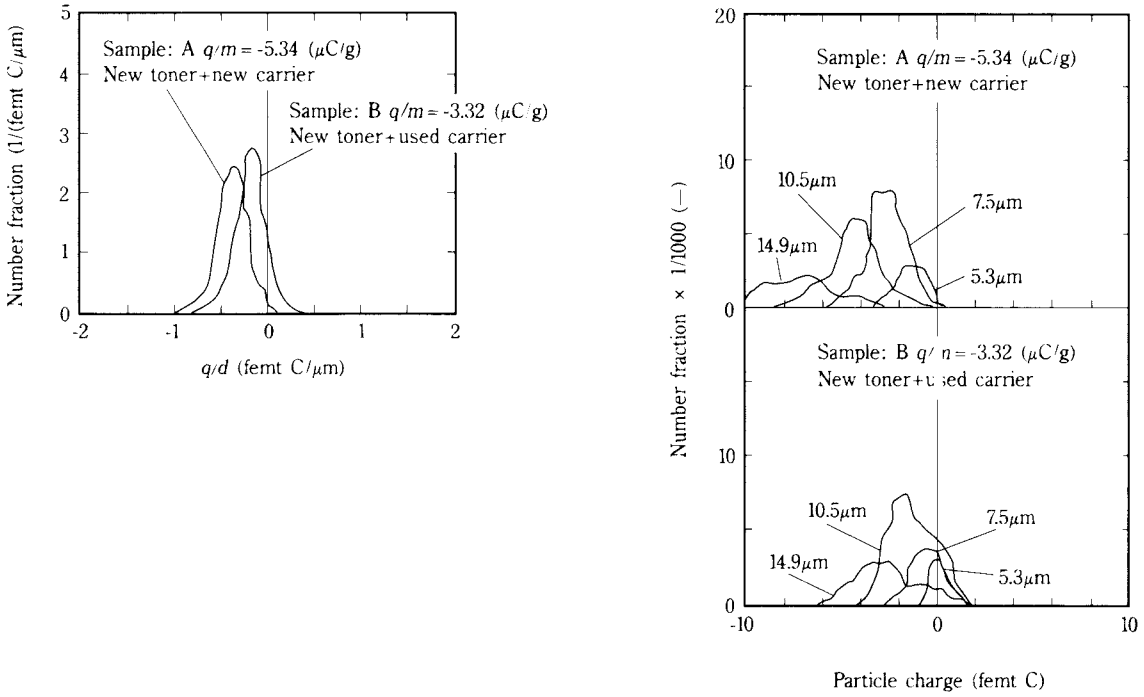

Fig. 8 Effects of new and used carriers on toner

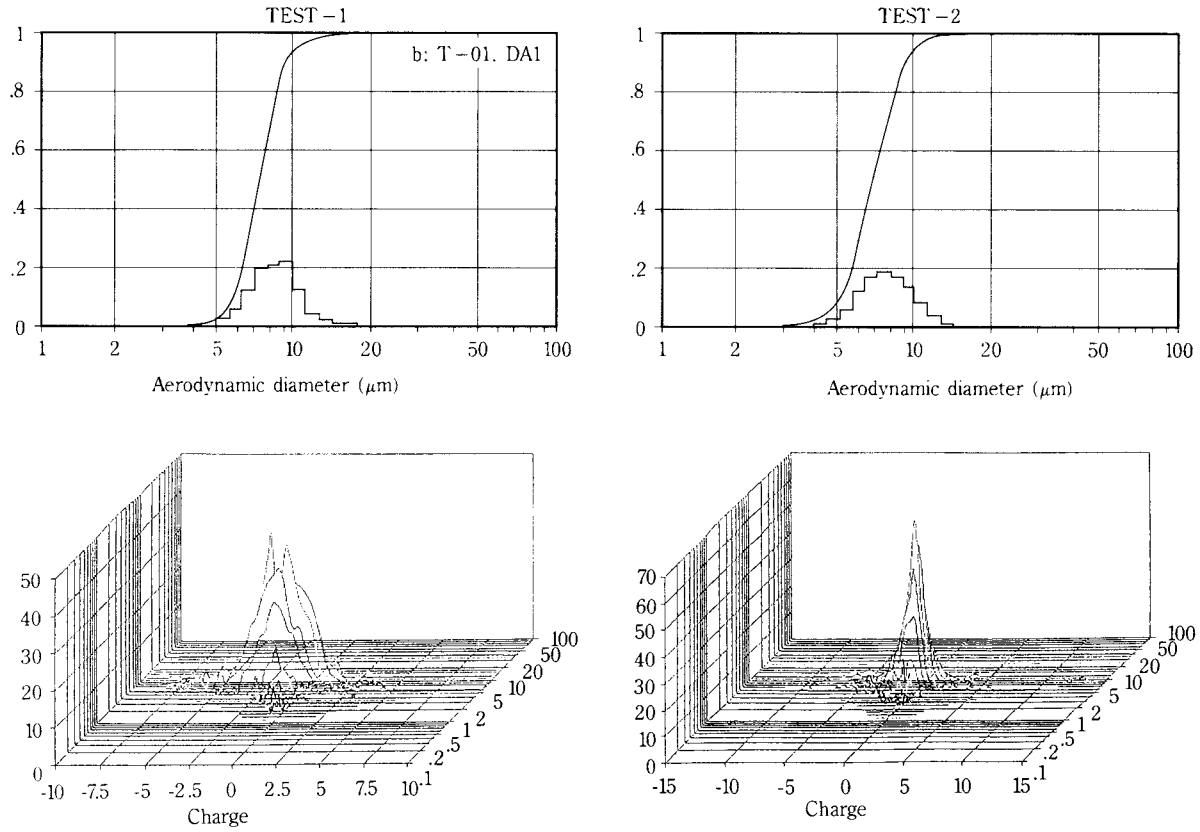

Fig. 9 Comparison example of measurement of single-component toners

recently deviced a method for measuring mono-component toner charges by physically removing a machine's charging mechanism and adapting it to our feeding device for accurate measurement. An example of a measurement for a mono-component toner is shown in **Figure 9. Figure 10** shows a feeding device for mesuring mono-component toner charges. To measure a mono-component toner with

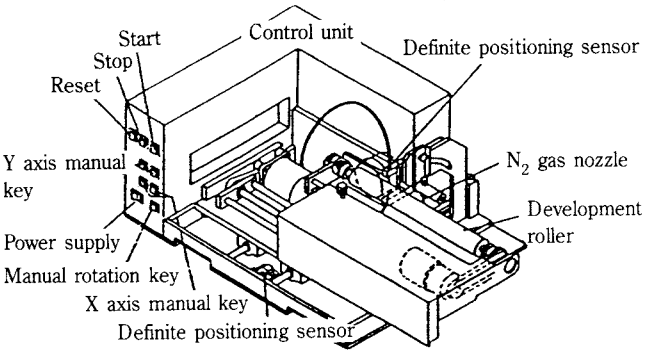

Fig. 10 Feeding device of charged single-component toner

the feeding device, a developing roller with a mono-component toner affixed to it (i.e.-after the toner has been charged) is removed from the copying machines and set directly onto the feeding device. The toner on the roller surface is fed into the measurement area by a jet of nitrogen gas. The roller is moved into a different position after each jet to ensure that all of the toner particles are blown from the roller surface. The results of measuring two different mono-component toners show that the measurements are substantially identical in terms of the distribution of particle size, but different in the distribution of particle charge. It is assumed that these different measurements reflect two samples having different compositions of the charge control agent and the like, althrough the particle sizes are similar to each other.

5. Conclusion

We have presented a method for simultaneously measuring the size and charge of toner particles by observing their velocity and oscillation in acoustic and electrical fields using the Laser Doppler method. In addition, we showed examples which evaluated the relationship between the particle size and the electrostatic charge of toners by measuring the toners using this Laser Doppler method.

Now we are making efforts to improve the accuracy and reproducibility of the measurement through further modifications in order to develop an apparatus that is easier to operate, and capable more accurate measurements, even at a production site.

Nomenclature

C_m	[−]	Cunningham's correction factor
D_p	[m]	particle diameter
E	[V/m]	electrical field strength
L	[m]	distance between parallel electrode plates
m_p	[kg]	mass of particle
q	[C]	charge of particle
u_g	[m]	amplitude of sound wave
V	[V]	applied voltage
ν_a	[m/s]	velocity of particle due to acoustic field
ν_e	[m/s]	velocity of particle due to electric field
ν_p	[m/s]	velocity of particle
η	[Pa·s]	viscosity of air
θ	[rad]	half crossing angle of laser beams
λ	[m]	wave length of laser
ρ_p	[kg/m^3]	density of particle
τ_p	[s]	relaxation time of particle
ϕ	[rad]	angle of phase lag
ψ	[rad]	inclination of movement of particle to crossing beam
ω	[rad/s]	angular velocity of sound
∇_f	[Hz]	beat frequency

Literature cited

1) Mazumder, M. K., et al.: IEEE Ind. Appl. Soc. Annual meeting, Part II p. 1606 (1987).
2) Yokoyama, T.et al.: Outline of Presentations at the 25th Symposium on Fine Particles, p. 82, Sapporo (1987)
3) Yatagai, T.: Applied Optics; Guide to Optical Instrumentation, p. 164, Maruzen (1988)
4) Kitabatake, Y.: *Funsai*, No. 32, p.86 (1988)
5) Tsujimoto, H., et al.: IS & T's 7th International Congress on Advances in Non-Impact Printing Technologies, 1, p.401 (1991).
6) Kutsuwada, N. et al.: IS & T's 7th International Congress on Advances in Non-Impact Printing Technologies, 2, p.84 (1991).

The Effect of Humidity on the Removal of Fine Particles on a Solid Surface using High-speed Air Jet†

Kuniaki Gotoh, Shyoji Takebe and Hiroaki Masuda
*Dept. Chem. Eng., Kyoto Univ.,**
Yoshiji Banba
*OMRON Co.,***

Abstract

The effect of operating conditions on the removal efficiency of deposited particles using high-speed air jet was studied with particular attention to the humidity of surrounding air during particle deposition and air-jet removal. The experimental results showed that the removal efficiency of particles deposited in a low humidity atmosphere, decreased with increasing drying time after the deposition. In the case of a deposition under high humidity, the removal efficiency increased at the beginning of drying and decreased rapidly after reaching the maximum efficiency. For drying over 80 hrs, however, the humidity of the surrounding air during the particle deposition didn't affect the removal efficiency.

The efficiency also depended on the humidity during the air-jet removal, and reached the maximum value at 67% relative humidity. Such a variation of the removal efficiency has been well explained by the change of Hamaker's constant with the adsorbed layer-thickness of water molecules and the variation of liquid surface tension with the thickness of liquid bridge.

1. Introduction

Contamination of products by fine particles has been a problem in many fields such as electric, electronic industries etc. Until today, although fine particles deposited on a product have been removed mainly by wet cleaning, the problem associated with wet cleaning is that such method is inapplicable to products sensitive to moisture, requires a drying process, and causes contamination of environments and the like by the cleaning agents. Accordingly, the authors paid attention to a method of removing particles by high-speed air jet which is a dry method using a removing apparatus of a relatively simple structure, and experimentally studied the effects of such flow control conditions as duration time of air jet, jet impinging angle, nozzle-surface distance on the removal efficiency[1]. We also studied the variation of the removal efficiency with jet impingement by continuously applying air jets for short durations. The pulse jets removal was also reported by Otani, et al.[2].

When a high-speed air jet is applied to a surface to remove particles, a separating force due to a resistance to the air jet acts on the particles deposited on the surface. On the other hand, an adhesive force is effective between the particle and the solid surface. Although the main adhesive forces are the van der Waals force, the liquid bridging force and the electrostatic force, they depend on the relative humidity of the air. Therefore, it is expected that the removal efficiency of particles may be affected by the humidity. Thus, in the study, we paid particular attention to the humidity during deposition of particles onto a surface and removal thereof, and studied the effect of the humidity, that is one of the environmental conditions in removing particles.

2. Apparatus and Method of Experiment

Figure 1 shows a schematic view of a particle removing apparatus used in the experiment. In the particle removing experiment, similar to our previous report[1], compressed air was adjusted to a predetermined pressure by means of a release valve after removal of mist, and supplied to a jet nozzle. For the jet nozzle, a two-dimensional slit-type nozzle having a nozzle area of 0.25×10 mm^2 was employed, as

* Sakyo-ku, Kyoto 606-01 JAPAN
** Kusatsu, Shiga 525 JAPAN
† This report was originally printed in *Kagaku Kougaku Ronbunshu*, **20**, 205 (1994) in Japanese, before being translated into English with the permission of the editorial committee of the Soc. Chemical Engineers, Japan.

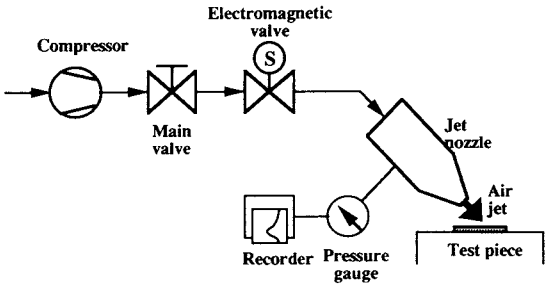

Fig. 1 Schematic diagram of experimental apparatus

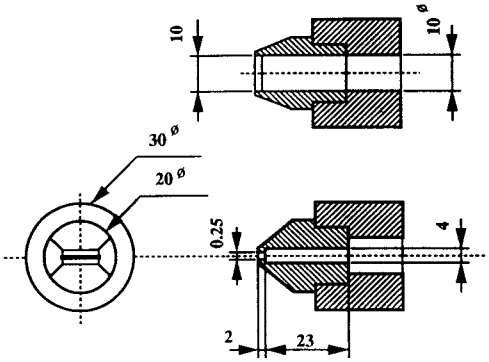

Fig. 2 Air jet nozzle

shown in **Figure 2**. The operating conditions of the air jet were constant such that the air pressure at the nozzle (gauge pressure) ΔP_n was set at 10^5Pa, the jet impinging angle at 45°, and the distance d between the nozzle tip and the surface at 10 mm. In addition, here, the duration time was constantly set to t = 10 sec, because the removal efficiency reached the highest value at that time and remained at that value throughout the duration time of air jet, when the air pressure at the nozzle ΔP_n was at 10^5Pa. During the removal of particles, the room temperature was maintained at constant (approximately 20°C) by means of an air-conditioner, and the relative humidity Ψ_r at removal was adjusted by varying the water content of the air mainly by means of an ultrasonic humidifier (Matsushita Electric Industry Co., Ltd., FE-05KVE).

In the experiment, the removal efficiency was obtained by microscopically counting the particles after they were deposited on a test piece surface (before removal) and after jet impingement (after removal), respectively, and dividing the difference of the counts by the total number of particles. The removal efficiency was measured at three points (measurement points 1, 2 and 3 in the previous report[1]) in the proximity of the air-jet impingement point, and an average value of the measurements was defined as the removal efficiency η. The measurement area for counting the particles was always set to 1 × 1 mm^2.

Other main conditions are shown in **Table 1.** Standard latex particles (Styrene/Divinylbenzene) of 3.7 μm in size were employed as test particles, and a glass (borosilicate glass) as a test piece. **Figure 3** shows an apparatus for depositing particles onto a test piece. Because the standard latex particles are dispersed and stored in a liquid containing surfactant, they were aerosolized by spraying with a nebulizer, and the particles were heated and dried in a buffer container. Water in the aerosol was removed by a diffusion drier filled with silica gel, and the particles were deposited on the wall by inertia impingement using an impactor. The impactor is of a jet diameter of 9 mm, and the mean velocity of aerosol was constant at about 6 m/s. At deposition, the humidity of the air jet was measured downstream of a baffle plate in the impactor by using a digital thermo-hygrometer, and the measurement was taken as the humidity Ψ_d at particle deposition. The humidity at deposition was changed by varying the heating temperature in the buffer container and the length of the diffusion dryer.

In studying the effect of the humidity Ψ_r at removal, the conditions at deposition were constant at about

Table 1 Experimental conditions

Surface material		Glass (Borosilicate)
Particle		Styrene/divinylbenzene
Particle size	D_p	3.7 μm
Nozzle pressure	ΔP_n	10^5 Pa
Jet impinging angle	θ	45 deg
Nozzle-surface distance	d	10 mm
Jet duration time	t	10 s
Relative humidity at deposition	Ψ_d	52 ~ 74 %
Relative humidity at removal	Ψ_r	55 ~ 82 %
Drying time in desiccator	t_d	1 ~ 180 hr

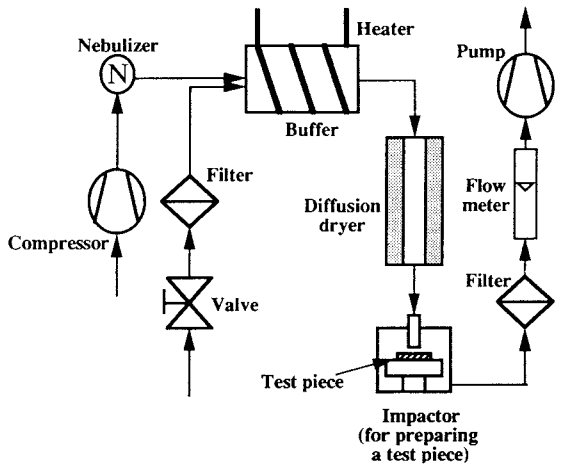

Fig. 3 Apparatus for preparing a test piece

60°C for the wall temperature of the buffer container and 66 cm for the length of the diffusion dryer (about 0.23 sec of average residence time of air). Although the number of particles deposited on a surface by inertia impingement is generally distributed in the radial direction, centering about an impingement point of air, it was confirmed that no significant difference in the number of particles was observed in the vicinity of the impingement point of air, which provides a measurement point in the experiment, and the particles were almost uniformly deposited. The depositing time of particles was adjusted such that about 200 particles were deposited on each measurement area.

After the particles were deposited, they were counted on the measurement surface by using an optical microscope, and dried in a desiccator of about 7×10^{-3} m^3 in content volume. It takes about 15 min to obtain a constant humidity (approximately 15%) in the desiccator after a test piece is placed in the desiccator, and the cover is closed. Therefore, the test piece was dried for at least 1 hr in order to assume a drying operation at a constant humidity.

3. Result of Experiment and Discussion

Figure 4 shows the result of the removal experiment by varying the drying time in the desiccator, taking the humidity at deposition as a parameter. The humidity Ψ_r at removal was constant at 59%. When the humidity at deposition was lowest at Ψ_d = 55%, the removal efficiency was reduced as the drying time was increased, and reached a constant level of about 10% after 5 hr of drying. At Ψ_d = 58%, reduction of the removal efficiency was minor until about 20 hr of drying, a high removal efficiency of 70 to 80% was obtained, and the efficiency rapidly decreased after the drying time exceeded 20 hr. When it exceeded 60 hr, the efficiency was equal to that at Ψ_d = 55%, and became constant. At Ψ_d = 64, 72%, although the removal efficiency was increased together with the drying time until about 3 and 6 hr of drying, respectively, it dropped rapidly thereafter. In other words: (1) The removal efficiency decreased as the drying time was increased, in the case when the deposition took place at a humidity not higher than the humidity Ψ_r at removal; (2) the removal efficiency increased at the beginning, and decreased after the maximum efficiency was achieved at a certain drying time, in the case when the deposition took place at a humidity not lower than that at removal; and (3) the removal efficiency was not affected by the humidity Ψ_d at deposition after 80 hr of drying. As a result, it is supposed that the removal efficiency is higher immediately after deposition of particles, in the case when the particles are deposited at a relatively low humidity, and after drying them to a certain level, in the case when the particles are deposited at a high humidity.

Figure 5 shows the result of the removal experiment conducted by varying the humidity Ψ_r at removal. Here, in order to avoid any effect of the humidity at deposition, the test piece was dried in a desiccator for 100 hr or longer after deposition of the particles according to the result of **Figure 4**. After drying, the test piece was transferred to a controlled removal environment, and the removal experiment was conducted after leaving the test piece in the environment for 2 min or longer. The removal efficiency was low at a low humidity, and rapidly increased as the humidity was increased. When the humidity Ψ_r at removal was 67%, the maximum efficiency was achieved, and it decreased at a humidity lower than that. From the figure, it is recognized that the removal efficiency can be increased, regardless of the humidity at deposition of the particles, by adjusting the humidity Ψ_r at removal, which is an environmental condition during the removal of the particles. Such tendency was observed not only on glass pieces used in the

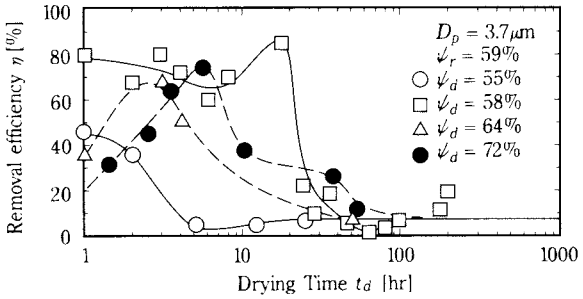

Fig. 4 Effect of drying time on removal efficiency

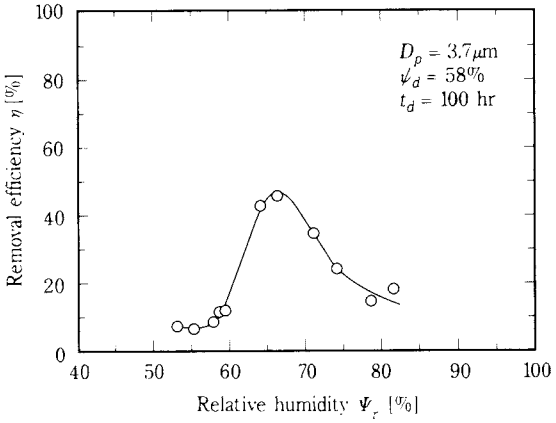

Fig. 5 Effect of relative humidity on removal efficiency

experiment, but also on test pieces made of polymer materials and metals. The result of the experiments using test pieces of different materials shall be discussed in the next report[3]. The experiment was conducted by varying the period during which the test pieces were left after they were set in place in a removal environment after drying, and it was confirmed that the removal efficiency was not affected by the period, if it is set to 1 min or longer. Thus, the results of the experiment shown in **Figure 5** are considered to be equilibrium values in the removal environment.

Since the conditions of jet impingement are unchanged in the environment, the particle removing force provided by the air jet is considered to be constant. It is, therefore, supposed that the removal efficiency depends on the humidity, because water molecules on a particle and wall surface may have an effect on the adhesive force between a particle and a solid surface. When the humidity is low, and the effect of water molecules is absent, the van der Waals force can be approximated by a value in vacuum, and represents an adhesive force higher than that in the presence of water molecules. It was reported that the liquid bridging force increases together with the humidity, when a liquid bridge formed between a particle and a surface at a high humidity[4]. Thus, it is considered that the removal efficiency is reduced mainly with an increase of the van der Waals force at a low humidity, and with an increase of the liquid bridging force at high humidity. Now, the variation of the adhesive force due to the humidity is typified.

At low humidity, it is generally considered that water molecules are adsorbed onto a particle and solid surface, and form an adsorbed layer of not more than a few molecules overlaid on each other (**Figure 6-a**). A variation of the thickness δ of the adsorbed water layer on a glass surface was presented by Chikazawa et al.[4], as shown in **Figure 7** , and the data is now approximated by the Halsey's formula[5] below.

$$\ln \psi = -\frac{k}{RT\theta_w^q}$$

$$\theta_w = \nu/\nu_m \tag{1}$$

At $\nu = S\delta$,

$$\ln \psi = -\frac{K_h}{\delta^q}$$

$$K_h = \frac{k\nu_m^q}{RTS^q} = 1.45 \times 10^{-17}$$

$$q = 1.81 \tag{2}$$

An approximate curve obtained by Eq. (2) is sufficiently consistent with plots, as shown in **Figure 7**. Additionally, it is found from the figure that about 0.5 nm (approximately 1.7 molecules) or more water molecules are adsorbed even at the lowest humidity within the range of the experiment. In such condition, the adsorbed water is different from bulk water, and no liquid bridging force acts as an adhesion force between the particle and the surface. However, the van der Waals force and an electrostatic are considered to be active. Here, taking only the van der Waals force, and neglecting the electrostatic force, an adhesive force F_d between the particle and the surface is assumed to be obtained by the following formula[6].

$$F_d = F_\nu = \frac{AD_p}{12z^2}\left(1+\frac{A^2k_p^2D_p}{108z^7}\right) \tag{3}$$

where

$$k_p = \frac{1-\nu_p^2}{E_p} + \frac{1-\nu_w^2}{E_w} \tag{4}$$

In Eq. (4), Young's modulus E and Poisson's ratio ν are independent of the humidity, and can be obtained as follows.

$E_w = 7.5 \times 10^{10}$ (Glass)[7]

$E_p = 0.38 \times 10^{10}$ (Polystyrene)[7]

$\nu_w = 0.17$ (Glass)[7]

$\nu_p = 0.34$ (Polystyrene)[7]

Accordingly, the modulus of elastic characteristic k_p in Eq. (3) is considered to be independent of the

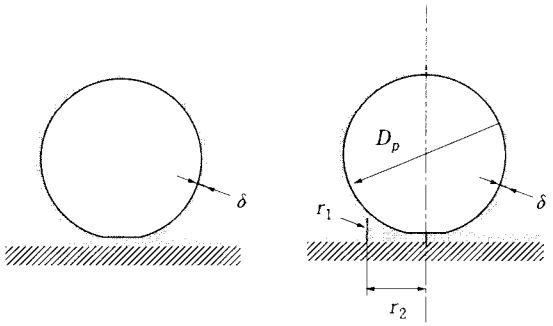

a) low humidity b) high humidity

Fig. 6 Schematic diagram showing effect of humidity

humidity and constant. Then, dependency of a gap z between a particle and a solid surface and Hamaker's constant A on the humidity is considered.

For this purpose, two models are assumed for the contact between a particle and a solid surface. In

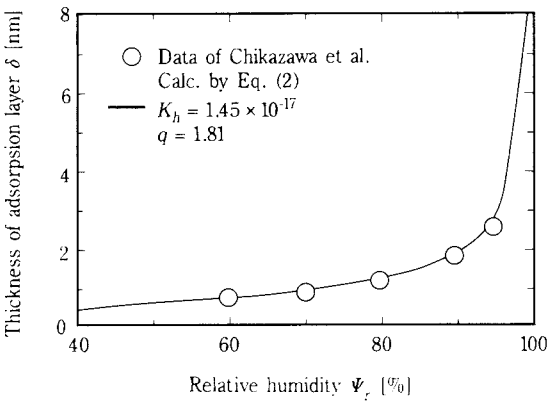

Fig. 7 Thickness of adsorbed water layer as a function of relative humidity

Model I (**Figure 8**), it is assumed that the medium between a particle and a surface is changed from air through an adsorbed water (air + water molecules) to a liquid (water). In this connection, it is assumed that the conditions of contact between the particle and the surface are unchanged. That is, an adsorbed layer of water is virtually considered as a medium different from air and liquid, and the gap z between the particle and the surface is assumed to be constant, although the Hamaker's constant of the medium is continuously changed as the humidity is increased. Since the gap z is determined by Born's repulsion between objects, and generally defined as being about 0.4 nm, it is also defined as z = 0.4 nm ($= z_0$) here.

The Hamaker's constant A is varied by the presence of water molecules, and can be approximated for dry air and a liquid by the following formulae, respectively[8].

$$A = \sqrt{A_p A_w} \tag{5}$$

$$A = (\sqrt{A_p} - \sqrt{A_l})\ (\sqrt{A_w} - \sqrt{A_l}) \tag{6}$$

However, according to the above formulae, the adhesive force created by water molecules should be changed stepwise from that in the air to that in the liquid, and such continuous change of the removal efficiency in relation to the humidity as observed in the experimental result cannot be expressed. On the other hand, the Hamaker's constant can be obtained by the following formulae, when an adsorption layer of macromolecules is present on a particle surface in a liquid[9].

$$A = (\sqrt{A_p} - \sqrt{A_j})\ (\sqrt{A_w} - \sqrt{A_j}) \tag{7}$$

$$A_j = [K_a\sqrt{A_a} + (1 - K_a)\sqrt{A_m}]^2 \tag{8}$$

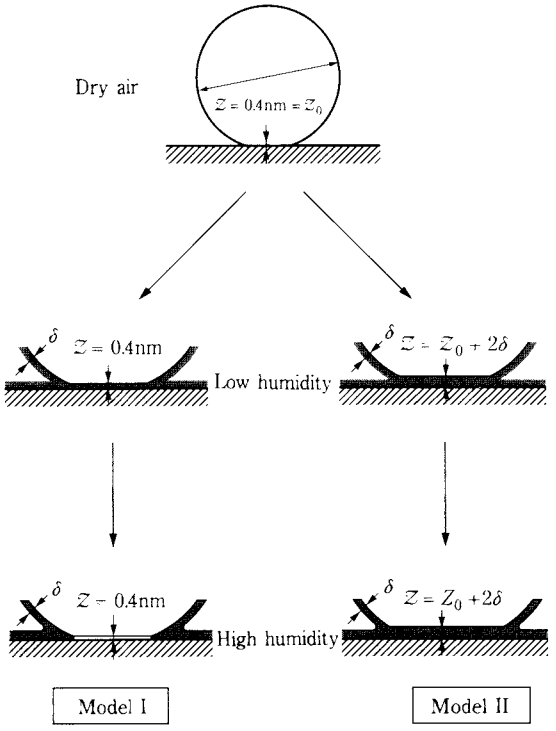

Fig. 8 Model showing water adsorption

$$K_a = 2\delta K_{a0}/z \leq 1 \tag{9}$$

where A_a is the Hamaker's constant of the adsorbate, and A_m the Hamaker's constant of the medium. In the experiment, as the medium is air, and the absorbate is water molecules, Eqs. (7) and (8) are equal to Eq. (5) at K_a = 0, as A_m = 0, and to Eq. (6) at K_a = 1. Therefore, the Hamaker's constant between a particle and a surface is expressed by the following formula.

$$A = (\sqrt{A_p} - K_a\sqrt{A_j})\ (\sqrt{A_w} - K_a\sqrt{A_j}) \tag{10}$$

In Eq. (9), K_{a0} represents the volume ratio between the adsorbate and the medium between two objects, and $2\delta/z_0$ the ratio of the thickness of the adsorption layer to the distance between the surfaces of the two objects. In the case when water molecules adsorbed are absent, K_{a0} = 0, therefore K_a = 0. If it is assumed that water molecules adsorbed are similar to those of bulk water, K_{a0} is constant at K_{a0} = 1. If z is assumed to be constant at 0.4 nm, $2\delta/z$ is 1 or more, and K_a is 1 or more within the range ($\delta \geq 0.5$ nm) of the experiment. Eq. (9) is, therefore, inapplicable to the experiment conducted in a gaseous phase. Then, by assuming that K_a depends only on the thickness δ of the adsorbed water, K_a is expressed by a linear function of δ. Because K_a = 0

when the thickness of the layer $\delta = 0$, while the thickness of a liquid film is 2.9 to 3.7 nm when adsorbed water film has the properties of a liquid, and capillary condensation is possible[10], K_{a0}/z is determined such that K_a becomes equal to 1 when the thickness 2δ of the liquid film between the particle and the surface is 3.5 nm. That is,

$$K_a = \delta / (1.75 \times 10^{-9})$$
$$0 \leq K_a \leq 1 \tag{11}$$

If the thickness of the layer of water molecules adsorbed onto the surface of a test particle is also obtained by Eq. (2), the variation of the adhesive force F_d created by the humidity Ψ_r can be calculated by using Eqs. (3) to (4) and (7) to (11).

On the other hand, in Model II (**Figure 8**), it is supposed that the number of water molecules between the particle and the surface is increased, and the distance z between the particle and the surface is changed, as the medium between the particle and the surface changes from air to liquid (water) along with the increase of humidity. Thus, Eqs. (7) to (10) are applicable to the variation of the Hamaker's constant caused by the thickness of the layer of water molecules, similarly to Model I, and the distance between the particle and the surface is given by the following formula as the sum of the initial distance z_0 between the particle and the surface and the thickness 2δ of the adsorbed water.

$$z = z_0 + 2\delta$$
$$z_0 = 0.4 \text{ nm} \tag{12}$$

For Models I and II, the variation of the adhesive force F_d was calculated, respectively, and the result of the calculation is shown in **Figure 9**. The Hamaker's constants used in the calculation are shown below.

$A_w = 1.6 \times 10^{-19}$ (Glass: SiO_2)[8]

$A_p = 1.2 \times 10^{-19}$ (Polystyrene)[8]

$A_l = 4.8 \times 10^{-20}$ (Water)[8]

As shown in the figure, by using either model, a continuous variation of the adhesive force caused by the humidity can be expressed successfully. However, within the range of the experiment (Ψ_r = 55 to 82%), the magnitude of the adhesive force is higher for Model I in which the distance z between the particle and the surface is constant.

Since the experimental result is expressed by the removal efficiency, the calculated value η_{cal} of the removal efficiency is obtained on the basis of the adhesive force F_d calculated. As shown in **Figure 10**, by taking the adhesive force F_d as a mean value, the distribution of the adhesive force between the particle and the surface should be given. The distribution of the adhesive force f_{ad} was assumed to

$$f_{ad} = \frac{1}{\sqrt{2\pi}\ln\sigma_g} \exp\left\{ - \frac{(\ln F - \ln F_d)^2}{2\ln^2\sigma_g} \right\} \tag{13}$$

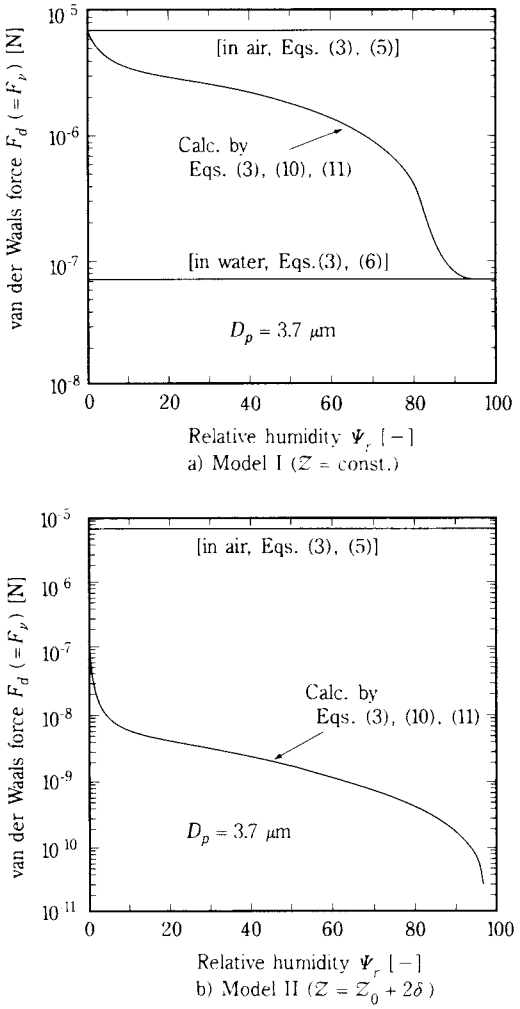

Fig. 9 van der Waals force as a function of relative humidity

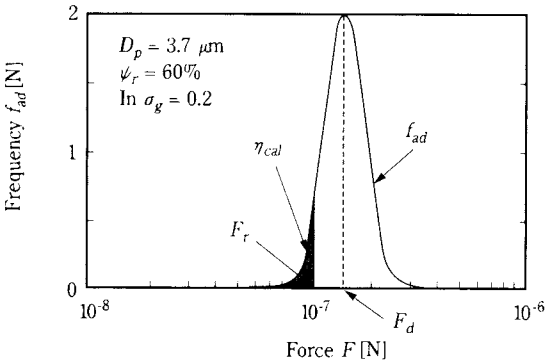

Fig. 10 Schematic diagram showing the distribution of the adhesive force

be a lognormal distribution as expressed by the following formula.

Now, defining the removal force by F_r, and assuming, as shown in **Figure 10,** that particles having an adhesive force F_d lower than the removal force F_r are removed, and those having an adhesive force F_d higher than the removal force F_r are not removed, the removal efficiency η_{cal} can be calculated from the distribution of the adhesive force using the following formula.

$$\eta_{cal} = \int_0^{F_r} f_{ad} dF \tag{14}$$

By means of Eqs. (13) and (14), the variation of the removal force can be calculated from the variation of the adhesive force F_d caused by the humidity.

The variation of the removal force caused by the humidity was calculated using ln σ_g as a parameter, and the result of the calculation is shown in **Figure 11.** Here, F_r was determined for each ln σ_g such that η_{cal} = 12% at the humidity Ψ_r = 60% that is obtained from the experimental result, at which no liquid bridge was considered to be formed. In a range of the humidity Ψ_r not higher than 67%, at ln σ_g = 0.2, the

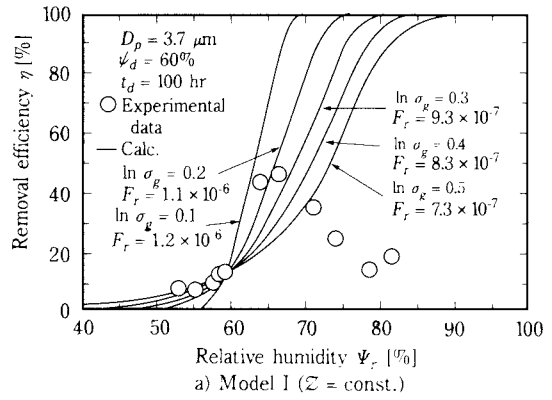

a) Model I ($\mathcal{Z}$ = const.)

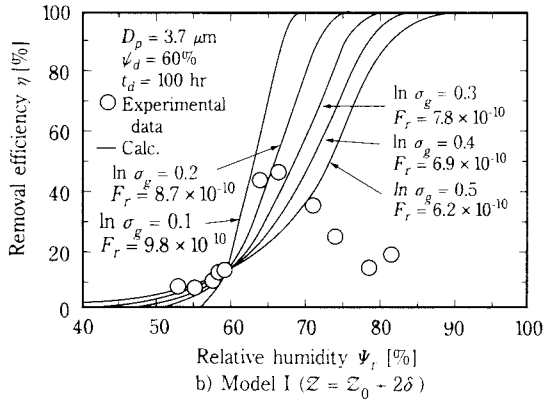

b) Model I ($\mathcal{Z} = \mathcal{Z}_0 + 2\delta$)

Fig. 11 Calculated removal efficiency considering about the change of van der Waals force

result of the calculation is generally consistent with the experimental result for both Models I and II. Accordingly, it is clear that the variation of the removal efficiency at a low humidity can be explained by using either model. However, the result of the calculation provides a curve rising rightward even when the humidity Ψ_r is 67% or more, and is inconsistent with the tendency of the experimental result of having a peak. It is considered to be because a liquid bridging force created by a liquid film formed at a high humidity is not taken into consideration.

It is known that a liquid film is formed in the vicinity of a contact point between a particle and a solid surface even at lower pressure than the saturated vapor pressure because water is condensed due to the Kelvin effect. It is considered that a liquid bridging force acts between a particle and a surface because of the liquid film. As impurities (surfactant, etc.) on the surface of a test piece and of a particle and impurities in the atmosphere at deposition and removal of particles are not removed, soluble impurities may be contained in the condensate. Therefore, a formula (Kelvin formula; see Appendix A) presented by Kousaka et al.[11,12] for a liquid bridge between two spheres of identical size was employed. Since the formula is derived for two spheres of identical size, it was converted for a sphere and a flat plate (d_1 = D_p, d_2 = ∞) using an equivalent diameter d_e that defines r_0 by the following formula.

$$d_e = \frac{d_1 d_2}{d_1 + d_2} = r_0 \tag{15}$$

By using the formula presented by Kousaka et al. and Eq. (15), the radii r_1 and r_2 of the liquid bridge when the humidity at removal is at Ψ_r can be obtained.

The thickness of the liquid film when a liquid bridge is formed, on the other hand, is defined by the distance t_l between points P and W formed by combining the thickness of the adsorption layer and that of the liquid bridge between a particle and a surface. Here, when the angle between the segment $\overline{CW}$ and the central axis of a deposited particle is at θ_p, the angle θ_p falls within the range expressed by the following formula (see Appendix B).

$$\theta_p \leq \tan^{-1}\left(\frac{r_2 + r_1}{D_p/2 + z}\right) \tag{16}$$

Because the particle size is 3.7 μm, and the radii r_1 and r_2 of the liquid bridge are 1.4 nm and 130 nm (N_s = 0.0035) at the maximum humidity of 82% within the range of the experiment,

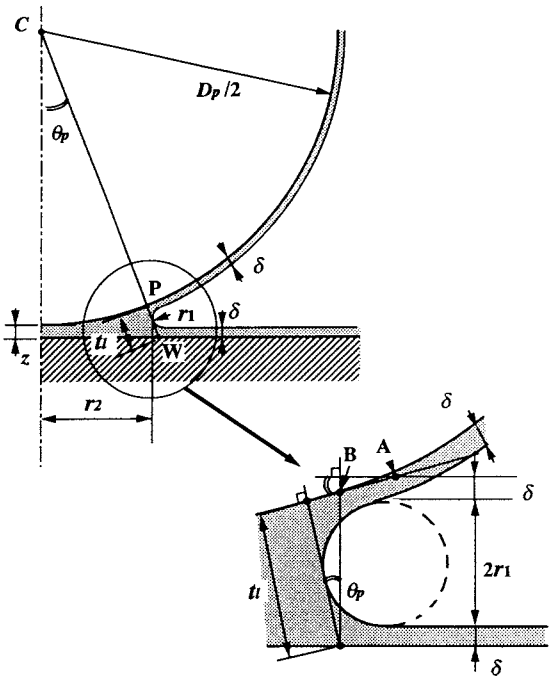

Fig. 12 Approximation of liquid film thickness t_l

$$\theta_p \leq \tan^{-1}(0.036) = 2.03 \text{ [deg]} \qquad (17)$$

(Note that $z = z_0 = 0.4$ nm is assumed.)

Thus, within the range of the experiment, the angle is assumed to be at $\theta_p = 0$, and the thickness of the liquid film is approximated by $2 \times (\delta + r_1)$. Although particles are deformed when they are deposited on a surface, since the radius of the deformed part is 71 nm (at the adhesive force $F = 10^{-6}$ [N]; see Appendix B), and is smaller than the radius r_2 of the liquid bridge, it is supposed that the calculation of the thickness of the liquid film is not affected.

Because a liquid bridge is formed when a liquid film is 2.9 to 3.7 nm thick, as described above, it was supposed that a liquid bridge was formed at such humidity that the thickness $2 \times (\delta + r_1)$ of the liquid film reached 3.5 nm or more. From the radii r_1 and r_2 of the liquid film, a liquid bridging force F_w was obtained by using the Laplace-Young's formula[13] expressed as follows.

$$F_w = 2\pi r_2 \gamma + \pi r_2^2 \gamma \{(1/r_1) - (1/r_2)\} \qquad (18)$$

The adhesive force F_d between a particle and a surface is given as the sum of the liquid bridging force F_w and the van der Waals force F_v by the following formula.

$$F_d = F_w + F_v \qquad (19)$$

The result of the calculation for the models using the adhesive force F_d given by Eq. (19), respectively, is shown in **Figure 13**, using the molecular number N_s of the impurity. Although the adhesive force continuously decreases as the humidity is increased to the level at which a liquid film is formed, similarly to **Figure 9**, it is discontinuously increased at a humidity at which a liquid film sufficiently thick to contribute to the liquid bridging force is formed. According to the result of the calculation using Model I for a constant gap z (**Figure 13-a**), the difference in adhesive force before and after formation of a liquid film is less than that of Model II, in which the gap z depends on the thickness of the adsorbed liquid film.

Similarly, the removal efficiency was calculated using the number of solute molecules devided by single particle volume N_s of the impurities as a parameter, and assuming a distribution of the adhesive force, taking the adhesive force given by Eq. (19) as

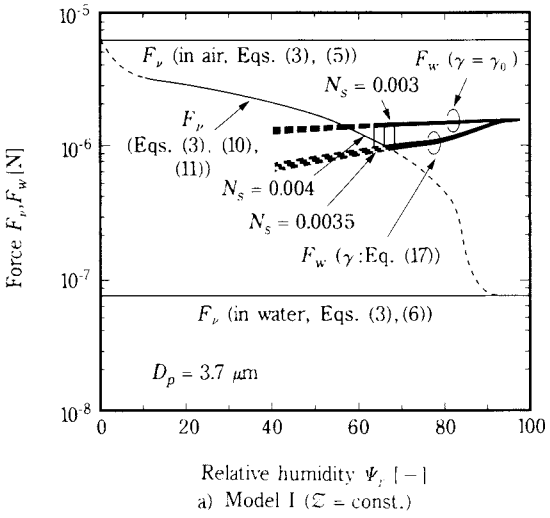

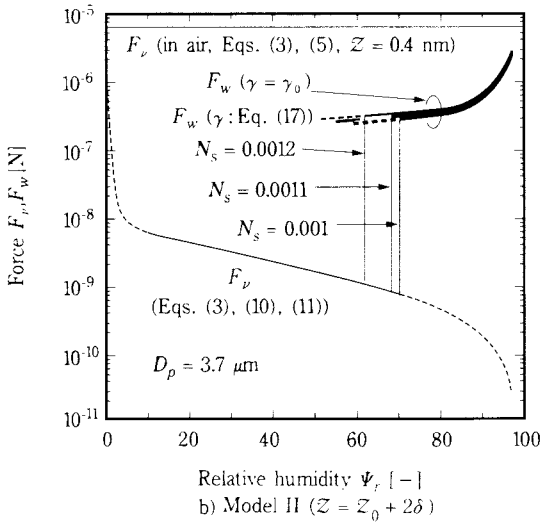

Fig. 13 Calculated results of adhesive force as a function of relative humidity

a mean value, and the result of the calculation is shown in **Figure 14**. In the calculation, ln σ_g was set to 0.2 that showed a sufficient consistency with the experimental result at a low humidity shown in **Figure 11**, and the removal force F_r was equal to that of **Figure 11** (1.1×10^{-6} in **Figure 14-a**, and 8.7×10^{-10} in b). The result of the calculation based on Eq. (18) is shown by a broken line in the figure. Although the removal efficiency increased with the humidity up to which a liquid film is formed, as in the case of **Figure 11**, after formation of the liquid film, the removal efficiency dropped to almost 0 in the calculation, and was completely different from the experimental result. The humidity at which the maximum efficiency is achieved is generally consistent with the experimental result at Ns = 0.0035 for Model I and N_S = 0.0011 for Model II. Therefore, it is considered that the optimum humidity can be estimated by calculating the humidity at which the minimum liquid film (= 3.5 nm) is formed.

The reason why the calculated value of the removal efficiency is inconsistent with the experimental result may be because the fact that the surface tension γ of a liquid bridge is lower than the value γ_0 of water,

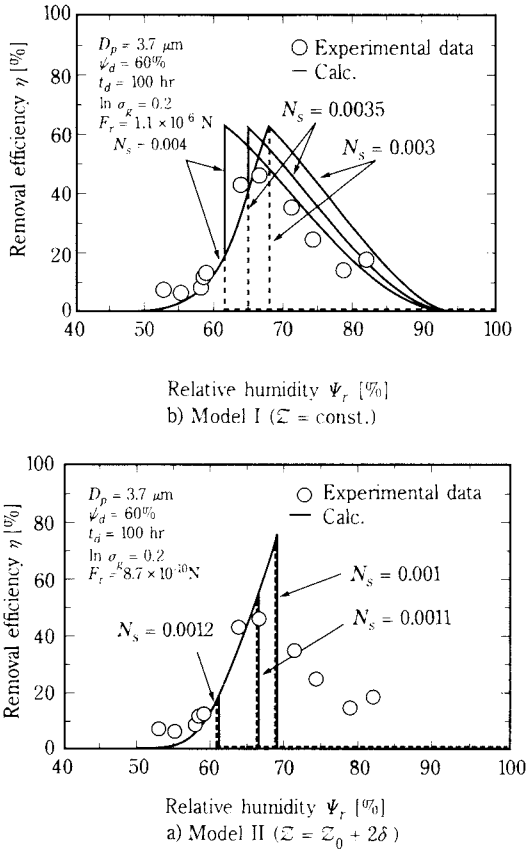

Fig. 14 Calculated removal efficiency considering about the liquid bridging force

when the liquid film is thin was not taken into consideration. From the experimental result using a porous glass, the variation of the surface tension with the thickness of the liquid film is approximated by the following formula[10].

$$\frac{\gamma}{\gamma_0} = 0.17 \times 10^9(\delta + r_1) + 0.32$$

$$\gamma \geq \gamma_0 = 7.3 \times 10^{-2} \qquad (20)$$

The removal efficiency was calculated by substitution of the above formula in Eq. (18), and the result of the calculation is shown by a solid line in **Figure 14**. Values calculated for a liquid bridging force F_w in such condition are shown in **Figure 13**. By assuming N_S = 0.0035 mol•m^{-3}, the result of the calculation (**Figure 14-a**) for Model I, in which the gap z is constant, is substantially consistent with the tendency of variation of the removal efficiency at high humidity. On the other hand, the result of the calculation (**Figure 14-b**) for Model II that assuming that the gap z is dependent on the thickness of the adsorbed layer is inconsistent with the experimental result, even if the variation of the surface tension with the thickness of the liquid film is taken into consideration. As shown in **Figure 13**, it is because the adhesive force (F_d = F_v) at a humidity not higher than that at which a liquid film is formed is underestimated in comparison with the liquid bridging force after formation of the liquid film. Thus, it is determined as a result of comparison with the experimental result that Model I assuming a constant gap z is preferable. In the study, the distance between a particle and a surface is, therefore, considered as being constant at $z = z_0$ = 0.4 nm.

Consequently, it is clear that the increase of the removal efficiency at a low humidity is explained by the variation of the Hamaker's constant due to adsorbed water, as shown in Model I, reduction of the removal efficiency at a high humidity is caused by an increase of the adhesive force due to formation of a liquid bridge, and a variation of the efficiency can be substantially explained by assuming that the surface tension linearly varies with the thickness of the liquid film. Thus, the removal efficiency has a maximum value, because the van der Waals force decreases with an increase of water molecules adsorbed, and a surface tension lower than that of bulk water gradually increases to the same level after a liquid bridge is formed.

From the result of the calculation by varying N_S of the impurities, a liquid film is formed at lower humidity, and the maximum efficiency is achieved at higher

humidity, when the quantity of impurities is lower. Accordingly, it is expected that a high removal efficiency as shown in **Figure 11** can be achieved by reducing the quantity of impurities deposited on a wall surface, because no liquid film is formed up to a higher humidity, and the van der Waals force is reduced.

A variation of the removal efficiency with the drying time as shown in **Figure 4** can be also explained quantitatively by considering that the effect of the variation of the van der Waals force caused by the quantity of water molecules adsorbed and that of the liquid bridging force described above are present during deposition of particles and drying as well. That is, when particles are deposited at high humidity, the liquid bridging force and van der Waals force are considered to be acting as adhesive forces. Because the liquid film is reduced, and the liquid bridging force is lower through the drying process, the adhesive force is reduced, and the removal efficiency is increased. It is considered that the adhesive force increases, and the removal efficiency decreases, as the drying time is increased, because the liquid film reduced to water molecules and disappears. In this process, the van der Waals force approaches the value in air from that in a liquid. When particles are deposited at a low humidity, the adhesion force increases, and the removal efficiency decreases through the drying process, because water molecules form no liquid film, and the van der Waals force is dominant.

Conclusions

We paid particular attention to the humidity at deposition of particles on a surface and that at removal, and studied the effects of humidity on the removal efficiency of particles by using a high-speed air jet. As a result, the following findings were obtained.

1) In the case when particles are deposited at low humidity, the removal efficiency decreases as the drying time is increased. In the case when particles are deposited at high humidity, the removal efficiency decreases once the maximum efficiency is reached after a certain drying time. After 80 hr of drying, no effect of humidity at deposition is observed.

2) Through experiments by varying the humidity at removal, it was found that the removal efficiency is low at low humidity, reaches its maximum value at a certain humidity (about 67% on a glass surface), and decreases at a humidity higher than that.

3) The variation of the removal efficiency at low humidity can be explained by considering the variation of the Hamaker's constant due to adsorption of water molecules. It is found that the variation of the efficiency at a high humidity can be also explained using a formula of the liquid bridging force, when the variation of the surface tension with the thickness of the liquid film is taken into consideration.

Appendices

Appendix A

A formula presented by Kousaka et al.[11,12] for a liquid bridge between two spheres of identical size was employed for expressing the Kelvin effect, as shown below.

$$\Psi_r = (1-\gamma_s)\exp\left(-\frac{M_s\sigma}{RT\rho_l}\frac{ds}{d\nu_w}\right) \tag{A-1}$$

$$\gamma_s = \frac{iM_w}{\rho_w}\Big/\left(\frac{3\nu_w}{4\pi N_s r_0^3} - \frac{M_s}{\rho_s} + \frac{iM_w}{\rho_w}\right) \tag{A-2}$$

$$0 \le \gamma \le 1$$

$$\nu = 2\pi r_0^3 R_1^2\left\{1+\frac{H}{2} - A_s\sqrt{(1+R_1)^2-\left(1+\frac{H}{2}\right)^2} - \frac{H^2(H+6)}{24R_1^2}\right\} \tag{A-3}$$

$$\frac{ds}{d\nu} = \frac{2}{r_0}\times\frac{(2R_1^2+3R_1-\frac{H^2}{4}-H)A_s - R_1(3R_1^2+5R_1-\frac{H^2}{2}-2H)A_s\dfrac{-\sqrt{(1+R_1)^2-\left(1+\frac{H}{2}\right)^2}}{+\sqrt{(1+R_1)^2-\left(1+\frac{H}{2}\right)^2}}}{\times R_1(2R_1+3)\left(1+\frac{H}{2}\right)/(1+R_1)^2 \times R_1(2+3R_1)\left(1+\frac{H}{2}\right)/(1+R_1)} \tag{A-4}$$

$$A_s \equiv \sin^{-1}\left\{(1+\frac{H}{2})/(1+R_1)\right\} \tag{A-5}$$

In Eq. (A-2), $M_s/\rho_s = 0$, assuming the impurities are at a low concentration. Although i varies according to the type and concentration of the solutes (impurities), it was taken as 2[11] in this study. R_1 is a dimensionless radius of the liquid bridge derived from the following formula.

$$R_1 = r_1/r_0 \tag{A-6}$$

where r_1 is the radius of the condensed liquid bridge shown in **Figure 12**. By approximating the condensed liquid bridge by an arc in contact with a wall surface, the following formula is obtained for radii r_1 and r_2.

$$\frac{r_2}{r_0} = \sqrt{(1+r_1)^2 - \left(1+\frac{H}{2}\right)^2} - R_1 \qquad \text{(A-7)}$$

From the formulae, the radius r_1 of the condensed liquid bridge and the radius r_2 of the liquid bridge formed at a humidity Ψ_r at removal were calculated.

Appendix B

The thickness of the liquid film at formation of a liquid bridge is defined, as shown in **Figure 12**, by the distance t_l between points P and W formed by combining the thickness of the adsorption layer and that of the liquid bridge between the particle and the surface. Here, when the angle between the segment $\overline{CW}$ and the central axis of the deposited particle is at θ_p, the following formula is given.

$$\overline{AW} = \frac{t_l}{\cos\theta_p} \qquad \text{(B-1)}$$

$$2\times(\delta+r_1) = \overline{AW} + \overline{AB}\sin\theta_p$$

$$2\times(\delta+r_1) = \frac{t_l}{\cos\theta_p} + \overline{AB}\sin\theta_p$$

Here, the angle θ_p falls within the range expressed by the following formula.

$$\tan^{-1}\left(\frac{r_2}{D_p/2+z}\right) \le \theta_p \le \tan^{-1}\left(\frac{r_2+r_1}{D_p/2+z}\right) \qquad \text{(B-2)}$$

Because the particle size D_p is 3.7 μm, and the radii r_1 and r_2 of the liquid bridge are 1.4 nm and 130 nm at the maximum humidity of 82% within the range of the experiment, from Eq. (B-2),

$$\tan^{-1}(0.035) = 2.01\,[deg] \le \theta_p \le \tan^{-1}(0.036) = 2.03\,[deg]$$

(Note that $z = z_0 = 0.4$ nm is assumed.)
By substituting this in Eq. (B-1),

$$2\times(\delta+r_1) = \frac{t_l}{0.999} + 0.035\overline{AB}$$

$$\theta_p = 2.01,\ 2.03\ [deg]$$

$$2\times(\delta+r_1) \cong t_l$$

Therefore, the thickness of the liquid film is approximated by $2\times(\delta+\gamma_1)$ within the range of the experiment.

On the other hand, the test particles (standard latex particles: Styrene/Divinylbenzene) are considered to be deformed in the vicinity of the contact point at deposition on a surface, because they are soft. From the theory of elasticity[14], the radius a_c of the contact area in the deformed part is given by the following formula.

$$a_c = 3\sqrt{\frac{3}{4}F_d\,k_p\frac{D_e}{2}} \qquad \text{(B-3)}$$

Here, by using values below, and assuming that the adhesive force F_d between the particle and the surface is equal to 10^{-6}[N] (**Figure 13-a**), a representative value within the range of the experiment, following formula is obtained;

$$D_e = D_p = 3.7\ [\mu m]$$

$$k_p = \frac{1-\nu_p^2}{E_p} + \frac{1-\nu_w^2}{E_w} = 2.6\times10^{-10}$$

$$a_c = 71\ [nm] \qquad (4)$$

On the contrary, the radius of the liquid bridge within the range of the experiment is equal to 105 nm even when a liquid film having the minimum radius is formed (Ψ_r = 65%, N_s = 0.0035, Model I). It means that the radius a_c in the deformed region is smaller than the radius r_2 of the liquid bridge within the range of the experiment, a model shown in **Figure 12** is applicable to the formation of a liquid bridge, and the thickness of the liquid film can be approximated by $2\times(\delta+r_1)$.

Nomenclature

A	:	Hamaker constant between particle and solid wall	[J]
A_a	:	Hamaker constant of adsorbate	[J]
A_j	:	Hamaker constant of interface with adsorbed layer	[J]
A_l	:	Hamaker constant of water	[J]
A_m	:	Hamaker constant of media	[J]
A_p	:	Hamaker constant of particle	[J]
A_w	:	Hamaker constant of solid wall	[J]
D_p	:	particle diameter	[m]
d	:	nozzle-surface distance	[m]
d_1, d_2	:	diameter	[m]
d_e	:	equivalent diameter	[m]

E_p	:	Young's modulus of particle	[N•m^{-2}]
E_w	:	Young's modulus of solid wall	[N•m^{-2}]
F	:	adhesive force between particle and solid wall	[N]
F_d	:	average adhesive force	[N]
F_r	:	removal force	[N]
F_v	:	van der Waals force	[N]
F_w	:	liquid bridging force	[N]
f_{ad}	:	frequency of adhesive force	[−]
H	:	nondimensional gap ($=z/r_0$)	[−]
i	:	von't Hoff factor	[−]
K_a	:	coefficient in Eq. (8)	[−]
K_{a0}	:	coefficient in Eq. (9)	[−]
K_h	:	coefficient in Eq. (2)	[m]
k_p	:	coefficient defined by Eq. (4)	[m^2•N^{-1}]
k	:	coefficient in Eq. (1)	[J•mol^{-1}]
M_s	:	molecular weight of solute	[kg•mol^{-1}]
M_w	:	molecular weight of water	[kg•mol^{-1}]
N_s	:	number of solute molecules divided by single particle volume	[mol•m^{-3}]
ΔP_n	:	air pressure at nozzle	[Pa]
q	:	exponent in Eq. (1)	[−]
R	:	gas constant	[J•K^{-1}•mol^{-1}]
R_1	:	nondimensional radius of liquid bridge	[−]
r_0	:	radius of equivalent diameter	[m]
r_1	:	radius of liquid bridge	[m]
S	:	surface area	[m^2]
s	:	surface area of liquid bridge	[m^2]
T	:	temperature	[K]
t	:	duration time of air jet	[s]
t_d	:	drying time	[hr]
v	:	adsorbed molecular volume	[m^3]
v_w	:	volume of liquid bridge	[m^3]
v_m	:	monolayer adsorption capacity	[m^3]
z	:	gap between particle and solid wall	[m]
z_0	:	initial gap between particle and solid wall	[m]
γ	:	surface tension of liquid bridge	[N•m^{-1}]
γ_0	:	surface tension of water	[N•m^{-1}]
δ	:	thickness of adsorption layer	[m]
η	:	removal efficiency	[−]
η_{cal}	:	calculated removal efficiency	[−]
θ	:	jet impinging angle	[deg]
θ_p	:	angle defined in Fig. 12	[deg]
ν_p	:	Poisson's ratio of particle	[−]
ν_w	:	Poisson's ratio of solid wall	[−]
ρ_l	:	density of liquid bridge	[kg•m^3]
ρ_w	:	density of water	[kg•m^3]
σ_g	:	geometric standard deviation	[−]
Ψ	:	relative humidity	[−]
Ψ_d	:	relative humidity at deposition	[−]
Ψ_r	:	relative humidity at removal	[−]

References

1) Masuda H., K. Gotoh, H. Fukada and Y. Banba: J. Soc. Powder Technol., Japan, **30**, 24-31 (1993)
2) Otani, Y., H. Emi and T. Morizane: Kagaku Kogaku Ronbunshu, **19**, 114-119 (1993)
3) Gotoh, K., S. Takebe and H. Masuda: Kagaku Kogaku Ronbunshu, **20**, 685-692 (1993)
4) Chikazawa, M., W. Nakajima and T. Kanazawa: J. Res. Assoc. Powder Technol., **14**, 18-25 (1977)
5) Young, D.M. and A.D. Crowell: ''PHYSICAL ADSORPTION of GASES (Trans. by Takaishi and S. Furuyama)'', p.156, Sangyo-Co. (1969)
6) Dahneke, B.: J. Colloid and Interface Sci., **40**, 1-13 (1972)
7) Nihon Kagaku Kai: ''Kagaku Binran'', p.564, Maruzen (1975)
8) Visser, J.: Advan. Colloid Interface Sci., **3**, 331-363 (1972)
9) Vincent, B.: J. Colloid and Interface Sci., **42**, 270-285 (1973)
10) Chikazawa, M., T. Yamaguchi and T. Kanazawa: Proc. Int. Symp. Powder Technol. '81, p.p.202-207 (1981)
11) Kousaka, Y., Y. Endo and Y. Nishie: Kagaku Kogaku Ronbunshu, **18**, 942-949 (1992)
12) Endo., Y., Y. Kousaka and Y. Nishie: Kagaku Kogaku Ronbunshu, **18**, 950-955 (1992)
13) Okuyama, K., H. Masuda and S. Morooka: ''BIRYUSI KOGAKU:, p40, Ohm-sha (1992)

Author's short biography

Kuniaki Gotoh

Dr. Kuniaki Gotoh graduated from Hiroshima University in 1986, and from the graduate school of Hiroshima University in 1988. He obtained the Doctor degree of Engineering from Kyoto University in 1995. He is Research Instructor of Chemical Engineering Department of Kyoto University since 1989.

His major research interests are the dynamics of aerosol particles relating to size classification and dry dispersion of aggregates, and particle adhesive force relating to the removal of deposited particles on a solid surface.

Shyoji Takebe

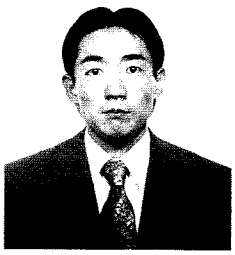

Mr. Shyoji Takebe graduated from Kyoto University in 1990 with B. Eng. He obtained M. Eng., from Kyoto University in 1992.

He has been engaged in Department of Pharmaceutics Technology, Production Technology division, TANABE SEIYAKU Co., Ltd. since 1992.

Hiroaki Masuda

Professor Hiroaki Masuda graduated from Hiroshima University in 1966, and from the graduate school of Hiroshima University in 1968. He entered in Dr. course of graduate school, Kyoto University and obtained the Doctor degree of Engineering from Kyoto University in 1973. From 1977 to 1988. He was an Alexander von Humboldt fellow at Frounhofer Institute of Aerosol research, Schmallenberg, Germany. He was appointed Associate Professor of Chemical Engineering Department of Hiroshima University in 1979, and Professor in 1986. Presently he is Professor of Chemical Engineering Department of Kyoto Univeristy since 1989.

His major research interests are dynamics of aerosol particles, electrostatic characteristics of powder and resuspension of particles.

Yoshiji Banba

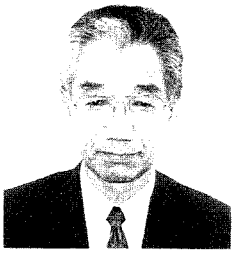

He has been engaged in OMRON Co., He worked on Production Control for the Factory of a Relay during 10 years. Technical Control of products 5 years, and Quality Control 5 years.

Presently he has worked on Production Technique for the Factory of a Relay since 15 years ago.

Flow Mechanism of Granular Materials Discharging from Bin-Hopper System †

Jusuke Hidaka, Junya Kano and Atsuko Shimosaka
*Dept. of Chem. Eng., Doshisha University**

Abstract

A new theory to estimate the state variables of flowing particles in a bin-hopper system was presented. The flowing behaviour of particles in the system was simulated by the particle element method. It was suggested that convergence of the flow path of particles in a hopper leads to a change in the bulk density of flowing particles, whereby particles in a hopper flow intermittently. On the basis of the microscopic behaviour of flowing particles observed through the simulation, a flow model was derived to analyse the flow of particles in a conical hopper. The values and fluctuation of dynamic pressure acting on the wall during the flow of particles in a bin-hopper system were estimated and the generation mechanism of over pressure during flowing of particles was also presented on the basis of the model.

1. Introduction

Conventionally, the flowing behavior of fine particles discharged from a bin-hopper system has been paid particular attention, and aggressively studied from different viewpoints. Although it was the object of such studies to find out a reasonable design for a bin-hopper system, interests in dynamic specificities found in such flowing behavior of fine particles constituted a strong motivation as well. The behavior of particles flowing in a bin-hopper system, in comparison with the flowing behavior of a fluid, shows such specificities that: (1) a very high pressure (overpressure) on hopper wall is generated immediately after initiation of flow; (2) the flow rate at discharge is independent of the height of the particle layer; (3) wall pressure and flow rate periodically pulsate; and (4) the flow rate is proportional to the orifice bore to the power 2.5 to 3.0. Regarding (1) and (2), although concepts of switching stress[12] and dynamic arch[11] were suggested, respectively, the position of the overpressure generated, the magnitude of the pressure and the physical meaning of dynamic arch remain unclear. Bransby et al.[2] observed flowing particles during discharge by X ray, and found that a slip line was periodically generated and dissipated, and a wall pressure thereby periodically fluctuated. However, the mechanism leading to such periodic generation of the slip line is unknown. A theory of Brown and Richards[3] concerning (4) is relatively conceptual, and a relation with the flowing mechanism of particles is quite uncertain.

Thus, although a gravitational flow out of a bin-hopper system is the simplest manner of flowing in flowing phenomena of fine particles, the flowing mechanism is still unknown despite a lot of experimental and theoretical studies. It may represent a limit of conventional approach in dynamic studies of fine particles. Specifically in the flowing behavior of fine particles, an observable quantity is limited to a very macroscopic one, and an engineering approach by means of a mathematical model is, therefore, very difficult.

Accordingly, in this study, we conducted a two-dimensional simulation of the flowing behavior of particles in a bin-hopper system by using the particle element method, and first microscopically observed the flowing state. Then, based on the result of the observation, we suggested a new theory to estimate the state variables of flowing particles in a bin-hopper system. In order to prove that the model is reasonable and useful, we presented a method for predicting a wall pressure in the bin-hopper system and frequency of fluctuation (pulsation) of the pressure.

* Karasuma Imadegawa-dori, Kamigyou-ku, Kyoto 602 Japan
† This report was originally printed in *Kagaku Kougaku Ronbunshu*, **20**, 397 (1994) in Japanese, before being translated into English with the permission of the editorial committee of the Soc. Chemical Engineers, Japan.

1. Computer simulation by the particle element method of the flowing behavior of particles discharged

Fine particles are an assembly of solid particles. Therefore, a particle constituting the assembly that is in motion has an independent rotational and translational displacement, and a discrete characteristic derived from them is found in the behavior of particles[5]. The particle element method[4, 7-9] is a simulation taking such discrete characteristic of particles in consideration, and sufficiently expresses the intermittent flowing behavior specific to particles[5].

Figure 1 is an example of the two-dimensional simulation by the particle element method of the behavior of particles flowing in a bin-hopper system which is provided with a hopper in its lower part. Material constants and computational conditions employed in the simulation are shown in **Table 1***). **Figure (a)** shows 1638 particles of equal size filled evenly in a bin-hopper system before initiation of flow. A straight line through the contact point between particles represents, by its length and direction, the magnitude and the direction of the force acting between the particles. A force acting against the wall of the system in a static state was generally consistent with the tendency observed in the distribution of particle pressures obtained by Jenssen's formula. **Figure (b)** shows the state 0.015 sec after opening an orifice in the lower end of the hopper to allow the particles to flow out of the hopper. In **Figure (b)** and succeeding ones, in order to avoid complication, only straight lines representing the forces between the particles are shown. When the orifice is opened, particles within a triangular zone immediately above the orifice flow out, while the direction of the force between particles is changed from the vertical to the horizontal direction. A change from such active stress to passive stress is referred to as switching[12], and it is known that the wall pressure in the location of switching is intermittent, as shown in **Figure (c)** and successive figures.

Table 1 Computational condition for simulation of flowing particles

Young's modulus	7.36×10^7Pa
Poisson's ratio	0.3
Particle density	2650kg/m^3
Coefficient of friction	0.7 (between two particles)
	0.176 (between particle and wall)
Radius of particle	5mm
Time step	1.0×10^{-4}s

* It is not required to use the material coefficient of a specific particle, because it is the object of the study to observe the general flowing behavior of particles. Thus, for facilitating a computational simulation, values shown in the table 1 were used.

The boundary of the triangular zone is a collapsing position of the particle layer, that is, a so-called "slip line". A flowing region surrounded by the slip line grows in the upper direction as time elapses, and the force against the wall of the hopper is much greater than that in a static state in the location where the slip line is generated. When the switching approaches the upper end of the hopper part (**Figures (e)** to **(j)**), a significantly high force acts in the vicinity of the connection between the upright wall and the hopper wall. The force is highest throughout the entire flowing process, and constitutes an overpressure that causes a problem immediately after discharge from the bin-hopper system. Referring to **Figure (e)** again, the particles below the slip line that is moving upward in the hopper are in a flowing state, and the interacting force between the particles and the wall is very low in such state. However, in **Figure (f)** showing a state immediately after the flow has increased, the force between particles in the vicinity immediately above the orifice is increased, and consolidation of particles has already begun in that area. Although the consolidated layer gradually grows upward (**Figure (g)**), when the layer reaches a certain height, the consolidated layer satisfies the collapsing conditions in a certain location thereof, and a collapsing flow is initiated (**Figure (h)**). Succeedingly, a similar consolidation starts in an area above that location (**Figure (i)**), and collapse is caused in that area (**Figure (j)**). Also in figures after **Figure (j)**, it is observed that the particles in the hopper part are periodically subjected to the consolidation and collapse of the particle layer by the same mechanism during flowing (**Figures (k)** to **(o)**). Immediately before the collapse of the consolidated layer, the horizontal component of the force between the particles is increased, and the force against the wall becomes several times higher than that in the static state. On the contrary, after the collapse, it is observed that the force against the wall is significantly reduced in the flowing particles, and the wall pressure of the hopper periodically fluctuates due to generation and dissipation of the slip line.

In **Figures 2 (a), (b)** and **(c)**, the distribution of the velocity of the particles in the states of **Figures 1 (k), (l)** and **(o)** is shown. The velocity of the particles during consolidation in the hopper part, as shown in **Figure (k)**, is practically low, and it is confirmed in **Figure (l)** that the particles are in a flowing state, as described above, when the force

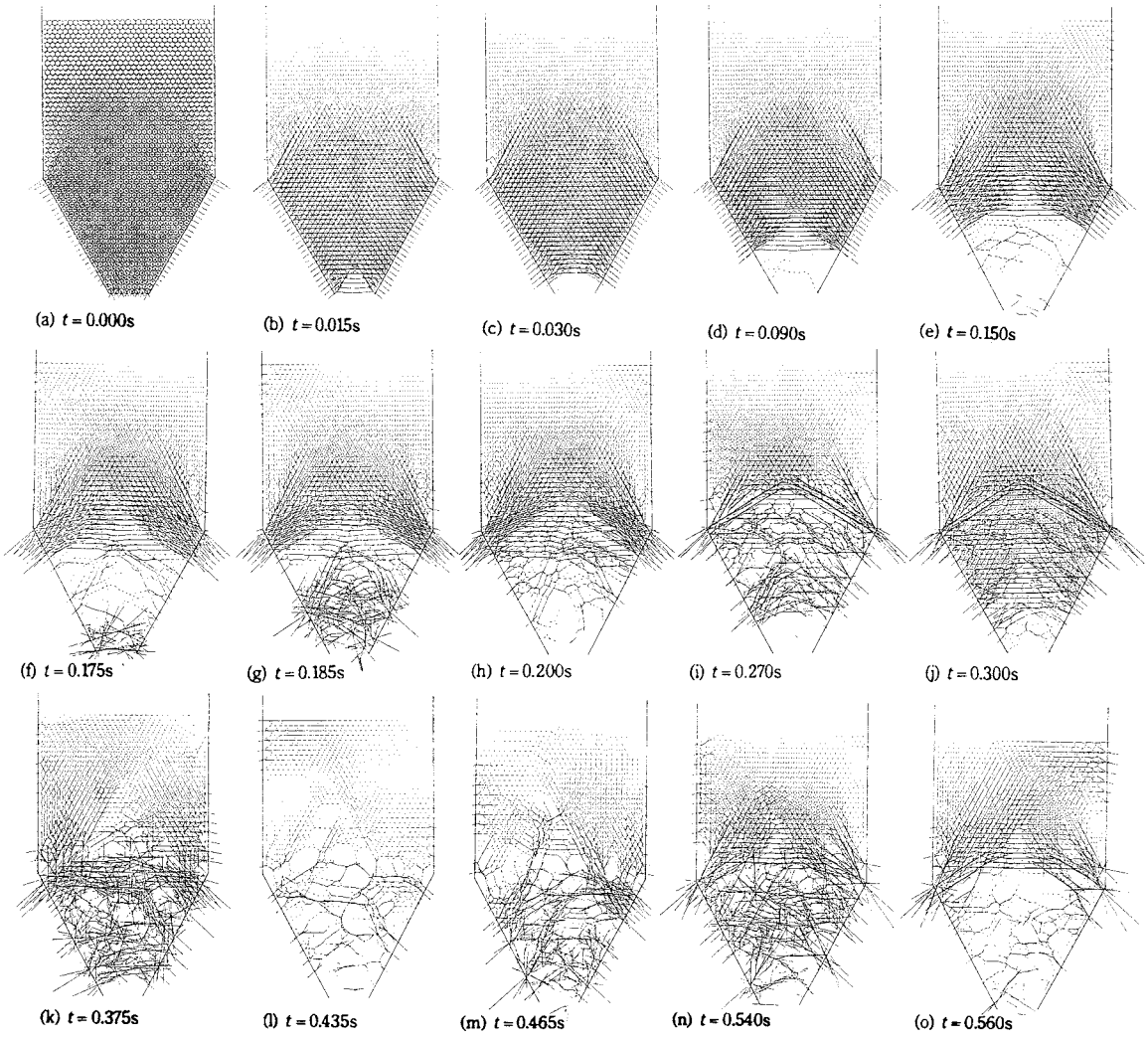

Fig.1 Two dimensional simulated results on the flowing behavior of particles in a bin

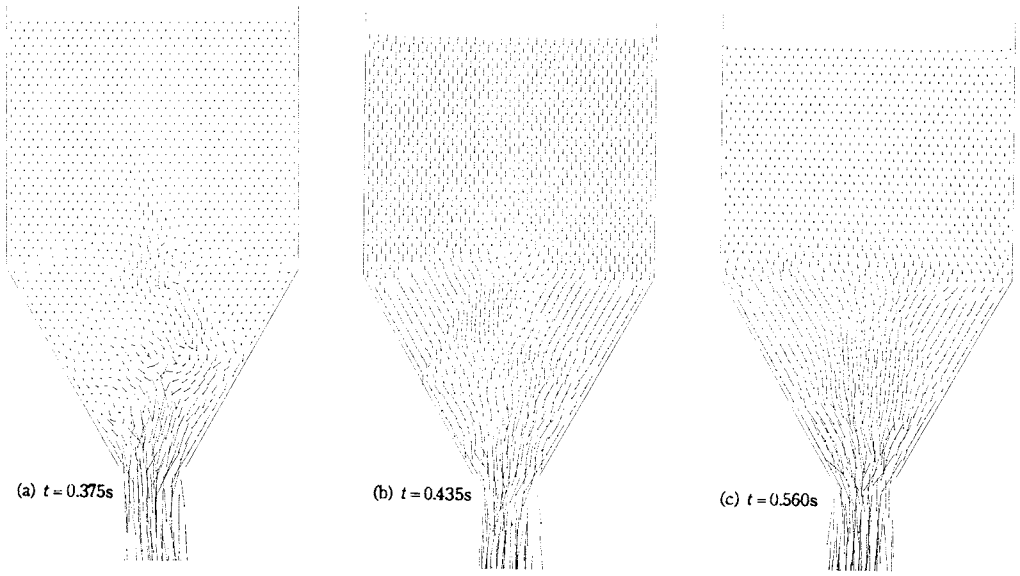

Fig.2 Velocity distribution of flowing particles in a bin

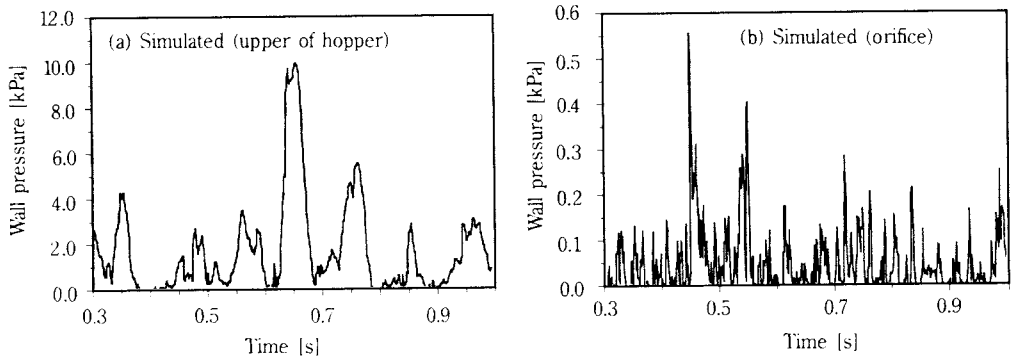

Fig.3 Fluctuatoin of dynamic pressure acting on wall of a bin

between the particles is low. **Figures 3 (a)** and **(b)** show a fluctuation of the wall pressure during discharge of the particles through the connection between the wall of the hopper and the upright wall and in the vicinity of the orifice. The wall pressure periodically fluctuates in response to the periodic collapse of the consolidated layer (generation of the slip line) in the hopper part, and the fluctuation of the pressure is more significant, and the frequency of fluctuation is longer in the upper part of the hopper.

The simulation is of the flowing behavior of a small group of particles during a short period. However, the result of the simulation is sufficiently consistent with a lot of prior findings obtained through experiments of flowing particles that are discharged from a bin-hopper system. Specifically, the behavior of an entire particle layer was identical to the result obtained by Bransby et al. through a direct observation by X ray. Thus, the microscopic behavior of flowing particles observed in the flowing and discharging simulation can be considered as being generally consistent with the basic flowing behavior of particles in a practical three-dimensional bin-hopper system. In other words, a practical flowing mechanism of particles in a bin-hopper system can be discussed by using the findings of this simulation.

2. Dynamic model of flowing behavior of particles

One of the important functions of a bin-hopper system is to discharge particles contained therein into a specific container. Therefore, the path of particles flowing in the bin-hopper system is necessarily reduced toward the outlet end. The result of the simulation described above shows that a bulk density of particles flowing in a bin-hopper system is changed with a geometric change of the path, and the constant flow of the particles is disturbed. In other words, it was found that the intermittent flow associated with consolidation and collapse of a particle layer was caused by a change in density, and the flow rate and the force against the wall thereby periodically fluctuated. By carefully examining the behavior of particles obtained through the simulation, such dynamic model as described below is established for the flowing behavior of particles discharged from a circular bin-hopper system that is most commonly used.

The stress of particles created before discharge can be approximated by a so-called active stress. As soon as discharge of the particles is initiated, a slip line is generated in the lower end, and switching to a passive state occurs. In a location where the slip line is generated, the wall of the system is subjected to a passive pressure higher than the pressure present in a static state. The slip line generated in a hopper part generally moves upwards, and the flow area is thereby increased. As described above, however, because the slip line is generated by the reduction of the flow path of the particles, the slip line in the upper end of the hopper, at which the reduction of the flow path begins, becomes the final one. At the beginning of the flow, particles in the cylindrical part above the final slip line are at a bulk density generally equivalent to that at initial loading, since they are still substantially immobile, and the connection between the cylinder and the hopper is, therefore, subjected to a very high passive pressure. This constitutes an overpressure at the beginning of the flow, and the higher bulk density at initial loading causes a higher pressure. It is clear that such overpressure is generated in a connection between the cylinder and the hopper at the beginning of the flow.

In the simulation, in order to clearly demonstrate the change in state during the flow of particles discharged from the system and generation of an over-

pressure, the particles were evenly loaded before discharge. Therefore, a transition period was required to form a structure of particles allowing a constant flow from the evenly loaded state. **Figures 1 (a)** to **(k)** correspond to the transition period, and a sufficient flowing condition is achieved in **Figure (l)**. Accordingly, examination of the mechanism of constant flow in the bin-hopper system should be reasonably started from the state of **Figure (l)**. Now, the bulk density of particles in a sufficient flowing condition in a bin-hopper system as shown in **Figure 4** is defined by γ_d. and the mean vertical mass velocity of the particles in such condition by $\bar{U}(\gamma_d)$. In such condition, as the flow path is reduced in the downward direction of the hopper, a consolidated particle layer of bulk density γ_d is formed by particles in the proximity of the orifice, and the flow velocity is reduced [**Figure 4 (b)**]. Because the particles forming the consolidated layer are built up with an inertial force corresponding to the velocity $\bar{U}(\gamma_d)$ from above, a horizontal force apt to separate the particles from each other dominantly acts on the particles that are falling, and the ratio of the radial component σ_r to the vertical component σ_z of the force is at $\sigma_r/\sigma_z > 1$. As soon as the consolidated particle layer reaches a height h_2 (**Figure (c)**), collapse conditions are met

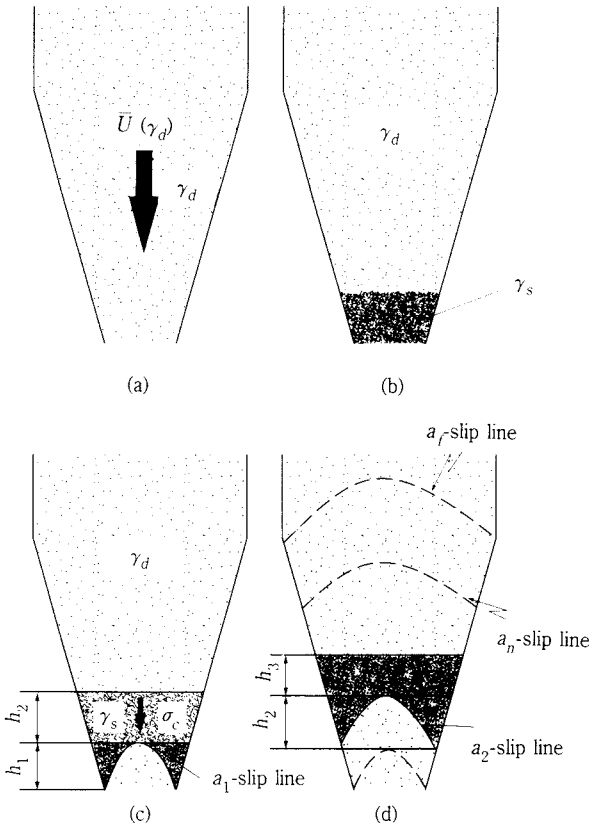

Fig. 4 Flow model of particles in a bin

at a certain position within the consolidated layer, and slip collapse occurs. The slip line generated in the consolidated layer at that time is indicated by a_1-slip line entering from the right side of the maximum main stress, and the height required to create the critical stress σ_{c1} on the slip line by h_2. After the collapse, particles below the a_1-slip line return to the flowing state of bulk density γ_d again. On the other hand, because a consolidated layer of a lower flowing velocity is already formed at the height h_2 above the slip line before the collapse, an a_2-slip line is formed similarly in the layer, causing collapse of the layer. While the formation of consolidated layer and the slip collapse are sequentially transferred upward in such manner, an a_f-slip line is finally formed in the upper end of the wall of the hopper, at which the reduction of the flow path begins. The particles flowing in the hopper part come out of the hopper, as generation and dissipation of the slip line are periodically repeated according to the mechanism of density variation due to the reduction of the flow path. Here, an interval of generation of an a_n-slip line corresponds to the time required for a consolidated layer to be built up from h_{n+1} to h_n. Therefore, the shape and interval of generation of a slip line depend on the shape of the bin-hopper system and on the characteristics ofthe particles. The fluctuation of the wall pressure caused by the slip line generated in the upper end of the hopper is highest and takes the longest interval, and causes the most significant effect on the flow in the hopper.

3. Prediction of pulsation frequency of flow rate and wall pressure

3.1 Shape and critical stress of slip line occurring in the hopper

Based on the model derived above, the pulsation frequency of the flow rate and wall pressure and the magnitude of the wall pressure are predicted. For this purpose, it is required first to obtain the shape of the slip line generated in the hopper part and the critical stress σ_c acting on the slip line. Thus, assuming that a fine particle layer forms a continuous mass satisfying Coulomb's breakage criteria, the shape of the slip line is estimated using the method of Takahashi et al.[10]. In the hopper shown in **Figure 5**, the r- and z-axes coordinates are established, and the radius of the hopper at a given location is defined by R. Now, assuming that the mean main stress σ_m acting on the slip line is constant for simplification, a coordinate of the-slip line generated in a consolidated

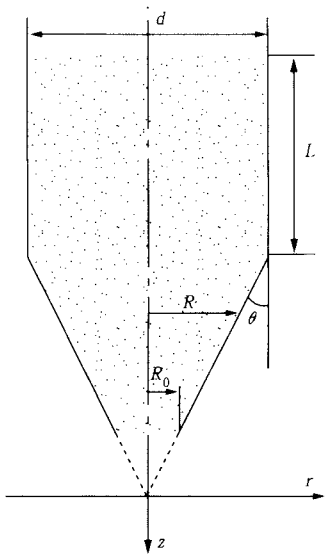

Fig. 5 Coordinate system in hopper

layer is given by:

$$\frac{r}{R}=\frac{R_o}{R}\cdot\frac{F(\alpha_w,\ \alpha,\ \eta)}{F(\alpha_w,\ \alpha_c,\ \eta)}-\frac{F(\alpha_w,\ \alpha,\ \eta)}{F(\alpha_w,\ \alpha_c,\ \eta)}+1 \tag{1}$$

$$-\frac{z}{R}=-\frac{z_w}{R}-\left(\frac{R_o}{R}-1\right)\cdot\frac{G(\alpha_w,\ \alpha,\ \eta)}{F(\alpha_w,\ \alpha_c,\ \eta)}$$

$$\alpha_w=(\phi_{ws}+\chi_p)/2+\theta,\ \alpha_c=0 \tag{2}$$

$$\chi_p=\sin^{-1}(\sin\phi_{ws}/\sin\phi_s),\ \eta=\frac{\pi}{4}-\frac{\phi_s}{2}$$

where

$$F(x,\ y,\ \eta)=(x-y)\cos 2\eta-\sin 2\eta\ \mathrm{In}\left|\cos(y-\eta)/\cos(x-\eta)\right|$$

$$G(x,\ y,\ -\eta)=(x-y)\sin 2\eta+\cos 2\eta\ \mathrm{In}\left|\cos(y-\eta)/\cos(x-\eta)\right|$$

α is the angle between the plane of the maximum main stress and the z-axis, α_w and α_c are boundary values at the wall and central axis, respectively, and ϕ_s and ϕ_{ws} are static friction angles of the particle layer and the wall.

In the central axis of the hopper, the critical stress σ_c acting on the slip line is a vertical stress, that is, the minimum main stress, and is given by:

$$\sigma_c=\frac{\tau_s R(1-\sin\phi_s)}{2\sin\phi_s F(\alpha_w,\ \alpha_c,\ \eta)} \tag{3}$$

Thus, using the friction angle ϕ_s of a consolidated layer, the friction angle ϕ_w of the wall and an open angle θ of the hopper, the shape and critical stress σ_c of the slip line generated at a given location of the hopper part can be predicted.

3.2 Height h_n of consolidated particle layer creating critical stress σ_c

The mean vertical stress $\bar{\sigma}_z$ acting in a given plane within the bin-hopper system is obtained by Walters's formula for predicting a particle pressure[12], and given for the cylindrical part and hopper part, respectively, by the following formulae.

Cylindrical part

$$\frac{\bar{\sigma}_z}{\gamma gd}=\frac{1}{4BD}\left(1-e^{-4BD(z/d)}\right) \tag{4}$$

Hopper part

$$\frac{\bar{\sigma}_z}{\gamma gd}=\frac{1-2(z/d)\tan\theta}{2\tan\theta\,(K-1)}\left[1-\left(\frac{1-2(z/d)\tan\theta}{1-2(z_0/d)\tan\theta}\right)^{K-1}\right]$$

$$+\frac{\sigma_{z,0}}{\gamma gd}\left(\frac{1-2(z/d)\tan\theta}{1-2(z_0/d)\tan\theta}\right)^{K} \tag{5}$$

where

$$BD=\frac{\tan\phi_w\cos^2\phi}{1+\sin^2\phi\ \pm 2y\sin\phi},\ y=\frac{2}{3c}\left[1-(1-c)^{3/2}\right],$$

$$c=\left(\frac{\tan\mu}{\tan\phi}\right)^2$$

$$D=\frac{\cos\mu(1+\sin^2\phi)-2(\sin^2\phi-\sin^2\mu)^{1/2}}{\cos\mu\,[1+\sin^2\phi\pm y\sin\phi]}$$

$$K=2\left(\frac{ED}{\tan\theta}+D-1\right)$$

$$\mu=\tan^{-1}\frac{\sin\phi\sin(2\varepsilon+\theta)}{1+\sin\phi\cos(2\varepsilon+\theta)},$$

$$E=\frac{\sin\phi\sin(2\varepsilon+\theta)}{1\pm\sin\phi\cos(2\varepsilon+\theta)},\ \varepsilon=\frac{(\phi_w+\chi_p)}{2}$$

BD is equal to the coefficient of particle pressure of Janssen multiplied by the coefficient of friction of the wall ($\tan\phi_w$), and $\bar{\sigma}_{z0}$ is a downward created stress. E is the ratio of the vertical to the shearing stresses, and D the coefficient of distribution for correlating the vertical stress of the wall and the mean vertical stress. They are obtained by a geometric study of Mohr's circle shown in **Figures 6 (a)** and **(b)**, and the positive symbol is for a flowing range, while the negative values are for a consolidated particle layer, considering the ratio of particle pressure. From Mohr's circle for a consolidated layer, the mean vertical stress ($\bar{\sigma}_z$) in a sectional plane creating the critical stress σ_c in the central axis of the bin-hopper system is given by:

$$\frac{(\bar{\sigma}_z)_T}{\gamma_s gd}=\sigma_c\frac{1+\sin^2\phi_s-2\sin\phi_s\cdot y_s}{1+\sin^2\phi_s-2\sin\phi_s} \tag{6}$$

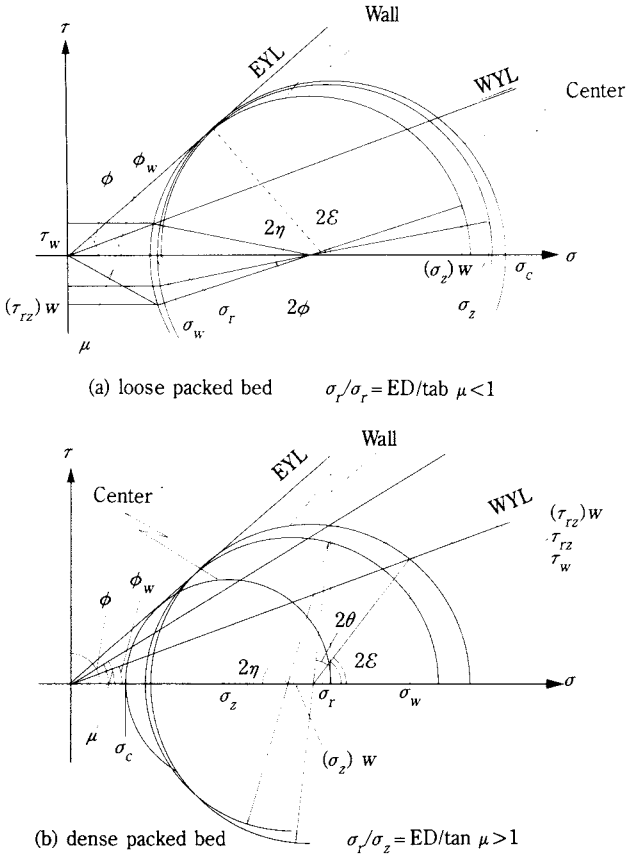

Fig. 6 Stress condition in a hopper

The maximum wall pressure σ_w at formation of a consolidated layer can be predicted from $(\bar{\sigma}_z)_T$ in by the following formula.

$$\sigma_w = \frac{ED\ (\bar{\sigma}_z)_T \sin 2\varepsilon}{\sin(2\theta + 2\varepsilon)\tan\phi_{ws}} \tag{7}$$

Then, by using the formulae, the height of the consolidated layer creating the critical stress σ_c at a given location within the bin-hopper system can be calculated in the following manner. Now, it is supposed that a consolidated particle layer is formed from the upper end of the hopper to a position z_3 in a bin-hopper system shown in **Figure 7**, and an a_n-slip line is generated at a position z_4. First, the mean particle pressure $\bar{\sigma}_{z1}$ in the bottom part of the cylinder is calculated by substituting the characteristics of the flowing particle in Eq. (4). Then, by using the positive symbol in Eq. (5), and taking $\bar{\sigma}_{z1}$ as the load stress, the mean stress $\bar{\sigma}_{z3}$ acting in a plane at a depth z_3 is obtained, Finally, by taking $\bar{\sigma}_{z3}$ as the load stress, and using the negative symbol and the characteristic values of the consolidated particle layer,

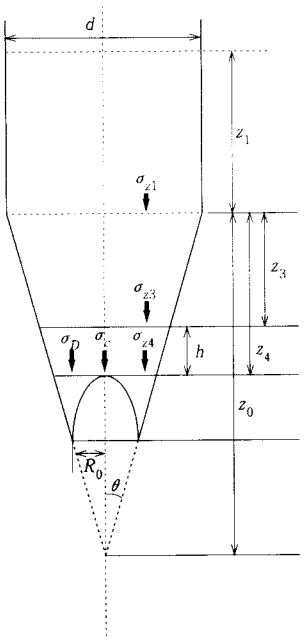

Fig. 7 Calculation of stress in a hopper

$\bar{\sigma}_{z4}$ acting in the consolidated layer at a depth z_4 is obtained. Although the vertical stress at a given depth and height of a consolidated layer can be obtained in such manner, a static fine particle layer under a critical stress has been analyzed above. However, in the flow model, the flow velocity of particles changes as the consolidated layer is formed, and it is required to take the dynamic pressure $\bar{\sigma}_D$ associated with the change into consideration. Then, by assuming that the particles at a mean flow velocity $\bar{U}$ are decelerated and momentarily stopped in the consolidated layer, $\bar{\sigma}_D$ is given from the change of momentum by:

$$\bar{\sigma}_D = \frac{\gamma_s \bar{U}}{3} \cdot \frac{(z_0 - z_4 + h)^3 - (z_0 - z_4)^3}{(z_0 - z_4)^2} \tag{8}$$

Then, by repeating the numerical calculation, h_n is obtained when the particle pressure $(\bar{\sigma}_{z4})_E$ given by the sum of Eqs. (4), (5) and (8) and the particle pressure $(\bar{\sigma}_{z4})_T$ equal to the critical stress σ_c meet the condition of the following formula, and are substantially equal.

$$|\ (\bar{\sigma}_{z4})_T - (\bar{\sigma}_{z4})_E\ | \leqq 10^{-5} \tag{9}$$

3.3 Prediction of pulsation frequency *f*

The pulsation frequency f is the inverse of the building-up time of the consolidated particle layer sufficient for the creation of the critical stress, and

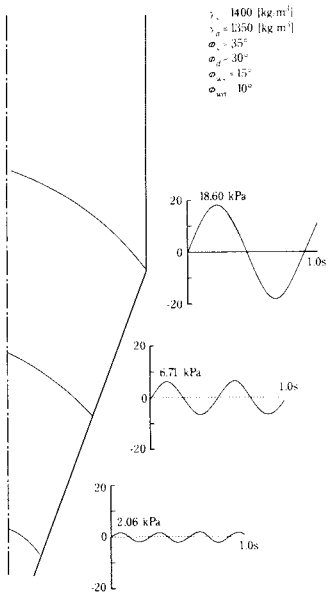

Fig. 8 Calculated slip line and waveforms of dynamic pressure acting on hopper wall

is given by the following formula, where W is the volume of the consolidated particle layer determined by h_n.

$$f = \frac{\pi \bar{U} \gamma_d [(z_0 - z_4) \tan\theta]^2}{W(\gamma_s - \gamma_d)} \tag{10}$$

In this way, the pulsation frequency and wall pressure at a given location in the hopper part can be predicted by using the geometric characteristics (θ, d, R_0, L) of the bin-hopper system and characteristics (γ_s, γ_d, ϕ_s, ϕ_d, ϕ_{ws}, ϕ_{wd}) of the particles.

Figure 8 shows a computational example of quartz sand (γ_p = 2650 kg/m^3) flowing out of a small bin-hopper system at θ = 20°, R_0 = 15 mm, d = 0.5 m, L = 0.6 m. The pulsation frequency at the connection between the cylindrical and the hopper parts is 1.11 Hz, and is consistent with the component of low frequency observed with such small bin-hopper system[6]. The pulsation frequency immediately above the orifice is not as high as that in the lower part of the hopper at 3.42 Hz, showing a consistency with the tendency observed in the simulation. Since the shape of the bin-hopper system, specifically, an opening angle θ and orifice bore R_0 determine the mean flow velocity U of particles flowing in the system, and the characteristics of the flow and those of the consolidated particle layer are determined by the velocity, a proper prediction of the characteristics of particles is essential. A detailed comparison of the pulsation frequency, flow rate and fluctuation of wall pressure according to the flow model suggested herein with actual measurements shall be reported separately.

Conclusion

We suggested a dynamic model for a flow mechanism of particles flowing in a bin-hopper system, and presented a method for predicting the particle pressure during discharge and the pulsation frequency of particles according to the model. First, a two-dimensional simulation was conducted for the flowing behavior of particles by using the particle element method. The result of the simulation was sufficiently consistent with prior findings experimentally known, and it was demonstrated that the flowing behavior of individual particles in a flowing state and the quantity of state can be microscopically observed using the simulation. Then, a model of flowing mechanism was obtained through a careful observation of the flowing behavior of particles using the simulation, and it was demonstrated that the flowing behavior of particles in a bin-hopper system can be dynamically analyzed by predicting the particle pressure fluctuating in a flowing state of the particles and the pulsation frequency as an example for confirming the usefulness of the model.

Nomenclature

d	= diameter of hopper	[m]
f	= frequency of fluctuation of wal pressure	[Hz]
g	= gravitational acceleration	[m/s^2]
h	= height of dense packed bed	[m]
L	= height of cylindrical part in bin	[m]
R	= radius of hopper	[m]
t	= time	[s]
U	= mean vertical velocity	[m/s]
W	= volume of dense packed bed	[m^3]
z	= distance from upper surface of hopper	[m]
α	= angle between major principal plane and vertical axis in bin	[deg]
γ	= bulk density	[kg/m^3]
η	= angle between faliure plane and minor principal plane	[deg]
θ	= half angle of hopper	[deg]
σ	= normal stress	[Pa]
τ	= shear stress	[Pa]
ϕ	= effective angle of friction	[deg]

<Subscript>

c = critical state
D = dynamic condition
d = dense packing state
E = estimated value
m = mean value
o = orifice

T = theoretical value
r = radial direction
s = static condition(loose packing state)
w = wall
z = vertical direcrion

Literature cited

1) Aoki, R.:Kagaku Kogaku, **49**, [7], 540－549 (1985).
2) Bransby, P.I., P.M. Blair-fish and R.G. James: Powder Technol., **8**, 197－206 (1973).
3) Brown, R.L. and J. C. Richards: "Principles of Powder Mechanics", pp. 135－202, Pergamon Press (1970).
4) Cundall, P.A. and O.D.L. Strack: Geotechnique, **29**, [1], 47－65 (1979)
5) Hidaka, J., Y. Kirimoto, S. Miwa and K. Makino: J. Soc. Powder Technol., **22**, [7], 427－435 (1985).
6) Hidaka, J., A. Shimosaka and S. Miwa: Preprints of the 56th Annual Meeting of The Soc. of Chem. Engrs., Japan, Tokyo, p.391 (1991).
7) Kano, J., A. Shimosaka and J. Hidaka:J. Soc. Powder Technol., **30**, [3], 188－193 (1993).
8) Hidaka, J.: J. Soc. Powder Technol., **29**, [6] 465－471 (1992).
9) Kiyama, H. and H. Fujimura: Dobokugakkai Ronbunsyu, [333], 137－146 (1983)
10) Takahashi, H. and H. Yanai: Kagaku Kogaku, **38**, [10], 746－751 (1974)
11) Pokrovskii, G.I. and A.I. Arefev: Zhur. Fiz., **7**, [4], 424 (1937)
12) Walters, J.K.: Chem. Eng. Sei., **28**, 13－21 (1973)

Author's short biography

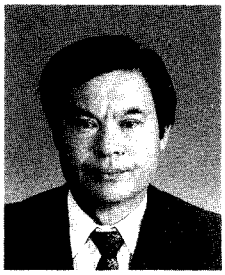

Jusuke Hidaka

Prof. Jusuke Hidaka has been at Doshisha University, Japan since 1976. His major research interests lie in mechanical analysis of powder flow using computer simulation, classification and instrumentation of powder industrial processes using acoustic emission. He is the secretary of the Society of Powder Technology, Japan.

Junya Kano

Junya Kano graduated in chemical engineering of post graduate course at Doshisha University in 1995. He is Research Assistant of Institute for Advanced Materials Processing, Tohoku University.

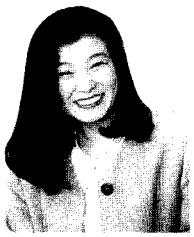

Atsuko Shimosaka

Atsuko Shimosaka is Lecturer of Chemical Engineering and Material Science Department at Doshisha University since 1993. Her main fields of research are in the mechanical analysis of granular behavior using computer simulations. Currently, she is editor of Journal of The Society of Powder Technology, Japan.

Adhesion Force Arising from Solid Salt Bridge Formed after Drying of Liquid Bridge †

Yoshiyuki Endo, Yasuo Kousaka and Hidenori Onitsuka
*Dept. of Chem. Eng., Univ. of Osaka Pref.,**

Abstract

Water bridges formed among particles in industrial process often contain soluble impurities such as salts. When such bridges are exposed to dry air, water in the bridges vaporizes and the salts crystallize to form solid bridges.

Solid bridges between two glass spheres were formed from NaCl, KCl, KNO_3 and Na_2SO_4 solution by controlling the humidity, and their tensile strength was measured. It was found from these experiments that 1) the adhesion force of a solid salt bridge which was uniformly formed in the gap between two spheres was one to two orders of magnitude larger than that of a water bridge without crystallization; 2) the average adhesion force of solid bridges was proportional to the 1/2 power of the product of salt volume and particle radius; and 3) the adhesion force of bridges of NaCl and KCl was influenced by the surrounding humidity, which it was below their deliquescent points, because they adsorbed water until complete recrystallization took place.

1. Introduction

Liquid bridges formed among fine particles in industrial processes often contain a small quantity of soluble impurities. When such soluble impurities are contained in a liquid bridge, depending on the kind and quantity of the solute, the liquid bridge may easily grow in size in comparison with the size of a liquid bridge formed by pure water (approximately 0.15 to 100 nm in neck radius of the bridge)[2]. This has been confirmed by experiments using several types of fine particles that have been industrially employed[3].

In connection with the problem associated with such phenomenon, we have studied the adhesion forces acting between particles when liquid bridges containing soluble impurities are exposed to dry air, and the solutes in the liquid bridge are crystallized. In the experiments, liquid bridges were formed from aqueous solutions containing NaCl, KCl, KNO_3 and Na_2SO_4 between two glass spheres of identical size, then solid bridges were formed by keeping the liquid bridges in an atmosphere of low humidity, and their adhesion force was measured. Additionally, a relation between the adhesion force arising from the initial liquid bridge and that of the solid bridge after crystallization was theoretically studied, and the results of the experiments were discussed.

* 1-1 Gakuen-cho, Sakai-shi 593 JAPAN

† This report was originally printed in *Kagaku Kougaku Ronbunshu*, 20, 542 (1994) in Japanese, before being translated into English with the permission of the editorial committee of the Soc. Chemical Engineers, Japan.

In most previous studies on such solid bridges, the strength in a consolidated state of a powder bed consisting of deliquescent particles as NaCl was studied[1, 5, 7, 8, 10-12], and the adhesion force of a solid salt bridge formed by vaporizing water from a liquid bridge containing a small amount of soluble salts has never been studied.

2. Theoretical discussion

In this paper, two spheres of identical size as shown in **Figure 1** are considered as particles. A liquid bridge containing the soluble salts is formed by the Kelvin effect and the effects of dissolving substances therein (effects of the vapor pressure drop on the surface of the liquid bridge, and as a result increase the size of the bridge)[2]. Generally, in the case of particles used in industrial processes, the effect of the solutes is greater than the Kelvin effect , which is negligible[3], and the size and profile of a liquid bridge are determined by the relative humidity of the atmosphere, the kind and the amounts of solutes in the liquid bridge etc[3]. The adhesion force F_L arising from a liquid bridge formed in such manner can be obtained from the following equation[4]:

$$F_L = \pi p_L r_2^2 + 2\pi\sigma r_2 \quad (1)$$

where r_2 is the neck radius of the liquid bridge shown in **Figure 1**, and p_L is the pressure deficiency in

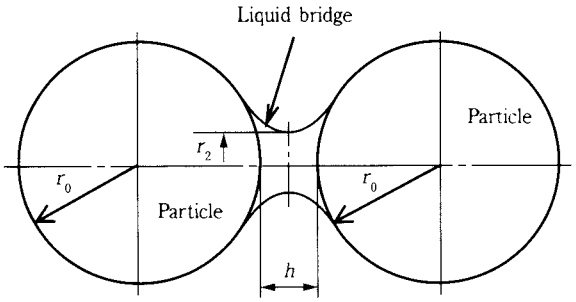

Fig. 1 Dimensions of liquid bridge between two spheres

the liquid bridge, which depends on the size and profile of the bridge determined in the above manner. Thus, the liquid bridge adhesion force F_L is determined by the type and amount of solutes, the surrounding humidity, the size of the particles, the distance between the particles and the like. When a large liquid bridge is formed because of a large amount of solutes contained in the liquid bridge, or when the gap between the particles forming the bridge can be considered as $h = 0$, for a liquid bridge formed between two spheres of identical size, Eq. (1) can be approximated by the following equation:

$$F_L = 2\pi r_0 \sigma \tag{2}$$

where r_0 is the particle radius.

Now, we consider that a solid bridge between two identical spheres is formed by crystallization of the solutes contained in the liquid bridge when the humidity becomes lower. It is assumed that the entire amount ($= N_S\ (4/3)\pi r_0^3$, where N_S is the number of solute molecules divided by the volume of a particle in the liquid bridge) of solute in the liquid bridge forms a solid bridge between particles in a form similar to that of the liquid bridge in **Figure 1**. This assumption will be discussed later in Result of Experiments. Now, the adhesion force arising from a solid bridge between particles is defined as the force required to break the solid bridge by separation of two particles as shown in **Figure 1**. We assume that the breakage occurs at $x = 0$ in **Figure 1**, and a relation is derived between the surface area of breakage and the volume of the solid bridge. The volume v of the bridge in **Figure 1** is related to a neck radius r_2 for the gap between the particles $h = 0$[2] as follows.

$$v = (\pi/2)\ r_2^4/r_0 \tag{3}$$

If the above relation exists also in a solid bridge, the surface area $A_S\ (= \pi r_2^2)$ of breakage can be expressed as follows.

$$A_S = (2\pi r_0 v)^{1/2} \propto (r_0 v)^{1/2} \tag{4}$$

Also, as the volume v of the solid bridge is proportional to the number of solute molecules ($= N_S\ (4/3)\pi r_0^3$), the following equation is obtained from Eq. (4):

$$A_S \propto \left\{ N_S\ (4/3)\pi r_0^4 \right\}^{1/2} \tag{5}$$

Here, if the solid bridge is assumed to have uniform strength at any section, because the tensile breakage force is proportional to the sectional area of breakage, the adhesion force F_S arising from the solid bridge can be expressed by the following formula:

$$F_S \propto A_S \propto \left\{ N_S\ (4/3)\pi r_0^4 \right\}^{1/2} \tag{6}$$

Further, if the liquid bridge adhesion force can be obtained by Eq. (2), the following relation is derived from Eqs. (2) and (6):

$$F_S/F_L \propto N_S^{1/2} r_0 \tag{7}$$

If breakage occurs in a solid bridge, it is expected that the relation between the adhesion force arising from a liquid bridge and that of a solid bridge formed by vaporization of water is given by the above formula.

On the other hand, when the amount of soluble salts is reduced, no solid bridge forms in the gap between particles, and the fine crystals are deposited onto the particle surface. In such case, it seems that adhesion force arises from van der Waals force, and the force is smaller than that of the initial liquid bridge. Moreover, if the gap between two particles is increased by deposition of the fine crystal particles in the gap, the van der Waals force becomes even lower.

2. Experimental Method

Glass spheres of 2.5, 5.0 and 7.5 mm in radius were used as particles. In order to form uniform liquid bridges, the glass spheres were dipped in a concentrated hydrochloric acid solution, held by pincers to avoid any contact with hands, washed in flowing ultrapure water, and dried in a thermo-hygrostat (at 298K and 30% humidity) in a clean tunnel. The glass spheres were set-up as shown in **Figure 2** so that the centerline of the two spheres coincided with the vertical direction. Then, liquid bridges of aqueous solution containing solutes (2×10 to 4×10^3 mol/m^3 -ultrapure water) were formed between two glass spheres by means of a microsyringe. The liquid bridge volume is 2×10^{-9} m^3. Solutes used in the experiment are Nacl, KCl, KNO_3 and Na_2SO_4, considering that

such ions as Na^+, K^+, Cl^-, NO_3^-, SO_4^{2-} are contained in tap water. The liquid bridge was left in a thermo-hygrostat operated at various constant humidities below the deliquescent points of the salts shown in **Table 1** (at a temperature of 289K) until it reached

Table 1 Relative humidity above which salts deliquesce (at 298K)[14)]

Soluble salt	Critical relative humidity (%)
Nacl	76
KCl	84
KNO_3	92
Na_2SO_4	83

an equilibrium condition (for about 24 hrs). Once the solid bridge was formed in such manner, the glass spheres set as shown in **Figure 2** were removed from the thermo-hygrostat, and placed on an electronic balance, as shown in **Figrue 3**. Then, the moving stage was slowly moved downward to separate the two spheres. Readings of the electronic balance were constantly inputted to a personal computer, and the highest reading of the balance at breakage of the solid bridge was taken as the adhesion force of the solid bridge. Although the measurement was carried out in a room at a temperature of 293 to 298K and a relative humidity of 60 to 70%, it took only a few minutes to measure a sample, and it is considered that no change in crystal conditions such as absorption of moisture occurred during the measurement.

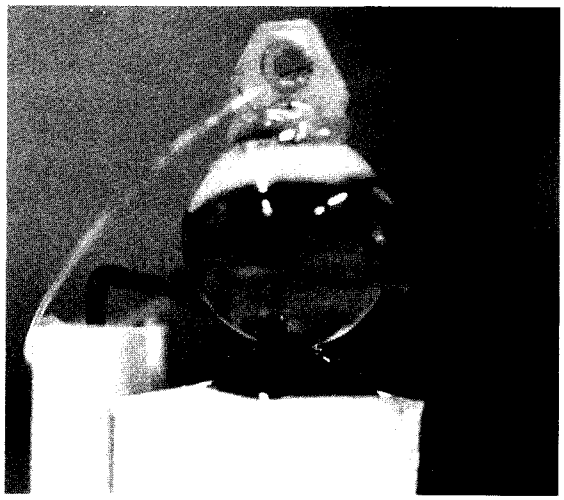

Fig. 2 Photograph of setting of two glass spheres

3. Experimental Results and Discussion

Figure 4 shows the measurement results of the solid bridge force. Only 20 points of measurement data are shown for each salt in **Figures 4 (a)** to **(d)**, because it is a very time-consuming operation to form a solid bridge between two glass spheres as described above. However, the results follow the Weibull distribution, widely distributed within a range of nearly two orders of magnitude. Similar results were obtained under conditions different from those shown in **Figure 4** (quantity N_s of the salt, radius r_0 of the glass sphere, etc.).

The measurement results are summarized in **Figure 5**, containing the results of **Figure 4**. The abscissa represents the amount of crystals (number of molecules) forming the solid bridge multiplied by the radius, which corresponds to the value between braces in the right term of Eq. (6), and the ordinate shows the average value of adhesion forces measured for 20 solid bridges as shown in **Figure 4**. Although data for individual pieces are distributed within a wide

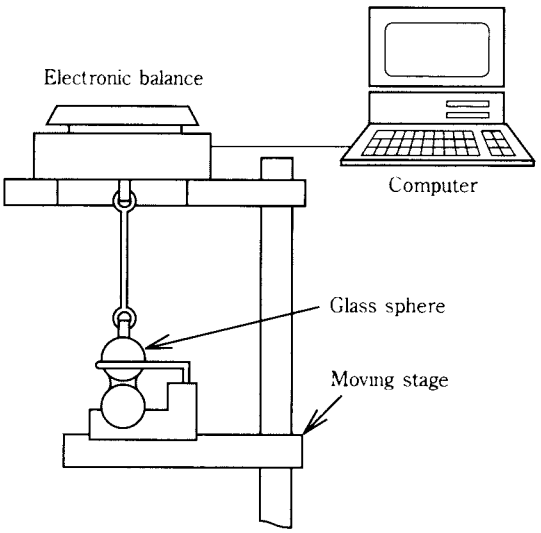

Fig. 3 Experimental set up

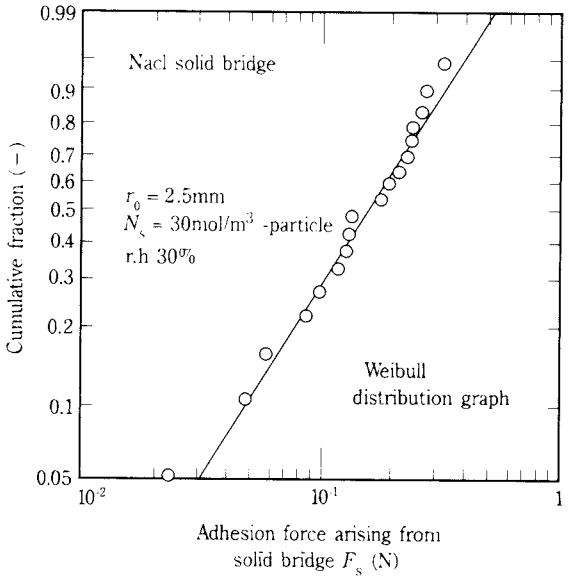

Fig. 4 (a) Distribution of adhesion force arising from solid bridge formed between two spheres (NaCl)

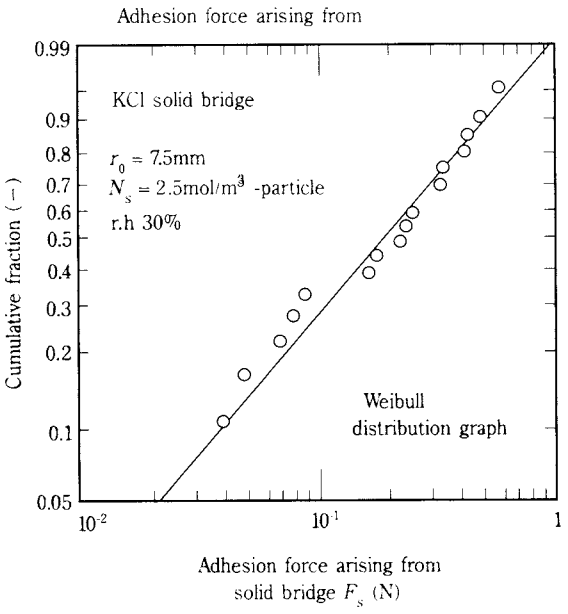

Fig. 4 (b) Distribution of adhesion force arising from solid bridge formed between two spheres (KCl)

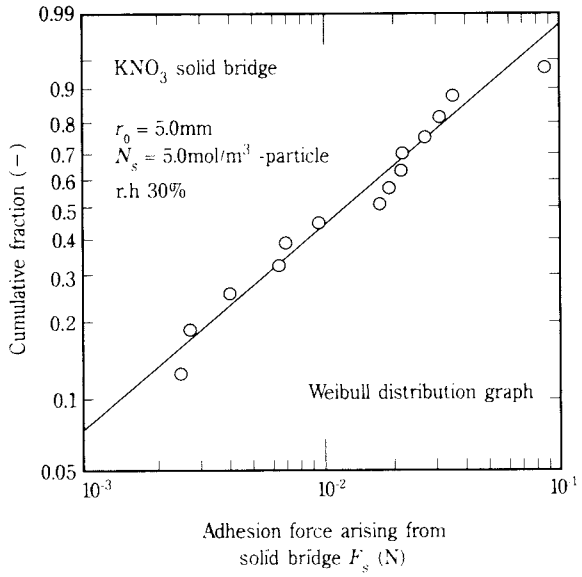

Fig. 4 (c) Distribution of adhesion force arising from solid bridge formed between two spheres (KNO_3)

range as shown in **Figure 4**, the adhesion force F_S of a solid bridge formed by any of the salts tends to comply with the relation given by Eq. (6). In the case of NaCl in **Figure 5 (a)**, the adhesion force decreases, as the humidity increases when the crystals are formed in the solid bridge. As shown in **Table 1**, NaCl is deliquescent at a humidity of 76%, and deliquescence of crystals begins at a humidity of 76% when the humidity is increased from a low level. However, water is not completely vaporized even if the humidity is reduced below 76%, although crystals are formed, when the humidity is reduced from a level higher than that level. In this case the water is completely vaporized at a humidity of

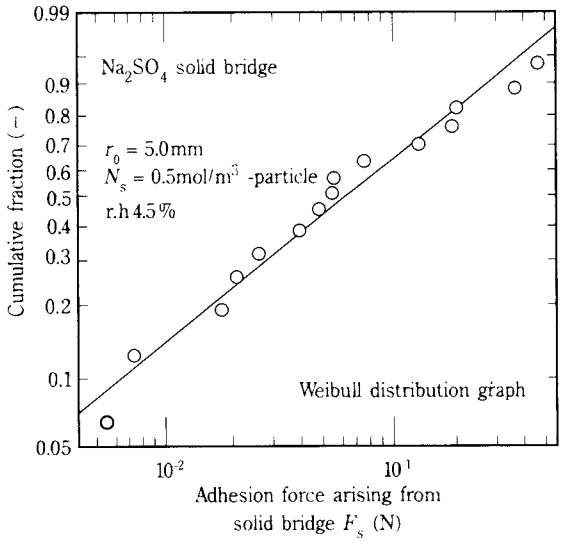

Fig. 4 (d) Distribution of adhesion force arising from solid bridge formed between two spheres (Na_2SO_4)

40%[9,13]. Because NaCl has such hysteresis, the results at a humidity of 45 and 60% account for the reduction in the adhesion force due to a small amount of water (undetected by microscopic observation) contained in the crystals. Also, in the case of KCl, a slight difference was found, although it is not as significant as that of NaCl, and it is caused by a hysteresis similar to that of NaCl (KCl is deliquescent at a humidity of 84%, and water is completely vaporized at a humidity of about 45%). In the results of KNO_3 in **Figure 5 (c)** and Na_2SO_4 in **Figure 5 (d)**, no difference was detected for different humidities. Since no reference describing the hysteresis of KNO_3 and Na_2SO_4 was found, changes in weight of the saturated aqueous solution of each salt were examined at various humidities. The hysteresis was not confirmed for both salts within the measurement range. Therefore, the adhesion force for both salts was not affected by humidity as shown in **Figures 5 (a)** and **(d)**.

Figure 6 shows photographs of a NaCl solid bridge formed between glass spheres. In **Figure 6 (a)** (before breakage), it is recognized that the profile of the solid bridge is similar to that of the liquid bridge in **Figure 1**, and the solid bridge is formed so as to fill the gap between the glass spheres. A solid bridge of substantially similar profile was formed in other salts, KCl, KNO_3 and Na_2SO_4. In **Figure 6 (b)** (breakage section viewed from above), because the solid bridge has some local voids, and has not a uniform structure, the individual measurement data for adhesive force are distributed within a wide range as shown in **Figure 4**. Although the adhesive forces

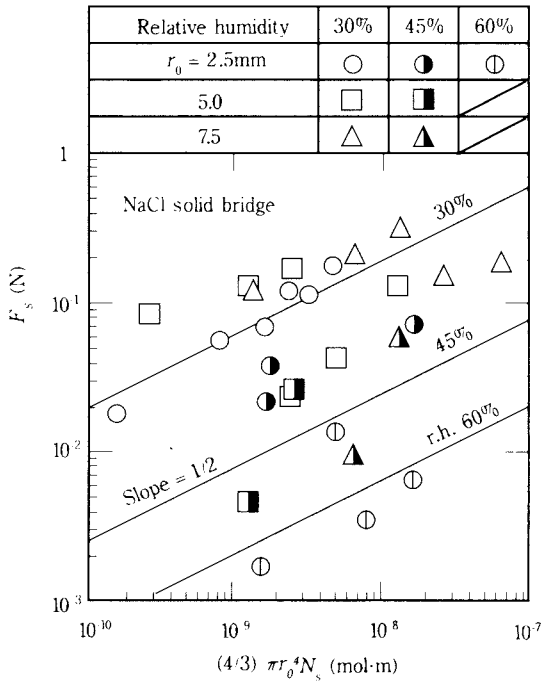

Fig. 5 (a) Experimental results of adhesion force arising from solid bridge (NaCl)

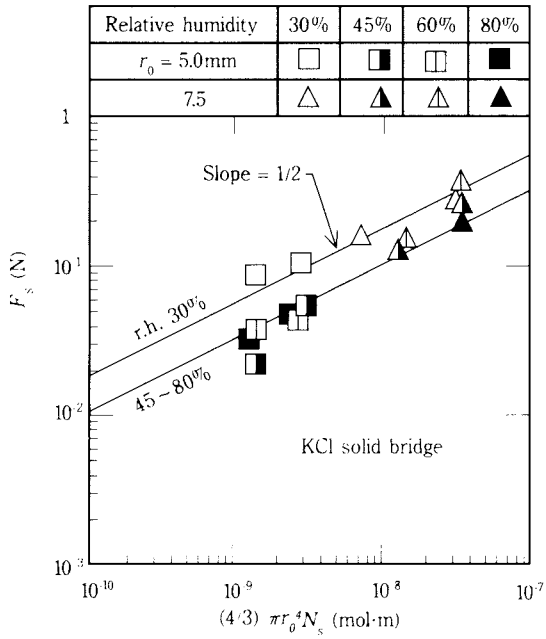

Fig. 5 (b) Experimental results of adhesion force arising from solid bridge (KCl)

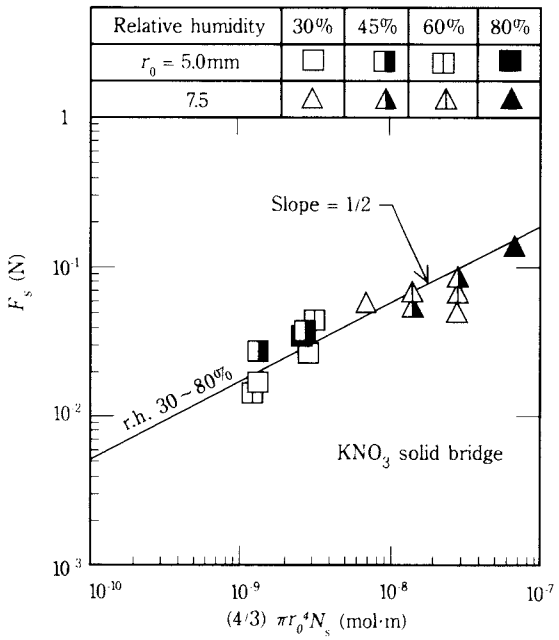

Fig. 5 (c) Experimental results of adhesion force arising from solid bridge (KNO_3)

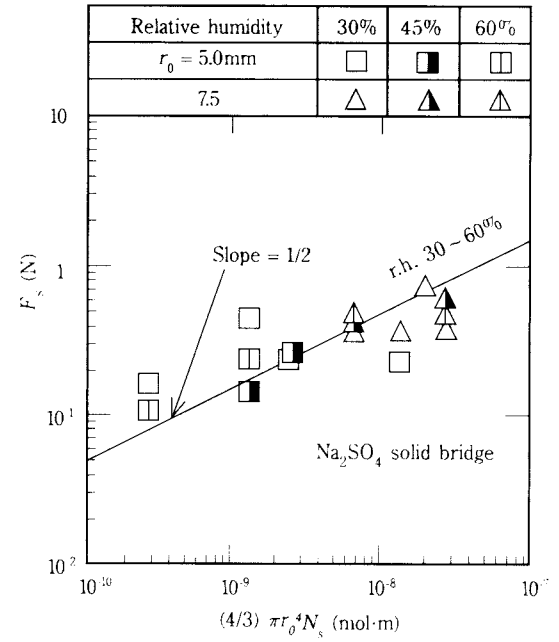

Fig. 5 (d) Experimental results of adhesion force arising from solid bridge (Na_2SO_4)

of solid bridges formed by the salts in the experiments are distributed within such range, it is found that Eq. (6) is satisfied by taking the average adhesive force.

A condition for the formation of a solid bridge between glass spheres is that the liquid bridge be kept in an atmosphere at the deliquescent point shown in **Table 1** or at a higher humidity. The liquid bridge force F_L can be calculated from Eq. (2). In **Figure 7**, F_L is compared with the solid bridge force F_S shown in **Figure 5**. It is clear that the adhesion force of a solid bridge formed by any salt is one to two orders of magnitude larger than that of liquid bridge in high humidities. F_S/F_L agrees with the relation of the Eq. (7) in **Figure 7** as well.

In the experiment, the measurement of the adhesion force in a section with a smaller amount of crystals was not achieved, because the solid bridge was broken by a very small force before measurement

of adhesion force. When the amount of crystals was much smaller, deposits of small crystals on the particle surface were observed, in which the van der Waals force is the main mechanism of adhesion between particles, as described in the Theoretical Discussion. The adhesion force in such state should be studied in the future.

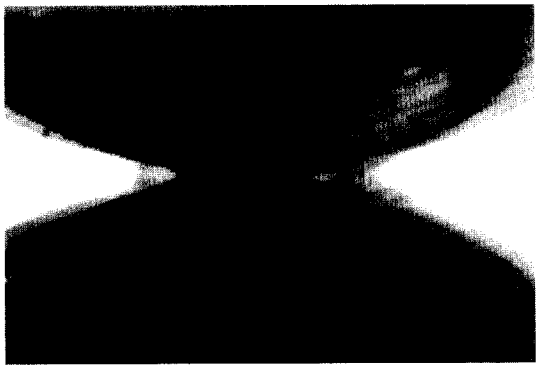

(a) ⌊⌋ 1mm

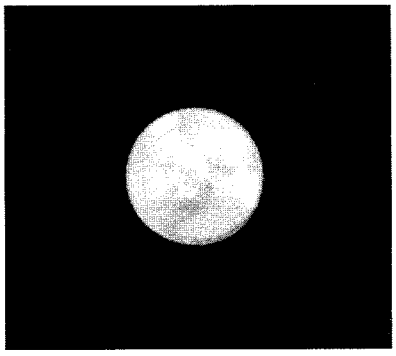

(b) ⌊⌋ 10mm

Fig. 6 Photographs of solid bridge (NaCl) formed between two glass spheres

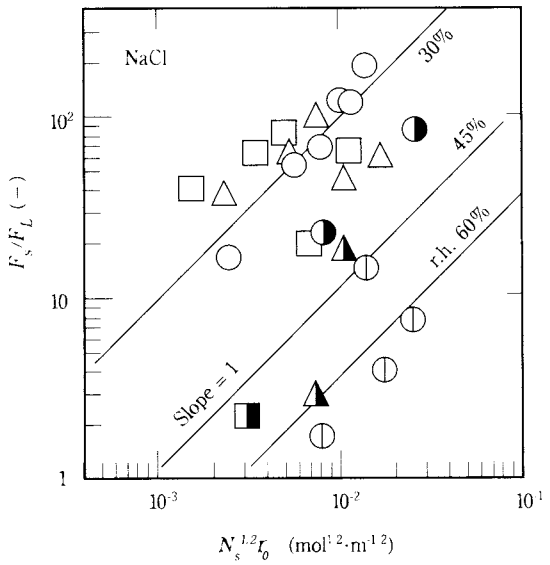

Fig. 7 (a) Ratio of adhesion force arising from solid bridge to liquid bridge force (NaCl) (Keys are the same as those in Fig. 5)

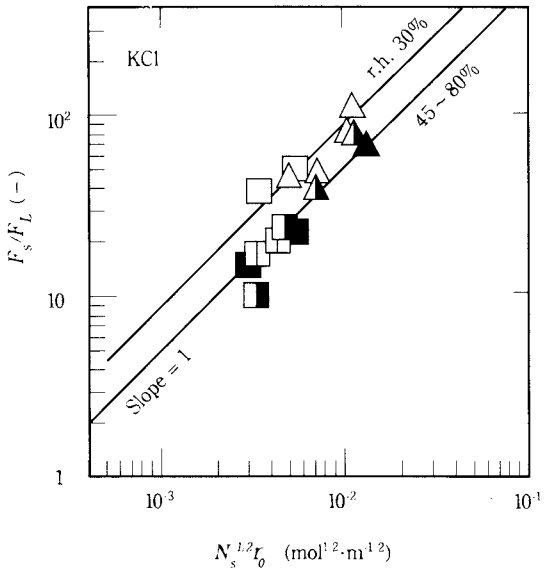

Fig. 7 (b) Ratio of adhesion force arising from solid bridge to liquid bridge force (KCl) (Keys are the same as those in Fig. 5)

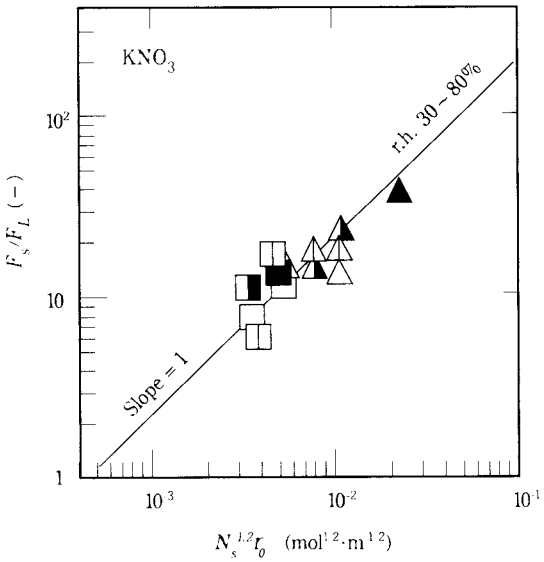

Fig. 7 (c) Ratio of adhesion force arising from solid bridge to liquid bridge force (KNO_3) (Keys are the same as those in Fig. 5)

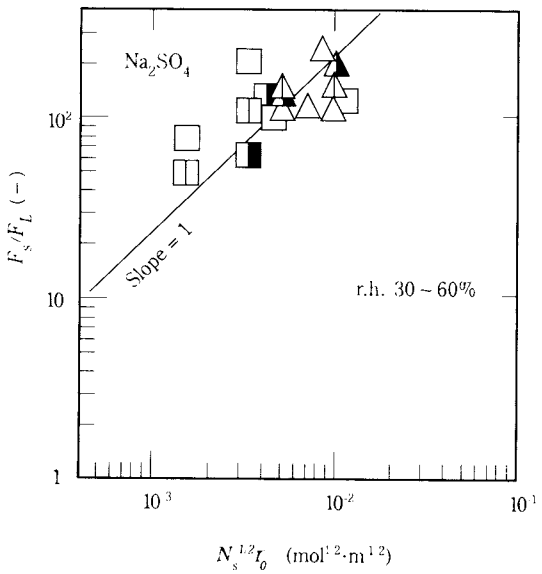

Fig. 7 (d) Ratio of adhesion force arising from solid bridge to liquid bridge force Na_2SO_4 (Keys are the same as those in Fig. 5)

Conclusions

A solid bridge formed after drying a liquid bridge containing such water-soluble salts as NaCl, KCl, KNO_3 and Na_2SO_4 in a low humidity atmosphere, was experimentally studied. The results of the experiments are described below.

1) When a large amount of solutes was contained in an initial liquid bridge, it was found that a solid bridge forms so as to fill the gap between particles, and its adhesion force is one to two orders of magnitude higher than that of the liquid bridge before crystallization.
2) Although the adhesion forces of individual solid bridges were distributed within a wide range, the average value of such forces was proportional to about 1/2 power of the product of the volume of crystals forming the solid bridge and the particle radius. This could be explained by a theoretical model.
3) It was found that the adhesion forces arising from NaCl and KCl bridges increase as the humidity decreases (below their deliquescent points), because they adsorbed water until complete recrystallization took place.

Literature cited

1) Adoms, J.R. and W.H. Ross: *Ind. Eng. Chem.*, **33**, 121-127 (1941)
2) Endo, Y., Y. Kousaka and Y. Nishie: *Kagaku Kogaku Ronbunshu*, **18**, 950-955 (1992)
3) Endo, Y., Y. Kousaka and Y. Nishie: *Kagaku Kogaku Ronbunshu*, **19**, 411-417 (1993)
4) Endo, Y., Y. Kousaka and Y. Nishie: *Kagaku Kogaku Ronbunshu*, **19**, 55-61 (1993)
5) Ezaki, S. and M. Sugiyama: *Nippon Engakkaishi (Japan Salt Soc.)*, **14**, 199-211 (1960)
6) Kousaka, Y., Y. Endo and Y. Nishie: *Kagaku Kogaku Ronbunshu*, **18**, 942-949 (1992)
7) Masuzawa, T.: *J. Res. Assoc. Powder Technol. (Japan)*, **7**, 554-560 (1970)
8) Nash, J.H., G.G. Leiter and A.P. Johnson: *Ind. Eng. Chem. Prod. Res. Dev.*, **4**, 140-145 (1965)
9) Orr, C., F.K. Hurd and W.J. Corbett: *J. Colloid Sci.*, **13**, 472-482 (1958)
10) Pietsch, W.G.: *Canadian J. Chem. Eng.*, **47**, 403-409 (1969)
11) Ross, W.H., J.Y. Yee and S.B. Hendricks: *Ind. Eng. Chem.*, **37**, 1079-1083 (1945)
12) Tanaka, T.: *Ind. Eng. Chem. Prod. Red. Dev.*, **17**, 241-246 (1978)
13) Tang, I.N., H.R. Munkelwitz and J.G. Davis: *J. Aerosol Sci.*, **8**, 149-159 (1977)
14) Wasshborn E.W. (ed.): "International Critical Table I", p.67, McGraw-Hill, New York (1926)

Author's short biography

Yasuo Kousaka

The author is Professor of Chemical Engineering Department at University of Osaka Prefecture since 1979. His major research interests are dynamic behavior of aerosol particles, sizing techniques of aerosol particles and powders, and dispersion of aggregate particles in air and water. He is currently editor in chief of Journal of the Society of Powder Technology, Japan, and vice president of Japan Association of Aerosol Seience and Technology.

Yoshiyuki Endo

The author is Research Associate of Chemical Engineering Department at University of Osaka Prefecture since 1991. His research interests are almost same as those of Professor Kousaka.

Creep Failure Process for Fine Powder Beds by Tensile Loading †

Hidehiro Kamiya*, Makio Naito**, JunIchiro Tsubaki***** and Genji Jimbo******
*Department of Chemical Engineering, Nagoya University**

Abstract

To investigate the process of creep failure phenomena in fine powder beds, the change in the tensile failure strength and the displacement of powder beds during the creep failure process was analyzed. The increasing displacement is divided into three sections (I, II, III). The increasing rate of displacement slows in the first stage (section I), remains almost constant in section II, and rapidly increases and falls in section III. By using the experimental equation to relate the creep failure life to the increasing rate of displacement in section II, the change in tensile strength of powder beds can be estimated during the creep failure process. No decrease in tensile strength is observed during the first stage (section I). However, in the second and third stages (section II and III), the strength decreased remarkably with increasing creep time. The increasing displacement can be fitted by a Voigt model in the region of section I, in which the tensile strength is almost constant. According to the elastic/viscous parameters of a Voigt model decrease in relation to the decrease in fracture strength of powder beds, the complex increase of displacement in the region of sections II and III can be quantitatively estimated. The deformation resistance of powder beds was quantitatively related to the fracture strength.

1. Introduction

Because fine powder of less than 10 μm in primary particle size, due to a high adhesiveness, causes such problems as blockage, measurements and analyses of adhesive force of fine particles have been conventionally conducted for primary particles[2] or powder beds[16]. In addition, with fine particles of high adhesiveness, such time-dependent phenomena as fatigue, creep and stress relaxation are significantly observed even in a dry powder bed. Such phenomena cannot be explained simply by the adhesive force alone, and need to be analyzed by considering the time-dependence change of micro structure in powder beds constituting the fine powder. In the field of soil engineering, the time-dependent phenomena have been conventionally addressed to in the setting of wet particle beds[3,9], and studied as a continuum by means of various viscoelasto-plastic models[1,17,21] and using models with microscopic changes in the configuration of particles taken into consideration[11,12]. On the other hand, it is reported that a dry fine powder bed is also highly densified by repetitive consolidation and creep consolidation[4,7,8] in relation to a ceramics forming operation. Naito, et al.[13,14,20] pointed out that fatigue and creep failure were caused also by tensile loading and shearing force experimentally by repetitively wiping off a collected powdery dust bed, and confirmed the presence of such phenomena using a fundamental experiment[5,6]. Although a macroscopic behavior of deformation to failure of a dry fine powder bed is similar to that of a wet bed of relatively large particles, for wet particles, interstitial water in gaps between particles significantly affects the time-dependent phenomena. In the case of dry fine particles, the time-dependent phenomena are considered to be caused by gradual deformation in such secondary particle structure as an aggregation of particles, and although the macroscopic behavior is similar to that of wet particles, the driving mechanism is supposed to be different.

Such similar phenomenon is reported whereby the ratio of removal and/or dispersion is increased with an increase in the number of repetitions, when a removal force is repetitively applied to a powder bed for the removal of particles collected onto a substrate[15]

* Furo-cho, Chigusa-ku, Nagoya 464-01 JAPAN
** Now with Fine Ceramics Center, Nagoya 456
*** Now with Tokyo University of Agriculture and Technology
**** Now with Chubu Powtech Plaza Laboratory
***** Now with Department of Micro-system Engineering Graduate school of, Nagoya University
† This report was originally printed in *Kagaku Kougaku Ronbunshu*, **20**, 556 (1994) in Japanese, before being translated into English with the permission of the editorial committee of the Soc. Chemical Engineers, Japan.

and dispersion of particles from the surface of a particle bed[9]. It has been attempted to explain such phenomenon as a probable phenomenon of failure due to fluid-dynamic unevenness of the removal force. However, it can be considered based on a theoretical phenomenon of failure that the configurational structure in a powder bed is gradually changed by the action of a repetitive force, and a final failure is caused because the resistance against failure stress is reduced. However, such failure mechanism is rarely taken into consideration, and the process leading to failure has rarely been determined and examined in detail.

Accordingly, we measured the rate of displacement and change in failure stress during a process leading to a creep tensile failure in two kinds of inorganic fine powder beds, and considered the changes in the dynamic characteristics of a powder bed in a process leading to creep failure. Then, we devised a viscoelastoplastic model for commonly expressing changes of failure stress and behavior of deformation.

2. Experiments

For the experiments, a suspended-type adhesion measurement apparatus (Hosokawa Micron Co., Ltd., Cohetester) shown in **Figure 1** was employed. The apparatus is a two-piece tensile failure tester of vertical consolidation and horizontal tension type, as described in detail in our previous report. It allows testing at a constant stress loading rate by employing a spring of low modulus of elasticity between a movable cell and a pulley which is rotated at a constant speed to load the cell. The density and mean particle size of powder samples used in the experiments are comprehensively shown in **Table 1**. Sample I is a standard powder sample (Kanto Loam JIS Classification 11), and Sample II is a fused alumina powder (Showa Denko K.K., WA#8000) used as an abrasive. Both are fine powders of about 1 μm in mean particle size.

The powder samples were loaded onto the measurement cell in an atmosphere of constant temperature and humidity (20°C ± 5°C, 60% ± 10%), and subjected to a preliminary loading of 5 kPa for 10 min to achieve an approximately constant porosity of 0.75 and 0.74 for Samples I and II, respectively. Three

Table 1 Powder properties of each sample.

Sample name		Mean diameter [μm]	True density [kg/m^3]
Sample I	Kanto loam (JIS No.11)	2.0	3.0×10^3
Sample II	Fused alumina (WA #8000)	1.3	3.9×10^3

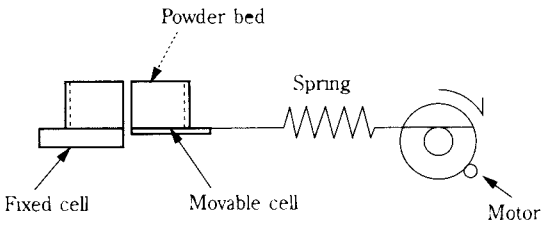

Fig. 1 Scheme of the test apparatus for measurement of tensile strength of powder beds.

types of tensile failure tests outlined in **Figure 2** were conducted on the powder beds. **Figure 2 (a)** shows a directional tensile displacement of the powder beds during the experiments, and **Figure 2 (b)** a time-course change of loading stress. Experiment 1 is a simple tensile failure test for measuring the tensile stress (σ_z) and determining a relation between the stress and displacement to failure by increasing the tensile stress at a constant rate. Experiment 2 is a creep failure test for determining time (t_b) to creep failure by increasing the tensile stress to a specified stress (σ_s) equal to or lower than the mean tensile failure stress of the powder bed obtained in Experiment 1, then, maintaining the stress constant, and measuring the increasing displacement as shown in **Figure 2 (a)**. The increasing displacement to creep tensile failure is divided into three sections, Section I or an early stage showing a low increasing rate of displacement, Section II with an almost constant increasing rate and linear time-course increase of displacement and Section III showing a rapid increase of displacement leading to creep failure[6, 10]. It was also confirmed for creep or fatigue failure of such ductile material as metals and in the soil-dynamic field that the increasing displacement in creep and other time-dependent failure can be divided into three sections. This was also observed in a high frequency repetitive stress fatigue test of dry fine powders. Presently, no model is proposed for commonly evaluating the complex increase of displacement. We studied a relation between life to creep failure (t_b) and time (t_I, t_{II}) from Section I to Section II and Section II to Section III, and determined a method for estimating the life to creep failure from the behavior of deformation before failure. In Experiment 3, a tensile stress (σ_E) was obtained by increasing the tensile stress again at a predetermined time (t_C) during the creep failure test. From the result, the change in strength of the powder bed during the process to creep failure was evaluated. The specified creep stress (σ_S) and time for starting the measurement of the strength were determined from the results of Experiments 1 and 2.

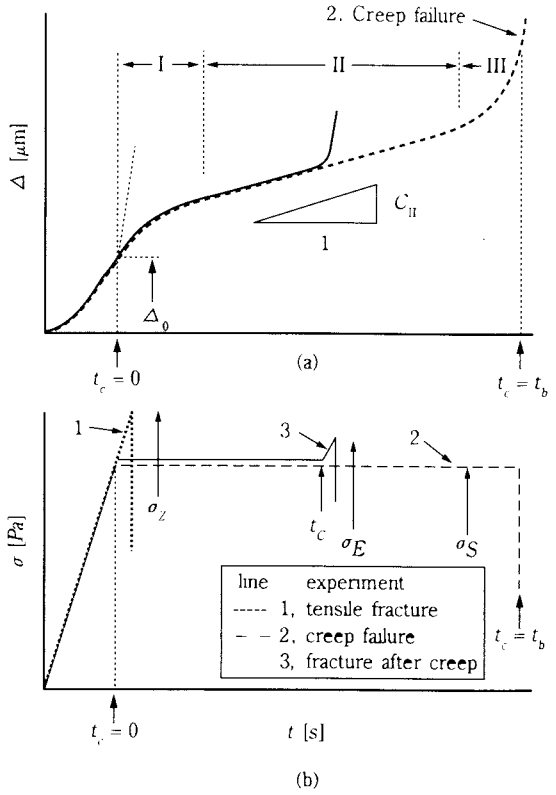

Fig. 2 Changing process of the displacement of powder beds and loading stress during simple tensile failure test (test 1), creep failure test (test II) and tensile failure test during creep failure process.
(a) Increasing process of displacement during each test.
(b) Changing process of tensile stress during each test.

3. Results

3.1 Tensile failure test (Experiment 1)

The result for Sample I is shown in **Figure 3** as an example of the relation between stress and displacement obtained by a simple tensile failure test of powder beds. The stress (σ_Z) at failure widely varied, and the coefficient of variation of the tensile stress at failure was 2.67% for 10 samples measured. However, the relation between stress and displacement shows a relatively similar curve, the displacement at failure is almost at the same point, and it is observed that the samples tend to break when the displacement reaches a certain value. Thus, in **Figure 3 (b)**, the loading stress and displacement in the ordinate and abscissa are changed into dimensionless values by means of the stress (σ_Z) and displacement (Δ_Z) at failure, and shown as a ratio of loading stress (σ/σ_Z) and dimensionless displacement (Δ/Δ_Z). In terms of the ratio of loading stress, a significant coincidence is observed in the relation between stress and displacement, and the coefficient of variation is reduced to 1.25% for a variation of displacement at σ/σ_Z = 0.95. A similar result is obtained with Sample II, and it

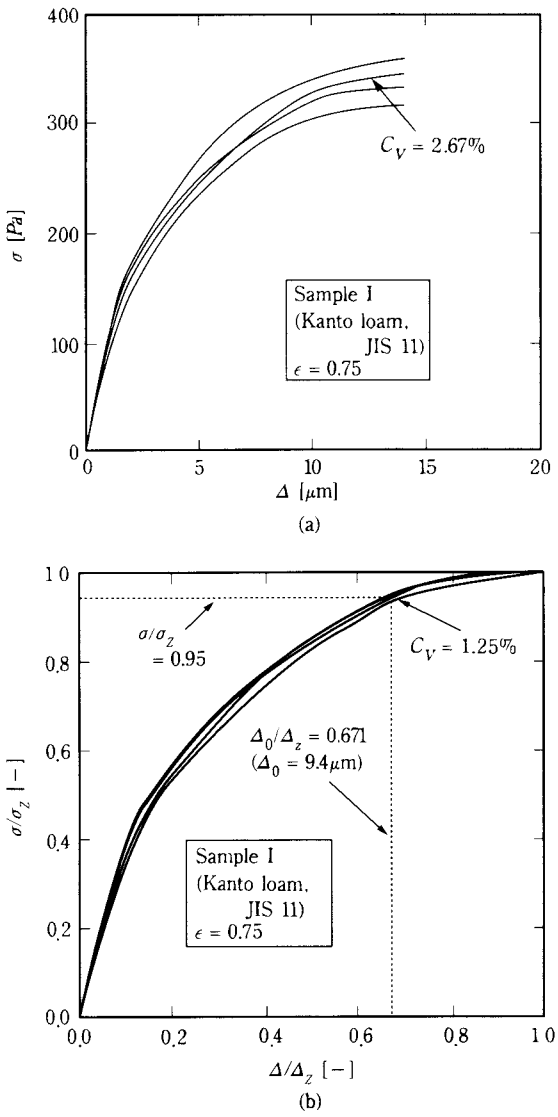

Fig. 3 Examples of tensile stress and displacement relations during simple tensile failure test (test 1).

is considered that a simple tensile failure of powder beds is a phenomenon attributed to displacement such that failure occurs as the displacement reaches a certain value, and the variation is reduced when it is determined from the aspect of displacement. Accordingly, an average curve of the ratio of stress against the displacement is obtained, as shown in **Figure 3 (b)**, and defined by a function f.

$$\sigma/\sigma_Z^* = f(\Delta/\Delta_Z) \quad (1)$$

In the creep tensile test, the stress is increased to a specified stress (σ_S) lower than the tensile failure strength (σ_Z) before starting the creep test. From a displacement (Δ_0) at the beginning of the creep test and Eq. 1, an estimated tensile failure strength (σ_Z^*)

of a powder bed subjected to the creep test can be obtained by the following equation.

$$\sigma_Z^* = \sigma_Z / f(\Delta/\Delta_0) \quad (2)$$

Life to creep failure and the change in strength of a powder bed during the creep test are not sufficiently high compared to the variation in the tensile failure strength of the powder bed without such hysteresis. Therefore, it is required to estimate the tensile failure strength of the powder beds that are subjected to the creep test and the like to evaluate the change in the strength.

3.2 Creep tensile failure test (Experiment 2)

A relation between the loading strength and life obtained by the creep test is shown in **Figure 4**. In the ordinate, the specified stress (σ_S) is changed into a dimensionless value by means of the estimated tensile failure strength (σ_Z^*) that is obtained by Eq. 2. By estimating the tensile failure stress, and obtaining the ratio of loading stress, a variation of life at the same value in the ordinate can be reduced. From the figure, if the ratio of loading stress is set to 0.9 or less, n_o failure occurs within 10^4s, which is the test range specified for the study. Because a fine powder bed may be stabilized, and have a higher strength, if no failure occurs due to a tensile force for 10^4s or a longer period[13], the measurement of the strength during the process to creep failure (Experiment 3) is conducted at $\sigma_S/\sigma_Z^* = 0.95$ to ensure the occurrence of a creep failure within 10^4s.

The increasing displacement before creep failure can be divided into three sections, as shown in **Figure 2 (a)**. The result of plotting the deformation rate (C_{II}) against life to creep failure during Section II of the process, in which the displacement increasing rate remains almost constant, is shown in **Figure 5**. Both Samples I and II are substantially approximated to a straight line of slope − 1. Thus, if Section II is confirmed, the life to creep failure can be estimated in a non-destructive way from the deformation ratio

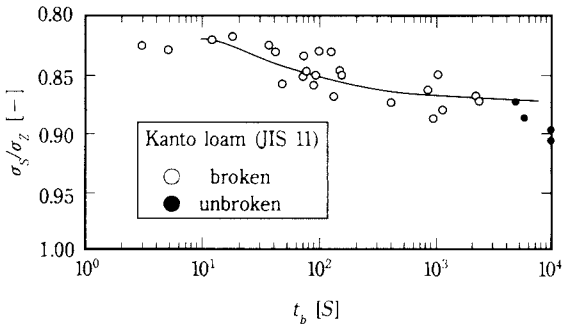

Fig. 4 Stress and creep failure life relations of sample 1.

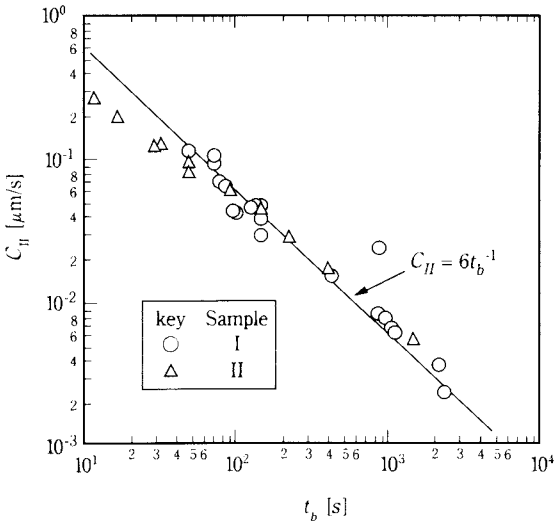

Fig. 5 Relations between creep failure life and constant deformation velocity of powder beds during section II.

(C_{II}) by means of the following equation.

$$C_{II} = -6t_b^{-1} \quad (3)$$

A similar relation is reported for a repetitive stress fatigue test of a fine powder bed[5] and a creep failure test of wet clay[18]. As an alternative method for estimating the life from the behavior of deformation, times (t_I, t_{II}) from Sections I to II and II to II can be employed. In **Figure 6**, a relation between (t_I, t_{II}) and life values is shown. In both Samples I and II, it is observed that t_b and t_I, t_{II} are proportional, and the ratio of Sections before creep failure is almost constant. In addition, t_{II} is almost unchanged between two types of samples, which means the occupying ratio of Section III is almost identical.

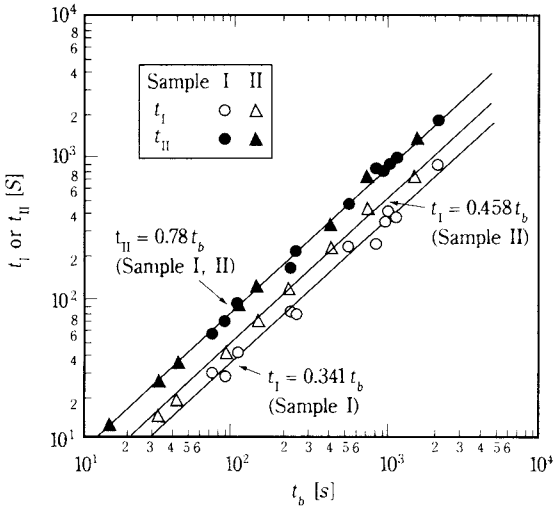

Fig. 6 Relations between creep failure life and the ending time (t_I, t_{II}) of section I and II.

3.3 Strength measurement test during the process to creep failure (Experiment 3)

The result of Experiment 1 indicates that the effect of variation in the tensile strength on the life to creep failure can be reduced in a creep test by maintaining the displacement (Δ_0) constant during the simple tensile test before the creep test. From Experiment 2, it was found that the life to failure can be estimated in a non-destructive manner from the rate of deformation, if the onset of the constant rate deformation, section II, can be confirmed in a creep test. On the basis of such results, an experiment for measuring the strength during the process to creep failure was conducted, and changes in strength were determined. In **Figures 7, 8**, the results of strength measurement at $\sigma_S/\sigma_Z^* = 0.95$ during a process to creep failure are shown respectively for Sections I, II and III. With regard to the strength measurement data in Sections II and III, the life value (t_b^*) was estimated by means of Eq. 3, and the ratio to start time (t_C) of the strength measurement test was obtained for the abscissa. The ordinate shows the strength measurements with the hysteresis of creep tension changed into a dimensionless value by means of the estimated strength when no hysteresis is applied. From the result of **Figure 6**, the ratios of Sections I, II and III remain unchanged between samples. Since the data of strength measurements during Section I is not useful for life estimation, it is comprehensively shown at 0.2 of (t_C/t_b^*) in the abscissa.

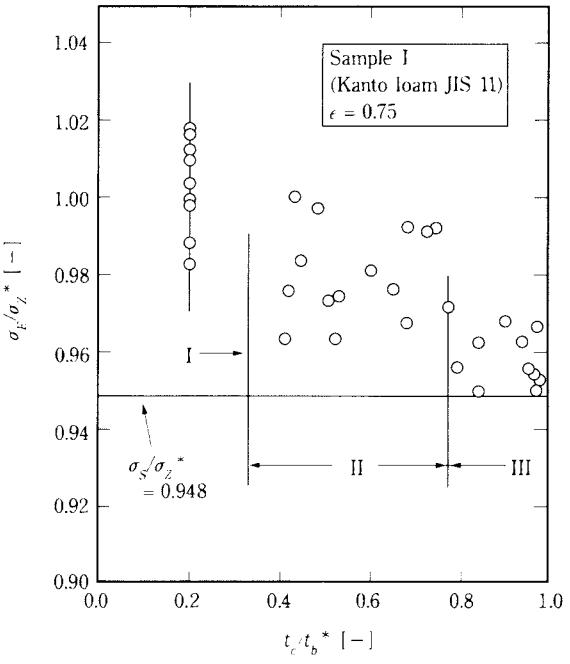

Fig. 7 Change of tensile strength during creep failure process. (Sample 1)

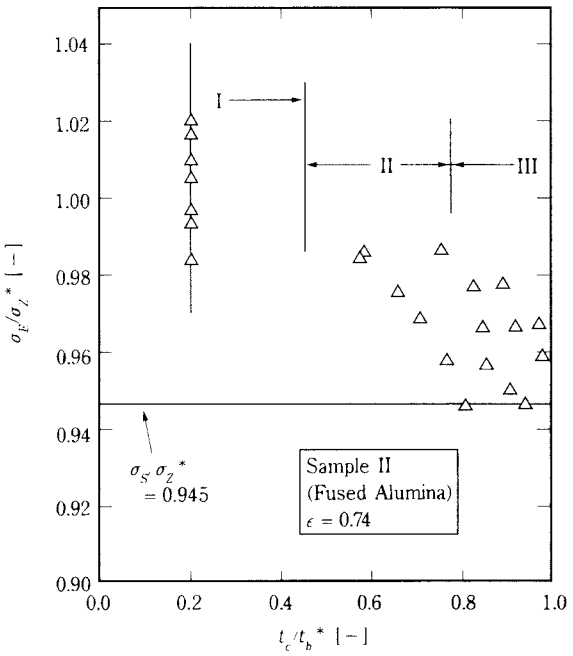

Fig. 8 Change of tensile strength during creep failure process. (Sample 2)

The strengths measured during Section I are distributed around 1.0 of the ordinate, and no reduction in strength is observed. Therefore, it is considered that Section I does not represent a deformation accompanied by a reduction in strength but a deformation for balancing and stabilizing the structure of the powder bed against creep tensile stress. In Section II, the value of the ordinate exceeds 1.0 in very few data, which means that the strength is lower than that of Section I. In Section III, the strength is further reduced approximately to the specified stress. In **Figure 8** showing the result for Sample 2, a similar result is obtained. Accordingly, it can be considered that reduction in strength to creep failure of a powder bed does not gradually occur through an entire process. Almost no reduction occurs during Section I, the strength begins to decrease in Section II, and creep failure occurs as soon as $s_E = s_S$ is reached. As a result, it is expected that some correlation may be present between the change in strength and the complex increasing displacement to creep failure.

4. Discussion

The reduction in strength and behavior of deformation during a process to creep failure is now quantitatively evaluated by means of a Voigt model in **Figure 9 (a)**. For the Voigt model, a relation between stress

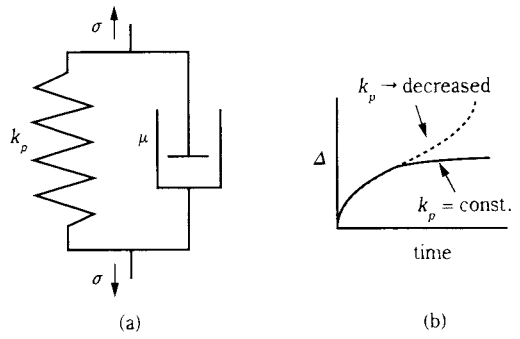

Fig. 9 Rheological model to analyze the increasing process of displacement.
(a) Voigt model
(b) Scheme of increasing process of displacement described by a Voigt model

and displacement is expressed by the fundamental equation shown below.

$$\sigma = k_p \Delta + \mu \, d\Delta/dt \tag{4}$$

where kp is the modulus of elasticity of the spring element, and μ the coefficient of viscosity of a dash pot element. By solving the equation at $\sigma = \sigma_S$ = constant as in the creep test, a time-course change of displacement Δ can be expressed by the following equation.

$$\Delta(t) = \sigma_S/k_p \{1 - exp(-k_p \, t/\mu)\} \tag{5}$$

The equation represents a process of deformation at a rate gradually decreasing to a constant value. For a specified tensile stress ($\sigma_S/\sigma_Z < 0.9$), an increasing displacement is sufficiently approximated by the Eq. 5, and the rate of deformation is found to be about 0 after a creep time of $10^4{}_S$. Even in a condition causing creep failure, the deformation process can be sufficiently approximated within the range of Section I. It is very difficult to express the complex process of deformation through Sections II and III to creep failure by a single viscoelasto-plastic model.

Therefore, it is assumed in this paper that the viscoelastic parameters (k_p, μ) change together with the tensile stress of a powder bed. Such assumption is made in the field of soil dynamics for the study of wet particles whereby a viscoelastic parameter indicative of a deformation resistance is a function of failure criterion determining the strength[1, 17, 21]. Here, it is assumed that the viscoelastic parameters are constant (k_{pI}, k_{pII}) in Section I, but decrease progressively in Sections II and III. A change in tensile displacement (Δ) in Sections II and III is approximated by the following equations.

(Section II) $$\Delta(t) = C_{II}(t - t_I) + \Delta_I \tag{6}$$

(Section III)
$$\Delta(t) = C_{III}(t - t_{II})^2 + C_{II}(t - t_I) + \Delta_I \tag{7}$$

where Δ_I is a cumulative displacement at the end of Section I, and C_{II}, C_{III} are constants. By substitution of Eq. 6 and Eq. 7 in Eq. 4, respectively, assuming k_p and μ are in such relation as shown in Eq. 8[4]:

$$\mu(t)/k_p(t) = C = \text{constant} \tag{8}$$

and solving for $k_p(t)$, a time-course change of the elastic parameter (k_p) that represents the behavior of deformation in Sections II and III can be expressed by the following equations.

(Section II)
$$k_p(t) = k_{pI} \, \sigma_S/[C\{exp(-C \, t_I)\}(t - t_I) + 1] \tag{9}$$

(Section III)
$$k_p(t) = k_{pI} \, \sigma_S \, C/[k_{pI} \, C_{II} \, C(t - t_{II})^2 + C \, \sigma_S\{exp(-C \, t_I)\}(t - t_I) + \Delta_I \tag{10}$$

Figure 10 shows the result of obtaining a time-course change of the elastic parameter (k_p) by using

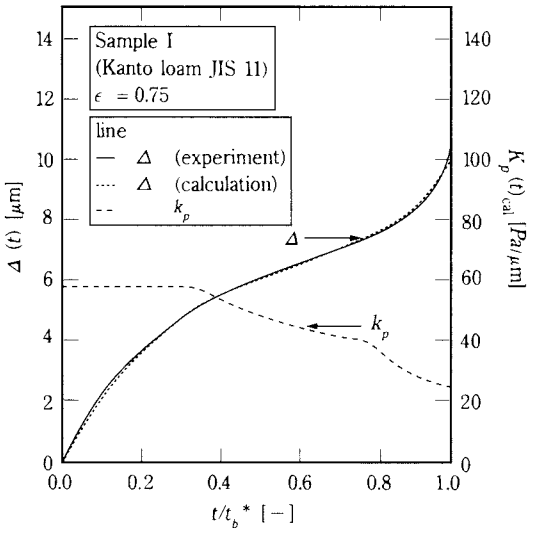

Fig. 10 Examples of fitted and calculated results of increasing and changing process of displacement and elastic parameter in Voigt model.

Eqs. 6 to 10, and approximating the creep deformation process. The creep deformation process is sufficiently approximated by Eqs. 5 to 7. The time-course change of the elastic parameter (k_p) used for approximation is constant in Section I, and decreases in Sections II and III. The tendency of reduction of the elastic parameter (k_p) is relatively similar to the reduction of the tensile strength shown in **Figures 7** and **8**. Then, with the data of strength measurements for Sections II and III, by obtaining the value (t_C/t_b) in the abscissa of each strength measurement, and substituting it in Eqs. 9 and 10, a value of k_p corresponding to the strength measurement is obtained. The ratio (k_p/k_{pI}) of the k_p value to the elastic parameter (k_{pI}) for Section I is obtained, and a relation with the corresponding ratio of strength (σ_E/σ_Z*) is shown in **Figures 11** and **12**. The solid line in the figures shows a proportional relation of slope 1, and the broken line the range of variation of σ_E/σ_Z* for Section I. Between the strength and elastic parameter, a substantially proportional relation is established within a range of variation for two types of samples.

Accordingly, by assuming that the viscoelastic parameter representative of a deformation resistance is reduced proportionally with a reduction in strength due to the hysteresis of creep tensile stress, the complex behavior of deformation to creep failure can be approximated to a single viscoplasto-elasticity model. Thus, it is suggested that a close relation

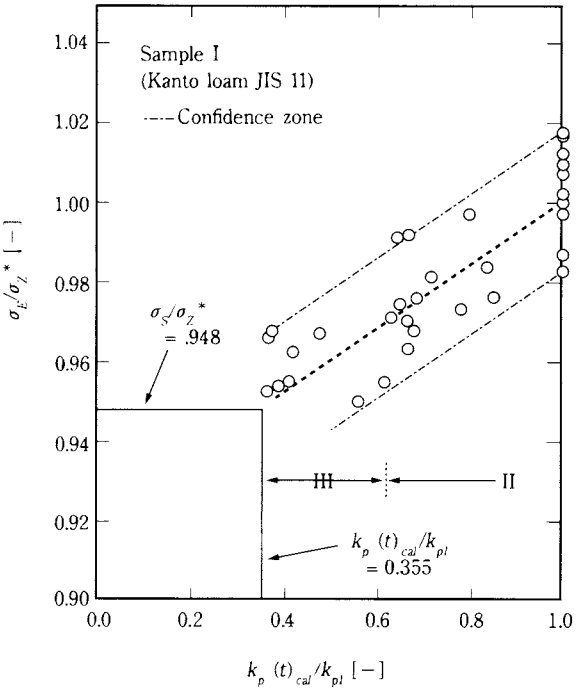

Fig. 11 Relations between tensile strength and elastic parameter during creep failure process. (Sample 1)

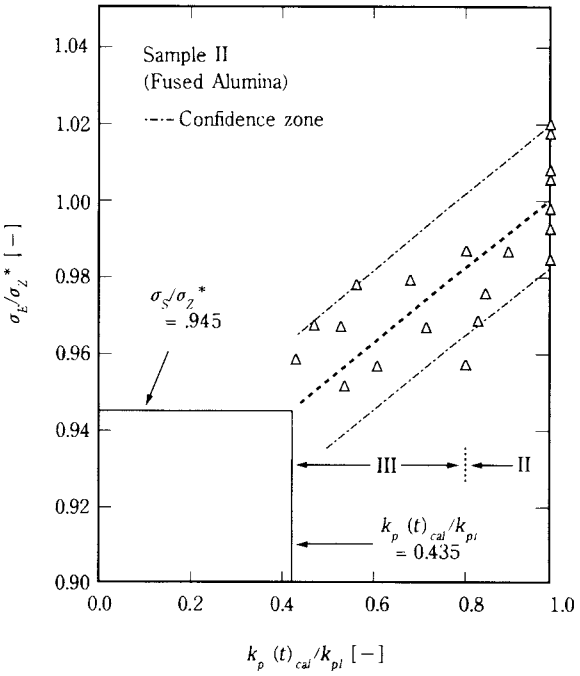

Fig. 12 Relations between tensile strength and elastic parameter during creep failure process. (Sample 2)

exists between the strength of a fine powder bed and the deformation behavior, and that the strength and failure characteristics of a powder bed can be estimated by evaluating the displacement.

5. Conclusions

Following the measurement and analysis of the strength and deformation behavior during a process leading to creep tensile failure using two types of fine powders, the following results were obtained.

(1) By means of a simple tensile test, it was confirmed that the tensile failure of a fine powder bed is displacement-dependent. In addition, the deformation process to creep failure is divided into three sections, and an equation (Eq. 3) for estimating the life from the rate of deformation for Section II of a constant deformation was obtained after analyzing the deformation behavior of the sections.

(2) Although a change in strength to creep failure is substantially identical to that of a sample with no hysteresis of creep tensile stress in Section I, where the rate of deformation gradually decreases, in Sections II and III, the strength gradually decreases, and failure occurs as the strength decreases to a specified stress.

(3) By means of a Voigt model assuming that the viscoelastic parameter decreases proportionally with a reduction in strength, the reduction in

strength and the complex process of deformation to creep failure of a powder bed was expressed in a simple manner.

Acknowledgement

We express our gratitude to Messrs. Nobuaki Kishi (presently in INAX) and Shinichi Furukawa (presently in Showa Denko) for their assistance in our experiment during the study.

Nomenclature

C	= Ratio of elastic parameter to viscous parameter ($= kp/\mu$ = constant)	[s^{-1}]
C_V	= Coefficient of variance	[−]
C_{II}	= Mean increasing rate of displacement in section II	[m/s]
C_{III}	= Constant in Eq. (7)	[m/s^2]
$f(\Delta)$	= Function of tensile stress and displacement during simple tensile test	[−]
k_p	= Elastic parameter in Voigt model	[Pa/m]
k_{pI}	= Elastic parameter in Voigt model duirng section I (=constant)	[Pa/m]
k_p $(t)cal$	= Calculated elastic parameter from Eq. (9) or (10)	[Pa/m]
t_b	= Creep failure life	[s]
t_b	= Estimated creep failure life from Eq. (3)	[s]
t_I	= Creep time at the end of section I	[s]
t_{II}	= Creep time at the end of section II	[s]
t_C	= Creep time at the start of test 3	[s]
Δ	= Displacement of powder beds	[m]
Δ_0	= Displacement of powder beds at the start of creep test	[m]
Δ_I	= Displacement of powder beds at the end of section I	[m]
ϵ	= Porosity of powder beds	[−]
σ	= Tensile stress	[Pa]
σ_E	= Tensile strength of powder beds after creep damage	[Pa]
σ_S	= Set tensile stress during creep test	[Pa]
σ_Z	= Tensile strength of powder beds determined by simple tensile fracture test	[Pa]
σ_Z	= Estimated tensile strength from Eq. 2	[Pa]
μ	= Viscous parameter in a Voigt model	[Pa s/m]

Literature cited

1) Adachi, T. and M. Okano: Soils and Foundations, 14, 55-62 (1974)
2) Asakawa, S., and G. Jimbo: J. Mat. Sci. Jpn, 16, 358-61 (1967)
3) Bjerrum, L.: Geothechnique, 17, 82-90 (1967)
4) Kamiya, H., N. Kishi, J. Tsubaki and G. Jimbo: J. Soc. Pow. Tech. Jpn., 23, 832-38 (1986)
5) Kamiya, H., J. Tsubaki and G. Jimbo: Kagaku Kogaku Ronbunshu, 11, 189-94 (1985)
6) Kamiya, H., J. Tsubaki and G. Jimbo: Kagaku Kogaku Ronbunshu, 11, 210-15 (1985)
7) Kamiya, H., S. Furukawa, J. Tsubaki and G. Jimbo: J. Soc. Pow. Tech. Jpn., 22, 618-25 (1985)
8) Matsuo, Y., T. Nishimura, K. Yasuda, K. Jimbo and S. Kimura: J. Ceram. Soc. Jpn., 99, 187-90 (1991)
9) Matsuzaka, S., M. Shimizu and H. Masuda: ibid., 251-57 (1993)
10) Mitchell, J.K., P.G. Campanella and A. Singh: Proc. ASCE, 94, SM1, 231-40 (1968)
11) Mitchell, J.K.: Proc. ASCE, 95, SM1, 29-35 (1964)
12) Mitchell, J.K., A. Singh and R.G. Campanera: Proc. ASCE, 95, SM5, 1219-20 (1969)
13) Naito, M., J. Tsubaki and G. Jimbo: Kagaku Kogaku Ronbunshu, 10, 744-50 (1984)
14) Naito, M. and J. Tsubaki: J. Soc. Pow. Tech. Jpn., 22, 17-19 (1985)
15) Otani, Y., H. Emi, T. Morizane and J. Mori: ibid., 19, 114-19 (1993)
16) Rumpf, H.: Chem. Eng. Tech., 42, 538-48 (1970)
17) Sekiguchi, H.: Soils and Foundations, 24, 129-131 (1984)
18) Singh, A. and K. Mitchell: Proc. ASCE, SM1, 94, 21-28 (1968)
19) Taylor D.W. and W. Merchant: J. Math. Phys., 19, 167-74 (1940)
20) Tsubaki, J., M. Naito, H. Takami, F. Kousaka and G. Jimbo: Kagaku Kogaku Ronbunshu, 8, 481-87 (1982)
21) Zienkiewicz, O.Z., C.Humpheson and R.W.Rewis: Geothechnique, 25, 671-79 (1975)

Author's short biography

Dr. Hidehiro Kamiya

Dr. Hidehiro Kamiya is Associate Professor of Graduate School of Bio-Application & Systems Engineerings at Tokyo University of Agriculture and Technology. His major research interests are adhesion, dispersion and aggregation behavior of fine particles in water, ceramic powder processing and science, and fine ash powder behaviors in coal and solid waste (included RDF) combustion and gasifier.

Dr. Makio Naito

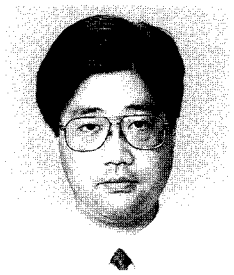

Dr. Makio Naito is Manager of Standardizing Project Division at JFCC. His major research interests are processing technology of fine particles and composite particle etc.

Dr. Tsubaki Jun-ichiro

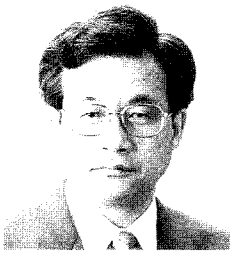

Dr. Tsubaki Jun-ichiro is Professor of Department of Micro-system Engineering Graduate School of Nagoya University. His major research interests are particle characterization of ceramics powder, porous ceramic materials and ceramic process before firing.

Dr. Genji Jimbo

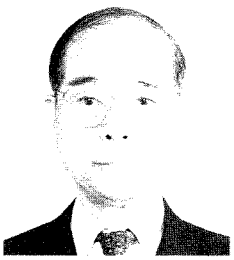

Dr. Genji Jimbo is the head of Chubu Powtech Plaza Laboratory and Professor of Gifu University of Economics. His major research interests are Powder Technology general.

Information Articles

The 29th Symposium on Powder Technology

The 29th Symposium on Powder Technology, sponsored by the Hosokawa Powder Technology Foundation was held on August 28, 1995 at the Foundation of Osaka Science and Technology Center. Over 230 people attended the symposium and with earnest lectures and heated discussions, the symposium was a great success.

This year, the mode of the symposium was changed slightly with emphasis placed on the theme of safety and health problems in the powder process. Lectures were given on "Impediments to Health," "Dust Explosions," "High temperature Dust Collection," and "Clean Rooms." Also, a special lecture, commemorating the receipt of the KONA Award was given by the recipient, Professor Emi of the Kanazawa University.

The 29th Symposium on Powder Technology

Session 1 Health Impediments by Dust and Explosions

Chairmanship: Y. Kousaka (University of Osaka Prefecture)

- Effects on Health by Powders — Isamu Tanaka (University of Occupational and Enviromental Health)
- Prevention of Powder Explosion — Heiji Enomoto (Tohoku University)

Session 2 KONA Award Special Lecture

Chairmanship: N. Yoshioka (Hosokawa Powder Technology Foundation)

- Various Problems on Dust Relevant to Clean Room Technology — KONA Awardee, Hitoshi Emi (Kanazawa University)

Session 3 Practices on Dust Collection and Clean Room Technology

Chairmanship: K. Miyanami (University of Osaka Prefecture)

- Dust Collecting Technology of High Temperature Gas — Takao Makino (Central Research Institute of Electric Power Industry)
- Practices on Biological Clean Technology — Yoshio Okuma (Former Hosokawa Micron Corporation)

The 4th KONA Award

The 4th KONA Award sponsored by Hosokawa Powder Technology Foundation and given to the scientists or groups who have achieved excellence in the researches related to the basic powder technology, was presented to Professor Hitoshi Emi of Kanazawa University by Masuo Hosokawa, President of the Foundation on January 19, 1995 at the R&D Center of Hosokawa Micron Corporation in Hirakata.

Professor Emi's research achievements are related to studies on filtering of aerosol. He established the theoretical basis for the design of fibrous bed filtration of aerosols, which is the key technology of clean room applications.

Academic publication concerning powder technology in Japan (1994)

Journal of the Society of Powder Technology, Japan Vol. 31 (1994)

Title	Author(s)	Page
<Research Papers>		
• Analysis of the Micropore Structure of Silica Gel Surface-treated with Various kinds of Alcohol through Ar Adsorption Isothems	N. Suzuki, M. Koseki, Y. Hoshino A. Endo, T. Kato and H. Utsugi	4 – 9
• The Preparation of Microcapsules which Include Silicon Carbide Particles in a Wall Material	I. Kimura, A. Souma, N. Saito and M. Tanaka	10 – 17
• An XPS Study on the Interaction of the Fe_3O_4/SiO_2 Boundary on the Surface of Composite Microspheres Prepared via the Shear-compressive Mechanical Route	I. Saito and M. Senna	18 – 24
• Determining the Optimum Diameter of a Grinding Media Used for Ultrafine Grinding Mechanisms	T. Tanaka	25 – 31
• The Vertical Component of the Circulation Velocity of Particles in Two Dimensional Vibrating Particle Beds	T. Akiyama, T. Iguchi, S. Kono and A. Ohta	80 – 85
• The Internal Flow of a Cylinder – type Jet Mill – The Classyifying Zone –	H. Ueno	86 – 91
• Cut Size Simulation of a Centrifugal Air Classifier – The Influence of Relative Velocity, Shape and the Agglomerate of Particles	M. Ito	92 – 99
• Experiment of the Vertical Conveyance of Bulk Solids in a Pipe Belt Conveyor System	H. Tsunakawa	100 – 103
• The Effect of Surface Characteristics of Silica Particles on Electrorheology	A. Kawai, I. Uchida, K. Kamiya A. Gotoh, S. Hayashi and F. Ikazaki	146 – 150
• Uniform Dispersion of Fine Particles in a Magnetic Fluid and its Evaluation	M. Horizone, R. Itoh and K. Gotoh	151 – 156
• Characterizing the Electrostatic Charging of Polymer Particles by Impact Charging Experiments	T. Matsuyama and H. Yamamoto	157 – 162
• Characterization of Magnetic Powders by the Electromagnetic Induction Method	Y. Fujihara	163 – 169
• The Separation of Mixed Fine Powders by Electrophoresis	M. Sando, A. Towata, Y. Uwamino and Y. Kuwahara	170 – 175
• Synthesis and Study of the Properties of Barium Titanate Powder by the Mechanochemical Process	O. Abe and Y. Suzuki	176 – 181
• A Study of the Internal Packing Characteristics of an Ultrafine Particle Bed by the X – ray Computed Tomography Method	M. Mizuno and G. Jimbo	181 – 187
• Some Proposals for a Wet Grinding Process for Ceramic Row Materials	N. Asai, T. Sugie and S. Toyama	236 – 240
• Rheological Behavior of Highly Filled Ceramic Suspensions	H. Nakamura, Y. Tawara and Y. Nagase	241 – 247
• Measurements of the Tortuosity Factor and Surface Diffusivity in Luquid – Filled Pores	C. Arai, H. Maruyama, N. Nakagawa K. Hioki, S. Hinata and Y. Sano	248 – 255

Title	Author(s)	Page
• The Formation of Germanium Oxide Particles in a Flame	K. Ueyama, T. Ono, T. Araki M. Matsukata and R. Oshima	314 – 319
• Formation of Gradient Composites Using a Infiltration Mechanism made of Chloride Reduced Particles	H. Mori, Y. Sakurai, M. Nakamura and S. Toyama	320 – 326
• Preparation and Application of Magnetic Particles Encapsulated with Polymer by the Use of Heterogeneous Polymerization in Water	M. Hasegawa, T. Aita, T. Nino and Y. Kanda	327 – 332
• A Design Procedure for Various Types of Closed Circuit Grinding Systems including Plural Mills and Classifiers	T. Tanaka	333 – 337
• Investigation of Cyclone Pressure Loss by a Coiled Tube Model	T. Fuyuki, M. Furuuchi and C. Kanaoka	390 – 395
• Deposition of an Aerosol Particle and Pressure Loss in a Coiled Tube	T. Fuyuki, C. Kanaoka and H. Emi	396 – 401
• The Perfoemance of an Electorostatic Granular Bed Filter	H. Makino, S. Ito and M. Kimoto	402 – 408
• The Development of an Air Purifing Technique by a Nucleation and Condensation Method	Y. Manabe, A. Tatani, M. Hino Y. Fukaya, M. Tanaka and K. Okuyama	409 – 415
• Electrostatic Scavenging of Submicron Particles Aided by the Hydrodynamic Effect of Particle Vibration	Y. Nakajima, Y. Komuro, and T. Sato	416 – 423
• The Dust Cleaning Mechanism of a Pulse Jet-Type Bag Filter	C. Kanaoka, M. Furuuchi and J. Murai	424 – 429
• Effects of UV Irradiation on the In-situ Surface Modification of Calcium Carbonate with a Crosslinked Polymer during Impact Comminution	T. Murata, K. Hamada, T. Tanaka K. Watanabe and M. Senna	468 – 475
• The Effect of the Amount of Collected Coagulant Droplets on the Coagulation Phenomena of Polymer Latex	N. Furukawa, T. Yoshimi and W. Okada	476 – 482
• Compounding Operation of a Thermoplastic Resin Powder – Charge Control Agent and its Triboelectricity	T. Tesima, A. Kuroki, T. Itakura K. Terasita and K. Miyanami	483 – 489
• The Synthesis of Nial Fine Powder from Organometallic Salt Precursors	O. Abe and K. Morimoto	540 – 548
• The Adsorption of Alcohols on Silica Gel from Aqueous Solutions	S. Shioji, M. Kawaguchi, Y. Ohara K. Tokami and H. Yamamoto	549 – 555
• The Flow Properties of a Gas – solid Contactor with Baffle Plates	K. Nagata, M. Nakamura, N. Yamagishi H. Yamaguchi, H. Mori, S. Toyama Y. Hamada and S. Tamura	556 – 560
• A Pneumatic Conveying System for Strongly – adhesive Powders and its Features	M. Futamura	561 – 567
• The Preparation of Monodispersed, Spherical Ferric Oxide Particles by the Hydrolysis of Metal Alkoxide Using a Continuous Tube – type Reactor	T. Ogihara, M. Yabuuchi, T. Yanagawa N. Ogata, K. Yoshida, N. Nagata K. Ogawa and U. Maeda	620 – 625

Title	Author(s)	Page
• The Evaluation of the Fine Grindability of Solid Materials based on the Work Index	N. Kotake, H. Shoji, M. Hasegawa and Y. Kanda	626 – 630
• Real – Time Imaging of a Nanometer-Scale Thin Film Including Fine Particles	E. Adachi, H. Yoshimura and K. Nagayama	631 – 634
• Aggregation and Dispersion of a Mineral Material Having Many Elements	T. Ueda, H. Kitamura, S. Omote H. Kitawaki and M. Nakamura	635 – 639
• The Correlation Between Dividing and Packaging Weight Loss and the Physical Properties of a Powder on Dispensing – Measurement of Apparent Adhesion –	M. Takada and T. Fukuda	640 – 646
• Preparation of Fine Sericite, a kind of Clay, by Chemically Assisted Dry Comminution: The Effect of Nitrate on Grindability	F. Ikazaki, K. Uchida, K. Kamiya A. Kawai, S. Yoda and A. Gotoh	647 – 651
• A Study of the Pressure of a Fine Powder in a Bin	H. Eitoku, M. Hirota, M. Suzuki and T. Osima	652 – 657
• The Preparation of Core Particles for coating by Rotating Fluid Bed Equipment	H. Sakamoto	658 – 662
• The Relationship Between the State of Kneading and the Dispersion of a Magnetic Powder and the Toughness of Magnetic Paint Film	K. Sakamoto, Y. Takai and K. Terashita	663 – 667
• Solid Bed Displacement Induced by Air Hammer Impact	T. Akiyama and M. Kono	698 – 702
• The Collision Efficiency of Unequally – sized Fine Particles Settling in Air	T. Umekage and S. Yuu	703 – 710
• A Method for the measurement of Particle Diameter Distribution in a Particle Group under High Speed Flow using Real – time Image Processing	M. Kamiwano, M. Kaminoyama K. Arai and T. Amari	711 – 718
• Evaluation of Adhesive Strength Distribution Based on Reentrainment Phenomena – Discrimination between Particle-particle and Particle-wall Interaction –	S. Matsusaka, K. Mizumoto, M. Koumura and H. Masuda	719 – 725
• High-efficiency Removal of Fine Particles Deposited on a Solid Surface	K. Gotoh, K. Karube, H. Masuda and Y. Banba	726 – 733
• Adsorption and Dispersion Stability of Hydrophilic Fine Particles by Polybutadienes with Polar Group Terminations	K. Osaka, Y. Yamagata and T. Omori	778 – 782
• The Development of a Rotary-intrusion-type Rheometer for a Powder Bed and the Measurement of the Dynamic Physical Properties of Powders	M. Satoh, N. Kondo, T. Iwasaki K. Miyanami, Y. Okudaira and H. Ando	783 – 788
• Evaluation of the Performance of a High-speed-Elliptical Rotor-type Powder Mixer	M. Satoh, T. Yoshida, K. Miyanami and Y. Okudaira	789 – 794
• Preparation of Monodispersed $MTiO_3$ (M = Ba, Sr, Pb) Fine Powders by the Hydrolysis of Metal Alkoxide	T. Ogihara, T. Yanagawa, N. Ogata K. Yoshida, M. Iguchi, N. Nagata and K. Ogawa	795 – 802

Title	Author(s)	Page
• Optimum Delamination Conditions by Wet Grinding and the Characterization of Talc Platelets	T. Isimori and M. Senna	803 – 807
• The Size Segregation of Polydispersed Particles During Feeding into a Vessel	K. Gotoh, T. Maki and H. Masuda	842 – 849
• The Influence of the Initial Stress Condition on the Dynamic Overpressure of a Silo Wall	T. Yahiro	850 – 861
• The Study of a High Efficiency Generation Process of Metallic Ultra Fine Particles with Arc Energy	Y. Endo, T. Araya, M. Kanamura Y. Ibaraki, R. Okada and S. Hiroki	862 – 868
• The Flow Properties of a Gas-solid Contactor with Inclined Baffle Plates	K. Nagata, K. Murase, H. Yamaguchi K. Kanai, M. Nakamura and S. Toyama	869 – 874

Kagaku Kogaku Ronbunshu Vol. 20 (1994)

Title	Autor(s)	Page
• Separation of Flyash Particle by Revised Cyclone with High Accuracy	H. Yoshida, H. Ami, K. Imai and Y. Yokomichi	105 – 112
• Shape and Stability of Axisymmetric Liquid Bridge Between Two Discs	M. Suzuki	113 – 120
• Formation Characteristics and Mechanisms of N_2O in Bubbling Fluidized-Bed Coal Combustion	I. Naruse, M. Imanari, K. Koizumi J. -Wei Yuan and K. Ohtake	178 – 185
• Permeability characteristics of a Spherical-Particle Bed Based on Cross-Sectional Void-Size Distribution	K. Shinohara and T. Murai	198 – 204
• The Effect of Humidity on the Removal of Fine Particles on a Solid Surface Using a High-Speed Air Jet	K. Gotoh, S. Takebe, H. Masuda and Y. Banba	205 – 212
• The Physical and Chemical Structure of Temperature Sensitive Polymer Gel and Its Surface Property	Y. Seida and Y. Nakano	213 – 218
• Study on Ignition Characteristics of Solid Fuels	H. Taniguchi, K. Kubo, M. Kamide Y. Oka and S. Sayama	233 – 239
• Coating in Spouted Bed by Rapid Expansion of Supercritical Fluid Solutions	A. Tsutsumi, A. Sasaki, M. Aihara and K. Yoshida	248 – 253
• Structural Property Changes of Fine Zinc Ferrite Sorbent during Sulfidation and Regeneration	T. Sakurai, M. Okamoto, H. Miyazaki and K. Nakao	268 – 274
• High-Temperature Desulfurization Performance and Durability of Fine Zinc-Iron-Aluminum Oxide	T. Sakurai, M. Okamoto, H. Miyazaki and K. Nakao	275 – 282
• Failure Behavior of Aerated Fine Powder Beds and Their Transition to Fluidization	K. Nishii and M. Horio	387 – 396
• Flow Mechanism of Granular Materials Discharging from Bin-Hopper System	J. Hidaka, J. Kano and A. Shimosaka	397 – 396
• A Method of Power Measurements for Vibrating Ball Mill	N. Asai, K. Tajiri, G. Jimbo and S. Toyama	411 – 417

Title	Author(s)	Page
• Catalytic Pyrolysis of Coal in a Powder-Particle Fluidized Bed – Control of catalytic activity by adjusting the sulfur content	C. Wang, T. Takarada, Y. Fusegawa N. Nakagawa and K. Kato	445 – 452
• Recognition of Overlapped Particle Image by Arc Interpolation	F. Koizumi, S. Toyoda, E. Kunugita and H. Nishitani	521 – 528
• Preparation Fine Particles of Metal-Metal Oxide Semiconductors by the Spray Pyrolysis Method	S. Deguchi, H. Matsuda, M. Hasatani and N. Kobayashi	529 – 534
• Adhesion Force Arising from Solid Solt Bridge Formed after Drying of Liquid Bridge	Y. Endo, Y. Kousaka and H. Onitsuka	542 – 548
• Creep Failure Process for Fine Powder Beds by Tensile Loading	H. Kamiya, M. Naito, J. Tsubaki and G. Jimbo	556 – 563
• Effect of Surface Material on Particle Removal Using High Speed Air Jet	K. Gotoh, S. Takebe and H. Masuda	685 – 692
• Effect of Particle Diameter on Removal of Surface Particles Using Hight Speed Air Jet	K. Gotoh, M. Kida and H. Masuda	693 – 700
• Flocculation of Fine Hematite in Aqueous Solution Containing Surface Active Agents	J. Shibata and H. Tamakoshi	701 – 707
• Dispersion Mechanism of Coagulated Particles by Acceleration in a Convergent Nozzle – Dispersion of Coagulated particles consisting of same-size spheres –	T. Horiuchi, Y. Kousaka and Y. Endo	708 – 716
• Flash Pyrolysis of Coal as a Means for Obtaining Valuable Chemicals	K. Miura and K. Mae	733 – 746
• Low NOx Conbustion Technology in Pulverizd Coal Combustion	H. Makino and M. Kimoto	747 – 757
• Development of a Spouted Bed-Type Coal Gasifier with Cycling Thermal Medium Particles [T]	Y. Hatase, Y. Uemura, S. Tanaka Y. Tokumasu, Y. Tanaka, D. F. King and K. Ijichi	758 – 765
• Reactivity of Catalysts for Coal Gasification – Effects of gases formed on reactivity – [F]	Y. Nishiyama and K. Terada	793 – 798
• Catalytic Coal Gasfication by Physical Mixing of K – Exchanged Brown Coal in a Fluidized Bed [F]	T. Takarada, U. Komori, T. Atsuta, N. Nakagawa and K. Kato	799 – 804
• Estimation of Particle Residence Time in Flow Model Furnace for Rotational Entrained-Bed Coal Gasifier	A. Morihara and S. Koyama	813 – 819
• Mathematical Modeling of a Spouted Bed Coal Gasifier [F]	T. Tsuji, T. Shibata and O. Uemaki	820 – 826
• Development of Catalyst for Simultaneous Oxidative Adsorption of SO_2 and NO [F]	E. Sasaoka, K. Tanaka, Y. Inami Y. Sakata and S. Kasaoka	880 – 888

Multi-functional Fluidized-bed Granulator "Agglomaster"

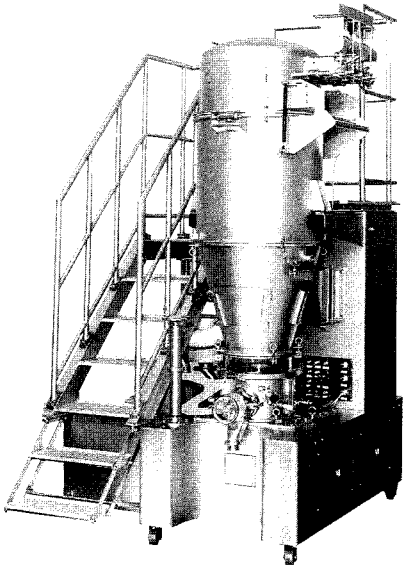

Agglomaster can perform the processes of mixing, granulating, drying, cooling, coating etc. of powders by one machine. The automatic operation of the system is possible using the sophisticated computer software which realized the fussy control of the system. In addition, newly developed countercurrent pulsed jet mechanism has made possible the film coating of fine particles down to 10 microns.

Features

- The combination of fluidized-bed, rotating disc and agitation blades of different shape has realized the control of particle size, shape and density in a wide range.
- Applying the countercurrent pulsed jet in the fluidized bed, the sequential operation of the dispersion of agglomerated material and the following granulation is also possible.
- The automatic control based on the in-line monitoring sensors of moisture content and fluidized condition of particles realize the narrow distribution of granule size and higher yield of product.
- Various models of the machine are available and have been installed from the lab-size AGM-1 (1 liter) to the large scale one AGM-150 (1,250 liter).
- The machine is constructed for easy disassembling and cleaning.

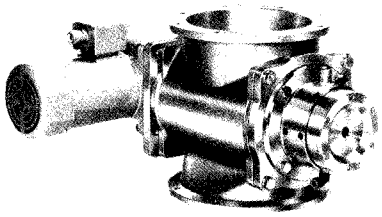

MICRON COMPACTOR (Patent pending)

Micron compactor is a new densifier specially developped to deaerate powders for filling in bags or containers with compacted condition.
With this unit, densification of powders can be achieved without damaging particles. It also has a simple and compact configuration.

Applications – Features

- Combined with filling machine to increase filling efficiency
- Saving transportation cost
- By combining with vibrating discharger, high accurate discharge is possible
- Pre-compactor for increasing the efficiency of granulators
- Improvement of powder characteristics to prevent flashing phenomenon and dust emission.

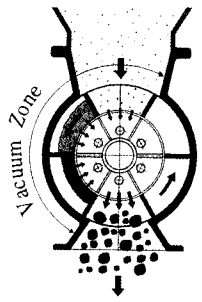

Powder is sucked into a pocket of the rotor, thereby the deaeration is achieved by the suction of air from the roots blower through the metal filter. When the pocket reaches to the lowest position, compressed air is pulsed into the metal filter to discharge the powder. This air pulse also enables the metal filter to prevent from cloggings, consequently stable deaeration process can be maintained for a long period of time.

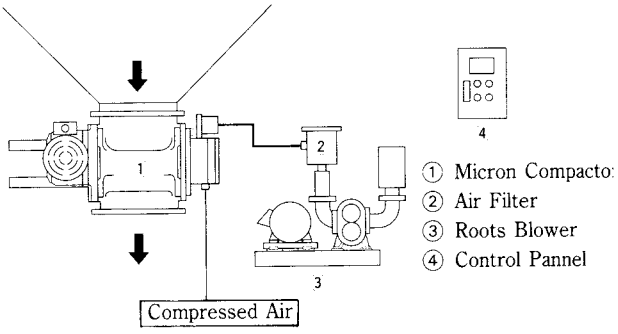

For more information contact; **HOSOKAWA MICRON CORPORATION**
No.9, 1-chome, Shoudai Tajika, Hirakata-shi, Osaka 573 JAPAN
Telephone: 81-720-55-2220 Facsimile: 81-720-55-3288

Laboratory Mill 100 UPZ-II: Design Stainless Steel

A Completely New Laboratory Mill Concept

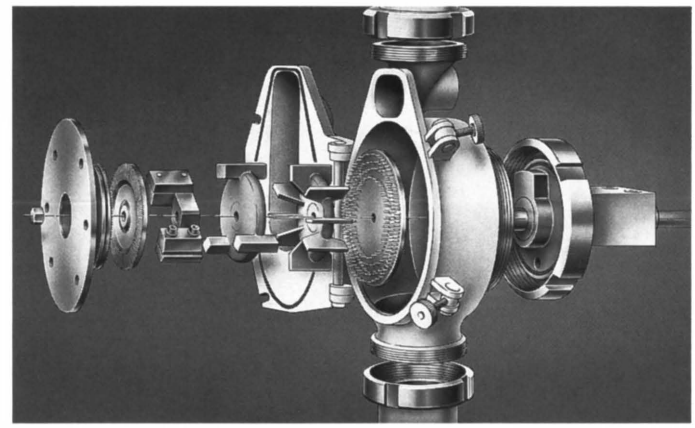

New mill concept offers more advantages.

Alpine has developed a laboratory mill with a completely new concept:

The 100 UPZ-II, design stainless steel.

No other mill of this type offers such a multitude of technical advantages and flexibility in application.

Five exchangeable grinding tools optimally cover versatile requirements.

Equipments to order:

- Stud discs (1 off rotating; 1 off stationary).
- Plate beater system combined with various grinding tracks.
- Beater disc system.
- Shearing discs (1 off rotating; 1 off stationary).
- Cutting knives (2 off rotating; 2 off stationary).

Cleaning and product recovery.

The mill is completely dismountable for:

- Cleaning in the sink or ultrasonic bath.
- Sterilizing in the autoclave.

The material inlet is freely accessible and integrated into the mill door. This constructional novelty facilitates dry cleaning and product recovery.

STRATOPLEX AIR CLASSIFIERS ASP

Low-energy fine classification

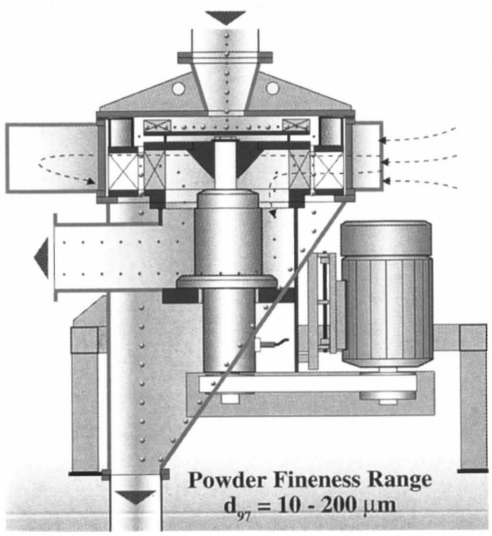

Alpine's Stratoplex air classifiers are newly developed high-efficiency air classifiers for the fine to medium separation range with a d_{97} of approx. 10 – 200μm.

The Stratoplex concept – a compact and modular system – permits not only top performance despite minimum dimensions, but also a trouble-free, space saving system installation.

Stratoplex-Air Classifiers ASP

Model Range	Type	315	400	500	630	800	1000	1250	1500
Scale-up factor	F = approx.	0.25	0.4	0.63	1	1.6	2.5	4	5.6
Drive	approx. kW	5.5	7.5	11	15	22	37	55	90
Speed range	rpm	800-4000	640-3200	500-2500	400-2000	320-1600	250-1250	200-1000	170-840
Air volume	approx. m^3/h	2500	4000	6300	10000	16000	25000	40000	56000
Fines yield*	approx.	t/h	t/h	t/h	t/h	t/h	t/h	t/h	t/h
powder fineness	d_{97} = 20 μm	0.6	1	1.6	2.5	4	6	10	14
powder fineness	d_{97} = 63 μm	1.4	2.2	3.5	5.5	9	14	22	30
powder fineness	d_{97} = 90 μm	1.8	2.8	4.5	7	11	18	28	39

*Reference values relating to approx. 60 % fines in feed, bulk density 2.7 g/cm^3.

HOSOKAWA ALPINE Aktiengesellschaft P.O.Box 101109, D-86001 Augsburg/Germany
Tel.: +821/5906-0 Fax: +821/57 35 58

HOSOKAWA MICRON

Global Capability of Hosokawa Micron Group

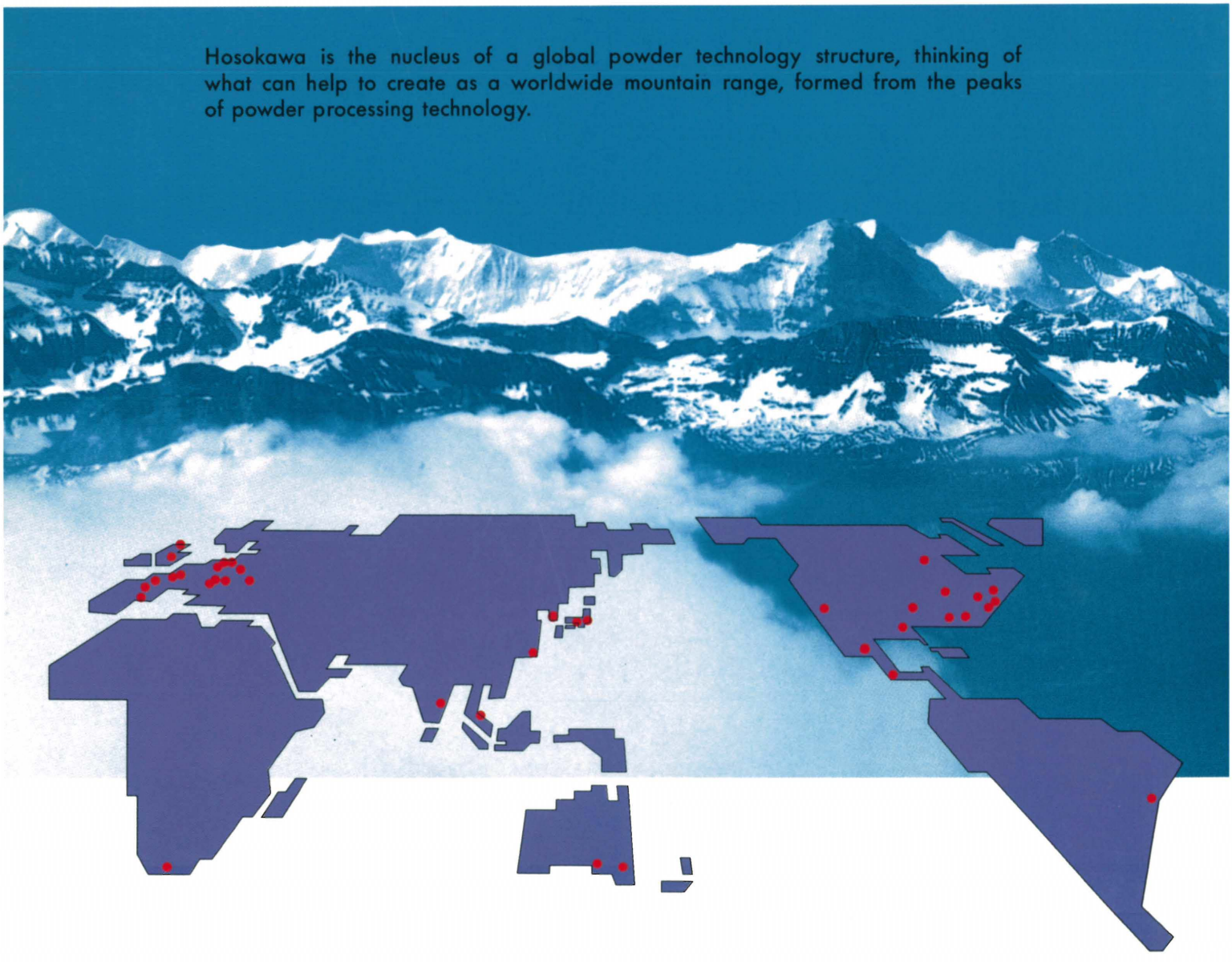

HOSOKAWA MICRON THROUGHOUT THE WORLD

HOSOKAWA MICRON

Asia/Australian Block
HOSOKAWA MICRON CORPORATION
5-14, 2-chome, Kawaramachi, Chuo-ku,
Osaka 541, Japan
Tel: 81-6-233-3968
Fax: 81-6-229-9267

Americas Block
HOSOKAWA MICRON INTERNATIONAL INC.
780 Third Avenue, New York,
NY 10017, U.S.A
Tel: 1-212-826-3830
Fax: 1-212-826-6612

European Block
HOSOKAWA MICRON INTERNATIONAL B.V.
World Trade Center, Strawinskylaan
249, 1077XX Amsterdam, Holland
Tel: 31-20-673-5571
Fax: 31-20-676-2061